

Endurance Limit for HMA Based on Healing Phenomenon

Using Viscoelastic Continuum Damage Analysis

by

Waleed Zeiada

A Dissertation Presented in Partial Fulfillment
of the Requirements for the Degree
Doctor of Philosophy

Approved July 2012 by the
Graduate Supervisory Committee:

Kamil Kaloush, Co-Chair
Matthew Witzak, Co-Chair
Claudia Zapata
Michael Mamlouk

ARIZONA STATE UNIVERSITY

August 2012

ABSTRACT

Perpetual Pavements, if properly designed and rehabilitated, it can last longer than 50 years without major structural rehabilitation. Fatigue endurance limit is a key parameter for designing perpetual pavements to mitigate bottom-up fatigue cracking. The endurance limit has not been implemented in the Mechanistic Empirical Pavement Design Guide software, currently known as DARWin-ME. This study was conducted as part of the National Cooperative Highway Research Program (NCHRP) Project 9-44A to develop a framework and mathematical methodology to determine the fatigue endurance limit using the uniaxial fatigue test. In this procedure, the endurance limit is defined as the allowable tensile strains at which a balance takes place between the fatigue damage during loading, and the healing during the rest periods between loading pulses. The viscoelastic continuum damage model was used to isolate time dependent damage and healing in hot mix asphalt from that due to fatigue. This study also included the development of a uniaxial fatigue test method and the associated data acquisition computer programs to conduct the test with and without rest period. Five factors that affect the fatigue and healing behavior of asphalt mixtures were evaluated: asphalt content, air voids, temperature, rest period and tensile strain. Based on the test results, two Pseudo Stiffness Ratio (PSR) regression models were developed. In the first model, the PSR was a function of the five factors and the number of loading cycles. In the second model, air voids, asphalt content, and temperature were replaced by the initial stiffness of the mix. In both models, the endurance limit was defined when PSR is equal to 1.0 (net damage is equal to zero). The

results of the first model were compared to the results of a stiffness ratio model developed based on a parallel study using beam fatigue test (part of the same NCHRP 9-44A). The endurance limit values determined from uniaxial and beam fatigue tests showed very good correlation. A methodology was described on how to incorporate the second PSR model into fatigue analysis and damage using the DARWin-ME software. This would provide an effective and efficient methodology to design perpetual flexible pavements.

DEDICATION

To my parents Mr. Abdelaziz Mohammed Zeiada and Mrs. Anwar Kamal Zeiada
for their love and support.

To my wife Shimaa, without her support, patience, and love, none of this would
be possible.

To my Son Adam, Daughter Mariam, and expected baby, you warm my heart and
soul.

ACKNOWLEDGEMENT

All thanks and praise is due to God the most gracious the most merciful. He has given me the patience, guidance, and strength to overcome all the hardships I have encountered and helped me complete this work. Oh Allah, I always asks you to accept this work as for you and for the benefit of humanity. Oh Allah, accept this work to be on my scale of good deeds on the Day of Judgment.

This research is a part of the federally funded NCHRP Project 944-A, “Validating an Endurance Limit for HMA Pavements: Laboratory Experiment and Algorithm Development”. I would like to acknowledge Dr. Edward Harrigan of NCHRP and the project panel for their constructive comments throughout the project. My sincere gratitude goes to the Egyptian Government for their financial support.

It is with immense gratitude that I acknowledge the support and help of my Professor Dr. Kamil Kaloush who advised me tirelessly in both academic and personal levels throughout my research work. Dr. Kaloush has an amazing personality. The way he deals with his students on an academic and social level is truly incredible. The things I have learned from him will reflect upon my relation with the students when I go back to Egypt for my assistant professor job at Mansoura University. I still remember his encouraging statement to me after a few months after starting at ASU “Waleed- I am happy to have you in our program at ASU.” Thank you Dr. Kaloush for all you have done for me.

I would like to express my genuine appreciation to the co-chair of my Ph.D. supervisory committee, Dr. Matthew Witzak for his special guidance and intensive technical discussions and suggestions during this research work. I appreciate his trust in me to work on the NCHRP 944-A project. He knows how to push students beyond their limits to achieve important goals. After two years of hard work on my Ph.D. and I had not gotten to the main project work yet due to many challenges and obstacles he said to me, “Your Ph.D dissertation is the toughest one I’ve ever had, so do not give up.” This statement recharged me again with the enthusiasm needed to overcome all the remaining obstacles and to complete this work.

Special thanks go to Dr. Michael Mamlouk for his continuous mentoring and beneficial discussion. Every time I stopped by his office he would smile saying, “tell me about your new problem.” It was indeed an endless list of problems and issues I had to solve to become Dr. Zeiada. I would like to extend my gratitude to Dr. Claudia Zapata for her support and encouragement. My sincere appreciation is for Dr. Mohamed El-Basyouny for his advice and support at the beginning of the project and more importantly his friendship from my first day at ASU.

My appreciation also goes to Mr. Peter Goguen for his continuous help and lab support. I would like to acknowledge Mr. Kenny Witzak who helped me understand the lab test practices when I started my degree at ASU and for the great effort he exerted in manufacturing hundreds of specimens. Thanks are also extended to Dr. Manuel Padilla and Mr. Tamas Vicosean of GCTS for their

help and for providing the first data acquisition system and the test software used at the beginning of the project. Special Thanks go to Mr. Con Sinadinos, Mr. Alan Feeley, and Mr. Stephen King of IPC for their continuous and unconditioned help and support in developing the final test software for the uniaxial fatigue test. I would like to acknowledge Dr. Richard Kim and Dr. Shane Underwood for the beneficial discussions I have had with both of them during the ETG and TRB meetings as well as the valuable information and documents they provided me with which helped me immensely.

During my time at ASU, I have networked with many students who have helped me acquire many valuable lessons. I would like to acknowledge Dr. Sherif El-Badawy, Dr. Mohammed Arab, Dr. Mena Souliman, Jordan Reed, Jeffery Stempihar, Dr. Myung Jeong, Dr. Carolina Rodezno, Atish Nadkarni, Dr. Krishna Biligiri, Smita Dwivedi, Rashmi Shanker, Dr. Carlos Cary, Gustavo Torres-Hernandez, Elham Bani Hashem, Dr. Sam Abbaszadeh, Maie El-Keshky, Abdulaziz Alost, Ramadan Salim, Ashraf Alrajhi, Matild Dosa, David Ramsey, Daniel Rosenbalm, Tina Pourshams-manzouri, Rubben Lolly, Samuel Enmon, Quyen Banh, and Saeed Mohammad.

Now it is the turn for my great family. My deepest and sincere gratitude are to my mother, the one who sacrificed her interests and health in raising, inspiring, and helping me throughout my life. I can never do anything to return back her countless favors. My father, without you I wouldn't be the man I am today. Your support and love are endless. Now, being a father of two kids, I cannot imagine how great you are to raise six kids the best way with all other

huge responsibilities upon you. Indeed, I am lucky to have such wonderful parents. I will always remember how you both raised me with a love of gaining knowledge. Your vision and value in education have been very beneficial for me. To my sweet brothers and sisters, my deepest gratitude for your continuous encouragement and unwavering supports. The love and support of my father and mother in-laws are meaningful to me beyond words. I have received daily phone calls full of encourages and motivations. I would like to offer my recognition to my neighbor Hosaam Hassan and His family and my friend Magd Neyazy and his family for their appreciable friendship and support since day one at USA.

Finally, I would like to express my deep thanks from the bottom of my heart to my wife, Shimaa for cheering me up and standing by me through the good times as well as the hard times. You are really a good wife by what this entire word means. I now fully understand the statement “behind every great man, there stands a great woman.” Without your support, patience, and understanding, none of this could have accomplished. I cannot imagine how responsible and understandable you are with all of these hardships that I have faced in this research. You were the one I used to talk to when I come back by every midnight and complain about the issues that raised one after other, and you were the one who encouraged and strengthen me to keep going. I can say you believed in me more than what I believed in myself. For sure, I cannot forget to thank my son Adam and my daughter Mariam. You both are the light of my life. The stress and exhaustion melts away just by hugging you.

TABLE OF CONTENTS

	Page
LIST OF TABLES.....	xviii
LIST OF FIGURES.....	xxiii
CHAPTER	
1 INTRODUCTION AND RESEARCH APPROACH	1
1.1 Introduction.....	1
1.2 Problem Definition.....	7
1.3 Research Objectives.....	7
1.4 Research Outline.....	8
2 LITERATURE REVIEW	10
2.1 Fatigue Cracking of Hot Mix Asphalt	10
2.2 Mode of Loading.....	11
2.3 Fatigue Test Methods.....	14
2.3.1 Simple Flexure Tests.....	15
2.3.1.1 Three and Four-Point Bending Tests	16
2.3.1.2 Cantilever Beam Rotating Test.....	16
2.3.1.3 Trapezoidal Cantilever Beam Test.....	17
2.3.2 Supported Flexure Test.....	17
2.3.3 Direct Tension Test.....	18
2.3.4 Tension/Compression Test.....	19
2.3.5 Diametral Test.....	20
2.3.6 Triaxial Test.....	21

CHAPTER	Page
2.3.7 Wheel-Track Test.....	22
2.4 Fatigue Failure Criteria.....	24
2.5 Effect of Rest Period on HMA Fatigue Behavior.....	30
2.5.1 Need for Rest Period.....	30
2.5.2 Effect of Rest Period.....	31
2.5.3 Optimum Rest Period.....	37
2.6 Healing of Asphalt Concrete Mixtures.....	38
2.6.1 Mechanism of Healing.....	39
2.6.2 Studies on Healing.....	43
2.6.2.1 Mechanical Healing of Asphalt Mixtures.....	44
2.6.2.2 Chemical Healing of Asphalt and Mastic.....	48
2.6.3 Healing Models.....	51
2.7 Characterization of HMA Fatigue Behavior.....	55
2.7.1 Phenomenological Approach.....	55
2.7.1.1 Illinois DOT / University of Illinois Model.....	58
2.7.1.2 SHRP A-404 Model.....	59
2.7.1.3 The Asphalt Institute Model.....	59
2.7.1.4 SHELL Pavement Design Manual Model.....	60
2.7.1.5 Transport and Road Research Laboratory – TRRL United Kingdom Model.....	61
2.7.1.6 PDMAP – NCHRP Project 1-10B.....	61
2.7.1.7 NCHRP 1-37A Calibrated Fatigue Model.....	62

CHAPTER	Page
2.7.2 Mechanistic Approach	63
2.7.2.1 Dissipated Energy	63
2.7.2.2 Fracture Mechanics.....	72
2.7.2.3 Continuum Damage Mechanics	76
2.8 Fatigue Endurance Limit of HMA	82
2.8.1 Definition of HMA Endurance Limit	82
2.8.2 Importance of Endurance Limit in Perpetual Pavement Design	83
2.8.3 Evidence of HMA Endurance Limit in Laboratory and field Studies.....	85
2.8.4 Prediction of HMA Endurance Limit through Laboratory Studies.....	88
3 THEORY OF VISCOELASTICITY AND DAMAGE MECHANICS	102
3.1 Theory of Viscoelasticity	103
3.1.1 Background	103
3.1.2 Viscoelastic Constitutive Equation	105
3.2 Correspondence Principle	108
3.3 Uniaxial Constitutive Model Using Work Potential Theory	111
3.3.1 Constitutive Theory	111
3.3.2 Determination of Damage Parameter S	116
4 DESIGN OF EXPERIMENT, SPECIMEN PREPARATION AND TESTING PLAN	120

CHAPTER	Page
4.1 Background	120
4.2 Selection of Factors Affecting the Healing Experiment	121
4.3 Design of Experiment	122
4.3.1 Independent Variables (Factors)	122
4.3.2 Fractional Factorial Design with Partial Randomization...	124
4.4 Binder Characterization	126
4.4.1 Background	126
4.4.2 Binder Source.....	127
4.4.3 Aging Levels	127
4.4.4 MACTEC Test Results	128
4.4.4.1 Mixing and Compaction Temperatures	128
4.4.4.2 Superpave Binder Classification Tests	129
4.4.5 ASU Asphalt Binder Characterization.....	133
4.4.5.1 Test Methods.....	134
Penetration Test	134
Softening Point Test.....	135
Brookfield Viscosity Test	136
4.4.5.2 Data Analysis	137
4.5 Mix Design.....	140
4.6 Research Testing Plan.....	142
4.6.1 Dynamic Modulus Test (AASHTO TP 62-07) Experiment	143

CHAPTER	Page
4.6.2 Uniaxial Tension-Compression Fatigue Test Experiments	145
4.6.2.1 Fatigue Lives Experiment	145
4.6.2.2 Main Fatigue Experiment	146
4.6.2.3 Additional Fatigue Experiment.....	147
4.7 Laboratory Manufacturing of HMA Specimens	149
4.7.1 Preparation of Aggregates.....	149
4.7.1.1 Drying of Aggregate Stockpiles.....	149
4.7.1.2 Blending of Aggregate Stockpiles	149
4.7.1.3 Sieving of Blended Aggregates	149
4.7.1.4 Aggregate Batching	150
4.7.1.5 Wet Sieve Analysis	150
4.7.3 Preparation of Specimens	151
4.7.3.1 Mixing of Asphalt Mixture	151
4.7.3.2 Short Term Aging	151
4.7.3.3 Maximum Theoretical Specific Gravity (G_{mm})...	151
4.7.3.4 HMA Compaction.....	152
4.7.3.5 Air Voids Determination.....	152
4.7.3.6 Storing of Prepared Specimens.....	152
5 VISCOELASTIC PROPERTIES OF ASPHALT CONCRETE MIXTURES	153
5.1 Background.....	153
5.2 Complex Modulus.....	153
5.2.1 Theoretical Background.....	153

CHAPTER	Page
5.2.2 Testing System.....	155
5.2.3 Tested Mixtures	157
5.2.4 Measured G_{mm} and Air Void Values of Tested Specimens	158
5.2.5 Capping of Specimens	162
5.2.6 Summary of Test Procedure.....	163
5.2.7 Construction of LVE Material Properties Master Curves..	167
5.2.8 Time-Temperature Superposition Principle and Shift Factors	167
5.2.9 Effect of Air Voids and Asphalt Content on E^* Master Curve	179
5.2.10 Proposed Approach to Predict the Effect of Air Voids and Asphalt Content on E^* Master Curves.....	192
5.2.11 Proposed Approach Validation	194
5.3 Relaxation Modulus	202
5.4 Conversion between Linear Viscoelastic Material Functions	202
5.5 Conversion from Complex Modulus to Relaxation Modulus.....	203
5.5.1 Approximate Inter-Conversion Method.....	203
5.5.2 Exact Inter-conversion Method.....	207
6 DEVELOPMENT OF UNIAXIAL TENSION-COMPRESSION FATIGUE TEST PROTOCOL AND SOFTWARE.....	211
6.1 Background.....	211
6.2 Current Proposed Uniaxial Fatigue Test Methods.....	212

CHAPTER	Page
6.2.1 Pennsylvania State University (PSU) Test Method	212
6.2.2 North Carolina State University (NCSU) Method.....	213
6.2.3 Advanced Asphalt Technologies (AAT) Method	215
6.3 Adequacy of the Available Test Methods.....	215
6.3.1 Pennsylvania State University (PSU) Test Method	216
6.3.2 North Carolina State University (NCSU) Method.....	216
6.3.3 Advanced Asphalt Technologies (AAT) Method	217
6.4 Testing System Setup.....	218
6.4.1 Testing Machine.....	218
6.4.2 Controller Systems.....	218
6.4.3 Temperature Control	219
6.4.4 Deflection Measurement.....	219
6.4.5 Load Measurement.....	219
6.5 Specimen Alignment.....	220
6.6 Development of ASU Uniaxial Fatigue Test Method.....	223
6.6.1 Selection of Appropriate Glue Type and Platens.....	224
6.6.2 Machine Compliance	227
6.6.3 Failure Location and Specimen Height during Compaction	230
6.6.4 Investigation of Strain Controlled Methods.....	243
6.6.4.1 Crosshead Controlled-Strain Test	243
6.6.4.2 On-Specimen LVDT Controlled-Strain Test	243

CHAPTER	Page
6.7 Development of ASU Uniaxial Fatigue Test Software.....	246
6.7.1 Software without Rest Period	246
6.7.2 Software with Rest Period	248
6.8 Why Tension-Compression Fatigue Test?	252
7 ENDURANCE LIMIT METHODOLOGY AND RESULTS OF EXPERIMENTS	257
7.1 Background.....	257
7.2 Methodology Development	257
7.2.1 Determination of Fatigue Endurance Limit	261
7.2.1.1 Healing Index Method	263
7.2.1.2 Pseudo Stiffness Ratio Method.....	265
7.2.2 Effect of Different Strain Levels and Rest Periods.....	267
7.3 Determination of Pseudo Stiffness.....	268
7.4 Fatigue Lives Experiment.....	270
7.4.1 Fatigue Failure Criterion.....	270
7.4.2 Definition of the Initial Number of Cycles	272
7.4.3 Fatigue Lives Experiment Results	274
7.4.4 Main Experiment Results.....	283
7.4.4.1 Results of Tests without Rest Period	284
7.4.4.2 Results of Tests with Rest Period	287
7.4.5 Additional Experimental Results	289

CHAPTER	Page	
8	ENDURANCE LIMIT MODEL DEVELOPMENT AND SENSITIVITY ANALYSIS.....	297
	8.1 Background.....	297
	8.2 Development of First Generation PSR Model.....	298
	8.2.1 Effect of Rest Period on PSR.....	305
	8.2.2 Effect of N on PSR.....	306
	8.2.3 Estimating Endurance Limits Using First Generation PSR Model.....	308
	8.3 Development of Second Generation PSR Model.....	311
	8.3.1 Effect of Rest Period on PSR.....	315
	8.3.2 Effect of N on PSR.....	315
	8.3.3 Estimating Endurance Limits Using Second Generation PSR Model.....	317
	8.4 Comparison of Endurance Limits Computed from Beam Fatigue Experiment.....	322
	8.5 Methodology for Incorporating the Endurance Limit into the DARWin-ME.....	332
	8.5.1 Calculation of Endurance Limit.....	332
	8.5.2 Incorporating Endurance Limit into Fatigue relationships	335
	8.5.3 Incorporating Endurance Limit into Fatigue Damage	338
9	SUMMARY, CONCLUSIONS AND RECOMMANDATIONS FOR FUTURE RESEARCH.....	340

CHAPTER	Page
9.1 Summary	340
9.2 Conclusions.....	342
9.2.1 Viscoelastic Properties.....	342
9.2.2 Development of Uniaxial Fatigue Protocol and Software .	343
9.2.3 Results of the Uniaxial Fatigue Experiments.....	344
9.2.4 Development of PSR Regression Models and Endurance Limit Analysis.....	346
9.3 Recommendations for Future Research	348
REFERENCES	349
APPENDIX A.....	370
APPENDIX B	399
APPENDIX C	421

LIST OF TABLES

TABLE	Page
1. List of factors that can affect the fatigue endurance limit (NCHRP 944, 2008)	121
2. Factor combinations for the 5-factor rational factorial completely randomized design	125
3. Factors and factor interactions estimated from the experiment	126
4. Summary of laboratory mixing and compaction temperatures for mix design, °F (°C).....	129
5. Summary of superpave binder characterization tests.....	130
6. Summary of BBR test results (S and m-value).....	131
7. Example of binder sample preparation scheme	133
8. Summary of conventional and Superpave binder characterization tests	134
9. Designed aggregate gradation.....	141
10. Composite aggregate properties.....	142
11. Summary of the volumetric mix design at different binder types	142
12. Number of complex modulus tests under different conditions.....	144
13. Number of fatigue tests under different conditions	146
14. Number of uniaxial tension-compression fatigue test under different conditions.....	147
15. Testing plan of additional fatigue test.....	148
16. Aggregate batching sheet.....	150

TABLE	Page
17. Number of specimens for different combinations of specimens for the PG64-22 asphalt mixture.....	158
18. Number of specimens for different combinations of specimens for the PG58-28 and PG76-16 asphalt mixtures.....	158
19. Bulk Sp. Gr., maximum Sp. Gr., and Saturated surface dry air voids of the PG 64-22 specimens.....	159
20. Bulk Sp. Gr., maximum Sp. Gr., and Saturated surface dry air voids of the PG 58-28 specimens.....	160
21. Bulk Sp. Gr., maximum Sp. Gr., and Saturated surface dry air voids of the PG 76-16 specimens.....	161
22. Test conditions of the dynamic modulus (E^*) test (AASHTO TP 62-07)...	164
23. E^* test results of PG 76-16 mixture at 4.2% AC and 7.0% Va	166
24. E^* Sigmoidal and shifting parameters of PG 64-22 mixtures	174
25. E^* Sigmoidal and shifting parameters of PG 58-28 mixtures	175
26. E^* Sigmoidal and shifting parameters of PG 76-16 mixtures	176
27. Temperature shift factors of PG 64-22 mixtures	177
28. Temperature shift factors of PG 58-28 mixtures	177
29. Temperature shift factors of PG 76-16 mixtures	178
30. Regression models of the sigmoidal parameters for the three groups of mixtures.....	193
31. Calculation of relaxation modulus values of PG 76-16 binder at 4.2% AC and 7.0% Va.....	206

TABLE	Page
32. Prony series parameters for different term values of PG 76-16 mixture at 4.2% AC and 7.0% Va	210
33. Summary of monotonic direct tension tests for 4 inch diameter specimens.	225
34. Summary of monotonic direct tension tests for 3- inch diameter specimens	226
35. Testing plan of the compaction study	233
36. Average of air void calculations for 6.7-inch height at 8.0% Va	237
37. Average of air void calculations for 7.1-inch height at 9.5% Va	237
38. Average of air void calculations for 7.1-inch height at 7.0% Va	238
39. Average of air void calculations for 7.1-inch height at 4.5% Va	238
40. Average of air void calculations for 7.9-inch height at 9.5% Va	239
41. Locations of failure for specimens with different compaction heights.....	242
42. Finger print and uniaxial fatigue tests results at 9.5% Va and 4.2% AC.....	274
43. Finger print and uniaxial fatigue tests results at 4.5% Va and 4.2% AC.....	275
44. Finger print and uniaxial fatigue tests results at 9.5% Va and 5.2% AC.....	275
45. Finger print and uniaxial fatigue tests results at 4.5% Va and 5.2% AC.....	276
46. Low and medium tesnile strain values for all mixtures at different temperatures	281
47. k_1 , k_2 and k_3 values for each individual mixture and all mixtures together .	281
48. Finger print and uniaxial fatigue test results at 9.5% Va and 4.2% AC	285
49. Finger print and uniaxial fatigue test results at 4.5% Va and 4.2% AC	285
50. Finger print and uniaxial fatigue test results at 9.5% Va and 5.2% AC	286
51. Finger print and uniaxial fatigue test results at 4.5% Va and 5.2% AC	286

TABLE	Page
52. Finger print and uniaxial fatigue test results at 9.5% Va and 4.2% AC	287
53. Finger print and uniaxial fatigue test results at 4.5% Va and 4.2% AC	288
54. Finger print and uniaxial fatigue test results at 9.5% Va and 5.2% AC	288
55. Finger print and uniaxial fatigue test results at 4.5% Va and 5.2% AC	289
56. High tesnile strain values for all mixtures at different temperatures	293
57. Updated k_1 , k_2 and k_3 values for each individual mixture and all mixtures together	293
58. Summery results of uniaxial fatigue test without rest period for all mixtures	295
59. Summery results of uniaxial fatigue test with rest period for all mixtures...	296
60. Regression coefficient values of first generation model.....	302
61. Regression coefficient values of second generation model	312
62. Regression coefficient values of first generation SR model using beam fatigue data for the PG 64-22 mixtures.....	323

LIST OF FIGURES

FIGURE	Page
1. Commonly used fatigue test arrangements.	14
2. Energy ratio versus number of repetitions (a) controlled-strain mode; (b) controlled-stress mode.	25
3. Phase angle and on-specimen LVDT microstrain amplitude as a function of time for specimen CLO7 (Daniel, 2001).	27
4. Stress-strain hysteresis loop through the progress of fatigue failure (Al-Khateeb and Shenoy, 2004).	28
5. R^2 vs N on semi-logarithmic scale, (Al-Khateeb and Shenoy, 2011).	29
6. Example of three stage weibull versus cycle repetitions (salt river base aggregate, Chevron 76-16 binder, strain control test, 70 °F).	30
7. Rest times between vehicle’s axles passing over the pavement.	31
8. Tests without rest.	31
9. Fatigue tests (a) with rest intervals; (b) with intermittent loads.	32
10. Change in pseudo stiffness before and after a rest period (Kim et., al 1990). .	41
11. Energy equilibrium flow chart, (Shen, 2006).	43
12. Typical dynamic modulus of elasticity through fatigue damage and rest periods: (a) 68°F healing; (b) 140°F healing (Daniel and Kim, 2001).	47
13. Comparison between measured and predicted stiffness moduli (Pronk, 2009).	54
14. Comparison between measured and predicted phase angles (Pronk, 2009). .	54
15. Stress-strain curve for viscoelastic solid.	65

FIGURE	Page
16. Typical ratio of dissipated energy change versus loading cycles plot, (Carpenter et al., 2003).	71
17. The three modes of loading to describe crack growth, (Anderson, 1995).	74
18. Continuum damage analysis of flexural fatigue (Christensen and Bonaquist, 2005).	80
19. Stresses and strains in a transverse section of a beam subjected to a harmonic sine loading, (Mello et al., 2009).	81
20. Typical S-N curve.	82
21. Endurance limit concept in perpetual HMA pavement design.	85
22. Typical failure criteria (fatigue limit) (Monismith et al., 1970).	86
23. Strain – load relationship illustrating the fatigue endurance limit, (Thomson and Carpenter, 2006).	87
24. Various methods of extrapolation, (Prowell and Brown, 2006).	90
25. One-stage v.s. three-stages Weibull extrapolation (Prowell et al, 2010).	90
26. PV vs. N_f @ 50% stiffness reduction curve for all data, (Shen and Carpenter, 2005).	92
27. Traditional fatigue plots for all the data, (Shen and Carpenter, 2005).	92
28. Relationship between the PV and N_f for direct tension samples, (Underwood and Kim, 2009).	93
29. Schematic of loading in stages I, II and III (Soltani et al., 2006).	94
30. Typical loading and strain history for increasing amplitude uniaxial fatigue test (Bhattacharjee et al., 2009).	96

FIGURE	Page
31. Stress-vs-pseudo strain at increasing strain levels (Bhattacharjee et al., 2009).	96
32. Effect of healing on traditional fatigue relationship at 5°C (Underwood and Kim, 2009).	98
33. Typical damage ratio curves collapsed into a unique damage relationship using continuum damage analysis, (Christensen and Bonaquist, 2009).	101
34. Stress-strain curve for linear elastic (Hookean) solid.	104
35. Stress-strain curve for linear viscous (Newtonian) fluid.	104
36. Stress-Strain curve for a viscoelastic material.	105
37. Stress application of correspondence principle to cyclic data with negligible damage: (a) stress-strain; (b) stress-pseudo strain (Lee and Kim, 1998b)..	110
38. Stress-pseudo strain curve behavior and pseudo stiffness changes in: (a) controlled-strain mode; (b) controlled-stress mode (Lee and Kim, 1998b).	115
39. Stiffness versus number of loading cycles with and without rest period.	124
40. RTFO equipment and specimen preparation.	128
41. PAV equipment and specimen preparation.	128
42. Temperature-viscosity relationship from DSR results, (PG 58-28).	131
43. Temperature - viscosity relationship from DSR results, (PG 64-22).	132
44. Temperature - viscosity relationship from DSR results, (PG 76-16).	132
45. Penetration test apparatus and specimen preparation.	135
46. Softening point test apparatus and specimen preparation.	136
47. Brookfield test apparatus and specimen preparation.	137

FIGURE	Page
48. Viscosity – temperature relationship of PG 58-28 binder.	138
49. Viscosity – temperature relationship of PG 64-22 binder.	139
50. Viscosity – temperature relationship of PG 76-16 binder.	139
51. Designed aggregate gradation distribution curve.	141
52. Flow chart of research testing plan.	143
53. Complex modulus test.....	155
54. Complex modulus test setup	157
55. Capping device.....	162
56. Specimen instrumentation of E* testing (AASHTO TP 62-03).	165
57. Construction of storage modulus master curve.....	172
58. Log shift factor as a function of temperature obtained by the construction of storage modulus master curve.....	172
59. Phase angle master curve using the same shift factors obtained from storage modulus master curve.	173
60. Dynamic modulus master curve using the same shift factors obtained from storage modulus master curve.....	173
61. Effect of air void on dynamic modulus master curves of PG 64-22 mixture at 4.0% AC.....	181
62. Effect of air void on dynamic modulus master curves of PG 64-22 mixture at 4.5% AC.....	181
63. Effect of air void on dynamic modulus master curves of PG 64-22 mixture at 5.0% AC.....	182

FIGURE	Page
64. Effect of air void on dynamic modulus master curves of PG 58-28 mixture at 4.2% AC.....	182
65. Effect of air void on dynamic modulus master curves of PG 58-28 mixture at 4.7% AC.....	183
66. Effect of air void on dynamic modulus master curves of PG 58-28 mixture at 5.2% AC.....	183
67. Effect of air void on dynamic modulus master curves of PG 76-16 mixture at 4.2% AC.....	184
68. Effect of air void on dynamic modulus master curves of PG 76-16 mixture at 4.7% AC.....	184
69. Effect of air void on dynamic modulus master curves of PG 76-16 mixture at 5.2% AC.....	185
70. Effect of asphalt content on dynamic modulus master curves of PG 64-22 mixture at 4.0 % Va.	185
71. Effect of asphalt content on dynamic modulus master curves of PG 64-22 mixture at 7.0 % Va.	186
72. Effect of asphalt content on dynamic modulus master curves of PG 64-22 mixture at 10.0 % Va.	186
73. Effect of asphalt content on dynamic modulus master curves of PG 58-28 mixture at 4.5 % Va.	187
74. Effect of asphalt content on dynamic modulus master curves of PG 58-28 mixture at 7.0 % Va.	187

FIGURE	Page
75. Effect of asphalt content on dynamic modulus master curves of PG 58-28 mixture at 9.5 % Va.	188
76. Effect of asphalt content on dynamic modulus master curves of PG 76-16 mixture at 4.5 % Va.	188
77. Effect of asphalt content on dynamic modulus master curves of PG 76-16 mixture at 7.0 % Va.	189
78. Effect of asphalt content on dynamic modulus master curves of PG 76-16 mixture at 9.5 % Va.	189
79. Effect of asphalt content and air void on on dynamic modulus master curves of PG 64-22 mixture.	190
80. Effect of asphalt content and air void on on dynamic modulus master curves of PG 58-28 mixture.	190
81. Effect of asphalt content and air void on on dynamic modulus master curves of PG 76-16 mixture.	191
82. An example shows the comparison between the predicted and shifted $ E^* $ master curve (PG 64-22, 7.0% Va and 4.0% AC).	195
83. Effect of different air void levels on shifted $ E^* $ master curves of PG 64-22 mixture.	196
84. Predicted $ E^* $ master curves at different air void and binder content levels of PG 64-22 mixture.	196
85. Comparison of $ E^* $ values obtained from constructed and predicted master curves of PG 64-22 mixtures.	197

FIGURE	Page
86. Effect of different air void levels on shifted $ E^* $ master curves of PG 58-28 mixture.....	198
87. Predicted $ E^* $ master curves at different air void and binder content levels of PG 58-28 mixture.....	198
88. Comparison of $ E^* $ values obtained from constructed and predicted master curves of PG 58-28 mixtures.	199
89. Effect of different air void levels on shifted $ E^* $ master curves of PG 76-16 mixture.....	200
90. Predicted $ E^* $ master curves at different air void and binder content levels of PG 76-16 mixture.....	200
91. Comparison of $ E^* $ values obtained from constructed and predicted master curves of PG 76-16 mixtures.	201
92. Relaxation modulus master curve of PG 76-16 binder at 4.2% AC and 7.0% V_a	207
93. Generalized Maxwell (Wiechert) model.	208
94. Detailed test setup: test specimen, fixtures, transducers, and thermocouples (Soltani et al., 2006).....	213
95. Specimen test setup (Daniel and Kim, 2001).....	214
96. UTM-25 uniaxial tension-compression test setup	219
97. Gluing jig for uniaxial tension-compression test specimen.....	220
98. Typical monotonic direct tension test results (specimen MC944-05)	226
FIGURE	Page

FIGURE	Page
99. Location of failure; (a) Between platen and glue; 4-inch, (b) Close to specimen end; 4-inch, and (c) Middle of specimen; 3-inch.....	227
100. Locking joints: a) slipped locked joint; b) thread locked joint	229
101. Comparison of actuator to on-specimen LVDT deformations using the slipped locked joint.....	229
102. Comparison of actuator to on-specimen LVDT deformations using the thread locked joint.....	230
103. Different failure types of uniaxial fatigue test: (a) end-failure, (b) middle-failure at top, (c) middle-failure, and (d) middle-failure at bottom	231
104. Compaction of plugs with different height	233
105. Steps of specimen cutting for different air void calculations	234
106. An example of air void calculations for each part	235
107. Air void distribution along the specimen height for 6.7-inch height at 8.0% Va.....	240
108. Air void distribution along the specimen height for 7.1-inch height at 9.5% Va.....	240
109. Air void distribution along the specimen height for 7.1-inch height at 7.0% Va.....	241
110. Air void distribution along the specimen height for 7.1-inch height at 4.5% Va.....	241
111. Air void distribution along the specimen height for 7.9-inch height at 9.5% Va.....	242

FIGURE	Page
112. On-specimen LVDT deformation using crosshead controlled-strain test...	245
113. Comparison of waveform shape: (a) On-specimen LVDTs controlled- strain test, (b) crosshead controlled-strain test.....	245
114. Typical actuator and average on-specimen strain over time relationships for test without rest period.....	248
115. Uniaxial tension-compression fatigue test with rest period.....	250
116. Average on-specimen strain and actuator strain over time relationships for test with rest period.....	251
117. Load cell during loading and rest time with a close up of one loading cycle.	252
118. Total, permanent, and cyclic strain for cyclic direct tension fatigue test, (<i>Daniel and Kim, 2002</i>).	253
119. Actuator deformation wave shape over time; A) direct tension and B) tension-compression.	255
120. On-specimen deformation wave shape over time; A) direct tension and B) tension-compression.	255
121. Stress wave shape over time; A) direct tension and B) tension-compression.	256
122. Pseudo stiffness ratio versus time relationship for with and without tests. ...	259
123. Determination of the high and low strain levels at each temperature.	261
124. Pseudo stiffness ratio at four different number of cycles.	262
125. Healing parameters versus strain levels at different temperatures.....	264

FIGURE	Page
126. Determination of endurance limit at each temperature using HI parameter.	265
127. Effect of strain and rest period of the PSR as a function of the loading cycles.	266
128. Determination of endurance limit at each temperature using PSR parameter.	266
129. Expected rest period versus healing parameters relationship.	268
130. Typical phase angle versus loading cycle's relationship at 40°F temperature.	270
131. Typical phase angle versus loading cycle's relationship at 70°F temperature.	271
132. Typical phase angle versus loading cycle's relationship at 100°F temperature.	271
133. Fatigue lines at different temperatures using 50 th cycle initial stiffness.	273
134. Fatigue lines at different temperatures using 100 th cycle initial stiffness. ...	273
135. Fatigue lives at different temperatures (9.5% Va and 4.2% AC).	277
136. Fatigue lives at different temperatures (4.5% Va and 4.2 AC%).	278
137. Fatigue lives at different temperatures (9.5% Va and 5.2% AC).	278
138 . Fatigue lives at different temperatures (9.5% Va and 5.2% AC).	279
139. Measured versus predicted cycles to failure based on individual generalized fatigue models.	282

FIGURE	Page
140. Measured versus predicted cycles to failure based on generalized fatigue model for all mixtures together.	282
141. Updated fatigue lives at different temperatures (9.5% AV and 4.2% AC). 290	
142. Updated fatigue lives at different temperatures (4.5% AV and 4.2% AC). 291	
143. Updated fatigue lives at different temperatures (9.5% AV and 5.2% AC). 291	
144. Updated fatigue lives at different temperatures (4.5% AV and 5.2% AC). 292	
145. Measured versus predicted cycles to failure based on individual generalized fatigue models.	294
146. Measured versus predicted cycles to failure based on generalized fatigue model for all mixtures together.	294
147. PSR and RP relationship fitted by Tanh function.	300
148. Measured versus predicted PSR for the first generation model.	303
149. Residual versus raw number for the first generation model.	304
150. Standerdized error versus measured PSR values.	304
151. Effect of rest period on PSR for all mixtures.	305
152. Effect N on PSR- ϵ_t relationship at different RP and temperatures for the 4.5Va-4.2AC mixture.	307
153. PSR versus tensile strain for all mixtures at 40°F (RP = 5.0 sec, and N = 20,000).	309
154. PSR versus tensile strain for all mixtures at 70°F (RP = 5.0 sec, and N = 20,000).	310

FIGURE	Page
155. PSR versus tensile strain for all mixtures at 100°F (RP = 5.0 sec, and N = 20,000).	310
156. Endurance limit values for all mixtures at different temperatures using the first generation PSR model.	311
157. Measured versus predicted PSR for the second generation model.	313
158. Residual versus raw number for the second generation model.....	314
159. Standerdized error versus measured PSR values.	314
160. Effect of rest period on PSR at different N values.....	316
161. Effect of N on PSR at different initial stiffness and RP values.	317
162. PSR versus tensile strain at different initial stiffness values (RP = 1.0 sec, N=20,000 cycles).	318
163. PSR versus tensile strain at different initial stiffness values (RP = 2.0 sec, N=20,000 cycles).	319
164. PSR versus tensile strain at different initial stiffness values (RP = 5.0 sec, N=20,000 cycles).	319
165. PSR versus tensile strain at different initial stiffness values (RP = 10.0 sec, N=20,000 cycles).	320
166. PSR versus tensile strain at different initial stiffness values (RP = 20.0 sec, N=20,000 cycles).	320
167. Endurance limit values at different rest periods and stiffness values using second generation model (N = 20,000).....	321

FIGURE	Page
168. Endurance limit values at different rest periods and stiffness values using second generation model (N = 100,000).....	322
169. Measured versus predicted SR using the beam fatigue, PG 64-22 model. .	324
170. Residual versus raw number using the beam fatigue, PG 64-22 SR model.	325
171. Standerdized error versus measured SR values using the beam fatigue, PG 64-22 SR mode.	325
172. Effect N on SR- ϵ_t relationship at different RP and temperatures for the beam fatigue, PG 64-22, 4.5Va-4.2AC mixture.	326
173. Effect N on SR- ϵ_t relationship at different RP and temperatures for the beam fatigue, PG 64-22, 4.5Va-4.2AC mixture.	327
174. SR versus tensile strain for the beam fatigue, PG 64-22 mixtures at 40 °F (RP = 5.0 sec, and N = 20,000).....	329
175. SR versus tensile strain for the beam fatigue, PG 64-22 mixtures at 70 °F (RP = 5.0 sec, and N = 20,000).....	329
176. SR versus tensile strain for the beam fatigue, PG 64-22 mixtures at 100 °F (RP = 5.0 sec, and N = 20,000).....	330
177. Endurance limit values for the beam fatigue, PG 64-22 mixtures at different temperatures using SR model (RP = 5 sec and N = 20,000 cycle).	330
178. Comparison of endurance limit values for all mixtures using beam fatigue versus uniaxial fatigue test (PG 64-22, RP = 5 sec, N = 20,000 cycles). ...	331

FIGURE	Page
179. Relationship between initial stiffness and dynamic modulus using the uniaxial fatigue results.	334
180. Assumed truck axle distribution during the 24 hours of the day.	335
181. Fatigue relationships for different stiffness values at 2 second rest period.	337
182. Fatigue relationships for different stiffness values at 5 second rest period.	337
183. Fatigue relationships for different stiffness values at 20 second rest period.	338

CHAPTER 1

INTRODUCTION AND RESEARCH APPROACH

1.1 Introduction

Fatigue damage is one of the primary distresses in asphalt pavements besides thermal cracking and rutting. Fatigue cracks are a series of longitudinal and/or interconnected cracks caused by fatigue failure of the HMA surface (or stabilized base) under repeated traffic loading. Better understanding of fatigue damage mechanisms would enable researchers to develop accurate models to enhance the prediction of fatigue life and damage and consequently, significant advances in the design and construction of flexible pavements can be reached.

The action of repeated loading caused by traffic induces tensile and shear stresses in the bound layers, which eventually leads to loss in the structural integrity of a stabilized layer material. Fatigue typically initiates cracks at points where critical tensile strains and stresses occur. Once the damage initiates at the critical location, the action of traffic ultimately causes these cracks to propagate through the entire bound layer. Two mechanisms of fatigue cracking typically take place depending on the pavement structure. In thin pavements, cracks initiate at the bottom of the HMA layer, where the tensile stress is the highest, and then propagate to the surface. This is usually referred to as “bottom-up” or “classical” fatigue cracking. In thick pavements, cracks most likely initiate at the top in areas of high localized tensile stresses resulting from tire-pavement interaction and asphalt binder aging (usually referred to as top-down cracking).

Different test protocols have been developed over the past few decades for measuring the fatigue behavior of asphalt concrete mixtures. The prediction quality of the fatigue life using any of these test methods depends on how accurate the method is able to simulate the condition of loading, support, stress state and environment. The most popular fatigue tests used all over the world are beam fatigue test, trapezoidal cantilever beam test, direct tension test, tension-compression test, indirect diametral test, triaxial test, and wheel track test. Even with the existence of current advanced technology, it is still difficult to accurately simulate the actual field conditions using available fatigue tests. Therefore, a shift factor is always used to account for the difference between fatigue life obtained from field and laboratory conditions. The magnitude of the shift factor varies depending upon many factors. It has been reported that shift factors varied between 10 and 100 (Harvey et al., 1997).

Fatigue behavior of asphalt concrete mixtures can be characterized using two main approaches. The first is the phenomenological approach where the stress or strain in the HMA layer is related to the number of loading repetitions that causes failure (SHRP A-404, 1994). The Phenomenological approach is simple to use; however, it does not account for damage evolution through the fatigue process. The second approach is the mechanistic approach which is inherently more complex than the Phenomenological one but it is more widely accepted because it uses material properties based on stress-strain relationships (Kim et al., 2003). The mechanistic approach can be implemented through three different methods: dissipated energy, fracture mechanics, or continuum damage mechanics.

The dissipated energy is defined as the area under the stress-strain curve due to the viscoelastic nature of the asphalt concrete mixtures at ambient temperature. The earliest work using the dissipated energy with asphaltic materials was reported by Chomton and Valayer (1972) and van Dijk et al. (1972). The use of dissipated energy for fatigue life prediction has been investigated. Current applications of dissipated energy to describe fatigue behavior assume that all of the dissipated energy goes into damaging the material (Ghuzlan, 2001). In reality, this is not the case. For asphalt concrete, a hysteresis loop is created due to the viscoelasticity of the material, even if no damage is induced. Only part of the total dissipated energy goes to damaging the material, and the remainder (or recovered energy) is due to the viscoelasticity of the material and other factors (Little, 1995). The basic concept of fracture mechanics to define the fatigue properties of asphalt mixtures was initially introduced by Griffith (1921) , which considers fatigue as a process of cumulative damage. In this approach, fatigue cracking is characterized by three stages: crack initiation, stable crack propagation, and unstable crack fracture. It is usually assumed that the stable crack propagation consumes most of the fatigue life. The prediction of crack propagation life using fracture mechanics can be described by the well-known Paris' law (Paris and Erdogan, 1963). A Continuum Damage Mechanics approach (CDM) developed through research efforts at North Carolina State University and Texas A&M University. This approach utilizes the viscoelastic correspondence principle and Work Potential Theory (WPT) described by Schapery (1984) to remove viscous effects in monitoring pseudo-stiffness changes in repeated

uniaxial tensile tests. Kim (1988) developed a nonlinear elastic-viscoelastic uniaxial constitutive model by employing the extended elastic-viscoelastic correspondence principle in the concept of CDM. This approach successfully accounted for damage growth through crack initiation and propagation and healing for any load history or mode of loading. The main difference between CDM and fracture mechanics is that in CDM, cracks occur at a level and number such that they are modeled as smeared out continuously. In Fracture Mechanics some small numbers of cracks are considered which are of size of the scale of interest. To generalize, CDM is useful to model the degradation of a mechanical body leading up to macro-cracks and fracture mechanics is useful for modeling the mechanical body after cracks on the scale of the structure have formed.

Current flexible pavement design methods assume that a cumulative damage occurs where each load cycle uses up a portion of the finite fatigue life of the Hot Mix Asphalt (HMA). However, recent studies show that HMA may exhibit an endurance limit, where properly constructed thick HMA pavements can be exposed to a very large number of loading cycles without exhibiting fatigue damage.

In 1870, the concept of the Endurance Limit (EL) was originally introduced for metals by August Wöhler (Walter Schlitz, 1996) and was defined as the stress level below which failure never occurs. The same concept was implemented for the concrete roads, which was expressed by the stress ratio level. It was recognized that the endurance limit of concrete is attained when the stress level does not exceed 45 percent of the modulus of rupture value (Huang, 1993).

For the HMA pavement, it has been shown that when the controlled strain/damage level is very low, distinctively different fatigue behavior can be found even for the same mixture where any small decrease in the strain level will result in a large fatigue life extension (Thomson and Carpenter, 2006). The endurance limit is an important parameter to design the optimal thickness of long lasting or perpetual pavements where any additional thickness will not provide any extra service life.

Monismith has firstly showed that there appears to be a strain below which there is no fatigue damage to the HMA. Monismith and McLean proposed 70 micro-strains as a likely value for the endurance limit (Monismith and McLean, 1972). As perpetual pavements gained more attention in the United States, a substantial amount of laboratory fatigue testing has recently been performed to demonstrate that HMA does exhibit an endurance limit. Most of this work has been performed at the University of Illinois by Carpenter and his colleagues and at the National Center for Asphalt Technology (NCAT) (Prowell et al., 2010).

In the National Cooperative Highway Research Program (NCHRP) Project 9-38, beam fatigue and uniaxial tension testing were conducted to determine fatigue life (Prowell et al., 2010). By conducting a small strain control beam fatigue test, a fatigue life in excess of 50 million cycles was achieved. Structural sections were also constructed at the NCAT test track as a part of the study to evaluate the effect of increased asphalt binder content and polymer modification on fatigue life (Priest and Tim, 2006). Data from the Long Term Pavement Performance (LTPP) studies were also analyzed to determine if they support the

endurance limit concept. The results obtained from that study support the existence of endurance limit in HMA mixes (Prowell et al., 2010).

The NCHRP Project 9-44 developed a detailed plan to validate an endurance limit for HMA pavements and to incorporate the concept of an endurance limit into a mechanistic-empirical algorithm for bottom initiated fatigue cracking in flexible pavements (NCHRP Project 9-44). Therefore, a concentrated research effort is needed to validate the endurance limit concept, and to devise effective methods for incorporating it in the DARWin-ME software.

It has been proposed that the healing of micro-crack damage is the main reason for the HMA endurance limit where endurance limit represents the balance point between damage and healing. For strain levels above the endurance limit, the damage done is considerably greater than the healing potential for the HMA. When strains are below the HMA-EL value, the damage is small enough that it is completely healed during the rest period between load applications (Shen and Carpenter, 2005). Over the last 4 decades, numerous researchers have studied the significance of rest periods and healing of asphalt binders as well as asphalt concrete mixture (Monismith et al., 1961; Bazin and Saunier, 1967; Raithby and Sterling, 1970, McElvaney and Pell, 1973; Verstraeten, 1976; Van Dijk and Visser, 1977; Francken, 1979, Bonnaure et al., 1982; Kim et al., 1990; Hsu and Tseng, 1996; Jacobs, 1995; Lytton et al., 1998; Bahia et al., 1999; Little et al., 2001; Daniel and Kim, 2001; Si et al., 2002; Breyse, et al. 2003; Castro et al., 2006; Carpenter and Shen, 2006; Shen, 2006; Seo and Kim, 2008; Shinhui et al., 2009; Pronk, 2005 and 2009; Mamlouk et al., 2012). The outcomes of this

research and others provide a clear and comprehensive understanding of the effect of rest period on fatigue damage and healing mechanisms.

1.2 Problem Definition

The endurance limit of HMA is defined as the allowable tensile strain below which fatigue cracking does not occur. NCHRP Project 9-44 stated that the endurance limit does not reflect an absence of load induced damage in the HMA. It is the result of a balance of damage caused by loading and healing or damage recovery that occurs during rest periods. This supports the theory that healing is considered as the main reason of the HMA endurance limit. However, previous research studied the two aspects separately and did not provide any certain methodology to correlate the fatigue endurance limit to the healing of HMA. On the other hand, the implementation of the HMA endurance limit into the DARWin-ME is still incomplete. The current DARWin-ME procedure allows for the use of only one value of endurance limit for the whole analysis. However, the endurance limit is believed to vary depending on the mixture properties, pavement temperature and traffic conditions.

1.3 Research Objectives

This research is part of the NCHRP project 9-44A. The main objective of that project is to validate the concept of endurance limit for HMA pavement through laboratory experiments and algorithm development for the determination and implementation into the DARWin-ME. The experimental plan of the NCHRP 944-A project consists of two fatigue tests. The first one is the beam fatigue test, while the second is the uniaxial fatigue test. The beam fatigue laboratory

experiment includes three binders; PG 58-28, PG 64-24, PG 76-16. The uniaxial fatigue experiment was duplicated for the PG 64-24 binder for the evaluation of the uniaxial fatigue test as well as for comparison purposes. The current study covers the uniaxial fatigue test on a PG 64-22 mixture and a comparison with the corresponding beam fatigue test results. The main objectives of this research are as stated below:

1. Carry out a laboratory experimental program using the uniaxial fatigue test to evaluate the main factors affecting fatigue and healing of HMA.
2. Validate and determine HMA fatigue endurance limit models that mainly consider the healing in HMA.
3. Compare the endurance limit from the uniaxial fatigue experiment and the beam fatigue experiment using the PG 64-22 binder.
4. Develop a methodology to incorporate the endurance limit into the DARWin-ME software.

1.4 Research Outline

This dissertation is composed of nine Chapters and three Appendices. Following will be Chapter 2, which presents the literature review on fatigue damage, laboratory tests, models and characterization methods, rest periods and healing, and fatigue endurance limit of HMA. Chapter 3 includes the theory of viscoelasticity and the uniaxial constitutive model based on the continuum damage mechanics. Chapter 4 describes the design of experiment, materials, specimen preparation and testing plan. Chapter 5 contains a description of the complex modulus experiment conducted to capture the viscoelastic properties

represented by the relaxation modulus of the tested asphalt concrete mixtures. This Chapter also contains a methodology developed to shift the entire dynamic modulus master curve based on air voids and asphalt content levels. Chapter 6 illustrates the development of proposed uniaxial tension-compression test protocol including test setup, test method, test condition, test software to run both tests, with and without rest period. Chapter 7 shows the uniaxial test results and the methodology developed to determine the fatigue endurance limit based on the healing of the fatigue damage. The development of the Pseudo Stiffness Ratio (SPR) regression models to determine the endurance limit is presented in Chapter 8. In addition, the endurance limit determined based on the uniaxial fatigue test and beam fatigue test are compared in Chapter 8. Chapter 9 includes summary, conclusions, and recommendations for future research.

Appendix A includes the dynamic modulus test results for the different mixtures; Appendix B contains proposed test protocol for the uniaxial fatigue test; and Appendix C shows the test results of the uniaxial fatigue test experiments.

CHAPTER 2

LITERATURE REVIEW

2.1 Fatigue Cracking of Hot Mix Asphalt

Load-associated fatigue cracking is one of the most significant distress modes in flexible pavements besides thermal cracking and rutting. The action of repeated loading, caused by traffic induced tensile and shear stresses in the bound layers, eventually leads to a loss in the structural integrity of a stabilized layer material. Fatigue cracking is a progressive distress and can be distinguished into three different stages. The early stage of fatigue cracking consists of intermittent longitudinal wheel path cracks. The intermediate stage of fatigue cracking is called alligator cracking because the cracking pattern resembles an alligator's skin. In some extreme cases, the final stage of fatigue cracking is disintegration when potholes form.

Over the last several decades of pavement technology, it has been common to assume that fatigue cracking normally initiates at the bottom of the asphalt layer and propagates to the surface (bottom-up cracking). However, recent worldwide studies have also clearly demonstrated that fatigue cracking may be also initiated from the top and propagates down (top-down cracking). This type of fatigue is not as well defined from a mechanistic viewpoint as the more classical "bottom-up" fatigue. In general, it is hypothesized that critical tensile and/or shear stresses develop at the surface and cause extremely large contact pressures at the tire edges-pavement interface, coupled with highly aged

(stiff) thin surface layer that have become oxidized is felt to be responsible for the surface cracking that developed (Abojaradeh, 2003).

The mechanism of fatigue failure (bottom-up cracking) can be described as a three stage process involving the crack initiation, propagation, and final fracture failure. During the crack initiation, micro-cracks grow from microscopic size until they reach a critical size of about 7.5-mm (Little et al., 2001). Fatigue initiated cracks develop at points where critical tensile strains and stresses occur. Additionally, the critical strain is also a function of the stiffness of the mix. The location of the initiation may be extremely small and difficult to distinguish from the succeeding stage of propagation, or crack growth. In crack propagation, a single crack or a few cracks grow, followed by more and larger cracks propagating and coalescing to complete the disintegration process. As the propagation of the fatigue crack continues, gradually reducing the cross-sectional area and eventually weakens the material greatly that final complete fracture occurs.

2.2 Mode of Loading

Fatigue tests are carried out in two different modes of loading: controlled strain (displacement) or controlled stress (force) mode. The type of loading is characterized by the ratio R of the minimum force (or displacement) over the maximum force. Thus, a pure sinusoidal signal is characterized by $R = -1$. A haversine signal is characterized by $R = 0$. A variety of loading patterns, such as sinusoidal, haversine, square and triangular-shaped waveforms with or without rest periods have been used to simulate field traffic load pulses. The most

commonly used wave forms in the characterization of the mix and development of fatigue life prediction models are sinusoidal and haversine (Huang, 2004).

In the controlled strain test, the strain amplitude is maintained constant and the force required maintaining the initial strain level decreases gradually after crack initiation, as the flexural stiffness of the mix is effectively decreased. The failure, or termination point, is commonly selected as a certain reduction in the initial stiffness from that at the commencement of the test, generally 50-percent, as discussed in Section 2.4.

The controlled strain mode of loading simulates conditions in thin asphalt pavement layers usually less than 2-inches. In this case, the pavement layer is not the main load-carrying component. The strain in the asphalt layer is governed by the underlying layers and is not greatly affected by the change in the asphalt layer stiffness. This situation is conceptually more related to the category of constant strain.

In the controlled stress mode of loading, the stress amplitude is maintained constant. Because of the repetitive application of the stress, the strain amplitude increases until it reaches twice the initial amplitude, when the flexural stiffness is reduced to half the initial flexural stiffness, which constitutes failure. According to Button et al. (1987), the constant stress type of loading is generally considered applicable to thick asphalt pavement layers usually more than 8 inches. In this type of structure, the thick asphalt layer is the main load-carrying component and the strain increases, as the material gets weaker under repeated loading. However,

with the reduction in the stiffness, because of the thickness, changes in the stress are not significant and this fact leads to a constant stress situation.

The strain mode of loading accounts for both crack initiation and propagation while the stress mode of loading does not account for both crack initiation and propagation, because the number of cycles to crack propagation is small compared to the number of cycles to failure which is defined by the fracture of the sample (Pell, 1973). Therefore, fatigue life is usually greater in control strain than control stress (in general approximately 2.4 times greater) (Tayebali et al., 1994)

The fatigue performance of asphalt mixes with lower flexural stiffness is superior under controlled strain loading than under controlled stress testing at similar initial strain amplitudes. While in the controlled stress mode, mixes with higher flexural stiffness have been shown to have longer fatigue lives, and flatter slopes in the stress-fatigue relationship irrespective of whether the repeated flexure testing was conducted using two- or four-point bending (Epps and Monismith, 1969; Pell and Cooper, 1975).

Controlled stress tests are more severe than controlled strain tests and the energy is absorbed more rapidly. The initial dissipated energy per cycle is high, and the rate of energy dissipation is faster, in the controlled stress mode of loading. It is well known that there will be variability and scatter in the results of fatigue testing. However, when the stress in a controlled stress test is converted to strain, and strain is plotted against the number of cycles to failure, then the scatter is considerably reduced (Monismith, 1966b). This suggests that controlled strain

tests reduce the scatter and variability associated with fatigue testing. Variability is also associated with sample (test specimen) dimensions, with the larger the sample size, the smaller is the scatter and variability in the fatigue test results.

2.3 Fatigue Test Methods

Different test methodologies have been developed over the past several decades for measuring the fatigue behavior of asphalt concrete mixtures. The prediction quality of the fatigue life using any of these test methods depends on how accurate the method to simulates the condition of loading, support, stress state and environment. Moreover, selecting any of these test methods can be influenced by the availability and cost of equipment, in addition to ease of use. FIGURE 1 represents a schematic diagram showing most of the available fatigue tests.

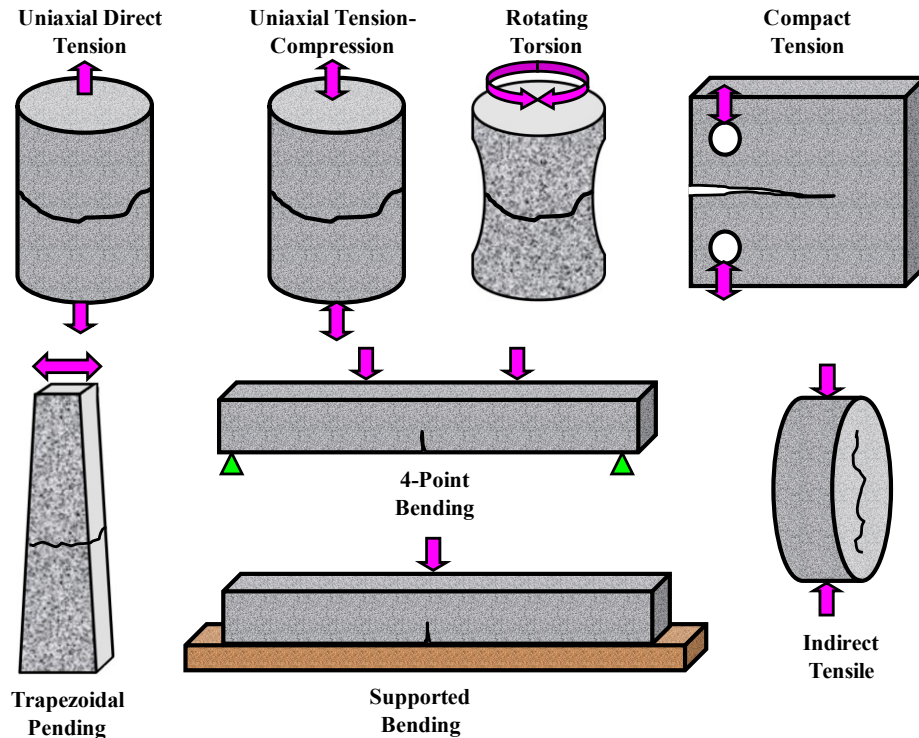


FIGURE 1 Commonly used fatigue test arrangements.

It is almost impossible for laboratory fatigue tests to completely simulate the field conditions as there are too many field variables that are not considered, such as specimen fabrication, compound loading, random rest periods and multi stress state. Therefore, there is difference in fatigue life obtained based on field and laboratory conditions. To account for this difference in fatigue life, a shifting factor usually used to relate laboratory to field performance. The magnitude of the shift factor is vary and depending upon many factors such as the thickness of the asphalt layer, the mix properties, traffic volume and composition, environmental conditions, fatigue failure criterion, and type of fatigue test. Harvey et al. (1997) reported shifting factors varied between 10 and 100.

Brief description along with the advantages and disadvantages and limitations of selected test methodologies can be found in SHRP's "Summary Report on Fatigue Response of Asphalt mixes (Tangella, 1990). Following is a summary of most popular fatigue tests as listed on the SHRP summary report:

2.3.1 Simple Flexure Tests

Simple flexure tests are widely used for measuring the stiffness modulus and assessing the fatigue resistance of asphaltic paving materials. This method is well known, widespread in use, and readily understood. A number of different types of flexural equipment have been developed to study the fatigue characteristics of asphalt-concrete mixtures including:

2.3.1.1 Three and Four-Point Bending Tests

The flexural fatigue test has been used by various researchers to evaluate the fatigue performance of pavements (Witczak et al., 2001). The Shell Laboratory at Amsterdam has used the center-point loading equipment to test specimens with dimensions 1.2-inch (30-mm) x 1.6-inch (40-mm) x 9-inch (230-mm). In this test, specimens are tested in the controlled-deflection (strain) mode.

In four-point test, the dimension of the beams can vary from one laboratory to another. The AASHTO T321-2003 and SHRP M-009, flexural fatigue testing protocol, require preparation of oversize beams that later have to be sawed to the required dimensions. The final required dimensions are $15\pm\frac{1}{4}$ -inch (380 ± 6 -mm) in length, $2\pm\frac{1}{4}$ inch (50 ± 6 -mm) in height, and $2.5\pm\frac{1}{4}$ -inch (63 ± 6 -mm) in width. The procedure does not specify a specific method for preparation. Several methods have been used to prepare beam molds in the laboratory including full scale rolling wheel compaction, miniature rolling wheel compaction, and vibratory loading.

2.3.1.2 Cantilever Beam Rotating Test

At the University of Nottingham, U. K., Pell and Hanson (1973) used a rotating cantilever machine where specimen is mounted vertically on a rotating cantilever shaft. A load is applied at the top of the specimen to induce a bending stress of constant amplitude through the specimen. The tests were usually conducted at a temperature of 50°F (10°C) and a speed of 1,000 rpm. Dynamic stiffness was measured by applying constant sinusoidal amplitude deformations.

Another way to carry out this test was done also by Pell using a controlled-strain torsional fatigue machine where the sample is clamped vertically on a shaft. The bottom of the sample is clamped to the bottom of the machine and the loading arrangement gives a sinusoidal varying shear strain of constant amplitude into the specimen.

2.3.1.3 Trapezoidal Cantilever Beam Test

The trapezoidal cantilever beam test has been popular in Europe. Tests on trapezoidal specimens have been conducted by the Shell researchers (Van Dijk, 1975) and LCPC (Bonnot, 1986). The larger dimension of the trapezoidal specimen is fixed and the smaller end is subjected to either a sinusoidal applied strain or stress. The trapezoid shape of the specimens can promise to have failure at about mid height where the bending stress is largest rather than at the base where boundary conditions might adversely affect interpretation of test results. As an example, specimens tested by van Dijk had a base cross section of 2.2-inch by 0.8-inch (55-mm by 20-mm), a top cross section of 0.8-inch by 0.8-inch (20-mm by 20-mm), and a height of 10-inch (250-mm).

2.3.2 Supported Flexure Test

Supported flexure test was used to better simulate stress state and mode-of-loading in field conditions. Several researchers have used this test with mainly two different specimens shape: circular slab and beam. Majidzadeh (Majidzadeh et al., 1971) and others used circular samples supported on a rubber mat and subjected to a circular shaped repeated load applied to the center of the slab resulting in a stress state in the slab which is very similar to that occurring in the

pavement structure. Barksdale (1977) used asphalt concrete beams placed on 4 in thickness of rubber mate supporting the beam subjected to a haversine load pulse of 0.06 second duration and 45 cpm frequency.

This test method can reduce the scatter of test results by duplication of field conditions in a better way.

2.3.3 Direct Tension Test

The Transport and Road Research Laboratory (TRRL) of the United Kingdom has performed uniaxial tensile tests without stress reversal using a loading frequency of 25 Hz; duration of 40 milliseconds; and rest periods varying from 0 to 1 sec. Starting from very short rest periods, fatigue life increases rapidly with an increase in rest period before reaching a limiting value at about 0.4 seconds, beyond which increasing the duration of the rest period had very little further effect (Raithby and Ramshaw, 1972). These tests were conducted in the controlled-stress mode. Later on, direct tension tests have been performed in the Netherlands (Kunst, 1989) at frequencies of 1 and 0.1 Hz using haversine loading in the controlled-strain mode. More recently, this test have been used in U.S. by Texas A &M and North Carolina State Universities to characterize micro-damage healing in asphalt and asphalt concrete using viscoelastic continuum damage, fracture micromechanics and dissipated energy approaches.

One advantages of direct tension test is the test specimen may be circular as well as rectangular in cross section. In addition, it is less costly as testing time is shorter because fewer loading cycles can be sustained before failure. The

primary disadvantage of this test is that loading condition does not necessarily represent the field conditions.

2.3.4 Tension/Compression Test

The tension/Compression fatigue test was developed at the Transport and Road Research Laboratory (TRRL) (Raithby and Ramshaw, 1972). Axial tensile and compressive loading was applied using in a servo-controlled electro-hydraulic machine. Prism specimens were 3-inch (75-mm) square cross sections and 9-inch (225-mm) lengths. Loading frequencies were 16.7 and 25 Hz, and the effects of rest periods, shape of wave form, and the sequence of load application (compression/tension, tension/compression, compression only, and tension only) were evaluated.

It was concluded that short rest periods, such as occur in practice between successive axle load applications, have an important effect on the fatigue life, the effect of load form is not very great however, a sinusoidal load pulse would appear to be a reasonable representation, and pure compressive cyclic loading gives the largest fatigue life followed by tensile/compressive cyclic loading, tensile cyclic loading, and compressive/tensile cyclic loading.

Except for the ability to simulate the loading pulse observed in the field, this test does not well represent field conditions, required more time, are more costly and required more specialized equipment.

2.3.5 Diametral Test

The diametral fatigue test is an indirect tensile test (ITT) conducted by repetitively loading a cylindrical specimen with a compressive load which acts parallel to and along the vertical diametral plane. This loading configuration develops a reasonably uniform tensile stress in the specimen perpendicular to the direction of the applied load and along the vertical diametral plane. Test specimens are usually 4- or 6-inch diameter and 2.5- to 3.0-inch high. Load is transmitted to the sides of the right circular cylinder through a 0.5-inch wide loading strip. Usually a haversine/sine load pulse can be applied. The load frequency most commonly used are 20 to 120 cycles per minute.

The unique thing about this test is that it can be used to characterize a variety of asphalt concrete mixture properties, especially properties related to resilient elastic, thermal cracking, fatigue cracking and permanent deformation (Kennedy, 1977). Most of the repeated-load indirect tensile tests have been conducted at the Center for Highway Research at the University of Texas at Austin (Moore and Kennedy, 1971; Navarro and Kennedy, 1975; Cowher, 1975; Kennedy, 1977). The diametral test offers a biaxial state of stress, which is possibly of a type that better represents field conditions. A key problem with this method is that it will significantly underestimate fatigue life if the principal tensile stress is used as the damage determinant.

One of previous studies of fatigue characterization using the ITT was carried out in Sweden by Said (1975). Said in his work tested 300 cores from different pavement sections using repeated controlled stress loading at 2

temperatures, 39°F and 59°F (4°C and 15°C). Said concluded the ITT is sufficiently accurate for routine investigation of asphalt concrete fatigue characterization with a shift factor of 10 to correlate to field.

In summary, the diametral test is simple in nature; more representing to field condition due to biaxial state of stress exists and can be performed not only on laboratory specimens but on field cores as well. A key problem with this method is that it will significantly underestimate fatigue life if the principal tensile stress is used as the damage determinant. Also, there is possible concern about the absence of stress reversal and the accumulation of permanent deformation.

2.3.6 Triaxial Test

Several agencies such as the University of Nottingham (Pell and Cooper, 1975) and the University of California, Berkeley (Sousa, 1986) developed this type of device to best represent the state of stress in situ. Pell and Cooper used a setup where they tested cylindrical specimens with a diameter of 4-inch (100-mm) and a height of 8-inch (200-mm). Specimen was bonded to end caps with epoxy resin and was mounted on the rig. Specimens enclosed in a triaxial cell were subjected to a sinusoidal varying axial stress. One concern about this kind of test is that the shear strains must be well controlled, otherwise the predicted fatigue lives could be considerably different than the field results.

Sousa (1986) developed equipment which is capable of applying shear strains by torsion (repeated or constant) together with radial tensile stress using specimens fabricated as hollow cylinders. To date, only shear fatigue (torsion) tests have been conducted. This equipment can be further developed to apply repeated radial tensile stresses through the pulsating fluid within the hollow

cylinder, thus simulating the necessary conditions including shear stresses (through torsion) and vertical stresses.

Triaxial test simulate the field loading condition in which compression is followed by tension and the results can be used for mixture design and, with field correlation factors, for structural design. This type of test is costly, requires specialized equipment, and is time consuming.

2.3.7 Wheel-Track Test

In order to better simulate the effects of a rolling wheel on the pavement and to better understand the pattern of crack initiation and propagation, wheel-track tests have been developed to study fatigue characteristics of asphalt pavements. The Wheel-track test can be conducted in the laboratory and on full scale pavement sections.

Van Dijk (1975) has developed a laboratory loaded wheel with a pneumatic tire that rolled back and forth over a slab of asphalt concrete. The wheel has a diameter of 10-inch (0.25-m) and its path is 24-inch (0.60-m) long with a width in the range of 2- to 2.75-inch (0.05- to 0.07-m). The slab is supported by a rubber mat. Strains at the bottom of slabs, and the detection of crack initiation and propagation were measured. Results can be expressed in terms of three fatigue stages associated with the development of hairline cracks (N_1), real cracks (N_2), and failure of the slab (N_3). Based on the test results, Van Dijk suggested that controlled-strain data may be more appropriate to define pavement cracking than controlled-stress data.

The main limitations of laboratory wheel-track tests are the small dimensions and the slow speed of the rolling wheel as compared to field conditions. In addition, the test is time consuming and does not measure a fundamental mixture property. Moreover, for mixes of low stiffness, rutting becomes significant and may affect fatigue measurements.

Full-scale testing facilities have been built in several countries around the world. Well-known examples include the circular tracks located at Nantes in France, at Pullman, near the Washington State University campus, the Federal Highway Administration's ALF (Accelerated Loading Facility), CALTRAN's Heavy Vehicle Simulator in California, in Australia (ARRB), New Zealand (Canterbury), Denmark, and in United Kingdom (TRRL). The tracks are often divided into sections, each with a different pavement structure, and loads are applied by several sets of dual truck tires.

With full-scale testing facilities, it is possible to examine the effect of changes in the pavement structural section on pavement performance and other forms of pavement distress in addition to fatigue can be studied as well. High initial investment cost and annual operation and maintenance costs are the main disadvantages. Also, a parallel, supplementary laboratory testing program is still needed, since the field track tests do not directly measure fundamental mixture properties.

2.4 Fatigue Failure Criteria

A large diversity regarding the identification of fatigue failure point (N_f) due to fatigue damage has been found through the literature. According to the fatigue test mode of loading (stress or strain), N_f has been specified in different ways. In the constant stress mode of testing, one definition of the N_f was assumed to be a complete fracture at the end of the fatigue test when the specimen fails due to tensile strains (Pell and Cooper, 1975; Tayebali et al., 1992). Rowe (1993) defined N_f when the initial complex modulus is reduced by 90%. Van Dijk (1975) defined N_f as number of loading cycles at which the correspondence strain is twice the initial strain.

In the constant strain mode of testing, several N_f definitions have been adopted. The most common and widely used definition for N_f in the constant strain mode is the 50% reduction in the initial stiffness as defined by Pronk and Hopman (1990) and Tayebali et al. (1992, 1993). A 50% reduction in the initial modulus was also defined as fatigue failure by Van Dijk and Vesser (1977). Afterward, the 50% reduction in stiffness was adopted to define N_f point by the AASHTO as a provisional standard TP8-94 (2002).

Rowe and Bouldin (2000) identified N_f by plotting the load cycle value n_i versus the load cycle multiplied by the stiffness S_i at that cycle ($n_i \times S_i$). The fatigue failure point was defined for both controlled stress and strain test types as the point that produces a peak value. This point was found to represent the formation of cracks.

A rational fatigue failure criterion was developed by ASU based on the Rowe and Bouldin's failure definition (Abojaradeh, 2003). A new stiffness term (called stiffness degradation ratio) was defined by normalizing the Rowe and Bouldin's ratio $n_i \times S_i$ by dividing it by the initial stiffness S_0 taken at cycle number 50th. N_f was defined for both controlled strain and controlled stress modes as the number of load repetitions at the peak value of stiffness degradation ratio-cycle number relationship. The results of the ASU method verified that 50% of the initial stiffness was the best value for the failure fatigue criterion.

Energy-based failure concepts have been proposed by many researches as an alternative mean to define N_f . Hopman et al. (1989) proposed the use of an 'Energy Ratio' concept to define N_f . By plotting the energy ratio (Load cycle \times initial dissipated energy/ dissipated energy at that load cycle, $n_i \times w_0/w_i$) versus the number of load cycles, N_f was defined as the number of load cycles when the energy ratio deviates from a straight line for strain-control mode. In case of stress-control mode, N_f was defined as the peak of the curve (FIGURE 2).

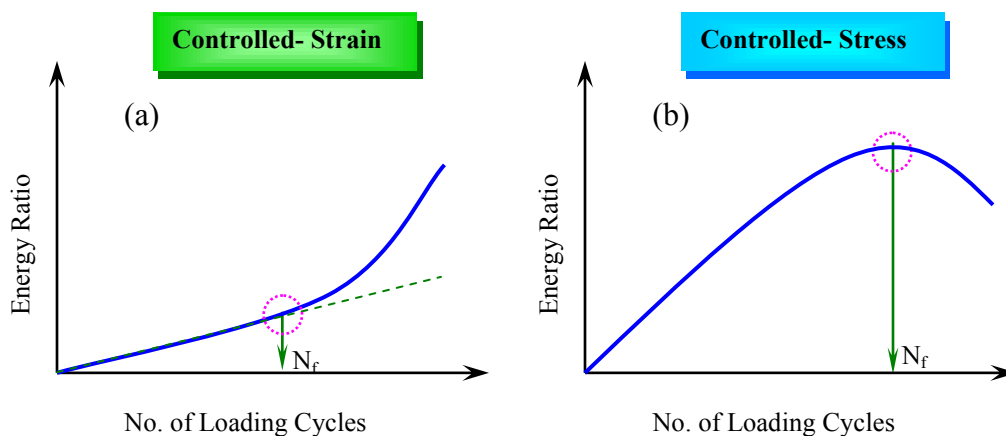


FIGURE 2 Energy ratio versus number of repetitions (a) controlled-strain mode; (b) controlled-stress mode.

In 1997, Pronk proposed a different expression of energy ratio as the ratio of the cumulative dissipated energy up to cycle n to the dissipated energy for cycle n (W_i/w_i). Under constant strain, N_f was defined as the number of load cycles when the energy ratio deviates from a straight line. Under controlled stress, N_f was defined as the peak of the curve. Ghuzlan and Carpenter (2000) used the ratio of the change in dissipated energy between two consecutive cycles (n_i, n_{i+1}) to the total dissipated energy in the load cycle n_i to define N_f . Failure was selected for both modes of loading as the point where this ratio increased rapidly after a consistent stable trend for this ratio with load cycles.

Kim et al. (1997) introduced the 50% reduction in pseudo stiffness as a failure point in fatigue testing, which was believed to be independent of mode of loading and stress/strain amplitude.

Reese (1997) used phase angle to define the N_f as the cycle at which the phase angle shows a maximum value with time where a sharp decrease in the phase angle values at the same point is occurred (FIGURE 3). Using phase angle failure criterion, Daniel (2001) found that the midpoint of the failure range has occurred at a pseudo stiffness reduction of 29% for cyclic uniaxial fatigue test and 31% for monotonic uniaxial test.

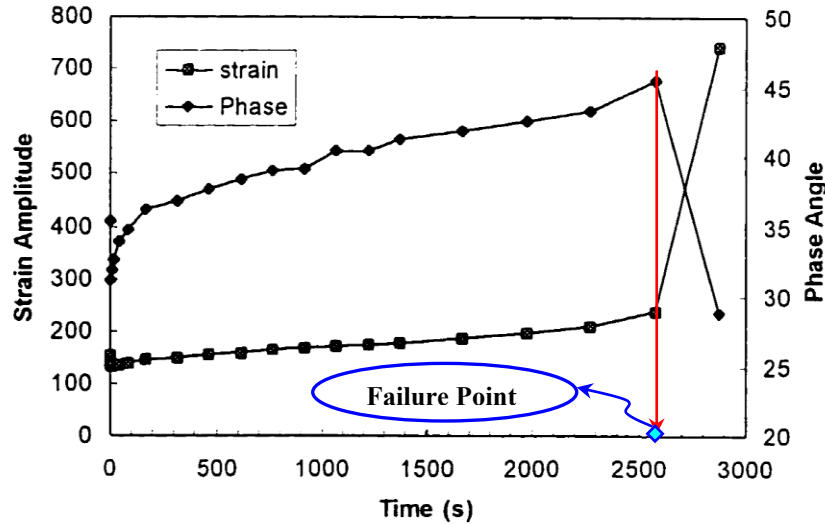


FIGURE 3 Phase angle and on-specimen LVDT microstrain amplitude as a function of time for specimen CLO7 (Daniel, 2001).

Al-Khateeb and Shenoy (2004) defined a new qualitative fatigue failure criterion through visual observations of the load-deformation (stress-strain) hysteresis loop. They defined the point of first fatigue failure N_{ff} as that point at which the hysteresis loop or the response waveform started to show the first signs of distortion. The point of complete fatigue failure N_{cff} , on the other hand, was defined as the point at which an extensive (or almost complete) distortion in the hysteresis loop or the response waveform is occurred (FIGURE 4).

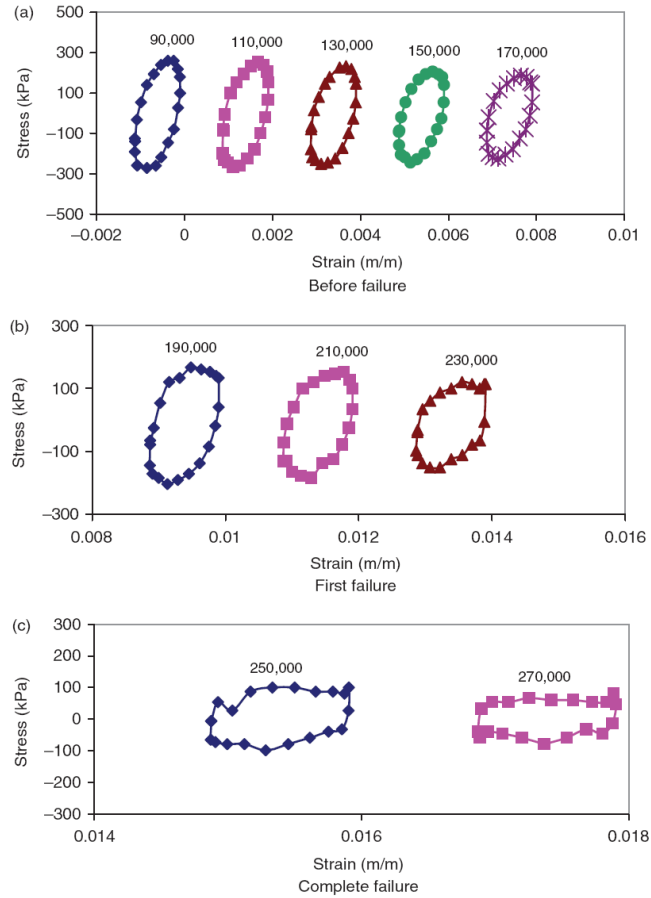


FIGURE 4 Stress-strain hysteresis loop through the progress of fatigue failure (Al-Khateeb and Shenoy, 2004).

Based on the same concept, Al-Khateeb and Shenoy (2011) developed a more quantitative method to identify the fatigue failure to any type of fatigue testing. In this method, the relationship between output signals for consecutive cycles with reference to initial stable cycle is used for computing ‘ R^2 ’. The ‘ R^2 ’ drops sharply from initial stable value of 1 to less than 0.5 and eventually to almost 0 with increasing loading cycles. The number of cycles determined from the fitted equation at ‘ R^2 ’ =1 marks the point of first fatigue failure N_{ff} and ‘ R^2 ’ =0 marks the point of complete fatigue failure N_{cff} (FIGURE 5).

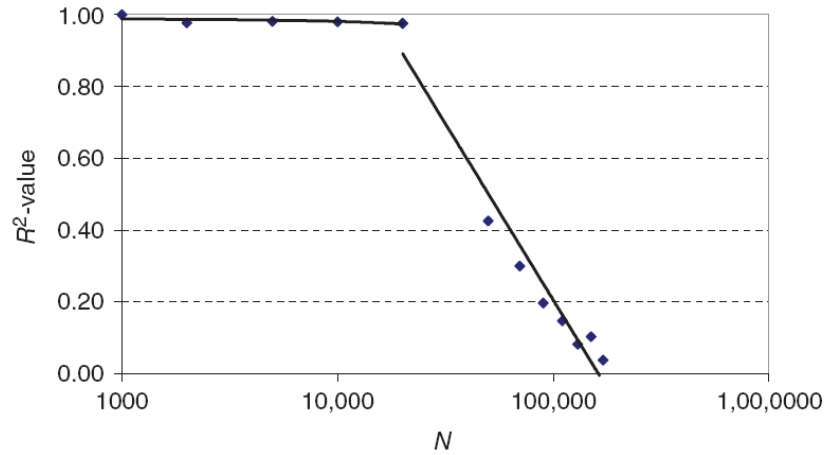


FIGURE 5 R^2 vs N on semi-logarithmic scale, (Al-Khateeb and Shenoy, 2011).

Tsai et al. (2005) used a 3-Stage Weibull model to define the fatigue failure of asphalt mixtures. The three stages defined are initial stage (warm-up), crack initiation and crack propagation. The 3-Stage Weibull model consists of three different equations that are based on the stiffness ratio, ($SR = S_i/S_o$). By plotting the $\ln(-\ln(SR))$ versus $\ln(\text{loading cycle, } n)$, three different curves can be distinguished that can be fitted using the three different equation of Weibull model. Once the data are fitted, the failure point is assumed to have a stiffness ratio of 0.5 as shown from FIGURE 6.

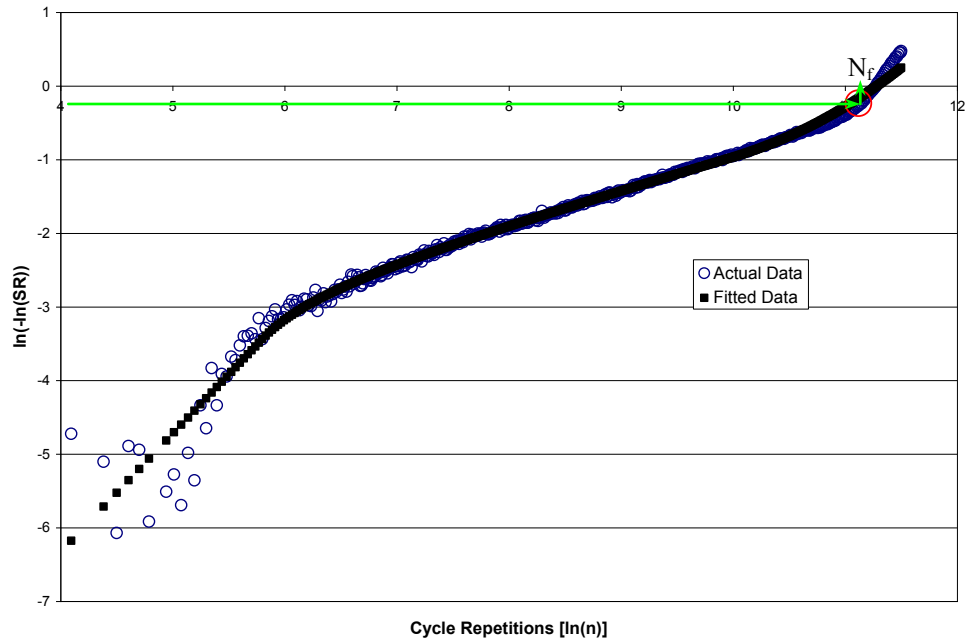


FIGURE 6 Example of three stage weibull versus cycle repetitions (salt river base aggregate, Chevron 76-16 binder, strain control test, 70 °F).

2.5 Effect of Rest Period on HMA Fatigue Behavior

2.5.1 Need for Rest Period

Under real traffic conditions the pavement structure is subjected to a succession of load pulses as the traffic flows past a particular point on the road. The duration and spacing of the load pulses depends on several factors, including vehicle speed, axle configuration and headway between following vehicles as shown from FIGURE 7. Another important factor that affect the rest period is the fact that loads are not always applied on the same part of the road, but distributed across the cross-section.

In most laboratory fatigue studies of asphalt concrete mixtures, fatigue is usually carried out by means of dynamic tests with loading cycles which are

repeated continually, without periods of non-loading (FIGURE 8), which contradict with the actual field traffic loading that is interrupted by rest periods because of the spaces between axles of the same vehicle or successive vehicles.

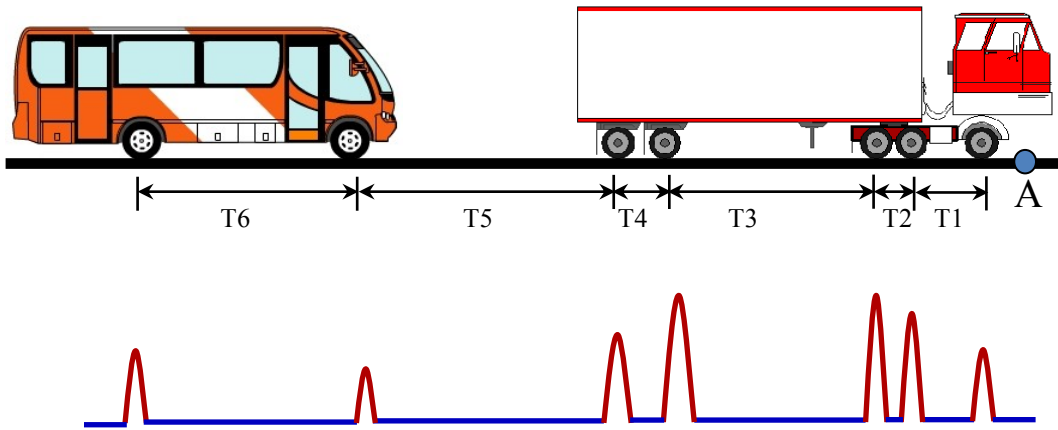


FIGURE 7 Rest times between vehicle's axles passing over the pavement.

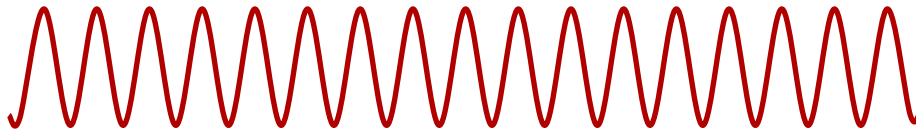


FIGURE 8 Tests without rest.

2.5.2 Effect of Rest Period

Over the last several decades, several researchers have studied the significance of rest periods between load applications during the fatigue testing of HMA. Dissimilar findings have been presented in literature showing diverse opinions on the effect of the rest period. Some researchers think that rest period only leads to a temporary modulus recovery without actually extending the fatigue life, while others found that the modulus recovery did extend fatigue life

by a certain amount. These different conclusions were mainly based on a large variety of tested mixtures, laboratory testing setups and research approaches.

Depending on the way the material is allowed to rest, there are two different ways of introducing rest periods into fatigue testing:

- With rest intervals: It is a classic fatigue test with continuous loading cycles where rest intervals (storage periods) are introduced after a certain number of continuous loading cycles. At the end of each rest interval, the test is continued until the next rest interval (FIGURE 9a).
- With intermittent loads: Each loading cycle is followed by a rest period with certain duration (FIGURE 9b).

It sounds as if the second method with intermittent loading resembles more closely the sequence of traffic pulses in the field than the first method, although both testing methods have been used by researchers for studying the effect of rest period and healing on the HMA fatigue behavior.

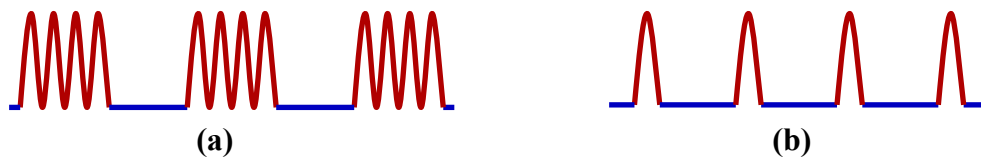


FIGURE 9 Fatigue tests (a) with rest intervals; (b) with intermittent loads.

Monismith et al. (1961) assessed the effect of rest period by conducting repeated flexure tests on beam specimens supported by a spring base. The loading cycles consisted of 1 sec of load and 1 sec, 3 sec, or 19 sec of rest period. The tests were performed at 77°F (25°C) temperature and three frequencies were used, 3, 15, and 30 load applications per minute. It was indicated from the test results

that increasing the rest period from 1 to 19 second had no effect on fatigue performance. This conclusion is different from other later research results that showed an enhancement of the fatigue life due to rest periods.

Bazin and Saunier (1967) quantified healing by introducing rest periods to asphalt concrete beams which were previously failed under both bending and uniaxial tensile loadings. In the tensile tests, beam specimens were stretched along the longest dimension and the tensile strength and strain at break were measured. In the bending test, the specimens were tested in a dynamic two-point bending apparatus (frequency 50Hz, temperature 50°F) until rupture occurred (fatigue life N). The broken samples were put in contact and samples were placed vertically resting on smallest base. After different rest periods and temperatures during rest, the samples were tested again to have both the new tensile strength and strain at break in uniaxial tensile the fatigue life N' in bend test. For the uniaxial tensile test, the amount of healing was evaluated based on healing index while the life ratio (N'/N) was used to evaluate the healing on bend test. The test results of the uniaxial tensile test showed that a dense graded asphalt concrete mixture could recover 90% of its original tensile strength after 3 days of recovery at 77°F (25°C) and that the healing seemed to become complete after one month at that temperature. Based on the bending test, a 50% increase in fatigue life for a previously failed sample after a one-day rest under a slight compressive stress 0.22 psi (1.5 kPa) was achieved.

Raithby and Sterling (1970) performed uniaxial tensile cyclic tests on beam samples sawed from a rolled carpet of asphalt concrete to have dimensions

of 3×3×8.6 inches (75-mm×75-mm×225-mm). The tests were conducted under a controlled stress mode at two loading frequencies (2.5Hz and 25Hz) and two temperatures 50°F and 77°F (10°C and 25°C), with sinusoidal load pulse, which has equal tensile and compressive stresses in each cycle. Pulsed loading without and with rest periods varying from 40ms to 800 μ s was applied until failure occurred. In the tests when rest periods were introduced, the specimens were rested at a zero stress. It was observed that the strain recovery during the rest periods resulted in longer fatigue lives by a factor of five or more than the fatigue life under continuous loading.

McElvaney and Pell (1973) performed rotating bending fatigue tests on a typical English base course mix at 50°F (10°C) using a 16.7 Hz frequency. The specimens were subjected to multi-level loading with random durations of rest period. It was concluded that rest periods have a beneficial effect on the fatigue life depending on the damage accumulated during loading periods. No evidence was found for a limiting value of the fatigue life extension.

Verstraeten (1976) performed dynamic two-point bending tests in a constant-stress mode (frequency 54 Hz, temperatures 23°F and 59°F). The loading conditions were maintained either until failure or 80% of stiffness reduction. Then, the specimens were stored for periods varying from 3 to 21 hours at temperatures from 23°F to 95°F (-5°C to 35°C). The author concluded that the longer the rest periods and the higher the temperatures, the greater the beneficial effect, although their effects on the susceptibility of mixtures to fatigue could not be quantified.

Francken (1979) carried out experiments on a typical Belgian mix using two-point bending apparatus. The test was run under constant stress mode of loading at 55.6 Hz frequency. The test results showed an increase in service life when rest periods were incorporated in the fatigue tests. From the test results, a new empirical relation that accounts for the effect of rest period was derived. It is a relation between the cumulative cycle damage ratio in Miner's law (N_i/N_c) and the loading ration (n_r/n_l):

$$\frac{N_i}{N_c} = 1 + 2.8\left(\frac{n_r}{n_l}\right)^{0.44} \quad (1)$$

where:

n_r = number of rest periods,

n_l = number of loading cycles.

The author pointed out that the use of this formula is restricted to a particular asphalt mix investigated.

Hsu and Tseng (1996) conducted a repeated load fatigue test on beam specimens using haversine wave with a loading duration of 0.1 sec. To study the effect of the rest period on the fatigue response of asphalt concrete mixtures, 1, 4 and 8 loading ratios, which represent the ratio of the duration of the rest period to that of loading, were applied. During the test, approximately 10% of the applied load was pulled upward on the specimen for each loading to simulate the rebound of the pavement for each passing of the vehicles. The test results of controlled stress test showed that asphalt concrete mixtures with higher loading ratios and asphalt content 0.5% more than optimum exhibited longer fatigue life.

Breysse et al. (2003) performed the two-point pending fatigue test on trapezoidal specimens, clamped at the lower base and submitted to a cyclic loading at its free end, to study the balance between damage and recovering in HMA. A controlled-displacement test was done at 68°F (20°C) temperature and 40 Hz loading frequency. In this study, specimens were continuously loaded until the overall stiffness reduction reached a given ratio $\alpha\%$ then the test is stopped. The stiffness recovery during the rest periods was then monitored by applying a low magnitude loading (supposed not to create any damage) until the response was stabilized. This process was repeated iteratively as many times as wanted, for the same $\alpha\%$ ratio. The tests were driven for various α values (10 – 50%) to study the effect of low and severe damage histories on the stiffness recovery values. The obtained results showed the maximum magnitude of recovery depends on the number of applied fatigue cycles that have been applied before. It was noticed that part of the recovery observed due to the interrupted loading sequence is a temporary stiffness recovery rather than true healing. This is why material will return its original status (damaged status) very quickly after reloaded.

Castro et al. (2006) had conducted flexural beam fatigue tests with and without rest periods. As a consequence, a constant rest period of 1 second following every 0.1 second loading was applied to the test. The fatigue curves had been evaluated by means of discriminate analysis so as to rigorously confirm that they were different. It was concluded that the rest period could increase the fatigue life of HMA specimens up to 10 times, compared to tests without rest periods.

2.5.3 Optimum Rest Period

Although an increase in the duration of the rest period produces an increase in fatigue life due to crack healing, exceeding certain value of rest time may have a small effect on the mixture fatigue life. At the same time, for the same number of cycles, the longer the rest period duration, the longer the test duration. Consequently, it is essential to find the rest period such that its increase would not cause a significant increase in fatigue life so as to avoid excessive test durations. This rest period duration can be referred to as the optimum rest period.

In an attempt to investigate a rational value of the optimum rest period, Raithby and Sterling (1972) applied a range of rest periods between null and 25 times the loading time on a rolled asphalt base course using a dynamic push-pull test. A constant stress mode was applying different waveforms (sine, triangle, and square). It was found that fatigue life does not increase significantly for rest periods greater than ten times the loading time and waveform influence was less important than the duration of rest periods.

Van Dijk and Visser, (1977) had tested a rolled asphalt base course mixture in a three-point bending apparatus in a constant strain mode (40 Hz frequency and 68°F (20°C) temperature) with loading ratios varying from 1 to 25. The results showed that the maximum beneficial effect of rest period on the fatigue life (life ratio of about 10) was determined by means of extrapolation to be achieved at a loading ratio of about 50.

Bonnaure et al. (1982) performed a three-point bending fatigue test with various rest period ratios (0, 3, 5, 10, and 25 times the length of the loading

cycle). The tests were done under both constant stress and constant strain modes of loading at three temperatures of 41°F, 68°F, and 77°F (5°C, 20°C, and 25°C) and 40Hz frequency. It was indicated that maximum beneficial effect of rest periods on the fatigue life was at a rest period equal to 25 times the loading cycle. It was concluded also that the constant-stress mode results in a greater increase in fatigue life than compared the constant-strain mode.

Although, in a rigorous sense, the optimum rest period would be different according to mixture properties (gradation, binder content, binder grade, mixture volumetric, etc.), test type (simple flexure, uniaxial, triaxial, etc.), and test conditions (mode of loading, temperature, frequency, stress or strain levels, etc.).

2.6 Healing of Asphalt Concrete Mixtures

Researchers have been trying to find answers to some of the issues regarding healing phenomenon of asphalt mixtures through some of outcomes of the conducted experiments. These queries are mainly to investigate the healing mechanism and if healing happens only during rest periods, during all the loading and unloading periods. Some other goals is to study the effect of mixture components and volumetric, test conditions (such as temperature, rest periods, stress or strain levels, frequency, and laboratory testing setup), material damage level, and the analysis approach on the healing rates. Although, some of these questions have been recognized, still there are lots of issues need to be investigated.

2.6.1 Mechanism of Healing

Healing is generally considered as the capability of a material to self-recover its mechanical properties (stiffness or strength) to some extent upon resting due to the closure of cracks. In fact, various engineering materials are found to have this ability whether they are metallic or non-metallic.

For metallic materials such as steel, aluminum, etc., Suresh (1998) categorized the various mechanisms of fatigue crack closure or healing that are induced by a variety of mechanical, microstructural and environmental factors based on his own results and of the work of other researchers. These mechanisms of crack closure include the followings:

1. Residual plastic stretch at crack wake (plasticity-induced crack closure),
2. Corrosion layers formed within a fatigue crack (oxide-induced crack closure),
3. Microscopic roughness of the fatigue fracture surfaces (roughness-induced crack closure),
4. Viscous fluids penetrated inside the crack (viscous fluid-induced crack closure), and
5. Stress- or strain- induced phase transformations at the crack tip (transformation-induced crack closure).

For non-metallic materials and composites such as glass, polymers, Portland cement concrete, and asphalt concrete mixtures, there are several other mechanisms which hinder the growth of fatigue cracks and induce crack healing, these mechanisms can be summarized as follow (Suresh, 1998):

1. Crack deflection,
2. Crack-bridging or trapping, and
3. Crack-shielding due to micro-cracking, phase transformations or dislocations.

For asphalt concrete mixtures, while a significant amount of work has documented the effect of rest periods on the fatigue life of asphalt mastics and mixtures, still little research has focused on the mechanism of healing.

Kim et al. (1990) defined two main “healing” mechanisms that occur during the rest period. One is the relaxation of stresses (time-dependent) in the system due to the viscoelastic nature of asphalt concrete, and the other is the chemical healing across microcrack and macrocrack faces. To separately evaluate chemical healing from the time-dependent effects of relaxation, the correspondence principle of nonlinear viscoelastic media was applied to asphalt concrete specimens subjected to intermittent cyclic uniaxial testing. After successfully accounting for the effects of relaxation, the authors were able to quantify the chemical healing using the concept of the healing index, which represents the healing potential of different binders at different rest times. This index is defined as the ratio of the recovered dissipated pseudo energy density following a rest period to the dissipated pseudo energy density measured prior to the rest period (FIGURE 10):

$$HI = \frac{\phi_{after} - \phi_{before}}{\phi_{before}} \quad (2)$$

where:

ϕ_{after} = dissipated PSE when the damaged sample is loaded, and

ϕ_{before} = dissipated PSE when the healed sample is loaded.

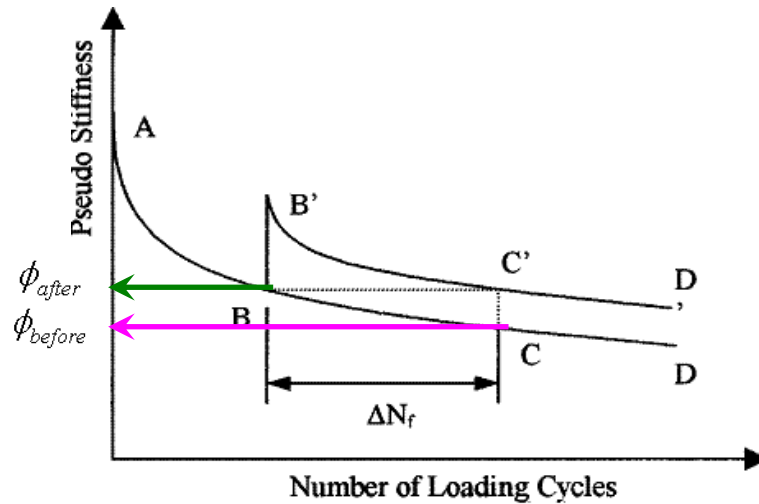


FIGURE 10 Change in pseudo stiffness before and after a rest period (Kim et., al 1990).

Phillips (1998) recently proposed that the healing of binders is a three-step process consisting of:

1. The closure of micro-cracks due to wetting (adhesion of two crack surfaces together driven by surface energy);
2. The closure of macro-cracks due to consolidating stresses and binder flow; and
3. The complete recovery of mechanical properties due to diffusion of asphaltene structures.

Step 1 is supposed to be the fastest, resulting only in the recovery of stiffness, while steps 2 and 3 are thought to occur much slower but improve both the stiffness and strength of the material such as those of virgin material.

Jacobs (1995) studied the fatigue properties of asphalt mixes under sinusoidal loading and found that the introduction of rest periods has a beneficial

effect on the fatigue resistance of the mixes. He proposed that this healing effect is caused by diffusion of maltenes (low molecular weight bitumen component) through the micro-cracks, re-establishing the bonds in the cracked area. The maltenes are involved, as they are the most mobile components of the bitumen, although higher molecular weight molecules could also diffuse during longer rest periods, resulting in completely restored material properties.

Lytton (2000) used the “dissipated pseudo strain energy concept” to explain the fracture and healing process. The fracture or healing of an asphalt mixture is related to two mechanisms: the surface energy storage, or the surface energy release. Which one dominates is related to polar or non-polar characteristic of the binder. The energy stored on or near the newly created crack faces governs the energy available to make the crack grow. This surface energy depends mainly on the chemical composition of the binder. The micro-fracture and healing of the asphalt-aggregate mixture is governed by the energy balance per unit of crack area between the “dissipated pseudo-strain energy” released and the energy that is stored on the surface of the crack.

Freund and Suresh (2003) showed that the actual fatigue behavior can be expressed as dynamic energy equilibrium between surface energy (SE) and dissipated energy (DE), can be formulated as:

$$\text{Chemical potential (healing potential)} = \text{SE} - \text{DE} \quad (3)$$

This can be clarified using the flow chart shown in FIGURE 11 Based on this equilibrium formula, the damage would occur if surface energy is smaller than the dissipated energy, i.e., the healing potential is negative, thus the material

has the tendency to increase surface energy through creating more surfaces. On the other hand, the healing would occur if the dissipated energy is at a very low level and the healing potential is positive, so the energy equilibrium leads to a decrease of surface energy, that is, some open crack surfaces will close.

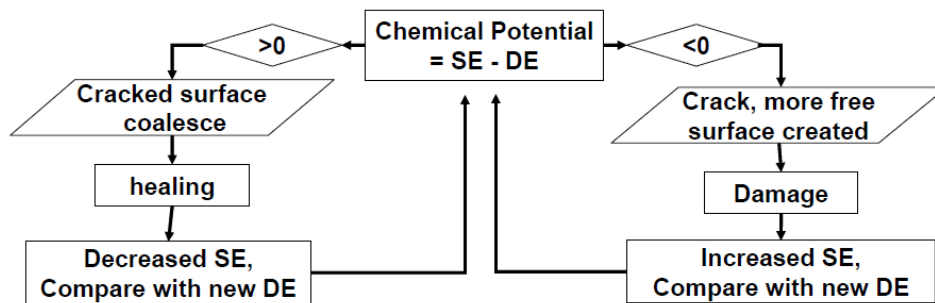


FIGURE 11 Energy equilibrium flow chart, (Shen, 2006).

2.6.2 Studies on Healing

Recently, healing of asphalt concrete mixtures became a hot research topic for the pavement engineers although it has been a well-known subject in other engineering branches, i.e., polymer and metal engineering's. Developing an improved methodology that can describe and quantify the healing of asphalt concrete mixtures would move forward towards more mechanistic design of pavement as well as more rational characterization of asphalt mixtures. Moreover, other important concepts such as endurance limit can be validated based on the healing phenomenon that is assumed to have a great influence on asphalt mixture's fatigue behavior.

As stated before, Kim et al. (1990) distinguished between mechanical healing and chemical healing. To explore both healing mechanisms, laboratory experiments to study healing have been done at the mixture level and asphalt and mastic level.

2.6.2.1 Mechanical Healing of Asphalt Mixtures

At the mixture level, there is plenty of works to investigate the healing phenomenon. Balbissi (1983) studied the effects of rest periods on the fatigue life of plasticized sulfur binders used in asphalt-like mixtures. The results indicated an increase in the fatigue life and more dissipation of energy as the number and length of the rest periods was increased. It was also indicated that although longer rest period durations tended to increase the amount of recovery, the incremental benefit was diminished as rest period duration increased above 30 minutes.

Kim (1988) used the pseudo strain concept to calculate the magnitude of pseudo strain energy that can be recovered following rest periods of various lengths. Kim found that the pseudo strain energy is substantial and dependent on the length of the rest period, the temperature of the sample during the rest period, and the chemistry and rheological nature of the binder. The fact that pseudo strain energy was used by Kim to evaluate the "healing" effects of rest periods is significant, as the use of pseudo strain allows the time-dependent, viscoelastic effects (mechanical healing) to be separated from healing of micro-cracks (chemical healing) in damage areas.

Kim and Kim (1996) performed a field study on fatigue damage growth and micro-damage healing during rest periods. The stress wave test technique and dispersion analysis method based on Short Kernel method (Douglas and Holt, 1993) employed in their study effectively assessed the changes in elastic modulus due to fatigue damage growth and micro-damage healing in asphalt surface layer. It was found that the elastic modulus decreases following a characteristic S-shape

curve when plotted against number of loading cycles. The major reduction in the elastic modulus occurred during early stage of fatigue life .when there was no visible cracks on the pavement surface. This reduction was concluded to be related to micro-crack initiation, propagation and densification. Moreover, it was found that the introduction of rest between loading cycles shifts the curve upward, resulting in a longer fatigue life.

Daniel and Kim (2001) evaluated the effect of rest periods and temperature on fatigue damage and healing potentials of two different asphalt mixtures when subjected to fatigue loading. This was accomplished using a three-point bending beam fatigue machine to induce damage. Then the impact resonance method was used to evaluate the stiffness of the specimens through cycles of damage and healing. It was considered that the impact resonance method measures the very short time or low temperature response, which is in the elastic range of a viscoelastic material. Thus, the increase in modulus after rest periods is not affected by time – dependent relaxation and is attributed to micro-crack healing in the asphalt concrete. The method used to study healing was based on a type of interrupted testing which introduced specific length of rest periods after a certain cycles of load repetition. Three groups of tests were performed: (1) testing under repetitive loading to failure at 68°F (20°C); (2) testing under repetitive loading at 68°F (20°C) with three rest periods at 68°F (20°C); and (3) testing under repetitive loading at 68°F (20°C) with three rest periods at 140°F (60°C). It was noticed that the higher healing temperature appeared to increase the amount of healing that occurred during the rest periods (FIGURE 12). The

qualitative study of the two asphalt mixtures showed a different healing potential for each mixture based on two different binder grades (AC-20 and AR-4000).

Zhang et al. (2001) used Superpave Indirect Diametral Test (IDT) with repeated load (0.1 second haversine load followed by a 0.9 second rest period) at 50°F (10°C) temperature to evaluate healing. A full 12-hour rest at an increased temperature condition 86°F (30°C) is introduced after certain amounts of load repetitions. Based on dissipated creep strain energy limit from strength test, they presented a threshold concept indicating that micro-damage is healable during rest periods and/or when temperature increases. Once the threshold of dissipated creep strain energy limit is exceeded, a non-healable macro-crack will propagate.

Si et al. (2002) performed a strain-controlled, repeated cyclic uniaxial fatigue test to evaluate the fatigue damage and healing of different asphalt concrete mixtures with two different types of both binder and aggregate by introducing a series of rest periods at 1,000 cycle intervals after the first 10,000 cycles. The test was terminated at 24,000 load cycles. The pseudo-strain concept was applied to characterize both damage and healing during the damage process. Both the pseudo-stiffness and dissipated pseudo-strain energy were adopted as they provide a clearer picture of damage by separating out the confounding effect of time dependency, viscoelastic effects from healing of micro-cracks. However, dissipated pseudo-strain energy was a strong and consistent quantifier of damage and healing. It was clear that the healing mechanism and process is complex; it was affected by the magnitude of damage prior to the rest period and hence the

amount of damage material to be healed. Furthermore, micro-damage healing is material property dependent.

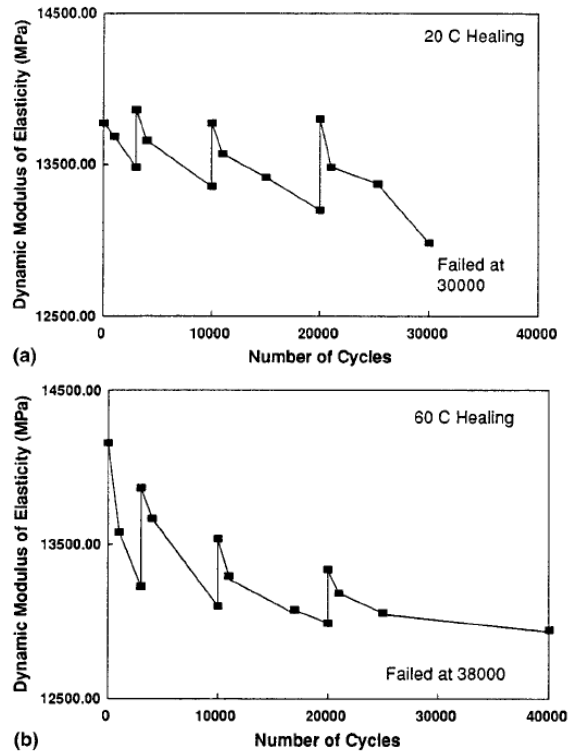


FIGURE 12 Typical dynamic modulus of elasticity through fatigue damage and rest periods: (a) 68°F healing; (b) 140°F healing (Daniel and Kim, 2001).

Seo and Kim (2008) used an Acoustic Emission (AE) to characterize the damage accumulation and strength recovery in Asphalt Concrete mixture. A series of uniaxial tensile cyclic tests with and without rest period had been conducted on a 19 mm nominal maximum size of aggregate asphalt concrete at 20 °C. During the fatigue tests, key AE parameters including emission counts were acquired from two piezo-type sensors attached to the middle of a 6-inch (150-mm) high, 3-inch (75-mm) diameter cylindrical specimen. Test results indicated that accumulative AE energy and AE count may be used not only to assess the

initiation and propagation of fatigue damage, but also to quantify the beneficial effect of rest period on the performance of asphalt concrete. The frequency-amplitude analysis showed that crack formations coincided with the peaks of maximum AE amplitude (A_{\max}) with higher frequencies, while healing is best described by A_{\max} with lower frequencies during the rest periods. In addition, it was demonstrated that the Kaiser effect, the stress dependence of AE generation, does not hold for fatigue in asphalt concrete.

2.6.2.2 Chemical Healing of Asphalt and Mastic

Usually, the term of chemical healing is used to refer to the healing of asphalt and mastic. According to Petersen (1984), the association force (secondary bond) is the main factor controlling the physical properties of asphalt cement. That is, the higher the polarity, the stronger the association force and the more viscous the fraction. Even if molecular weights are relatively low.

Kim et al. (1990) investigated the effect of asphalt composition on the healing of asphalt cement. It was proposed that the healing mechanism is related to the flow properties of the asphalt. As the longer aliphatic side chains on the various polynuclear aromatics hinder molecular structuring, allowing for greater fluidity and micellar dispersion. Based on that, healing potential was found to be directly proportional to the amounts of longer-chained aliphatic molecules in the saturates and long-chained aliphatic side chains in the naphthene aromatics, polar aromatics and asphaltenes generic fractions. The authors proposed the methylene (-CH₂) to methyl (-CH₃) ratio (MMHC) as a quantifier of the nature of the long-chained aliphatic molecules and side chains. The MMHC is defined as the ratio of

the number of methyl and methylene hydrogen atoms ($H_{-CH_2} + H_{-CH_3}$) to the number of methyl and methylene carbon atoms ($C_{-CH_2} + C_{-CH_3}$) in independent aliphatic molecules or aliphatic chains attached to cycloalkanes or aromatic centers. Based on the MMHC data, healing models were developed to correlate the Healing index, HI, to the MMHC ratio through a second order polynomial:

$$HI = -19.70 + 18.50 (MMHC) - 4.248(MMHC)^2, \quad (R^2 = 0.996) \quad (4)$$

where strain amplitude = 0.00674 unit,

and

$$HI = -11.14 + 0.82 (MMHC) - 2.529(MMHC)^2, \quad (R^2 = 0.966) \quad (5)$$

where the strain amplitude is 0.0092 units,

Bahia et al. (1999) studied the effect of rest periods on fatigue damage recovery in Dynamic Shear Rheometer (DSR) tests using various base and modified binders. In this study the asphalt specimens were tested first for 5000 cycles then it was allowed to rest for specific rest periods before testing again. The rest periods included in this work were 0.5, 3 and 12 hours. The benefit of different rest periods were evaluated by comparing the initial fatigue curve (G^* vs. number of cycles) to the second one after certain rest period. If the two curves are similar, this means that no permanent damage was occurring and the binder was fully recovered to its original status. The results confirmed that healing has a significant effect on recovery from fatigue damage and that recovery was a time dependent phenomenon and was a function of composition of the base asphalt and type of modifiers.

Kim et al. (2003) studied the effect of fatigue fracture and fracture healing during controlled-strain, Dynamic Mechanical Analysis (DMA) testing using sand asphalt samples. The sand asphalt samples were fabricated with two SHRP-classified binders: AAD-1 and AAM-1. DMA testing was performed at 77°F (25°C) and at 10 Hz. The mechanical response during dynamic mechanical analysis testing was monitored using three different damage indicators: change in dynamic modulus, change in pseudo stiffness, and change in dissipated strain energy. Dynamic mechanical analysis was found to be an effective when used to characterize the fatigue behavior and healing of asphalt binders and mastics in torsional fatigue. They reported that healing during several rest periods introduced at equal levels of damage increased the fatigue life. It was found that asphalt AAM-1 is a substantially better healer than asphalt AAD-1. This is in consistent agreement with previous studies on the fatigue and healing characteristics of these binders.

Chowdary (2004) investigated the healing of an asphalt sand mix in the laboratory. Cyclic triaxial tests were carried out on sand asphalt samples. The samples were tested at a constant load with rest periods introduced between successive loading cycles to observe the deformation response. A set of loading and rest cycles were applied and the recovery of deformation in the subsequent loading cycles after a rest period of one hour was chosen as a parameter to characterize the healing of sand asphalt mixtures. The experimental investigations and the results obtained have adequately proved the healing or beneficial deformation recovery of sand asphalt mixtures with rest periods. The amount of

healing was observed to be dependent on the magnitude of lateral pressure applied on the specimen in the triaxial test.

Shinhui et al. (2009) studied the fatigue and healing of asphalt binders using laboratory Dynamic Shear Rheometer (DSR) testing and a specifically designed intermittent loading sequence. The Ratio of Dissipated Energy Change (RDEC) approach was adopted to analyze the fatigue and healing characteristics of different asphalt binders. The test results showed that with the inclusion of 6-second rest period, the fatigue life was extended about 7 times for PG64-28 binder but 17 times for PG70-28 binder. It was proven that there was a strong correlation between healing of asphalt binder and the healing phenomenon observed in the HMA mixtures.

2.6.3 Healing Models

Schapery (1989) developed a model for healing in linear, isotropic viscoelastic materials assuming “interfacial forces of attraction and external” or applied “loading”. The inclusion of surface forces in Schapery's model is significant, accounting for the case where complete contact of the fractured surfaces is not initially achieved by dominating loading. After expanding the first principles approach to healing speed, Schapery (1989) derived a relationship between healing speed, h_2^\bullet , and several material properties including surface energy:

$$h_2^\bullet = \left[\frac{2\gamma_m E_R^2 D_{1c} \Gamma_h}{(1-\nu^2) C_m^{1/m} H_\nu} \right]^{1/mc} \beta \quad (6)$$

where:

- E_R =Reference modulus, a constant derived of the stress transformation,
- ν = Poisson's ratio,
- D_{1c} = Compressive creep compliance constant (@, is assumed to be zero),
- H_v = Healing integral,
- Γ_h = Wetting surface energy,
- m_c =Slope of compressive,
- γ_m =Creep compliance versus time, and
- C_m = Average microcrack length.

The healing rate (h_2^*) was directly related to the surface energy density, i.e., a greater surface energy density signifies a greater potential for healing, all other conditions being the same.

Lytton et al. (1998) developed a similar model to explain the healing rate between fracture surfaces. The recovery rate depends essentially on the same properties that appear in Schapery's earlier model, but a key difference is the assumption that the surface energy is an inhibitor of healing. Assuming that the surface energy is an energy density required to close a given area of crack face, the lower this surface energy density is then the greater is the amount of healing. A higher surface energy density reduces the amount of crack surface that can be closed with the same amount of available energy. Lytton derived the following relationship between "healing speed" and surface energy, among other factors:

$$h_1^{\bullet} = \left[\frac{(K_{th})E_R D_{1c} H_v}{2\Gamma_h} \right]^{1/mc} \beta \quad (7)$$

where K_{th} is a fitting constant.

Pronk (2005 and 2009) developed a model called Partial Healing (PH) model to describe the evolution of the complex stiffness modulus and phase angle during a bending test for certain loading condition as well as the healing (in complex stiffness modulus) after a rest period (FIGURES 13 and 14). The model is based on the assumption that the fatigue damage can be related to the dissipated energy per cycle. The PH model consists of two integral equations representing the evolution of the loss and storage modulus (Pronk, 2001).

$$\text{Loss modulus} = S \sin(\phi) = F\{t\} = F_0 e^{-Bt} [Cosh\{Ct\} + D Sinh\{Ct\}] \quad (8)$$

$$\text{Storage modulus} = S \cos(\phi) =$$

$$G\{t\} = G_0 - F_0 \left[\frac{\alpha_2}{C} e^{-Bt} Sinh\{Ct\} + \frac{\gamma_2}{\gamma_1} (1 - e^{-Bt}) [Cosh\{Ct\} + E Sinh\{Ct\}] \right] \quad (9)$$

in which: $B = \frac{\alpha_1 + \beta + \gamma_1}{2}$, $C = \sqrt{(B^2 - \beta\gamma_1)} \rightarrow \beta\gamma_1 = B^2 - C^2$, $D = (\beta - B)/C$, and

$$E = (B - \gamma_1)/C$$

where:

$$S = \text{Stiffness modulus,}$$

$$\phi = \text{Phase angle, and}$$

$$\alpha_1, \alpha_2, \gamma_1, \gamma_2 \text{ and } \beta = \text{Model parameter.}$$

These integrals represent the reversible (healing) and irreversible damage increase during loading. A mathematical deduction was applied for the solution to represents the case of load periods of N cycles followed by rest periods of M

cycles. It was concluded that prediction of the PH model was much better when the model parameters (α_1 , α_2 , γ_1 , γ_2 and β) were determined from a fit on the evolutions in the first and second load periods rather than using the first load period only.

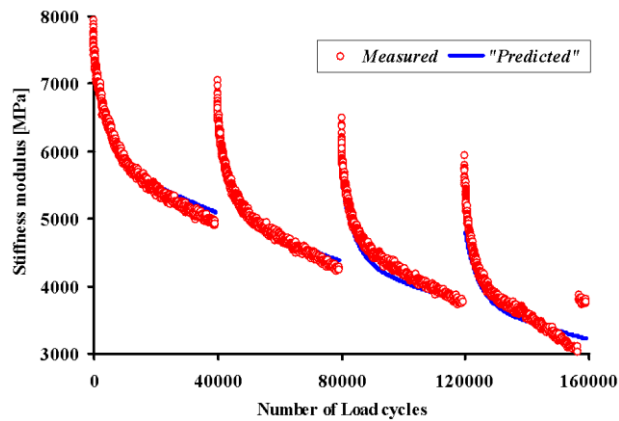


FIGURE 13 Comparison between measured and predicted stiffness moduli (Pronk, 2009).

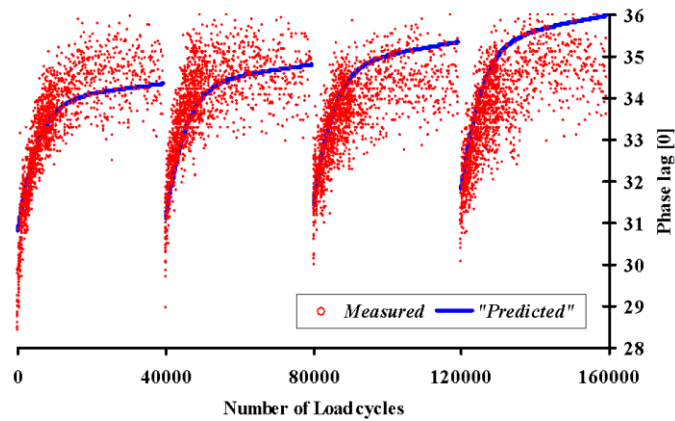


FIGURE 14 Comparison between measured and predicted phase angles (Pronk, 2009).

2.7 Characterization of HMA Fatigue Behavior

There are two main approaches that can be utilized to characterize the fatigue behavior of asphalt concrete mixtures: Phenomenological and mechanistic. The Phenomenological approach is simple to use, however, it does not account for damage evolution through the fatigue process. On the other hand, mechanistic approach is inherently more complex than the Phenomenological one but it is more widely accepted because it uses material properties based on stress-strain relationships (Kim et al., 2003). The mechanistic approach can be implemented through any of the followings:

- Dissipated energy,
- Fracture mechanics, and
- Continuum damage mechanics.

2.7.1 Phenomenological Approach

The phenomenological approach usually relates the stress or strains in the Hot Mix Asphalt (HMA) layer to the number of load repetitions that cause failure (SHRP A-404, 1994). It is a combination of the phenomenological observation and the laboratory- tabulated data derived from designated fatigue tests.

This approach has been widely used with Miner's (1945) linear law of cumulative damage in conventional asphalt pavement design and performance analysis. The damage is calculated as the ratio of the predicted number of traffic repetitions to the allowable number of load repetitions (to some failure level) as shown in Equation 10. Theoretically, fatigue cracking should occur at an accumulated damage value of 1.0. If a normal distribution is assumed for the

damage ratio calculated, the percentage of area cracked can be computed and checked with field performance.

$$D = \sum_{i=1}^T \frac{n_i}{N_i} \quad (10)$$

where:

D = damage.

T = total number of periods.

n_i = actual traffic for period i.

N_i = allowable failure repetitions under conditions prevailing in period i.

Results from fatigue test can be formulated depending on the mode of loading: stress or strain loading mode. Pell (1967) demonstrated that the tensile strain is more important parameter for fatigue cracking. He introduced the approach to relate the initial strain to load repetition, even in controlled stress mode of testing, as shown in follows:

$$N_f = K_1 \left(\frac{1}{\epsilon_o} \right)^{k_2} \quad (11)$$

where:

N_f = number of load applications to fatigue failure;

ϵ_o = tensile strain;

k_1, k_2 = material regression constants from the lab testing.

Because of the phenomenological nature of this relationship, some have proposed applying adjustments to this relation to obtain a “better fit” with observed

behavior differences. Bonnaure et al. (1980) and Finn et al. (1977) noted differences in the coefficients of this equation for different temperatures. They proposed a fatigue formula using modulus as follows:

$$N_f = K_1 \left(\frac{1}{\varepsilon_o} \right)^{k_2} \left(\frac{1}{E} \right)^{k_3} \quad (12)$$

where:

E = stiffness of the material;

k_1, k_2, k_3 = material regression constants from the lab testing.

As a drawback of the phenomenological approach, it doesn't provide a mechanism of damage accumulation in the mixture under the repetitive load. Furthermore, the accumulation of damage is treated as linear in the strain-fatigue life relationship which has been found incorrect at low strain/damage condition (Carpenter et al., 2003). Because it is material and loading mode dependent, this approach cannot be applied directly to the complex loading scenarios that are actually common to in-service pavements, the traditional phenomenological approach also does not account for the complexity of asphalt mixture mechanism such as healing and stress redistributions, which are known to have significant effect on fatigue behavior of asphalt mixtures (Shen, 2006).

These basic models have served as the framework for various agencies in calibrating these models to their specific pavements and mixtures. Carpenter (2006) presented most common fatigue models used by several agencies. Followings are some of the well-known fatigue models used by national and international agencies as well:

2.7.1.1 Illinois DOT / University of Illinois Model

Elliott and Thompson (1986) used both deflection-based performance equations from the AASHO road test at two Present Serviceability Index (PSI) to estimate the value of the k_3 coefficient. These two equations are based on the spring normal Benkelman beam deflection. They developed an algorithm that relates load repetitions to failure with the surface deflection:

$$N_{18} = 5.6 \times 10^{11} / \Delta^{4.6} \quad (13)$$

where:

N_{18} = Number of 18-kip loads to fatigue failure, and

Δ = Surface deflection (mils) for 18-kip axle load (Benkelman Beam).

This relation was substituted in the fatigue equation and the final estimate of the k_2 coefficient was established for each equation. Values of the k_2 and k_3 coefficients were used with the road test data and the design algorithm for asphalt strain to calculate an average K_1 value. On this analysis, the following fatigue model was developed by Elliot and Thompson (1986):

$$\text{Log } N = 2.4136 - 3.16 \times \text{Log } \epsilon - 1.4 \times \text{Log } E_{ac} \quad (14)$$

where:

N = number of load repetitions to cracking,

ϵ = predicted AC strain (in/in), and

E_{ac} = AC dynamic stiffness modulus (psi).

The typical fatigue relation used by the Illinois Department of Transportation, from Thompson (1987) is:

$$N_f = 5 \times 10^{-6} \left(\frac{1}{\varepsilon} \right)^{3.0} \quad (15)$$

2.7.1.2 SHRP A-404 Model

An accelerated performance test for defining the fatigue response of asphalt-aggregate mixes and their use in mix analysis and design systems was developed in SHRP A-404 (1994). The effect of the following variables on fatigue performance of asphalt concrete mixtures was investigated in this study: asphalt type (8 types), aggregate type (2 types), asphalt content, air-void content (2 levels), strain levels (2 levels), replicates (2 replicates), frequency (10 Hz), and test temperature (68°F). Based on the experiment, the following model was obtained:

$$N_f = 466.4e^{0.052VFB} (\varepsilon_0)^{-3.948} (S_0)^{-2.270} \quad (16)$$

where:

N_f = fatigue life,

ε_0 = initial strain (in/in),

S_0 = initial loss stiffness (psi), and

VFB = percentage of voids filled with bitumen.

2.7.1.3 The Asphalt Institute Model

The fatigue relation for the Asphalt Institute (AI) was developed based on laboratory fatigue data for selected sections of the AASHO road test by Asphalt Institute (1982), and Finn et al. (1977). The following fatigue relation was developed by the Asphalt Institute 1982:

$$N_f = 18.4 \times (C)(4.325 \times 10^{-3})(\epsilon_t)^{-3.291}|E^*|^{0.854} \quad (17)$$

where:

N_f = number of 18,000 lb equivalent single axle loads

ϵ_t = tensile strain in asphalt layer, (in/in)

$|E^*|$ = asphalt mixture dynamic modulus (psi)

C = function of volume of both voids and asphalt

$$C = 10^M \quad (18)$$

where:

$$M = \left(\frac{V_b}{V_v + V_b} - 0.69 \right)$$

V_b = volume of asphalt, percent

V_v = volume of air voids, percent

2.7.1.4 SHELL Pavement Design Manual Model

The SHELL fatigue criterion is based on strain and modulus. The following formula is used to predict fatigue life from Shell (1978):

$$N = 4.91 \times 10^{-13} (0.86 V_b + 1.08)^{5.0} (1/\epsilon)^{5.0} (1/S_{mix})^{1.8} \quad (19)$$

where:

N = number of load cycles to failure,

V_b = volume of asphalt in the mixture (%),

ϵ = maximum tensile asphalt concrete strain, (in/in), and

S_{mix} = dynamic modulus of the asphalt mixture, (ksi).

2.7.1.5 Transport and Road Research Laboratory – TRRL United Kingdom Model

The TRRL fatigue criterion was developed after TRRL report 1132, Powell et al, (1984), and is based on the field performance of 34 sections of experimental road with dense base macadam and 29 sections of experimental rolled asphalt base. A multi-layer elastic model was used to calculate the dynamic strains. The accumulation of fatigue damage was calculated based on Miner's hypothesis. Considerable adjustment was needed to correlate between laboratory fatigue relations and field performance.

The design life could be calculated using the following relationships:

For 85% probability of survival and an equivalent temperature of 20° C (68° F):

For dense bitumen macadam (100 pen.):

$$N_f = (4.169 \times 10^{-10})(1/\epsilon_r)^{4.16} \quad (20)$$

For hot rolled asphalt (50 pen.):

$$N_f = (1.660 \times 10^{-10})(1/\epsilon_r)^{4.32} \quad (21)$$

where:

N_f = the road life in standard axles, and

ϵ_r = the horizontal tensile strain at the underside of the bound layer

under a standard wheel load.

2.7.1.6 PDMAP – NCHRP Project 1-10B

The PDMAP program (Probabilistic Distress Models for Asphalt Pavements) was developed to enable the highway engineers to predict distress conditions of given pavement sections. The PDMAP program employs probabilistic analysis, which computes the expected amount of damage with

specified reliability factor at any time during the analysis period, Finn et al. (1977).

The prediction model for fatigue cracking used in PDMAP is based on the fatigue testing done by Monismith et al. (1970) as follows:

$$\text{Log } N_f = 14.82 - 3.291 \text{ Log } (\varepsilon/10^{-6}) - 0.854 \text{ Log } (|E^*|/10^3) \quad (22)$$

where:

N_f = load applications of constant stress to cause fatigue failure;

ε = initial strain on the bottom of the asphalt concrete;

$|E^*|$ = complex modulus (psi).

Cracking and rutting observations from the AASHO Road Test were used to calibrate the above equation. A shift factor of 13 was used for the 10 percent cracking and 18.4 for the 45 percent cracking.

2.7.1.7 NCHRP 1-37A Calibrated Fatigue Model

This model contains significant modifications to the standard form of the fatigue equation, but still relies on the basic strain-modulus form. Because thick and thin pavements exhibit different behavior when analyzed with the standard phenomenological model, changing from constant strain in a thin pavement to constant stress in a thick HMA layer, the 1-37A research team elected to add a variable to change coefficients as the HMA layer becomes thicker. This model takes its basic form from the Asphalt Institute equation.

An extensive calibration process using field data and LTPP sections was conducted to establish the coefficients for different mixtures and different parts of

the United States. The final form of the model from El-Basyouny and Witzcak, (2005) is:

$$N_f = \beta_{f1} k_1 (\epsilon_t)^{-\beta_{f2} k_2} (E)^{-\beta_{f3} k_3} \quad (23)$$

where:

N_f = Number of load repetitions to fatigue failure,

ϵ_t = tensile strain at the critical location,

E = the dynamic modulus of the HMA,

k_1, k_2, k_3 = Laboratory regression coefficients, and

$\beta_{f1}, \beta_{f2}, \beta_{f3}$ = Calibration parameters.

Basically, the exponents, k_2 and k_3 , are constants, and the coefficient k_1 contains the mixture variables. Other coefficients are included for constant stress to constant strain considerations. The calibration parameters are designed to reduce the bias and scatter in the prediction.

2.7.2 Mechanistic Approach

Mechanistic approach could explore the mechanisms of fatigue behavior on a more fundamental basis than the phenomenological approach. The dissipated energy, the fracture mechanics and the continuum damage mechanics methods may be categorized into a mechanistic approach to study the characteristics of asphalt concrete.

2.7.2.1 Dissipated Energy

When applying load to a material, the material will exhibit some stain induced by the acting stress. The area under the stress-strain curve represents the energy being input into the material. When the load is removed from the material,

the stress is removed and the strain is recovered as shown in FIGURE 15. If the loading and unloading curves coincide, all the energy put into the material is recovered after the load is removed. If the two curves do not coincide, there is energy lost in the material. This energy can be altered through mechanical work, heat generation, or damage in the material in a manner that it could not be used to return the material to its original shape. This energy difference is the dissipated energy of the material caused by the load cycle (Ghuzlan, 2001). So, dissipated energy can be defined as the damping energy or the energy loss per load cycle in any repeated or dynamic test.

The equation for calculating dissipated energy per cycle in a linear viscoelastic material in the flexural fatigue test is given by the following equation (Tayebali et al., 1994):

$$\omega_i = \pi \sigma_i \epsilon_i \sin \phi_i \quad (24)$$

where:

ω_i = Dissipated Energy at load cycle i ,

σ_i = Stress at the load cycle i ,

ϵ_i = Strain at the load cycle i , and

ϕ_i = Phase angle between stress and strain at load cycle i .

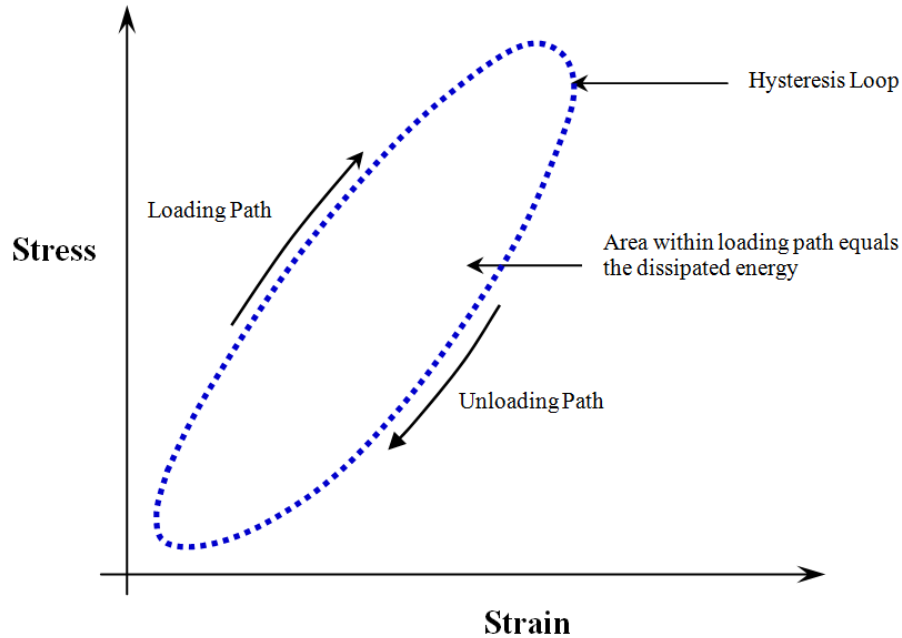


FIGURE 15 Stress-strain curve for viscoelastic solid.

Current applications of dissipated energy to describe fatigue behavior assume that all of the dissipated energy goes into damaging the material (Ghuzlan, 2001). In reality, this is not the case for asphalt concrete as a hysteresis loop is created due to the viscoelasticity of the material, even if no induced damage. Only part of the total dissipated energy goes to damaging the material, and the remainder is due to viscoelasticity and other factors.

It was experimentally demonstrated by Manfredi (2001) that energy dissipated during plastic cycles at low amplitude, without induced damage, will not contribute to damage and should be excluded from the total energy when damage is considered. It was observed for viscoelastic materials to have a capacity to store and dissipate mechanical energy. Subsequently, when sustaining external loading, part of the dissipated mechanical energy can be converted into thermal

energy through viscoelastic damping, therefore reducing material fatigue damage (Hilton and Yi, 1992). As a source of released energy, this part of dissipated energy won't create fatigue crack propagation and should be eliminated from the total dissipated energy calculation for predicting fatigue failure.

It was found in a study conducted by Van Dijk and Visser (1977) that the fatigue behavior under different dynamic tests, sets of conditions for different mixes can be described by a single mix specific relationship. This relationship is the number of the cycles to fatigue failure related mainly to the amount of energy dissipated during the fatigue test. All the factors including rest period, mode of loading, temperature, and frequency, did not significantly influence the dissipated energy relationship. They reported that the slopes of the lines representing different mixes are nearly the same and similar to the 0.67 slope suggested by Chomton and Valayer (1972). On the other hand, some of the researcher found that this relationship was mix dependent (Van Dijk et al., 1972; and SHRP A-404, 1994). The University of California at Berkley study (SHRP-A-404, 1994) reported that all lines are not parallel and have different slopes. Based on previous dissipated energy studies on fatigue life of asphalt concrete mixtures, various representations and applications were proposed as indicated below:

a. Initial Dissipated Energy Approach

Initial Dissipated Energy (IDE) is the dissipated energy measured at initial loading cycles which is usually, the dissipated energy at the 50th loading cycle. Initial dissipated energy can be a good indicator of fatigue performance for similar mixture type. It was found by Ghuzlan (2001) that the initial dissipated energy is

one of the most important factors that affect HMA's fatigue behavior. SHARP A - 404 (1994) used the following surrogate model to relate the initial dissipated energy to fatigue life:

$$N_f = 6.72 e^{0.049 \text{ VFB}} (w_o)^{-2.047} \quad (25)$$

where:

N_f = design life,

VFB = percentage of voids filled with bitumen, and

w_o = initial dissipated energy.

One disadvantage of the initial dissipated energy approach is that it is not appropriate for the whole loading range. Especially when dealing with low strain fatigue test (Carpenter and Shen, 2005 and 2006). It is also doesn't account for the effect of healing.

b. Cumulative Dissipated Energy Approach

The cumulative dissipated energy is the summation of all dissipated energy per cycle and is defined by the following equation:

$$W_N = \sum_{i=1}^{N_f} \pi \sigma_i \epsilon_i \sin \phi_i \quad (26)$$

A relationship between the cumulative dissipated energy and the number of the loading cycles is characterized as:

$$W_N = A (N_f)^Z \quad (27)$$

where:

W_N = cumulative dissipated energy to failure,

A, Z = experimentally derived mix coefficients, and

N_f = number of load cycles to failure.

It was concluded by Van Dijk (1975 and 1977) that there was a strong relationship between the cumulative dissipated energy and the number of loading cycles to failure. This relationship is not affected by the loading mode, the effect of frequency (between 10 and 50 Hz), temperature (between 50 and 104 °F), and the occurrence of rest periods where it is highly material dependant.

c- Work Ratio Approach

This approach was first introduced by Van Dijk and Visser (1997) and further developed by Rowe (1993). The work ratio, ψ_{N1} , is defined as the ratio between the products of the initial dissipated energy in cycle 1 and $N1$ divided by the cumulative dissipated energy, as shown in Equation 28:

$$\psi_{N1} = \frac{w_0 N1}{W_{N1}} \quad (28)$$

where:

w_0 = initial dissipated energy;

$N1$ = number of load cycles to crack initiation;

W_{N1} = cumulative dissipated energy at cycle $N1$.

Rowe (1993) found that the work ratio can be used effectively to predict the fatigue life to crack initiation through Equation 23. The crack initiation is assumed to occur at 60% reduction of original extensional complex modulus as shown in Equation 29.

$$N1 = 205 V_b^{6.44} w_0^{-2.01} \psi_{N1}^{1.64} = \quad (29)$$

where:

$N1$ = number of load cycles to crack initiation,

V_b = volume of binder (%),

w_0 = initial dissipated energy, and

Ψ_{N1} = work ratio.

d. Dissipated Energy Ratio Approach

Tayebali et al. (1992) introduced two terms: the stiffness ratio which is the ratio of stiffness at load cycle (i) to the initial stiffness; and the dissipated energy ratio which is defined as the ratio of the cumulative dissipated energy up to load cycle (i) to the cumulative dissipated energy. It was suggested by him that there is a unique relationship between the stiffness ration and the dissipated energy ratio, but not necessarily between cumulative dissipated energy and fatigue life which is also verified by SHRP A-404 (1994). This relationship was found to be mix and temperature dependent.

Carpenter and Jansen first initiated an improved implementation of the dissipated energy concept for HMA fatigue analysis, in which a dissipated energy ratio was used as a parameter to relate to fatigue life (Carpenter and Jansen, 1997). This approach believes that not all the dissipated energy is responsible for material damage. For each cycle, the loss of energy due to material mechanical work and other environmental influence remains almost unchanged. Therefore, if the dissipated energy starts to change dramatically, it could be explained as the development of damage. Later, this approach was examined and refined by Ghuzlan and Carpenter (Ghuzlan and Carpenter, 2000; Ghuzlan, 2001; and Carpenter et al., 2003). It is found that the relationship between dissipated energy

ratio and fatigue life is fundamental as it is independent of loading level, loading mode, and mix type (Carpenter et al., 2003).

e. Ratio of Dissipated Energy Change Approach

The dissipated energy ratio (DER) approach was further improved by Shen (2006) and was renamed as the ratio of dissipated energy change (RDEC) approach considering the fact that it is using the ratio of the amount of dissipated energy change between different loading cycles to represent the damage propagation. The ratio of dissipated energy change is defined as the average change in dissipated energy between two cycles divided by the dissipated energy from the first of the two cycles (NCHRP 9-44, 2008):

$$\text{RDEC}_a = \frac{(\text{DE}_a - \text{DE}_b)}{(b - a) \times \text{DE}_a} \quad (30)$$

where:

RDEC_a = ratio of dissipated energy change for cycle a,

DE_a = dissipated energy for cycle a, and

DE_b = dissipated energy for cycle b.

The basic premise of this approach is that the change in dissipated energy per cycle of loading is related to the growth of damage that occurs in HMA for a given mixture a plot of the ratio of dissipated energy change as a function of loading cycles forms a broad “U” shape as shown in FIGURE 16. Lower plateau values (PV) imply lower damage per cycle. The plateau value for a given mixture depends on the mixture properties, the applied strain level, and the duration of rest periods. Plateau values decrease with decreasing applied strain and increasing rest period duration (Carpenter and Shen, 2006).

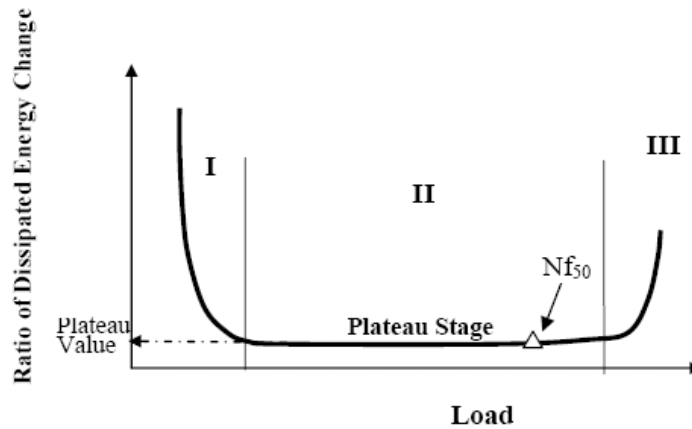


FIGURE 16 Typical ratio of dissipated energy change versus loading cycles plot, (Carpenter et al., 2003).

The distinctiveness of the RDEC approach is the relationship between the energy parameter, plateau value (PV), and the fatigue life (N_f). This relation, as presented in Equation 31, is unique for all HMA mixes, all loading modes (controlled stress and controlled strain), all loading levels (normal and low damage levels), and various testing conditions (frequency, rest periods, etc.) (Shen, 2006).

$$N_f = 0.4801(PV)^{-0.9007} \quad (31)$$

Furthermore, a preliminary PV prediction model was developed by Shen and Carpenter (2007) based on material properties and load response. The PV prediction model was constructed with a regression R^2 of 0.9017 and a standard error of estimate of 0.3437, as shown in Equation 32.

$$PV = 2.612 \times 10^{-10} IDE^{2.758} S^{2.493} VP^{3.055} GP^{-2.445} \quad (32)$$

where:

IDE = the initial dissipated energy,

ϵ = tensile strain, in/in,

S = the flexural stiffness of HMA mix from the laboratory fatigue test,
Mpa,

$$VP = \text{volumetric parameter } VP = \frac{AV}{AV + V_b},$$

AV = air voids %,

V_b = the asphalt content by volume,

$$GP = \text{the aggregate gradation parameter } GP = \frac{P_{NMS} - P_{PCS}}{P_{200}},$$

P_{NMS} = percent of aggregate passing the nominal maximum size sieve,

P_{PCS} = percent of aggregate passing the primary control sieve, and

P_{200} = percent of aggregate passing #200 (0.075mm) sieve.

2.7.2.2 Fracture Mechanics

Considering fatigue as a process of cumulative damage, fracture mechanics principals were utilized by several researchers to investigate cracking of paving mixtures. In this approach, fatigue cracking was characterized into three stages: crack initiation, stable crack propagation, and unstable crack fracture. It is usually assumed that the stable crack propagation consumes most of the fatigue life. The prediction of crack propagation life using fracture mechanics can be described by the well-known Paris' law (Paris and Erdogan, 1963):

$$\frac{dc}{dN} = A(\Delta K)^n \quad (33)$$

where:

dc/dN = crack propagation rate per load cycle,

N = number of loading repetitions,

C = crack length,

ΔK = stress intensity factor range during loading and unloading, and

A, n = material parameters.

Integration of the Paris equation between initial crack length, c_o , and critical crack length, c_f , gives the fatigue life (*Liang and Zhou, 1997*).

$$N_f = \int_{c_o}^{c_f} \frac{dc}{A(\Delta K)^n} \quad (34)$$

Schapery (1973) theoretically justified the use of Paris' law for the description of the crack growth process in viscoelastic material and presented a relationship between crack growth velocity and material properties such as the creep compliance, tensile strength and fracture energy to determine A and n on Paris' equation. Germann and Layton (1979) found that the calculated values of A and n agree fairly well with those determined experimentally for high asphalt content samples. However, at lower asphalt content, the theoretical and experimental values differ significantly. It has been stated that although Schapery's analysis may be applicable in some instances, it has not been widely accepted. Even if the constants A and n can be related to some material properties as Schapery suggested they are still used in a power law relationship which at best can only describe a linear region of fatigue crack propagation, i.e. it will not describe fatigue crack propagation over the entire range of the crack driving force (*Aglan and Figueroa, 1991*). Majidzadah et al. (1972) stated that, at all temperature for sand-asphalt and asphalt concrete beams, A in Paris' law becomes

a material constant. However, at higher temperature, A and n can no longer be considered as a material constant.

According to fracture mechanics theory, three possible fracture modes can be identified. These modes are Mode I-opening and closing mode (tension), Mode II-Shear sliding mode (shear), and mode III-Tearing mode (torsion). These different modes are shown in FIGURE 17. For thermal cracking of pavement materials, normally, Mode I is predominant. For fatigue cracking induced by traffic loads, normally, mode I and II could be considered to occur. Knowing that, under mode I, cracks would never propagate to the surface of the pavement and, consequently, Mode II solutions were generated for load associated fatigue crack propagation analysis.

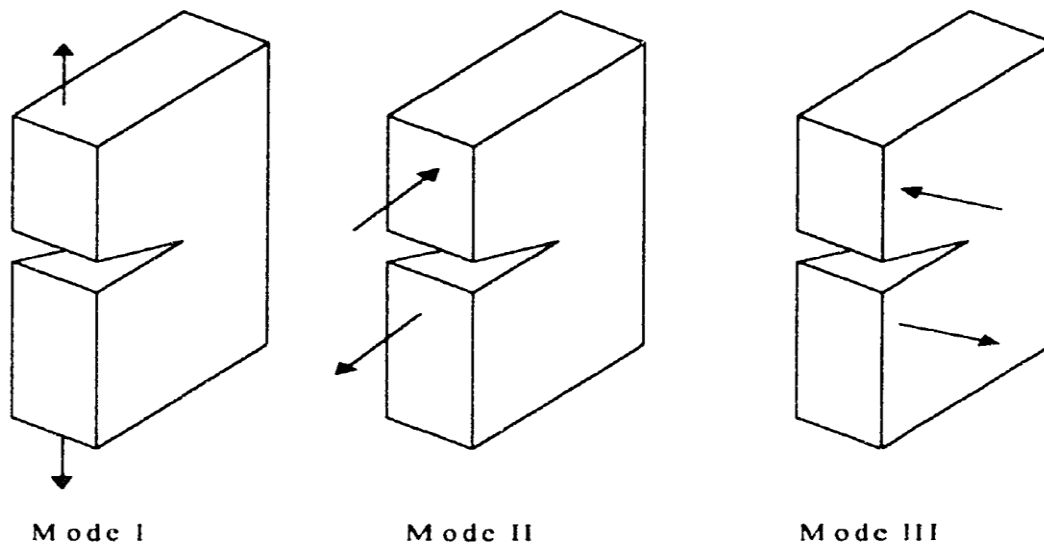


**FIGURE 17 The three modes of loading to describe crack growth,
(Anderson, 1995).**

Jacobs et al. (1996) investigated the applicability of fracture mechanics to asphalt concrete and showed that a crack in asphalt concrete grows discontinuously, indicating the limitation of the fracture mechanics approach for asphalt concrete (In linear elastic fracture mechanics, the crack propagates continuously). It was pointed out that the discontinuous crack propagation could be due to the inhomogeneity of asphalt concrete. Still, the measured discontinuous crack growth was treated as a continuous single crack in case the comparison was based on the maximum normal stresses occurring during the fracture process. Thus, the fracture mechanics principle was applied to describing the crack growth process. With finite element analysis, Jacobs found a relationship between the A and n value, as follows:

$$\log A = a + bn \quad (35)$$

where

a, b = regression parameters.

This relationship is important for practical purpose as Schapery (1973 and 1978) demonstrates that n-values could be estimated by using simple test instead of time money consuming fatigue and crack growth test.

The constant K represents the proportion in which the stress approaches infinity and completely defines the crack tip stress conditions. The stress intensity factor in the Paris' law can be replaced by the energy release rate J-integral. Many researchers have successfully calculated the energy dissipation with finite element methods instead of measuring the stress intensity factor from laboratory

specimens. Therefore, Paris' law fracture parameters A and n could be derived directly from the energy approach (Chen, 1997; and Si, 2001).

2.7.2.3 Continuum Damage Mechanics

Asphalt concrete is a history-dependent composite material. Therefore, accurate prediction of its behavior under realistic traffic loading conditions requires the application of the theory of viscoelasticity. To develop a realistic mechanistic model for asphalt concrete undergoing damage, the viscoelasticity and damage growth should be considered in the constitutive modeling.

In general, a continuum damage model consists typically of three major components:

- Selection of damage variables,
- Definition of strain energy density (as a function of damage variables and other state variables), and
- A damage evolution law.

If the model considers only fixed damage, the evolution law is not needed (Park et al., 1996).

A Continuum Damage Mechanics Approach (CDM) developed through research efforts at North Carolina State University and Texas A&M University. This approach utilizes the viscoelastic correspondence principle and Work Potential Theory (WPT) described by Schapery (1984) to remove viscous effects in monitoring changes in pseudo-stiffness in repeated uniaxial tensile tests. Therefore, physical variables were replaced by pseudo variables based on the extended elastic-viscoelastic correspondence principle to transform a viscoelastic

(linear and/or nonlinear) problem to an elastic case. Schapery (1990 and 1991) developed a series of damage models for elastic and viscoelastic media based on thermodynamics of irreversible process and work potential theories with internal state variable to describe evolution of micro-structural changes. The theories developed have been successfully employed to asphalt concrete mixtures (park et al., 1996).

Kim (1988) developed a nonlinear elastic-viscoelastic uniaxial constitutive model in his Ph.D. work by employing the extended elastic-viscoelastic correspondence principle in the concept of continuum damage mechanics that successfully accounted for damage growth through crack initiation and propagation and healing for any load history or mode of loading (Kim et al. 1997a, b). The major difference in Kim's approach from the dissipated energy approach stems from the recognition of the fact that the energy dissipation under cyclic loading is not only related to the damage growth, but also due to linear viscoelastic time-dependency of asphalt concrete. The damage-independent viscoelastic time dependency was eliminated by the extended elastic-viscoelastic correspondence principle and additional time dependency due to non-linear damage was used to develop the damage-induced viscoelastic constitutive relations. All response of asphalt concrete specimens under fatigue loading was assigned to three mechanisms (Kim et al., 1998): fatigue damage growth, time-dependence due to the viscoelastic nature of the material, and chemical healing across micro-cracks and micro-cracks interfaces.

Pseudo strain relation for viscoelastic body with damage and without temperature change can be identified by Equation 36.

$$\sigma = C(S_m)\varepsilon^R \quad (36)$$

where

σ = stress,

ε^R = pseudo strain,

S_m = internal state variable of damage, and

$C(S_m)$ = internal function of damage.

More recently, *Lee (1996)* extended Kim's work and developed a more generalized uniaxial constitutive fatigue model for asphalt concrete mixtures. The resulting model by Lee can predict damage growth and recovery due to compound loading histories, in both controlled-strain and controlled-stress modes, composed of randomly applied multi-level loading with different loading rates and varying rest periods. The general form of the general uniaxial pseudo variable constitutive equation for a viscoelastic body during damage can be expressed as follows (Kim, 2003):

$$\sigma = I_p C(S_m)\varepsilon^R \quad (37)$$

where

I_p = initial pseudo-stiffness.

The constitutive model seems to be an elastic model due to the use of pseudo variable and accounts for the response of the viscoelastic body and damage by a C function. The C function is then specially categorized into three

selected functions in the following constitutive equation that was developed by Kim et al. (1997a):

$$\sigma = I_p(\varepsilon^R)[F + G + H] \quad (38)$$

where:

F = damage function representing the change in the slope pseudo stiffness of each σ - ε^R loop,

G = hysteresis function representing the different between loading and unloading paths, and

H = microdamage healing function representing the change in secant pseudo-stiffness due to rest periods.

The damage function F is responsible for algebraically reducing the predicted stress evolved in the specimen during uniaxial fatigue loading and its counterpart for the healing regime of the test, H, accounts for the recovery during rest periods and the adjustment of the predicted stress levels thereafter. This constitutive model is capable of accurately predicting fatigue behavior of asphalt concrete under (1) constant-strain-rate monotonic loading; and (2) controlled-strain and controlled-stress cyclic loading.

Christensen and Bonaquist (2005) developed an approximate method to analyze the beam fatigue data using the continuum damage approach where damage estimates were based upon stresses and strains in the middle third of the beam but were applied to the entire beam. In this analysis, the beam was divided into ten equal layers from top to bottom, each 0.2-in. thick. The loading history is divided into ten logarithmically spaced intervals; damage is calculated during each

of these intervals for each beam layer, and then a new modulus value is calculated for the following loading interval, as described below in FIGURE 18. It was observed that the relationship between the damage ratio at the beam's lower surface and the overall flexural stiffness damage ratio, throughout the progress of a flexural fatigue test remained essentially constant regardless of the assumed material properties. So, this relationship was used to perform a continuum damage analysis using flexural fatigue data as opposed to uniaxial fatigue, by converting overall beam stiffness to pseudo-stiffness for the lower beam surface.

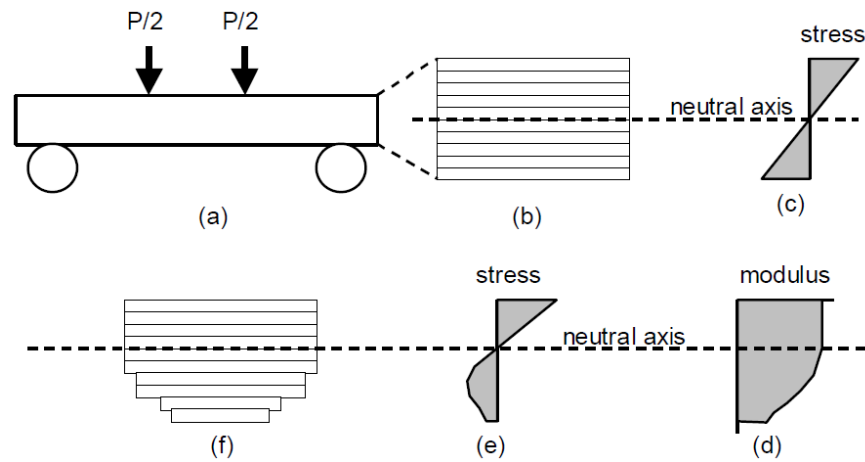


FIGURE 18 Continuum damage analysis of flexural fatigue (Christensen and Bonaquist, 2005).

In a parallel effort, Mello et al. (2009) successfully applied the continuum damage model to beam fatigue test. The damage parameter expression was used followed the same expression that Daniel (2001) proposed where the time intervals was corrected to account only for the time period during which the sample is under tension in haversine loading tests. In case of binding tests with

harmonic loading, the tension time is corresponding to only half of the total cycle time, as illustrated in FIGURE 19. Based on this, the expression to obtain the damage parameter from 4PB tests was obtained by accounting only to that time.

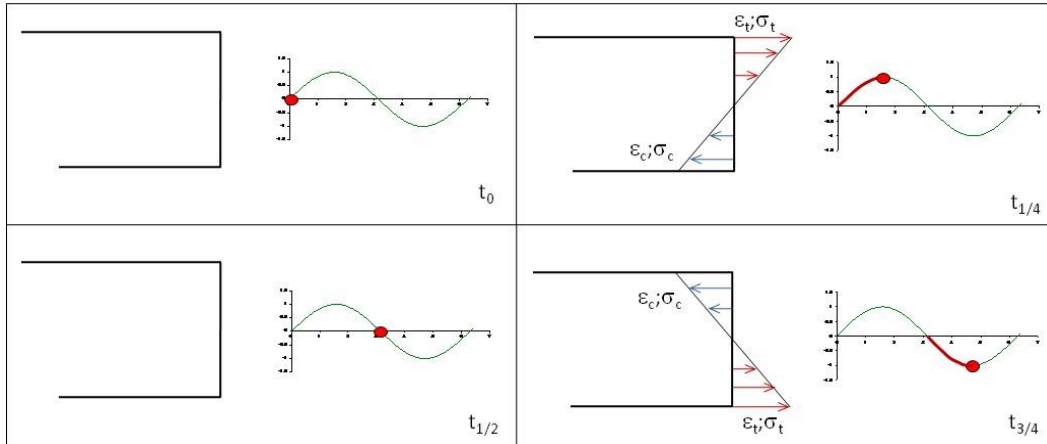


FIGURE 19 Stresses and strains in a transverse section of a beam subjected to a harmonic sine loading, (Mello et al., 2009).

2.8 Fatigue Endurance Limit of HMA

The concept of the Endurance Limit (EL) was originally introduced in for metals in 1870 by Wöhler (Walter Schlitz, 1996) and was defined as stress level below which failure never occurs, even for an indefinitely large number of loading cycles. Ferrous alloys and titanium alloys have a distinct limit, amplitude below which there appears to be no number of cycles that will cause failure. Other structural metals such as aluminum and copper do not have a distinct limit and will eventually fail even from small stress amplitudes (FIGURE 20). An effective endurance limit for these materials is sometimes defined as the stress that causes failure at 1×10^8 or 5×10^8 loading cycles.

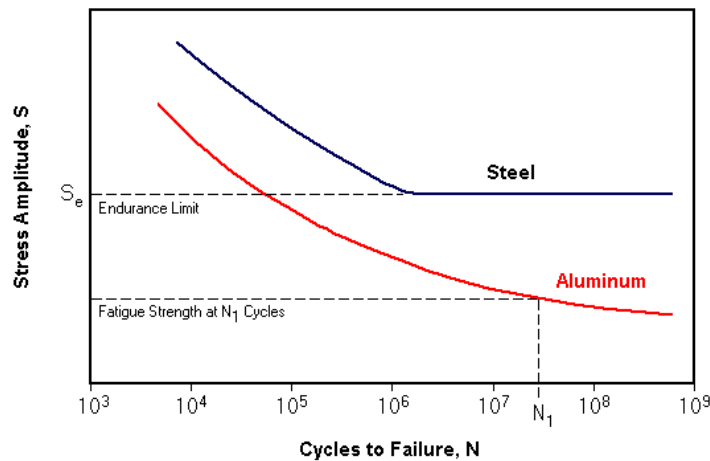


FIGURE 20 Typical S-N curve.

2.8.1 Definition of HMA Endurance Limit

The fatigue EL is a critical concept in the design of pavement structures that must resist large numbers of repeated loads. If the actual stress or strains level applied to the pavement are kept below the endurance limit, the structure will be able to withstand an infinite number of load applications. Based on a review of recent literature concerning the fatigue response of HMA, and recommendations

made through the NCHRP 9-44 project, a more formal definition of the endurance limit has been proposed as “A level of strain below which there is no cumulative damage over an indefinite number of load cycles”. It has been hypothetically assumed that “HMA does exhibit an endurance limit”. This endurance limit, however, does not reflect an absence of load induced damage in the HMA. It is the result of a balance of damage caused by loading and healing or damage recovery that occurs during rest periods. The endurance limit for HMA is, therefore, not a single value, but will change depending on the material properties, loading and environmental conditions applied to the HMA.

2.8.2 Importance of Endurance Limit in Perpetual Pavement Design

Asphalt Pavement Alliance, APA, has defined a perpetual pavement as “*an asphalt pavement designed and built to last longer than 50 years without requiring major structural rehabilitation or reconstruction, and needing only periodic surface renewal in response to distresses confined to the top of the pavement*” (APA, 2002). Ferne (2006) expanded upon this idea and define the perpetual pavement through its life as “*an asphalt pavement well-designed and constructed pavement that could last indefinitely without deterioration in the structural elements provided it is not overlooked and the appropriate maintenance is carried out*”. Therefore, the performance of perpetual pavements is not a function only of the design but also traffic, climate, subgrade and pavement parameters (such as modulus), pavement materials, construction, and maintenance levels. These factors all combined will contribute to how a pavement will perform over the course of its life (Walubita et al., 2008). Other expressions

such as “long-life”, “long-lasting”, and “extended life” have also been used to describe the perpetual pavements.

Recently, pavement engineers have begun to introduce methodologies of designing pavements to resist rutting and bottom-up fatigue cracking which are the two main pavement distresses seen on roadways. For perpetual HMA pavements, subgrade stress/strain levels are generally within acceptable limits and subgrade permanent deformations are not significant. Therefore, HMA thickness requirements for high-volume highway traffic are controlled by HMA fatigue cracking considerations (Brown et al., 2002).

There are two different approaches that mainly recommended in the perpetual pavement concept. The first one is by constructing a bottom lift for the base layer with softer binder grade and/or higher binder content. This type of mix in the bottom lift can stretch without cracking thus it will have an increased fatigue life. The second approach is by increasing the total thickness of asphalt layers as well as the stiffness for all layers such that the tensile strains at the bottom of the asphalt layer will be kept less than the endurance limit that the bottom-up fatigue cracking will not occur (Romanoschi et al., 2006). In this case, the endurance limit concept can provide a more mechanistic design tool where increasing the HMA layer thickness beyond that established by the endurance limit would provide no increased structural resistance to fatigue damage and would represent an unneeded expense as shown in FIGURE 21.

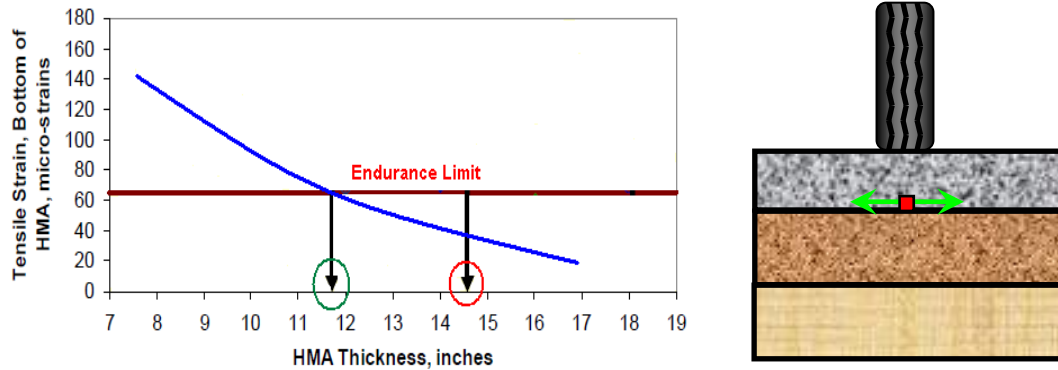


FIGURE 21 Endurance limit concept in perpetual HMA pavement design.

By controlling the bottom-up fatigue cracking by keeping the tensile strain at the bottom of the HMA asphalt layer lower than the endurance limit, the pavement structure will probably be limited only to top-down fatigue cracking as a result of tire interaction and binder aging of wearing courses (Mahoney, 2001). Moreover, the pavement structure may show a limit amount of rutting belong only to the surface layers. At this point, since the distresses in the pavement are kept in the wearing course, the deep structural maintenance could be avoided and only surface treatment such as “mill and fill” maintenance would be enough to eradicate the surface cracks and rutting.

2.8.3 Evidence of HMA Endurance Limit in Laboratory and Field Studies

A number of laboratory and field studies have been conducted over the last 5 decades to check the existence of fatigue endurance limit of hot mix asphalt. Monismith and McLean (1972) first proposed 70 micro-strain (ms) as a likely value of the endurance limit for asphalt pavements. However, there was not sufficient test data to substantiate this observation. They observed that the log-log relationship between strain and loading cycles converged below 70 ms at approximately 5 million cycles (FIGURE 22). Based on this finding, Monismith

and McLean designed a pavement structure that increased the fatigue life of the pavement from 12 to approximately 19-plus years using low-strain design principles. Maupin and Freeman (1976) performed several simple flexure fatigue tests (third point loading) on asphalt concrete beams using controlled stress and controlled strain mode of loadings. The test results also showed that the fatigue curves converged in a similar way that was found by Monismith and McLean.

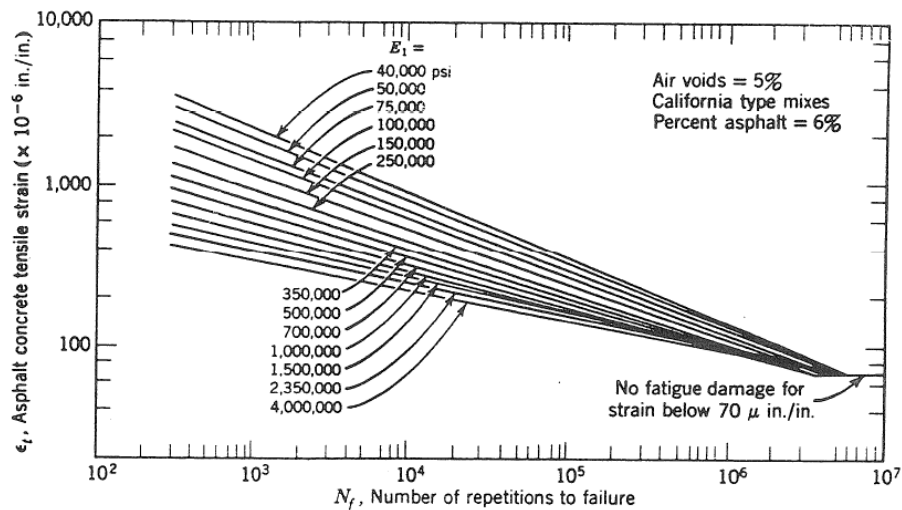


FIGURE 22 Typical failure criteria (fatigue limit) (Monismith et al., 1970).

Nishizawa et al. (1996) concluded that fatigue cracking does not occur when the tensile strain at the bottom of the asphalt pavement is held to be less than 200 μ s, and they suggested a design value of 150 μ s. Research at the NCAT Test Track (Willis et al., 2009) has shown that pavements can withstand bending strains greater than 70 to 100. It was observed that some of the field test sections well-built could be robust enough to withstand trafficking of close to 20 million ESALs even if they designed at higher strain levels.

Recent publications by Carpenter et al. (2003), Shen and Carpenter (2005), and Thomson and Carpenter (2006) investigated the fatigue endurance

concept in asphalt mixture. These researches strongly suggested that there is a fatigue endurance limit below which asphalt mixtures tend to have an extraordinary long fatigue life. It has been showed that when the controlled strain/damage level is very low, distinctively different fatigue behavior can be found even for the same mixture. That is, there is a breakpoint between the normal strain- N_f curve and low strain- N_f curve. For normal strain range, the strain- N_f can be defined with a good power law relationship (or linear relationship under log-log plot). For the lower strain range, the asphalt mixtures changed their fatigue behavior where any small decrease in the strain level will result in a big fatigue life extension (FIGURE 23). The strain level below the breakpoint can be considered as an endurance limit for each mixture type where HMA materials can have extremely long fatigue life.

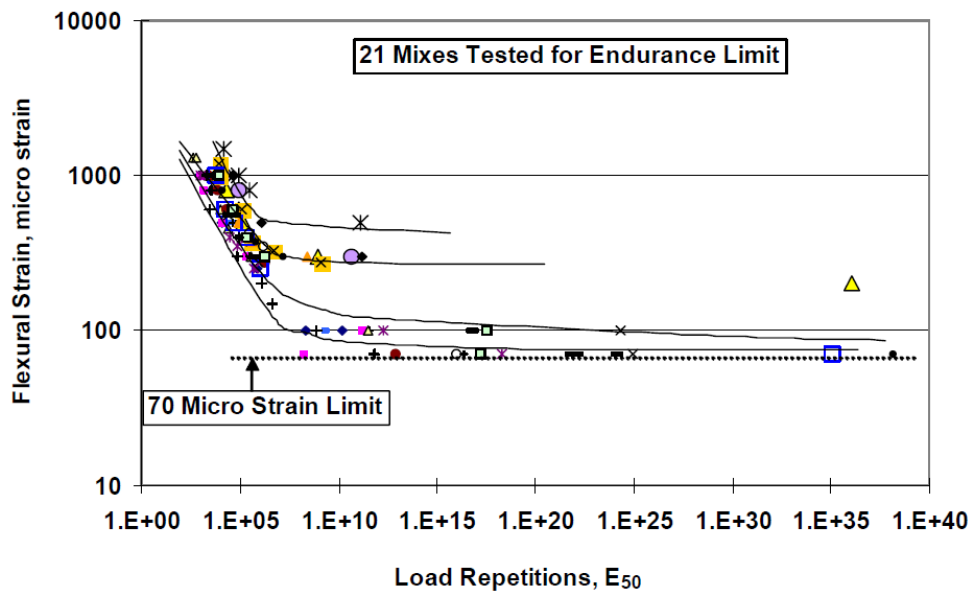


FIGURE 23 Strain – load relationship illustrating the fatigue endurance limit, (Thomson and Carpenter, 2006).

2.8.4 Prediction of HMA Endurance Limit through Laboratory Studies

The long-life pavement has several definitions that can vary from one place to another. Nunn (1997) defines long-life pavements in the United Kingdom (UK) as those that last at least 40 years without structural strengthening. A mirror studies have been done in the United States and confirmed the European experience on the performance of the perpetual pavement (Wu et al., 2004). Prowell et al. (2010) suggest that the maximum possible number of equivalent single-axle loads (ESALs) that a pavement would be subjected to over a 40-year period is approximately 500 million. Considering a shift factor of 10 between laboratory beam fatigue results and field performance for up to 10% fatigue cracking in the wheel path as recommended by Leathy et al. (1995), the fatigue endurance limit can be considered as the strain level that causes a beam fatigue specimen to fail at exactly 50 million loading cycles. Carrying out one fatigue test to such very high numbers of cycles can last for almost 58 days if the test is conducted continuously and at 10 Hz frequency. Methods based on extrapolating data or shortcut methods have certain defined methodologies are developed to show how test results with smaller cycles to failure can be used to predict the fatigue endurance limit of HMA.

There are a number of methods that can be used to extrapolate the fatigue life at lower strain value (close to the endurance limit) based on shorten fatigue testing results. The extrapolating methods will vary according to adopted model. These models include exponential models (AASHTO T-321), Logarithm model (Prowell and Brown, 2006), power models (Shen, unpublished data), Weibull

survivor function (Tsai et al., 2002), Two-Stage Weibull functions (Tsai et al., 2004) and Three-Stage Weibull functions (Tsai et al., 2005). In addition, Prowell and Brown (2006) utilized the linear portion of the stiffness versus loading cycles curve in the extrapolation analysis at low strain levels. Peterson et al. (2004) stated that extrapolation of fatigue life at failure (50% reduction of initial stiffness) at lower strain values can be done from a test that only tested to 4 million loading cycles. Shen and Carpenter (2005) extrapolated test results based on tests conducted to greater than 8 million cycles.

In the National Cooperative Highway Research Program (NCHRP) Project 9-38, Prowell and Brown (2006) performed beam fatigue tests performed at National Center for Asphalt Technology (NCAT). To determine the fatigue endurance limit of various asphalt concrete mixtures, different extrapolation methods were applied to fatigue tests carried out at low strain values up to 10 million loading cycles. In addition, a few tests were carried out up to 50 million cycles to confirm the existence of endurance limit. It was observed that both Logarithmic model and Weibull function showed better extrapolation of the test data at lower cycles to predict endurance limit. FIGURES 24 and 25 showed extrapolation comparisons of different applied models.

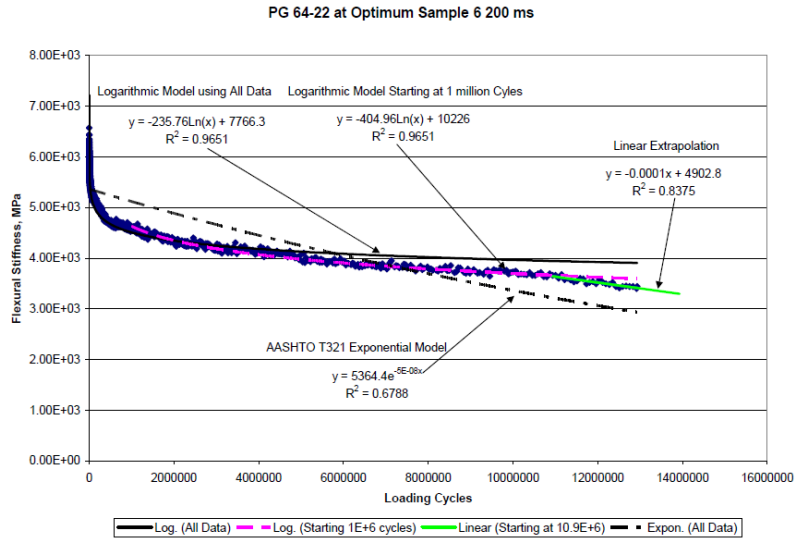


FIGURE 24 Various methods of extrapolation, (Prowell and Brown, 2006).

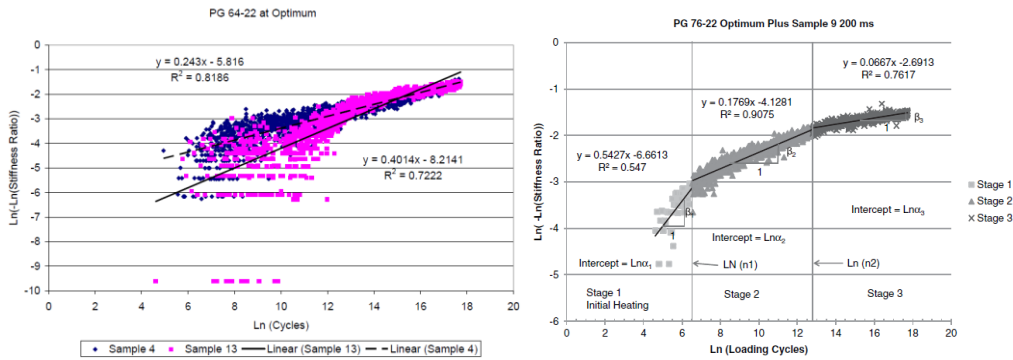


FIGURE 25 One-stage v.s. three-stages Weibull extrapolation (Prowell et al, 2010)

Based on researches that have been conducted at University of Illinois, Shen and Carpenter (2005) used the Plateau Value (PV) of the Ratio of Dissipated Energy Change (RDEC) to develop a new method for predicting the endurance limit of asphalt concrete mixtures. The PV is the value of RDEC when it becomes almost constant or minimum which means that there is a minimum percent of input energy being turned into damage. Shen and Carpenter refined this technique and suggested that the RDEC plateau value should be calculated at the number of

cycles that produced 50% of the initial sample stiffness. It has been indicated that there is a linear relationship between the log of the PV and the log of cycles to 50% initial stiffness for both normal and low (below the endurance limit) strain levels. This relationship was found to be unique for all HMA mixes, all loading modes (controlled stress and controlled strain), all loading levels (normal and low damage levels), and various testing conditions (frequency, rest periods, etc.) as indicated from FIGURE 26.

Considering this unique relationship between PV and N_f , the extremely long fatigue life under low strain/damage condition can be extrapolated for tests conducted for only limited amount of cycles. Laboratory tests and statistical analysis suggested that there is no significant difference between the PV predicted from shortened load repetitions as low as 500,000-cycle load repetitions and extended load repetitions as long as 3 millions cycle load. A tentative plateau value of $8.57E-9$ was identified as indicating the endurance which is corresponding to the breakpoint in the fatigue life at $1.10E+7$. This break point was identified based on enormous amount of fatigue test results that carried out at normal strain ranges and extrapolated results at low strain range as shown from FIGURE 27.

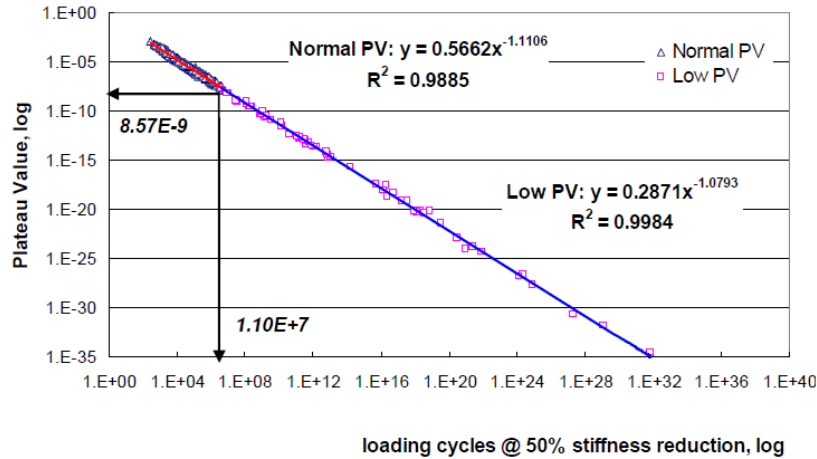


FIGURE 26 PV vs. Nf @ 50% stiffness reduction curve for all data, (Shen and Carpenter, 2005).

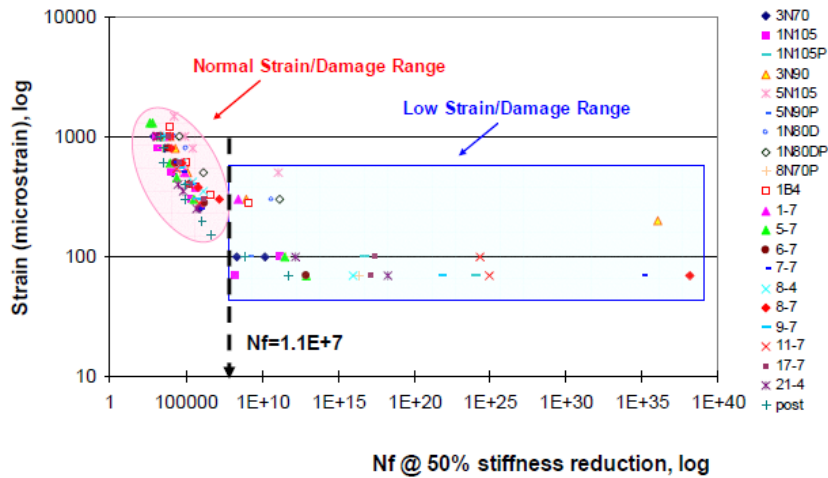


FIGURE 27 Traditional fatigue plots for all the data, (Shen and Carpenter, 2005).

Underwood and Kim (2009) tried for first time to validate the concept of PV using data from uniaxial direct tension fatigue test. The same procedure as for the beam fatigue test was followed (Shen and Carpenter, 2005). However, only limited experimental data were used which represent a small range of materials;

the analysis outputs have supported the existence of such a curve for direct tension tests as seen in FIGURE 28.

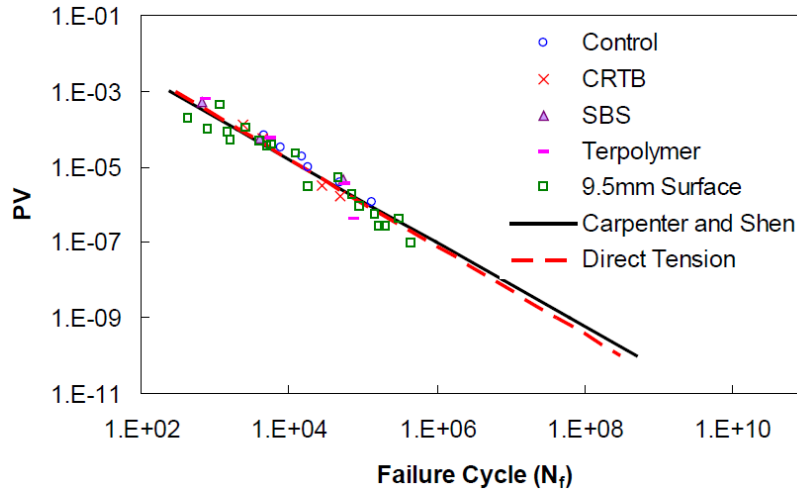


FIGURE 28 Relationship between the PV and N_f for direct tension samples, (Underwood and Kim, 2009).

Soltani et al. (2006) developed a method that can be used to investigate the existence of endurance limit for HMA using a new uniaxial fatigue testing protocol. Cylindrical specimens, 4.7-inch (120-mm) in height and 3.1-inch (80-mm) in diameter, were tested by applying a tension-compression loading at 50°F (10°C) and 10 Hz. The test method consists of applying three stages of continuous loading without any rest period. At Stage I and III, the same strain value is applied at a level lower than the endurance limit so no fatigue damage would occur. During stage II, a variable strain level is applied starting with high value enough to produce damage in the first test and gradually decreased at the following tests. The difference between the moduli at the end of stage I and III was used to indicate the level of fatigue damage imposed during stage II. If the modulus values in stage III are lower than those in stage I, Damaged occurred at

stage II as the applied strain level is higher than the endurance limit as showed in FIGURE 29a. On the other hand, if the modulus values at stages III and I are equal, the strain level at stage II is the fatigue endurance limit as showed in FIGURE 29b.

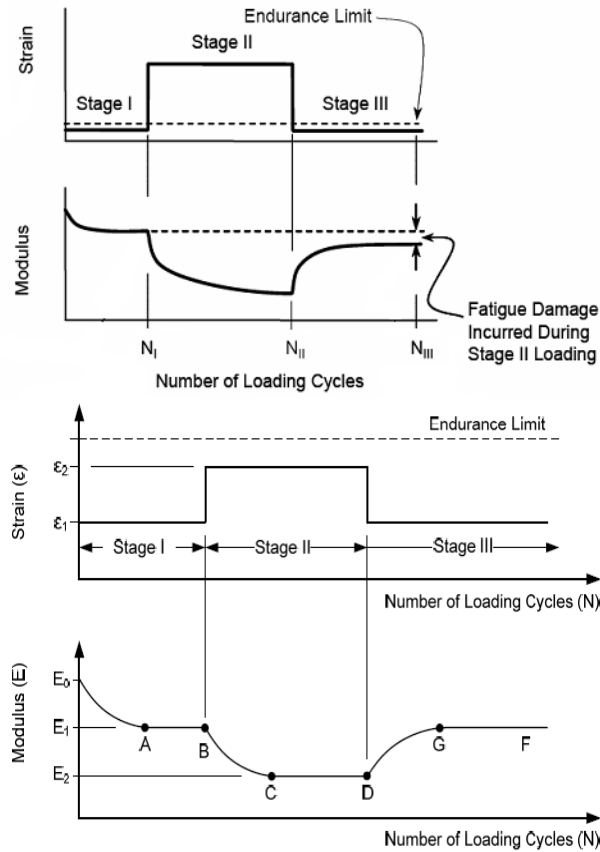


FIGURE 29 Schematic of loading in stages I, II and III (Soltani et al., 2006).

As a part of the NCHRP 9-38, Bhattacharjee et al. (2009) at University of New Hampshire developed an alternative approach to determine the endurance limit of asphalt concrete using the elastic-viscoelastic correspondence principle. This was done by separating the effect of viscoelasticity from damage development and without the need for long term fatigue tests. Uniaxial direct tension fatigue tests under crosshead stain-controlled were conducted by applying

blocks of haversine loading to a uniaxial test specimen. Initially, relatively low strain amplitude that is thought to be below the fatigue endurance limit is applied. Approximately 10,000 cycles are applied at this amplitude to allow the specimen to reach steady-state response. The applied strain amplitude is then increased and 10,000 more cycles are applied. The time lag between the loading blocks was about 5 to 10 seconds. This procedure is continued until the specimen fails as shown in FIGURE 30. The strain data then was converted to pseudo strain using elastic-viscoelastic correspondence principle. The endurance limit was determined by identifying the strain level at which loop between stress and pseudo strain began to develop which means damage started to develop (FIGURE 31).

The major disadvantage of this methodology is that the identification of the loop formation in some cases is tricky and unclear to visually recognize whether a loop has truly formed or has only apparently formed due to data noise and/or other experimental difficulties. To overcome this drawback, Underwood and Kim (2009) suggested using the slope of the stress-pseudo strain graph or the secant pseudo stiffness value (C), as a damage indicator is less subjective than identifying a loop. In case of no damage where the applied strain is considered as the endurance limit, the secant pseudo stiffness will equal to unity where in case of damage, the secant pseudo stiffness will be less than unity. The researchers recommended a more practical threshold value of 0.95 for the secant pseudo stiffness at the end of cycling of a given strain level to account for specimen-to-specimen variability and data noise. This threshold value means that the damage growth is so slow to be neglected.

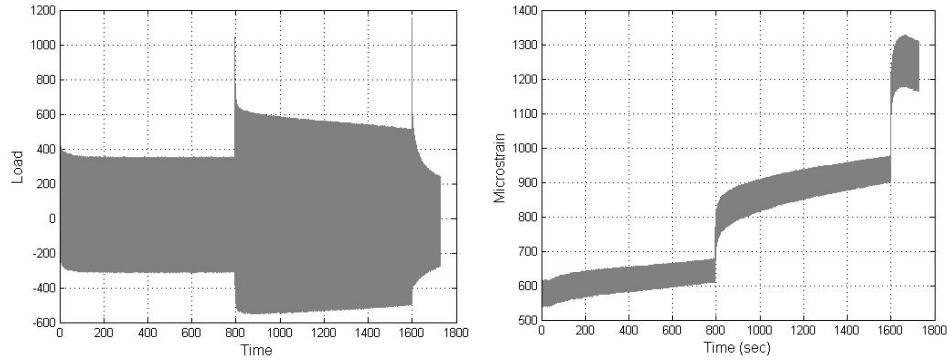


FIGURE 30 Typical loading and strain history for increasing amplitude uniaxial fatigue test (Bhattacharjee et al., 2009).

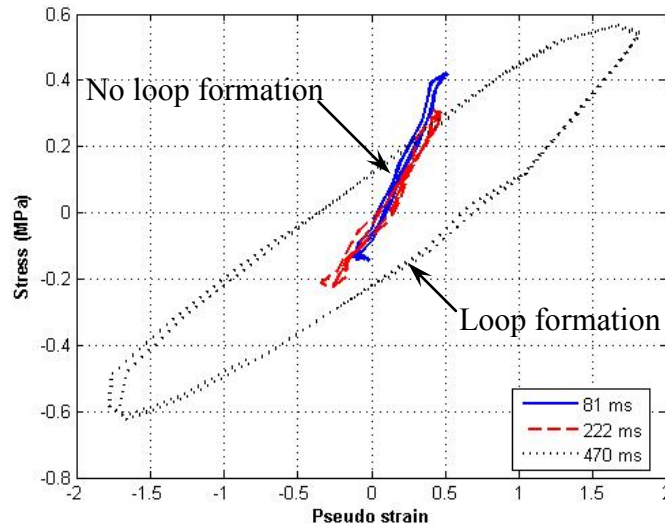


FIGURE 31 Stress-vs-pseudo strain at increasing strain levels (Bhattacharjee et al., 2009).

Underwood and Kim (2009) used the Viscoelastic and Continuum Damage (VECD) approach to predict the fatigue endurance limit with the incorporation of the temperatures effect and rest periods as well. The effect of rest period was considered explicitly in this approach by incorporating the model that was given by Lee and Kim (1998b). The method required at the beginning to define the material damage characteristic curve which is the relationship between

the pseudo stiffness, C , (removes the material time effects) and the damage parameter, S , (represents any microstructural change that leads to a reduction in material integrity). A relationship to accurately predict the fatigue life at failure based on the VECD model was mathematically derived by Hou (2009). This relationship as viewed in Equation 39 was developed for controlled-strain direct tension cycle test assuming the power law damage model.

$$N_f = \frac{(f_R)(2^{3\alpha})S_f^{\alpha-\alpha C_{12}+1}}{(\alpha-\alpha C_{12}+1)(C_{11}C_{12})^\alpha \left[(\beta+1)(\varepsilon_{0,pp}) \left(|E^*|_{LVE} \right) \right]^{2\alpha} K_1} \quad (39)$$

where:

- N_f = number of loading cycles at failure,
- A = damage evolution rate,
- f_R = reduced Frequency,
- S_f = damage parameter at failure,
- C_{11}, C_{12} = regression coefficients of the power model used to fit the C-S curve,
- β = correction factor based on the mean of strain amplitude,
- $\varepsilon_{0,pp}$ = peak-to-peak strain amplitude,
- $|E^*|_{LVE}$ = linear viscoelastic dynamic modulus at the particular temperature and frequency, and
- K_1 = calculated parameter depend on the time history of loading.

Having this closed form solution, the endurance level can be obtained as the strain level corresponding to certain defined high number of load repetition (50,000,000) for certain temperature and rest period. The researchers also suggested another method by using the traditional fatigue approach. In this method, the VECD model was used to predict the N_f for three to five different strain magnitudes. These predicted failure curves were then fit to the traditional fatigue relationship where K_1 and K_2 are regression coefficients that reflect the effect of temperature, frequency of loading, rest period, modulus or other factors.

Using the definition of EL proposed by Prowell et al. (2009), The strain amplitude that yields N_f of 50,000,000 for any given rest period and temperature is considered to be the EL as shown in FIGURE 32.

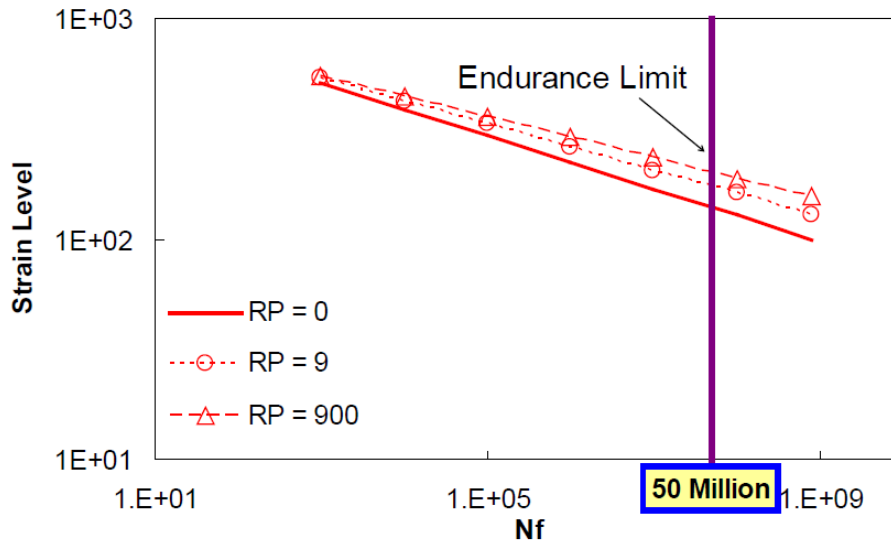


FIGURE 32 Effect of healing on traditional fatigue relationship at 5°C

(Underwood and Kim, 2009).

Christensen and Bonaquist (2009) followed the same methodology of Underwood and Kim but by using a similar mathematical formula (Equation 40)

that predicts the strain level required to sustain any number of design load repetitions with generalized power law (Christensen and Bonaquist, 2005).

$$\varepsilon_o^{2\alpha} = \frac{fS_f^p}{p(0.125IC_{11}C_{12})^\alpha N_f(|E^*|)^{2\alpha}} \quad (40)$$

where:

- f = Frequency,
- I = normalized pseudo stiffness, and
- p = $1 + (1 - C_{12}) \alpha$.

Where S_f is the damage parameter value at failure measured from the damage characteristic curve for the mixture at the point where $C = 0.3$ (Daniel and Kim, 2002).

Another methodology was created by Christensen and Bonaquist, (2009). They developed a simplified continuum damage analysis using the concept of reduced cycles defined by Equation 41 in which the damage parameter, S is replaced by reduced cycles that also collapse all the data at different strains and different temperatures into a unique relationship as shown in FIGURE 33. This method directly accounts for the endurance limit by applying the concept of effective strain which defined as applied strain minus the endurance limit. The analysis allows for the calculation of endurance limits from relatively limited fatigue data. One advantage of this method is that the reduced cycles is easier to be calculated and understood compared to the damage parameter, S that can only be computed using approximate, numerical integration.

$$N_R = N_{R-ini} + N \left(\frac{f_0}{f} \right) \left(\frac{|E^*|_{LVE}}{|E^*|_{LVE/0}} \right)^{2\alpha} \left(\frac{\varepsilon^E}{\varepsilon_0^E} \right)^{2\alpha} \left[\frac{1}{a(T/T_0)} \right] \quad (41)$$

where:

N_R = reduced cycles,

N_{R-ini} = initial value of reduced cycles, prior to the selected loading

period,

N = actual loading cycles,

f_0 = reference frequency (10 Hz suggested),

f = actual test frequency,

$|E^*|_{LVE}$ = undamaged (LVE) dynamic modulus under given conditions,
lb/in²,

$|E^*|_{LVE/0}$ = reference initial (LVE) dynamic modulus, lb/in² (the LVE
modulus at 68°F (20°C) is suggested),

α = continuum damage material constant with a typical value of
about 2.0,

ε^E = effective strain level = applied strain minus the endurance limit
strain,

ε_0^E = reference effective strain level (0.0002 suggested), and

$a(T/T_0)$ = shift factor at test temperature T relative to reference
temperature T_0 .

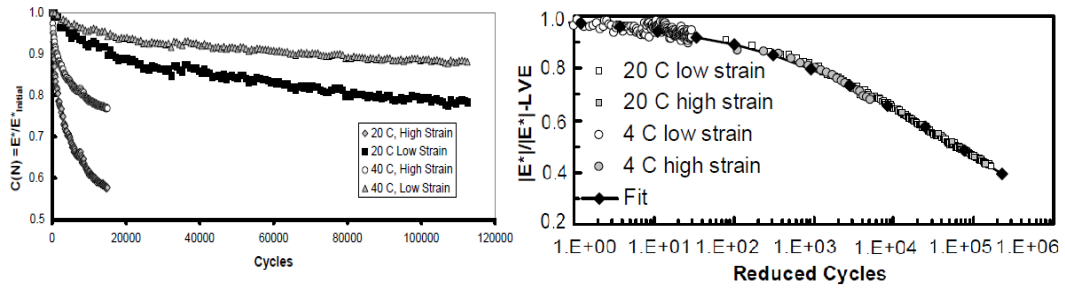


FIGURE 33 Typical damage ratio curves collapsed into a unique damage relationship using continuum damage analysis, (Christensen and Bonaquist, 2009).

CHAPTER 3

THEORY OF VISCOELASTICITY AND DAMAGE MECHANICS

In modeling the hysteretic behavior of asphalt concrete mixtures under multi-repetitive loading with random duration of rest, the following constitutive factors are deemed important (Lee, 1996):

- I. Viscoelasticity of the matrix that cause hysteretic behavior under cyclic loading and relaxation during rest periods,
- II. Fatigue damage growth under cyclic loading,
- III. Healing during the rest periods, and
- IV. Temperature dependence of asphalt matrix.

Effects of temperature on the constitutive behavior can be included in the viscoelastic material properties, such as creep compliance and relaxation modulus, using time temperature superposition principle (Kim and Lee, 1995a). It is difficult to evaluate the effect of the remaining three factors as their mechanisms occur simultaneously under cyclic loading with rest periods. For example, the inelastic response of the material during loading and unloading paths can be due to damage incurred in the material and/or the viscoelastic nature of the material. Also, relaxation and healing also occur at the same time during rest periods. Consequently, it is essential to separate the viscoelasticity from damage and healing in order to accurately predict the inelastic response of the material.

This chapter represents the basic theories that are applied in this research, starting with the theory of viscoelasticity, followed by the elastic-viscoelastic correspondence principle and time-temperature superposition to eliminate the

time-dependence of the material of the material from the hysteretic stress-strain behavior by using the pseudo strain concept. Finally the work potential theory (Schapery, 1990), one of the continuum damage mechanics principles based on irreversible thermodynamics, is employed to model damage and microdamage healing. In addition, the constitutive model developed by Lee (Lee, 1996) is also presented.

3.1 Theory of Viscoelasticity

3.1.1 Background

The classical theory of elasticity, in accordance with Hook's law, deals with the mechanical properties of elastic solids where the stress is always directly proportional to the strain by a material constant (Young's modulus) where the deformation is small and is independent of the rate of strain, as shown in FIGURE 34. In this case, the strain energy is completely recovered during unloading. On the other hand, the classical theory of hydrodynamics deals with the mechanical properties of viscous liquids, in accordance with Newton's law, where the stress is directly proportional to the rate of strain by a material constant (Viscosity) and is independent of the strain itself, as shown in FIGURE 35. In this case, the strain energy is completely dissipated during loading. These two theories are idealizations of characteristics of elastic solids for infinitesimal strain and viscous liquids for infinitesimal strain rates. Some of engineering materials, especially those soft enough to be deformed substantially without breaking such as asphalt concrete, may exhibit behavior that combine liquidlike and solidlike characteristics. In this case, some of the energy input is stored and recovered in

each cycle, and some is dissipated. The energy dissipated during a full cycle of loading and unloading represents the material damping characteristic and is graphically represented by the area contained with a stress-strain diagram as seen in FIGURE 36 (Zhiming, 2001). Material whose behavior exhibits such characteristics called viscoelastic.

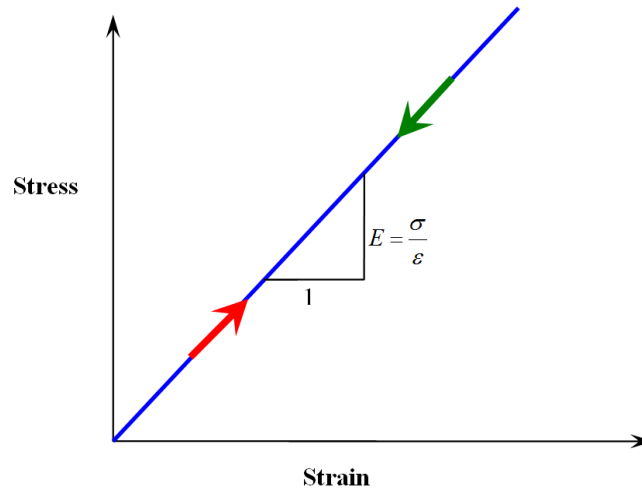


FIGURE 34 Stress-strain curve for linear elastic (Hookean) solid.

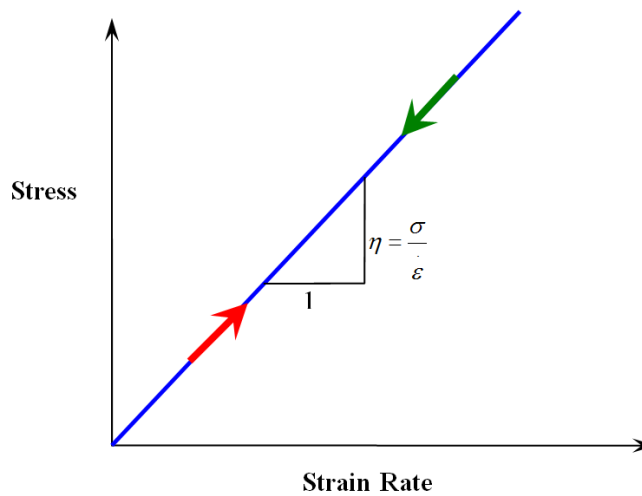


FIGURE 35 Stress-strain curve for linear viscous (Newtonian) fluid.

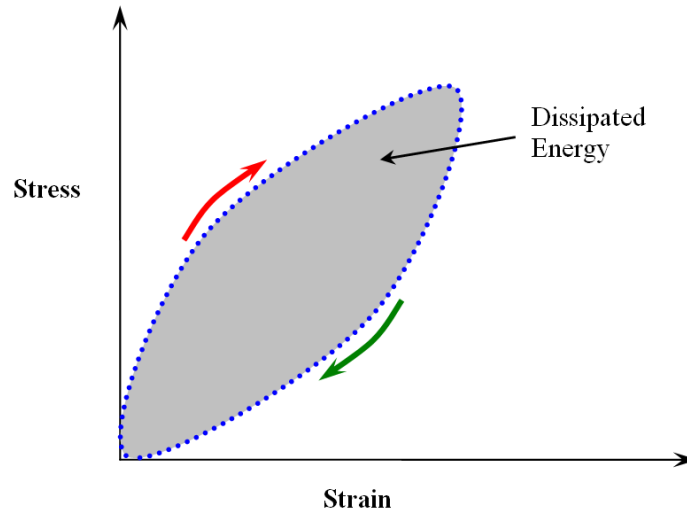


FIGURE 36 Stress-Strain curve for a viscoelastic material.

3.1.2 Viscoelastic Constitutive Equation

Viscoelastic materials such as asphalt concrete mixtures exhibit time or rate dependence. Demonstrating that, the response of such materials depends not only on current state of input (load or deformation), but also on all past history of input, i.e., the materials have a memory for all past history of input. Viscoelastic material behavior is separated into two main categories: linear and nonlinear. Linear viscoelastic materials show dependence of the time history of the loading or deformation and the response due to change in the level of stress or strain may be superimposed. Nonlinear viscoelastic materials have behavior that is dependent on stress or strain history and the response in stress or strain may not be superimposed.

The response of a linear viscoelastic material to any input history is described using the convolution integral. A system is considered to be a linear if the conditions of homogeneity and superposition are fulfilled:

$$\text{Homogeneity:} \quad R \{AI\} = A R \{I\} \quad (42)$$

$$\text{Superposition: } R \{I_1+I_2\} = R \{I_1\} + R \{I_2\} \quad (43)$$

where:

I, I_1, I_2 = input histories,

R = response, and

A = arbitrary constant.

The brackets $\{ \}$ indicate that the response is a function of the input history. The homogeneity, or the proportionality, condition means that the output is directly proportional to the input. For example, if the input is doubled, the response doubled as well. On the other hand, the superposition condition means that response to the sum of two inputs is equivalent to the sum of the responses from the individual inputs.

Considering the linear response of a viscoelastic material, and the homogeneity and superposition concepts, the following input-response relationship can be expressed using the following hereditary integral that represent the constitutive behavior of a viscoelastic materials:

$$R = \int_{-\infty}^t R_H(t, \tau) \frac{dI(\tau)}{d\tau} d\tau \quad (44)$$

where:

R_H = response function,

t = time,

τ = time-history integration variable, and

I = input history.

The relationship is called hereditary integral because the conditions at a time t depend on prior history.

With a known unit response function, the response to any input history can be calculated. The lower limit of the integration can be reduced to 0^- (0^- , just before time zero) if the input starts at time $t = 0$ and both the input and response are equal to zero at $t < 0$. The value of 0^- is used instead of 0 to allow for the possibility of a discontinuous change in the input at time $t = 0$. For notational simplicity, 0 is used as a lower limit in all successive equations and should be interpreted as 0^- unless specified otherwise. Equation 44 is applicable to an aging system in which response measurement at any time is a function of both of the time of loading and the time of fabrication. The unit response function, R_H , is then a three dimensional surface.

Usually, the assumption that asphalt concrete mixtures behave as a non-aging system is made. Then the unit response function is simplified to a two-dimensional line and Equation 44 reduces to:

$$R = \int_0^t R_H(t - \tau) \frac{dI(\tau)}{d\tau} d\tau \quad (45)$$

For uniaxial loading, the corresponding hereditary integrals of stress-strain relationship for non-aged & linear viscoelastic material are:

$$\varepsilon = \int_0^t D(t - \tau) \frac{d\sigma}{d\tau} d\tau \quad (46)$$

$$\sigma = \int_0^t E(t - \tau) \frac{d\varepsilon}{d\tau} d\tau \quad (47)$$

where:

ε, σ = physical strains and physical stresses, and

$E(t), D(t)$ = relaxation modulus and creep compliance, respectively.

3.2 Correspondence Principle

The theory of linear viscoelasticity and some nonlinear viscoelasticity models have been established in the past. However, solution of various kinds of viscoelastic boundary value problems still remains a complex problem. Fortunately, theory of viscoelasticity allows viscoelastic problems to be transformed so that they are mathematically equivalent to those for elastic problems with the substitution of elastic moduli. This correspondence can be made by taking appropriate transformation of the governing field and boundary equations of viscoelastic problems with respect to time. In general, the principle employs the Laplace transformation for linear viscoelastic materials.

Schapery (1984) proposed the extended elastic-viscoelastic correspondence principle (CP) which can be applicable to both linear and nonlinear viscoelastic materials. Schapery suggested that constitutive equations for certain viscoelastic media are identical to those for the elastic cases, but stresses and strains are not necessarily physical quantities in the viscoelastic body. Instead, they are *pseudo variables* in the form of convolution integrals.

The following uniaxial version of constitutive equations for linear elastic and linear viscoelastic bodies without and with damage is presented. They also show how models of different complexity may evolve from simpler ones:

➤ Elastic Body without Damage: $\sigma = E_R \varepsilon$ (48)

➤ Elastic Body with Damage: $\sigma = C(S_m) \varepsilon$ (49)

➤ Viscoelastic Body without Damage: $\sigma = E_R \varepsilon^R$ (50)

➤ Viscoelastic Body with Damage: $\sigma = C(S_m) \varepsilon^R$ (51)

where ϵ , σ are physical stresses and physical strains, ϵ^R is the pseudo strain, E_R is a constant and $C(S_m)$ indicates that C is a function of Internal State Variables (ISVs) S_m that represents the changing stiffness of the material due to microstructure changes such as accumulating damage or healing. In Equation 50, E_R is the Young's modulus.

A correspondence is seen between the elastic and viscoelastic constitutive equations: the viscoelastic behavior can be described by the elastic equations with pseudo strain replacing corresponding physical strain. For example, a correspondence can be found between Equation 50 and a linear elastic stress-strain relationship (Hooke's law). The power of pseudo strain can be seen in FIGURE 37. FIGURE 37a shows the stress strain behavior of a controlled-stress cyclic loading with within the material's linear viscoelastic range (such as a complex modulus test). Because the material is being tested in its linear viscoelastic range, no damage is induced and the hysteretic behavior and accumulation strain are due to the viscoelasticity only. FIGURE 37b shows the same stress data plotted against the calculated pseudo strain. All of the cycles collapse to a single line with a slope of 1.0 ($E_R = 1.0$). The use of pseudo strain essentially accounts for the viscoelasticity of the material and allows for the separate characterization of damage within the specimen.

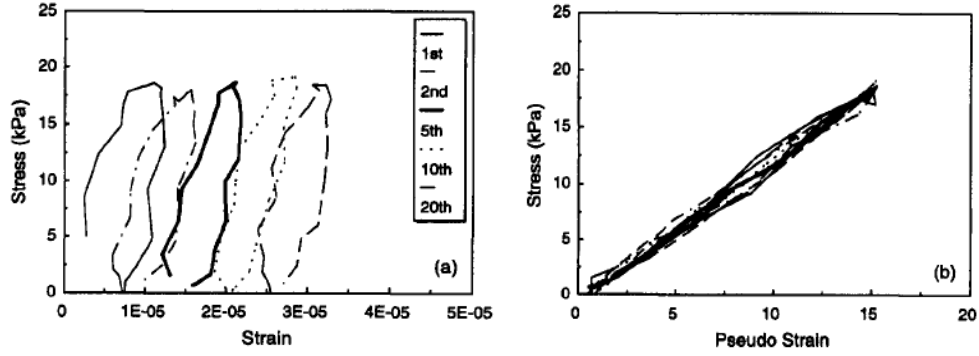


FIGURE 37 Stress application of correspondence principle to cyclic data with negligible damage: (a) stress-strain; (b) stress-pseudo strain (Lee and Kim, 1998b).

In order to introduce pseudo strain and pseudo stress, consider a uniaxial stress-strain relationship for linear, non-aging viscoelastic materials, Equation 47, which can be written as:

$$\varepsilon^R = \frac{\sigma}{E_R} \quad (52)$$

By substituting the stress value from Equation 47 to Equation 52, the pseudo strain relationship can be written such as:

$$\varepsilon^R = \frac{1}{E_R} \int_0^t E(t-\tau) \frac{d\varepsilon}{d\tau} d\tau \quad (53)$$

The same way, the pseudo stress relationship can be represented by the following equation:

$$\sigma^R = E_R \int_0^t D(t-\tau) \frac{d\sigma}{d\tau} d\tau \quad (54)$$

where:

ε^R, σ^R = pseudo stresses and pseudo strains,

t = elapsed time from specimen fabrication and time of interest, and

τ = time when loading began.

Using the concept of pseudo variables, Schapery (1984) introduced three different correspondence principles. The first case is by using both pseudo strain and stress (general boundary condition). The physical stress and pseudo strain were used in the second case (as the crack increases, the traction boundary condition grows). The last correspondence principle employs the pseudo stress and physical strain (as the crack heals, the traction boundary condition reduces).

For the case of a growing traction boundary surface, such as crack growth, the viscoelastic problem can be reduced to an elastic case by using physical stresses and pseudo strains. The uniaxial pseudo strain (ε_{ij}^R) is defined as:

$$\varepsilon_{ij}^R = \frac{1}{E_R} \int_0^t E(t-\tau) \frac{d\varepsilon_{ij}}{d\tau} d\tau \quad (55)$$

Calculation of pseudo strain using Equation 55 requires the expression of relaxation modulus as a function of time.

3.3 Uniaxial Constitutive Model Using Work Potential Theory

3.3.1 Constitutive Theory

Schapery (1990) applied the method of thermodynamics of irreversible processes and the observed phenomenon of path independence of work in damage-inducing processes to develop the work potential theory to describe the mechanical behavior of elastic composite materials with growing damage. The theory is general enough to allow for strong nonlinearities and to describe variety mechanisms including micro- and macro-crack growth in monolithic and

composite materials. Three fundamental elements comprise the work potential theory:

1. **Strain energy density function:**

$$W = W(\varepsilon, S_m) \quad (56)$$

2. **Stress-strain relationship:**

$$\sigma_{ij} = \frac{\partial W}{\partial \varepsilon_{ij}} \quad (57)$$

3. **Damage evolution law:**

$$-\frac{\partial W}{\partial S_m} = \frac{\partial W_s}{\partial S_m} \quad (58)$$

where σ_{ij} and ε_{ij} are stress and strain tensors, respectively. S_m are internal state variables, ISVs, (or damage parameters) representing structural changes in the material (e.g., damage, healing, etc.) and $W_s = W_s(S_m)$ is the dissipated energy due to structural changes. Using Chapery's elastic-viscoelastic correspondence principle (CP) and rate-type evolution law (Schapery, 1984; Schapery, 1990 and Park et al., 1996), the physical strains, ε_{ij} , are replaced with pseudo strains, ε_{ij}^R , to include the effect of viscoelasticity. However, the damage evolution laws cannot directly be translated into evolution laws for viscoelastic materials through the correspondence principle. It is to be understood that not only the available force for growth of S_m is rate-dependent (through pseudo strains), but the resistance against the growth of S_m is rate-dependent for most viscoelastic materials. Therefore, a form which is similar to the well-known power-law crack growth laws for viscoelastic materials (Schapery, 1984), will be adopted as it can

reasonably represent the actual damage evolution processes of many viscoelastic materials as shown in Equation 61:

Finally, the work potential theory applied to viscoelastic media with the rate type damage evolution law presented by the following three components for uniaxial loading condition:

- **Pseudo strain energy density function:** A pseudo strain energy function exists in the following form:

$$W^R = W^R(\varepsilon_{ij}^R, S_m) \quad (59)$$

- **Stress-strain relationship:** The pseudo-strain energy function has the following property:

$$\sigma_{ij} = \frac{\partial W}{\partial \varepsilon_{ij}^R} \quad (60)$$

- **Damage evolution law:** Damage evolution in viscoelastic material is governed by the following:

$$\dot{S}_m = \left(-\frac{\partial W^R}{\partial S_m} \right)^{\alpha_m} \quad (61)$$

where ε^R and σ^R are the pseudo strain and stress tensors respectively. S_m are internal state variables, ISVs, (or damage parameters) representing structural changes in the material (e.g., damage, healing, etc.). S_m overdot is the damage evolution rate, and α_m , are material constants.

Using Schapery's work potential theory (Schapery, 1990) and correspondence principle that eliminate the time dependence of material, Lee and Kim (1998b) developed a mode of loading-independent constitutive model for the

fatigue and microdamage healing of asphalt concrete under cyclic loading. They used uniaxial tensile cyclic loading tests with various loading amplitudes under controlled-strain and controlled-stress modes. FIGURE 38 show typical stress-pseudo strain hysteresis loops at different numbers of cycles in the controlled-strain and controlled-stress modes respectively. Relatively high stress and strain amplitudes are used to induce significant damage in the specimen. The following three characteristics can be observed from these figures due to the damage incurred in the specimens:

1. Nonlinear behavior of the loading and unloading paths in each cycle,
2. Change in the slope of each σ - ε^R cycle as cyclic loading continues (i.e., reduction in the pseudo stiffness of the material as damage accumulates), and
3. Accumulation of permanent pseudo-strain in the controlled-stress mode (i.e., shift of the loop from the origin as cyclic loading continues).

The first two characteristics are observed in both modes of loading, while the third characteristic is unique to the controlled-stress mode.

To represent the change in the slope of σ - ε^R loops in both modes of loading using single parameter, secant pseudo stiffness, S^R , defined as:

$$S^R = \frac{\sigma_m}{\varepsilon_m^R} \quad (62)$$

where ε_m^R is the peak pseudo strain in each stress pseudo-strain cycle, and σ_m is a stress corresponding to ε_m^R .

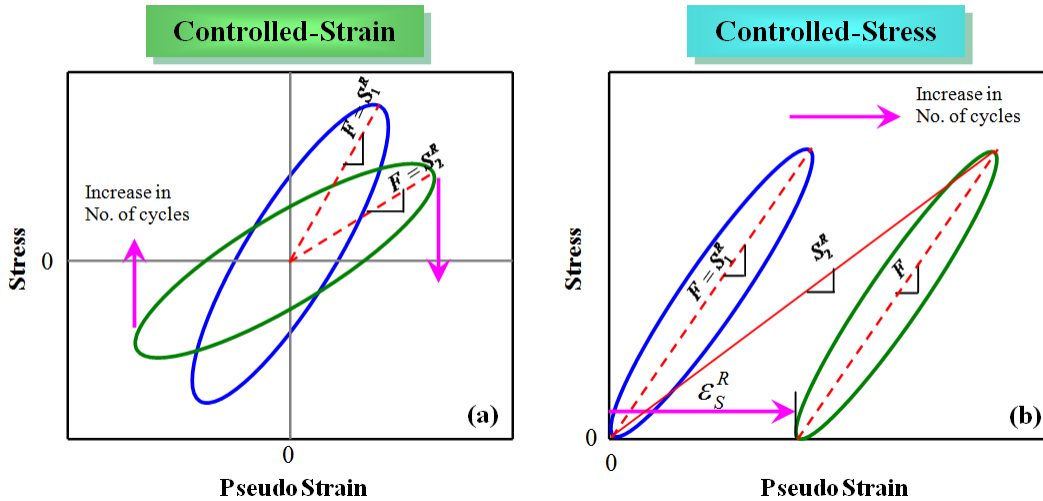


FIGURE 38 Stress-pseudo strain curve behavior and pseudo stiffness changes in: (a) controlled-strain mode; (b) controlled-stress mode (Lee and Kim, 1998b).

Since S^R is determined from stress and pseudo-strain values, instead of physical strain, the advantage of using pseudo strain, that is eliminating the time-dependence from the hysteretic behavior, is still effective. Thus, the change in S^R represents damage growth and healing separately from the time-dependence, which allows a simple function of S^R to describe these mechanisms under complicated loading histories. In modeling, Lee (Lee, 1996) found it necessary to normalize the pseudo stiffness by the initial pseudo stiffness, I , to account for sample-to-sample variation. The normalized pseudo stiffness, C , is then:

$$C = \frac{S^R}{I} \quad (63)$$

3.3.2 Determination of Damage Parameter S

The work potential theory specifies an internal state variable S_m to quantify damage, which is defined as any microstructure changes that result in stiffness reduction. For asphalt concrete in tension, this variable is related primarily to microdamage phenomenon. Therefore, only one internal state variable (i.e., S_1) is used to model the damage growth in tension.

Kim et al. (1997a) characterized the growing damage by using the function C in Equation 51 for a controlled-strain testing mode through the following constitutive equations:

$$W_m^R = \frac{1}{2} C_1(S_1) (\varepsilon_m^R)^2 \quad (64)$$

$$\sigma_m = I C_1(S_1) \varepsilon_m^R \quad (65)$$

where W_m^R is the pseudo strain energy density function when $\varepsilon^R = \varepsilon_m^R$ and C_1 is defined as in Equation 63, and S_1 is an internal state variable. The subscript on the C and S variables indicates that damage is occurring in the virgin material opposed to a material that has undergone healing.

The function C_1 represents S^R , as can be seen from Equations 63 and 65 since $I = 1.0$. The evolution law becomes:

$$\dot{S}_m = \frac{dS}{dt} = \left(- \frac{\partial W_m^R}{\partial S_m} \right)^{\alpha_m} \quad (66)$$

To characterize the function C_1 in the Equation 65, the damage evolution law and experimental data are used. With the measures stresses and calculated pseudo strains, C_1 values can be determined through Equation 63. To find the dependence of C_1 and S_1 , the value of S_1 must be obtained through Equation 66.

The current form of Equation 66 is not suitable for finding S_1 because it requires prior knowledge of the $C_1(S_1)$ function through Equation 64. Substituting Equation 66 into 64, Equation 67 is derived:

$$\frac{dS_1}{dt} = \left[-\frac{1}{2} \frac{dS_1}{dC_1} (\varepsilon_m^R)^2 \right]^{\alpha_m} \quad (67)$$

To eliminate S from the dS/dC term of the evolution Equation 67, Lee (1996) proposed a solution that utilizes the chain rule:

$$\frac{dC}{dS} = \frac{dC}{dt} \frac{dt}{ds} \quad (68)$$

From Equations 67 and 68, the damage evolution rate, dS/dt , is represented by Equation 68:

$$\frac{dS_1}{dt} = \left[-\frac{1}{2} \frac{dC_1}{dt} (\varepsilon_m^R)^2 \right]^{\alpha_m} \quad (69)$$

As a result, S_1 can be obtained:

$$S_1 = \int_0^t \left[-\frac{1}{2} \frac{dC_1}{dt} (\varepsilon_m^R)^2 \right]^{\frac{\alpha}{(1+\alpha)}} dt \quad (70)$$

Both the function C_1 and ε_m^R are dependent upon time t , thus a numerical approximation can be used with the measured data to obtain S_1 as a function of time (Daniel, 2001; Daniel and Kim, 2002):

$$S_1(t) = \sum_{i=1}^N \left[-\frac{1}{2} (C_i - C_{i-1}) (\varepsilon_m^R)^2 \right]^{\frac{\alpha}{(1+\alpha)}} (t_i - t_{i-1})^{\frac{1}{(1+\alpha)}} \quad (71)$$

Daniel and Kim (2002) showed that the damage characteristics of a material are independent of the mode of loading and can be determined using a simpler test, such as the constant crosshead rate monotonic test. Chehab et al.

(2002) and Underwood et al. (2006) verified that the time-temperature superposition (t-TS) principle at high levels of damage is equally significant.

Based on this validation, Equation 71 can be modified as following:

$$S_1(\xi) = \sum_{i=1}^N \left[-\frac{I}{2} (C_i - C_{i-1}) (\varepsilon_m^R)^2 \right]^{\frac{\alpha}{(1+\alpha)}} (\xi_i - \xi_{i-1})^{\frac{1}{(1+\alpha)}} \quad (72)$$

where ξ is the reduced time. Equations 71 or 72 can also be written in the following form (Kim, 2009):

$$S_{i+1} = S_i + \left[-\frac{I}{2} (C_i - C_{i-1}) (\varepsilon^R)^2 \right]^{\frac{\alpha}{(1+\alpha)}} \Delta \xi_i^{\frac{1}{(1+\alpha)}} \quad (73)$$

Underwood et al. (2010) developed a simplified VECD modeling technique based on the analysis of cyclic data. This method allows the prediction of the fatigue lives of asphalt concrete at various strain–stress amplitudes under different temperatures using the dynamic modulus master curve and the cyclic fatigue data from a single temperature and single stress or strain amplitude. The proposed S function had the following form:

$$S_{N+1} = S_N + \left[-\frac{DMR}{2} (C_N - C_{N-1}) (\varepsilon^R)^2 \right]^{\frac{\alpha}{(1+\alpha)}} (\Delta \xi_i)^{\frac{1}{(1+\alpha)}} (K_1)^{\frac{1}{(1+\alpha)}} \quad (74)$$

where:

DMR = Dynamic Modular Ratio = $|E^*|_{fp} / |E^*|_{LVE}$ and $|E^*|_{fp}$ is finger print modulus,

Δt_R = the change in the average reduced time between analysis cycles,

and

K_1 = a developed functional parameter to account for the analysis of cyclic data.

The parameter α is supposed to be a material property. A few correlations have been proposed to estimate the value of this constant, relating it to viscoelastic properties of asphalt mixtures. Lee and Kim (1998a, b) attempted to relate α to the slope m in the central part of the Master Curve for the $\log E(t)$ - $\log(t)$ relationship. It was suggested that it is most appropriate to use $\alpha = 1/m$ for the type of stress-controlled tests $\alpha = 1/m + 1$ for the cross-head strain tests.

This relationship is valid by cross-plotting the measured C_1 values against the S_1 values obtained from Equation 71 to obtain the damage characteristic curve. The relationship between C_1 and S_1 can be found by performing a regression on the data. Lee (1996) found that the function follows the form:

$$C_1(S_1) = C_{10} - C_{11}(S_1)^{C_{12}} \quad (75)$$

where the C_{1x} are the regression coefficients. The regression coefficient C_{10} is close to 1.0, as would be expressed at a negligible damage level (S_1 goes to zero) because the material is in linear viscoelastic range of behavior and there exists a one-to-one relationship between the stress and pseudo strain (i.e., $S^R = 1.0$). Using this model, Lee (Lee, 1996) was able to successfully predict the damage growth of asphalt concrete under monotonic loading at various strain rates and cyclic loading under both controlled stress mode and controlled strain as well.

The S_1 - C_1 relationship can be also fitted to some analytical form represented in Equation 76 (Lee, 2007 and Kim, 2009).

$$C = e^{aS^b} \quad (76)$$

CHAPTER 4

DESIGN OF EXPERIMENTS, SPECIMEN PREPARATION AND TESTING PLAN

4.1 Background

Recommendations were made during the HMA Endurance Limit Workshop conducted early in NCHRP Project 9-44 (Hot Mix Asphalt Endurance Limit Workshop, 2007). It was hypothesized that: “HMA does exhibit an endurance limit. This endurance limit, however, does not reflect an absence of load induced damage in the HMA. It is the result of a balance of damage caused by loading and healing or damage recovery that occurs during rest periods.”

Based on this hypothesis, the main objective of this research is to develop an algorithm and test methodology to validate an endurance limit for hot asphalt mixture (HMA) using uniaxial tension-compression fatigue test and based on the Viscoelastic and Continuum Damage Model (VECDM). The experimental program of this research was developed to fulfill the main objectives of this research. The main experimental plan investigates the healing of fatigue damage for a PG 64-22 HMA by building a statistical model and considering the effect of different experimental factors on healing. Once the healing model is developed, the second step is to develop an algorithm to get the fatigue endurance limit from the healing model.

4.2 Selection of Factors Affecting the Healing Experiment

There are many variables that can possibly influence the fatigue endurance limit of HMA. Some of these main factors are shown in TABLE 1. The selection of the number of factors and design of experiment should be carefully evaluated. For example, if 10 factors are considered and 3 levels of each variable are pursued in a full factorial plan, it would require $3^{10}=59,049$ tests.

TABLE 1 List of factors that can affect the fatigue endurance limit (NCHRP 944, 2008)

Topic	Factors
Mixture Compositional Factors	Binder Type
	Binder Age
	Asphalt Content
	Air Voids
	Design Compaction
	Gradation
	Filler Content
Testing Inputs and Conditions	Strain Level
	Loading Frequency
	Loading Wave Shape
	Rest Period Duration
Environmental Condition	Temperature

Furthermore, this number considers only a single replicate. If 2 or 4 replicates were used; the number of tests would increase to about 118,000 (2 replicates) and 236,000 (4 replicates). If one were to go one step further and recognize that a typical lab (with one fatigue apparatus) can conduct about 30 tests per month; the total number of years required to complete the lab testing experiment, with one lab, would be 164 (1 replicate), 328 (2 replicates), or 656 (4

replicates).It is clearly obvious that some type of reduced statistical plan, other than a full factorial, to address all variables and levels, had to be executed. In addition, it was decided to eliminate some of the variables to reduce the number of required tests.

4.3 Design of Experiment

4.3.1 Independent Variables (Factors)

The design of experiment for the work plan using only one asphalt binder (PG 64-22) is designed for uniaxial tension-compression fatigue test. Five important factors were selected, which are:

1. Asphalt content, AC% (2 levels: optimum \pm 0.5 %)
2. Air voids, Va% (2 levels: 4.5, 9.5 %)
3. Strain Level, ϵ (2 levels: L, M)
4. Temperature, T (3 levels: 40, 70, 100°F)
5. Rest period, RP (2 levels: 0, 5 sec)

It is initially planned to start the experiment using three replicates for each factor combination. As results were obtained and evaluated; a statistical analysis was conducted to re-evaluate the efficiency and accuracy of the use of three replicate specimens as discussed later.

In this design, all 5 factors stated above would be evaluated. From the uniaxial fatigue test results with and without rest periods, the Pseudo Stiffness Ratio (PSR) values are calculated at a certain number of loading cycle. The PSR is simply the pseudo stiffness at certain loading cycles divided by the initial

pseudo stiffness. A regression model would be developed to estimate the PSR as a function of all five factors.

$$PSR = f(AC, Va, \varepsilon_t, T, RP) \quad (79)$$

where:

- AC = Asphalt content,
- Va = Air voids,
- ε_t = Tensile strain level,
- T = Temperature, and
- RP = Rest period.

To estimate the Healing Index at certain parameters values, the PSR values are calculated using the PSR regression model at two different rest periods. The first PSR is calculated at a rest period equal to zero that represents the test without rest period. The second PSR is obtained at a target or assumed rest period greater than zero. Considering the number of cycles till failure for the test without rest period, the Healing Index (HI) is then calculated as shown from FIGURE 39 and Equation 78.

$$HI = \frac{PSR_{WRP} - PSR_{W/ ORP}}{1 - PSR_{W/ ORP}} \quad (78)$$

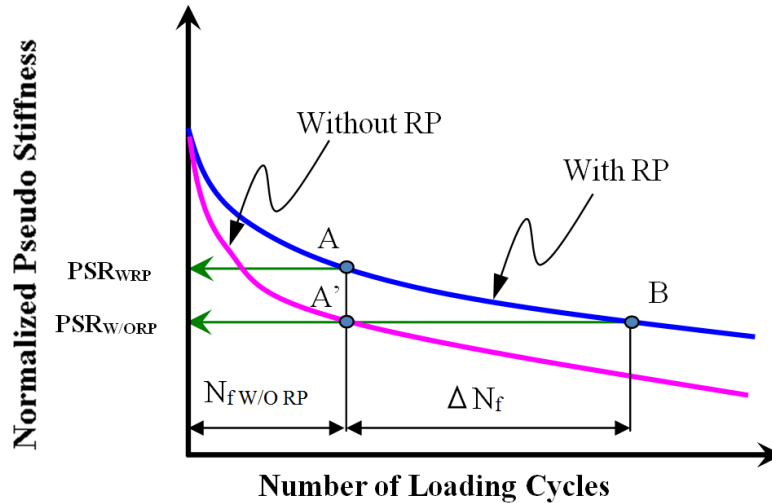


FIGURE 39 Stiffness versus number of loading cycles with and without rest period.

4.3.2 Fractional Factorial Design with Partial Randomization



In order to reduce the number of tests and at the same time to determine important effects of all variable, a 5-factor fractional factorial statistical design was developed as part of the NCHRP 9-44A project. The statistical fractional factorial design considers the effect of all 5 factors, two-factor interactions, and 3-factor interactions (Jump® Software). Higher factor interactions are ignored in this design since they are unlikely significant.

Within the fractional factorial statistical design, there are many design optimality criteria and the most popular criterion is called D-optimality (Montgomery, 2008), which was used in this study. The D-optimality design minimizes the volume of the joint confidence region on the vector of regression coefficient. A computer generated design is used to reduce the number of runs using the JMP software. TABLE 2 shows the factor combinations at which the test would be performed. The table shows that 32 combinations would be tested

with 3 replicates for each combination. This design would require a total of 96 tests required for the 5-factor full factorial design.

TABLE 2 Factor combinations for the 5-factor rational factorial completely randomized design

Asphalt Content (%)		4.2		5.2	
Air Voids (%)		4.5	9.5	4.5	9.5
Temp. (°F)	Strain Level	Rest Period (sec)			
40	L	0		--	
		5		--	
	M	0		--	
		5	--		
70	L	0	--		--
		5			--
	M	0			--
		5		--	
100	L	0		--	
		5	--		--
	M	0	--		--
		5			--

 Test combinations used in the study
 Empty cells

Test combinations used in the study

TABLE 3 shows the lists of the main and the two and three-factor interaction terms that can be estimated from this experimental design. Using this fractional factorial design, a model with up to 25 variable parameters can be developed.

TABLE 3 Factors and factor interactions estimated from the experiment

All main effect	Two-factor interactions	Three-factor interactions
Asphalt Content	Asphalt Content*Air Voids	Asphalt Content*Air Voids* Strain Level
Air Voids	Asphalt Content* Strain Level	Asphalt Content*Air Voids*Rest Period
Strain Level	Asphalt Content*Rest Period	Asphalt Content*Air Voids*Temperature
Rest Period	Asphalt Content*Temperature	Asphalt Content* Strain Level*Rest Period
Temperature	Air Voids* Strain Level	Asphalt Content* Strain Level*Temperature
	Air Voids*Rest Period	Asphalt Content* Rest Period*Temperature
	Air Voids*Temperature	Air Voids* Strain Level*Rest Period
	Strain Level*Rest Period	Air Voids* Strain Level*Temperature
	Strain Level*Temperature	Air Voids*Rest Period*Temperature
	Rest Period*Temperature	Strain Level*Rest Period*Temperature
Total of 5	Total of 10	Total of 10

4.4 Binder Characterization

4.4.1 Background

The characterization of the asphalt binder properties can be used as direct input to estimate the Complex Modulus properties of asphalt mixtures. A full characterization of three binders used in this study has been conducted by two laboratories: MACTEC in Phoenix, Arizona, and Arizona State University as a part of the NCHPR 9-44A project (Quarterly Progress Report, 2010)

The binder tests performed at MACTEC were mainly to: 1) Determine the range of compaction and mixing temperatures, 2) Characterize asphalt binders using the Superpave binder tests including Dynamic Shear Rheometer (DSR) and Bending Beam Rheometer (BBR), and 3) Design of mixture. On the other hand, ASU conducted a comprehensive characterization study of the rheological properties of asphalt binder, using one Superpave test (Brookfield viscometer) and two conventional binder tests (penetration and softening point) at a wide

range of temperatures. All test results from MACTEC and ASU are presented in the following sections.

4.4.2 Binder Source

Three grades of AC binder were provided by Holly Asphalt Company in Phoenix, Arizona, and used by both MACTEC and ASU, in order to conduct the mix design and binder characterization tests. They are all unmodified and classified as PG 58-28, PG 64-22, and PG 76-16.

4.4.3 Aging Levels

For the binder characterization tests (MACTEC and ASU), samples of the three asphalt binder grades were aged for the short-term (RTFO) and long-term (PAV) conditioning. The RTFO and PAV aging were conducted in accordance with AASHTO T240 and AASHTO R28, respectively.

The basic RTFO procedure (FIGURE 40) includes poring un-aged asphalt binder samples in cylindrical glass bottles and places these bottles in a rotating carriage within an oven. The carriage rotates within the oven for 85 minutes at 325°F (163°C) temperature. Samples are then stored for use in physical properties tests or the PAV.

The basic PAV procedure (FIGURE 41) consists of placing the RTFO aged asphalt binder samples stainless steel pans and then aging them for 20 hours in a heated vessel pressurized to 305 psi (2.10 MPa) at 212 °F (100°C). Samples are then stored for use in physical property tests.

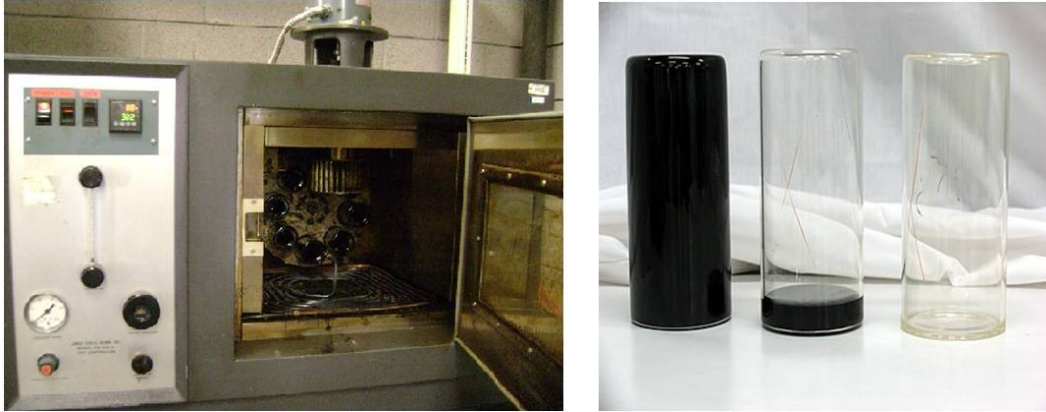


FIGURE 40 RTFO equipment and specimen preparation.



FIGURE 41 PAV equipment and specimen preparation.

4.4.4 MACTEC Test Results

4.4.4.1 Mixing and Compaction Temperatures

The laboratory mixing and compaction temperatures for the mix design were determined using the viscosity–temperature relationship. The temperatures were selected corresponding with binder viscosity values of 0.17 ± 0.02 Pa·s for mixing and 0.28 ± 0.03 Pa·s for compaction. Viscosity values were determined using a Brookfield Rheometer (ASTM D 4402). To develop the viscosity binder temperature curves, three viscosity values were measured at temperatures of 275,

311, and 347°F (135, 155, and 175°C) for the PG 58-28 and PG 64-22 binders, while two viscosity values were measured at temperatures of 275 and 347°F (135 and 175°C) for the PG 76-16 binder. TABLE 4 summarizes the lab mixing and compaction temperatures determined.

TABLE 4 Summary of laboratory mixing and compaction temperatures for mix design, °F (°C)

Temperature, °F (°C)		Binder Type		
		PG 58-28	PG 64-22	PG 76-16
Compaction	Min	275 (135)	287 (142)	310 (154)
	Max	284 (140)	296 (147)	318 (159)
Mixing	Min	295 (146)	308 (153)	329 (165)
	Max	305 (152)	320 (160)	340 (171)

4.4.4.2 Superpave Binder Classification Tests

The Dynamic Shear Rheometer (DSR) and Bending Beam Rheometer (BBR) tests were performed to characterize the three asphalt binders used for the mix design and to confirm that the binders meet the specification.

For the characterization of binder at intermediate and high temperatures, the DSR test was conducted at 59, 86, 113, 158, 203, and 239°F (15, 30, 45, 70, 95, and 115°C). The complex shear modulus (G^*) and phase angle was measured at a constant frequency (10 rad /sec). For the low temperature binder response, the BBR test was conducted and the flexural creep stiffness (S) at 60s at a specified temperature and slope (m-value) were measured. The temperatures used to measure the flexural creep stiffness were -0.4, 10.4, and 21.1°F (-18, -12, and -6°C) for PG 58-28, PG 64-22, and PG 76-16, respectively. TABLE 5 summarizes

the test methods and their properties and test conditions. It should be noted that the DSR test was separately conducted with each aging condition: Neat or Tank, RTFO, RTFO+PAV, while the BBR test was conducted only with the PAV condition.

TABLE 5 Summary of superpave binder characterization tests

Test	Property	Method	Conditions
Dynamic Shear Rheometer	Complex Shear Modulus (G^*) and Phase Angle (δ)	AASHTO T315	10 rad/sec 59, 86, 113, 158, 203, and 239°F (15, 30, 45, 70, 95, and 115°C)
Bending Beam Rheometer	Creep Stiffness (S) and Slope (m-value)	AASHTO T313	60 sec -0.4, 10.4, and 21.2 °F, (-18, -12, and -6°C)

A viscosity–temperature relationship was developed using the DSR test results (e.g., G^* and phase angle) at three aging conditions for the three binders as shown from FIGURES 42 to 44. It is obvious that, from the plots, the binder becomes more viscous as the binder is aged. Note that the viscosity values in each plot were obtained from the G^* and phase angle values at the specified test temperatures (Witczak,1998) by converting them into viscosity by the Cox-Merz equation (Cox and Merz, 1958).

$$\eta = \frac{G^*}{10} \left(\frac{1}{\sin \delta} \right)^{4.8628} \times 1000 \quad (79)$$

where,

η = viscosity, cP

G^* = complex shear modulus, Pa

δ = phase angle, degree

The creep stiffness results from the BBR test were found satisfactory with the Superpave specification. TABLE 6 shows the test results for each binder types indicating that they were all met with the specification.

TABLE 6 Summary of BBR test results (S and m-value)

Property	Binder Type			Spec
	PG 58-28	PG 64-22	PG 76-16	
Creep Stiffness, S	232	191	138	300 max
Slope, m-value	0.323	0.316	0.337	0.300 min

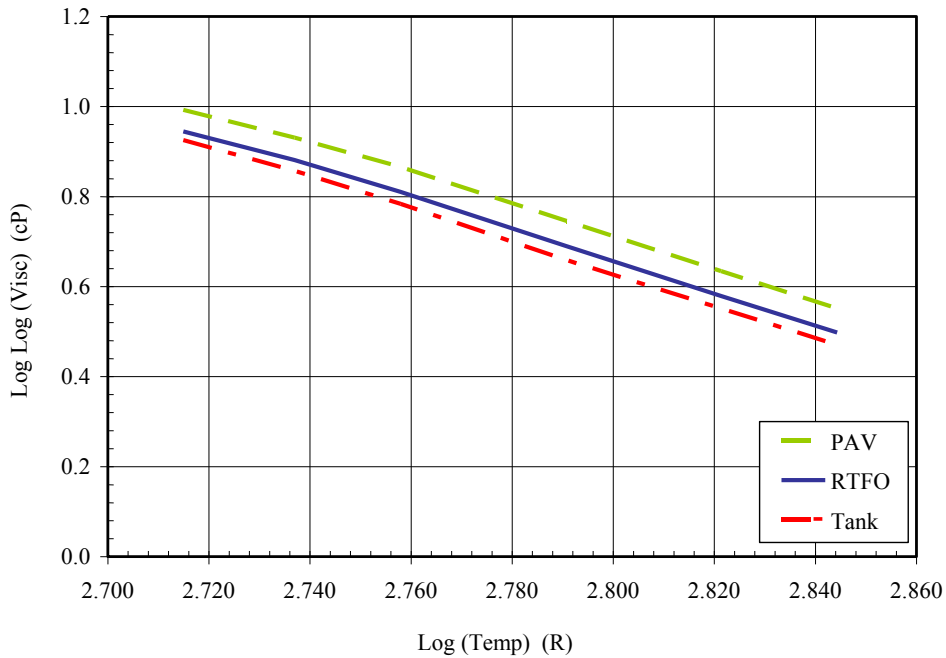


FIGURE 42 Temperature-viscosity relationship from DSR results, (PG 58-28).

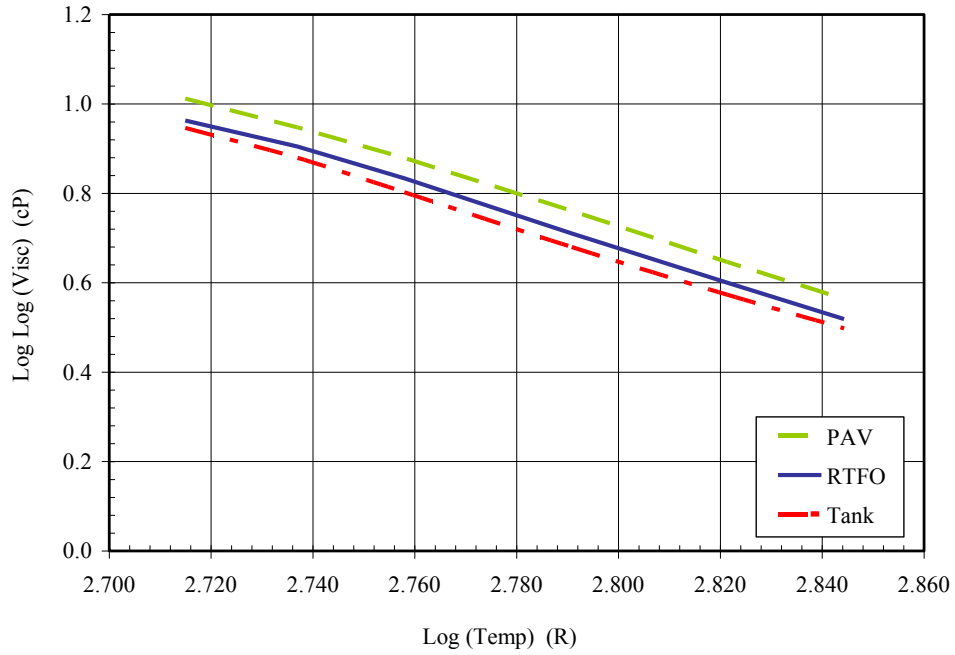


FIGURE 43 Temperature - viscosity relationship from DSR results, (PG 64-22).

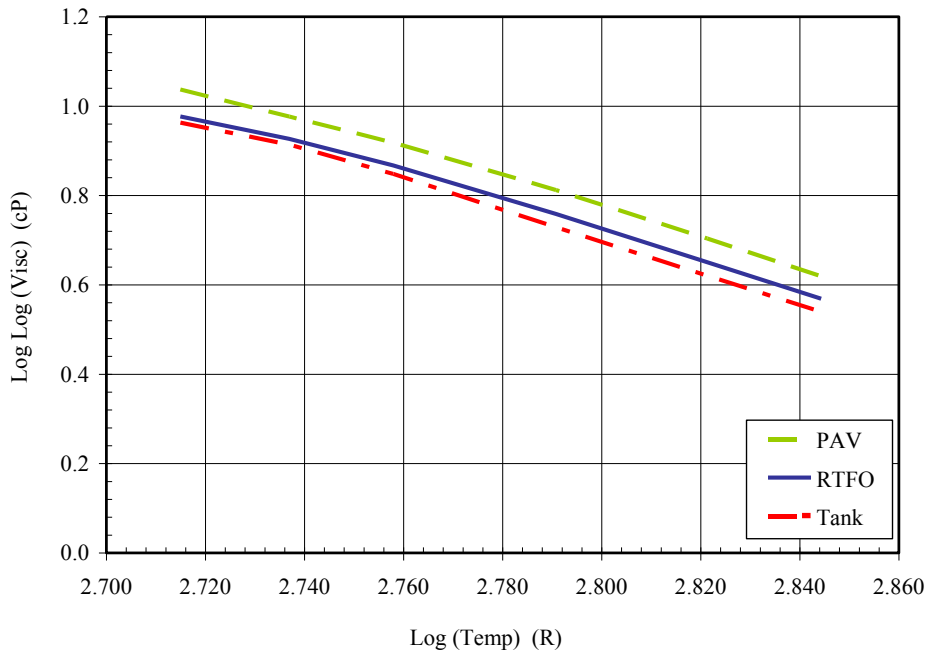


FIGURE 44 Temperature - viscosity relationship from DSR results, (PG 76-16).

4.4.5 ASU Asphalt Binder Characterization

A comprehensive characterization study of the rheological properties of three binder types (PG 58-28, PG 64-22, and PG 76-16) was conducted by ASU as a part of the NCHRP 9-44A project, using one Superpave test and two conventional binder tests. The objective of this work is to characterize the asphalt binder used in this project over a wide range of temperatures and subsequently to develop a linear relationship between temperature and viscosity (e.g., Ai-VTSi relationship). All binder tests were performed at three aging conditions: Neat (Tank) or Original, Short-Term Aged (RTFO), and Long-Term Aged (RTFO + PAV). The conventional binder tests used in this study include Penetration test and Softening Point (Ring and Ball test). The Superpave binder test was the Rotational Viscosity (Brookfield) test.

It is also worthy to mentioned that each of the three binder types was distributed with two sample cans (Sample 1 and 2); and each can was again duplicated (Replicate A and B). This scheme applies to each aging condition. Thus, for one PG binder at a certain aging condition, four specimens (2 cans * 2 duplicates) were tested for the three binder tests. These four specimens were called a set and a unique number was assigned for each set as a set number. TABLE 7 shows an example of this set numbering scheme.

TABLE 7 Example of binder sample preparation scheme

Binder Type	Aging Condition	Sample Can	Replicate	Set Number
PG 58-28	Neat	1	A	10
			B	12
		2	A	11
			B	13

4.4.5.1 Test Methods

Two conventional binder tests (penetration and softening point) and one Superpave binder tests (Brookfield viscometer) were conducted. Each test was essential to develop the linear relationship of temperature-viscosity susceptibility. TABLE 8 summarizes the properties measured, the test standard, and the test condition for each test. Following is a summary of the three binder tests:

TABLE 8 Summary of conventional and Superpave binder characterization tests

Test Type	Property	Method	Conditions
Conventional Test	Penetration	AASHTO T49	100 g, 5 sec, 40, 55, 77, and 90°F (4, 12.8, 25, and 32°C)
	Softening Point	AASHTO T53	Measured Temperature
Superpave Test	Brookfield Viscosity	AASHTO T316	200, 250, 300, 350°F (93, 121, 149, 177°C)

Penetration Test

The Penetration test was conducted to measure viscosity at low and intermediate temperatures. The penetration of an asphalt binder is the distance in tenths of a millimeter that a standard penetrates vertically into a sample of the material under fixed conditions of temperature, load and time. This test is commonly used as a measure of consistency. Higher values of penetration indicate softer consistency. The binder sample was heated and cooled under controlled conditions. The penetration was measured with a penetrometer using a standard needle under a specified condition. Penetration tests were conducted at

40, 55, 77, and 90°F (4, 12.8, 25, and 32°C) using a 100 g load for 5 second.

FIGURE 45 shows the penetration test apparatus and specimen preparation. The

penetration value can be converted into viscosity by the Equation 80:

$$\log \eta = 10.5012 - 2.2601 \log(\text{Pen}) + 0.00389 [\log(\text{Pen})]^2 \quad (80)$$

where;

η = viscosity, P

Pen = measured penetration for 100g, 5 sec loading, 0.1 mm

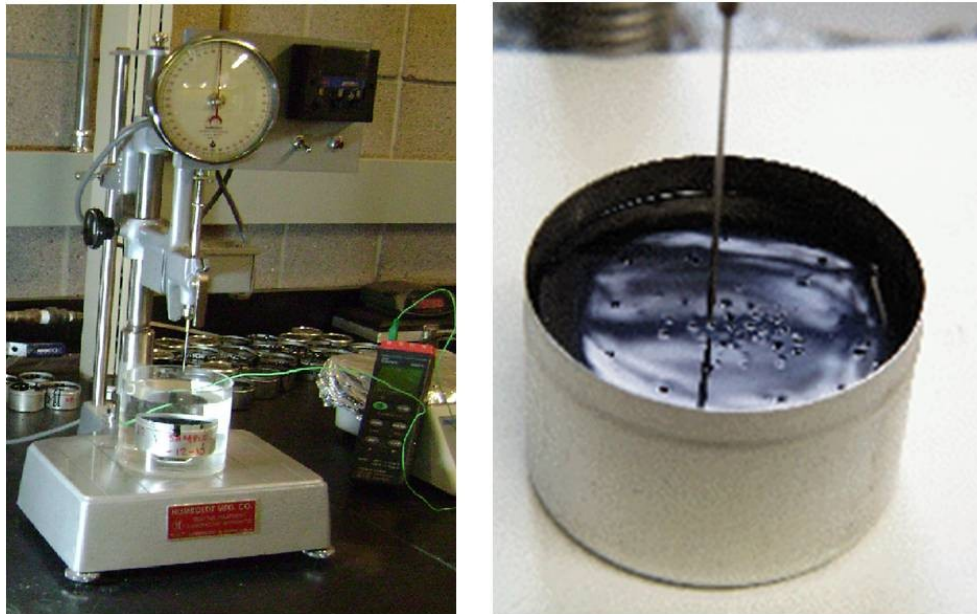


FIGURE 45 Penetration test apparatus and specimen preparation.

Softening Point Test

This test covers the determination of the softening point of asphalt binders using the ring-and-ball apparatus. Two horizontal disks of binder, cast in shouldered brass rings, are heated at controlled rate in a liquid bath while each

supports a steel ball. The softening point is reported as the mean of the temperatures at which the two disks softens enough to allow each ball, enveloped in asphalt binder, to fall a vertical distance of 1-inch (25-mm). The softening point is used in the classification of asphalt binders and as one of the elements in establishing the uniformity of shipments or sources of supply. The softening point is indicative of the tendency of the binder to flow at elevated temperatures encountered in service. For most asphalt binders, the ring and ball softening point corresponds to a viscosity of 13,000 Poise. FIGURE 46 shows the test apparatus and specimen preparation.

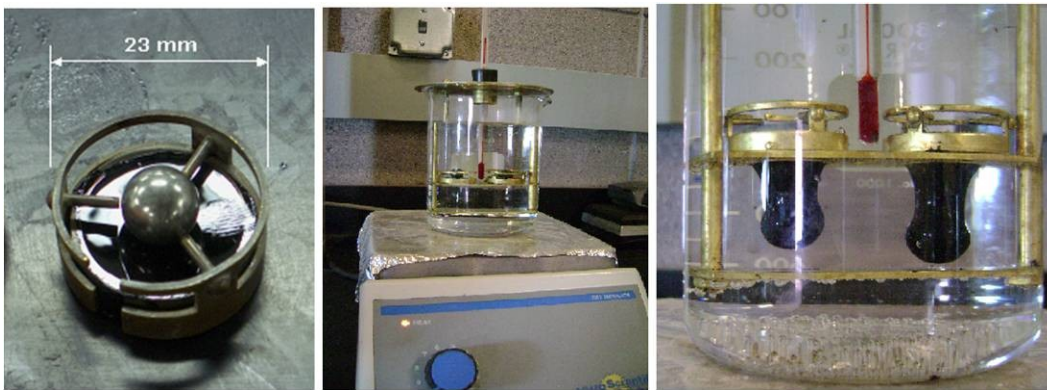


FIGURE 46 Softening point test apparatus and specimen preparation.

Brookfield Viscosity Test

This test determines the viscosity i.e. flow characteristics of asphalt binders at higher temperatures. A Brookfield rotational coaxial viscometer was used with a Thermosel™ temperature control system. The rotational viscometer automatically calculates the viscosity at the test temperature. The rotational viscosity is determined by measuring the torque required to maintain a constant rotational speed of a cylindrical spindle while submerged in a binder at a constant temperature. This torque is directly related to the binder viscosity. A rotational

viscometer can measure viscosity of asphalt binder both at Newtonian and non-Newtonian binder conditions. Unlike capillary tube viscometers, the rotational viscometers have larger clearances between the components and, therefore, are applicable to modified as well as unmodified asphalt binders. The viscosity at different shear rates at different temperatures can be used to determine the viscosity-temperature susceptibility of asphalt binders. The Brookfield viscometer measures viscosity at four elevated temperatures (200, 250, 300, and 350°F). FIGURE 47 shows the test apparatus and specimen preparation.



FIGURE 47 Brookfield test apparatus and specimen preparation.

4.4.5.2 Data Analysis

A combination of eight viscosity-temperature data points (four penetration, one softening, and four Brookfield) are plotted together in a viscosity-temperature graph, in order to characterize the viscosity temperature susceptibility relation over a wide range of temperature. The linear relationship can be established based upon Equation 81. FIGURES 48 to 50 illustrate the viscosity-temperature relationship for each binder type at all aging levels (tank condition, RTFO, and PAV).

$$\log \log \eta = A + VTS \log T_R \quad (81)$$

where;

η = viscosity, cP

T_R = temperature, Rankine

A = regression intercept

VTS = regression slope of viscosity temperature susceptibility

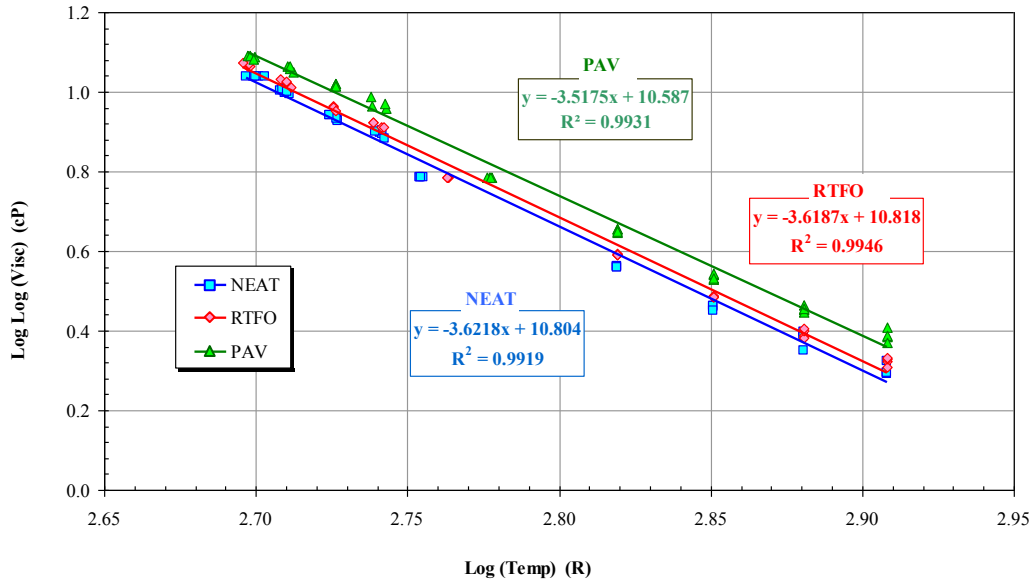


FIGURE 48 Viscosity – temperature relationship of PG 58-28 binder.

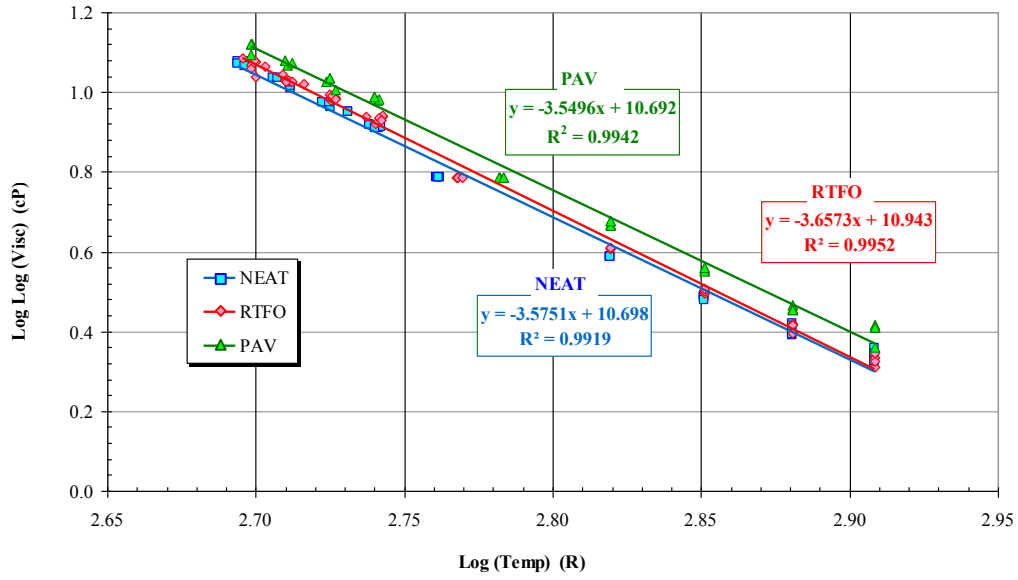


FIGURE 49 Viscosity – temperature relationship of PG 64-22 binder.

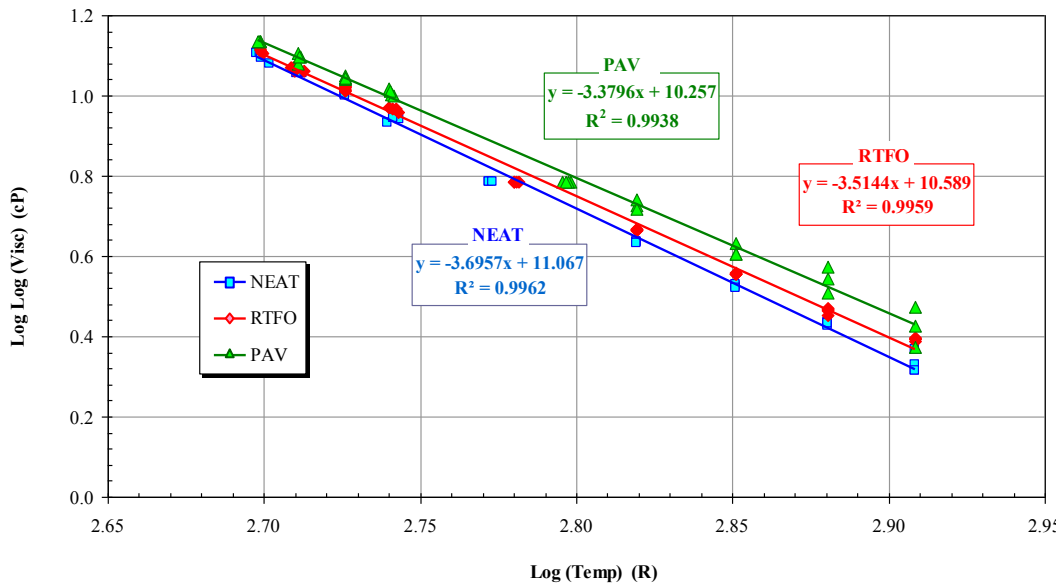


FIGURE 50 Viscosity – temperature relationship of PG 76-16 binder.

4.5 Mix Design

The aggregate for this research was crushed Salt River gravel. The aggregate stockpiles were provided by CEMEX U.S.A., and were delivered from their Plant #111 – 1386 in Phoenix, Arizona. The aggregate stockpiles being delivered included different aggregate sizes including: ¾”, ½” 3/8”, sand, and crushed fines.

The ¾-inch (19-mm) Superpave high traffic asphalt concrete mix design was prepared by MACTEC for this research according to the requirements of Maricopa County, Uniform Standard Specifications for Public Works Construction Section 710. The Superpave mix design prepared herein is to provide typical paving materials used for paving arterial roads. While three different asphalt concrete mixes were designed each of which used a particular binder type: PG 58-28, PG 64-22, and PG 76-16, the same aggregate gradation was consistently used for all mix designs. TABLE 9 shows the designed aggregate gradation along with the minimum and maximum design specification. FIGURE 51 illustrates the designed aggregate gradation distribution curve.

TABLE 10 includes composite aggregate properties conducted by MACTEC. The summary of the key volumetric properties from the mix design results using three binders are presented in TABLE 11.

TABLE 9 Designed aggregate gradation

Size	% Passing		
	Design	Minimum	Maximum
1 in.	100.0	100.0	100.0
¾ in.	95.0	90.0	100.0
½ in.	80.0	43.0	89.0
3/8 in.	59.0		
No. 4	39.0		
No. 8	29.0	24.0	36.0
No. 16	23.0		
No. 30	17.0		
No. 50	10.0		
No. 100	5.0		
No. 200	3.3	2.0	6.0

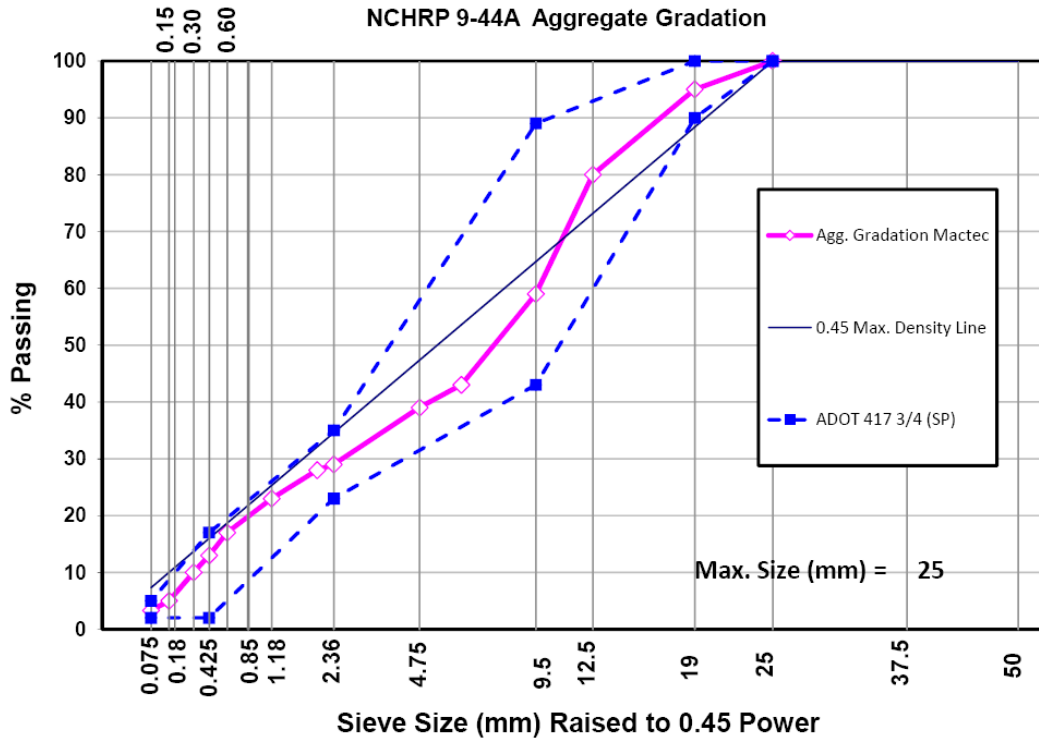


FIGURE 51 Designed aggregate gradation distribution curve.

TABLE 10 Composite aggregate properties

Property	Value	Specifications
Bulk (Dry) Sp. Gravity	2.614	(2.35-2.85)
SSD Sp. Gravity	2.638	
Apparent Sp. Gravity	2.677	
Water absorption (%)	0.90	(0-2.5)
Sand Equivalent Value	71	Min 50
Fractured Face One (%)	99	Min 85
Fractured Face Two (%)	96	Min 80
Flat & Elongation (%)	1.0	Max 10
Uncompacted Voids (%)	46.8	Min 45
L.A. Abrasion @ 500 Rev.	16	Max 40

TABLE 11 Summary of the volumetric mix design at different binder types

Volumetric Property	Binder Type			Specs.
	PG 58-28	PG 64-22	PG 76-16	
Target Asphalt Content (%)	4.8	4.5	4.7	4.5 ~ 5.5
Bulk Specific Gravity (G_{mb})	2.365	2.367	2.351	N/A
Theoretical Max. Sp. Gr. (G_{mm})	2.461	2.467	2.454	N/A
Design Air Voids (%)	3.9	4.1	4.2	3.8 ~ 4.2
VMA (%)	13.9	13.5	14.3	Min. 13
VFA (%)	71.9	69.9	70.8	N/A
Asphalt Sp. Gr. (G_b)	1.024	1.024	1.042	N/A

4.6 Research Testing Plan

The research testing plan included conducting two main testing methods: the first test method is the Complex Modulus test, the second test is the uniaxial tension-compression fatigue test which is a damage inducing test. The research

testing plan for each test is shown in FIGURE 52 and described in the following session.

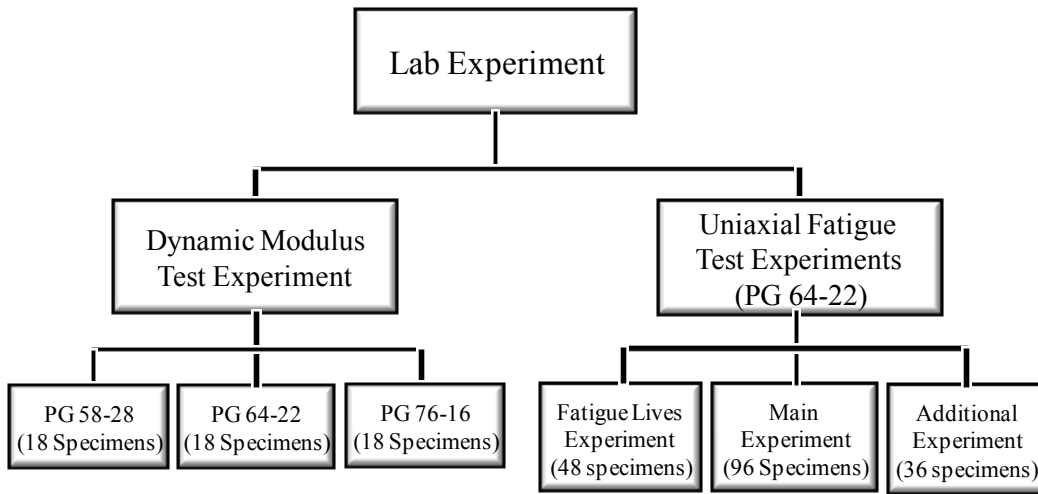


FIGURE 52 Flow chart of research testing plan.

4.6.1 Dynamic Modulus Test (AASHTO TP 62-07) Experiment

One important part of the research plan was to develop the dynamic modulus master curves and temperatures shifting for different tested asphalt concrete mixtures. These results will be used for two main purposes. The first purpose is to use the dynamic modulus master and phase angle master curves to estimate the viscoelastic properties of asphalt concrete mixtures by predicting the relaxation modulus that required in the analysis of the viscoelastic and continuum damage model. Another important purpose of this test is to use the shift factors of different temperatures in the shifting analysis of fatigue damage and healing at different temperatures.

The complex modulus test is conducted according to the AASHTO TP 62-07 protocol in a stress-control mode of loading within the linear viscoelastic range using sinusoidal loading wave in compression. The stress magnitudes vary

according to the mixture type, test temperature, and test frequency so that the recoverable strain is limited to 150 microstrains to insure that there is no damage occurred during the test. The cylindrical specimens used in this test had a diameter of 100 mm (4 inches) and 150 mm (6 inches) height.

Complex modulus test plan included testing of three asphalt concrete mixtures based on the binder type. The three binder types are PG 58-28, PG 64-22, and PG 76-16. Each asphalt concrete mixture was tested at three levels of asphalt contents and air void including nine different combinations of both factors. Two identical replicates were tested for each combination which means a total number of 18 specimens for each mixture or 54 specimens for the three mixtures. Each one of these specimens was tested at five temperatures and six frequencies as explained in details in Chapter 5. TABLE 12 shows the number of complex modulus tests under different conditions.

TABLE 12 Number of complex modulus tests under different conditions

Mixture Type	Asphalt Cement (%)	Air Void (%)		
		Low	Optimum	High
PG 58-28	Low	2 replicates	2 replicates	2 replicates
	Optimum	2	2	2
	High	2	2	2
PG 64-22	Low	2	2	2
	Optimum	2	2	2
	High	2	2	2
PG 76-16	Low	2	2	2
	Optimum	2	2	2
	High	2	2	2
Total number of specimens		54		

4.6.2 Uniaxial Tension-Compression Fatigue Test Experiments

Test uniaxial fatigue test experiments included the testing of PG 64-22 asphalt concrete mixture only. Four asphalt concrete mixtures with different asphalt content and air void combinations were used on these experiments (4.2% AC& 4.5 %Va, 5.2% AC& 4.5 %Va, 4.2% AC& 9.5 %Va, and 5.2% AC& 9.5 %Va). The research plan of the uniaxial tension compression fatigue test consists of three experiments: fatigue lives experiment, main experiment, and additional experiment.

4.6.2.1 Fatigue Lives Experiment

The main purpose of this experiment was to determine the strain levels for each mixture type used in the main experiment at different temperatures. Based on the main experiment, it is required to select two different strain levels at each test temperature (40, 70 and 100°F). The criterion of selecting the two strain levels at each temperature was to reach a fatigue life of 20,000 cycles at the high strain level and 100,000 cycles at the low strain level. To establish each fatigue life, four uniaxial tension-compression fatigue tests were conducted at different strain levels, which required 12 tests for one mixture at three temperatures (40, 70 and 100°F) or 48 tests for the four asphalt concrete mixtures. The number of fatigue tests under different conditions is shown in TABLE 13.

TABLE 13 Number of fatigue tests under different conditions

Air Voids (%)	Temp. (°F)	Asphalt Content (%)	
		4.2	5.2
4.5	40	4	4
	70	4	4
	100	4	4
9.5	40	4	4
	70	4	4
	100	4	4
Total		48 Tests	

4.6.2.2 Main Fatigue Experiment

The main objective of the main experiment is to investigate the healing of fatigue damage of asphalt concrete mixtures and mathematically correlate the healing properties to different factors identified before in the design of experiment section. In addition, the results from this experiment are used to develop a methodology to predict the endurance limit of hot mix asphalt based mainly on healing properties. The fatigue healing in this research is evaluated by observing the difference between fatigue damage using two different methods of the uniaxial fatigue test. The first method is a damaged test where the loading is running continuously without any rest between the loading cycles inducing fatigue damage. The second method is the healing or intermittent-load test where a constant rest period is inserted between the loading cycles to allow for healing of fatigue damage. The amount of rest period used on this experiment is 5 seconds inserted between the 0.1-second loading cycles throughout the entire test (loading ratio of 50).

Based on the results of the fractional factorial design of experiment, TABLE 14 shows the testing plan for uniaxial tension-compression fatigue test.

TABLE 14 Number of uniaxial tension-compression fatigue test under different conditions

Rest Period (sec)			0		5	
Air Voids (%)			4.5	9.5	4.5	9.5
Temp. (°F)	Strain Level	Asphalt Content (%)	Number of Specimens			
40	L	4.2	3	3	3	--
		5.2	--	3	3	3
	M	4.2	3	--	--	3
		5.2	3	3	3	3
70	L	4.2	--	3	3	3
		5.2	3	--	--	3
	M	4.2	3	3	3	--
		5.2	--	3	3	3
100	L	4.2	3	--	--	3
		5.2	3	--	3	--
	M	4.2	--	3	3	3
		5.2	3	--	--	3
Total Number of Specimens			45 Specimens		51 Specimens	

4.6.2.3 Additional Fatigue Experiment

As only two strain levels were considered in the main experiment, the relationship between the Pseudo Stiffness Ratio (PSR) and the strain levels is linear. However the real relationship may have a different trend. The same situation is also considered for the rest period as only two levels of the rest periods are applied (0, and 5 seconds). Based on earlier research, the effect of the rest period on the fatigue life and healing might be insignificant beyond certain value. Therefore, the relationship between the PSR and the rest period is not a linear relationship. In this experiment, an additional strain level (high) and two additional rest periods of 1.0 and 10.0 seconds (10 and 100 loading ratio) were added. The selection of the required combinations is justified by using the fractional factorial technique considering only two levels of interaction as shown

in TABLE 15 (Jump® Software). Based on this, additional 20 combinations are required. Because of the overlap with the main experiment, only 18 new combinations are required. Two replicates were considered for each combination.

TABLE 15 Testing plan of additional fatigue test

Asphalt Content (%)		4.2		5.2		
Air Voids (%)		4.5	9.5	4.5	9.5	
Temp., °F	Strain Level	Rest Period (sec)				
40	L	0				
		1				
		5		X	XX	
		10				
	M	0				
		1		X		
		5				
		10			X	
	H	0				X
		1			X	
		5	X			
		10				
70	L	0	X			
		1				
		5				
		10			X	
	M	0				
		1			X	
		5		X		
		10				
	H	0				
		1				X
		5				
		10				
100	L	0			X	
		1	X			X
		5				
		10				
	M	0				X
		1				
		5	XX			
		10		X		
	H	0		X		
		1				
		5				X
		10				

X New combinations of additional experiment
 XX Overlapped combinations with the main experiments

4.7 Laboratory Manufacturing of HMA Specimens

4.7.1 Preparation of Aggregates

4.7.1.1 Drying of Aggregate Stockpiles

Five different stockpiles were used in this study including: $\frac{3}{4}$ " , $\frac{1}{2}$ " $\frac{3}{8}$ " , sand, and crushed fines. The aggregates were placed in large ovens to dry over night at 110 °F before the blending and sieving.

4.7.1.2 Blending of Aggregate Stockpiles

Dried aggregate stockpiles were blended at percentages provided by CEMEX, U.S.A. The percentages used for each stockpile gradation were as follows:

Sieve Size	Percent Passing
$\frac{3}{4}$ "	= 18%
$\frac{1}{2}$ "	= 12%
$\frac{3}{8}$ "	= 12%
Sand	= 15%
Crushed Fines	= 43%

4.7.1.3 Sieving of Blended Aggregates

Once the aggregates from each stockpile have been weighed and blended at the determined percentages, a shovel was used to place 3-4 heaping shovel fills into the top of a Gilson Test Master TM-4 Floor Sieve Shaker. The Sieve shaker was run for a 20 minute period and once completed; the contents of each size sieve were emptied into pre labeled 5 gallon plastic buckets.

4.7.1.4 Aggregate Batching

Batches were created using the Mix Design Gradation from MACTEC's mix design (TABLE 16). Batches were made using empty, clean 1 gallon metal paint cans. Paint cans were filled with the calculated weights from each aggregate size as per mix design gradation in order to create one individual specimen.

TABLE 16 Aggregate batching sheet

Sieve Size	Total Passing (%)	Retained (%)	Weight per Core Batch (gm)	Weight per Core Batch (gm)
¾"	95.0	5.0	325	350
½"	80.0	15.0	975	1050
3/8"	59.0	21.0	1365	1470
No. 4	39.0	20.0	1300	1400
No. 8	29.0	10.0	650	700
No. 16	23.0	6.0	390	420
No. 30	17.0	6.0	390	420
No. 50	10.0	7.0	455	490
No. 100	5.0	5.0	325	350
No. 200	3.3	1.7	110.5	119
Pan (<No. 200)		3.3	214.5	231
Total		100	6500	7000

2.7.1.5 Wet Sieve Analysis

In order to pinpoint the proper amount of fines used in each specimen, ASU (Arizona State University) performed (AASHTO T-11) Wet Sieve Analysis of Aggregates. Two 1,500 gram samples were washed on a weekly basis as a quality assurance quality control. Those results were analyzed and any adjustments were made to the batching gradation for that week's worth of batching.

4.7.3 Preparation of Specimens

4.7.3.1 Mixing of Asphalt Mixture

Prior to the specimen mix manufacturing process; batched aggregate cans were placed in a heated oven at 295 °F (145 °C) overnight to insure that no moisture is present in the aggregate specimens. The day of the sample mixing, an appropriate of binder was placed in a heated oven for approximately 60 minutes to gently bring the temperature of the binder up to the desired mixing temperature. The preheated aggregates and the desired amount of binder were then placed into mixing bucket and mixed together using the mixing machine for 120 seconds.

4.7.3.2 Short Term Aging

The properly mixed HMA was then emptied and evenly spread about into a heated metal tray, approximately 3' x 3' and 3" deep in size, and placed uncovered into a preheated 275°F (135°C) convection oven for Short Term Aging. This procedure is as specified in the AASHTO PP-2 aging procedure for Superpave mixture performance testing.

4.7.3.3 Maximum Theoretical Specific Gravity (G_{mm})

HMA specimen that was heated and mixed, as per the standard mixing protocol, was poured loose on a table to cool overnight. The next day, the cooled HMA is crumbled and separated by hand and the Theoretical Maximum Specific Gravity (G_{mm}) is established for the mix using the AASHTO T209 Pycnometer Method. This G_{mm} of the specific HMA is used to calculate the Air Voids (V_a %) of all specimens.

4.7.3.4 HMA Compaction

For the preparation of gyratory specimens used in this study, an IPC (Industrial Processing Services) SERVOPAC gyratory compactor is used. The compactor is set with a vertical stress of 600 kPa at a rate of 38 gyrations per minute and a 1.25° gyration angle. The molds used are 6-inch (150-mm) in diameter. All gyratory plugs are compacted to a standardized height of 6.7-inch (170-mm). The 6-inch (150-mm) diameter plug is then cored with a 4-inch (100-mm) diamond tipped coring bit for E* specimens or with a 3-inch (75-mm) diamond tipped coring bit in case of uniaxial fatigue specimens. The 6.7-inch (170-mm) height is trimmed to 6-inch (150-mm) using a 14-inch diamond tipped asphalt circular saw blade.

4.7.3.5 Air Voids Determination

The cored and cut specimens were left out for enough time to get dry. The air voids (V_a) of the dried specimens were then obtained using the Bulk Specific Gravity of Bituminous Mixtures Using Saturated Surface Dry Specimens method (AASHTO T166- 93).

4.7.3.6 Storing of Prepared Specimens

After measurement of air voids, the specimens were left for one day to dry out. The specimen is then placed inside a Zip-Loc bag and stored in a shelving cabinet at room temperature to minimize aging. The storing time is limited to less than a month before testing.

CHAPTER 5

VISCOELASTIC PROPERTIES OF ASPHALT CONCRETE MIXTURES

5.1 Background

The viscoelastic response of asphalt concrete mixtures can be captured through mechanical tests conducted in the linear viscoelastic range. Viscoelastic behavior of asphalt concrete mixtures can be described by different mechanical properties. These mechanical properties are complex modulus, relaxation modulus and creep compliance. In this study, the complex modulus was determined for three mixtures with binder grades of PG 58-28, PG 64-22, and PG 76-16 according to AASHTO TP 62-07 test procedure.

5.2 Complex Modulus

5.2.1 Theoretical Background

For linear viscoelastic materials such as asphalt mixes, the stress-strain relationship under a continuous sinusoidal loading is defined by a complex number called the complex modulus E^* (Pellinen, 2001; NCHRP 465, 2002). It is a true complex number that contains both a real and imaginary component of the modulus that defines the elastic and viscous behavior of the linear viscoelastic material. These components are:

$$E^* = E' + iE'' \quad (82)$$

or

$$E^* = \sqrt{(E')^2 + (E'')^2} \quad (83)$$

with

$$E' = (\sigma_o / \epsilon_o) \cos \phi \quad \text{or} \quad E' = E^* \cos \phi \quad (84)$$

$$E'' = (\sigma_o / \varepsilon_o) \sin \phi \quad \text{or} \quad E'' = E^* \sin \phi \quad (85)$$

where:

σ_o = peak dynamic stress amplitude (psi or kPa),

ε_o = peak recoverable strain (in/in or mm/mm), and

ϕ = phase lag or angle (degrees).

The E' value is generally referred to as the storage (elastic) modulus component of the complex modulus, while E'' is referred to as the loss (viscous) modulus. The loss tangent ($\tan \phi$) is the ratio of the energy lost to the energy stored in a cyclic deformation and is equal to:

$$\tan \phi = E'' / E' \quad (86)$$

According to the current protocol, complex modulus testing of asphalt materials is conducted using a uniaxial sinusoidal load (AASHTO TP 62-03, 2005). Under such conditions, the complex modulus is defined as the ratio of the amplitude of the sinusoidal stress (at any given time, t , and angular load frequency, ω), $\sigma = \sigma_o \sin(\omega t)$ and the amplitude of the sinusoidal strain $\varepsilon = \varepsilon_o \sin(\omega t - \phi)$, at the same time and frequency, that results in a steady state response (FIGURE 53)

$$E^* = \frac{\sigma}{\varepsilon} = \frac{\sigma_o e^{i\omega t}}{\varepsilon_o e^{i(\omega t - \phi)}} = \frac{\sigma_o \sin \omega t}{\varepsilon_o \sin(\omega t - \phi)} \quad (87)$$

where,

ω = angular velocity = $2\pi f$,

t = time, seconds, and

f = loading frequency (Hz).

$$\phi = (t_i / t_p) \times (360^\circ) \quad (88)$$

or

$$\phi = 2\pi f (t_i) \quad (89)$$

where:

t_i = time lag between a cycle of stress and strain (sec), and

t_p = time for a stress cycle (sec).

The absolute value of the complex modulus $|E^*|$, is defined as the dynamic modulus. Mathematically, the dynamic modulus is defined as the maximum (peak) dynamic stress (σ_o) divided by the recoverable axial strain (ϵ_o):

$$|E^*| = \frac{\sigma_o}{\epsilon_o} \quad (90)$$

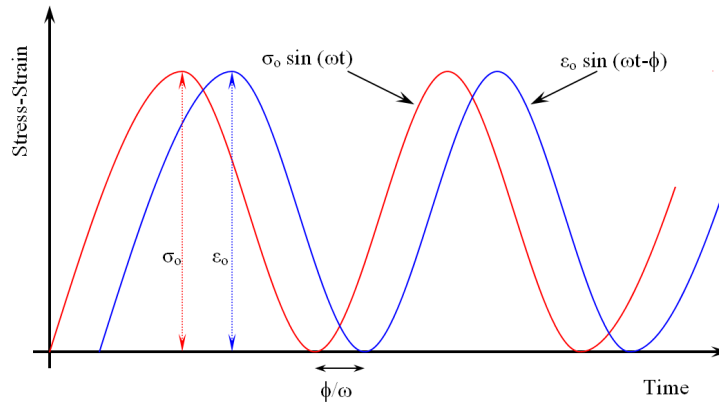


FIGURE 53 Complex modulus test

5.2.2 Testing System

An Industrial Process Controls (IPC) Universal Testing Machines (UTM-25) was used to conduct the complex modulus test. The UTM-25 machine have two closed-loop servo-hydraulic testing system manufactured by IPC in Australia. The load frame capacity is 5,600 lb (25kN) in static loading and 5,600 lb (25kN) in dynamic loading. The machine is capable of applying load over a wide range of

frequencies (from 0.1 to 20 Hz). The servo hydraulic system is controlled by an IPC controller

The temperature control system of the UTM is refrigeration-based. The temperature control system is able to provide temperatures in the range of 5 to 140°F (-15 to 60°C), and for extended periods. The excellent temperature homogeneity and gradients is achieved with internal fans and baffles to control air circulation, gives greater confidence in test results. Asphalt dummy specimen with both skin and core temperature probes is used to ensure consistency in testing temperature.

The measurement system is computer controlled and capable of measuring and recording a minimum of 16 channels, simultaneously. The channels are assigned to various sensors. Of the 16 channels, 7 channels are using; 2 channels for on-sample vertical deformation measurements, 2 channels for the load cell and the actuator LVDT, 2 channels for the skin and core temperature probes, and one channel for the confinement pressure measurement.

Loads are measured using electronic load cells capable of measuring loads with an accuracy of ± 0.1 %. Vertical deformations are measured using two spring loaded linear variable differential transducers (LVDTs). FIGURE 54 illustrates different components of the testing system.

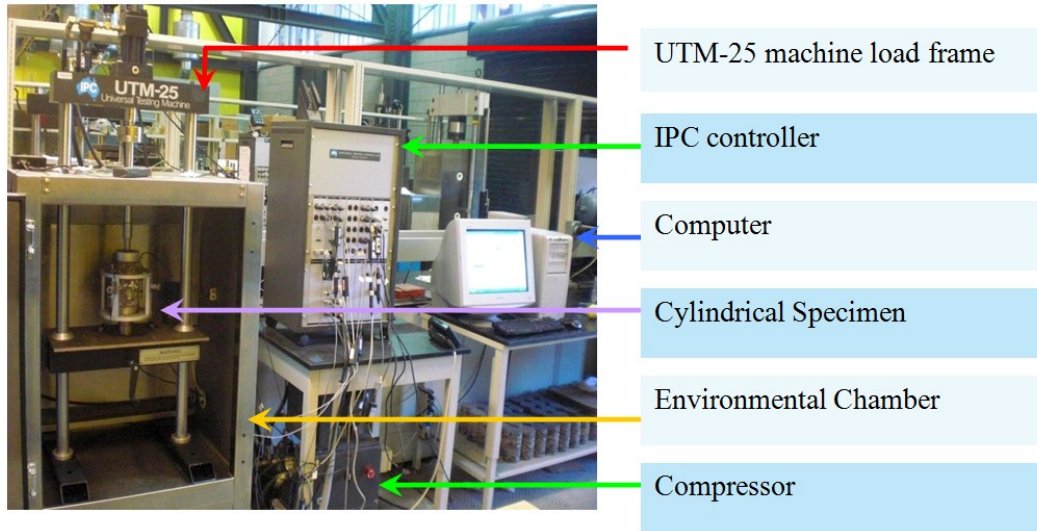


FIGURE 54 Complex modulus test setup

5.2.3 Tested Mixtures

As discussed before in Chapter 4, the testing plan of the dynamic modulus experiment includes the testing of three different mixtures. Each mixture has different binder type (PG 58-28, PG 64-22, and PG 76-16). For each mixture, a number of 18 different cylindrical specimens of 4-inch (100 mm) in diameter and 6-inch (150 mm) in height are. These specimens represent 9 different combinations of the air voids and the asphalt content with 2 replicate for each combination. For the 64-22 asphalt mixture, the air voids values are the designed $V_a \pm 3\%$ (4, 7, and 10%). The asphalt content values are the optimum AC and $\pm 0.5\%$ (4.0, 4.5, and 5%). For PG 58-28 and PG 76-16 mixtures, the air voids values are the designed V_a and $\pm 2.5\%$ (4.5, 7, and 9.5). The asphalt content values were fixed for these two mixtures as 4.2, 4.7, and 5.2%. TABLE 17 shows the different combinations of specimens used for the PG 64-22 asphalt mixture. TABLE 18 illustrates the combinations of specimens required for the other two mixtures.

TABLE 17 Number of specimens for different combinations of specimens for the PG64-22 asphalt mixture

Binder Type	Asphalt Content (%)	Air Voids (%)		
		4	7	10
PG64-22	Optimum-0.5 = 4.0	2	2	2
	Optimum = 4.5	2	2	2
	Optimum+0.5 = 5.0	2	2	2

TABLE 18 Number of specimens for different combinations of specimens for the PG58-28 and PG76-16 asphalt mixtures

Binder Type	Asphalt Content (%)	Air Voids (%)		
		4.5	7	9.5
PG58-28	4.2	2	2	2
	4.7	2	2	2
	5.2	2	2	2
PG76-16	4.2	2	2	2
	4.7	2	2	2
	5.2	2	2	2

5.2.4 Measured G_{mm} and Air Void Values of Tested Specimens

All E* test specimens are prepared according to the AASHTO TP 62-03 protocol. First, the maximum specific gravity (G_{mm}) has been measured according to the AASHTO T209-00 for each binder type at different asphalt content value (OAC and $\pm 0.5\%$). Also, gyratory compacted trials have been done to get the proper mixture weights required to get the targeted air voids levels in each case. Mixes are compacted in a Servopac gyratory compactor to 6-inch (150-mm) diameter x 6.7-inch (170-mm) high. All test specimens are sawed and cored to obtain the final 4-inch (100-mm) diameter x 6-inch (150-mm) high E* test

specimens. Before the E* testing, AASHTO T166-00 is followed to measure the bulk specific gravity, air voids and water absorption of the specimens using saturated surface-dry specimens. The measured SSD air voids and the bulk specific gravity for the fabricated specimens are listed on TABLES 19 to 21.

TABLE 19 Bulk Sp. Gr., maximum Sp. Gr., and Saturated surface dry air voids of the PG 64-22 specimens

Specimen ID	Bulk S. G. G_{mb}	Measured Max. S. G. G_{mm}	SSD Air Voids (%)
6-105	2.254	2.491	9.52
6-106	2.248		9.74
6-703	2.304		7.51
6-704	2.317		7.00
6-404	2.403		3.53
6-405	2.398		3.73
6O103	2.222	2.471	10.07
6O104	2.214		10.42
6O701	2.294		7.16
6O702	2.293		7.21
6O401	2.366		4.26
6O402	2.366		4.23
6+105	2.218	2.459	9.80
6+106	2.207		10.24
6+705	2.271		7.28
6+706	2.287		6.99
6+405	2.355		4.22
6+406	2.354		4.26

TABLE 20 Bulk Sp. Gr., maximum Sp. Gr., and Saturated surface dry air voids of the PG 58-28 specimens

Specimen ID	Bulk S. G. G_{mb}	Measured Max. S. G. G_{mm}	SSD Air Voids (%)
5-901	2.246	2.482	9.53
5-902	2.245		9.56
5-701	2.295		7.55
5-702	2.296		7.49
5-401	2.364		4.74
5-402	2.365		4.72
5O901	2.222	2.465	9.84
5O902	2.224		9.79
5O702	2.281		7.46
5O703	2.284		7.36
5O402	2.340		5.07
5O403	2.347		4.77
5+901	2.201	2.444	9.95
5+902	2.204		9.81
5+703	2.255		7.74
5+704	2.271		7.06
5+401	2.333		4.53
5+402	2.329		4.72

TABLE 21 Bulk Sp. Gr., maximum Sp. Gr., and Saturated surface dry air voids of the PG 76-16 specimens

Specimen ID	Bulk S. G. G_{mb}	Measured Max. S. G. G_{mm}	SSD Air Voids (%)
7-901	2.251	2.470	8.87
7-902	2.239		9.34
7-703	2.299		6.92
7-704	2.304		6.71
7-403	2.347		4.99
7-404	2.349		4.89
7O903	2.229	2.453	9.12
7O904	2.225		9.30
7O701	2.282		6.97
7O702	2.277		7.13
7O401	2.338		4.69
7O403	2.354		4.56
7+903	2.197	2.437	9.85
7+904	2.199		9.77
7+703	2.259		7.32
7+704	2.274		6.70
7+401	2.329		4.45
7+402	2.319		4.84

5.2.5 Capping of Specimens

During cutting the tops and the bottoms of the specimens, especially at high air voids and low asphalt cement combination, some of the aggregates were torn off leaving void gaps on the top and the bottom surfaces. A special attention was given to treat these surfaces by capping the top and the bottom of the specimen with a suitable capping compound so that the thickness of the cap is about 1/8-inch (3-mm) and not more than 5/16-inch (8-mm) in any part. Before the specimen is tested, the cap was left to cure in order to have strength comparable to that of the specimen material. FIGURE 55 shows the capping device.



FIGURE 55 Capping device.

5.2.6 Summary of Test Procedure

The complex modulus test is conducted in a stress-controlled mode within the linear viscoelastic range. The main purpose of this test is to obtain the viscoelastic properties of the material and to determine the shift factors for the undamaged state by constructing the dynamic modulus master curve. The AASHTO TP 62-07 is followed for the E^* testing. For each mixture, two replicates were prepared for testing. For each specimen, E^* tests are conducted at 14, 40, 70, 100 and 130°F for 25, 10, 5, 1, 0.5 and 0.1 Hz loading frequencies starting with the highest frequency. A 120 second rest period was used between each frequency to allow some specimen recovery before applying the new loading at a lower frequency. TABLE 22 presents a summary of the E^* test conditions.

The stress amplitude was selected by trial and error at the beginning of each temperature for each replicate so that the recoverable strain at the beginning of the test at 25 Hz frequency is in the range of 30 to 60 micro-strains. For moderate and high temperatures (70 to 130°F) the stress levels is decreased as the frequency get decreased to insure that the produced strain is smaller than 150 micro-strains. This ensures, to the best possible degree, that the response of the material is linear across the temperature used in the study. The dynamic stress values are 10 to 160 psi for low temperatures (14 to 70°F) and 2 to 20 psi for higher temperatures (100 to 130°F). All E^* tests are conducted in a temperature-controlled chamber capable of holding temperatures from 3.2 to 140°F (–16 to 60°C).

TABLE 22 Test conditions of the dynamic modulus (E^*) test (AASHTO TP 62-07)

Test Temp. (°F)	Freq. (Hz)	Cycles	Cycles to Compute E^* & ϕ
14, 40, 70, 100, 130	25	200	196 to 200
	10	100	196 to 200
	5	50	96 to 100
	1	20	16 to 20
	0.5	15	11 to 15
	0.1	15	11 to 15

The axial deformations of the specimens are measured using two spring-loaded Linear Variable Differential Transducers (LVDTs) placed vertically on diametrically opposite sides of the specimen. Parallel brass studs are used to secure the LVDTs in place. Two pairs of studs are glued on the two opposite cylindrical surfaces of a specimen; each stud in a pair, being 4-inch (100-mm) apart and located at approximately the same distance from the top and bottom of the specimen. FIGURE 56 shows the schematic presentation of the instrumentation of the test samples used in the dynamic modulus testing. TABLE 23 shows a typical tabulated E^* test results that include the dynamic modulus and phase angle of each replicate and the averages as well. To show the amount of variability between the replicates at different test temperatures and frequencies, coefficient of variation have been determined. Other E^* test results for a total of 27 tested mixtures are presented in Appendix A.

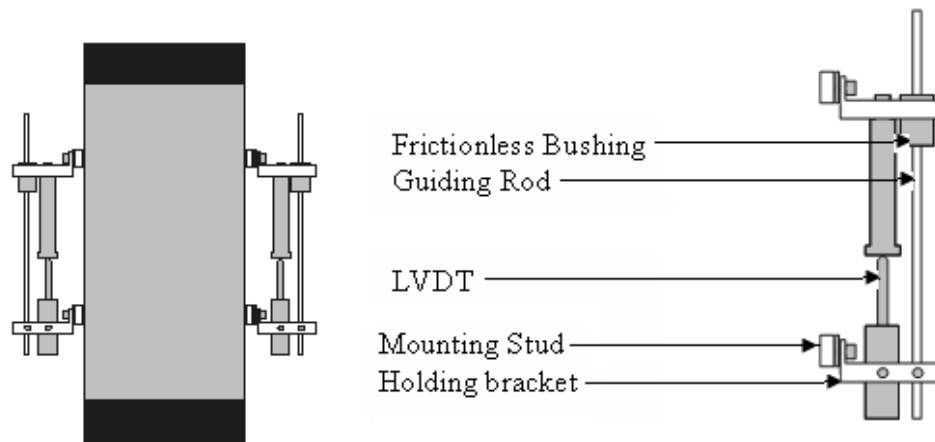


FIGURE 56 Specimen instrumentation of E* testing (AASHTO TP 62-03).

TABLE 23 E* test results of PG 76-16 mixture at 4.2% AC and 7.0% Va

Temp (°F)	Freq (Hz)	Dynamic Modulus, E*					Phase Angle, ϕ				
		Repl. 1 7-403 (ksi)	Repl. 2 7-403 (ksi)	Average (ksi)	Std. Dev. (ksi)	Coeff. of Var.	Repl. 1 7-403 (Deg.)	Repl. 2 7-403 (Deg.)	Average (Deg.)	Std. Dev. (Deg.)	Coeff. of Var.
14	25	4015	4089	4052	52	1.3	5.8	5.2	5.5	0.5	8.6
	10	3934	4042	3988	76	1.9	6.9	7.3	7.1	0.3	4.5
	5	3857	3931	3894	52	1.3	7.0	7.6	7.3	0.4	5.6
	1	3633	3682	3658	35	1.0	6.7	7.5	7.1	0.5	7.7
	0.5	3518	3583	3550	46	1.3	7.1	8.1	7.6	0.7	9.6
	0.1	3266	3382	3324	82	2.5	6.9	10.7	8.8	2.6	29.8
40	25	2974	3107	3041	95	3.1	8.3	8.2	8.2	0.1	0.9
	10	2853	2936	2895	59	2.0	10.7	10.1	10.4	0.4	3.6
	5	2735	2717	2726	13	0.5	11.6	11.2	11.4	0.2	2.0
	1	2412	2386	2399	18	0.8	12.7	13.4	13.1	0.5	4.1
	0.5	2282	2245	2264	26	1.2	13.2	14.2	13.7	0.7	5.4
	0.1	1941	1977	1959	26	1.3	14.2	15.6	14.9	1.0	6.7
70	25	1647	2198	1922	390	20.3	12.2	11.9	12.0	0.2	1.6
	10	1476	1953	1715	338	19.7	15.0	15.9	15.4	0.6	4.1
	5	1337	1759	1548	298	19.3	16.7	16.2	16.4	0.3	2.1
	1	1029	1305	1167	195	16.7	21.1	21.7	21.4	0.4	1.9
	0.5	913	1141	1027	161	15.7	23.1	23.9	23.5	0.6	2.6
	0.1	655	801	728	104	14.2	28.0	29.0	28.5	0.7	2.3
100	25	789	945	867	110	12.7	25.9	27.6	26.7	1.2	4.6
	10	690	736	713	33	4.6	28.0	29.4	28.7	1.0	3.6
	5	569	608	588	27	4.6	29.2	30.4	29.8	0.8	2.8
	1	355	369	362	10	2.7	32.7	33.3	33.0	0.4	1.2
	0.5	282	292	287	7	2.5	33.5	34.5	34.0	0.7	2.2
	0.1	171	161	166	7	4.4	34.0	35.3	34.6	0.9	2.6
130	25	252	283	268	22	8.2	34.3	35.2	34.8	0.6	1.8
	10	196	216	206	14	7.0	31.8	33.3	32.6	1.1	3.3
	5	160	175	168	10	6.0	30.5	31.8	31.1	0.9	3.0
	1	100	105	102	4	3.7	26.6	28.0	27.3	1.0	3.8
	0.5	81	84	82	2	2.7	24.5	25.0	24.8	0.4	1.5
	0.1	49	50	50	0	0.3	19.6	20.3	19.9	0.5	2.7

5.2.7 Construction of LVE Material Properties Master Curves

Asphalt concrete mixture is a viscoelastic material that exhibits time and temperature dependent. LVE property master curves of asphalt concrete mixtures enable comparison of viscoelastic materials when tested using different loading times (frequencies) and test temperatures. This can be done using the principle of time-temperature superposition. The data at various temperatures are shifted with regard to a reference temperature (generally taken as 70 °F) with respect to loading time or frequency until the curves merge into single smooth function. In general, the master modulus curve can be mathematically modeled by a sigmoidal function described as:

$$\log|E^*| = \delta + \frac{\alpha}{1 + \frac{1}{e^{\beta + \gamma(\log f_r)}}} \quad (91)$$

where:

f_r = reduced frequency of loading at reference temperature

δ = minimum value of E^*

$\delta + \alpha$ = maximum value of E^*

β, γ = parameters describing the shape of the sigmoidal function

5.2.8 Time-Temperature Superposition Principle and Shift Factors

Time-temperature (or frequency-temperature) superposition or the method of reduced variables is a recognized procedure applied either to determine the temperature dependency of a material or to expand the time or frequency range at a given temperature at which the material behavior is studied. Applicability of the time-temperature superposition principle is restricted to “Thermorheologically

Simple” materials, i.e., to materials in which the shift factor is identical for all relaxation times.

Construction of modulus master curve as a function of time or frequency describes the time dependency of the material is based on the time or frequency-temperature superposition concept. The amount of shifting at each temperature required to form the master curve describes the temperature dependency of the material. The same modulus value can be obtained either at low temperatures and long times or at high testing temperatures and short times. Intrinsically, allowing prediction of long-term behavior from short-term tests.

The shift factors $a(T)$ used to shift the dynamic modulus values along frequency values to form a continuous master curve with respect to a reference temperature can be shown in the following form:

$$a(T) = \frac{f_r}{f} \quad (92)$$

where:

$a(T)$ = shift factor as a function of temperature,

f = frequency of loading at desired temperature,

f_r = reduced frequency of loading at reference temperature, and

T = temperature.

While classical viscoelastic fundamentals suggest a linear relationship between $\log a(T)$ and T in degrees Fahrenheit (Anderson et al., 1991); years of testing by the Principal Investigator have shown that for precision, a second order polynomial relationship between the logarithm of the shift factor i.e. $\log a(T_i)$ and

the temperature in degrees Fahrenheit (T_i) should be used (Witczak et al., 1995).

The relationship can be expressed as follows:

$$\text{Log } a(T) = aT_i^2 + bT_i + c \quad (93)$$

where:

$a(T_i)$ = shift factor as a function of temperature T_i

T_i = temperature of interest, °F

a, b and c = coefficients of the second order polynomial

Many studies have showed that the time-temperature shift factors, which are a function of the material itself, should be the same regardless from which material property they are derived (Daniel, 2001). Shehab (2002) in his dissertation recommended having the shift factors from the storage modulus, E' master curve rather than dynamic modulus, E^* master curve. The reason beyond this is that the former method considers both dynamic modulus and phase angle while the last method ignores the representation of phase angle which symbolizes an important part of the material's behavior. In this research, the calculation of shift factors is done using Shehab approach is considered as it looks more rational. Based on that, the storage modulus master curve is constructed first to have the shift factors for different temperatures then the same shift factors was used to get dynamic modulus master curve as well as phase angle master curve.

In order to accomplish the horizontal shifting and sigmoidal function fitting for the storage modulus, an initial trial values for the coefficients of the shift factor polynomial relationship (a, b, c) in Equation 93 are assumed then least square technique was used to optimize their values by minimizing the amount of

error between actual E' values and the fitted ones using a log-sigmoidal function as shown in Equation 94. This procedure can be done using the Solver Function in Excel by optimizing both the sigmoidal function parameters (δ' , α' , β' , γ') in Equation 94 as well as (a, b, c) in Equation 93 so that the summation of errors in minimal and shift factor at the reference temperature (70 °F) is unity.

$$\log|E'| = \delta' + \frac{\alpha'}{1 + \frac{1}{e^{\beta' + \gamma'(\log f_r)}}} \quad (94)$$

where:

δ' = minimum value of E' ,

$\delta' + \alpha'$ = maximum value of E' , and

β' , γ' = parameters describing the shape of E' sigmoidal function.

FIGURE 57 shows the storage modulus values as a function of reduced frequency at various testing temperatures that are shifted around a reference temperature of 70 °F to construct the storage modulus master curve. FIGURE 58 illustrates the log shift factors as a function of the test temperatures. The sigmoidal and shifting parameters for the different mixtures are tabulated in TABLES 24 to 26. In addition, the shift factors at different test temperatures for all mixtures are summarized in TABLES 27 through 29

The phase angle master curve as well as the dynamic modulus master curve was obtained by shifting the data at different temperatures using the same shift factors. FIGURES 59 and 60 demonstrate the shifting of the phase angle and dynamic modulus values respectively to construct the master curves. The phase

angle shifted data then can be fitted using any appropriate function like sigmoidal, normal distribution or beta distribution functions (Biligiri et. al, 2010).

It can be observed that the phase angle increases with decreasing reduced frequency (increase of temperature or decrease of loading frequency) till certain point where it starts to decrease. This can be explained that at low temperature and high loading frequency, the asphalt binder dominates the behavior of asphalt mixtures and the mixture is more elastic so the phase angle is low. By increasing the temperature or decreasing the loading frequency, the asphalt mixture becomes more viscous as the binder becomes softer so the phase angle increases. With the increase/decrease of temperature/frequency, the asphalt binder becomes very soft and the aggregates dominate the behavior of asphalt mixture. As the aggregates and the asphalt mixture exhibits more elastic behavior again as the aggregate particles are more elastic then the phase angle will decrease again by decreasing the reduced frequency. This is a typical behavior for the conventional mixtures but it may not be the case for modified asphalt mixtures (modified asphalt rubber/polymer mixture).

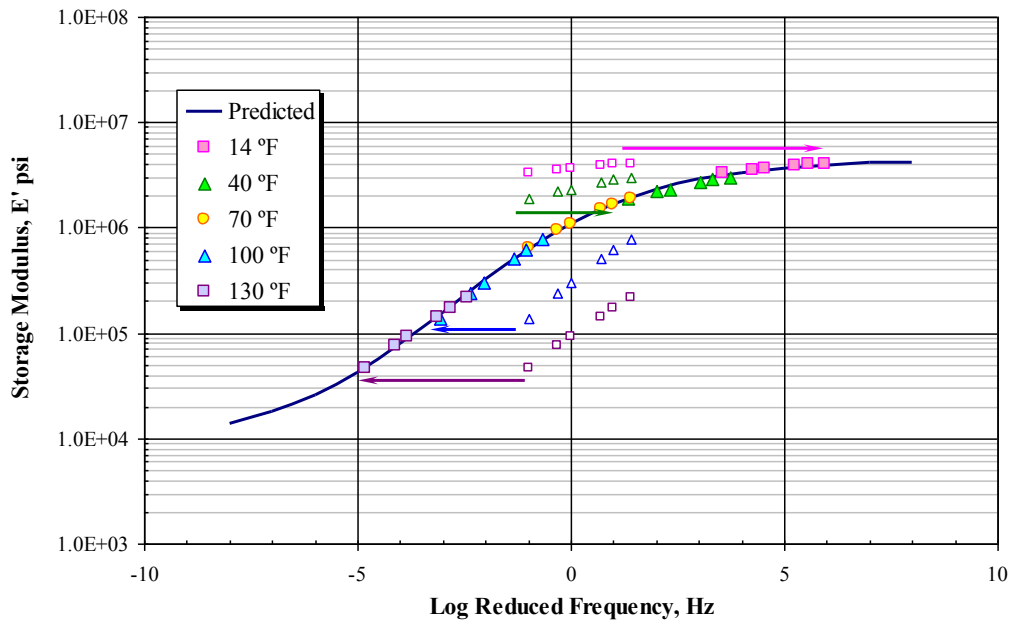


FIGURE 57 Construction of storage modulus master curve.

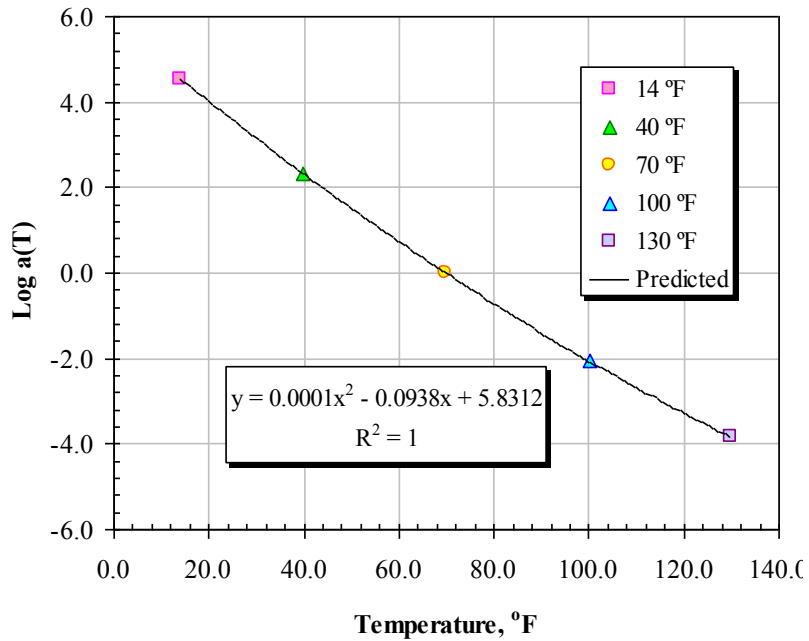


FIGURE 58 Log shift factor as a function of temperature obtained by the construction of storage modulus master curve.

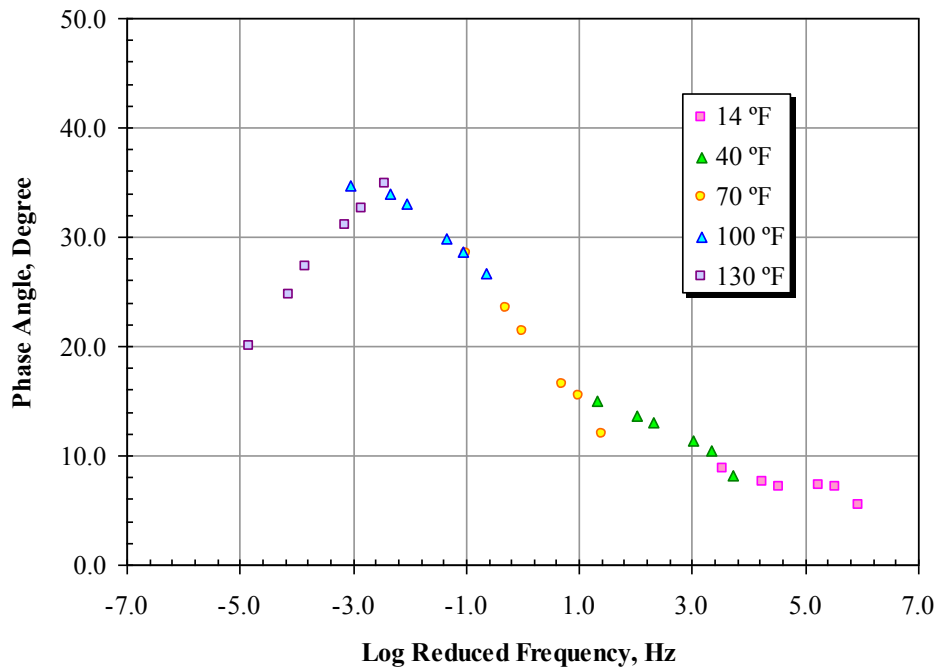


FIGURE 59 Phase angle master curve using the same shift factors obtained from storage modulus master curve.

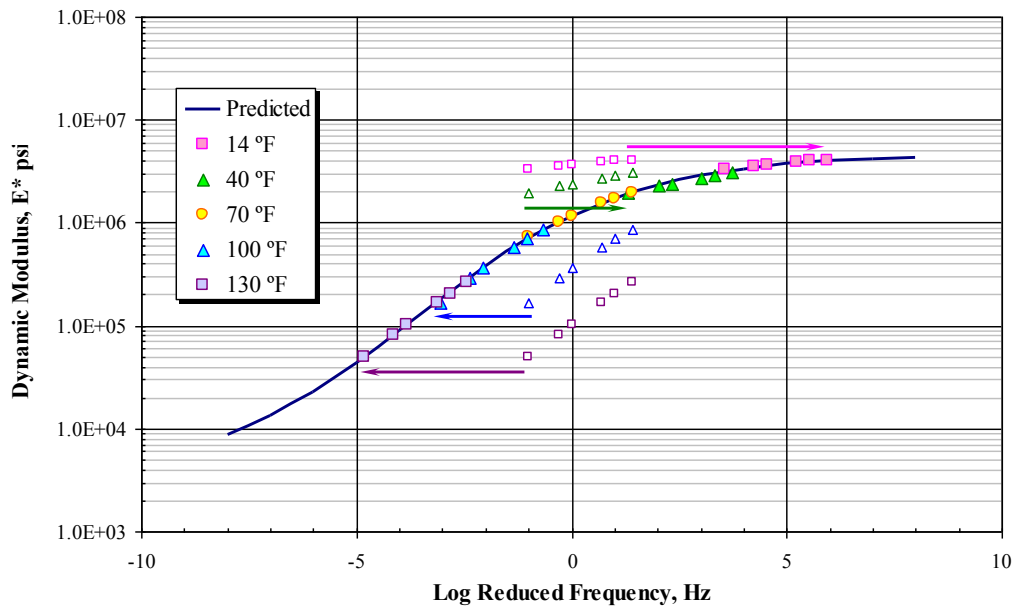


FIGURE 60 Dynamic modulus master curve using the same shift factors obtained from storage modulus master curve.

TABLE 24 E* Sigmoidal and shifting parameters of PG 64-22 mixtures

Binder Content	Parameter	Air Voids		
		4.0 % Va	7.0 % Va	10.0% Va
4.0% AC	δ	3.8670	3.1049	2.9736
	α	2.8194	3.4173	3.5837
	β	1.3622	1.5286	1.0946
	γ	0.4778	0.3758	0.3315
	a	0.000255	0.000435	0.000205
	b	-0.1218	-0.1564	-0.1018
	c	7.2745	8.8141	6.1178
4.5% AC	δ	3.9641	3.4270	2.5035
	α	2.7773	3.1963	4.0883
	β	1.1104	1.1199	1.0443
	γ	0.4531	0.3934	0.2759
	a	0.000033	0.000256	0.000264
	b	-0.0804	-0.1133	-0.1115
	c	5.4608	6.6776	6.5132
5.0% AC	δ	3.5145	3.4975	3.6367
	α	3.1038	3.0937	2.6642
	β	1.3412	1.0357	1.1614
	γ	0.3989	0.3914	0.4650
	a	0.000190	0.000236	0.000238
	b	-0.1064	-0.1078	-0.1112
	c	6.5151	6.3929	6.6135

TABLE 25 E* Sigmoidal and shifting parameters of PG 58-28 mixtures

Binder Content	Parameter	Air Voids		
		4.5 % Va	7.0% Va	9.5% Va
4.2% AC	δ	3.9136	3.9742	3.4565
	α	2.6523	2.4793	3.0600
	β	1.0610	0.9246	0.8641
	γ	0.4705	0.5315	0.3912
	a	0.000268	0.000306	0.000224
	b	-0.1167	-0.1203	-0.1064
	c	6.8500	6.9189	6.3464
4.7% AC	δ	3.6716	3.5602	3.6349
	α	2.9068	3.0335	2.7437
	β	1.0578	0.7921	0.8259
	γ	0.4539	0.4006	0.4496
	a	0.000206	0.000238	0.000205
	b	-0.1012	-0.1046	-0.0975
	c	6.0711	6.1512	5.8209
5.2% AC	δ	3.9508	3.2547	3.5436
	α	2.6120	3.3257	2.8190
	β	0.7883	0.7315	0.6583
	γ	0.5047	0.3336	0.4216
	a	0.000237	0.000293	0.000221
	b	-0.1050	-0.1136	-0.1012
	c	6.1923	6.5092	5.9990

TABLE 26 E* Sigmoidal and shifting parameters of PG 76-16 mixtures

Binder Content	Parameter	Air Voids		
		4.5 % Va	7.0% Va	9.5% Va
4.2% AC	δ	3.8027	3.4867	3.6750
	α	2.9418	3.1785	2.8923
	β	1.2590	1.4572	1.3382
	γ	0.4184	0.4048	0.4404
	a	0.000185	0.000150	0.000285
	b	-0.1002	-0.0938	-0.1213
	c	6.1028	5.8312	7.0942
4.7% AC	δ	3.5381	3.7658	3.6179
	α	3.2352	2.8811	2.9303
	β	1.4347	1.3604	1.3374
	γ	0.3751	0.4282	0.4185
	a	0.000167	0.000142	0.000311
	b	-0.0963	-0.0934	-0.1257
	c	5.9214	5.8447	7.2708
5.2% AC	δ	3.7149	3.9177	3.2502
	α	2.9737	2.6827	3.2307
	β	1.3025	1.1970	1.2411
	γ	0.3911	0.4683	0.3634
	a	0.000311	0.000086	0.000239
	b	-0.1314	-0.0806	-0.1100
	c	7.6733	5.2246	6.5267

TABLE 27 Temperature shift factors of PG 64-22 mixtures

Binder Content	Temperature (°F)	Temperature Shift Factor		
		4.0 % Va	7.0 % Va	10.0% Va
4.0% AC	14	5.619	6.710	4.733
	40	2.819	3.264	2.382
	70	0.000	0.000	0.000
	100	-2.358	-2.479	-2.012
	130	-4.245	-4.164	-3.645
4.5% AC	14	4.342	5.141	5.004
	40	2.306	2.561	2.482
	70	0.000	0.000	0.000
	100	-2.245	-2.099	-2.005
	130	-4.417	-3.727	-3.526
5.0% AC	14	5.063	4.929	5.104
	40	2.571	2.463	2.555
	70	0.000	0.000	0.000
	100	-2.228	-2.037	-2.124
	130	-4.103	-3.641	-3.809

TABLE 28 Temperature shift factors of PG 58-28 mixtures

Binder Content	Temperature (°F)	Temperature Shift Factor		
		4.5 % Va	7.0 % Va	9.5% Va
4.2% AC	14	5.269	5.295	4.901
	40	2.620	2.605	2.457
	70	0.000	0.000	0.000
	100	-2.135	-2.053	-2.051
	130	-3.777	-3.545	-3.688
4.7% AC	14	4.695	4.734	4.496
	40	2.361	2.356	2.255
	70	0.000	0.000	0.000
	100	-1.988	-1.926	-1.885
	130	-3.595	-3.414	-3.392
5.2% AC	14	4.768	4.977	4.626
	40	2.376	2.444	2.312
	70	0.000	0.000	0.000
	100	-1.949	-1.913	-1.913
	130	-3.462	-3.290	-3.418

TABLE 29 Temperature shift factors of PG 76-16 mixtures

Binder Content	Temperature (°F)	Temperature Shift Factor		
		4.5 % Va	7.0 % Va	9.5% Va
4.2% AC	14	4.737	4.547	5.451
	40	2.399	2.325	2.705
	70	0.000	0.000	0.000
	100	-2.065	-2.054	-2.190
	130	-3.787	-3.828	-3.856
4.7% AC	14	4.606	4.564	5.572
	40	2.343	2.341	2.750
	70	0.000	0.000	0.000
	100	-2.041	-2.085	-2.187
	130	-3.770	-3.904	-3.805
5.2% AC	14	5.895	4.112	5.034
	40	2.923	2.141	2.517
	70	0.000	0.000	0.000
	100	-2.362	-1.987	-2.085
	130	-4.153	-3.808	-3.729

5.2.9 Effect of Air Voids and Asphalt Content on E* Master Curve

As mentioned before, E* tests have been conducted on three different asphalt mixtures. Each mixture has nine different combinations of asphalt contents and air voids. Two test replicates were prepared for each asphalt mixture. The effects of air voids on the dynamic modulus master curves at each binder content are presented in FIGURES 61 through 69. It was noticed that the dynamic modulus master curves are shifted from each other in a general pattern, where the higher the air voids, the lower the dynamic modulus master curve. This is rational, as the asphalt mixture becomes weaker at high air voids because of the poor interlock of the aggregate skeleton as well as lower cohesion strength. In general, the Witczak predictive model shows the same trend in $|E^*|$ versus the air voids. However, this linearity is only prevalent at air voids above 4-5%. Below this value a higher non-linearity trend is observed (Jeong, 2010).

Similarly, the effects of the asphalt content on the dynamic modulus master curves at each air void level was studied as shown in FIGURES 70 through 78. It was observed that the effect of the asphalt content (within the used range ± 0.5) on the dynamic modulus master curves is lower compared to the effect of the air void range (± 2.5 or ± 3.0). It was also noticed that there is no general pattern regarding the effect of the asphalt content on the dynamic modulus master curves. However, it can be observed that the effect of the binder on the dynamic modulus master curve follows certain recognized trend for each binder type. For the PG 64-22 mixtures, the dynamic modulus master curves, at different binder contents and the same air voids, are overlapped with no specific trend

(FIGURES 70 to 72). In case of PG 58-28 mixtures, the master curves with lower asphalt contents exhibit higher dynamic modulus values compared to those at higher asphalt contents as shown in FIGURES 73 to 75. Regarding the PG 76-16, the master curves at Optimum Asphalt Content (OAC) show higher dynamic moduli compared to the ones with $\pm 0.5\%$ (FIGURES 76 to 78). For both PG 58-28 and PG 76-16 mixtures, the effect of the binder content in shifting the dynamic modulus master curves from each other is high for the higher air void levels. For the PG 64-22 mixtures, the effect of the air void values on the dynamic modulus master curves is minimal at higher temperatures and compared to lower and intermediate temperatures. The reason being that, at higher temperatures, the aggregate dominate the behavior of the asphalt mixtures; therefore, there role for the asphalt content diminishes. Whereas at lower temperatures, the binder dominates the elastic behavior of the asphalt mixtures; and consequently has higher impact on the dynamic modulus of asphalt concrete mixtures.

FIGURES 79 through 81 show the effect of both asphalt contents and air voids combinations for the different mixture groups: PG 64-22, PG 58-28, and PG 76-16, respectively. It is clear that the mixture combination that have lower asphalt content and air voids showed the highest modulus values where increasing the asphalt content and air voids decreases the dynamic modulus.

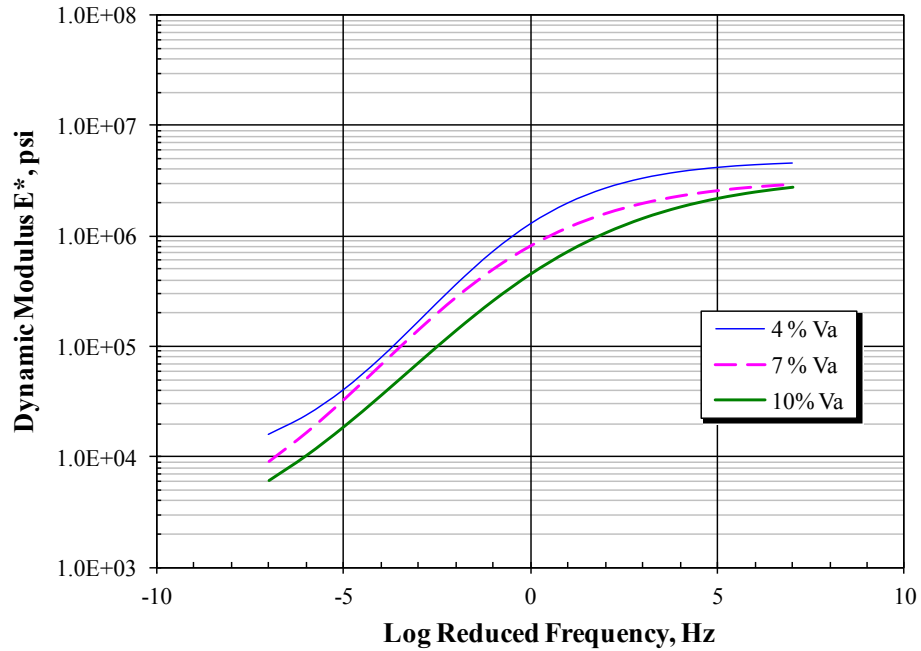


FIGURE 61 Effect of air void on dynamic modulus master curves of PG 64-22 mixture at 4.0% AC.

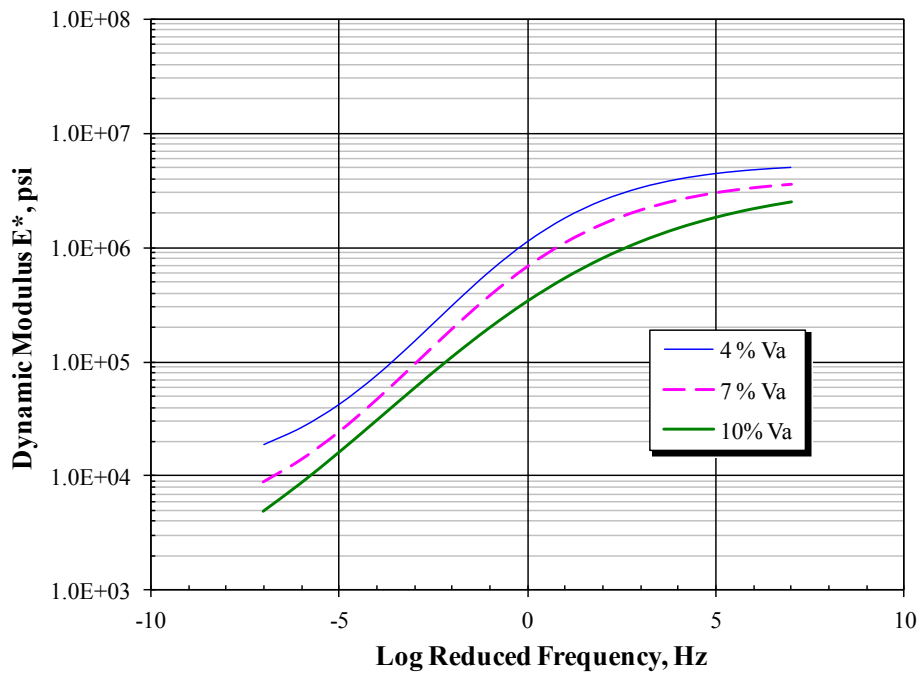


FIGURE 62 Effect of air void on dynamic modulus master curves of PG 64-22 mixture at 4.5% AC.

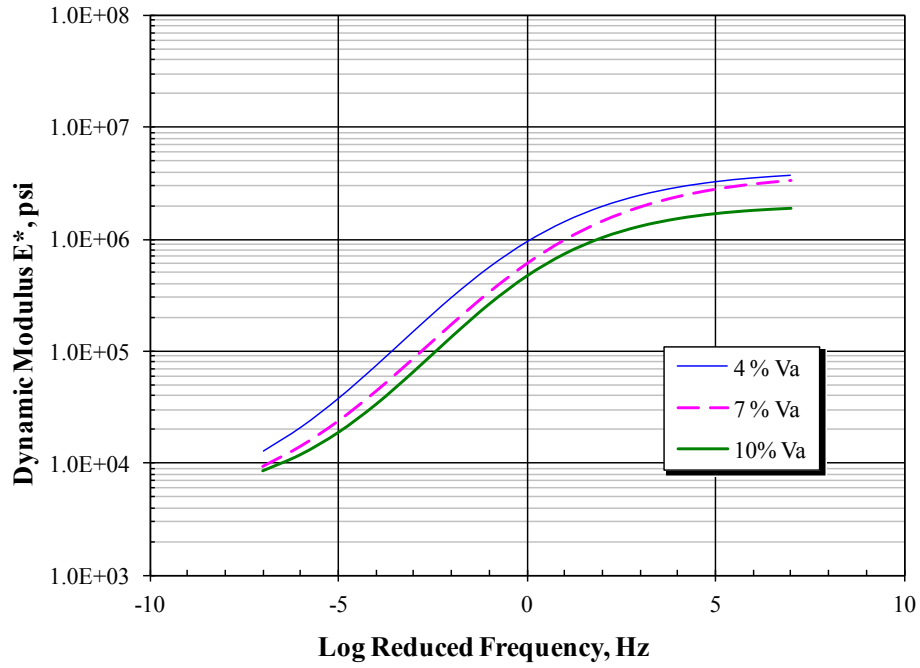


FIGURE 63 Effect of air void on dynamic modulus master curves of PG 64-22 mixture at 5.0% AC.

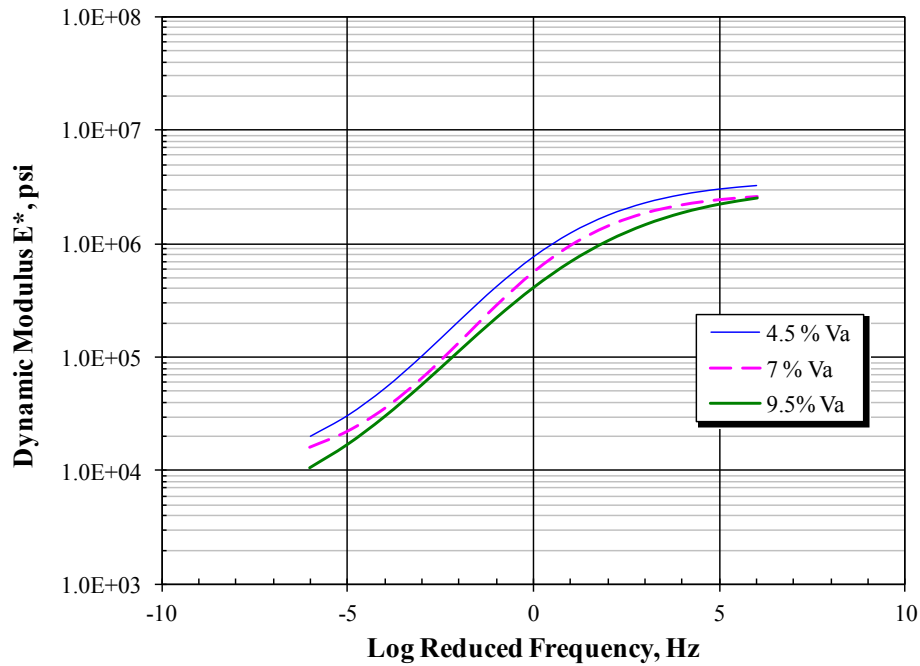


FIGURE 64 Effect of air void on dynamic modulus master curves of PG 58-28 mixture at 4.2% AC.

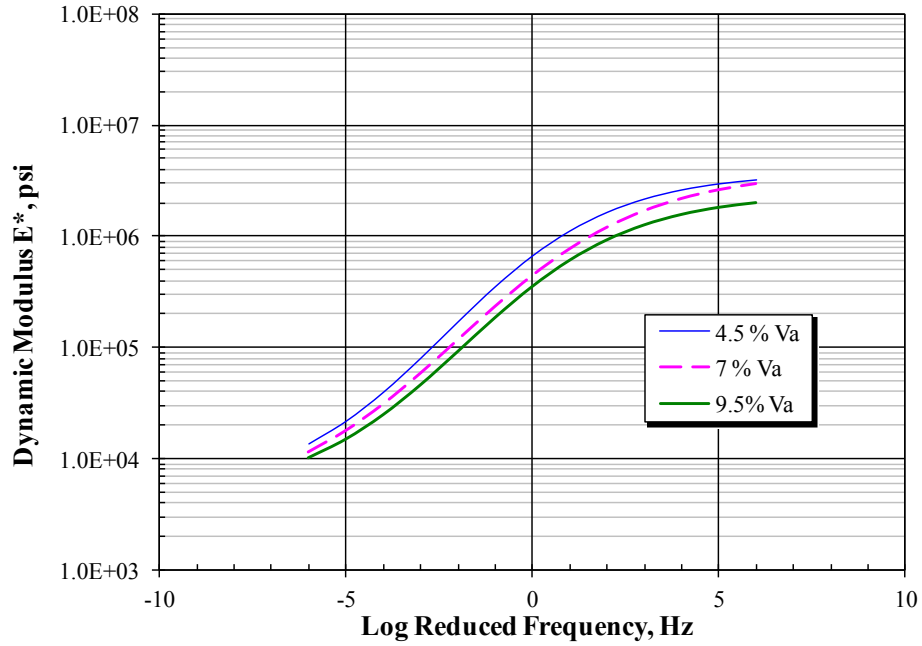


FIGURE 65 Effect of air void on dynamic modulus master curves of PG 58-28 mixture at 4.7% AC.

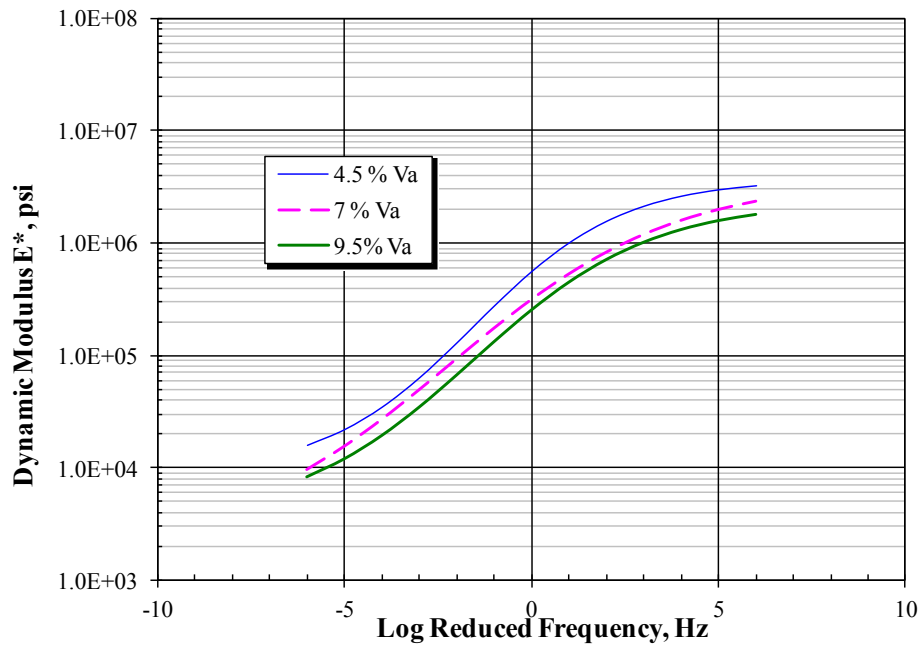


FIGURE 66 Effect of air void on dynamic modulus master curves of PG 58-28 mixture at 5.2% AC.

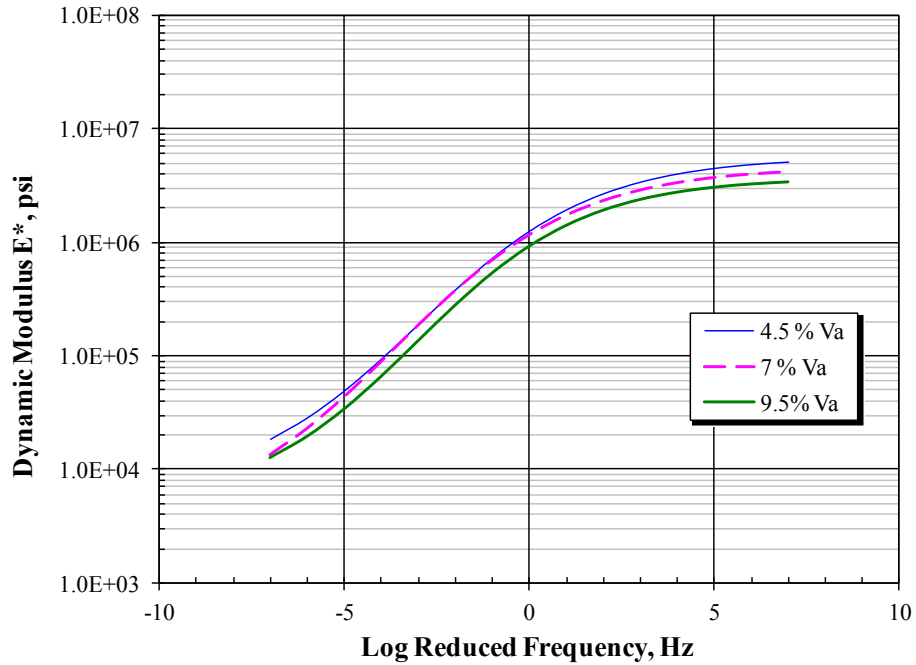


FIGURE 67 Effect of air void on dynamic modulus master curves of PG 76-16 mixture at 4.2% AC.

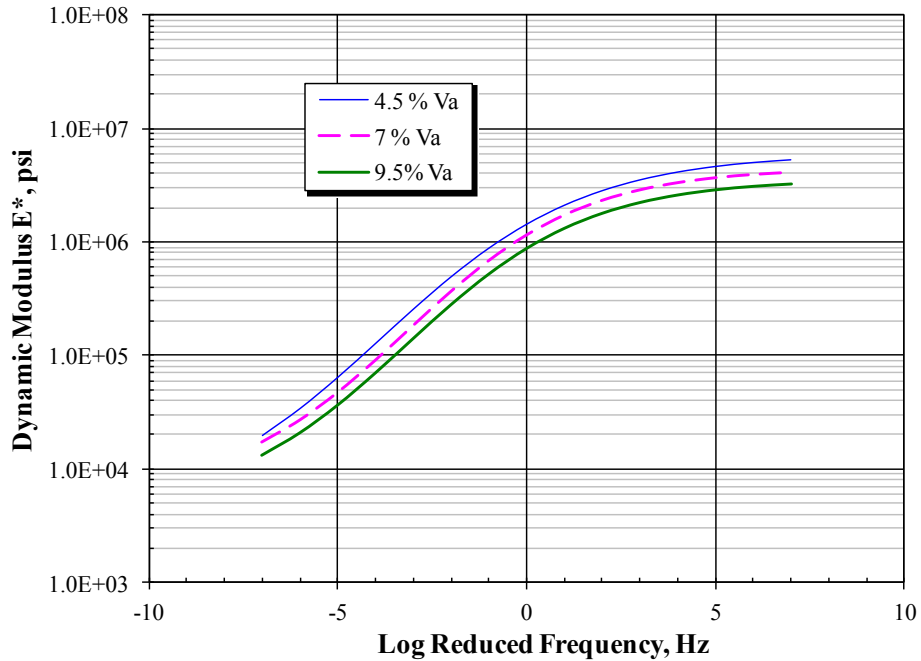


FIGURE 68 Effect of air void on dynamic modulus master curves of PG 76-16 mixture at 4.7% AC.

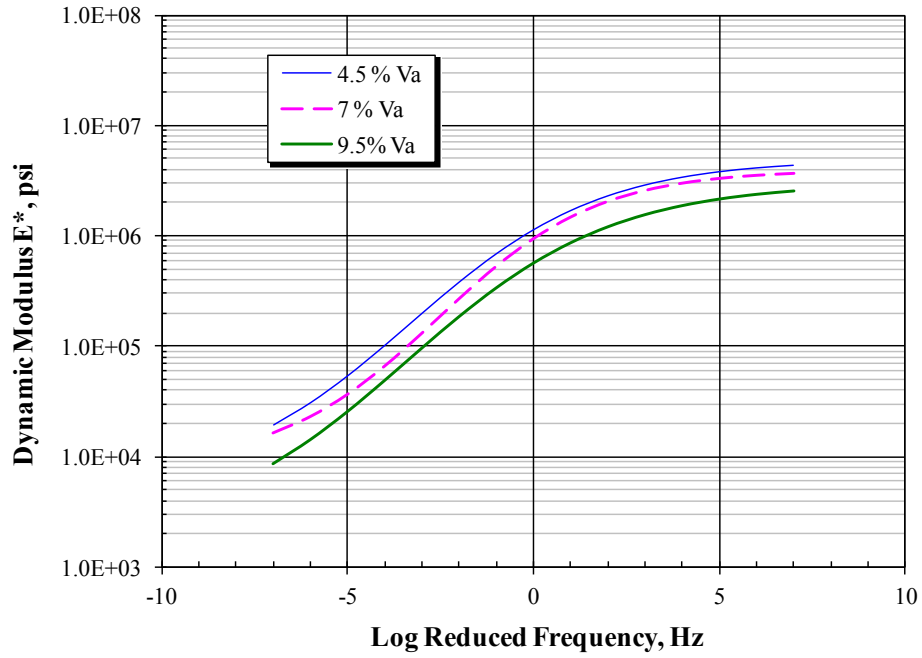


FIGURE 69 Effect of air void on dynamic modulus master curves of PG 76-16 mixture at 5.2% AC.

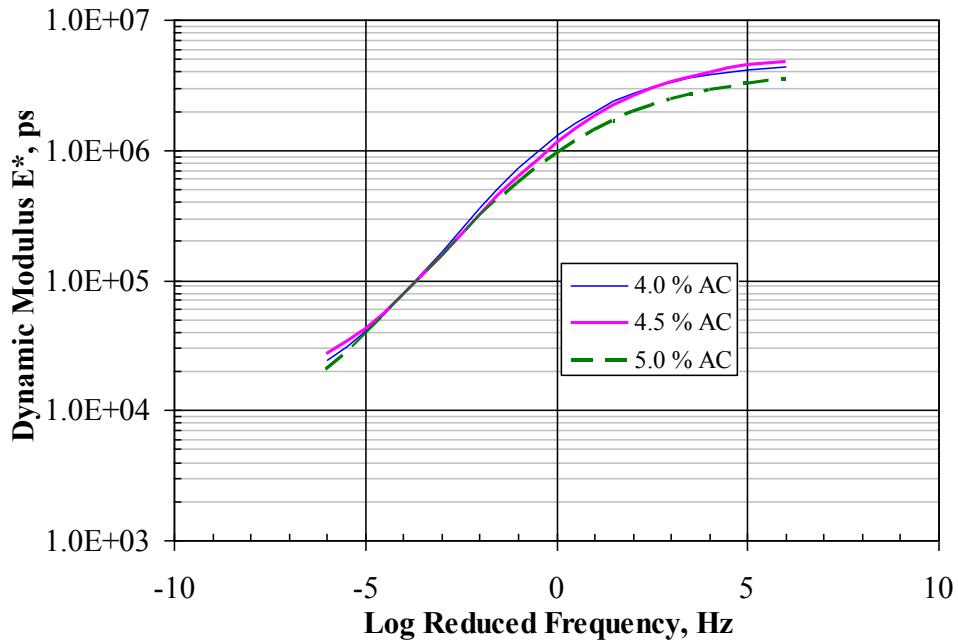


FIGURE 70 Effect of asphalt content on dynamic modulus master curves of PG 64-22 mixture at 4.0 % Va.

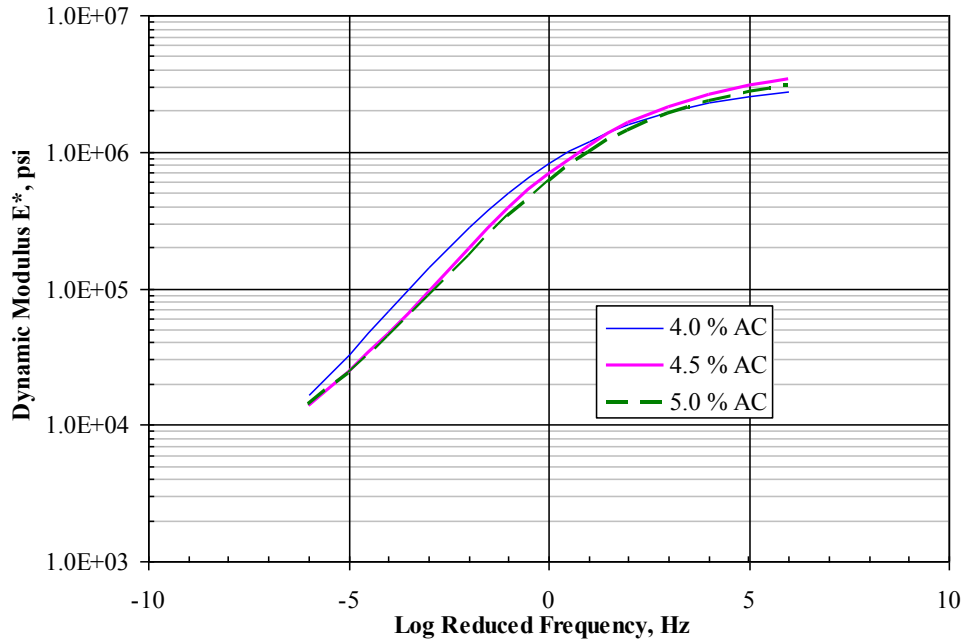


FIGURE 71 Effect of asphalt content on dynamic modulus master curves of PG 64-22 mixture at 7.0 % Va.

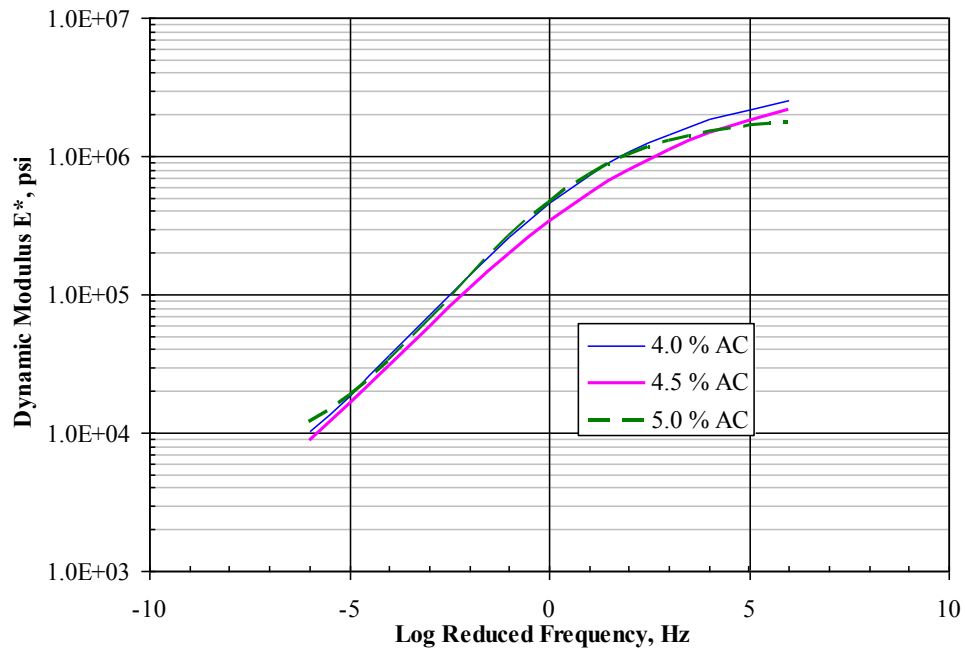


FIGURE 72 Effect of asphalt content on dynamic modulus master curves of PG 64-22 mixture at 10.0 % Va.

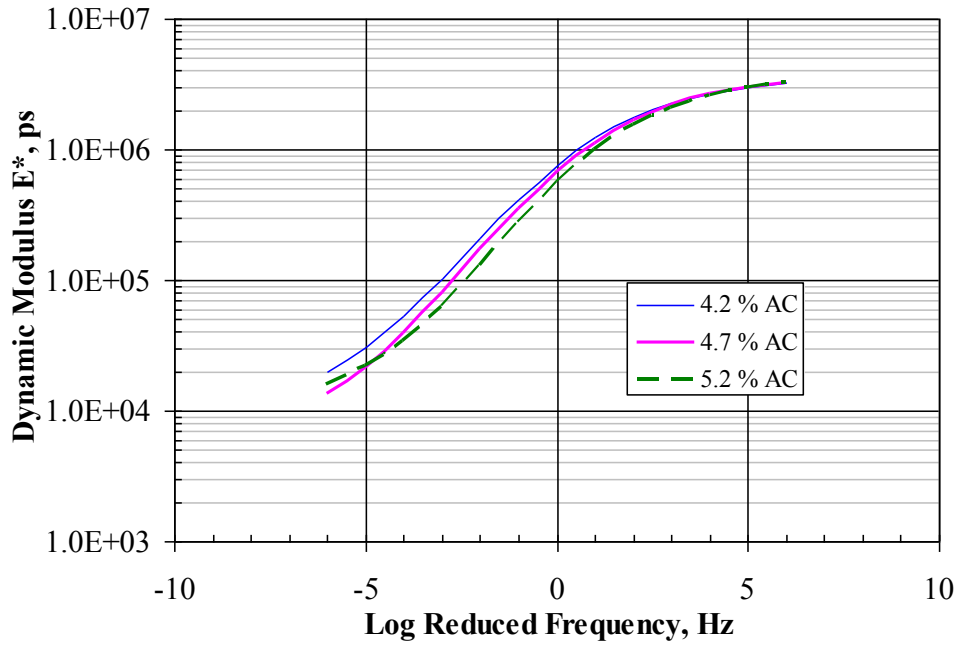


FIGURE 73 Effect of asphalt content on dynamic modulus master curves of PG 58-28 mixture at 4.5 % Va.

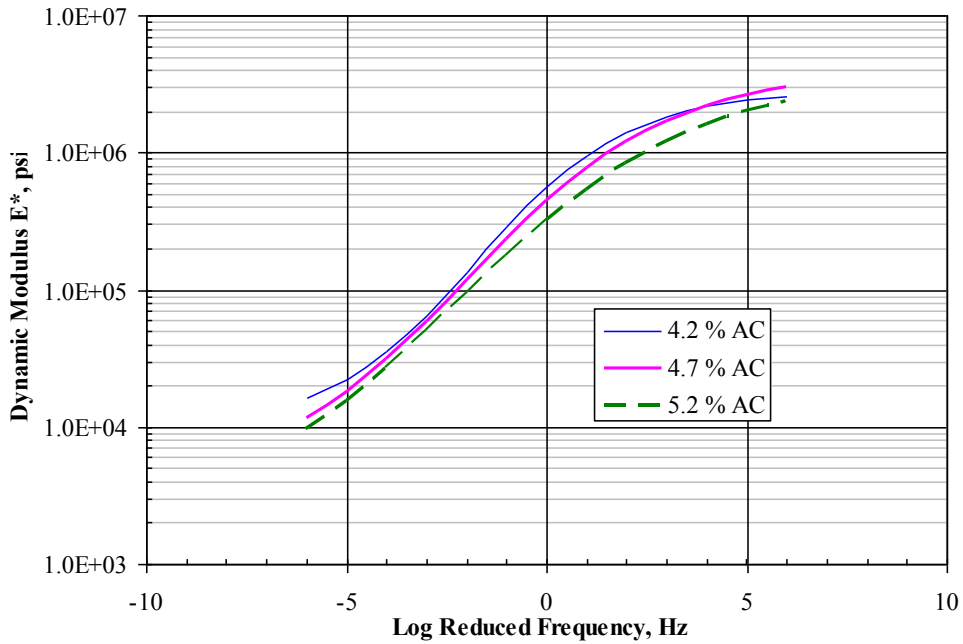


FIGURE 74 Effect of asphalt content on dynamic modulus master curves of PG 58-28 mixture at 7.0 % Va.

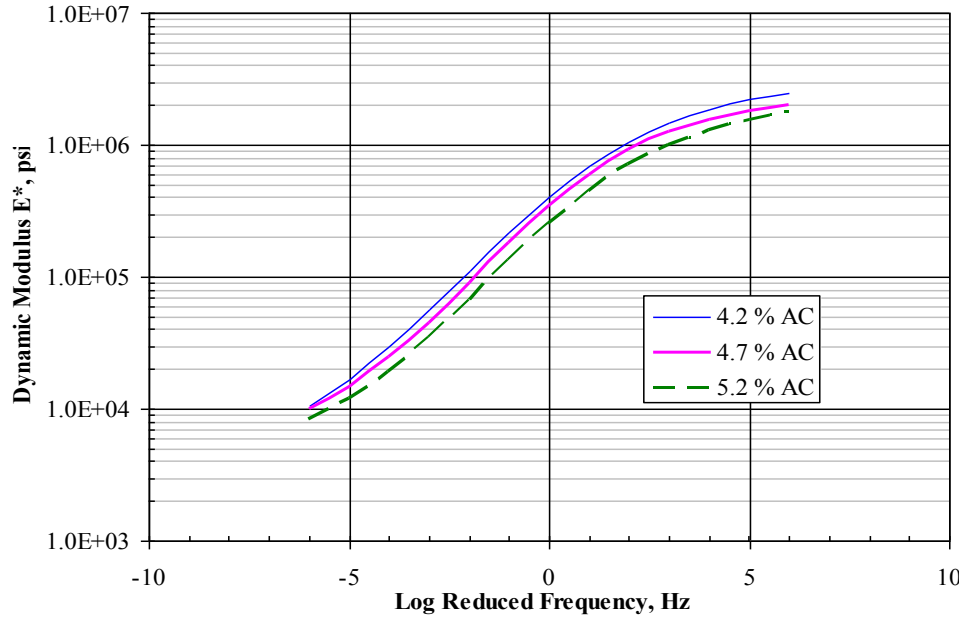


FIGURE 75 Effect of asphalt content on dynamic modulus master curves of PG 58-28 mixture at 9.5 % Va.

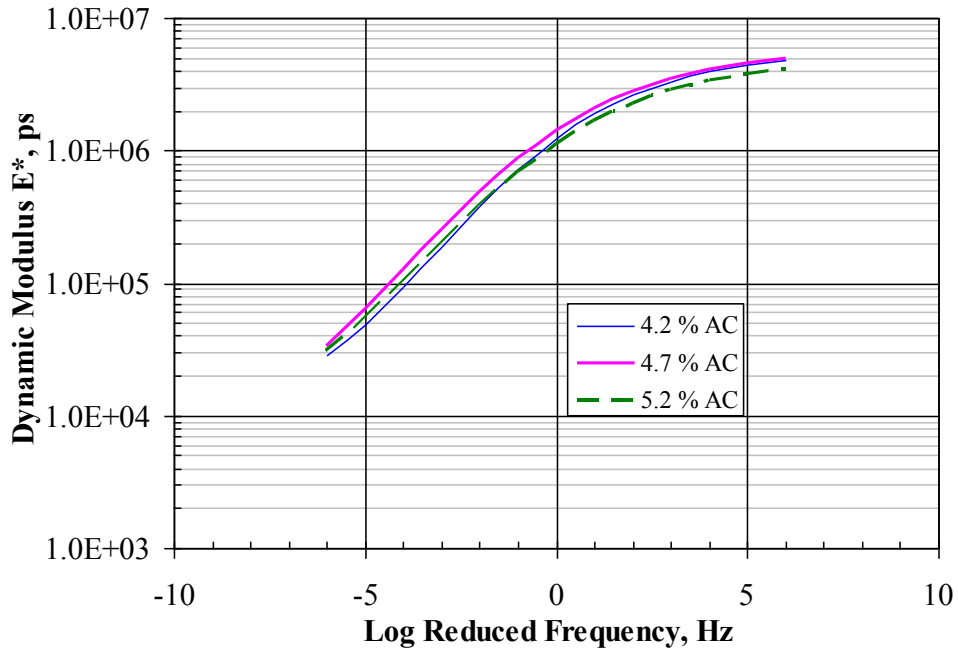


FIGURE 76 Effect of asphalt content on dynamic modulus master curves of PG 76-16 mixture at 4.5 % Va.

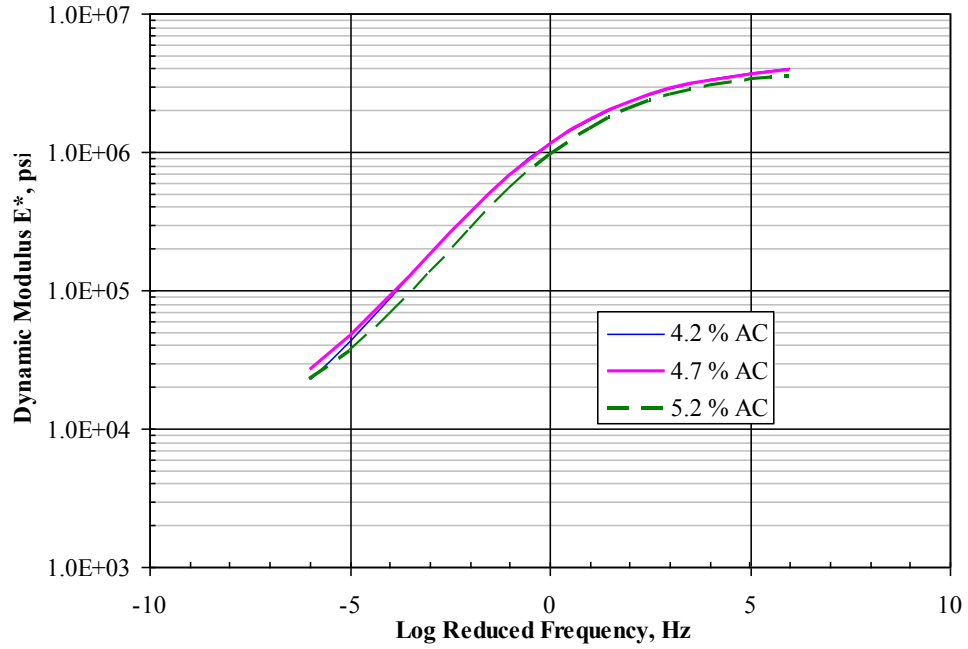


FIGURE 77 Effect of asphalt content on dynamic modulus master curves of PG 76-16 mixture at 7.0 % Va.

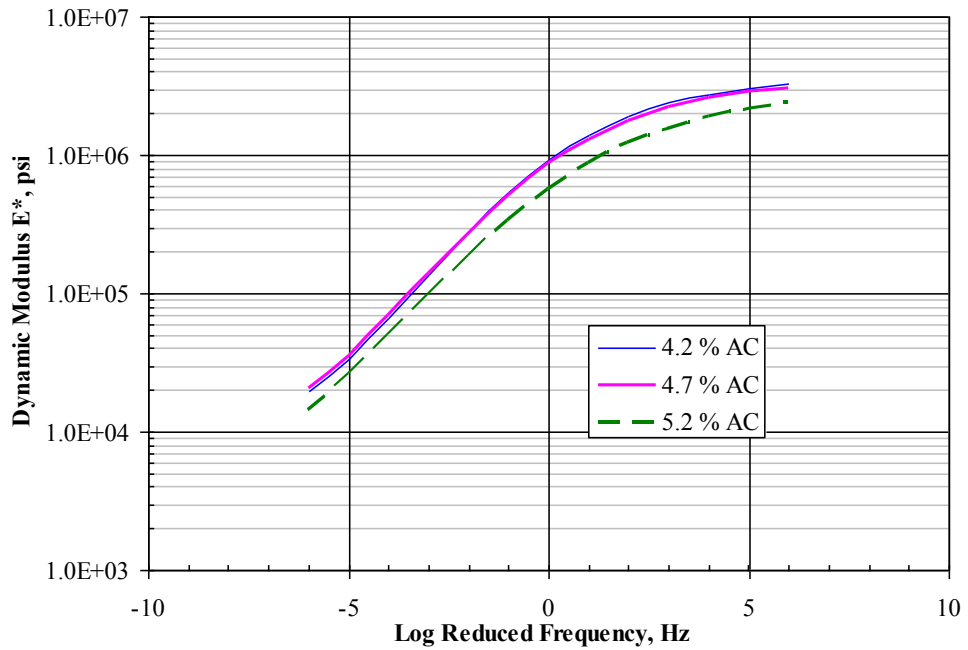


FIGURE 78 Effect of asphalt content on dynamic modulus master curves of PG 76-16 mixture at 9.5 % Va.

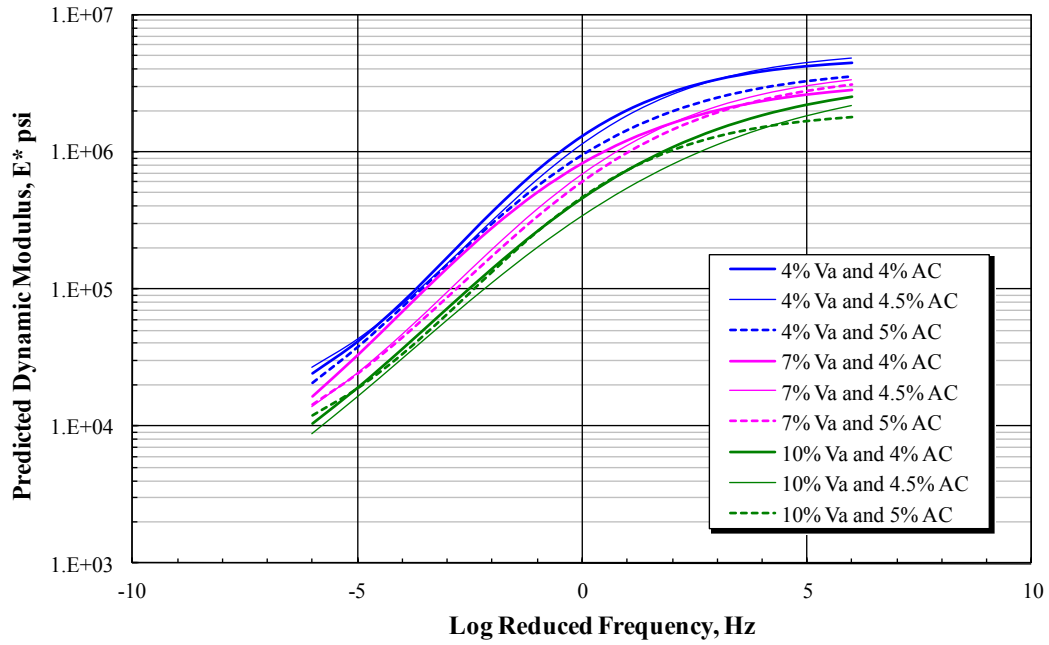


FIGURE 79 Effect of asphalt content and air void on on dynamic modulus master curves of PG 64-22 mixture.

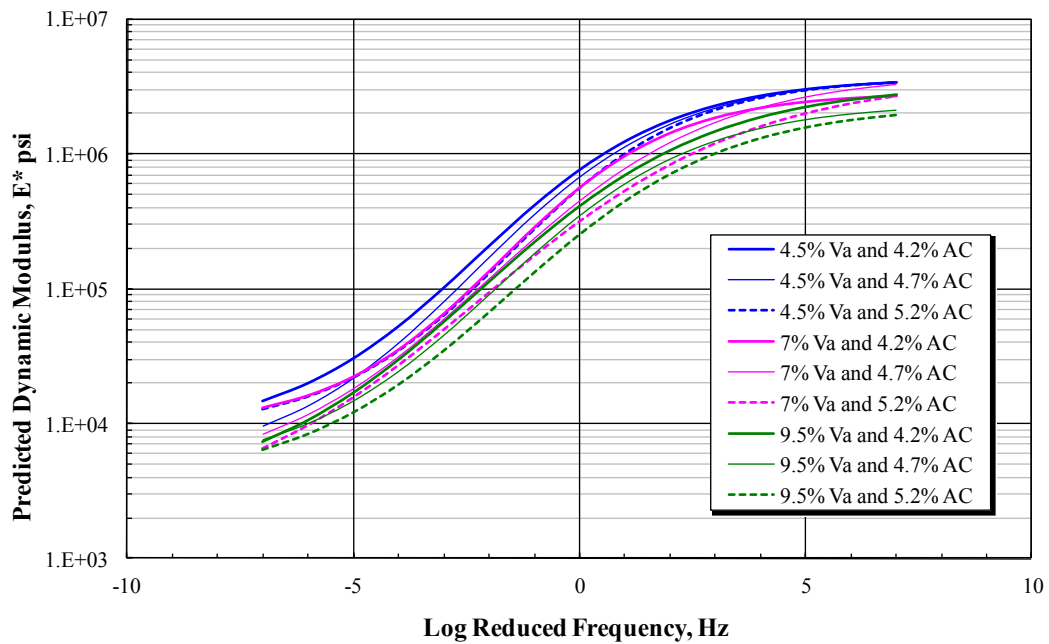


FIGURE 80 Effect of asphalt content and air void on on dynamic modulus master curves of PG 58-28 mixture.

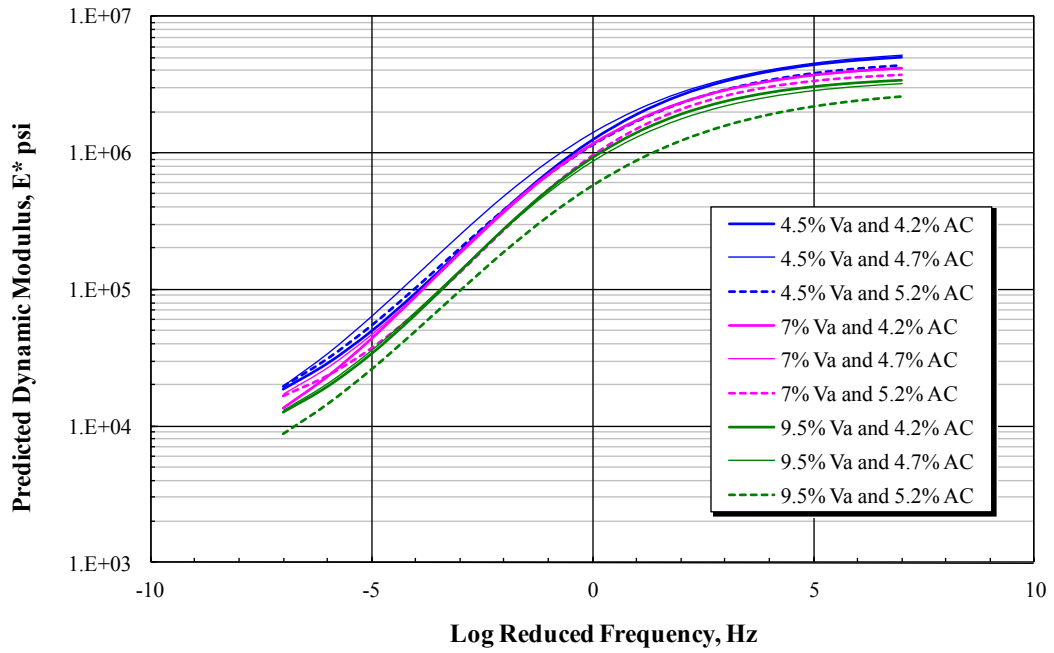


FIGURE 81 Effect of asphalt content and air void on on dynamic modulus master curves of PG 76-16 mixture.

5.2.10 Proposed Approach to Predict the Effect of Air Voids and Asphalt

Content on E* Master Curves

As shown earlier, the E* master curves were shifted or moved due the effect of the air void and the asphalt content. This section includes the proposed approach to predict the shifting of the entire master curve due to changes in air void, asphalt content, or both. These shifts were mainly dependent on the magnitude of volumetric parameter (asphalt content or air voids) change. In addition, the direction of the master curve change or shift depends on the decrease or increase of the volumetric property compared to that at a reference value.

Knowing that, the sigmoidal function used to fit the E* master curve is composed mainly of four parameters. Two of these parameters are used to determine the maximum and the minimum (δ and α) values of the master curve. The other two parameters (β and γ) are used to describe the shape of the sigmoidal function. The developed approach applies regression analysis to correlate the sigmoidal parameters obtained from the master curves to the values of air void and the asphalt content. Once the regression models are well established, then the sigmoidal parameters can be predicted at any level of air void and asphalt content, which are then used to generate the |E*| master curve.

For each group of mixtures, the regression models for each sigmoidal parameter fitted using the Minitab statistical software assuming two levels of interaction. The variables were chosen by best subsets regression. The values of the adjusted R-square, Mallows' Cp, and S-curve model were used in determining

final model. The adequacy of the final models was checked through the normal probability and residual plots.

It was noticed that there was good correlation between the volumetric factors and the maximum $\log |E^*|$ values ($\mu = \sigma + \delta$) compared to σ or δ alone. Therefore, the regression model for parameter μ was established first. The best regression model of either σ or δ was then considered, while the value of the remaining sigmoidal parameter (σ or δ) was obtained by subtracting the other two parameters. For each group of mixtures, regression models for the four sigmoidal parameters were obtained as summarized in TABLE 30.

TABLE 30 Regression models of the sigmoidal parameters for the three groups of mixtures

Binder Type	Parameter	Regression Model
PG 64-22	δ	$\mu - \alpha$
	α	$-2.32 + (1.08*AC) + (0.994*Va) - (0.201*AC*Va)$
	$\mu = \delta + \alpha$	$-1.56 + (3.79*AC) - (0.00756*AC*Va) - (0.425*AC^2)$
	β	$15 - (6*AC) + (0.65*AC^2) - (0.00208*Va^2)$
	γ	$1.51 - (0.224*AC) - (0.174*Va) + (0.0354*AC*Va)$
PG 58-28	δ	$4.12 - (0.0139*AC*Va)$
	α	$\mu - \delta$
	$\mu = \delta + \alpha$	$6.62 - (0.00224*AC*Va) - (0.000008*e^{AV})$
	β	$2.08 - (0.171*Va) - (0.024*AC^2) + (0.00957*Va^2)$
	γ	$0.528 - (0.00268*AC*Va)$
PG 76-16	δ	$\mu - \alpha$
	α	$3.9 - (0.275*AV) + (0.0192*Va^2)$
	$\mu = \delta + \alpha$	$4.18 + (1.18*AC) - (0.00863*AC*Va) - (0.127*AC^2)$
	β	$-5.03 + (2.84*AC) - (0.313*AC^2) - (0.000407*Va^2)$
	γ	$0.16 + (0.0756*Va) - (0.00522*Va^2)$

5.2.11 Proposed Approach Validation

To validate the proposed approach, regression models for random combinations of factors were used to predict the sigmoidal parameters. The constructed $|E^*|$ master curve and the curve predicted based on the regression models were compared. FIGURE 82 shows an example comparing the original and predicted dynamic modulus master curves at the same binder content and air void levels. It can be observed that both the original and predicted master curves are almost identical.

FIGURE 83 demonstrates an example of the sensitivity analysis using the sigmoidal parameters regression models of the PG 64-22 mixtures. The analysis was conducted by changing the air levels (4, 6, 8, 10, and 12%) and by keeping the asphalt content constant (5.0%). It can be seen that the prediction of the dynamic modulus master curves using the regression models is rational, where the dynamic modulus master curves exhibit higher values at lower air void levels. It can be also observed that the pattern of these master curves coincide with the pattern obtained from the actual data.

To further examine the prediction accuracy of the models, the regression models of the sigmoidal parameters for the PG 64-22 mixtures were used to predict the master curves at the same nine combinations of binder content and air void levels as shown in FIGURE 84. Again, the dynamic modulus master curves show a similar trend that was obtained from the actual data analysis presented in FIGURE 79. FIGURE 85 shows a comparison the dynamic modulus values obtained from the nine original master curves and the shifted master curves for

the PG 64-22 mixtures. It is quite noticeable that all the plotted data are almost at the equality line for the three mixture combinations. This is also supported by the excellent statistical measures of accuracy term (S_e/S_y) shown in the figures. FIGURES 86 to 91 show the same analysis for the other two mixtures groups, which also confirm the same findings explained earlier for the PG 64-22 mixtures.

As the dynamic modulus is a very important input and is required for the analysis in the MEPDG, the previous approach can be applied to many possible scenarios. One possible application of this approach is in QA/QC analysis, where the dynamic modulus master curves can be predicted based on changes in volumetric variables such as asphalt content or air void. This only requires testing certain mixtures that represent a combination of these volumetric variables to be able to predict the sigmoidal parameters. Then the master curves can be predicted at any volumetric combination, which would consequently save a considerable amount of E^* testing.

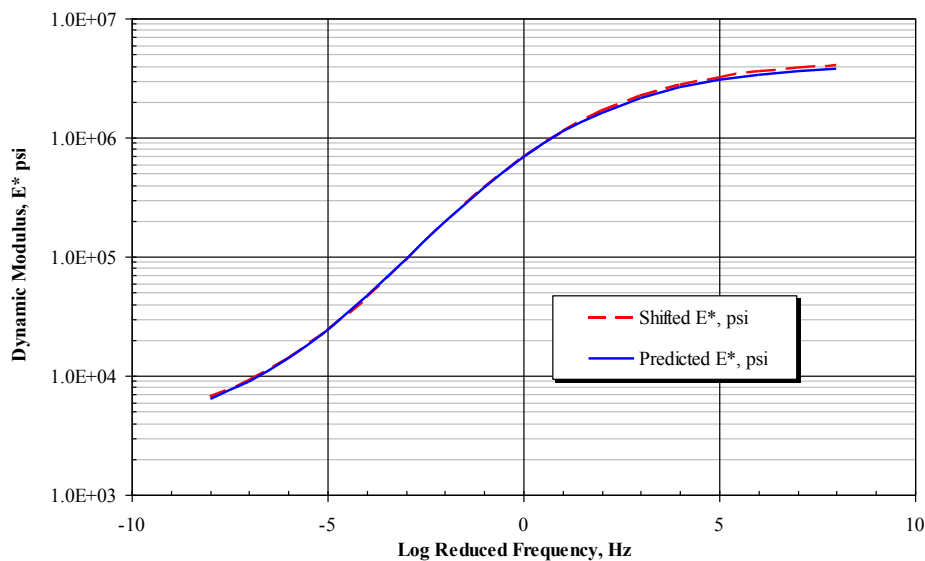


FIGURE 82 An example shows the comparison between the predicted and shifted $|E^*|$ master curve (PG 64-22, 7.0% Va and 4.0% AC).

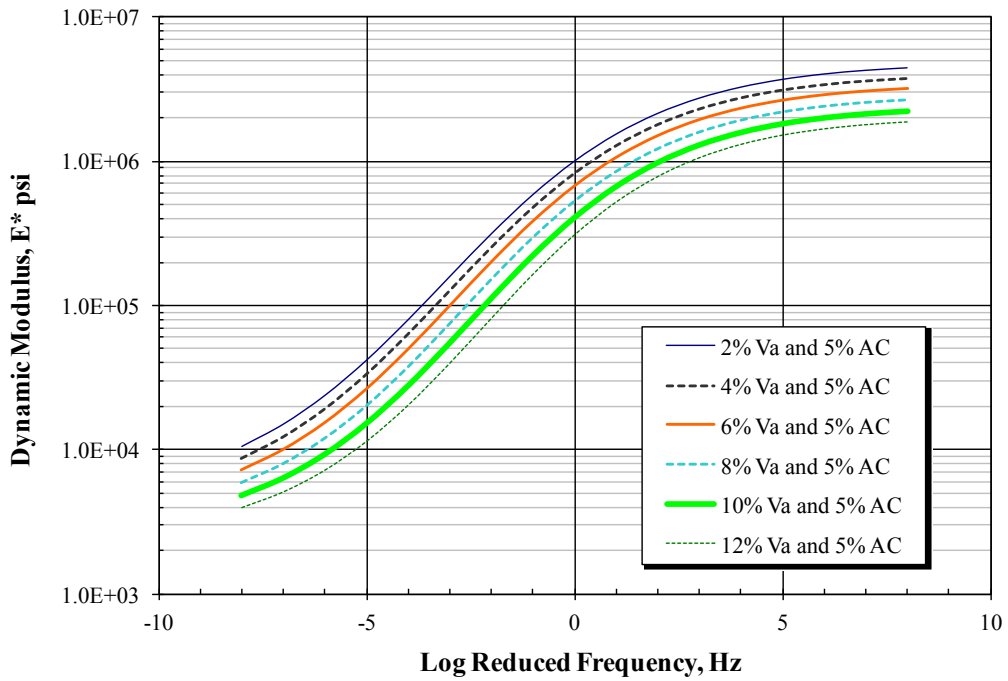


FIGURE 83 Effect of different air void levels on shifted $|E^*|$ master curves of PG 64-22 mixture.

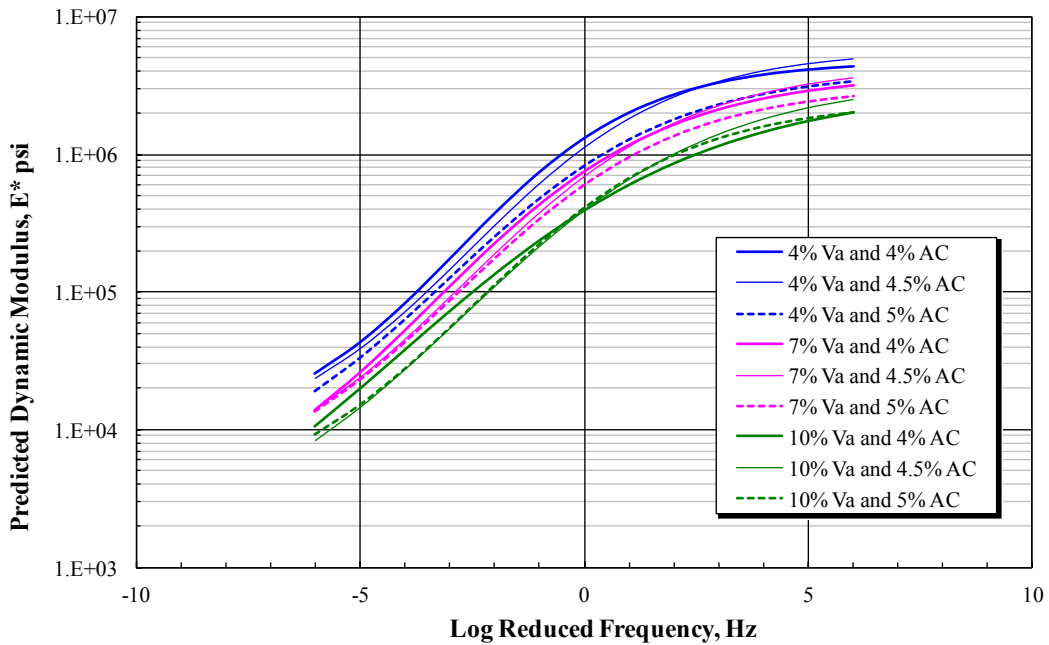


FIGURE 84 Predicted $|E^*|$ master curves at different air void and binder content levels of PG 64-22 mixture.

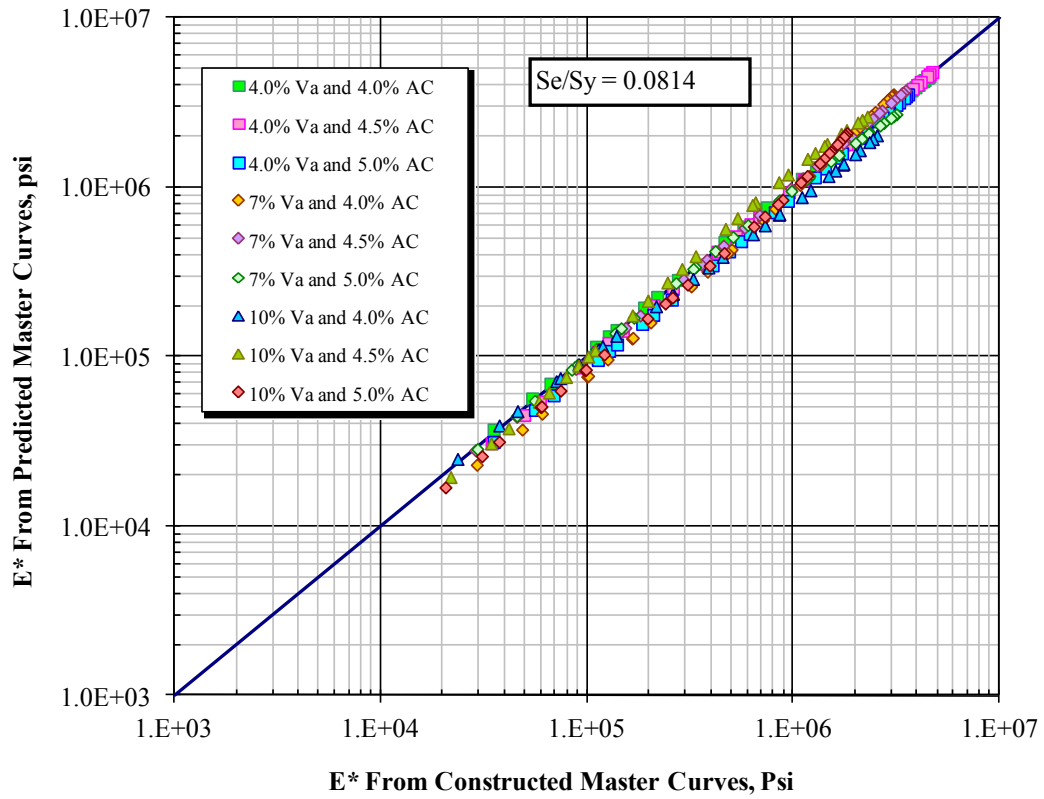


FIGURE 85 Comparison of $|E^*|$ values obtained from constructed and predicted master curves of PG 64-22 mixtures.

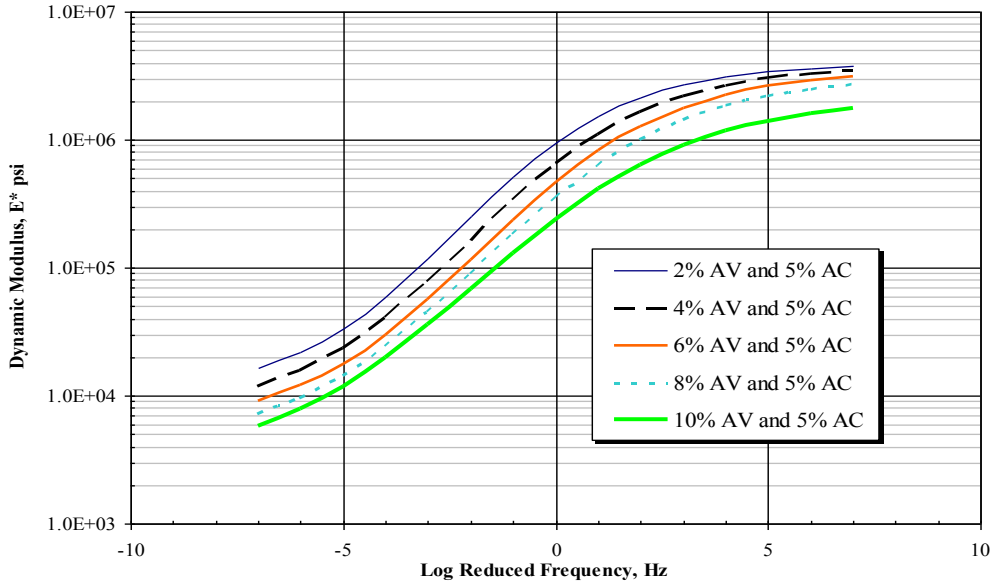


FIGURE 86 Effect of different air void levels on shifted $|E^*|$ master curves of PG 58-28 mixture.

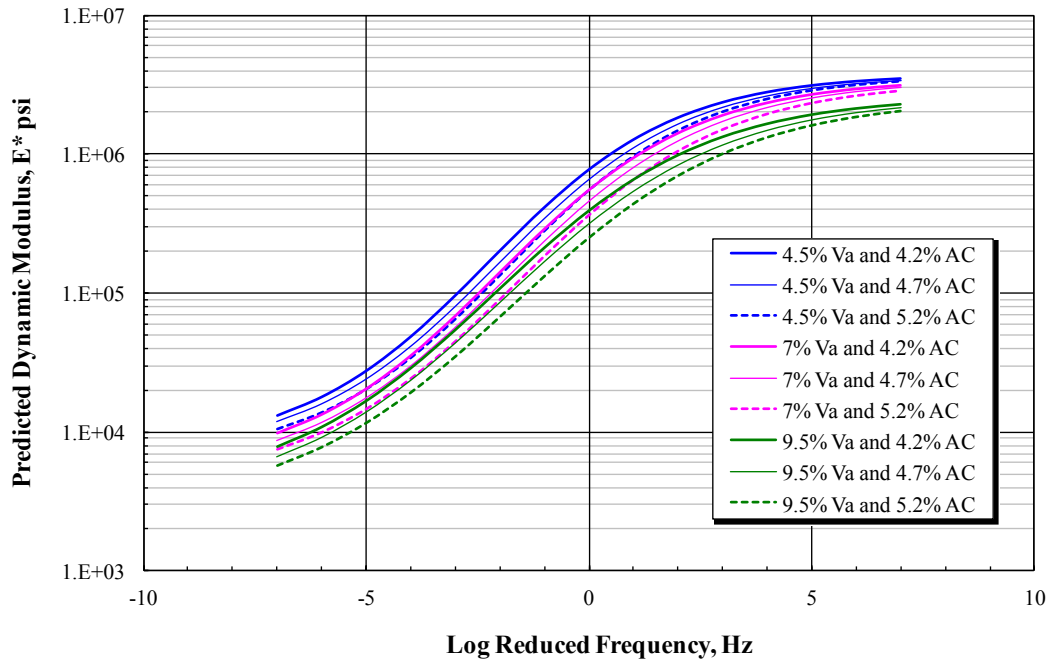


FIGURE 87 Predicted $|E^*|$ master curves at different air void and binder content levels of PG 58-28 mixture.

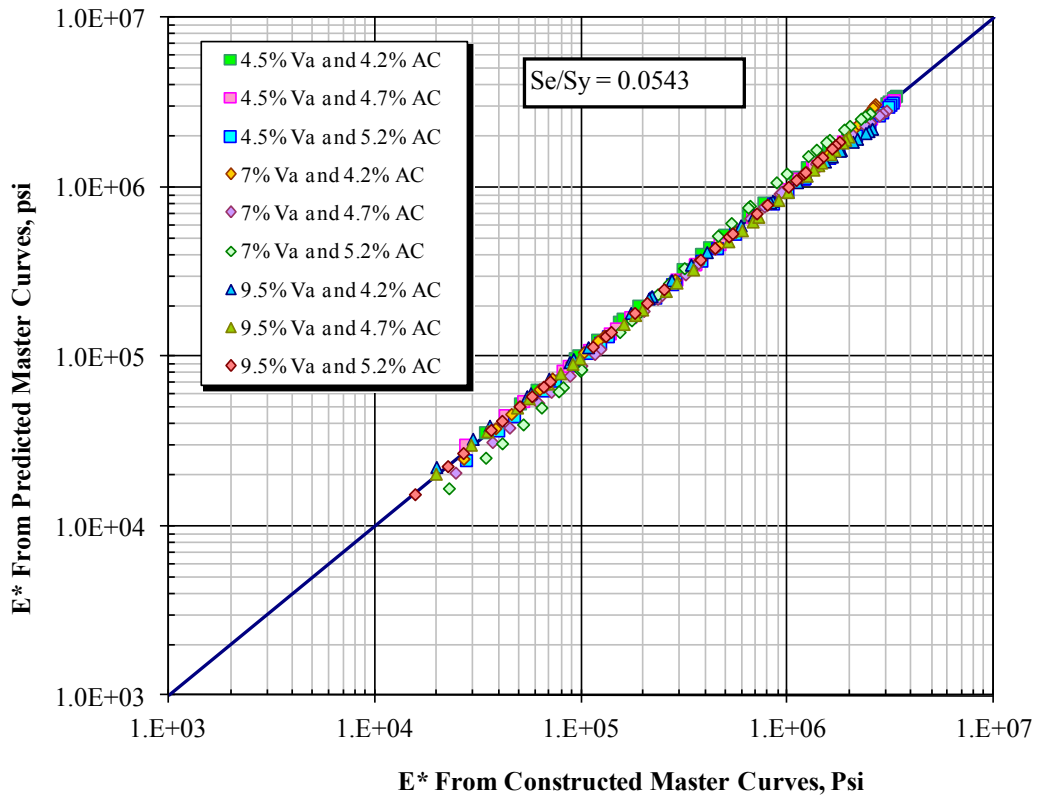


FIGURE 88 Comparison of $|E^*|$ values obtained from constructed and predicted master curves of PG 58-28 mixtures.

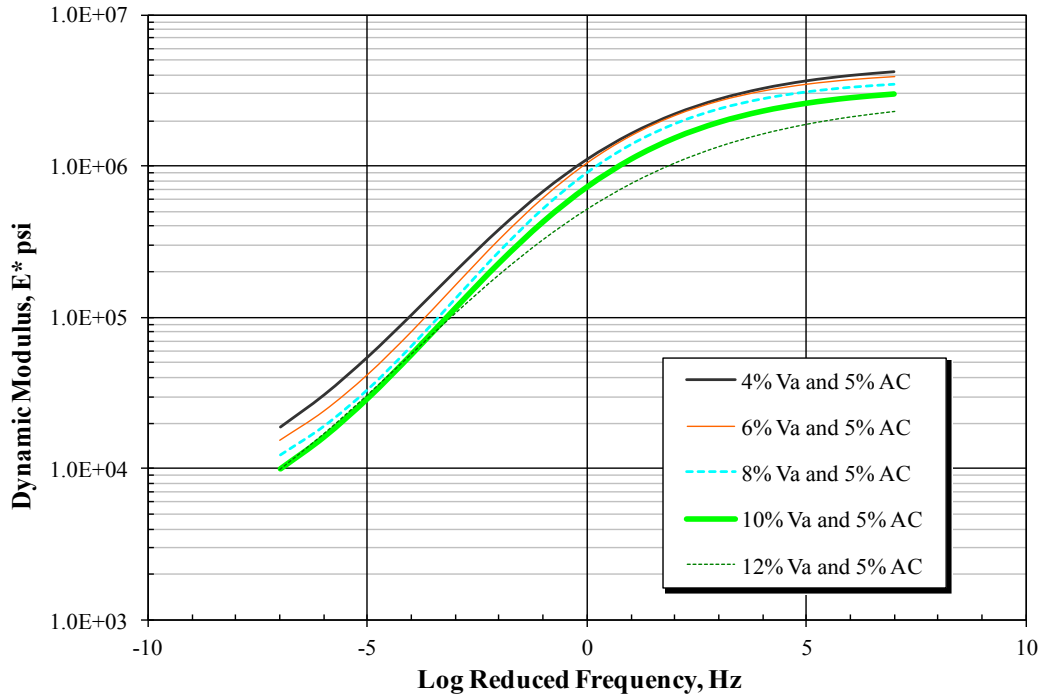


FIGURE 89 Effect of different air void levels on shifted $|E^*|$ master curves of PG 76-16 mixture.

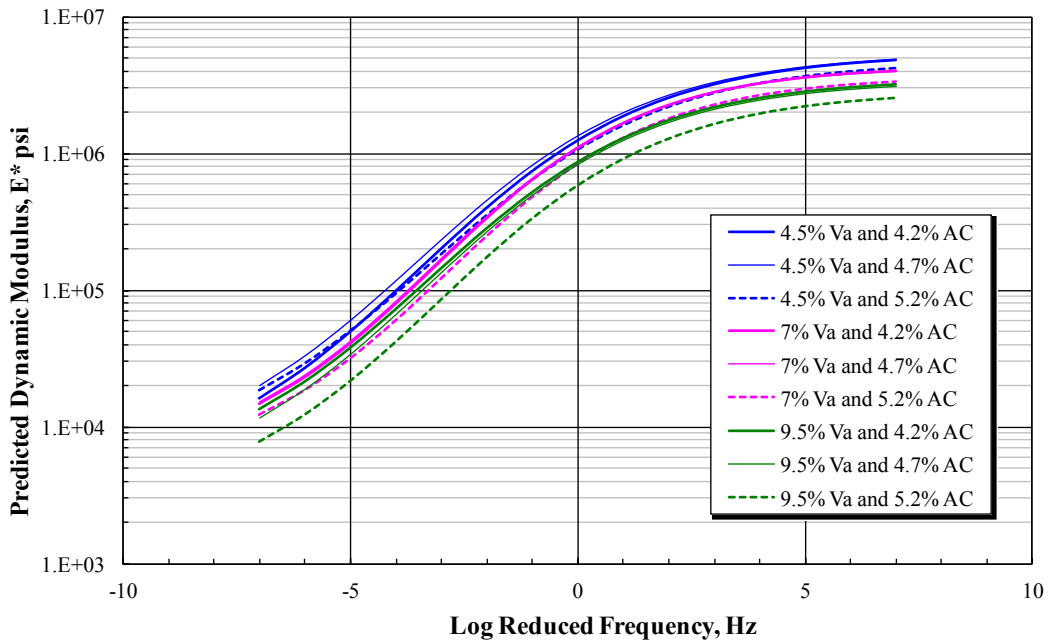


FIGURE 90 Predicted $|E^*|$ master curves at different air void and binder content levels of PG 76-16 mixture.

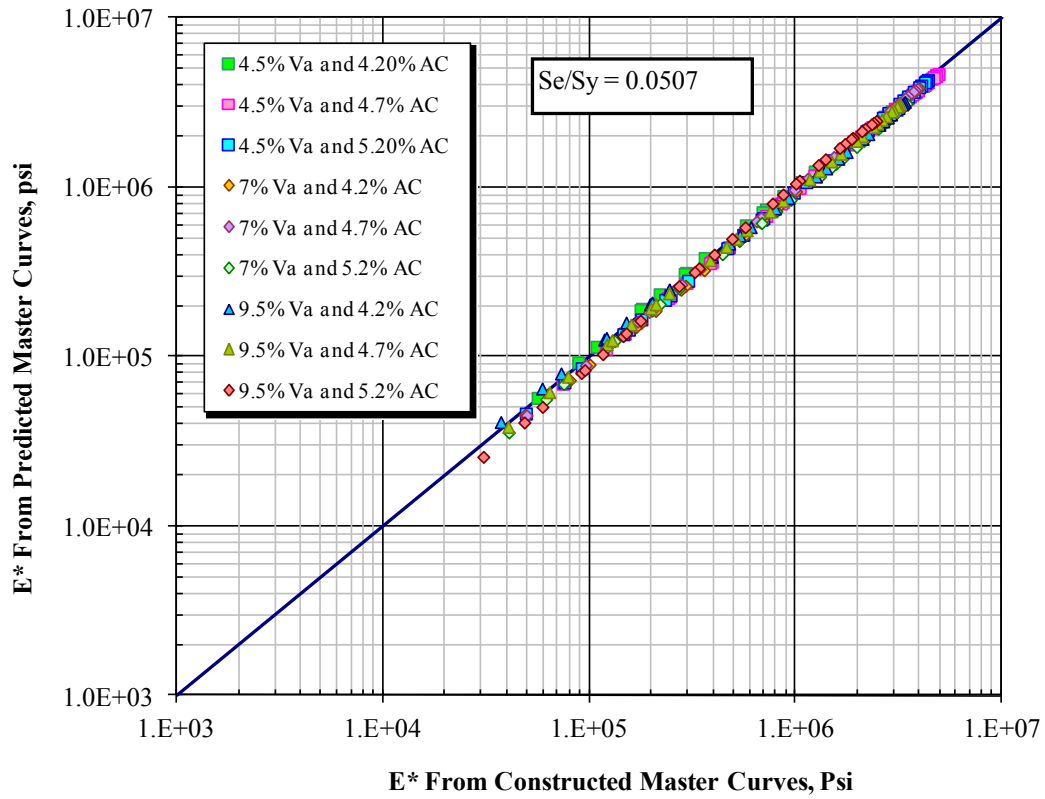


FIGURE 91 Comparison of $[E^*]$ values obtained from constructed and predicted master curves of PG 76-16 mixtures.

5.3 Relaxation Modulus

The relaxation modulus is considered as a key viscoelastic property needed for not only the characterization of the viscoelastic behavior but also the characterization of material damage where exhibits non-linear behavior. Having the viscoelastic properties of the investigated asphalt concrete mixtures represents the first step of applying the viscoelastic continuum damage model (VECDM) to validate the endurance limit of these mixtures.

The relaxation modulus, $E(t)$, is defined as the stress response of a viscoelastic material due to a unit step of strain input. The relaxation modulus can be calculated as the time-dependent stress divided by the applied strain level as shown by Equation 95:

$$E(t) = \frac{\sigma(t)}{\varepsilon_0} \quad (95)$$

where:

$E(t)$ = relaxation modulus at time t ,

$\sigma(t)$ = stress at time t , and

ε_0 = initial applied strain.

5.4 Conversion between Linear Viscoelastic Material Functions

All linear viscoelastic material functions are mathematically equivalent for each mode of loading such as uniaxial or shear. The mathematical interrelationships between linear viscoelastic material functions have been

established though detailed derivation of each interrelationship (Ferry, 1980; and Tschoegl, 1989).

There are different reasons on why the inter-conversion may be required. For example, a relaxation modulus for stiff material, which is difficult to obtain from a constant-strain relaxation test because it requires a robust testing machine, can be predicted through inter-conversion between relaxation modulus and creep compliance obtained from constant-stress creep test. Another reason is that material property often cannot be determined over the complete range of its domain from a single test input; in this case, the range can be extended by combining the responses to different input levels. This normally requires an inter-conversion between responses in time and frequency domains (Park and Schapery, 1999).

5.5 Conversion from Complex Modulus to Relaxation Modulus

Schapery et al. (1999) have demonstrated two methods of inter-conversion between frequency-domain complex modulus and time-domain relaxation modulus. The first method was based on an approximate analytical (Schapery and Park, 1999) while the second method was based on an exact mathematical formulation (Park and Schapery, 1999). Followings are an illustration for both methods.

5.5.1 Approximate Inter-Conversion Method

Having dynamic modulus and phase angle values at different test temperatures (14, 40, 70, 100 and 130 °F) and loading frequencies (25, 10, 5, 1, 0.5 and 0.1 Hz), the first step in this method is to have the storage modulus E'

master curve in a frequency-domain range as explained previously. The relaxation modulus can be determined using the following equation:

$$E(t) \cong \frac{1}{\lambda'} \times E'(\omega) \Big|_{\omega=(1/t)} \quad (96)$$

where:

t = reduced time,

ω = reduced frequency,

E(t) = relaxation modulus, and

λ' = adjustment function corresponding to use of storage modulus

conversion which can be defined as following:

$$\lambda' = \Gamma(1-n) \times \cos(n \times \pi / 2) \quad (97)$$

and:

$$n \equiv \frac{d \log E'(\omega)}{d \log(\omega)} \quad (98)$$

Where $\Gamma()$ is the Gamma function and n is the local log-log slope value of storage modulus used for calculating each relaxation modulus point. The n values at different reduced frequencies can be obtained by differentiating the sigmoidal function of the storage modulus master curve which can be written in the following form:

$$n = \frac{d \log E'(f_r)}{d \log(f_r)} = \frac{\alpha' \times \gamma' \times e^{-\beta' - \gamma'(\log f_r)}}{\left(1 + e^{-\beta' - \gamma'(\log f_r)}\right)^2} \quad (99)$$

TABLE 31 shows an example of relaxation modulus prediction using the approximate method. It can be noticed that the relaxation modulus values are actually close to the storage modulus values.

Having the predicted relaxation modulus values at different temperatures and frequencies, the relaxation modulus master curves are constructed for all mixtures by using the sigmoidal function and the same shift factors of the storage modulus as shown in FIGURE 92. It is observed that at the same asphalt cement content, the relaxation modulus values are higher when air voids are lower.

**TABLE 31 Calculation of relaxation modulus values of PG 76-16 binder at
4.2% AC and 7.0% Va**

Temp (°F)	Freq (Hz)	Predicted Storage Modulus, E' (psi)	n	$\Gamma(1-n)$	λ'	Relaxation Modulus, E(t) (psi)
14	25	3,906,388	0.023	1.014	0.999	3,908,971
	10	3,816,960	0.028	1.017	0.999	3,820,531
	5	3,739,951	0.031	1.019	0.999	3,744,493
	1	3,526,207	0.042	1.026	0.998	3,533,997
	0.5	3,417,735	0.048	1.030	0.997	3,427,467
	0.1	3,124,907	0.064	1.041	0.995	3,140,769
40	25	3,204,008	0.060	1.038	0.996	3,218,094
	10	3,019,649	0.070	1.046	0.994	3,037,999
	5	2,867,927	0.079	1.052	0.992	2,890,088
	1	2,478,933	0.103	1.071	0.987	2,511,801
	0.5	2,298,487	0.115	1.081	0.984	2,336,592
	0.1	1,863,067	0.147	1.109	0.974	1,913,632
70	25	1,908,949	0.143	1.106	0.975	1,958,256
	10	1,659,375	0.163	1.125	0.967	1,715,208
	5	1,474,231	0.179	1.141	0.961	1,534,189
	1	1,073,007	0.216	1.183	0.943	1,138,095
	0.5	918,397	0.233	1.203	0.934	983,264
	0.1	613,762	0.267	1.249	0.913	672,192
100	25	753,547	0.251	1.227	0.923	816,126
	10	593,498	0.270	1.253	0.912	651,121
	5	490,060	0.282	1.271	0.903	542,587
	1	305,272	0.304	1.304	0.888	343,628
	0.5	246,865	0.309	1.312	0.885	279,013
	0.1	149,852	0.309	1.313	0.884	169,435
130	25	234,088	0.309	1.313	0.884	264,747
	10	176,130	0.311	1.315	0.883	199,405
	5	142,104	0.308	1.311	0.885	160,560
	1	87,496	0.292	1.286	0.897	97,590
	0.5	71,720	0.281	1.269	0.904	79,336
	0.1	46,747	0.249	1.225	0.924	50,578

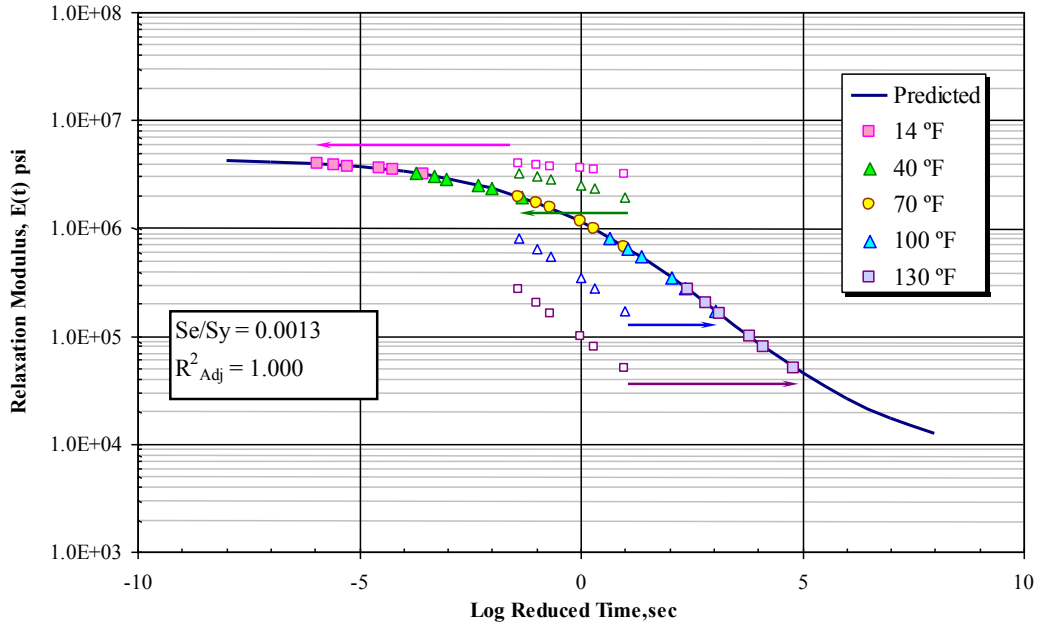


FIGURE 92 Relaxation modulus master curve of PG 76-16 binder at 4.2% AC and 7.0% Va.

5.5.2 Exact Inter-conversion Method

This method also requires the storage modulus, E' master curve. It is based on the Prony series representation of E' to allow simple inter-conversion between the frequency and time domains (Park and Schapery, 1999). This representation of E' is based on Wiechert model (or generalized Maxwell model) where the mechanical model consisting of multiple Maxwell elements (a spring and a dashpot in series) placed in parallel as shown in FIGURE 93. E' can be expressed by the following Prony series representations in the frequency domain.

$$E'(\omega) = E_{\infty} + \sum_{i=1}^N \frac{\omega_i^2 \rho_m^2 E_m}{\omega_i^2 \rho_m^2 + 1} \quad (100)$$

where:

$E'(\omega)$ = the storage modulus as a function frequency, ω (kPa or psi),

E_∞ = the long-time equilibrium modulus (kPa or psi),

E_m = the modulus of Prony term number m (kPa or psi),

P_m = the relaxation time of Prony term m (s), and

N = the number of Prony terms used.

The long-time equilibrium (Rubbery) E_∞ is basically the modulus that corresponding to the lower asymptote of the master curve and is independent of test temperatures and loading frequency. The equilibrium modulus can be obtained using Equation 101.

$$E_\infty = 10^{\delta'} \tag{101}$$

Where δ' is minimum value of E' .

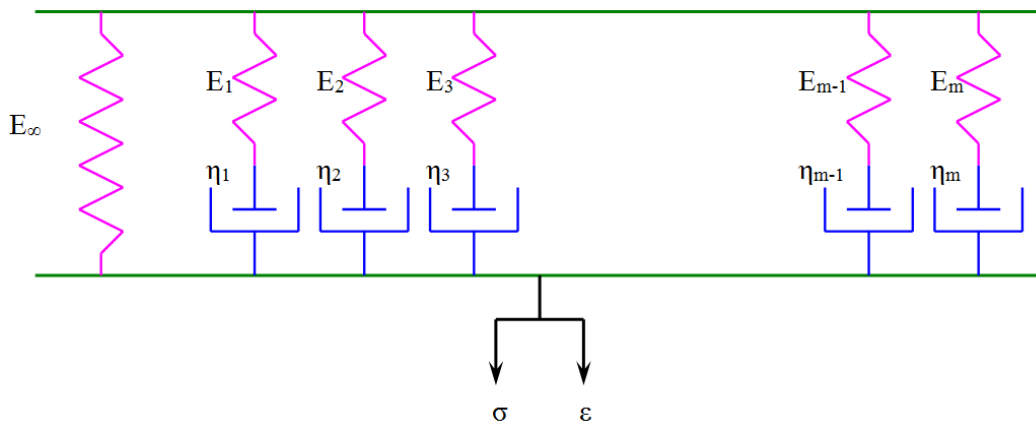


FIGURE 93 Generalized Maxwell (Wiechert) model.

The Prony series coefficient (E_∞ , E_m , and ρ_m) can be established by solving the following linear equation:

$$E_m = [B]_{mi}^{-1} \times \{E^i\}_{norm} \quad (102)$$

where:

$$B_{mi} = \frac{\omega_i^2 \rho_m^2}{\omega_i^2 \rho_m^2 + 1} \quad (103)$$

and:

$$E'_{norm} = E' - E_\infty \quad (104)$$

B_{mi} = relaxation kernel matrix for determining the Prony coefficients

ω_i = reduced frequency at the temperature and frequency condition, i
(rad/s).

Once the Prony series coefficients are calculated, the relaxation modulus values along desired time range are fitted to prony series function using the collocation method. This method is more practical in the analysis purpose of the Pseudo strain (Park and Kim, 2001). The prony series function can be expressed using the following formula:

$$E(t) = E_\infty + \sum_{i=1}^N E_m \exp \frac{-t}{\rho_m} \quad (105)$$

where:

$E(t)$ = the relaxation modulus as a function of time, t , (kPa or psi).

TABLE 32 illustrates an example the prony series coefficients at different series terms.

**TABLE 32 Prony series parameters for different term values of PG 76-16
mixture at 4.2% AC and 7.0% Va**

No. of Series	7 Terms		9 Terms		11 Terms		13 Terms		15 Terms		17 Terms	
	ρ_m (s)	E_m (psi)	ρ_m (s)	E_m (psi)	ρ_m (s)	E_m (psi)	ρ_m (s)	E_m (psi)	ρ_m (s)	E_m (psi)	ρ_m (s)	E_m (psi)
1	2.E+03	177172	2.E+04	83827	2.E+05	41278	2.E+06	21536	2.E+07	11878	2.E+08	6849
2	2.E+02	149323	2.E+03	71329	2.E+04	31709	2.E+05	14086	2.E+06	6539	2.E+07	3231
3	2.E+01	325638	2.E+02	176845	2.E+03	84881	2.E+04	38779	2.E+05	17986	2.E+06	8787
4	2.E+00	487250	2.E+01	318754	2.E+02	173456	2.E+03	83113	2.E+04	37804	2.E+05	17423
5	2.E-01	610717	2.E+00	488972	2.E+01	319602	2.E+02	173898	2.E+03	83357	2.E+04	37944
6	2.E-02	630799	2.E-01	610249	2.E+00	488761	2.E+01	319491	2.E+02	173837	2.E+03	83322
7	2.E-03	584921	2.E-02	631846	2.E-01	610303	2.E+00	488788	2.E+01	319507	2.E+02	173845
8	-	-	2.E-03	561460	2.E-02	631806	2.E-01	610296	2.E+00	488784	2.E+01	319504
9	-	-	2.E-04	463998	2.E-03	562154	2.E-02	631808	2.E-01	610297	2.E+00	488785
10	-	-	-	-	2.E-04	446780	2.E-03	562134	2.E-02	631808	2.E-01	610297
11	-	-	-	-	2.E-05	340899	2.E-04	447262	2.E-03	562135	2.E-02	631808
12	-	-	-	-	-	-	2.E-05	328885	2.E-04	447249	2.E-03	562134
13	-	-	-	-	-	-	2.E-06	237863	2.E-05	329210	2.E-04	447249
14	-	-	-	-	-	-	-	-	2.E-06	229761	2.E-05	329202
15	-	-	-	-	-	-	-	-	2.E-07	160432	2.E-06	229975
16	-	-	-	-	-	-	-	-	-	-	2.E-07	155086
17	-	-	-	-	-	-	-	-	-	-	2.E-08	105850

CHAPTER 6

DEVELOPMENT OF UNIAXIAL TENSION-COMPRESSION FATIGUE TEST PROTOCOL AND SOFTWARE

6.1 Background

Various laboratory testing methods have been developed to characterize the fatigue properties of HMA. The prediction precision of the fatigue damage using any of these test methods depends on how close that method is to simulate the condition of loading, support, stress state, and environment which the material is subjected to in the pavement. The beam fatigue test is well-known and the mostly used testing method. The uniaxial fatigue test, either the direct tension (pull) or the tension-compression (push-pull), is a promising fatigue test.

In this research, the uniaxial fatigue test is conducted to evaluate the fatigue damage and healing of asphalt concrete mixtures using the viscoelastic and continuum damage model. The fatigue healing is evaluated by observing the difference between fatigue damage using two different methods of the uniaxial fatigue test. The first method is a test run continuously without any rest between the loading cycles inducing fatigue damage. The second method includes healing, where a constant rest period is inserted between the loading cycles to allow for healing of fatigue damage.

However, there are many studies conducted to propose a rational test protocol for the uniaxial fatigue test. Currently, there is no standard ASTM or AASHTO test procedure to conduct the uniaxial fatigue test. One main objective of this chapter is to highlight the available proposed uniaxial fatigue test protocols

or test methods and to check their suitability to be used in this project. The other important objective is to propose uniaxial fatigue test method and software that is more general and at the same time relevant to the project goals.

6.2 Current Proposed Uniaxial Fatigue Test Methods

6.2.1 Pennsylvania State University (PSU) Test Method

Soltani and Anderson (2005) developed new test protocol, testing machine, and software for the uniaxial fatigue test. The uniaxial fatigue test protocol includes three stages of continuous loading without rest period. In stages I and III, a strain level, not exceeding the endurance limit of the HMA, is applied. In Stage II, a strain with a magnitude exceeding the endurance limit and consequently causing fatigue damage is applied. The effects of non-fatigue phenomena such as self heating, self cooling are investigated by using eighteen thermocouples for the measurement of temperature at various locations in the specimen. FIGURE 94 shows the test setup including test specimen, fixtures, transducers and thermocouples. The following test conditions were used for this test method:

- Test loading: sinusoidal centered at zero (push-pull configuration),
- Test frequency: 10 Hz,
- Test temperature: 50°F (10°C),
- Specimen: cylindrical, 3-inch diameter by 4.7-inch height (75.5-mm diameter by 120-mm height),
- Gauge length: 3-inch (75-mm),
- Number of LVDTs : 3 LVDTs, and

- Test mode: On-specimen controlled strain (controlled by one LVDT only).

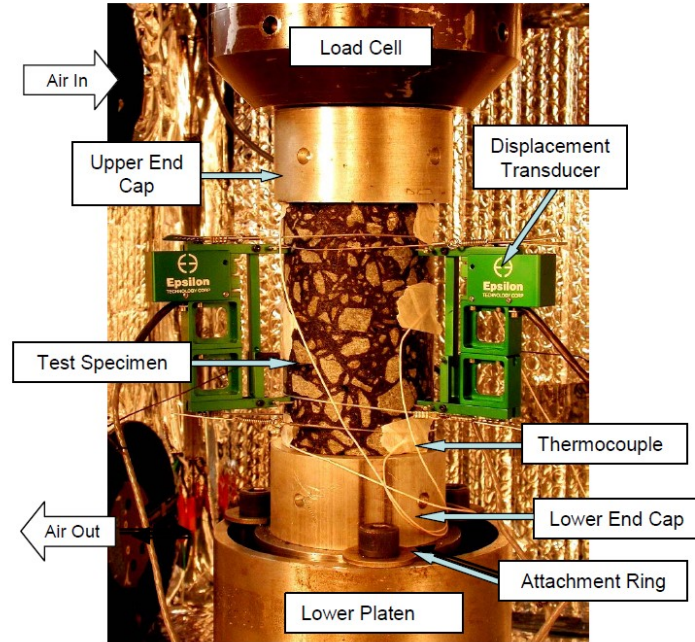


FIGURE 94 Detailed test setup: test specimen, fixtures, transducers, and thermocouples (Soltani et al., 2006)

6.2.2 North Carolina State University (NCSU) Method

As a result of several studies, a uniaxial fatigue test method was developed at NCSU (Daniel and Kim, 2001; Chehab, 2002; and Underwood et al., 2010). The developed test method was named Simplified Viscoelastic Continuum Damage Fatigue Test (S-VECD). Recently, test software was developed for the S-VECD fatigue test by IPC (Industrial Process Control) company. FIGURE 95 showed a specimen test setup for the S-VECD fatigue test method.



FIGURE 95 Specimen test setup (Daniel and Kim, 2001)

The following test conditions were used for the S-VECD fatigue test method:

- Test loading: haversine loading wave shape (direct tension configuration),
- Test frequency: 10 Hz,
- Test temperature: 41 and 77°F (5 and 25°C),
- Specimen: cylindrical, 3-inch diameter by 6-inch height (75-mm diameter by 150-mm height),
- Gauge length: 4-inch (100-mm),
- Number of LVDTs : 4 LVDTs, and
- Test mode: Crosshead strain controlled (controlled by actuator).

6.2.3 Advanced Asphalt Technologies (AAT) Method

Christensen and Bonaquist (2009), at AAT, developed a uniaxial fatigue test method. IPC Company developed test software called Simplified Continuum Damage Uniaxial (SCDU) fatigue test.

The following test conditions were used for the SCDU fatigue test method:

- Test loading: sinusoidal centered at zero (tension-compression configuration),
- Test frequency: 10 Hz,
- Test temperature: 68°F (20°C),
- Specimen: cylindrical, 4-inch diameter by 6-inch height (100-mm diameter by 150-mm height),
- Gauge length: 3-inch (75-mm),
- Number of LVDTs: 3 LVDTs, and
- Test mode: On-specimen strain controlled (controlled from the 3 LVDTs).

6.3 Adequacy of the Available Test Methods

After a comprehensive investigation of the available test methods and software for the uniaxial fatigue test, it was obvious that none of them can directly be used in this research without either certain modifications of test software or further examinations of the test method itself. Followings are the main issues regarding these test methods that disallowed using any of them directly.

6.3.1 Pennsylvania State University (PSU) Test Method

- The test software was developed for a different test machine and controller than the ones available at the ASU laboratory,
- Controlling the on-specimen strain through only one LVDT and ignoring the other specimen sides is not reasonable as there is always differences among measurements at different specimen sides,
- The test software can only perform the tension-compression fatigue test and there is no option to run the direct-tension test which disallows investigation of the most appropriate one for this study,
- The test method includes 3 different stages with different strain values, which are not appropriate for this study,
- The software does not allow for rest periods between loading cycles, which is one of the main requirements of the current project, and
- There is a reported issue with the loading synchronization that causes a partial data loose.

6.3.2 North Carolina State University (NCSU) Method

As the test uniaxial test software of NCSU was developed by IPC which matches the available test setup at ASU, few tests were conducted and the following issues were found.

- The software was capable of running the uniaxial direct-tension fatigue test only and not the tension-compression test,
- The feedback signal is controlled by the actuator strain and not by the on-specimen strain,

- The number of loading cycles was limited to a maximum of 100,000 cycles,
- The software was not able to apply rest periods between the loading cycles; which is one of the main requirements of the current project,
- There was no option to stop the test after a certain stiffness reduction value (i.e., 50% of the initial stiffness), and
- There was no option to save the dynamic raw data for the saved loading cycles.

6.3.3 Advanced Asphalt Technologies (AAT) Method

The IPC Company provided ASU with the uniaxial fatigue software developed for AAT. The following comments were found after running few tests:

- Although the software is capable of running the tension-compression uniaxial fatigue test, it cannot run the direct tension test,
- Although the software can conduct the test by controlling the on-specimen LVDTs strain, it cannot control the actuator strain,
- The software was not able to apply rest periods between the loading cycles,
- There was no option to stop the test after a certain reduction of the stiffness;
- There is no figure print test to evaluate the variability between replicates as in the NCSU software, and

Based on the evaluation of the available software, it was clear that none of them can satisfy the requirements of this research. A new uniaxial fatigue

software had to be developed that can conduct the uniaxial fatigue test according to the test conditions required in this study.

6.4 Testing System Setup

The description of the different components of the testing system used to develop the ASU uniaxial fatigue test is presented as follows:

6.4.1 Testing Machine

A Universal Testing Machine, UTM-25, was used in this study. The machine can perform the test using two closed-loop servo-hydraulic testing system manufactured by IPC. The load frame capacity of the UTM-25 machine is 25 kN in static loading and 20 kN in dynamic loading. The machine is capable of applying load over a wide range of frequencies from 0.1 to 20 Hz.

6.4.2 Controller Systems

Two different controller systems have been examined to perform the uniaxial fatigue test using the available UTM-25 IPC machine. The first system consisted of two parallel controllers manufactured by IPC and GCTS companies. The second system consists of a new IPC IMACS controller (FIGURE 96). Although both controller systems are capable of producing the required loading function, it was concluded that the second system was the best in order to avoid the incompatibility issues between the two different controllers of the first system.

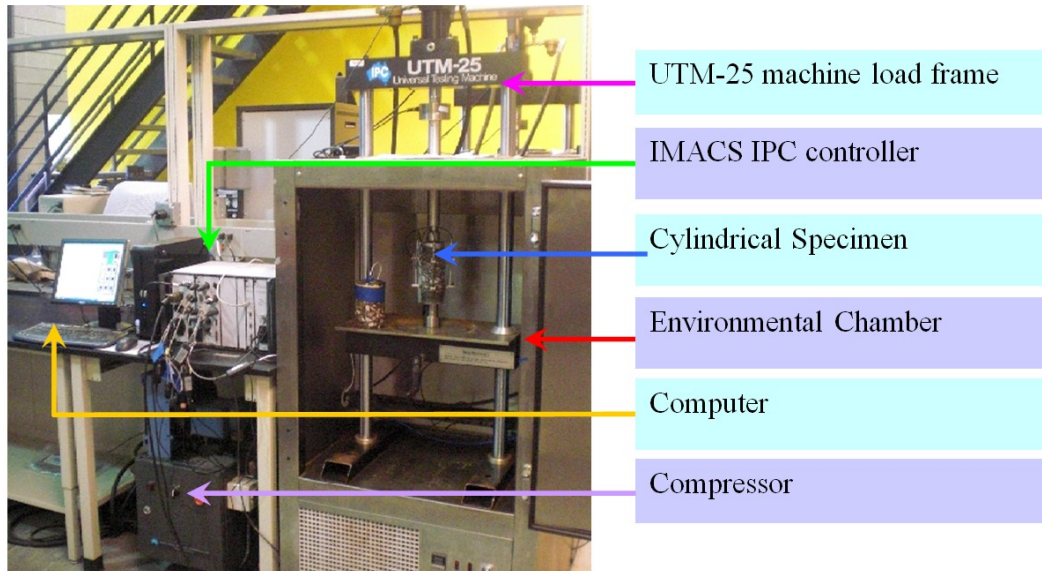


FIGURE 96 UTM-25 uniaxial tension-compression test setup

6.4.3 Temperature Control

The temperature control of the UTM system is refrigeration-based. The temperature control system is able to provide a temperature between 5 °F and 140 °F for extended periods. The temperature homogeneity is achieved with internal fans and baffles to ensure air circulation. An asphalt dummy specimen with a temperature probe is used to ensure consistency in testing temperature.

6.4.4 Deflection Measurement

The vertical deformation is measured with three spring-loaded LVDTs spaced 120 degrees apart. The LVDTs are attached to the specimen using parallel brass studs to secure the LVDTs in place. Three pairs of studs are glued on the surface of the specimen with gauge lengths of 4-inch (100-mm).

6.4.5 Load Measurement

Loads are measured using electronic load cells. The UTM-25 is equipped with a 5,000 lb. load cell.

6.5 Specimen Alignment

The uniaxial fatigue test requires special attention to the vertical alignment and the centering of the specimen to have accurate test results (SHRP-A -641, 1993; Chehab, 2002; Soltani and Anderson, 2005; and others). The sample preparation technique is of paramount importance in order to ensure that the failure plane occurs far enough from the end platens and perpendicular to the sample axis. For this purpose, a gluing jig was manufactured to ensure proper alignment between the end platens and the specimen axis. At the same time, the device will aid in centering the specimen within the end plates and ensures that no eccentricity exists between the specimen and end plates. FIGURE 97 shows the gluing jig that was designed and manufactured at ASU.

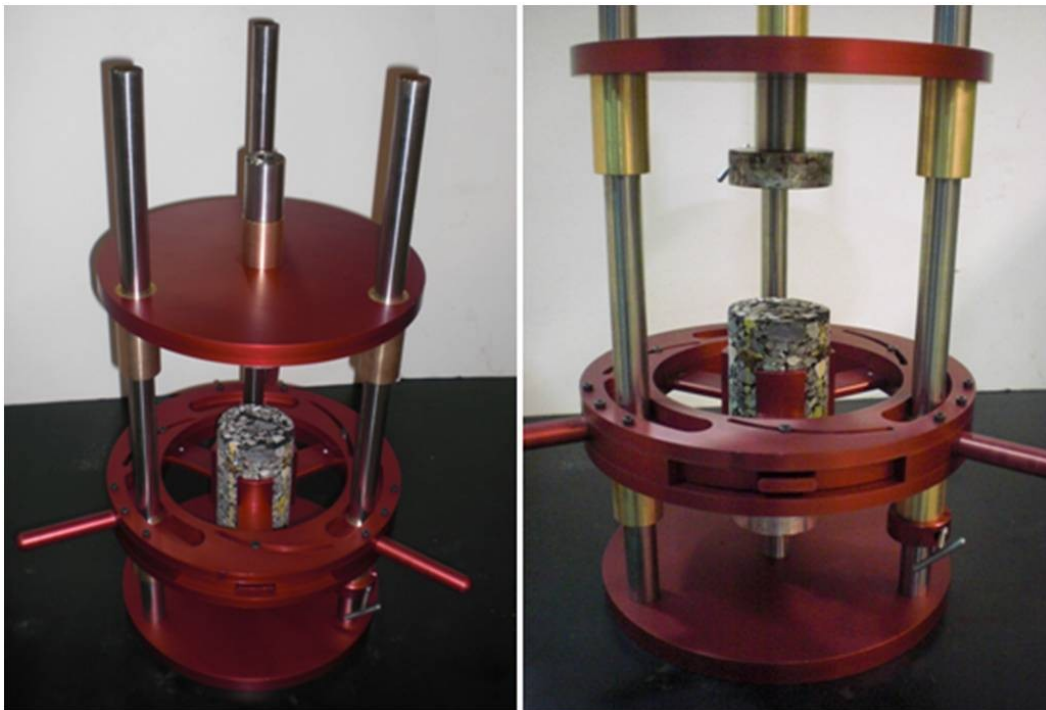


FIGURE 97 Gluing jig for uniaxial tension-compression test specimen

A detailed gluing procedure is presented as stated below:

- Clean the ends of the specimen from any residual dust using a towel or the operator hand.
- Screw the top and the bottom end platens to the gluing jig.
- Place the specimen approximately on the center of the bottom end platens.
- Rotate the middle part of the gluing jig till the three vertical rods hold the specimen firmly to be exactly on the center of the bottom plate.
- Move the upper part of the jig upward.
- Weigh out an appropriate amount of adhesive for the top side of the specimen only.

Note 1 –The following epoxy types were found to be satisfactory for gluing the specimens without having any failure between the platens and the glue:

- Davcon plastic steel 5 minutes putty 10240 (2800 psi strength)
- Loctite metal /concrete epoxy (2700 psi strength)
- Loctite Fixmaster Superior Metal (5500 psi strength)
- ACE plastic repair epoxy (3431 psi strength)

Note 2 –approximately 40 grams epoxy was found to be enough for one side of 75 mm diameter specimen.

- Mix the two components of the epoxy by the required percentages very well for 30 seconds until homogeneous putty is obtained.
- Take around 60% of the epoxy and spread it at the top surface of the specimens.

- Move the top part of the jig downward until the upper end platens rest on the upper surface of the specimen.
- Apply enough pressure on the top part of the jig to squeeze any extra glue between the top end platen and the top surface of the specimen.
- Use the other 40% plus the squeezed epoxy to glue the outer surface of both the specimen and the top end platen to cover around 0.4-inch (10-mm) from each.

Note 3 –gluing about 0.4-inch (10-mm) from the outer surface at top and bottom of the specimen was found to decrease the opportunity of having edge failure.

- Allow the adhesive to reach its initial set. Follow the manufacturer's recommendation to determine the time needed to the initial set.
- Rotate the middle part to lose the specimen then move the upper part upward with the upper end platens and the specimen.
- Prepare the epoxy amount for the bottom side of the specimen.
- Spread 60% of the epoxy amount on the top of the lower end platens.
- Move down the upper part of the jig till the specimen rest on the upper end platen.
- Apply pressure to the upper part of the jig to squeeze any extra glue amount outside.
- Use the remaining amount of the glue plus the squeezed amount to cover a 10 mm height around both the lower end platen and bottom surface of the specimen.

- Leave the specimen until the initial set is reached then remove the specimen from the gluing jig.
- After approximately two hours, attach the mounting studs for the axial LVDTs to the sides of the specimen using epoxy cement.

6.6 Development of ASU Uniaxial Fatigue Test Method

In this research, the uniaxial fatigue test will be conducted to evaluate the fatigue damage and healing of asphalt concrete mixtures using the viscoelastic and continuum damage model. The results will then be used through a developed methodology based on the crack healing to predict the fatigue endurance limit of HMA mixtures. The healing in this research is evaluated by observing the difference between fatigue damage for tests with and without rest periods inserted between load cycles. New software was developed to meet the test requirements as discussed in Section 6.7.

At the beginning, four available softwares (Three provided by IPC and one provided by GCTS) were used to address different issues regarding the proper test conditions to be used according to the research requirements. The name of these softwares is as following:

1. GCTS universal software.
2. IPC User programmable software (UTS-019, V1.07b)
3. IPC S-VECD software (UTS-032, V1.00)
4. IPC SCUDU software (UTS-021)

The outcomes from these preliminary studies were considered in the development of the new softwares. The purpose and the main findings of the different ancillary studies are discussed in the next section.

6.6.1 Selection of Appropriate Glue Type and Platens

A special study was performed to select the appropriate epoxy type and metal platens that would be used in the rest of the research. In this study several monotonic direct tension tests at different strain rates and cyclic uniaxial tension-compression tests were conducted. The GCTS universal software was used in this study. The selection of the appropriate type was based on failure location to ensure that failure occurs in the middle portion of the specimen and not close to the specimen end, or through the epoxy. Two specimen sizes were used; 3-inch diameter by 6-inch height (75-mm by 150-mm) and 4-inch diameter by 6-inch height (100-mm by 150-mm). In this special study, only the actuator LVDT reading was used in order to reduce the specimen preparation time. TABLES 33 and 34 summarize the different monotonic tests for 4- and 3-inch specimens, respectively. FIGURE 98 shows test results for a successful test.

Based on the outcome and the test results, the following findings were recommended:

- Aluminum platens are better than steel ones in providing a better cohesion between specimen and platens.
- Loctite metal/concrete epoxy, Loctite Fixmaster Superior Metal and Davcon plastic steel liquid (10210) are appropriate for 3-inch diameter specimens. However, ACE Plastic repair epoxy is

suitable for 4-inch diameter specimens due to its higher shear strength.

- 3-inch diameter specimens have higher tendency to fail within the middle of the specimen, while the 4-inch diameter usually fail more frequently near to the end platens as shown in FIGURE 99.

TABLE 33 Summary of monotonic direct tension tests for 4 inch diameter specimens

Specimen ID	Glue Type	Glue Strength (Psi)	Upper Plate	Lower Plate	Strain Rate (mm/min)	Max Load (N)	Test Time (min)	Failure Location
LP702	Devcon 5 min epoxy	1500	Aluminum	Steel	1.0	65	1.76	between glue and lower plate
LP701	Loctite metal /concrete epoxy	2700	Aluminum	Steel	0.25	5805	2.24	between glue and lower plate
LP705	Devcom 2 ton epoxy	2500	Steel	Aluminum	0.1	4493	2.4	between glue and upper plate
MC 94404	Loctite metal /concrete epoxy	2700	Aluminum	Aluminum	0.1	5162	1.34	between glue and upper plate
MC 94403	ACE Plastic repair epoxy	3431	Aluminum	Aluminum	0.1	7417	3.99	Successive failure at top of specimen

TABLE 34 Summary of monotonic direct tension tests for 3- inch diameter specimens

Specimen ID	Glue Type	Glue Strength (Psi)	Upper Plate	Lower Plate	Strain Rate (mm/min)	Max Load (N)	Test Time (min)	Failure Location
MC944-01	Loctite metal /concrete epoxy	2700	Aluminum	Aluminum	0.1	2060	60	Successive failure at top of specimen
MC944-02	Devcon 2 ton epoxy	2500	Aluminum	Aluminum	0.1	2400	17.3	between glue and upper plate
MC944-05	Loctite metal /concrete epoxy	2700	Aluminum	Aluminum	0.1	2800	60	Successive failure at middle of specimen
MC944-06	Loctite Fixmaster Superior Metal	5500	Aluminum	Aluminum	0.15	2750	30	Successive failure at top of specimen
MC944-07	Davcon plastic steel liquid (10210)	2800	Aluminum	Aluminum	.25	2520	18	Successive failure at top of specimen

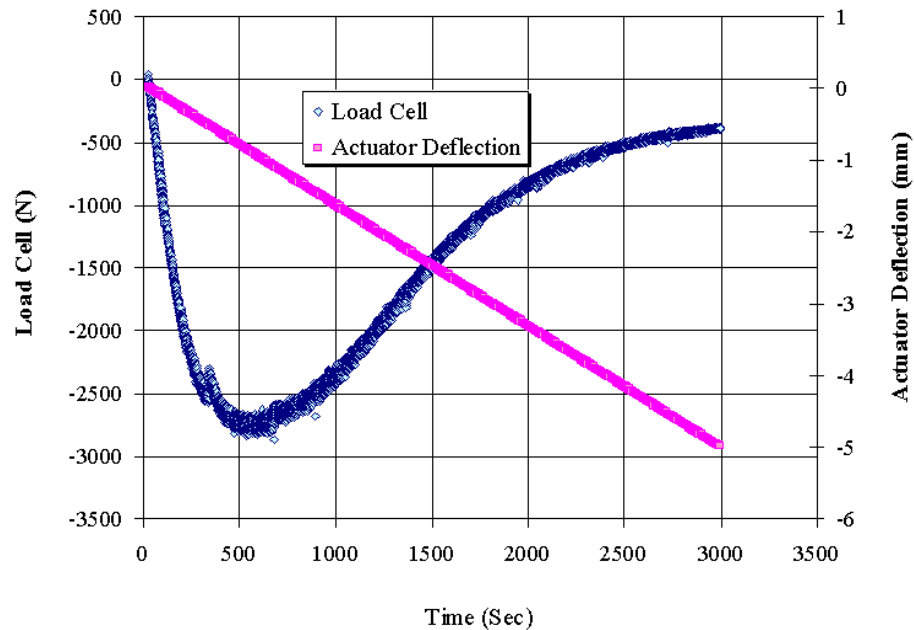


FIGURE 98 Typical monotonic direct tension test results (specimen MC944-05)

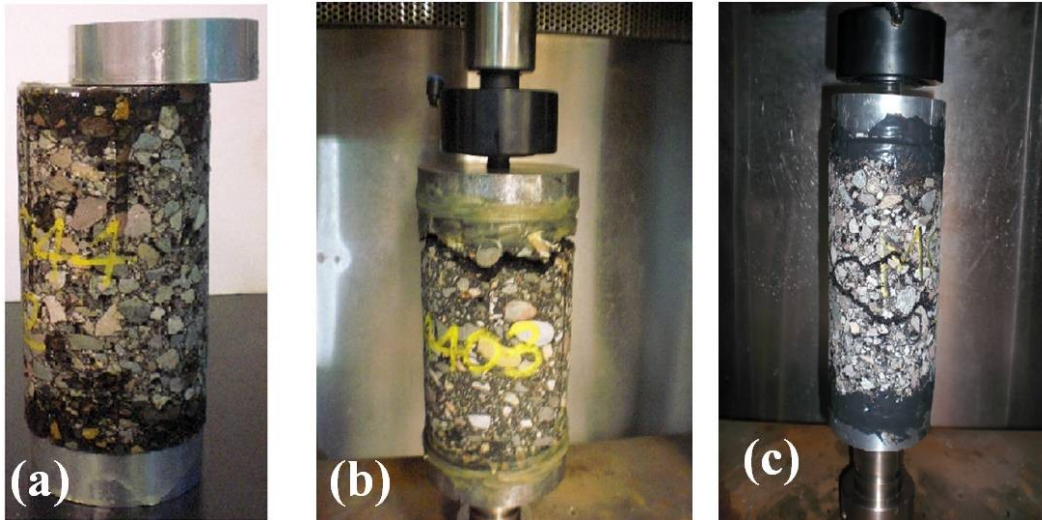


FIGURE 99 Location of failure; (a) Between platen and glue; 4-inch, (b) Close to specimen end; 4-inch, and (c) Middle of specimen; 3-inch

6.6.2 Machine Compliance

Machine compliance is a very important issue in uniaxial fatigue tests. In this type of testing, not all the actuator movements are transferred to the specimen due to the inadequate machine compliance. Different reasons may contribute to the machine compliance. One reason is that one or more components of the loading system may yield under the applied loads. Machine compliance can be easily investigated by comparing the deformations measured from the actuator LVDT and on-specimen LVDTs or by calculating the machine compliance factor which is the actuator LVDT displacement divided by the on-specimen LVDT displacement. If the machine compliance factor is equal to one, this means that all the actuator deformation is transferred to the specimen. In reality, the machine compliance factor is always greater than one, which means that a portion of the actuator displacement is missed before getting to the tested specimen. Knowing

the machine compliance factor of the testing machine, a requisite on-specimen displacement can be achieved by applying an actuator displacement equal to the required on-specimen displacement times the machine compliance factor. A machine compliance factor in the range of 5 to 10 is usually common (Chehab, 2002).

Chehab (2002) stated that the magnitude of the machine compliance depends upon the stiffness of the material. The higher the stiffness of the material being tested the higher the machine compliance factor. Based on that, it can be concluded that the machine compliance will be high at lower temperatures where the HMA stiffness is high. It was also mentioned that the machine compliance factor increases as the testing frequency increases. The machine compliance can be reduced by regularly maintaining the testing machine. It is important also to clean all the threads and connections and ensure they are very well tightened.

For the purpose of this research, the machine compliance was evaluated for the UTM-25 machine. The GCTS universal software was used to evaluate two types of locking joints. The first one was an air-vacuum locked joint where the other one was a thread locked joint as shown in FIGURE 100. It was noticed that the machine compliance is too high when using the air-vacuum locked joint, while the thread locked joint improved the machine compliance (FIGURES 101 and 102)

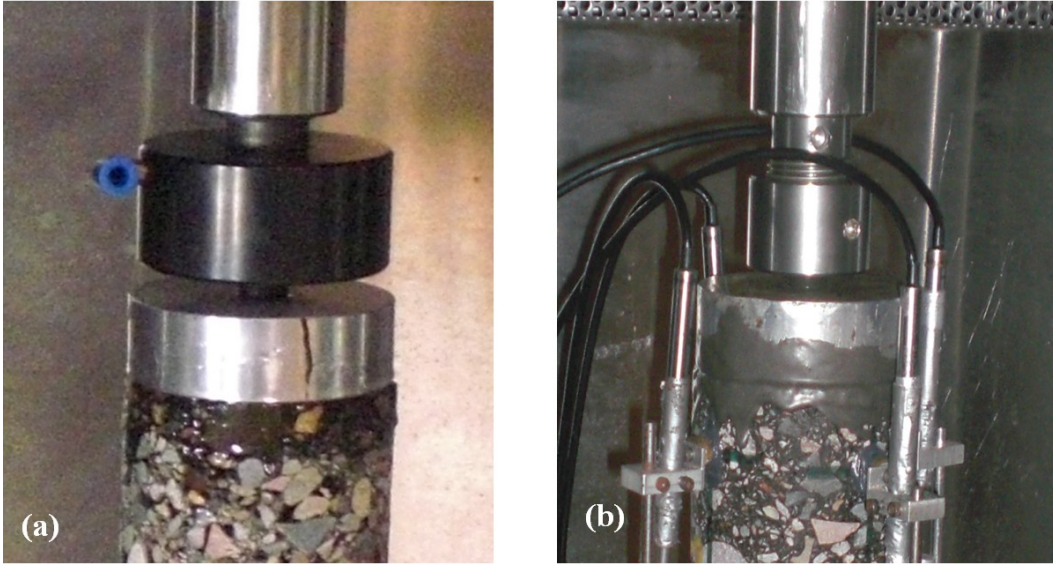


FIGURE 100 Locking joints: a) air-vacuum locked joint; b) thread locked joint

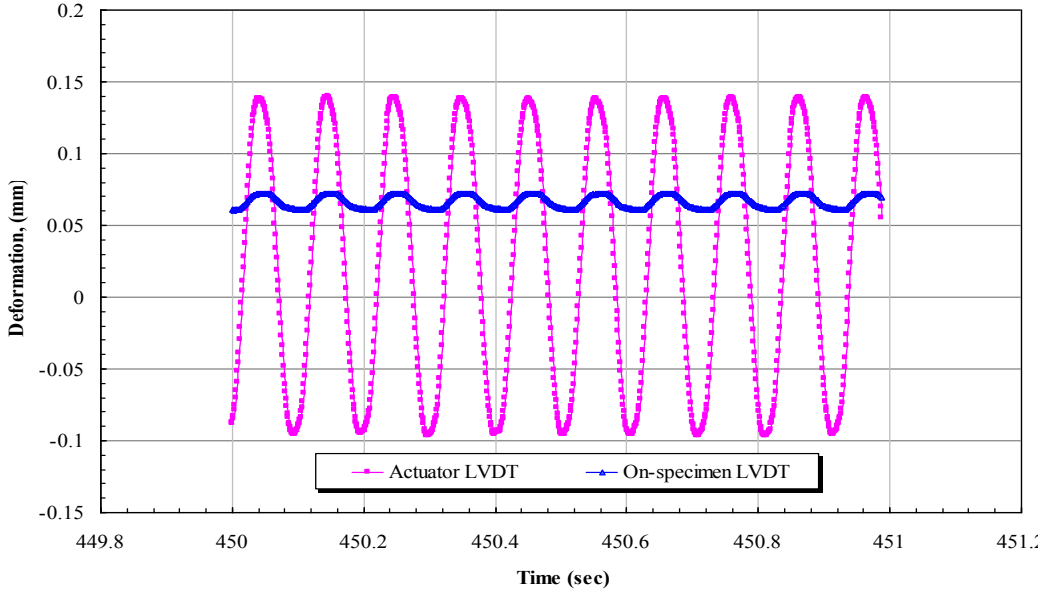


FIGURE 101 Comparison of actuator to on-specimen LVDT deformations using the air-vacuum locked joint

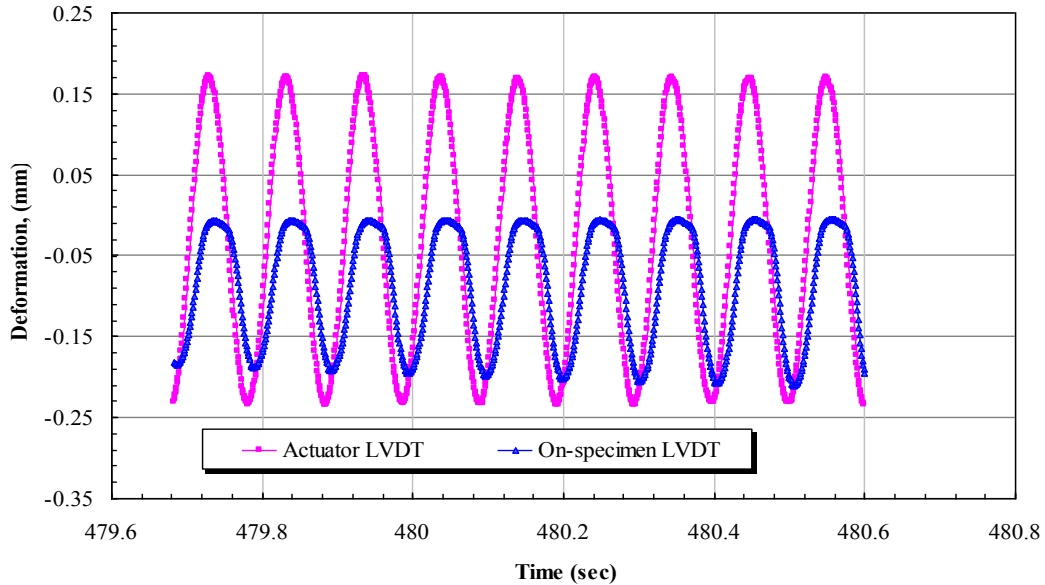


FIGURE 102 Comparison of actuator to on-specimen LVDT deformations using the thread locked joint

6.6.3 Failure Location and Specimen Height during Compaction

In uniaxial fatigue tests, two types of failure are recognized based on the location of the failure plane. The first failure type is when the specimen fails in the middle and within the LVDTs gauge length. The second failure type is when the specimen fails at one of the ends, either top or bottom, and out of the LVDT measuring zone. Furthermore, the middle-failure type can also have three different modes as shown in FIGURE 103, when failure occurs at the top, middle or bottom of the LVDTs measuring zone. Middle-failure within the LVDT measuring zone is essential, as the LVDTs are able to capture the specimen response during the whole period. Conversely, end-failure test is doubtful as the acceptable LVDT measurements are only available for the test range before the failure starts to take place.

Hou et al. (2010) concluded that both middle-failure and end-failure results do not affect the damage characterization. However, the end-failure test results can't be considered in the fatigue failure (fatigue life) analysis. As the analysis in this research requires having the fatigue life at failure data, it is crucial to have the failure occurs anywhere within the LVDTs measuring zone.

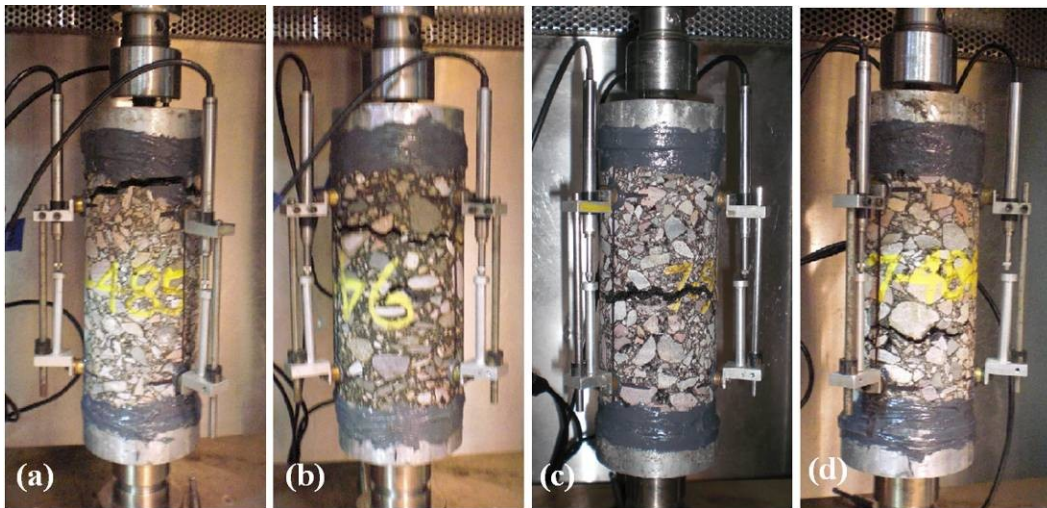


FIGURE 103 Different failure types of uniaxial fatigue test: (a) end-failure, (b) middle-failure at top, (c) middle-failure, and (d) middle-failure at bottom

Assuming proper alignment, special care has to be taken regarding the air void distribution along the specimen height in order to achieve middle failure.

Specimens compacted using gyratory compactors tend to have non-uniform air void distribution both along the diameter and height, where the air void distribution is usually higher for the outside shell compared to the inside core (Chehab, 2002). To obtain a uniform air void distribution within a specimen for testing, it has to be cored from a larger compacted specimen with the top and bottom sections being cut off. The gyratory plug is usually compacted to 6.7-inch (170-mm) height and 6-inch (150-mm) diameter. The gyratory plug is then cored

to have a cylinder specimen of certain lower diameter based on the test type and specification (usually 3- or 4-inch diameter). The upper and lower specimen ends are then trimmed to have a specific specimen height according to the test protocol (usually 6-inch height).

It was hypothesized that higher compaction heights would allow for more cuts, from the two ends with high air voids. This would leave a more homogeneous air void distribution along the remaining specimen height (6-inch), which promises to have more frequent failure in the middle of the specimen in the uniaxial tension-compression fatigue test.

To investigate the above hypothesis, a pilot study was performed, in which gyratory plugs were compacted at three compaction heights, (6.7-, 7.1-, and 7.9-inch (170-, 180- and 200-mm) (FIGURE 104). A 3-inch (75-mm) diameter and 150-mm height specimens were cored and cut from the different-height plugs. Some of these specimens were used to investigate the air void distribution at different compaction heights, while the other specimens were tested using uniaxial tension-compression fatigue test up to failure to determine the failure location. All the manufactured specimens for this study were prepared using the PG 76-16 binder at 4.2% asphalt content. TABLE 35 summarizes the testing program of the pilot study. Since the volume of the material needed for the 200 mm height plugs was too large to put in the mold, it was possible to compact two plugs at 9.5% air void only.

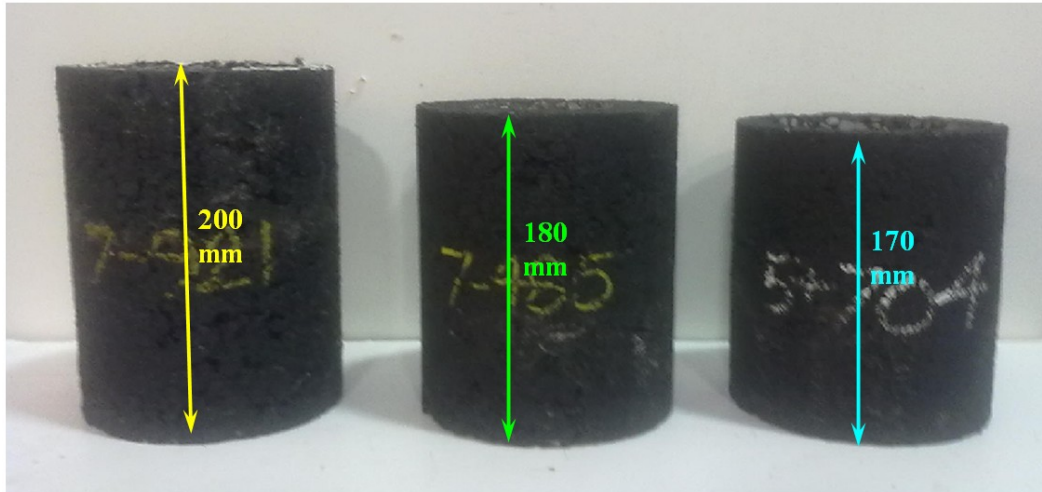


FIGURE 104 Compaction of plugs with different height

TABLE 35 Testing plan of the compaction study

Compaction Height (inch)	Target Air Void (%)	No. of Specimens for Air Void Distribution	No. of Specimens for Fatigue Test
6.7	8.0	3	5
7.1	9.5	3	3
	7.0	3	0
	4.5	3	3
7.9	9.5	1	1

In gyratory compacted specimen, the air voids at the top is usually higher than the air voids at the bottom. Therefore, a higher thickness is usually trimmed from the top compared to the bottom of the specimen (Chehab et al., 2000). In this study, for 6.7-inch (170-mm) compaction height specimens, 0.3-inch (8-mm) were trimmed from the bottom and 0.5-inch (12-mm) were trimmed from the top. For the 7.1-inch (180-mm) specimens, 0.4-inch (10-mm) was trimmed from bottom and 0.8-inch (20-mm) was trimmed from top. Finally, in the case of the

7.9-inch (200-mm) height plugs, 0.6-inch (15-mm) was trimmed from bottom and 1.4-inch (35-mm) was trimmed from top.

To examine the air void distribution along the specimen height, the air voids for both cored and cut specimens were determined initially. The second step was to cut the specimen into two halves, 3-inch (75-mm) in height each; designated as top half (T) and bottom half (B). The two halves were then completely dried for 24 hours and the air voids were determined for both halves. The last step was to divide the specimen into four quarters by cutting each half into two quarters with approximately 1.5-inch (37-mm) height each. The two quarters from the top half were designated as top-top quarter (TT) and top-bottom quarter (TB), where the two quarters from the bottom half were designated as bottom-top quarter (BT) and bottom-bottom quarter (BB). The air voids were then determined for the four quarters after being dried for 24 hours. FIGURE 105 shows the steps of specimen cutting, while

FIGURE 106 illustrates an example of air voids calculation for each part.



FIGURE 105 Steps of specimen cutting for different air void calculations

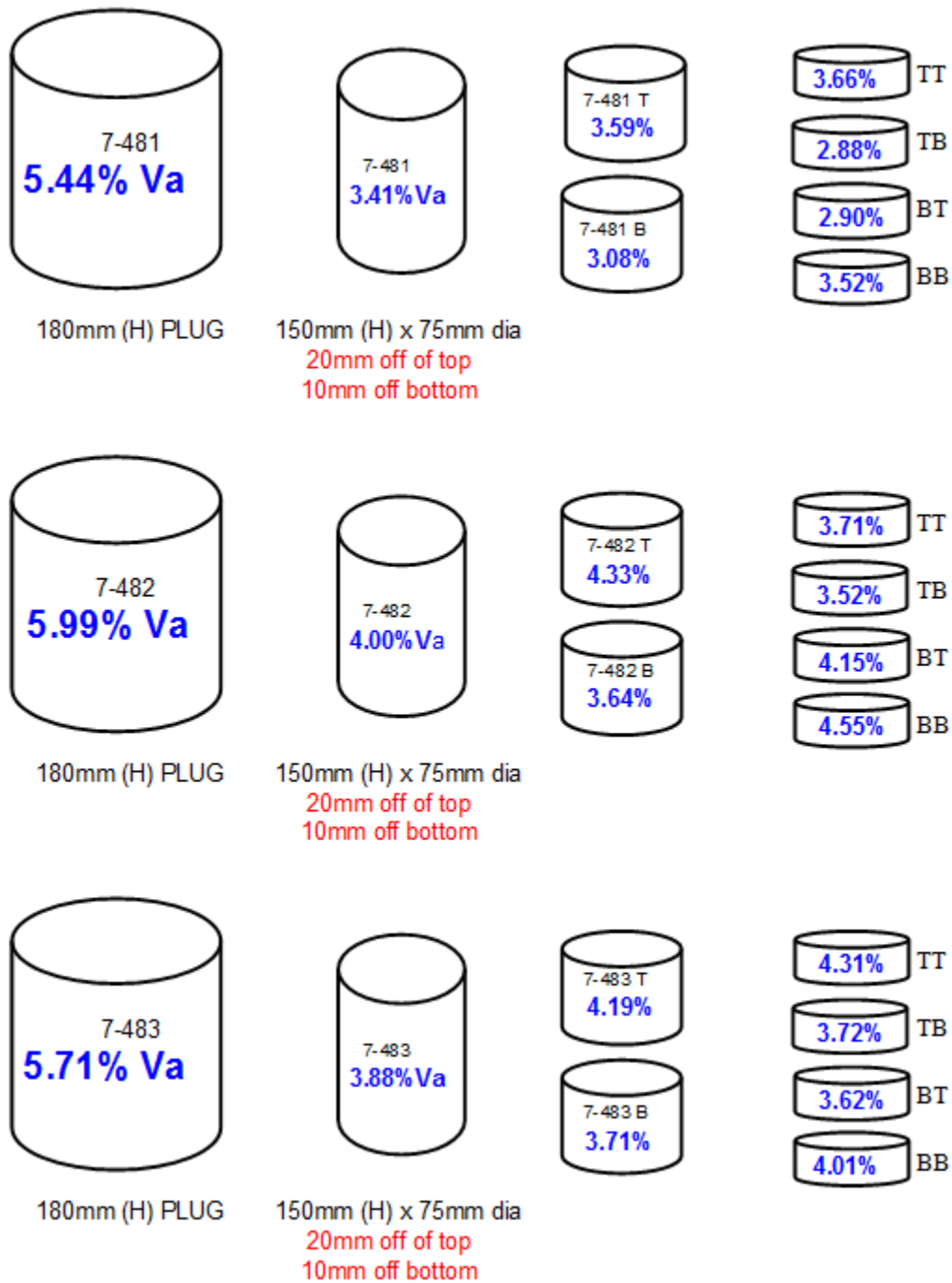


FIGURE 106 An example of air void calculations for each part

The air void calculations and analysis are summarized for each group of replicates based on the compaction height and the air void levels in TABLES 36 through 40. Each table contains the air void calculations based on the whole specimen, two halves, and 4 quarters. The percent air voids difference between the top and bottom halves as well as the top and bottom quarters within the same group were determined. To have a better chance in specimen failure in the middle or at least within the LVDT measuring zone, the average percent difference of the air voids between the top and the bottom quarters of the same half should be minimal. It can be observed from the different tables that the average top and bottom air voids percent difference is lower for the 7.1-inch (180-mm) height samples (for the three groups at 4.5, 7.0, and 9.5%) compared to the 6.7-inch (170-mm) height samples. This means that specimens cored and cut out of the 7.1-inch (180-mm) compacted plugs will have a better chance to fail in the middle compared to those compacted at 6.7-inch (170-mm) height. The specimen compacted at 7.9-inch (200-mm) height showed higher air voids percent difference compared to both 6.7- and 7.1-inch (170- and 180-mm) plugs. However, this observation was only based on one replicate.

TABLE 36 Average of air void calculations for 6.7-inch height at 8.0% Va

Sample ID	1 Parts	2 Parts			4 Parts						
	Air Void	Air Void	Difference	Average Difference	Air Void	Difference	Ave. Top Difference	Ave Bottom Difference			
944-18	8.29	8.45	0.71	0.85	8.56	0.94	1.42	1.21			
		7.62			7.49						
		7.74			9.27	1.78					
		944-19			8.19	8.59			1.23	9.50	1.85
7.36	7.65		0.78								
944-20	8.40					8.82				0.61	8.77
			8.08			9.56					1.07
7.66		8.08									
8.21		8.73									

TABLE 37 Average of air void calculations for 7.1-inch height at 9.5% Va

Sample ID	1 Parts	2 Parts			4 Parts						
	Air Void	Air Void	Difference	Average Difference	Air Void	Difference	Ave. Top Difference	Ave Bottom Difference			
7-981	8.67	9.27	0.34	0.88	9.66	0.82	1.21	1.55			
		8.93			8.84						
		7-982			9.66	9.87			1.52	10.02	1.2
						8.35				7.74	1.7
7-983	9.82		10.28			0.78				10.49	1.6
			9.50							8.89	2.01
		8.38	10.39								
		10.39	10.39								

TABLE 38 Average of air void calculations for 7.1-inch height at 7.0% Va

Sample ID	1 Parts	2 Parts			4 Parts						
	Air Void	Air Void	Difference	Average Difference	Air Void	Difference	Ave. Top Difference	Ave Bottom Difference			
7-781	6.27	6.55	0.56	0.77	7.17	1.12	0.84	0.68			
		5.99			6.05						
		7-782			6.71	7.26			0.94	7.39	0.29
						6.32				7.10	
7-783	7.22	7.41	0.77		6.12	0.44					
		8.18			6.56						
		7-481			3.41	3.59			0.51	3.66	0.78
						3.08				2.88	
7-482	4.00	4.33	0.69		2.90	0.62					
		3.64			3.52						
7-483	3.88	4.19	0.54		3.71	0.19					
		4.73			3.52						
		7-481		3.41	3.59	0.51	4.15	0.4			
					3.08		4.55				
7-482	4.00	4.33	0.69	4.31	0.59						
		3.64		3.72							
7-483	3.88	4.19	0.54	3.62	0.39						
		4.73		4.01							

TABLE 39 Average of air void calculations for 7.1-inch height at 4.5% Va

Sample ID	1 Parts	2 Parts			4 Parts						
	Air Void	Air Void	Difference	Average Difference	Air Void	Difference	Ave. Top Difference	Ave Bottom Difference			
7-481	3.41	3.59	0.51	0.58	3.66	0.78	0.52	0.47			
		3.08			2.88						
		7-482			4.00	4.33			0.69	3.71	0.19
						3.64				3.52	
7-483	3.88	4.19	0.54		4.15	0.4					
		4.73			4.55						
		7-481			3.41	3.59			0.51	4.31	0.59
						3.08				3.72	
7-482	4.00	4.33	0.69		3.62	0.39					
		3.64			4.01						

TABLE 40 Average of air void calculations for 7.9-inch height at 9.5% Va

200 mm Plugs, 9.0%AV					
Sample ID	1 Parts	2 Parts		4 Parts	
	Air Void	Air Void	Difference	Air Void	Difference
7-922	8.67	9.55	0.46	10.52	1.79
				8.73	
		11.01		9.28	1.63
				11.91	

The air void distributions for each group based on the compaction height and the air void level are plotted in FIGURES 107 to 111. The following can be observed as a general trend:

- The air void values at the specimen ends are relatively higher compared to the values at the middle of the specimen,
- The upper half of the specimen has higher air voids than the lower half.
- Despite larger thicknesses were trimmed from the top compared to the bottom of specimens, the top of the specimens in most cases had higher air voids than the bottom; which emphasized the approach followed in trimming the top and bottom ends.

Regarding the uniaxial fatigue test, the results concerning the failure location were very encouraging and showed the same conclusion from the air void distribution analysis. For the 6.7-inch (170-mm) compaction height group, only one specimen out of five failed in the LVDT measuring zone (20 % success). On the other hand, the 7.1-inch (180-mm) compaction height groups at 4.5 and 9.5% had five out of six specimens failed in the LVDT measuring zone (83% success). For the 7.9-inch (200-mm) compaction height, the specimen failed in the LVDT measuring zone, but this was only for one specimen. TABLE 41 summaries the failure location at different compaction heights.

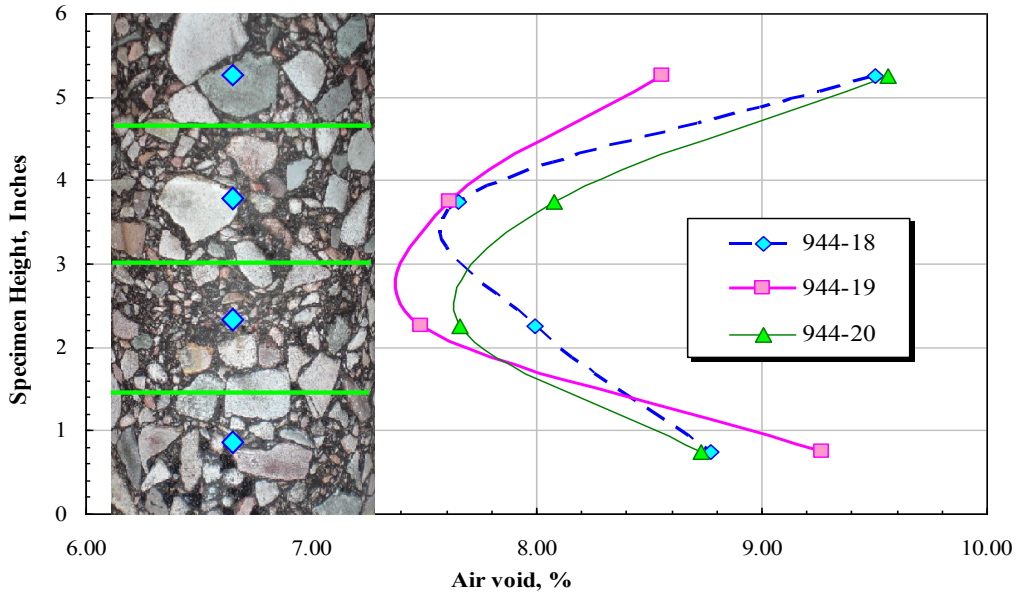


FIGURE 107 Air void distribution along the specimen height for 6.7-inch height at 8.0% Va.

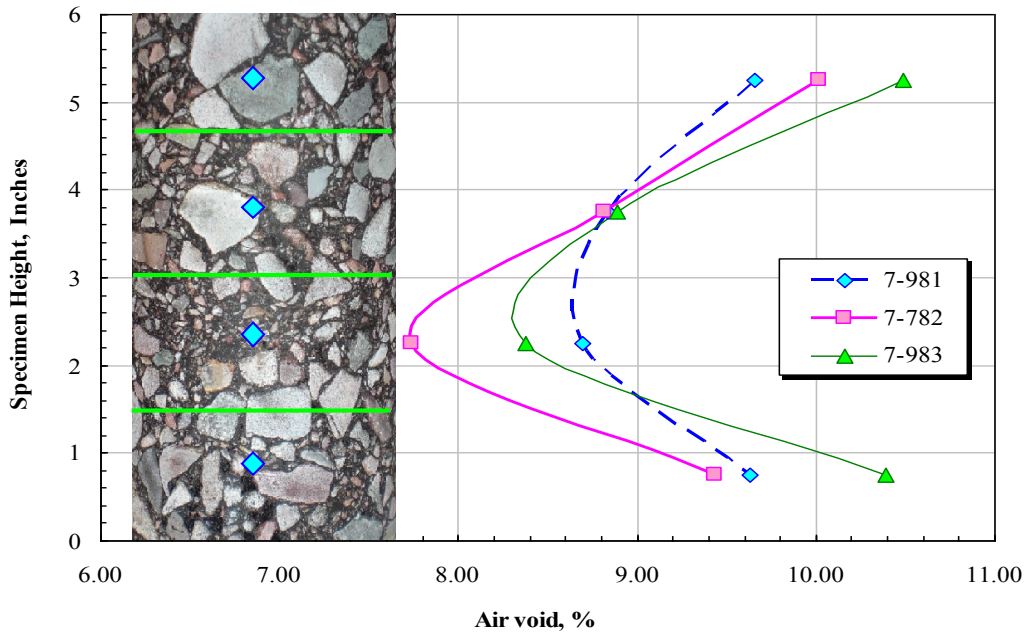


FIGURE 108 Air void distribution along the specimen height for 7.1-inch height at 9.5% Va.

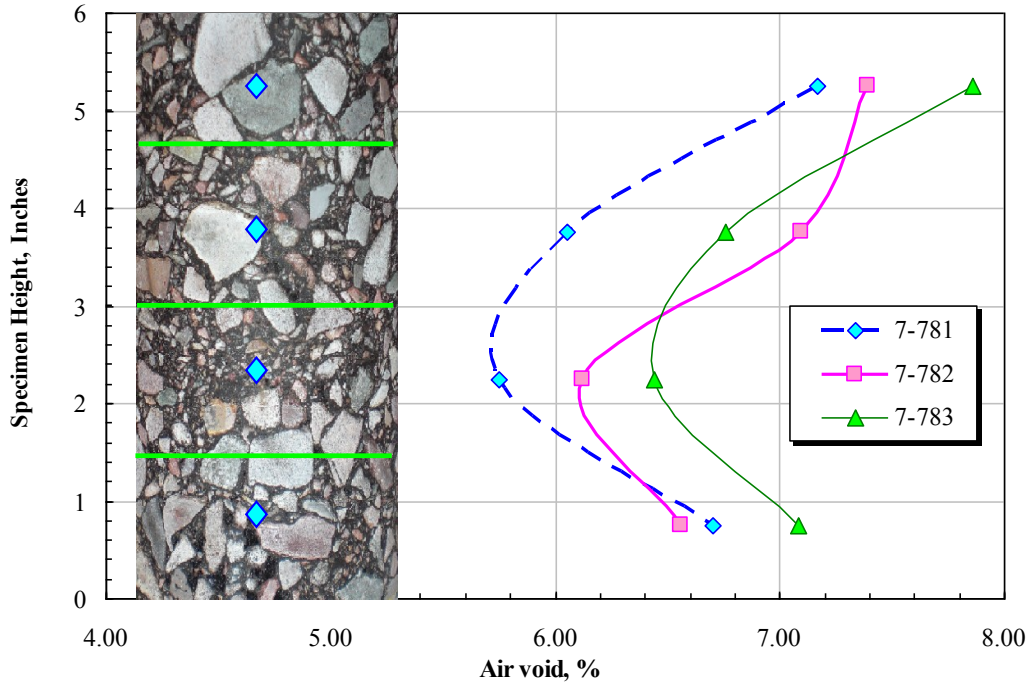


FIGURE 109 Air void distribution along the specimen height for 7.1-inch height at 7.0% Va.

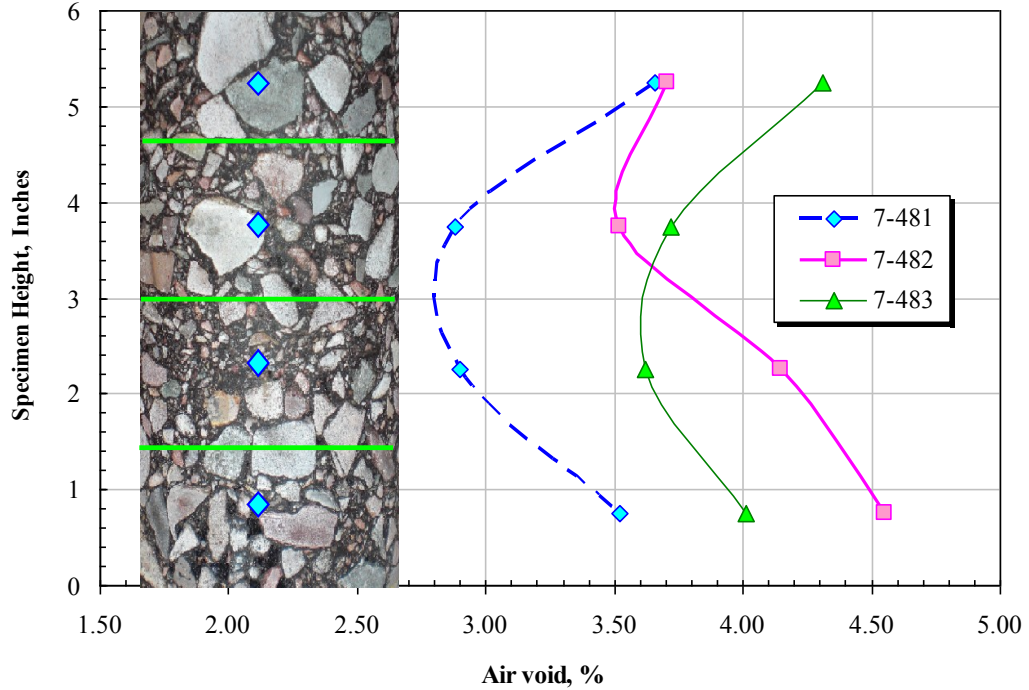


FIGURE 110 Air void distribution along the specimen height for 7.1-inch height at 4.5% Va.

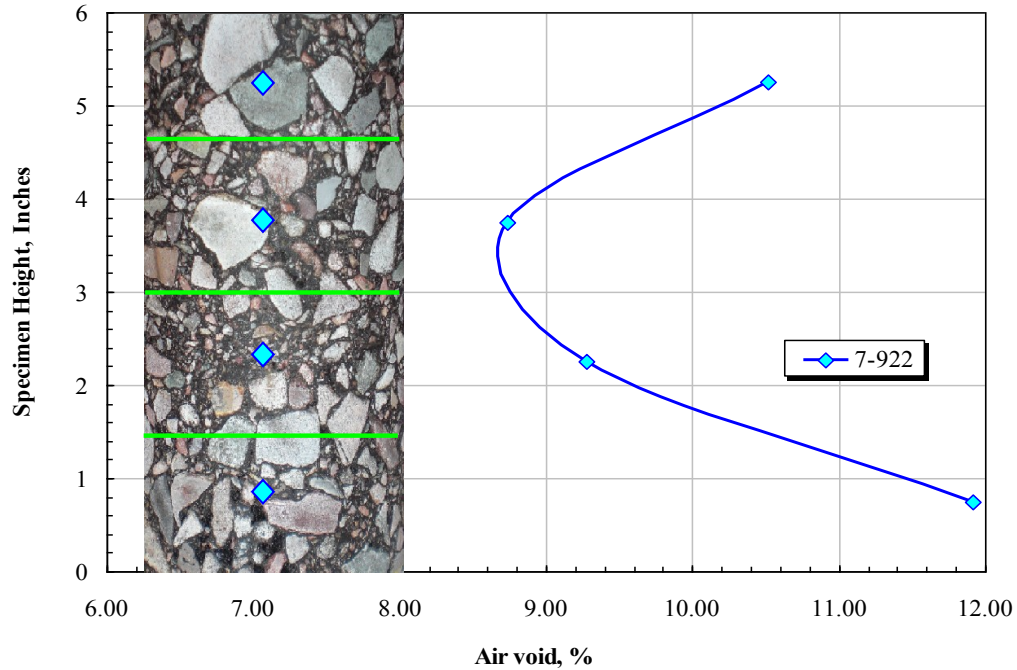


FIGURE 111 Air void distribution along the specimen height for 7.9-inch height at 9.5% Va.

TABLE 41 Locations of failure for specimens with different compaction heights

Specimen ID	Compaction Height (inches)	Target Air Void (%)	Actuator Displacement (mm)	Failure Location	Fatigue Life Analysis
MC944A-17	6.7	7.0	±0.3	At top of specimen	Not applied
MC944A-21			±0.3	At bottom of specimen	Not applied
MC944A-22			±0.3	In the LVDT gauge length near top	Applied
MC944A-23			±0.3	At bottom of specimen	Not applied
MC944A-25			±0.3	At bottom of specimen	Not applied
944A-7-984	7.1	9.5	±0.2	In the LVDT gauge length near top	Applied
944A-7-985			±0.2	In the LVDT gauge length at middle exactly	Applied
944A-7-986			±0.2	In the LVDT gauge length near bottom	Applied
944A-7-484		4.5	±0.25	In the LVDT gauge length near bottom	Applied
944A-7-485			±0.25	At top of specimen	Not applied
944A-7-486			±0.25	In the LVDT gauge length near top	Applied
944A-7-921	7.9	9.5	±0.25	In the LVDT gauge length near top	Applied

6.6.4 Investigation of Strain Controlled Methods

A preliminarily controlled-strain tension-compression (Push-Pull) uniaxial fatigue test was performed to compare crosshead (actuator) strain control and on-specimen LVDT strain control. The description of each test is explained below.

6.6.4.1 Crosshead Controlled-Strain Test

In this test, the strain was controlled by the actuator while the strain values of on-specimen LVDTs were used for the analysis. In this case, the actuator displacement amplitude is maintained constant during the test, while the on-specimen LVDT displacement amplitude varied during the test. Several tests have been conducted using both the GCTS Universal software and the IPC user programmable software (UTS-019, V1.07b). The following test parameters were used at following:

- Frequency values: 1, 2, 5 and 10 Hz.
- Strain levels: ± 300 , ± 500 and ± 750 μs .

6.6.4.2 On-Specimen LVDT Controlled-Strain Test

In this test, the strain was controlled by the on-specimen LVDTs. In this case, the on-specimen displacement amplitude was kept constant during the test, whereas the actuator displacement amplitude varied during the test. Controlling the on-specimen LVDTs displacements were achieved through a channel created to represent the average displacement from the four on-specimen LVDTs. In this test, ± 300 μs amplitude was applied to the on-specimen LVDTs at 10 Hz frequency.

Based on the results obtained from the two tests, the following conclusions were made.

- The on-specimen strain values using the crosshead-control constant-strain method cannot be maintained constant, but actually increased during the test. This is mainly because the decrease of the machine compliance factor with time due to the gradual decrease in specimen stiffness as illustrated in FIGURE 112.
- It was observed that controlling the strain directly from the on-specimen LVDTs is unsafe as the actuator strain can go too high to transfer the assigned amount of strain to the specimen especially when the machine compliance factor is high. Another issue is that the shape of the load and strain waveform became distorted as the final strain wave was based on the average of the four on-specimen LVDTs (FIGURE 113).
- Since it is important to maintain constant on-specimen strain and to ensure machine safety at the same time, it is recommended to perform a crosshead strain-controlled test and continuously adjust the wave form during the test. This can be done by having a continuous feedback between the actuator and the on-specimen LVDTs.

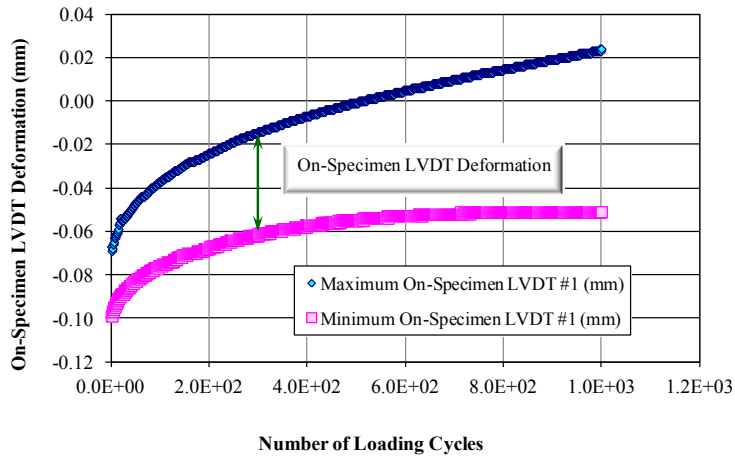


FIGURE 112 On-specimen LVDT deformation using crosshead controlled-strain test

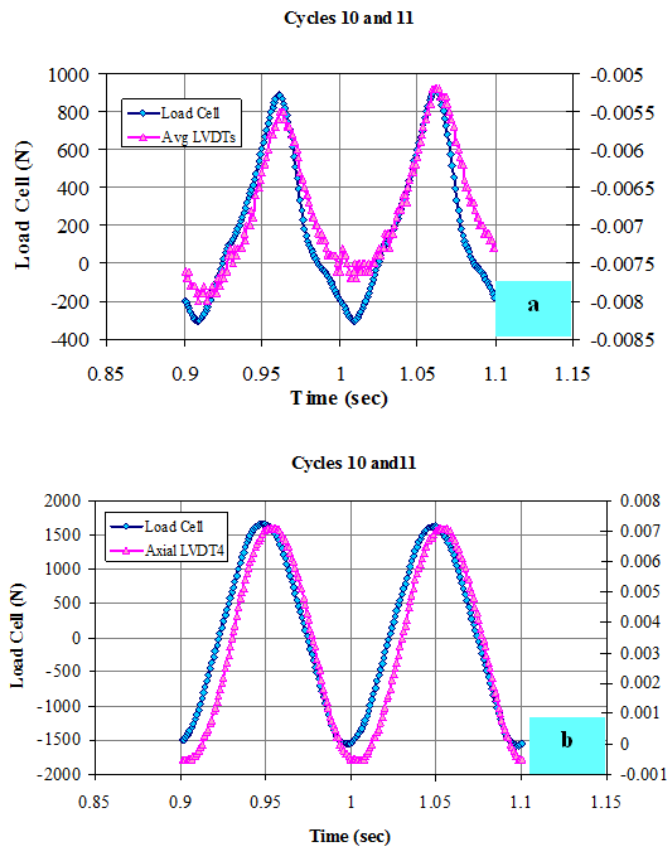


FIGURE 113 Comparison of waveform shape: (a) On-specimen LVDTs controlled-strain test, (b) crosshead controlled-strain test

6.7 Development of ASU Uniaxial Fatigue Test Software

Since the beginning of this research, it was obvious that running the uniaxial fatigue test is a big challenge because of the unavailability of the proper commercial software and the limited literature on hardware setup, test parameters, test procedure, and data acquisition system. After conducting several preliminary studies as explained before, most of the issues regarding the uniaxial fatigue test were solved except two main issues. The first issue was that none of the available software was able to conduct the tension-compression fatigue test with rest period inserted after each loading cycle. The second issue was the ability to keep the target on-specimen LVDT stain constant during the test.

Throughout collaborating efforts, IPC Company delivered to the research team two new softwares. The first software was developed to run the test without rest period so that it can achieve the target on-specimen strain value and to keep it constant throughout the entire test. This issue was critical as the developed methodology to determine the endurance limit requires the target on-specimen average strain to be constant until the end of the test. The second software that was developed for this study was for the test with rest period that have the same other features of the test with rest period.

6.7.1 Software without Rest Period

The software without rest period was developed by IPC for ASU by modifying and adding additional features to the NC State software. The software name is “UTS-032 V1.01b S-VECD Fatigue Test”. The following is a list of its main features.

- The software is capable of running both the direct tension and the tension-compression uniaxial fatigue tests.
- The software is capable of conducting the test by controlling either the actuator strain or the on-specimen LVDT strain.
- The software is able to run a test up to 999,999,999 loading cycles.
- The test can be stopped according to three different criteria that can be used separately or together (number of loading cycles, stiffness reduction percent, and/or adaptive strain control limit factor).
- The software is able of saving the dynamic raw data file for the saved loading cycles.
- The software allows for a varying number of LVDTs (2 to 4).
- The software has a finger print test to evaluate the variability between replicates.
- The saved output data can be used for the viscoelastic continuum damage analysis as well as the reduced cycle analysis.

At the beginning, a few tests were conducted to check out the applicability of the software for the test without rest period. It was clear from the first test that the software was able to achieve the target on-specimen strains within few seconds at the beginning of the test by correcting the actuator strain. The amount of actuator strain correction at the beginning depends on the proximity of the seed dynamic modulus value that is required by the software to the actual or measured value. The estimated input dynamic modulus value helps the software to determine the initial stress value to be applied. The actuator correction (iteration)

procedure is achieved through the adaptive strain control (ASC) option in the software.

As the test proceeds, the specimen stiffness reduces with time due to fatigue damage which, in turn, decreases the machine compliance factor and increases the average on-specimen strain compared to the target value. To solve this issue, the software keeps using the ASC option to readjust the actuator displacement every 10 cycles to keep the target on-specimen strain constant. FIGURE 114 shows typical relationships of the actuator and on-specimens strain values over time. It can be seen that the actuator strain values decrease over time in order to keep the target on-specimen strain values constant.

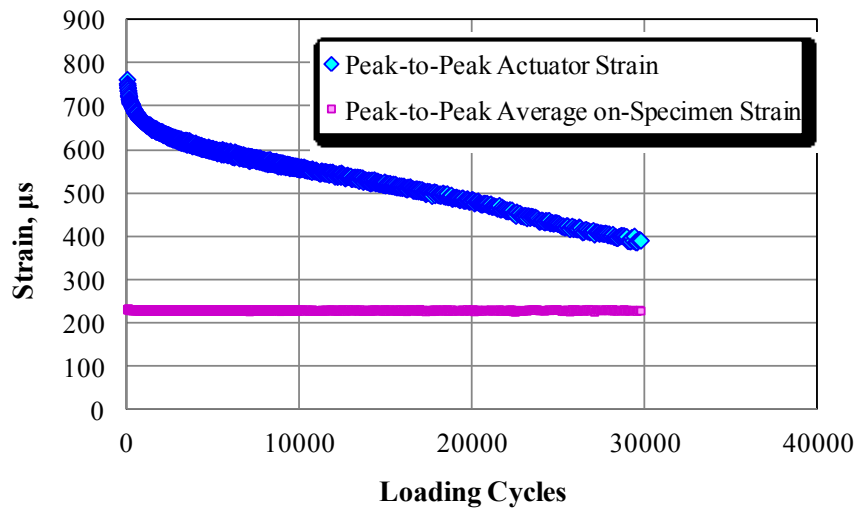


FIGURE 114 Typical actuator and average on-specimen strain over time relationships for test without rest period

6.7.2 Software with Rest Period

Since none of the available software was capable of incorporating a rest period to meet the requirements of this research project, the development of such software was a big challenge. After detailed discussion with the IPC staff and

numerous trials, it was concluded that the IPC programmer had to develop separate software for the test with rest period as it was almost impossible to combine the software with and without rest period. The main reason was that the software without rest period used the technique of performing a sinusoidal "best fit" of the data results using a proto-type equation based on a sinusoidal function. This is basically the same approach used in the AASHTO TP-62 protocol and the NCHRP 9-29 project. This best fit was applied over 5 continuous sine waves dynamically. From this best fit equation, the amplitude and phase angle were determined. Therefore, the best fit technique cannot be applied in the case of rest periods as the sinusoidal wave shape will be broken by straight lines representing the rest periods as shown in FIGURE 115. During the development of that software, many technical issues were raised which required enormous effort and time to overcome. Finally, and after almost six months of work, IPC was able to deliver the final version of the software with rest period. The new software was examined by running a few tests and showed that the software is very efficient. The new software name is "UTS-320 V1.00b S-VECD Fatigue Test with Rest Period." The following is a list of the main features of the UTS-320 software.

- The software is capable of running the tension-compression uniaxial fatigue tests, but not the direct-tension test.
- The software is capable of conducting the test by controlling either the actuator strain or the on-specimen LVDTs strain.
- The software is able to run a test up to 999,999,999 loading cycles.
- This software is able to apply rest periods ranging from 0 to 10 seconds.

- The test can be stopped according to three different criteria that can be used separately or together (number of loading cycles, stiffness reduction percent, and/or adaptive strain control limit factor).
- The software is able to save a dynamic raw data file for the saved loading cycles.
- The software allows for a varying number of LVDTs (2 to 4).
- The software has a finger print test to evaluate the variability between replicates.
- The saved output data can be used for the viscoelastic continuum damage analysis as well as the reduced cycle analysis.

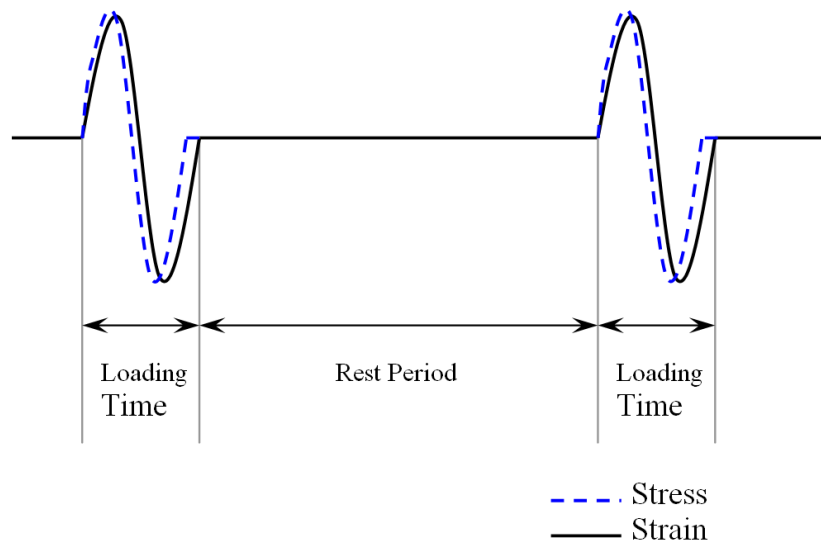


FIGURE 115 Uniaxial tension-compression fatigue test with rest period.

It was noticed that the software with rest period was able to reach the target on-specimen strain and to maintain this value over time as shown in FIGURE 116. To capture the real healing due to rest period, it is very important to insure that the specimen is not subjected to any load during the rest period. One

great advantage of that software is that loads and deformations can be recorded not only during the loading time but also during the rest time. These output data were used to check out if there is any remaining stress applied on the specimen during the rest time due to the viscoelastic nature of the HMA mixture which means that the specimen is subjected to damage during the rest period. FIGURE 117 illustrates that the software releases any loads or stresses from the specimen during the rest time so that the load is almost zero during the rest time.

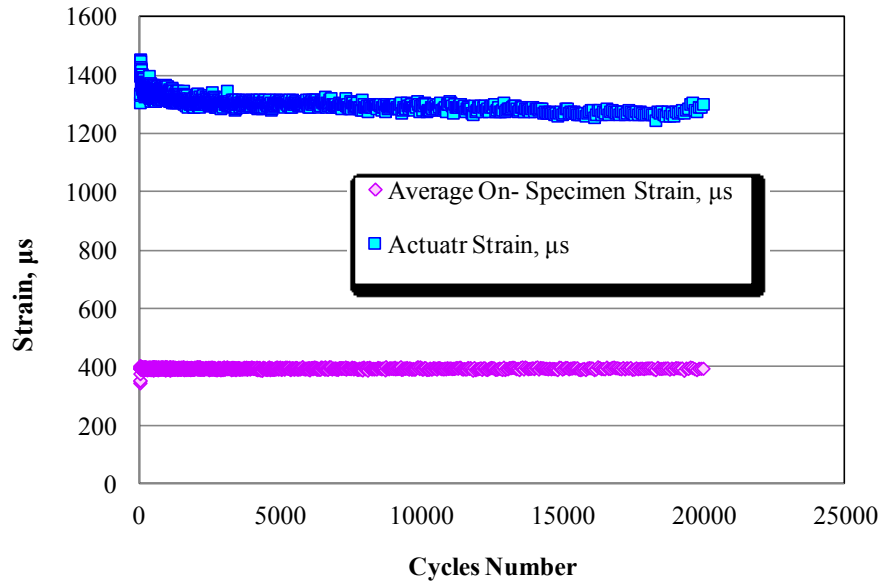


FIGURE 116 Average on-specimen strain and actuator strain over time relationships for test with rest period.

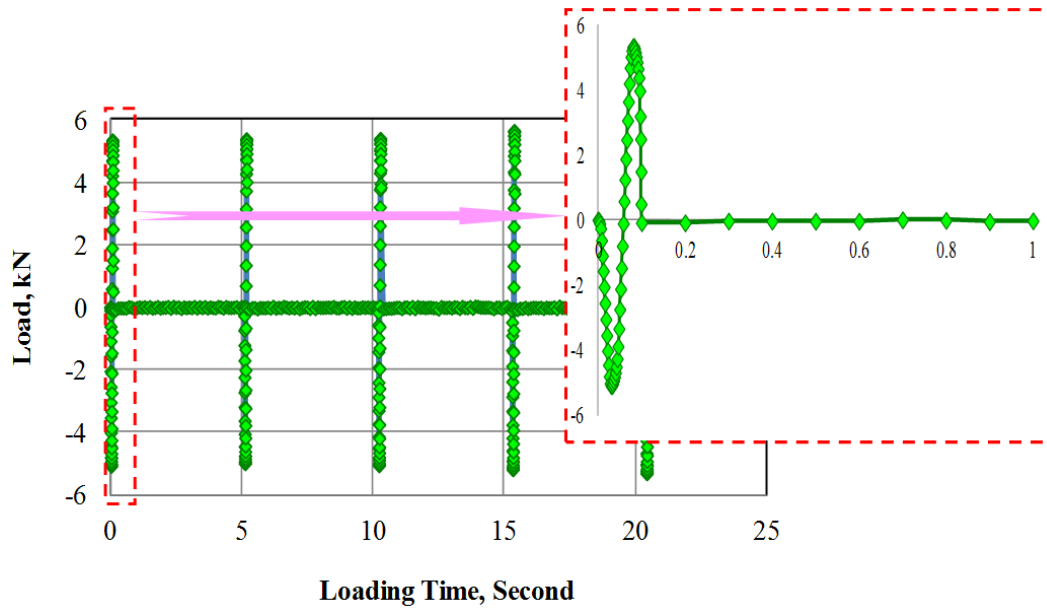


FIGURE 117 Load cell during loading and rest time with a close up of one loading cycle.

6.8 Why Tension-Compression Fatigue Test?

Uniaxial tension-compression test was proposed for this research as a fatigue test instead of uniaxial direct tension test to validate the endurance limit for HMA. This main thought was derived based on previous studies as shown in FIGURE 118 (Daniel and Kim, 2002). In case of the direct tension test, the specimen tends to accumulate a significant amount of permanent deformation accumulated during the test as the specimen stretched in only one direction. It is anticipated that the tension-compression fatigue test would decrease the amount of permanent deformation significantly compared to the direct tension fatigue test.

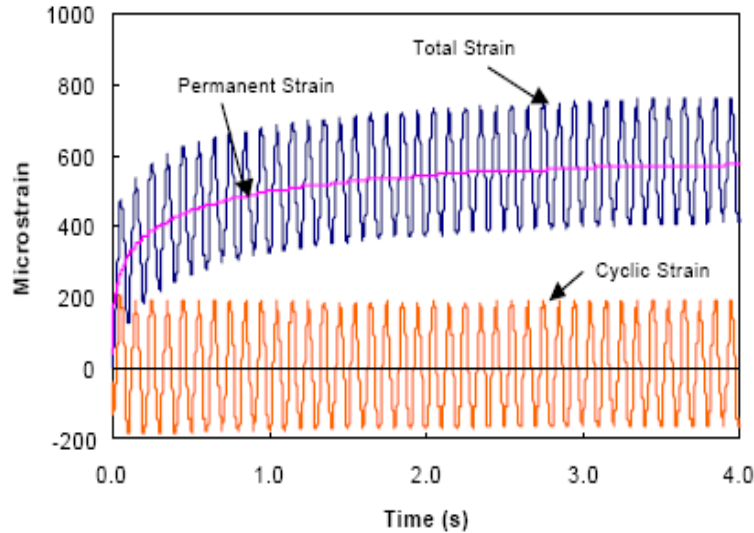


FIGURE 118 Total, permanent, and cyclic strain for cyclic direct tension fatigue test, (Daniel and Kim, 2002).

To elaborate on the behavior of asphalt concrete mixture under uniaxial fatigue test in case of direct tension versus tension-compression conditions, two replicates (5.2% AC and 9.5% Va) were tested under each condition using the developed software for the test without rest period. Both uniaxial fatigue tests were conducted at 70°F (21.1°C) using peak to peak on-specimen strain of 310 μs .

FIGURE 119 shows the actuator deformation over time for both direct tension and tension-compression uniaxial fatigue tests. It can be noticed that there is no difference between wave amplitude for both tests as the two specimens belong to the same mixture. The only difference was regarding the wave shape where it is haversine in case of direct-tension and sinusoidal for tension-compression test. By looking into the on-specimen deformation or strain, it was clear that the specimen exhibited permanent deformations especially at the beginning for the direct tension test before it vanished after only about 10 loading

cycles. At the same time, the tension-compression test showed very minimal permanent deformation as expected (FIGURE 120) due to the fact that the behavior of HMA in tension is slightly different than in compression, where the asphalt concrete mixture is strained in tension slightly more than in compression (Kallas, 1970).

To understand more about the reason for this behavior, the wave shape of the applied stress for both tests over time was plotted in FIGURE 121. It was obvious that the stress wave shape in case of the direct tension test changed very quickly after only about 10 cycles from haversine to sinusoidal which seems to be the equilibrium condition for the asphalt mixture. The main reason for that is the permanent deformation that the specimen experienced over the early 10 cycles which increased the height of the specimen and shifted the neutral axis of the stress wave to be sinusoidal. This would cause erroneous fatigue results as the amplitude of the tensile stress and strain are considered to be the peak-to-peak values in case of direct-tension fatigue test. However, the actual direct-tension test results showed that only half of the peak-to-peak stress and strain are on tension. For the tension-compression test, it was noticed that the stress wave shape remained the same as sinusoidal.

Based on the outcomes from this small study, the tension-compression test type was selected instead of the direct tension as the direct tension test switched to tension-compression test due to the viscoelastic behavior of the asphalt mixture. For the strain controlled uniaxial fatigue test, it was found that there is no existence for the haversine test condition as it will switch quickly to a sinusoidal

wave shape. This conclusion was also supported by previous studies but for the beam fatigue test (Pronk et al., 2010 and Mamlouk et al., 2012)

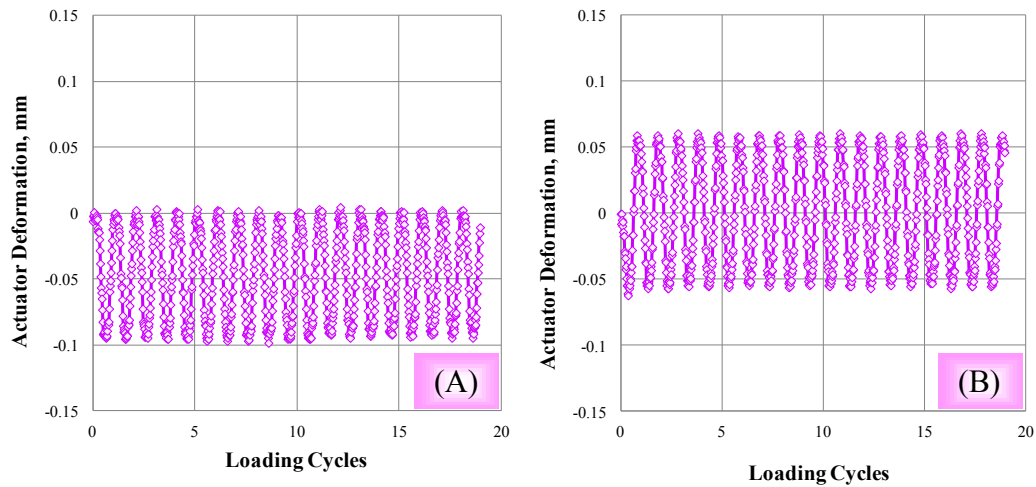


FIGURE 119 Actuator deformation wave shape over time; A) direct tension and B) tension-compression.

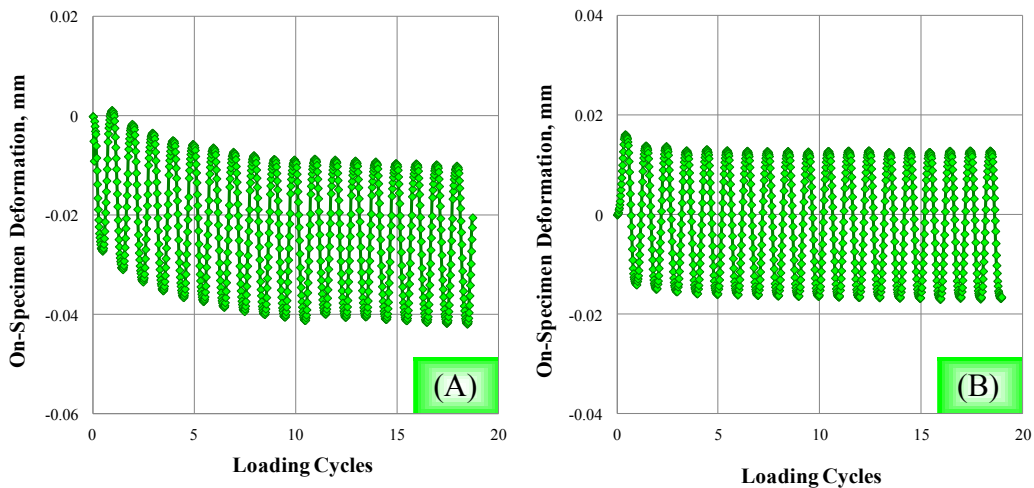


FIGURE 120 On-specimen deformation wave shape over time; A) direct tension and B) tension-compression.

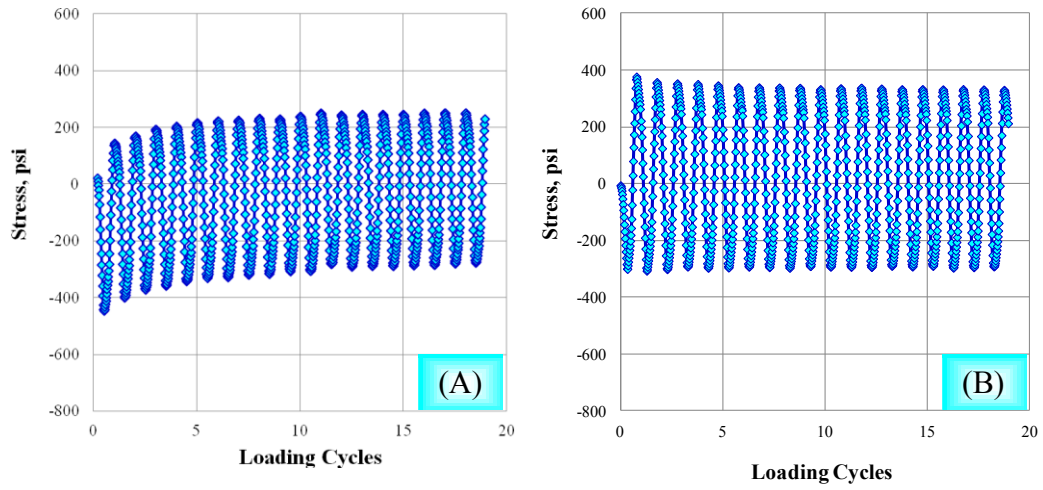


FIGURE 121 Stress wave shape over time; A) direct tension and B) tension-compression.

CHAPTER 7

ENDURANCE LIMIT METHODOLOGY AND RESULTS OF EXPERIMENTS

7.1 Background

Many recent studies showed that HMA mixtures exhibit an endurance limit. All these studies are based on the concept that the endurance limit is a strain level below which there is no cumulative fatigue damage; or the HMA will last for an indefinite number of load cycles. The proposed methodology in this research is based on the fatigue damage healing phenomena. The endurance limit in this situation does not reflect an absence of HMA fatigue damage, but it represents the state where there is a balance of damage induced by loading and healing, or damage recovery that occurs during rest periods. The endurance limit for HMA is, typically, not a single value, but will change depending on the material properties, traffic loading, and environmental conditions.

7.2 Methodology Development

As mentioned earlier, the developed methodology of predicting the HMA endurance limit is based mainly on fatigue healing using viscoelastic and continuum damage analysis. To evaluate the fatigue healing, two uniaxial tension-compression fatigue tests were conducted. The first test was conducted under continuous loading condition and referred to as the without rest period test. The second test introduced rest periods between loading cycles and referred to the test with rest period. The inclusion of the rest periods decreases the stiffness deterioration through partial healing of fatigue damage. That is, the stiffness tends to deteriorate at a slower rate compared to the test without rest period.

Based on the above, the healing of fatigue damage is expressed as the Healing Ratio Difference (HRD), which is articulated as the mathematical difference between the pseudo stiffness ratios of the tests without and with rest period at a certain loading cycle, N. The main advantage of using the pseudo stiffness is to separate healing caused by cracks re-bonding from time-dependant healing due to the material relaxation or viscoelasticity. FIGURE 122 shows Pseudo Stiffness Ratio (PSR) over time relationship for two tests conducted using 0 and 5 seconds rest periods less than 310 peak-to-peak microstrains at 70°F. Because the initial pseudo stiffness varies between replicates, the PSR is used. The PSR is the pseudo stiffness value at any cycle (PS_n) normalized to the initial stiffness (PS_o), or the stiffness value at the initial cycle number.

$$PSR_n = PS_n/PS_o \quad (106)$$

To determine the effect of applying rest period, two different healing parameters are measured. The first healing parameter is the healing ratio difference (HRD), which is simply the arithmetic difference between the stiffness ratios with and without rest period measured at any number of cycles.

$$HRD = PSR_{WRP} - PSR_{W/ORP} \quad (107)$$

where,

PSR_{WRP} = Pseudo stiffness ratio with rest period at loading cycle N, and

$PSR_{W/ORP}$ = Pseudo stiffness ratio without rest period at the same N.

The other healing parameter is the healing index (HI), which is the healing ratio difference divided by full healing ($1-PSR_{W/ORP}$).

$$HI = (PSR_{WRP} - PSR_{W/ORP}) / (1 - PSR_{W/ORP}) \quad (108)$$

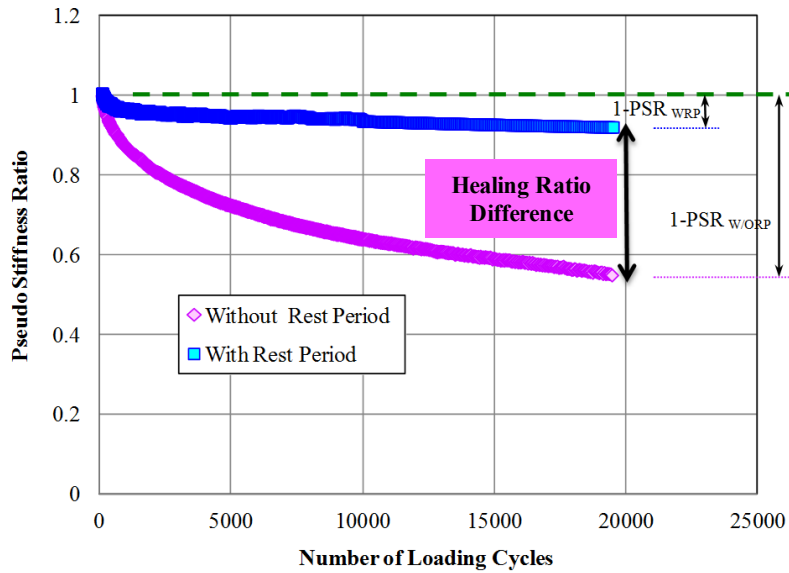


FIGURE 122 Psudo stiffness ratio versus time relationship for with and without tests.

Note that the several definitions of the healing index (HI) are available in the literature. For example, the HI defined in this uniaxial fatigue study is different from that defined in the beam fatigue study within the same NCHRP 9-44A project (Souliman, 2012).

As mentioned previously, the design of experiment for the uniaxial tension-compression test main experiment consisted of five main factors. The partial factorial design required 32 different combinations to be tested with 3 replicates for each combination. This design would require a total of 96 tests. The experimental factors are as follows:

- Binder content (2 levels: 4.2, 5.2 %)
- Air voids (2 levels: 4.5, 9.5 %)

- Strain Level (2 levels: medium to fail the specimen at 20,000 cycles and low to fail the specimen at 100,000 cycles for the tests without rest period). Note that a high strain level will be added as discussed in Section 7.2.2.
- Temperature (3 levels: 40, 70, 100°F)
- Rest period (2 levels: 0, 5 sec)

To determine the strain levels at different temperatures that correspond to the two levels of N_f w/ORP, fatigue tests were performed for the four asphalt mixtures at the three temperatures of 40, 70 and 100°F as shown in FIGURE 123. These fatigue curves were used to determine the recommended strain levels at each temperature. The criterion for selecting the two strain levels at each temperature was to reach an N_f value (for tests without rest period) of 20,000 and 100,000 cycles at the medium and low strain levels, respectively. For the fatigue tests with rest period, all the tests were stopped at 20,000 cycles because of time limitations. The test would take 50 times more to reach the N_f w RP due to the long time of the rest period. . In addition, it was anticipated that the N_f WRP would be extremely higher than that without rest period due to the damage healing.

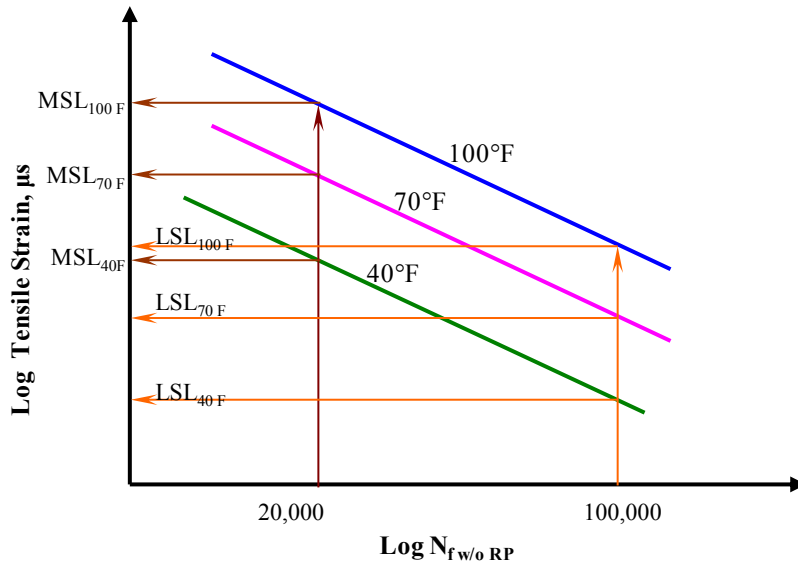


FIGURE 123 Determination of the high and low strain levels at each temperature.

7.2.1 Determination of Fatigue Endurance Limit

The first step in calculating the fatigue endurance limit was to determine the PSR values for the main experiment combinations. A regression model was then established to correlate PSR to the five factors. The PSR model can take the following form:

$$\text{PSR} = a_0 + a_1 T + a_2 AC + a_3 Va + a_4 \epsilon_t + A_5 RP + A_6 N + 2\text{-factor interactions} \quad (109)$$

where

- PSR = Pseudo stiffness ratio
- $a_0, a_1 \dots a_n$ = Regression coefficients
- AC = Percent asphalt content
- Va = Percent air voids
- RP = Rest period (sec)
- T = Temperature (°F)
- ϵ_t = Tensile Strain, μs

- N = Number of loading cycles

To consider the nonlinear effect of N on the PSR value, several PSR values were measured at different N along the same PSR-Time relationship. As the tests with rest period are more of interest to calculate the endurance limits, PSR values were selected at four N values. For the test without rest period, only one PSR value was considered, which is at the failure where PSR is equal to 0.5 (FIGURE 124). This also would help reduce the regression model bias toward the tests conducted at zero rest periods as it represents almost 50% of the tests. Tests at 1, 5, and 10 second rest periods represent the rest of the overall tests. It also prevents overlap of the PSR ranges for tests with and without rest periods and provides a better regression model.

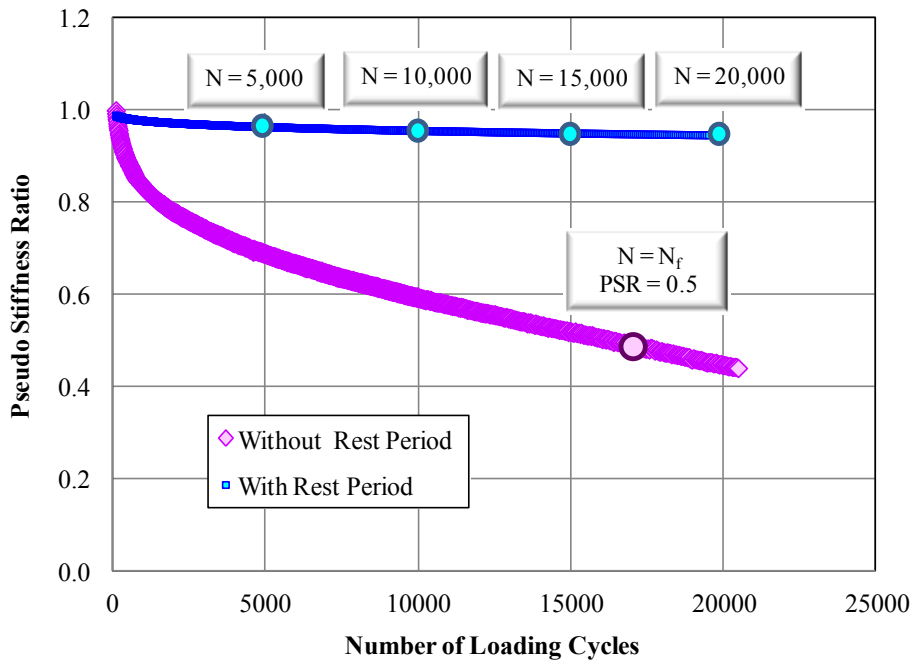


FIGURE 124 Pseudo stiffness ratio at four different number of cycles.

Two methods can be followed to determine the fatigue endurance limit. The first method is by using the HI parameter; while the second method is by using the PSR regression model.

7.2.1.1 Healing Index Method

The first step in this method is to calculate the HI values for all test combinations (i.e., at different tensile strains and temperatures). The HI can be calculated by running the regression model for each test combination two times. The first time is to calculate the $PSR_{W/ORP}$ by using a rest period value equals to zero. In the second time, a specific rest period value is used with the same test condition and volumetric properties to calculate the PSR_{WRP} . Subsequently, the second step is to plot the HI values versus the tensile strain at each temperature and for each mixture type. This is because it is anticipated to have a different endurance limit value for each mixture at each temperature. The expected relationship between the strain level and the HI is shown in FIGURE 125. In the figure, the HI values increases as the tensile strain decreases. Because the main experiment has only two strain levels, the HI-tensile strain relationships are assumed to be linear.

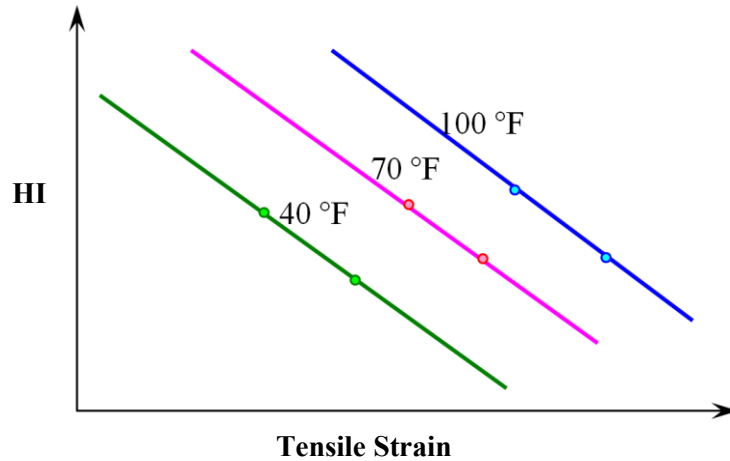


FIGURE 125 Healing parameters versus strain levels at different temperatures.

As proposed, the endurance limit will occur when a complete healing happens during the rest period. In this case, the endurance limit is estimated at HI value of 1.0, as the PSR_{WRP} is equal to 1.0, which is the healing ratio at no damage with rest period (FIGURE 126). This method can be used for any mixture even without using the PSR regression model; given the mixture is tested at least two strain levels, with and without rest periods, and at a certain temperature. This analysis is usually done at a single N value. If the N value is considered as the number of cycles until failure for the test without rest period ($N_{FW/GRP}$), the $PSR_{W/GRP}$ will be equal to 0.5. In this case, the endurance limit can be determined at $HRD = 0.5$, when the HRD is plotted against the tensile strain instead of the healing index as the PSR_{WRP} is equal to 1.0 ($HRD = 1.0 - 0.5 = 0.5$).

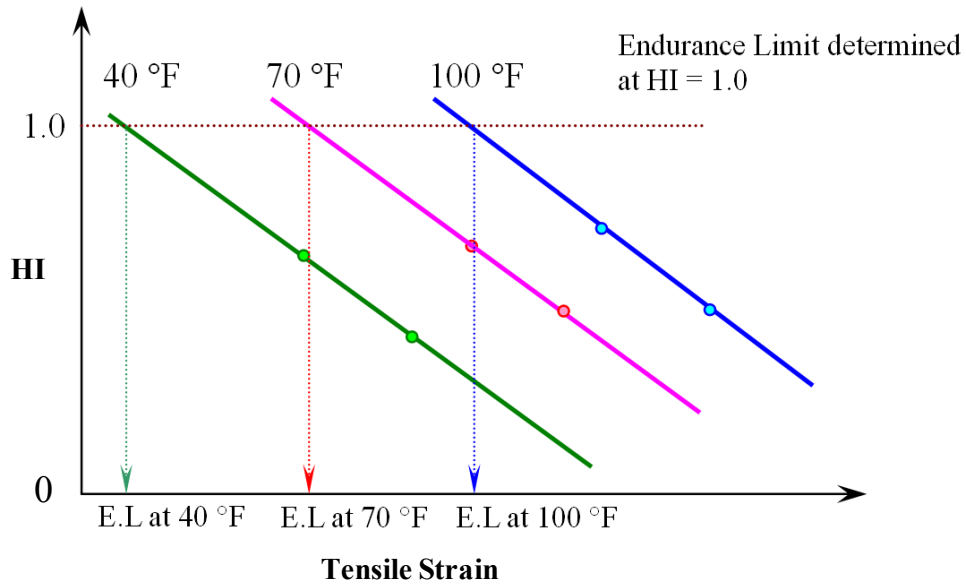


FIGURE 126 Determination of endurance limit at each temperature using HI parameter.

7.2.1.2 Pseudo Stiffness Ratio Method

This method depends on using the PSR regression model to calculate the PSR values at two different strain levels for the same test conditions, same volumetric properties, and any rest period. For any rest period value and N value, it is expected that the PSR decreases as the strain level increases (FIGURE 127). The endurance limit in this case can be defined as the strain level where the PSR equal to 1.0, when plotting relationship between the PSR and the strain level as shown in FIGURE 128. This method is recommended to use when a PSR regression model is established for the non-linear effect between N and the PSR. The powerful use of this method is that, for the endurance limit case, the PSR is independent of N as the PSR is equal to 1.0 at any N values. A second advantage is that this method can be used to determine the EL value for the continuous test condition. Based on this discussion, the second method is adopted for this study

as a regression model can be developed over a reasonable range of volumetric properties, rest period, and strain values.

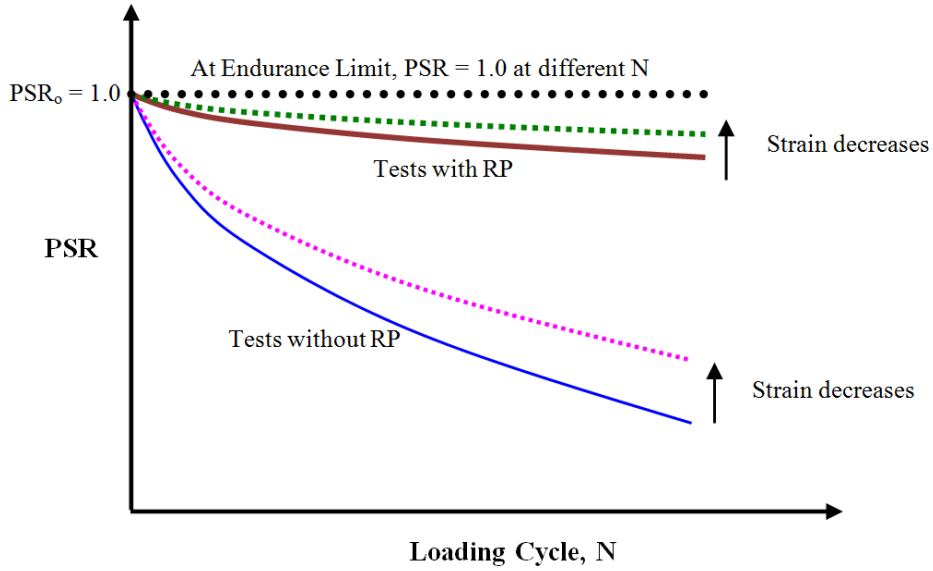


FIGURE 127 Effect of strain and rest period of the PSR as a function of the loading cycles.

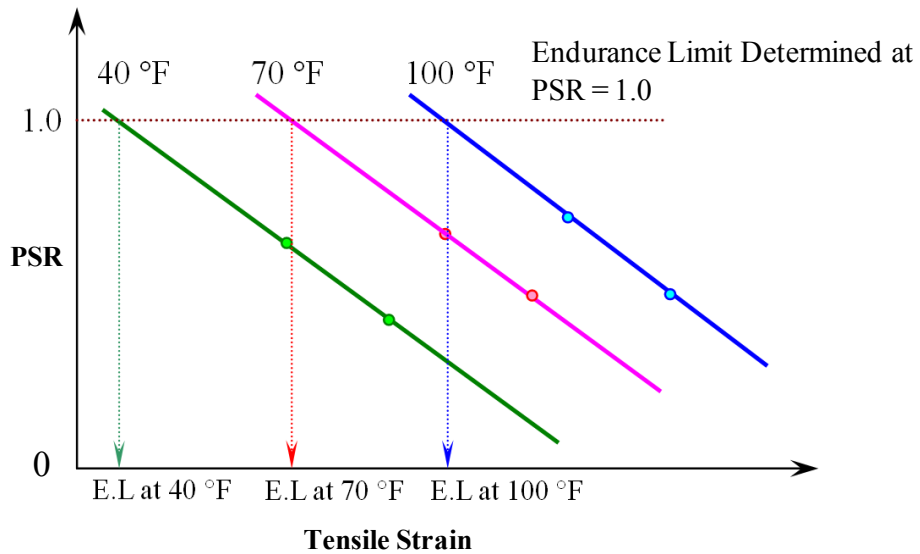


FIGURE 128 Determination of endurance limit at each temperature using PSR parameter.

7.2.2 Effect of Different Strain Levels and Rest Periods

As only two strain levels were considered in this study, the relationship between the HI and the strain levels has to be linear. However the true relationship may have a different trend. The same assumption is also considered for the rest period as only two rest periods were applied (0, and 5 seconds). As it was mentioned in the Literature Review Chapter, the rest period may not have a significant effect on the fatigue life as well as the healing parameters after a certain value as was shown in FIGURE 129. Therefore, the relationship between the PSR and the rest period is not linear. Therefore, it is important to have additional tests to be done at different rest periods to validate how the true relationship. For the extra tests, an additional strain level (high) and two rest periods (1 and 10 seconds) were added. The selection of the required combinations is justified using a fractional factorial statistical technique considering two levels of interaction. Based on this, additional 18 combinations were required for testing. The same analysis was repeated again by compiling the whole data to get an integrated regression model that accounts for the nonlinear effect of strain level and rest period.

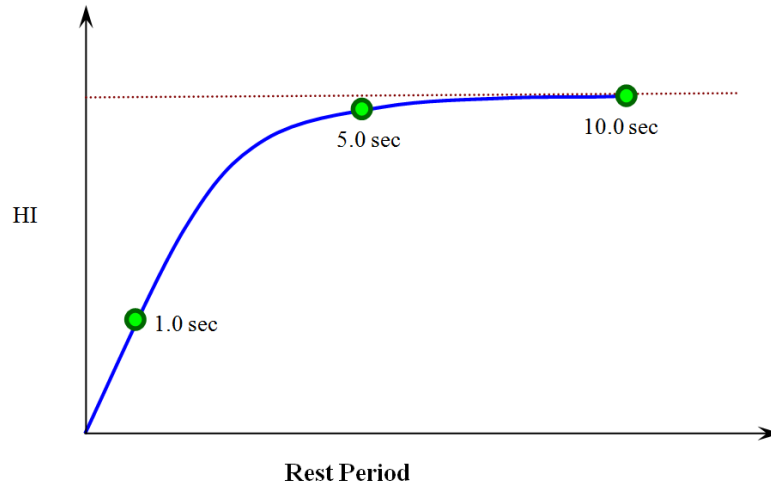


FIGURE 129 Expected rest period versus healing parameters relationship.

7.3 Determination of Pseudo Stiffness

The calculation of the pseudo stiffness (PS) requires the calculation of pseudo strain (ε^R). The pseudo strain can be calculated rigorously using Equation 110, where ε is the measured strain, $E(t)$ is the linear viscoelastic relaxation modulus and E_R is the reference modulus (typically taken as 1) used for dimensional compatibility (Schapery, 1984). Equation 110 was used to calculate the pseudo strain for the first loading cycle.

$$\varepsilon^R = \frac{1}{E_R} \int_0^t E(t-\tau) \frac{d\varepsilon}{d\tau} d\tau \quad (110)$$

The pseudo strains for the rest of the loading cycles were calculated using Equation 111 proposed by Kim et al. (2003) using a simplified approach for the steady-state assumption to calculate the pseudo strain. This equation is based on the assumption that fatigue damage accumulates only under the tensile loading condition, the pseudo strain tension amplitude, $\varepsilon^R_{0,1a}$. In such conditions, the pseudo strain can be rigorously computed as the product of strain and dynamic

modulus, $|E^*|_{LVE}$ (at temperature and frequency matching with the test under investigation).

$$\left(\varepsilon_{0,ta}^R\right)_i = \frac{1}{E_R} \cdot \frac{\beta+1}{2} \left(\left(\varepsilon_{0,pp}\right)_i \cdot |E^*|_{LVE} \right) \quad (111)$$

where β is a factor used to quantify the duration that a given stress cycle is tensile (1 means always tensile, 0 means fully reversed loading and -1 means always compressive), and $\varepsilon_{0,pp}$ stands for peak-to-peak strain amplitude.

Once the pseudo strain is calculated, the pseudo stiffness is also calculated through Equation 112 using the pseudo strain as defined in Equations 110 and 111 (Underwood et al., 2010).

$$C = \begin{cases} \frac{\sigma}{\varepsilon^R \times DMR} & \text{first cycle} \\ \frac{\sigma}{\varepsilon_{0,ta}^R \times DMR} & \text{rest of cycles} \end{cases} \quad (112)$$

where the DMR is the dynamic modular ratio to account for specimen-to-specimen variability (Underwood et al., 2010) and is defined as shown in Equation 113. In this equation $|E^*|_{LVE}$ is the linear viscoelastic dynamic modulus of the material at the particular temperature and frequency of the test and it can be determined from $|E^*|$ master curve. $|E^*|_{fp}$ is the fingerprint dynamic modulus that is measured from a fingerprint experiment which is performed before the uniaxial fatigue test.

$$DMR = \frac{|E^*|_{fp}}{|E^*|_{LVE}} \quad (113)$$

7.4 Fatigue Lives Experiment

7.4.1 Fatigue Failure Criterion

As discussed in Section 2.4, several methods are available to define fatigue failure. Based on results of initial tests in this study, it was concluded that determining the fatigue life based on 50% reduction of the initial stiffness was feasible at different test conditions, especially at different temperatures. On the other hand, using the phase angle relationship to determine the fatigue life (Reese, 1997) was not possible, especially for tests conducted at 100°F as the point where the phase angle relationship has a sharp decrease is not found compared to tests conducted at 40 and 70°F (FIGURES 130 to 132).

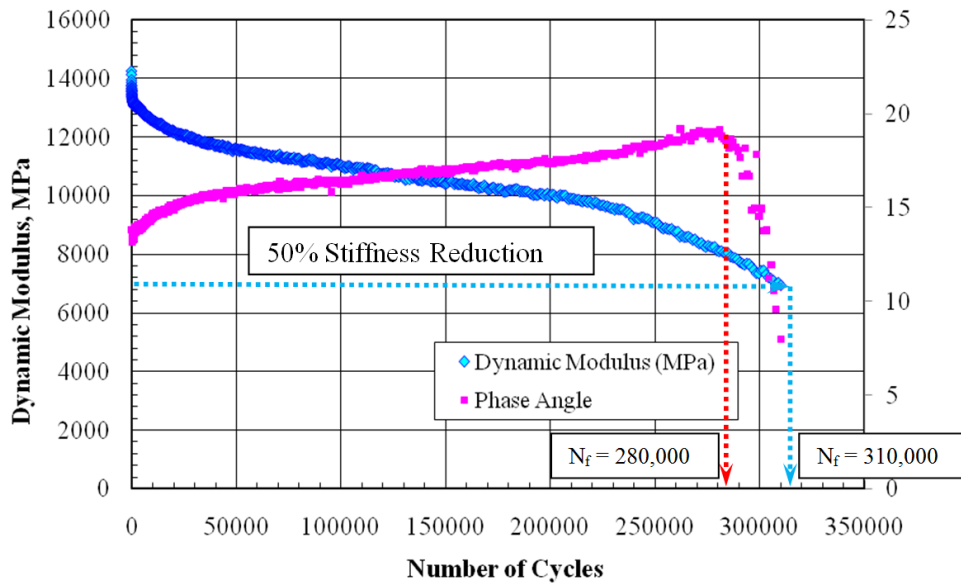


FIGURE 130 Typical phase angle versus loading cycle's relationship at 40°F temperature.

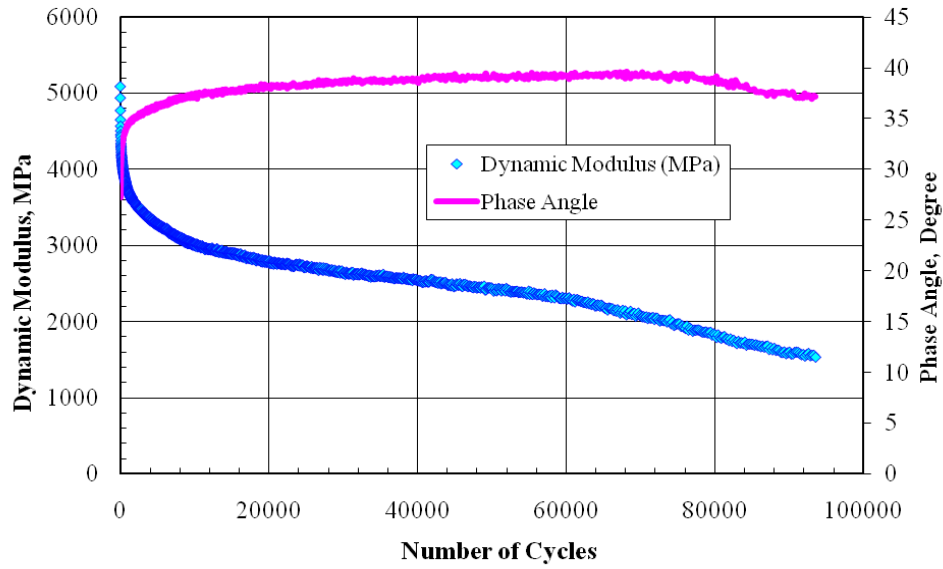


FIGURE 131 Typical phase angle versus loading cycle's relationship at 70°F temperature.

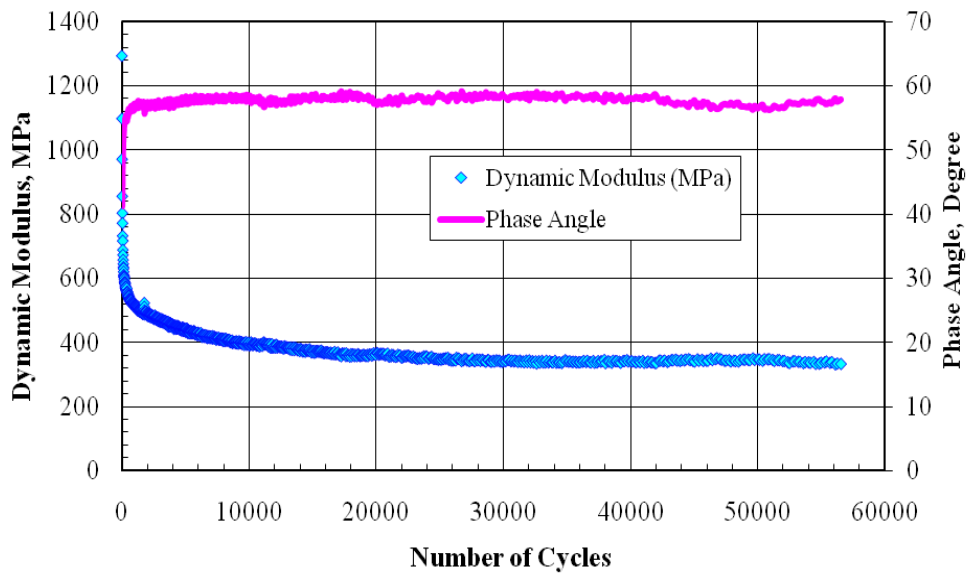


FIGURE 132 Typical phase angle versus loading cycle's relationship at 100°F temperature.

7.4.2 Definition of the Initial Number of Cycles

In this study, specimens were manufactured only at the optimum mix design conditions (4.7% asphalt content and 7% air voids). A series of tests without rest periods were conducted at different strain levels at the three temperatures of 40, 70 and 100°F. The 50% reduction in the initial stiffness criterion was used to determine the fatigue lives for the different test conditions.

As per the current AASHTO T321, the initial stiffness is the stiffness at the 50th cycle for the beam fatigue test. Consequently, the fatigue life values were initially calculated using initial stiffness at the 50th cycle. It was noticed that there is a significant drop of stiffness at the beginning of tests conducted at 100°F compared to those conducted at 40 and 70°F as shown previously in FIGURES 130 to 132. This means that using the stiffness at the 50th cycle as an initial stiffness at 100°F will notably decrease the calculated fatigue life. For that reason, two different initial numbers of cycles were investigated.

Fatigue analysis using initial stiffness values at both the 50th and the 100th cycles are illustrated in FIGURES 133 and 134, respectively. It can be noticed that the fitting of fatigue life at 100°F improved significantly using the initial stiffness at 100th cycle compared to 50th cycle. Therefore, the fatigue life determination in this research will be based on an initial stiffness measured at the 100th cycle.

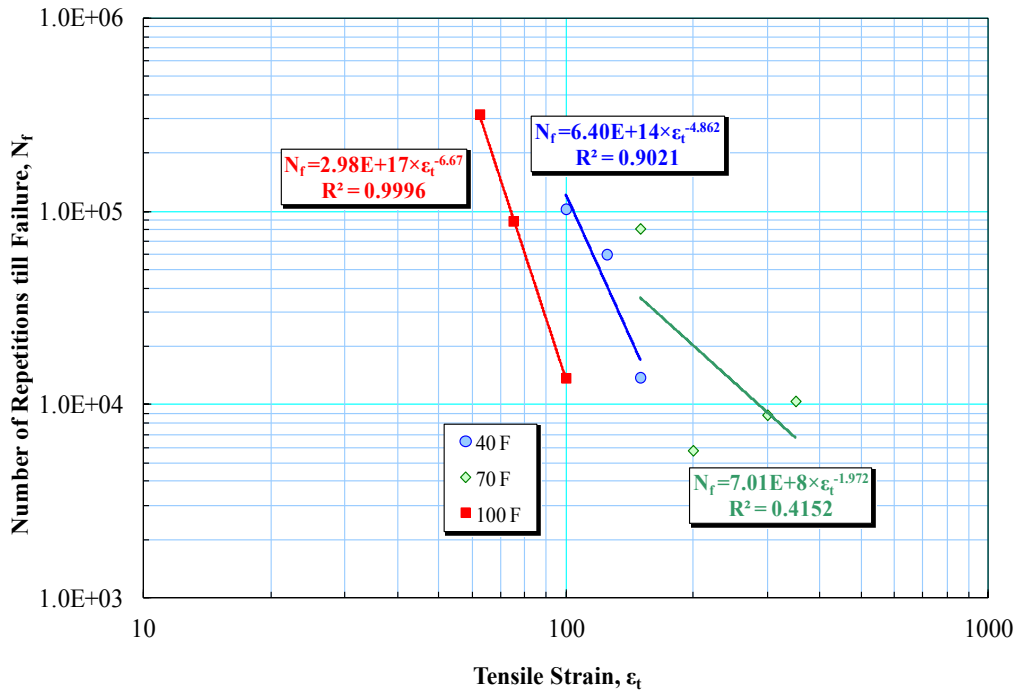


FIGURE 133 Fatigue lines at different temperatures using 50th cycle initial stiffness.

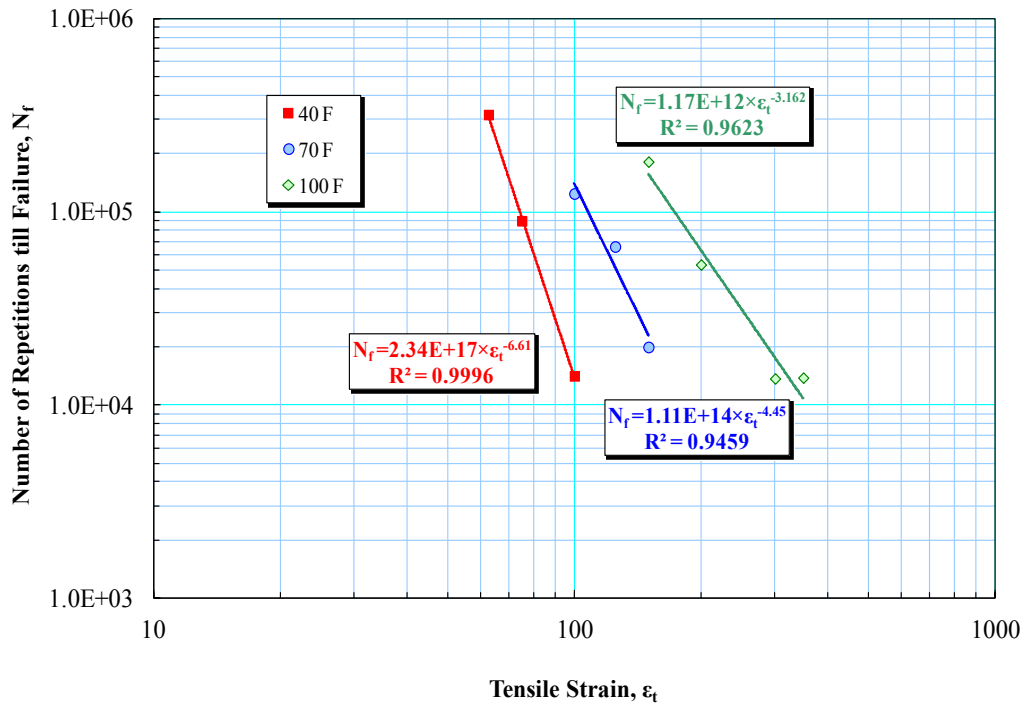


FIGURE 134 Fatigue lines at different temperatures using 100th cycle initial stiffness.

7.4.3 Fatigue Lives Experiment Results

As stated earlier, the criterion for selecting the two strain levels at each temperature for the main experiment was to reach a fatigue life of 20,000 cycles for the medium strain level, and 100,000 cycles for the low strain level. For the additional experiment, the high strain level was selected at fatigue life of 5,000 cycles.

To construct the fatigue lives for the four tested mixtures (4.2% AC & 4.5 %Va, 5.2% AC & 4.5 %Va, 4.2% AC & 9.5 %Va, and 5.2% AC & 9.5 %Va), three to four tests without rest period were conducted at different strain levels and temperatures. The results of the finger print as well as the uniaxial tension-compression fatigue tests are tabulated for the four mixtures in TABLES 42 to 45.

TABLE 42 Finger print and uniaxial fatigue tests results at 9.5% Va and 4.2% AC

Temp (°F)	Specimen ID	Air Voids (%)	Peak to Peak Strain (µs)	Tensile Strain (µs)	FP Modulus (psi)	Phase Angle ϕ Degree	MCF	Initial Stiffness (psi)	Initial ϕ Degree	Cycles to Failure (N_f)
100	D-960	10.28	300	150.0	141,890	34.8	2.25	83,194	51.7	469,540
	D-962	9.28	450	225.0	152,300	31.4	2.10	70,546	50.3	32,030
	D-964	9.49	350	175.0	164,200	38.0	2.03	86,892	49.1	168,530
	D-963	9.91	550	275.0	145,500	34.8	1.95	65,949	51.5	7,100
70	D-945	9.60	210	105.0	669,784	26.6	3.62	500,815	32.4	14,270
	D-946	9.22	175	87.5	648,028	27.5	3.50	514,739	29.9	94,770
	D-947	8.52	250	125.0	827,585	25.2	3.46	617,135	29.7	22,260
	D-951	9.31	200	100.0	724,318	25.4	3.90	596,830	29.0	84,000
	D-957-1	9.00	125	62.5	740,708	24.6	4.13	661,923	26.7	1,280,000
	D-955	9.26	200	100.0	638,746	24.0	3.20	539,540	27.9	73,570
40	D-959	9.65	150	75.0	1,936,543	13.0	12.92	1,701,002	13.5	17,920
	D-965	9.52	125	62.5	2,404,145	14.6	11.61	2,031,978	16.0	132,340
	D-968	9.31	175	87.5	1,589,613	13.2	7.88	1,355,087	14.0	10,500
	D-972	9.49	140	70.0	1,595,270	14.4	7.38	1,478,514	14.4	57,250

**TABLE 43 Finger print and uniaxial fatigue tests results at 4.5% Va and
4.2% AC**

Temp (°F)	Specimen ID	Air Voids (%)	Peak to Peak Strain (μ s)	Tensile Strain (μ s)	FP Modulus (psi)	Phase Angle ϕ Degree	MCF	Initial Stiffness (psi)	Initial ϕ Degree	Cycles to Failure (N_f)
100	D-406	4.63	350	175.0	316,617	41.6	2.46	147,895	53.1	184,080
	D-407	4.09	510	255.0	346,785	39.8	2.45	140,687	53.0	15,930
	D-408	4.56	350	175.0	321,259	31.9	2.30	163,167	48.2	261,000
	D-414	4.24	510	255.0	427,426	34.1	2.52	195,018	45.8	12,120
70	D-401	3.77	150	75.0	984,226	29.3	5.74	984,226	29.2	431,740
	D-402	4.72	290	145.0	1,101,996	28.5	5.29	851,154	31.3	9,070
	D-404	4.08	290	145.0	1,307,370	33.0	6.23	1,105,767	40.6	3,430
	D-405	4.33	210	105.0	1,333,332	31.9	6.03	1,020,630	31.5	26,300
	D-432	4.03	210	105.0	1,344,064	22.6	6.74	1,099,821	25.7	27,340
40	D-411	4.48	140	70.0	2,986,906	8.5	14.87	2,808,510	10.3	172,460
	D-412	4.84	190	95.0	2,573,694	9.3	11.89	2,393,992	10.5	9,470
	D-434	4.53	150	75.0	2,770,800	10.8	11.96	2,519,595	13.5	149,630
	D-435	4.49	175	87.5	2,801,548	13.7	14.83	2,498,274	14.3	23,000

**TABLE 44 Finger print and uniaxial fatigue tests results at 9.5% Va and
5.2% AC**

Temp (°F)	Specimen ID	Air Voids (%)	Peak to Peak Strain (μ s)	Tensile Strain (μ s)	FP Modulus (psi)	Phase Angle ϕ Degree	MCF	Initial Stiffness (psi)	Initial ϕ Degree	Cycles to Failure (N_f)
100	D+952	9.66	400	200.0	110,230	34.3	1.59	54,389	49.7	357,550
	D+956	9.77	500	250.0	107,210	30.3	1.78	52,591	51.0	74,140
	D+957	10.25	600	300.0	109,095	33.1	1.78	50,908	52.5	71,340
	D+953	10.37	700	350.0	99,694	37.1	1.76	41,959	53.2	13,560
70	D+943	9.52	190	95.0	516,624	28.3	2.85	409,296	31.4	372,300
	D+944	8.90	250	125.0	643,532	24.1	3.57	483,121	31.3	63,910
	D+948	9.34	400	200.0	613,219	26.8	3.93	356,938	36.3	4,070
	D+949	9.99	375	187.5	501,250	31.8	2.97	328,365	39.0	9,740
40	D+949	10.15	150	75.0	1,691,430	15.7	7.86	1,476,194	16.5	151,360
	D+959	9.10	200	100.0	1,443,415	12.2	7.92	1,332,316	13.6	53,760
	D+958	8.80	225	112.5	1,777,437	14.4	8.19	1,423,545	14.4	17,380
	D+962	9.40	260	130.0	1,610,644	14.1	8.15	1,434,713	15.4	8,320

**TABLE 45 Finger print and uniaxial fatigue tests results at 4.5% Va and
5.2% AC**

Temp (°F)	Specimen ID	Air Voids (%)	Peak to Peak Strain (μs)	Tensile Strain (μs)	FP Modulus (psi)	Phase Angle φ Degree	MCF	Initial Stiffness (psi)	Initial φ Degree	Cycles to Failure (N _f)
100	D+432	4.57	300	150.0	220,457	35.8	1.99	103,412	51.0	460,610
	D+430	4.89	500	250.0	149,389	47.6	1.75	72,475	59.4	64,570
	D+438	3.99	900	450.0	201,167	45.7	1.77	79,597	58.2	8,810
	D+439	3.91	850	425.0	238,442	43.4	2.01	81,946	57.8	9,670
	D+440	4.46	400	200.0	157,656	49.8	1.74	94,420	57.0	245,470
70	D+402	3.46	210	105.0	1,038,905	28.2	4.80	842,988	31.2	218,000
	D+403	3.63	290	145.0	1,049,058	30.5	5.25	756,981	33.0	50,500
	D+404	3.37	350	175.0	924,035	30.2	4.41	670,669	34.3	30,000
	D+406	3.54	150	75.0	982,630	31.4	4.80	845,309	32.5	476,800
40	D+418	4.07	140	70.0	2,716,846	12.3	12.03	2,481,624	13.5	280,000
	D+419	4.32	140	70.0	2,341,489	10.7	10.86	2,319,385	10.8	135,420
	D+442	4.79	175	87.5	2,129,444	11.8	9.67	2,044,741	11.6	130,320
	D+443	4.20	200	100.0	2,440,549	12.8	14.21	2,164,253	12.7	74,710
	D+445	4.37	275	137.5	2,648,388	13.2	11.99	2,263,603	13.1	9,470

Based on the uniaxial fatigue test results for the four mixtures, the fatigue lives were constructed at the three test temperatures (40, 70, and 100 °F) as shown in FIGURES 135 to 138. The fatigue life at each temperature is represented by linear relationship between the number of cycles to failure (N_f) and the applied tensile strain levels (ε_t) on a log-log scale. This relationship is represented by the form of Equation 114.

$$N_f = k_1 \times (1/\epsilon_t)^{k_2} \quad (114)$$

where k₁ and k₂ are the intercept and slope of the fatigue life relationship, respectively, as was shown in FIGURES 135 to 138. It is noticed that as the binder content increases, the k₂ value decreases. This means that adding more

binder to the asphalt mixtures would reduce the fatigue degradation of that mixture. On the other hand, the effect of air voids on k_2 values looks insignificant, especially at lower asphalt contents. At higher asphalt contents, it is clear that decreasing the air voids result in decreasing the k_2 values. It can be noticed that changing the asphalt content by 1% has more effect on the k_2 values than changing the air voids by 5%.

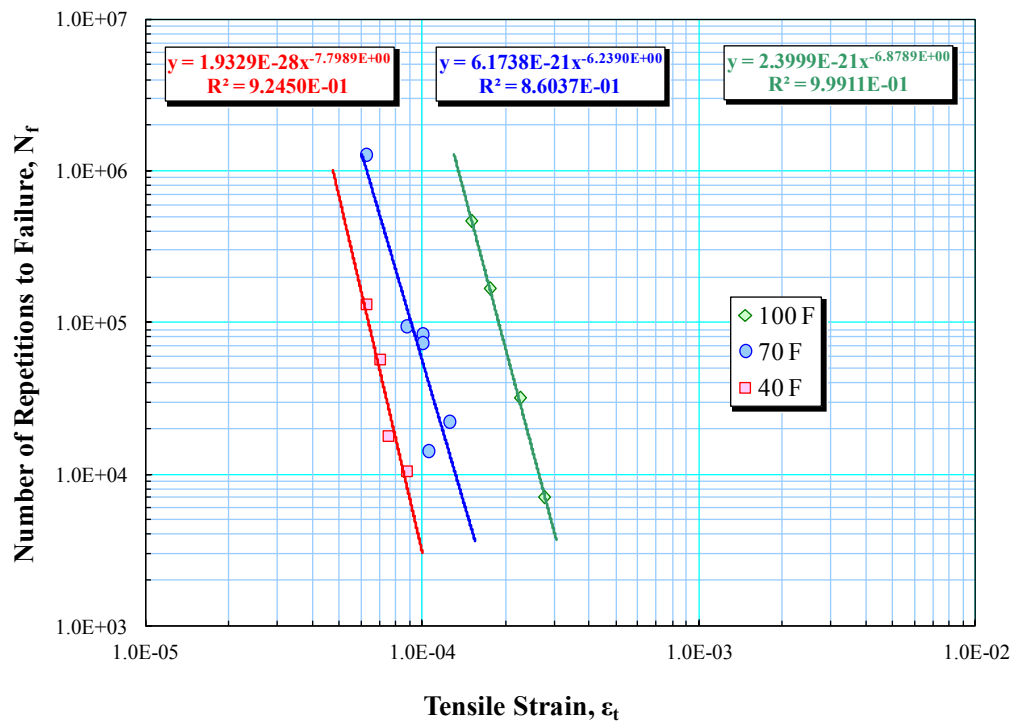


FIGURE 135 Fatigue lives at different temperatures (9.5% Va and 4.2% AC).

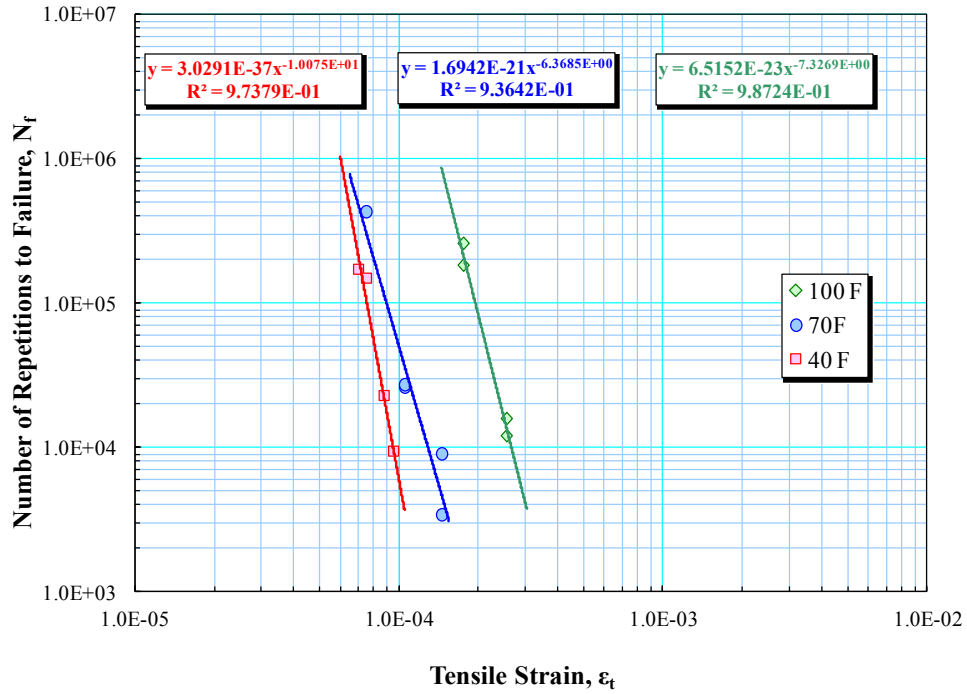


FIGURE 136 Fatigue lives at different temperatures (4.5% Va and 4.2 AC%).

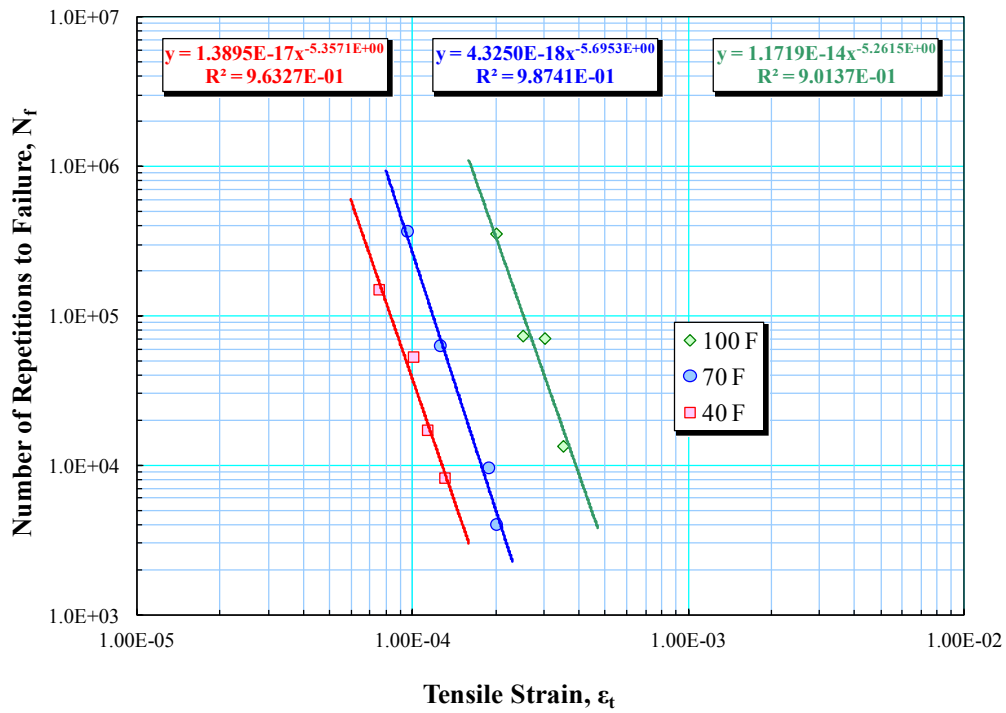


FIGURE 137 Fatigue lives at different temperatures (9.5% Va and 5.2% AC).

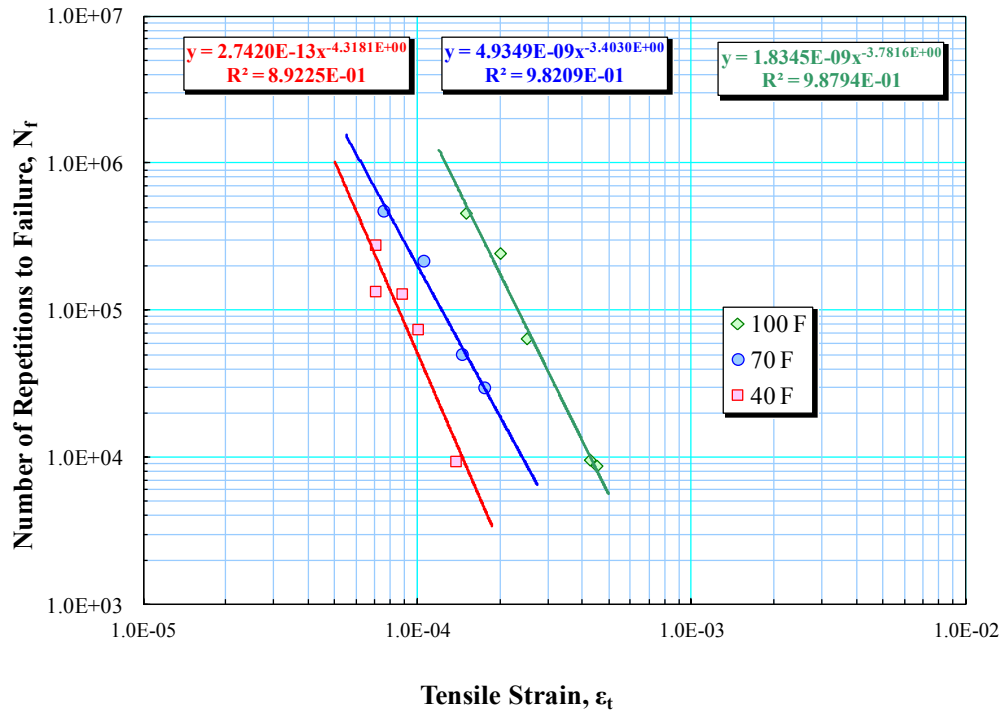


FIGURE 138 Fatigue lives at different temperatures (9.5% Va and 5.2% AC).

Using the k_1 and k_2 values, the low and medium strain levels at each temperature for the four mixtures were determined at fatigue lives of 100,000 and 20,000 loading cycles, respectively. TABLE 46 contains the low and medium strain levels at different temperatures for all mixtures.

The fatigue test results for each mixture at different test temperatures were used to generate the generalized fatigue model coefficients (k_1 , k_2 , and k_3) as in Equation 115.

$$N_f = k_1 \times (1/\epsilon_t)^{k_2} \times (1/E)^{k_3} \quad (115)$$

where k_1 , k_2 , and k_3 are regression coefficients and E is the initial stiffness in psi. Table 7 shows the k_1 , k_2 , and k_3 values for the four mixtures. In addition, all the test results of the four mixtures were pooled together in one data set and used to

get regression coefficients for all mixtures together (TABLE 47). It can be easily recognized that the lower the air voids, the lower the k_2 and k_3 values. Also, increasing the asphalt content reduces both k_2 and k_3 values. It can be concluded that high binder content and lower air voids increase the asphalt mixture resistance to fatigue damage, which agrees with previous fatigue research work. All the generalized fatigue models showed an excellent to good levels of goodness of fit measured by the coefficient of determination (R^2), ranging from 98.7 to 88.43% for the individual mixtures. When combining the test results for all the mixtures, the R^2 value was reduced slightly to 82.2%, which still shows a good level of prediction.

In order to evaluate the accuracy of the generalized fatigue models, the fatigue lives predicted from these models were compared to corresponding measured values. FIGURE 139 shows a comparison of the measured to the predicted fatigue lives based on the individual models for each mixture; while FIGURE 140 shows the same comparison using the all-data model. As discussed earlier, the individual models showed better predictions as compared to the combined model. However, the combined data model to describe the behavior of the different mixtures looks very reasonable. In this case, it is understood that the effect of using different binder contents and air voids can be easily captured by considering their effect on the corresponding stiffness values, which are represented in the generalized fatigue model.

TABLE 46 Low and medium tesnile strain values for all mixtures at different temperatures

Temp (°F)	4.2% AC				5.2% AC			
	9.5% Va		4.5% Va		9.5% Va		4.5% Va	
	Low (100,000)	Medium (20,000)	Low (100,000)	Medium (20,000)	Low (100,000)	Medium (20,000)	Low (100,000)	Medium (20,000)
100	187.5	237.5	195	242.5	252.5	342.5	232.5	357.5
70	90	115	90	115	112.5	155	122.5	197.5
40	62.5	80	70	87.5	82.5	112.5	85	112.5

TABLE 47 k_1 , k_2 and k_3 values for each individual mixture and all mixtures together

Air voids Va (%)	Asphalt content AC (%)	k_1	k_2	k_3	R^2 (%)
9.5	4.2	2.901E-11	7.930	2.869	98.68
4.5	4.2	0.000514	4.599	1.674	88.43
9.5	5.2	1.682E-05	5.114	1.819	97.73
4.5	5.2	0.0424	3.172	1.016	93.19
All mixtures		1.246E-05	4.882	1.633	83.54

$$*N_f = k_1 \times (1/\epsilon_t E)^k_2 \times (1/E)^k_3$$

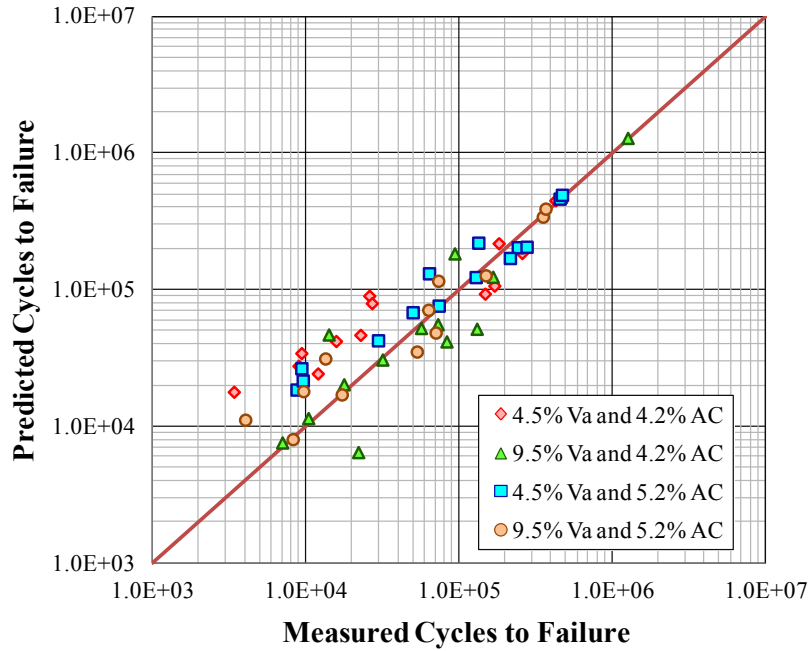


FIGURE 139 Measured versus predicted cycles to failure based on individual generalized fatigue models.

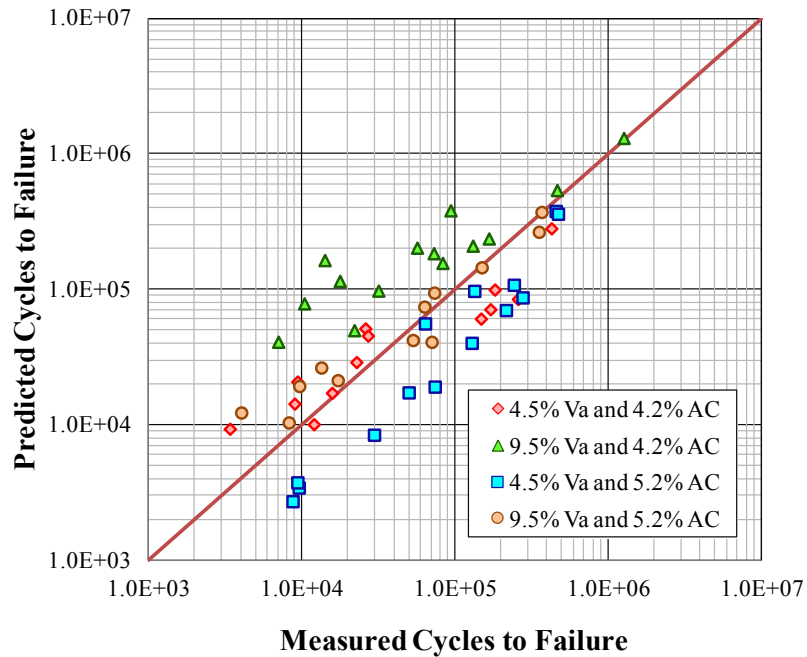


FIGURE 140 Measured versus predicted cycles to failure based on generalized fatigue model for all mixtures together.

7.4.4 Main Experiment Results

As explained earlier, the main objective of this experiment is to investigate the effect of five main factors on the fatigue damage and healing of HMA mixtures. These five factors are:

- Asphalt content (AC)
- Air voids (Va)
- Tensile strain level (ϵ_t)
- Temperature (T)
- Rest period (RP)

The main experiment included two levels for each factor except the temperature, where three levels were included. Thirty two (32) combinations were included as a result of the fractional factorial statistical design. Each combination was tested using three replicates. The 32 combinations include 15 combinations at zero rest period, and 17 combinations at five second rest period. Two different tests were used for each combination group. The first was without rest period (damage test), while the second with rest period (healing test). Two different softwares were developed for both tests. The main idea was to trace the change of the PS over time for the “without” and “with” rest period tests. The calculated differences of the PS between the “with” and “without” rest period tests for each combination represent the fatigue healing.

7.4.4.1 Results of Tests without Rest Period

Using three replicates, 45 specimens were tested without rest period in the main experiment for all PG 64-22 mixtures. Each mixture was tested using two selected strain levels at test temperatures of 40, 70 and 100°F. The criterion of selecting the two strain levels at each temperature was to reach a fatigue life of 20,000 cycles for the medium strain level, and 100,000 cycles for the low strain level. Prior to the uniaxial fatigue test, a dynamic modulus finger print test was conducted at 10 Hz to determine the dynamic modulus (E^*) value as well as the Machine Compliance Factor (MCF). The 50% reduction in the initial stiffness criterion was used to determine the fatigue life of material. The initial stiffness is the stiffness at the 100th cycle.

The results of the finger prints as well as the uniaxial tension-compression fatigue tests are tabulated for each mixture in TABLES 48 to 51.

**TABLE 48 Finger print and uniaxial fatigue test results at 9.5% Va and
4.2% AC**

Temp (°F)	Specimen ID	Air Voids (%)	Tensile Strain (µs)	FP Modulus (psi)	Phase Angle ϕ Degree	MCF	Initial Stiffness (psi)	Initial ϕ Degree	Cycles to Failure	Average Cycles	Standard Deviation	Coefficient of Variation (%)
100	D-985	8.84	237.5	130.5	51.65	1.29	72.4	56.7	9,810	13,897	3,563	25.6
	D-986	9.17	237.5	120.7	49.30	1.25	67.3	56.0	15,530			
	D-992	9.05	237.5	169.7	46.54	1.37	98.0	52.0	16,350			
70	D-969	9.52	115	538.4	24.58	2.83	433.6	28.1	31,150	25,753	4,793	18.6
	D-984	8.76	115	720.8	24.46	3.56	551.1	30.1	21,990			
	D-981	8.73	115	729.5	28.92	3.58	583.2	31.5	24,120			
	D-977	9.25	90	716.6	23.16	3.36	627.9	25.8	146,780	86,893	52,092	59.9
	D-978	9.45	90	672.8	24.26	3.45	557.3	28.2	61,820			
	D-983	9.32	90	768.8	27.53	4.26	572.5	32.3	52,080			
40	D-993	9.14	62.5	1,735	10.84	8.25	1,674	11.8	86,210	101,610	23,238	22.9
	D-988	8.39	62.5	2,175	12.95	9.29	2,175	13.6	90,280			
	D-987	9.01	62.5	2,066	12.66	9.13	1,960	13.4	128,340			

**TABLE 49 Finger print and uniaxial fatigue test results at 4.5% Va and
4.2% AC**

Temp (°F)	Specimen ID	Air Voids (%)	Tensile Strain (µs)	FP Modulus (psi)	Phase Angle ϕ Degree	MCF	Initial Stiffness (psi)	Initial ϕ Degree	Cycles to Failure	Average Cycles	Standard Deviation	Coefficient of Variation (%)
100	D-427	3.85	195	295.6	42.37	1.77	183.1	49.9	85,770	77,083	7,652	9.9
	D-467	4.12	195	244.7	51.49	1.77	140.3	56.1	71,340			
	D-466	4.50	195	203.6	50.02	1.51	132.9	55.4	74,140			
70	D-436	4.92	115	974.9	23.89	4.33	814.0	27.5	12,090	15,253	6,401	42.0
	D-437	5.09	115	1,133.2	26.63	5.53	862.0	30.1	22,620			
	D-488	4.99	115	1,220.3	23.34	5.01	901.2	28.3	11050			
40	D-442	3.81	87.5	3,145	11.52	12.70	2,712	13.1	21,660	16,147	5,353	33.2
	D-440	4.39	87.5	2,701	10.74	12.21	2,394	12.9	15,810			
	D-446	4.82	87.5	2,956	2,956	14.42	2,354	15.2	10,970			
	D-443	4.06	70	3,050	12.72	13.40	2,751	13.3	71,160	57,903	13,300	23.0
	D-452	4.52	70	2,969	10.64	12.95	2,756	11.7	44,560			
	D-455	4.46	70	3,137	12.22	13.09	2,823	14.4	57,990			

**TABLE 50 Finger print and uniaxial fatigue test results at 9.5% Va and
5.2% AC**

Temp (°F)	Specimen ID	Air Voids (%)	Tensile Strain (μs)	FP Modulus (psi)	Phase Angle φ Degree	MCF	Initial Stiffness (psi)	Initial φ Degree	Cycles to Failure	Average Cycles	Standard Deviation	Coefficient of Variation (%)
100	D+985	9.41	252.5	129.8	43.41	1.33	78.6	51.2	126,870	97,217	35,115	36.1
	D+989	9.89	252.5	80.0	56.86	1.21	48.4	59.1	58,440			
	D+984	9.39	252.5	122.3	44.21	1.21	76.4	49.5	106,340			
70	D+961	9.66	155	603.4	30.02	3.51	433.1	34.6	25,910	20,377	4,813	23.6
	D+974	9.61	155	459.6	29.08	2.55	368.3	34.1	18,060			
	D+9B2	9.34	155	540.3	27.94	2.66	412.9	33.5	17,160			
40	D+971	9.16	112.5	1,629	12.51	6.92	1,490	13.0	20,580	14,723	5,105	34.7
	D+968	9.98	112.5	1,471	12.21	6.73	1,348	13.1	11,220			
	D+967	9.04	112.5	1,612	11.74	7.72	1,510	14.2	12,370			
	D+965	9.38	82.5	1,380	12.16	5.97	1,334	12.5	93,810	119,010	32,788	27.6
	D+936	9.79	82.5	1,408	12.36	6.37	1,345	12.5	156,080			
	D+935	9.26	82.5	1,599	11.87	7.90	1,531	12.2	107,140			

**TABLE 51 Finger print and uniaxial fatigue test results at 4.5% Va and
5.2% AC**

Temp (°F)	Specimen ID	Air Voids (%)	Tensile Strain (μs)	FP Modulus (psi)	Phase Angle φ Degree	MCF	Initial Stiffness (psi)	Initial φ Degree	Cycles to Failure	Average Cycles	Standard Deviation	Coefficient of Variation (%)
100	D+457	4.63	357.5	142.7	51.90	1.26	75.4	59.6	29,520	24,897	7,060	28.4
	D+465	4.78	357.5	140.7	50.89	1.26	77.0	57.0	28,400			
	D+463	4.86	357.5	155.3	49.98	1.32	81.5	58.6	16,770			
70	D+449	4.79	122.5	872.0	30.02	4.31	679.4	33.0	129,320	92,577	31,918	34.5
	D+455	4.01	122.5	959.1	24.88	4.84	784.7	28.7	71,710			
	D+492	4.63	122.5	1,036	26.13	4.27	824.1	29.5	76,700			
40	D+459	4.79	112.5	2,291	11.17	10.86	2,095	13.0	23,270	17,270	6,035	34.9
	D+452	3.75	112.5	2,386	10.92	11.97	2,184	12.2	17,340			
	D+453	4.51	112.5	2,542	13.34	11.16	2,139	13.2	11,200			

7.4.4.2 Results of Tests with Rest Period

The main experiment included 17 different combinations of the tests with rest period. Using three replicates for each combination, 51 specimens were tested. Considering the long time needed for tests with rest period, all the tests were stopped after 20,000 cycles, which was reasonable to demonstrate a clear behavior of the mixtures tested with rest period. It takes 28 hours to complete one test with 5 seconds rest period run until 20,000 cycles. The results of the tests with rest periods for the different mixtures are summarized in TABLES 52 to 55.

TABLE 52 Finger print and uniaxial fatigue test results at 9.5% Va and 4.2% AC

Temp (°F)	Specimen ID	Air Voids (%)	Tensile Strain (µs)	Rest Period (sec)	FP Modulus (psi)	Phase Angle ϕ Degree	MCF	Initial Stiffness (psi)	Cycles N	PSR at N
100	D-996	9.28	187.5	5.0	135.2	47.45	1.35	113.0	20,000	0.934
	D-999	9.47	187.5	5.0	151.9	46.67	1.46	122.1	20,000	0.976
	D-9C9	8.64	187.5	5.0	145.9	50.02	1.37	122.9	20,000	0.899
	D-995	9.08	237.5	5.0	132.4	50.69	1.24	103.4	20,000	0.890
	D-9A2	9.48	237.5	5.0	126.0	48.24	1.21	92.0	20,000	0.853
	D-9C7	9.35	237.5	5.0	126.3	47.27	1.13	102.6	20,000	0.894
70	D-997	9.25	90.0	5.0	772.9	24.22	3.61	682.8	20,000	0.939
	D-9A1	9.29	90.0	5.0	699.1	25.54	2.34	636.1	20,000	0.957
	D-9C5	9.10	90.0	5.0	728.2	25.49	3.31	652.4	20,000	0.952
40	D-9A4	9.05	80.0	5.0	1,665.5	10.81	6.92	1,527.8	20,000	0.842
	D-9B9	9.29	80.0	5.0	1,720.4	11.68	7.13	1,604.8	20,000	0.890
	D-9C8	9.04	80.0	5.0	1,608.9	12.28	6.52	1,492.8	20,000	0.944

**TABLE 53 Finger print and uniaxial fatigue test results at 4.5% Va and
4.2% AC**

Temp (°F)	Specimen ID	Air Voids (%)	Tensile Strain (μs)	Rest Period (sec)	FP Modulus (psi)	Phase Angle φ Degree	MCF	Initial Stiffness (psi)	Cycles N	PSR at N
100	D-472	4.25	242.5	5.0	213.9	45.34	1.48	166.6	20,000	0.900
	D-474	4.68	242.5	5.0	226.1	47.19	1.56	163.3	20,000	0.872
	D-497	5.00	242.5	5.0	182.0	46.39	1.28	145.4	20,000	0.853
70	D-465	4.54	90.0	5.0	1,126.1	22.43	5.01	1,036.4	20,000	0.927
	D-468	3.95	90.0	5.0	1,343.3	24.12	5.81	1,183.2	20,000	0.948
	D-493	4.25	90.0	5.0	1,261.7	23.77	5.03	1,110.0	20,000	0.932
	D-471	4.66	115.0	5.0	1,208.7	26.62	5.25	987.8	20,000	0.905
	D-473	4.83	115.0	5.0	1,095.5	25.15	4.77	975.4	20,000	0.919
	D-494	4.34	115.0	5.0	1,195.7	20.98	4.75	1,066.6	20,000	0.882
40	D-475	4.62	70.0	5.0	3,145.4	11.51	14.20	2,731.2	20,000	1.000
	D-478	4.26	70.0	5.0	2,691.0	11.37	10.63	2,567.8	20,000	0.976
	D-495	3.99	70.0	5.0	2,763.7	9.85	10.20	2,763.7	20,000	0.956

**TABLE 54 Finger print and uniaxial fatigue test results at 9.5% Va and
5.2% AC**

Temp (°F)	Specimen ID	Air Voids (%)	Tensile Strain (μs)	Rest Period (sec)	FP Modulus (psi)	Phase Angle φ Degree	MCF	Initial Stiffness (psi)	Cycles N	PSR at N
100	D+993	9.43	342.5	5.0	84.9	54.36	1.20	66.2	20,000	0.860
	D+999	9.43	342.5	5.0	103.7	52.46	1.27	73.2	20,000	0.842
	D+9B8	8.98	342.5	5.0	77.6	51.23	1.14	59.3	20,000	0.810
70	D+991	8.73	112.5	5.0	656.7	26.28	3.13	584.1	20,000	0.940
	D+992	8.97	112.5	5.0	543.3	26.54	2.77	491.4	20,000	0.940
	D+9B4	9.35	112.5	5.0	570.7	27.69	2.77	501.2	20,000	0.950
	D+983	9.77	155.0	5.0	606.7	25.46	2.93	494.4	20,000	0.920
	D+988	8.76	155.0	5.0	782.0	20.20	3.65	676.8	20,000	0.895
	D+9B1	9.65	155.0	5.0	509.8	27.66	2.53	433.4	20,000	0.912
40	D+996	8.84	82.5	5.0	2,009.5	13.08	8.37	1,807.2	20,000	0.968
	D+9A0	9.06	82.5	5.0	1,616.3	10.55	7.08	1,552.9	20,000	0.974
	D+9C0	9.32	82.5	5.0	1,427.9	12.31	5.65	1,350.5	20,000	0.967
	D+995	9.66	112.5	5.0	1,443.9	13.08	5.96	1,336.3	20,000	0.960
	D+997	9.54	112.5	5.0	1,704.5	10.00	7.10	1,614.1	20,000	0.936
	D+9B0	8.77	112.5	5.0	1,543.5	12.23	5.98	1,427.1	20,000	0.921

**TABLE 55 Finger print and uniaxial fatigue test results at 4.5% Va and
5.2% AC**

Temp (°F)	Specimen ID	Air Voids (%)	Tensile Strain (μs)	Rest Period (sec)	FP Modulus (psi)	Phase Angle φ Degree	MCF	Initial Stiffness (psi)	Cycles N	PSR at N
100	D+466	4.57	232.5	5.0	151.6	51.59	1.44	124.3	20,000	0.941
	D+470	4.13	232.5	5.0	209.6	48.89	1.71	149.0	20,000	0.893
	D+493	4.70	232.5	5.0	165.9	52.00	1.41	135.1	20,000	0.906
70	D+468	4.39	197.5	5.0	1,155.8	24.00	5.15	865.7	20,000	0.873
	D+471	4.61	197.5	5.0	883.4	26.83	4.10	719.9	20,000	0.912
	D+495	4.68	197.5	5.0	907.5	24.99	3.82	761.8	20,000	0.877
40	D+473	4.57	82.5	5.0	2,268.8	10.51	11.49	2,168.4	20,000	0.997
	D+476	4.22	82.5	5.0	2,889.4	11.81	13.29	2,540.8	20,000	1.001
	D+491	4.95	82.5	5.0	2,402.4	12.55	9.21	2,180.0	20,000	0.963
	D+464	5.00	112.5	5.0	2,275.6	12.25	8.80	2,090.4	20,000	0.969
	D+477	4.54	112.5	5.0	2,664.1	11.86	11.30	2,330.6	20,000	0.968
	D+489	4.36	112.5	5.0	2,299.3	11.18	8.90	2,147.2	20,000	0.940

7.4.5 Additional Experimental Results

An additional experiment was conducted to study the nonlinear effect of the strain level and the rest period on the fatigue healing. The additional experiment included two additional rest periods and one additional strain level. The additional experiment included 5 combinations for tests without rest period and 13 combinations for tests with rest period. Considering two replicates for each combination, 36 tests were conducted for the additional experiment.

The new rest period levels were 1 and 10 seconds. The new strain level was high enough to fail the specimen at 5,000 loading cycles. The fatigue lives relationships were improved by adding the data of the tests without rest period from the main experiment to the existing fatigue life relationships. Consequentially, the fatigue life relationships can be fitted using more data points

(7 to 12 data points). The improved fatigue life relationships for each mixture at different temperatures are shown in FIGURES 141 to 144. The new k_1 and k_2 values at different temperatures are shown in the figures for each mixture.

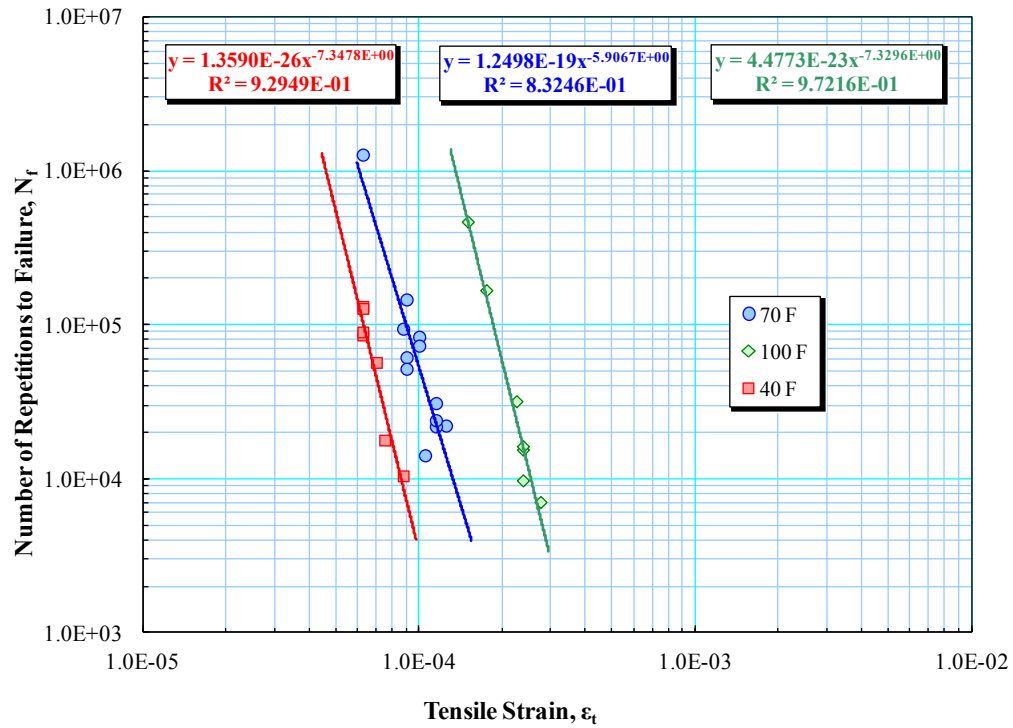


FIGURE 141 Updated fatigue lives at different temperatures (9.5% AV and 4.2% AC).

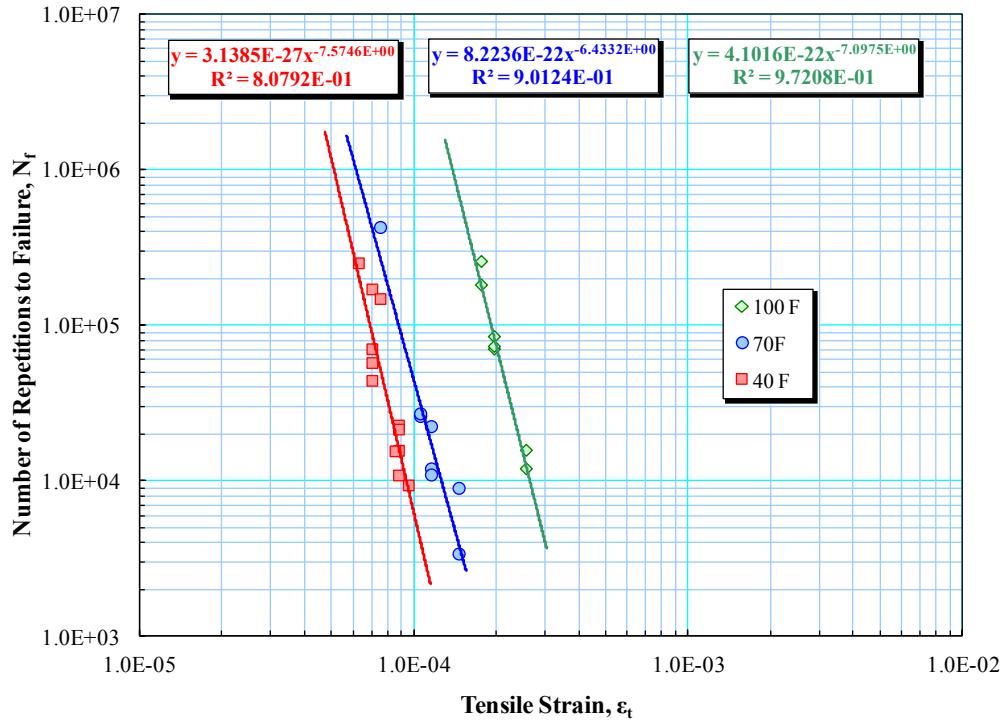


FIGURE 142 Updated fatigue lives at different temperatures (4.5% AV and 4.2% AC).

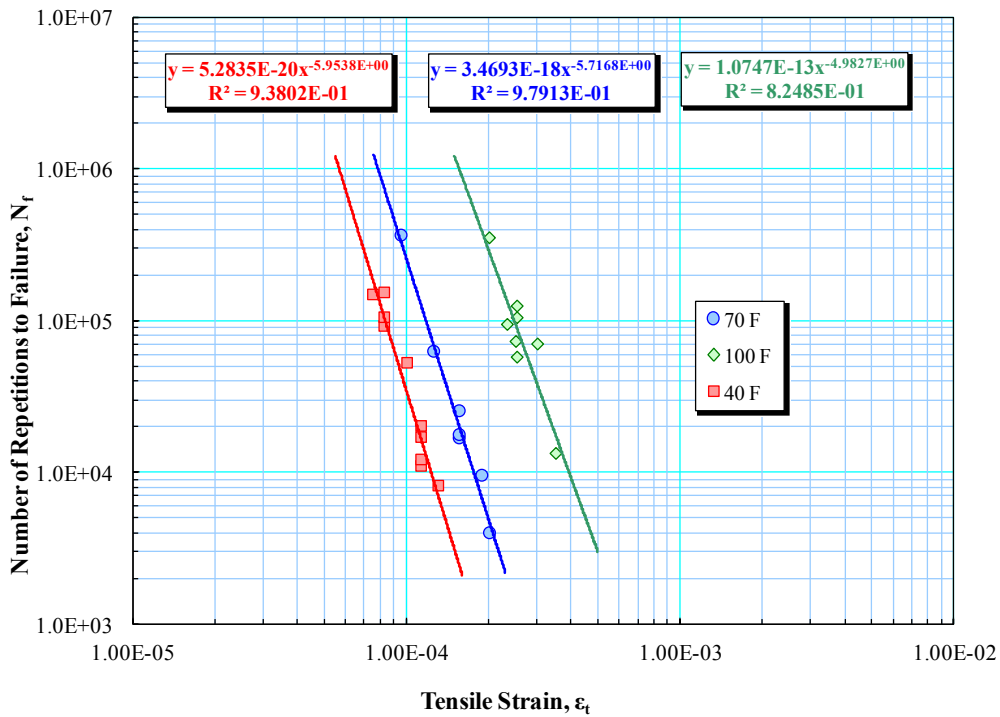


FIGURE 143 Updated fatigue lives at different temperatures (9.5% AV and 5.2% AC).

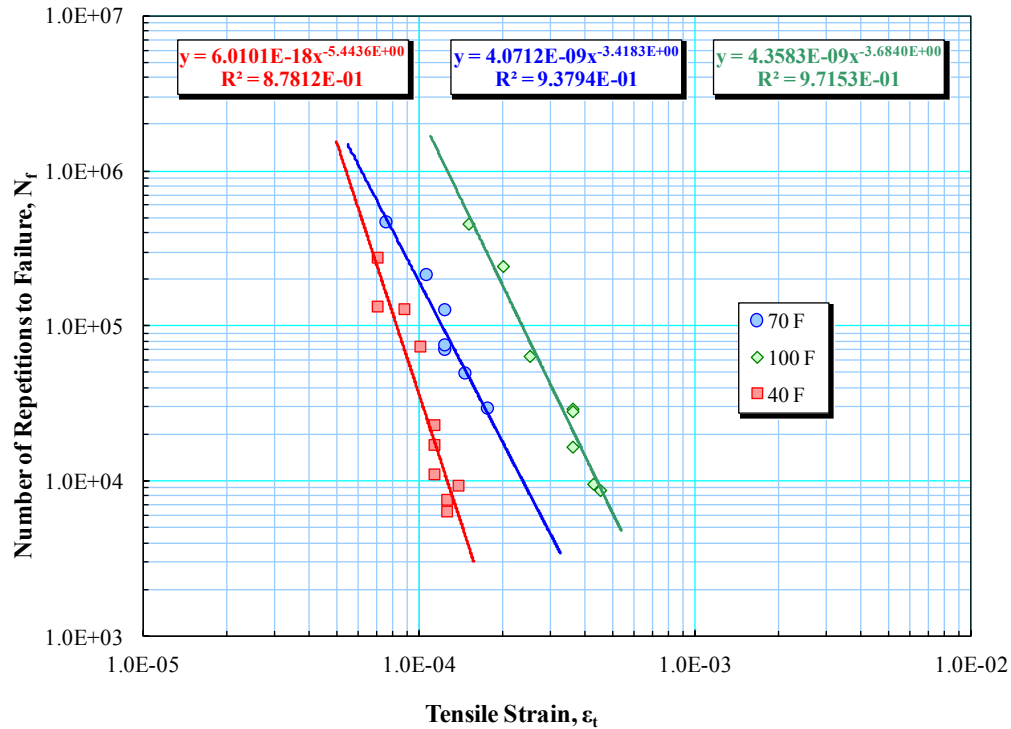


FIGURE 144 Updated fatigue lives at different temperatures (4.5% AV and 5.2% AC).

Based on a fatigue life criterion of 5,000 loading cycles, the high strain values for the asphalt mixtures at different temperatures were calculated as shown in TABLE 56. Using the combined data set for each mixture, the fatigue test results at different test temperatures were used to generate the generalized fatigue model coefficients (k_1 , k_2 , and k_3). TABLE 57 shows the k_1 , k_2 , and k_3 values for the four mixtures. In addition, all the test results for the four mixtures were pooled together in one generalized data set and used to get regression coefficients for all mixtures (TABLE 57). FIGURE 145 shows a comparison of the measured to the predicted fatigue lives based on the individual models for each mixture. FIGURE 146 displays the same comparison but using the generalized fatigue model for all mixtures together.

For the additional experiment, TABLE 58 contains a summary of the test results without rest period. For the tests with rest period, all the tests were stopped at 20,000 loading cycles. As stated before, this was a reasonable number of cycles due to time constrains; a test with 10 seconds rest period required 56 hours of testing. The results of the tests with rest period were summarized in TABLE 59. It is worthy to mention that the results for four tests without rest period and two tests with rest period at the lowest temperature (40 °F) could not be obtained even with many trials. The reason for that was that all test specimens failed quickly as the specimens were subjects to extreme levels of stresses.

TABLE 56 High tesnile strain values for all mixtures at different temperatures

Temp. (°F)	4.2% AC		5.2% AC	
	9.5% Va	4.5% Va	9.5% Va	4.5% Va
	(5000 Cycles)	(5000 Cycles)	(5000 Cycles)	(5000 Cycles)
100 °F	280	290	450	532.5
70 °F	145	142.5	207.5	302.5
40 °F	95	100	140	142.5

TABLE 57 Updated k_1 , k_2 and k_3 values for each individual mixture and all mixtures together

Air voids Va%	Asphalt content AC%	k_1	k_2	k_3	$R^2\%$
9.5	4.2	3.7904E-11	7.8325	2.8178	97.71
4.5	4.2	4.0851E-06	5.5693	1.9891	82.87
9.5	5.2	1.4200E-05	4.9422	1.6812	88.23
4.5	5.2	0.009953	3.4648	1.1127	93.35
All Mixtures		3.2761E-06	5.2812	1.8259	77.55

$$*N_f = k_1 \times (1/E)^{k_2} \times (1/\epsilon_t)^{k_3}$$

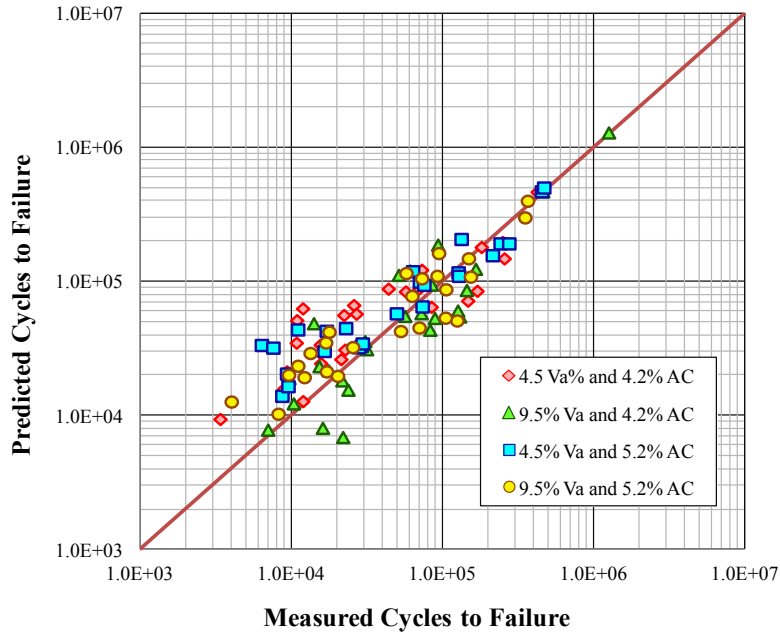


FIGURE 145 Measured versus predicted cycles to failure based on individual generalized fatigue models.

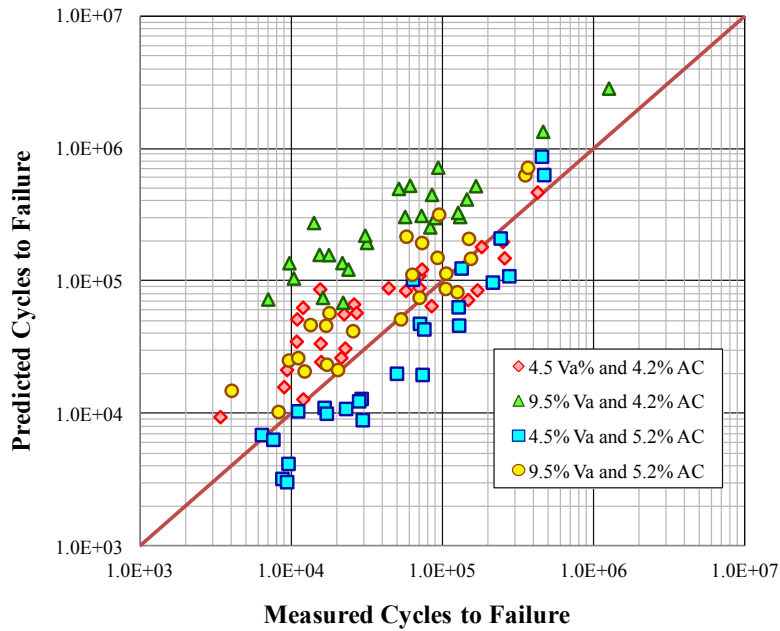


FIGURE 146 Measured versus predicted cycles to failure based on generalized fatigue model for all mixtures together.

**TABLE 58 Summary results of uniaxial fatigue test without rest period for
all mixtures**

Temp (°F)	Specimen ID	Air Voids (%0)	Tensile Strain (µs)	FP Modulus (psi)	Phase Angle φ Degree	MCF	Initial Stiffness (psi)	Initial φ Degree	Cycles to Failure	Average Cycles	Standard Deviation	Coefficien of Variation (%)
100	D-9A7	8.87	280.0	214.2	38.94	1.51	110.0	49.01	5,990	6,360	523	8.23
	D-9B3	8.83	280.0	152.7	46.54	1.44	80.0	55.6	6,730			
100	D+9B3	8.87	342.5	84.6	51.32	1.17	46.0	58.96	16,350	14,175	3,076	21.70
	D+9B5	8.83	343.5	90.0	52.38	1.41	46.1	58.24	12,000			
70	D-490	4.44	90.0	1,118.4	26.32	4.55	961.4	27.92	53,840	50,550	4,653	9.20
	D-491	4.48	90.0	1,058.1	23.50	4.50	896.7	26.82	47,260			

TABLE 59 Summary results of uniaxial fatigue test with rest period for all mixtures

Temp (°F)	Specimen ID	Air Voids (%)	Tensile Strain (μs)	Rest Period (sec)	FP Modulus (psi)	Phase Angle ϕ (Degree)	MCF	Initial Stiffness (psi)	Cycles N	PSR at N
40	D-484	4.11	100.0	5.0	2,928.6	11.17	11.10	2,586.5	20,000	0.863
100	D-476	4.07	195.0	1.0	298.6	39.64	1.97	221.8	20,000	0.791
	D-482	4.35	195.0	1.0	199.0	47.06	1.37	156.1	20,000	0.803
40	D+478	4.33	112.5	10.0	2,456.8	10.77	9.37	2,338.2	20,000	0.977
	D+483	4.44	112.5	10.0	2,528.3	11.16	9.72	2,277.3	20,000	0.992
	D+485	4.70	125.0	1.0	2,130.5	10.98	8.47	1,991.3	20,000	0.610
70	D+472	4.24	197.5	1.0	995.2	25.12	4.26	758.5	20,000	0.811
	D+475	4.18	197.5	1.0	991.3	24.17	4.27	783.8	20,000	0.750
	D+474	4.24	122.5	10.0	967.5	24.86	4.24	845.6	20,000	0.946
	D+479	4.17	122.5	10.0	977.0	29.22	4.56	807.9	20,000	0.946
40	D-9B2	9.32	62.5	5.0	1,790.5	13.25	7.38	1,699.1	20,000	0.976
	D-9B6	9.08	62.5	5.0	1,896.4	11.26	7.52	1,759.4	20,000	0.961
	D-9B8	9.30	80.0	1.0	1,520.3	13.21	6.14	1,369.7	20,000	0.689
	D-9C0	9.13	80.0	1.0	1,610.5	12.07	6.42	1,497.5	20,000	0.702
70	D-9A8	9.69	115.0	5.0	737.4	23.00	3.46	651.3	20,000	0.922
	D-9B0	9.76	115.0	5.0	678.1	23.90	3.29	599.3	20,000	0.940
100	D-9B5	9.46	237.5	10.0	122.0	47.36	1.37	98.3	20,000	0.909
	D-9C1	9.13	237.5	10.0	118.8	46.88	1.34	102.7	20,000	0.858
70	D+9A5	9.35	207.5	1.0	516.2	27.11	2.55	412.2	20,000	0.795
	D+997	9.54	207.5	1.0	548.2	27.59	2.78	440.2	20,000	0.757
100	D+9A6	9.42	450.0	5.0	82.1	50.96	1.13	56.3	20,000	0.729
	D+9A7	8.91	450.0	5.0	81.0	49.30	1.21	55.8	20,000	0.676
	D+9A8	9.06	252.5	1.0	86.4	51.22	1.15	69.3	20,000	0.802
	D+9A9	9.11	252.5	1.0	93.2	51.05	1.47	67.4	20,000	0.758

CHAPTER 8
ENDURANCE LIMIT MODEL DEVELOPMENT AND SENSITIVITY
ANALYSIS

8.1 Background

This chapter includes the methodology and implementation of the endurance limits developed using test results from the laboratory experiments. The developed methodology incorporates one important aspect, which is the healing of fatigue damage into the endurance limit estimation. This methodology is an inimitable and distinctive approach compared to the current methods. Healing of the fatigue damage is believed to be the main reason for the existence of asphalt mixtures endurance limits. As explained earlier in Section 7.2.1, there are two scenarios to determine the endurance limit values. In the first scenario, the endurance limit is calculated using the HI parameter where the endurance limit occurs at HI equal to one, or when all the fatigue micro-cracks are healed at certain number of cycles. In the second scenario, the PSR parameter is used to calculate the endurance limit where the endurance limit is defined; this is when the PSR is equal to one for the whole test time. As discussed earlier, the PSR method was used in this study to determine the endurance limit. Both methods entailed the development of PSR regression model. Five main factors that affect the fatigue behavior of asphalt mixtures were considered in this study. These factors are: air voids, binder content, temperature, tensile strain, and rest period.

This chapter also includes a comparison of the endurance limit values obtained from the uniaxial tension-compression fatigue study to those obtained

from the beam fatigue study that was conducted as a part of the NCHRP 944-A (Souliman, 2012).

8.2 Development of First Generation PSR Model

The test results from all uniaxial fatigue experiments were combined together to develop the first generation PSR model for the PG 64-22 mixtures. For each test with rest period, four PSR values were measured at different N values to represent the non-linear change of PSR over time. Only the PSR values at N_f were considered for the tests without rest period. A total number of 161 test results were used in the model development that included 385 data points. All data points are presented in Appendix C. The first PSR model includes the main five factors plus one additional factor, which is N where PSR values were measured.

One- and two-factor interactions were used in the statistical model. Two statistical techniques were used to develop the PSR model. The first technique was the regression analysis using the Minitab® software. The second technique was non-linear optimization technique. The non-linear optimization analysis can be done using the solver function in Excel® or other statistical software like Statistica®, Minitab®, and others. These different softwares use the Generalized Reduced Gradient (GRG) Algorithm for optimizing nonlinear problems. The only issue about this technique is that once a solution is found that seems producing favorable results, it will stop trying for new solutions. One other issue is the difficulty to get a reasonable solution when the number of adjustable parameters is quite large, which was the case for this model where one- and two-factor interactions between six different factors were considered. A more powerful non-

linear optimization technique that uses innovative Genetic Algorithm (GA) technology provides a more accurate optimization solution. Evolver®, one of the GA technology based softwares that is well-suited to find the best overall answer by exploring the entire universe of possible answers, was used in this study to develop the PSR model. The Evolver® software is completely compatible to work under Microsoft Excel®.

The optimization technique requires the main form of the regression model as an input. To construct a more rational model from, the relationship between the PSR and each factor was investigated to choose the best mathematical function to fit this relationship following an iteration process. It was found that there is a need for a logarithmic transformation for strain and number of loading cycles, while the second degree polynomial function was proper for temperature. For the rest period, a special function was used to fit its relationship with the PSR. It was noticed that by increasing the rest period, the PSR increases, indicating more healing. The rate of increase of PSR decreases as the rest period increases up to a certain value above which there is no more PSR increase. This value of rest period is called the optimum rest period. Using the tangent hyperbolic (Tanh) function to fit the PSR and RP relationship, the optimum rest period can be found. The shape and form of the Tanh function to fit the PSR and RP relationship is presented in FIGURE 147.

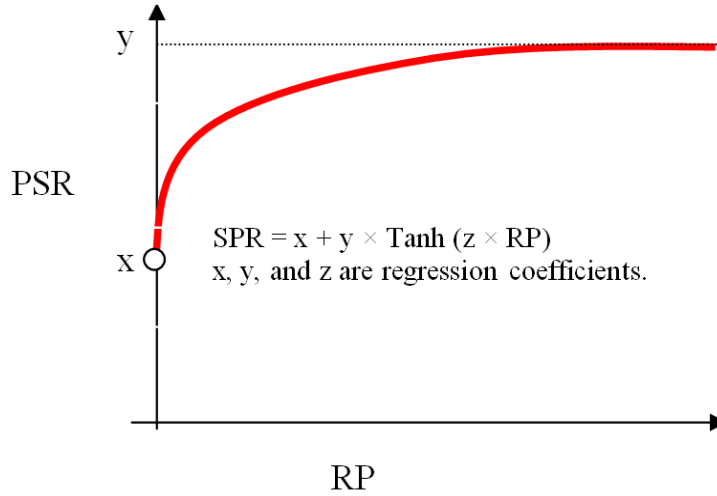


FIGURE 147 PSR and RP relationship fitted by Tanh function.

Based on the statistical accuracy, precision measurements, and the rationality of the sensitivity analysis, it was clear that the PSR models developed by the non-linear optimization technique were more accurate compared to the regression analysis technique. The regression analysis technique, however, was not able to include some of the essential function forms used by the first technique.

The form of the PSR model can be expressed as shown in Equation 116.

$$\begin{aligned}
 PSR = & a_0 + (a_1 T^2 + a_2 T) + a_3 AC + a_4 Va + a_5 \log \epsilon_t + (a_6 \text{Tanh}(a_7 RP) + a_8 \log N \\
 & + a_9 T^2 * AC + a_{10} T * AC + a_{11} T^2 * Va + a_{12} T * Va + a_{13} T^2 * \log \epsilon_t + a_{14} \\
 & T * \log \epsilon_t + a_{15} T^2 * \text{Tanh}(a_{16} RP) + a_{17} T * \text{Tanh}(a_{18} RP) + a_{19} T^2 * \log N + a_{20} \\
 & T * \log N + a_{21} AC * Va + a_{22} AC * \log \epsilon_t + a_{23} AC * \text{Tanh}(a_{24} RP) + a_{25} AC \\
 & * \log N + a_{26} Va * \log \epsilon_t + a_{27} Va * \text{Tanh}(a_{28} RP) + a_{29} Va * \log N + a_{30} \log \\
 & \epsilon_t * \text{Tanh}(a_{31} RP) + a_{32} \log \epsilon_t * \log N + a_{33} \log N * \text{Tanh}(a_{34} RP)
 \end{aligned}
 \tag{116}$$

where,

AC = Percent asphalt content by weight

Va = Percent air voids

ϵ_t = Tensile strain, micro-strains

T = Temperature (°F)

RP = Rest period (seconds)

To reduce the analysis time using the Evolver optimization function, the Solver function was used to have reasonable initial values for the regression coefficients (a_0 to a_{34}). The Evolver optimization function was used then to further reduce the sum of squared errors. The analysis was usually run for 12 hours and the best reasonable solution that has the least sum of squared errors was then considered. To have a non-biased regression model, the sum of errors was constrained to be zero. The model was further improved by removing two outlier data points using the method suggested by Montgomery (2008). The analysis was then repeated based on the remaining 383 data points and the following regression coefficients values were obtained (TABLE 60).

TABLE 60 Regression coefficient values of first generation model

Coefficient	Value	Coefficient	Value
a ₀	1.128166247	a ₁₈	0.000000000
a ₁	0.000013877	a ₁₉	0.000000485
a ₂	-0.001196544	a ₂₀	0.000106845
a ₃	0.044418678	a ₂₁	0.000032361
a ₄	-0.004845287	a ₂₂	0.000008648
a ₅	-0.318423391	a ₂₃	0.000000000
a ₆	0.415230129	a ₂₄	0.000000000
a ₇	0.899087837	a ₂₅	-0.000084625
a ₈	-0.046120564	a ₂₆	-0.000050235
a ₉	-0.000003538	a ₂₇	0.000000000
a ₁₀	0.000135597	a ₂₈	0.000000000
a ₁₁	-0.000001893	a ₂₉	-0.000799796
a ₁₂	0.000231228	a ₃₀	0.000000000
a ₁₃	0.000007109	a ₃₁	0.000000000
a ₁₄	-0.000047641	a ₃₂	-0.000104153
a ₁₅	0.000000000	a ₃₃	0.000000000
a ₁₆	0.000000000	a ₃₄	0.000000000
a ₁₇	0.000000000		

From the analysis of the results, it was noticed that there is no interaction between the rest period and other factors. The resulting first generation regression model is shown in Equation 117.

$$\begin{aligned}
 \text{PSR} = & 1.1282 + 0.00001388 T^2 - 0.0011197 T + 0.04442 AC - 0.004845 Va - \\
 & 0.3184 \log \varepsilon_t + 0.4152 \text{Tanh}(0.8991 RP) - 0.04612 \log N - 0.00000354 \\
 & T^2 * AC + 0.000136 T * AC - 0.00000189 T^2 * Va + 0.000231 T * Va + \\
 & 0.00000711 T^2 * \log \varepsilon_t - 0.0000476 T * \log \varepsilon_t + 0.000000485 T^2 * \log N + \\
 & 0.000107 T * \log N + 0.0000324 AC * Va + 0.00000865 AC * \log \varepsilon_t - \\
 & 0.0000846 AC * \log N - 0.0000502 Va * \log \varepsilon_t - 0.000800 Va * \log N - \\
 & 0.000104 \log \varepsilon_t * \log N \tag{117}
 \end{aligned}$$

The above model shows good predictions when compared with the measured PSR values. This also was supported by the excellent statistical measures of accuracy terms ($R^2_{adj} = 0.9563$ and $S_e/S_y = 0.291$).

The measured versus predicted PSR is shown in FIGURE 148. FIGURE 149 shows the model's adequacy using the residual versus raw data plot. The fitting model meets the requirement of normal distribution with constant variance. FIGURE 150 shows standardized error versus the measured PSR after deleting the two outlier data points.

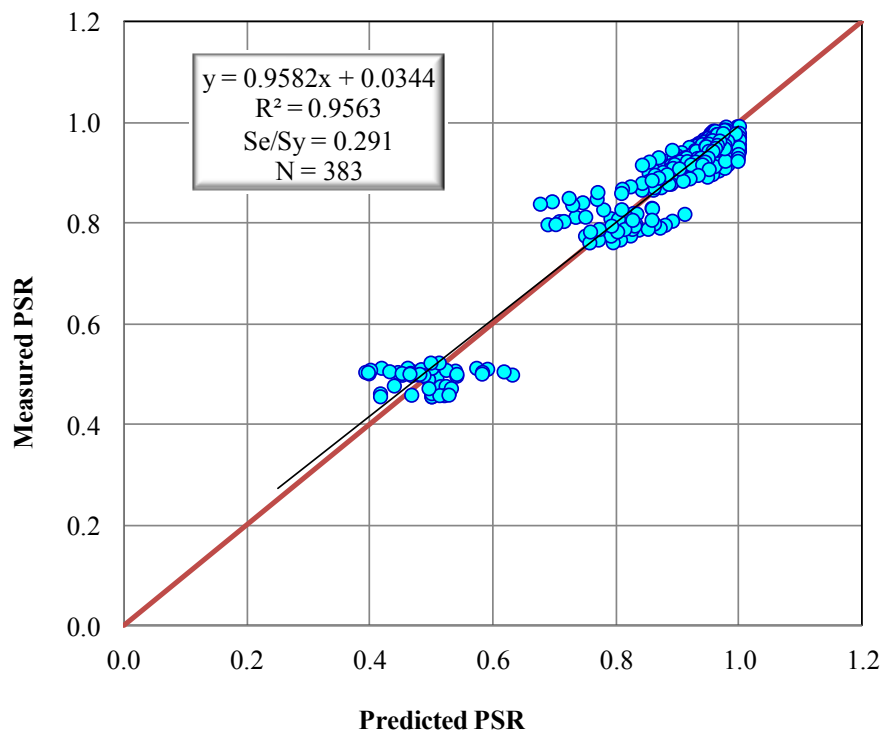


FIGURE 148 Measured versus predicted PSR for the first generation model.

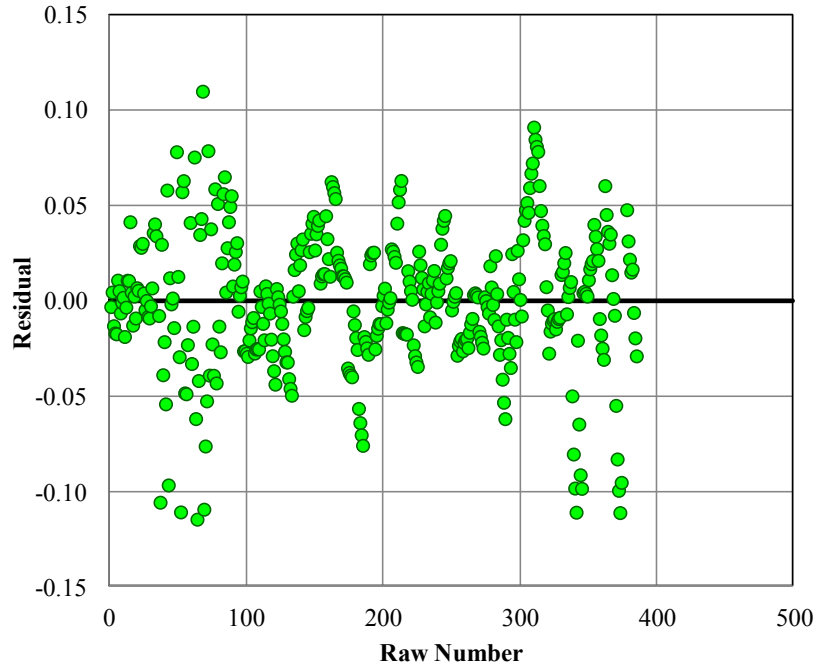


FIGURE 149 Residual versus raw number for the first generation model.

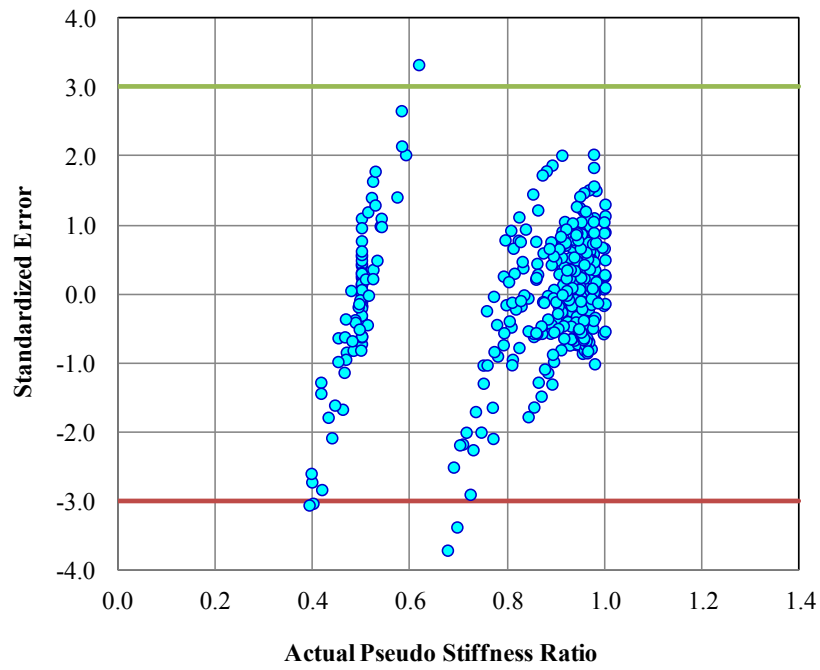


FIGURE 150 Standardized error versus measured PSR values.

8.2.1 Effect of Rest Period on PSR

The effect of rest period on the PSR for all mixtures at different temperatures is shown in FIGURE 151. For all the cases presented, it is clear that the PSR increases by increasing the rest period until a certain value after which the PSR is constant. This observed trend is supported with all the literature studies regarding the effect of rest period on fatigue behavior. The previous studies showed that there is an optimum rest period value beyond which there is no more enhancement of fatigue behavior. The optimum rest period values for all the cases (in FIGURE 151) are 3 seconds (loading ratio of 30), which almost fit in the middle range of optimum rest periods (1 to 5 seconds) reported in literature research work and was presented in Section 2.5.3.

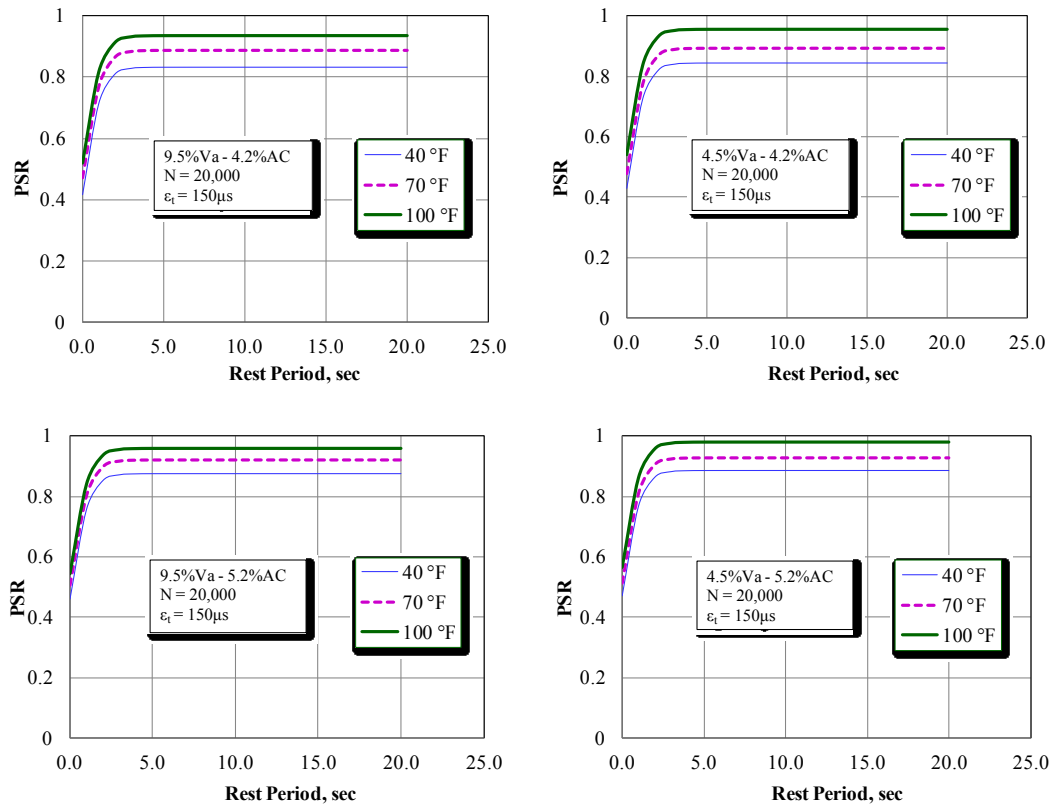


FIGURE 151 Effect of rest period on PSR for all mixtures.

8.2.2 Effect of N on PSR

To investigate the effect of N on the PSR and consequently on the endurance limit, a sensitivity analysis study was performed. In this analysis, the PSR versus the tensile strain relationships were investigated at rest periods of 1 and 10 seconds, N values of 25,000, 50,000, and 100,000 loading cycles, and temperatures of 40, 70, and 100°F. The results of the sensitivity analysis is shown in FIGURE 152 for only one asphalt mixture (4.5% Va-4.2%AC) as the other asphalt mixtures showed similar trends. Based on the sensitivity analysis results, N has small or almost no effect on the SR value for tests with rest period, where there is a trivial increase on the PSR by increasing N values. Consequentially, a rational N value of 20,000 loading cycles is recommended for the endurance limit calculation as it represents the end of all uniaxial fatigue tests with rest period.

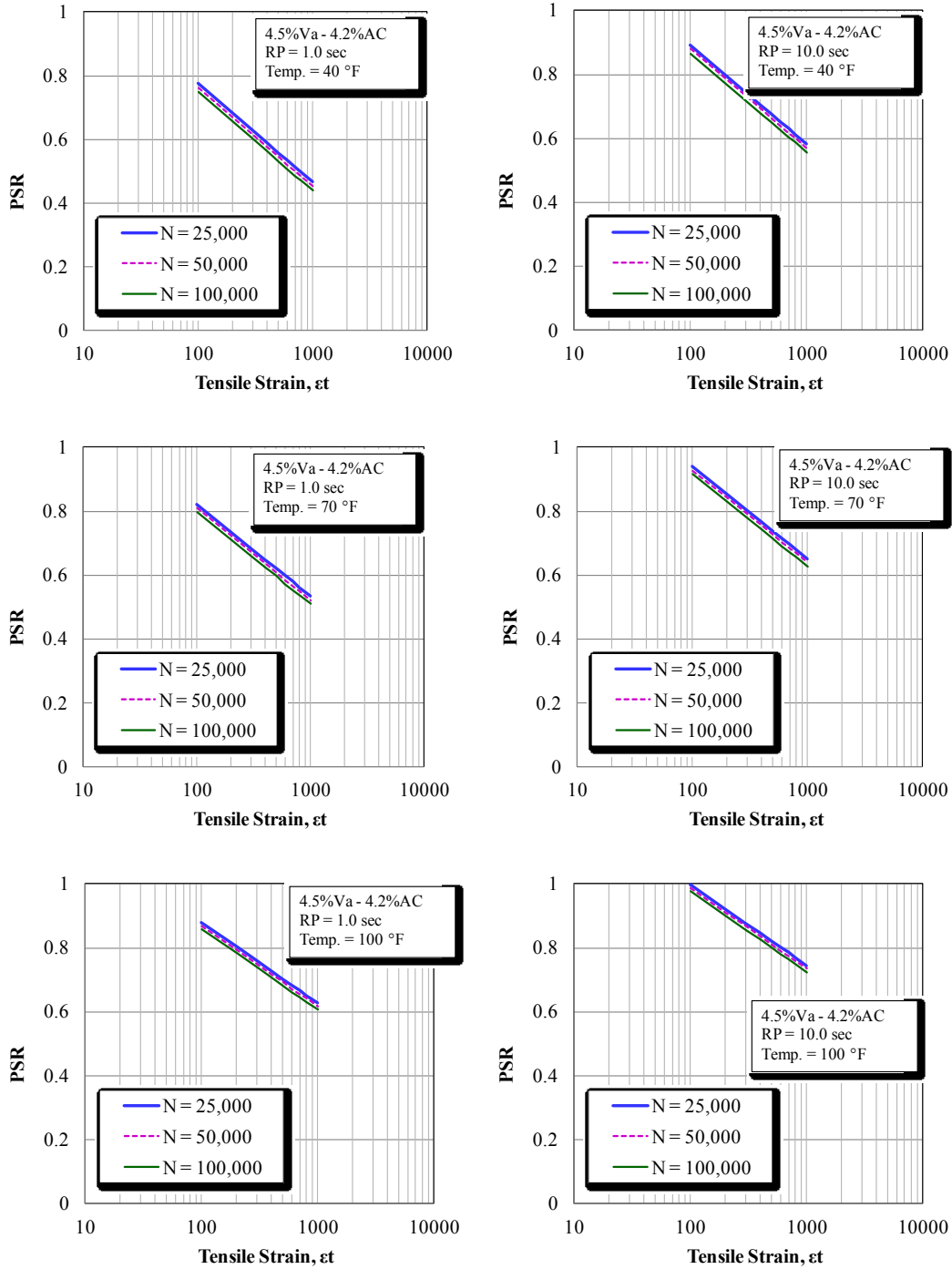


FIGURE 152 Effect N on PSR- ϵ_t relationship at different RP and temperatures for the 4.5Va-4.2AC mixture.

8.2.3 Estimating Endurance Limits Using First Generation PSR Model

The above model was used to predict the PSR values (when PSR is 1.0) at different tensile strains values for each mixture type at different temperatures (4 mixtures \times 3 temperatures). FIGURES 153 to 155 illustrate the relationship between the PSR and the tensile strain for different mixtures. In general, it is observed that the mixtures with higher asphalt contents showed considerably higher PSR values, especially at 40 and 70°F. At 100 °F, the effect of the asphalt content was less. This is totally agrees with a typical asphalt mixture behavior, where the asphalt cement dominates the mix behavior at low and medium temperatures. The opposite trend was observed for air voids, where the mixtures with high and low air voids (4.5 and 9.5% Va) showed a comparable PSR values at 40 and 70°F. At 100°F, the mixtures with 4.5% Va showed higher PSR values than the mixtures with 9.5% Va. The effect of both air voids and asphalt content on the healing of fatigue damage described by the PSR values emulates the fatigue behavior of the different mixtures under the uniaxial fatigue test conditions.

To estimate the endurance limit for each mixture, the endurance limit values were calculated at different temperatures where the PSR-tensile strain relationship intersects the line and the PSR is equal to 1.0. FIGURE 156 shows the endurance limit values of the asphalt mixtures at different temperatures for the 5 second rest period using N value of 20,000 cycles. As expected, the mixtures with higher binder contents and lower air voids exhibited high endurance limit values at all test temperatures. It is also noticed that the effect on asphalt content

is much more significant than the effect of air voids on the fatigue micro-cracks healing. This is, hypothesized, due to the fact that healing of micro-cracks occurs mainly due to the diffusivity of the asphalt binder along the surface of the micro-crack. Higher asphalt content increases the ability for the micro-cracks to heal. The same endurance limit trend was found at different rest periods.

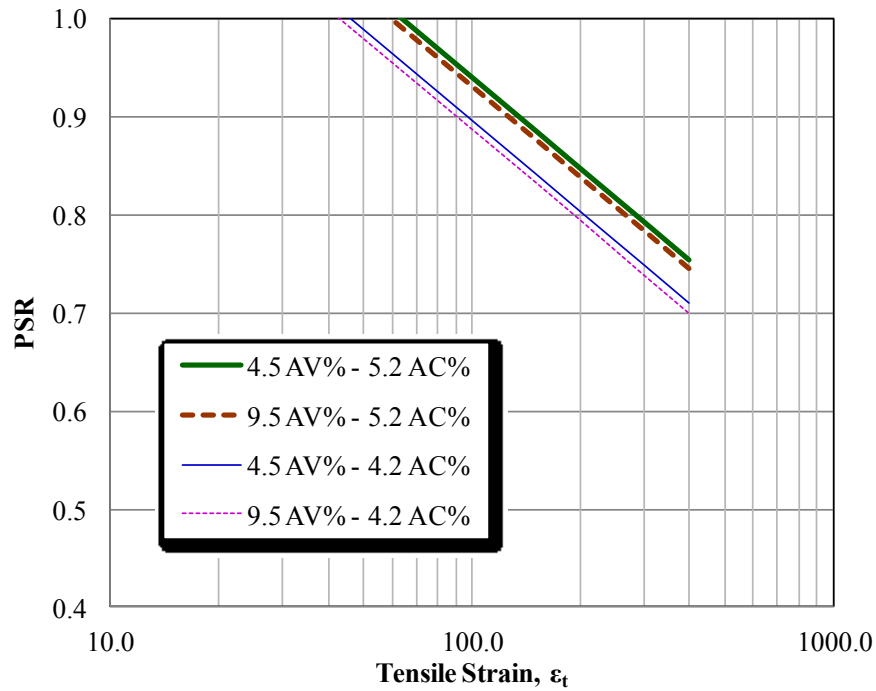


FIGURE 153 PSR versus tensile strain for all mixtures at 40°F (RP = 5.0 sec, and N = 20,000).

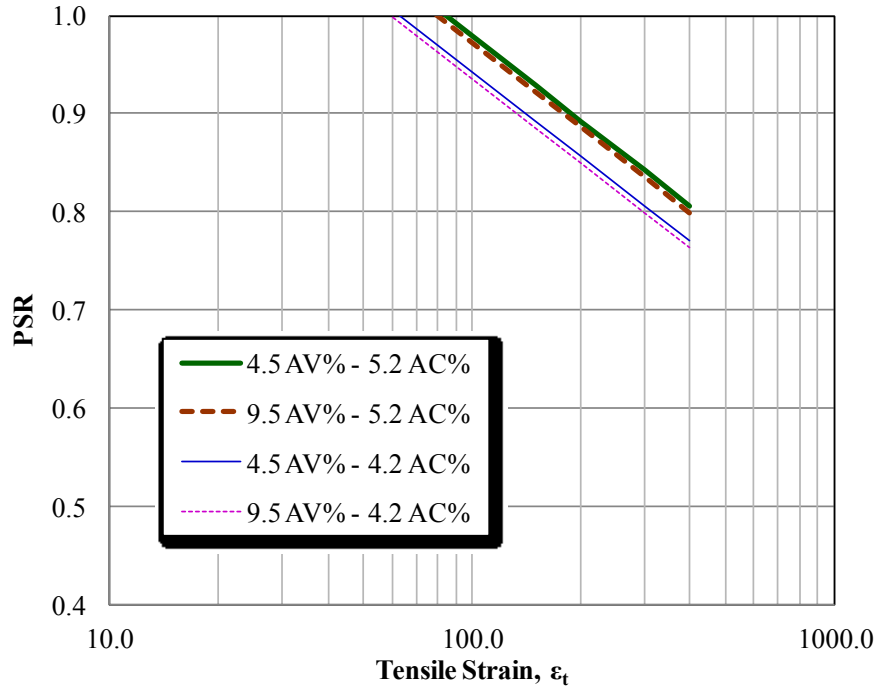


FIGURE 154 PSR versus tensile strain for all mixtures at 70°F (RP = 5.0 sec, and N = 20,000).

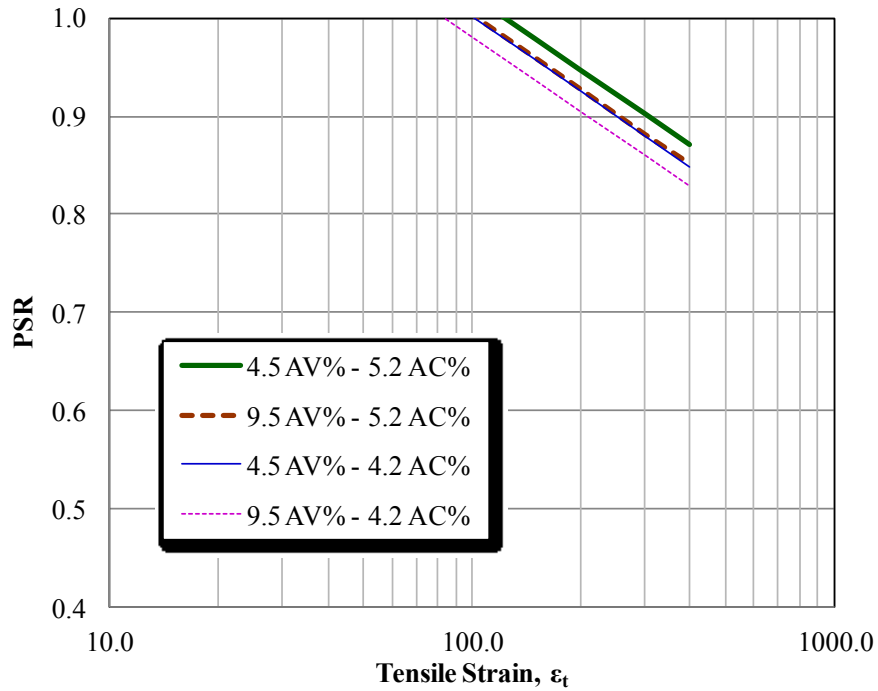


FIGURE 155 PSR versus tensile strain for all mixtures at 100°F (RP = 5.0 sec, and N = 20,000).

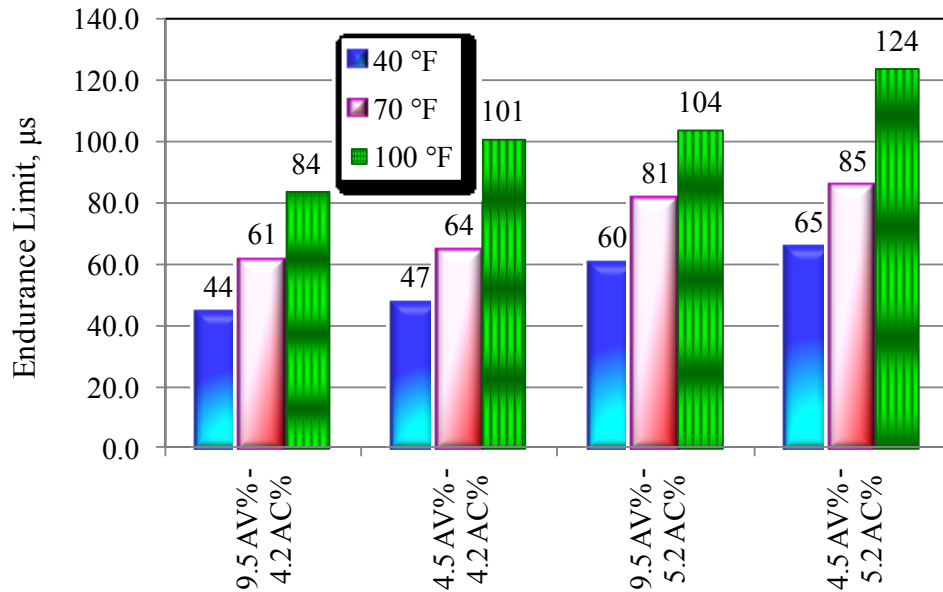


FIGURE 156 Endurance limit values for all mixtures at different temperatures using the first generation PSR model.

8.3 Development of Second Generation PSR Model

In the second generation model, the initial stiffness of the mixtures was used as a replacement of three main factors that are mainly affecting the stiffness value. These factors are asphalt content, air voids, and temperatures. Two main advantages can be achieved by this modification. The first advantage is to simplify the PSR model. The second advantage is to develop a PSR model that is more combatable with the DARWin-ME software, where the pavement performance prediction is mainly driven by the dynamic modulus of HMA mixture. The development of the second generation PSR model followed the same procedure used to develop the first generation model. Logarithmic transformation was required for the initial stiffness. In addition to the main factor effects, one-

and two-factor interactions were considered. The structure of the second generation model is shown in Equation 118.

$$\begin{aligned}
 \text{PSR} = & a_0 + a_1 * \log E_o + a_2 * \log \varepsilon_t + (a_3 * \text{Tanh} (a_4 * \text{RP}) + a_5 * \log N \\
 & + a_6 * \log E_o * \log \varepsilon_t + a_7 * \log E_o * \text{Tanh} (a_8 * \text{RP}) + a_9 * \log E_o * \log N \\
 & + a_{10} * \log \varepsilon_t * \text{Tanh} (a_{11} * \text{RP}) + a_{12} * \log \varepsilon_t * \log N + a_{13} * \log N * \text{Tanh} \\
 & (a_{14} * \text{RP})
 \end{aligned} \tag{118}$$

where E_o is the initial stiffness measured at 100th cycle in ksi.

Both Excel Solver and Evolver softwares were used, in order to minimize the sum of the squared errors using a non-linear optimization technique to estimate the regression analysis coefficients (a_0 to a_{14}). The model was further improved by removing the outliers using the method suggested by Montgomery (2008). Only two outlier data points were removed out of the 385 data points. The analysis was then repeated based on the remaining 383 data points which improved the R^2_{adj} from 0.9425 to 0.9511. The final regression coefficient values were obtained as tabulated in TABLE 61. The second generation regression model is shown in Equation 119.

TABLE 61 Regression coefficient values of second generation model

Coefficient	Value	Coefficient	Value
a_0	0.459539	a_8	0.000000
a_1	-0.090917	a_9	-0.041502
a_2	-0.104389	a_{10}	0.000000
a_3	0.417028	a_{11}	0.000000
a_4	0.875884	a_{12}	-0.077377
a_5	0.238893	a_{13}	0.000000
a_6	0.120018	a_{14}	0.000000
a_7	0.000000		

$$\begin{aligned}
 \text{PSR} = & 0.459539 - 0.090917 * \log E_o - 0.104389 * \log \epsilon_t + 0.417028 * \text{Tanh} \\
 & (0.875884 * \text{RP}) + 0.238893 * \log N + 0.120018 * \log E_o * \log \epsilon_t - 0.041502 \\
 & * \log E_o * \log N - 0.077377 * \log \epsilon_t * \log N \quad (119)
 \end{aligned}$$

FIGURE 157 presents the measured versus predicted PSR using the second generation model. The residual versus raw data plot is shown in FIGURE 158, which indicates that the fitting model meets the requirement of normal distribution with constant variance. The standardized error versus the measured PSR plot is illustrated in FIGURE 159.

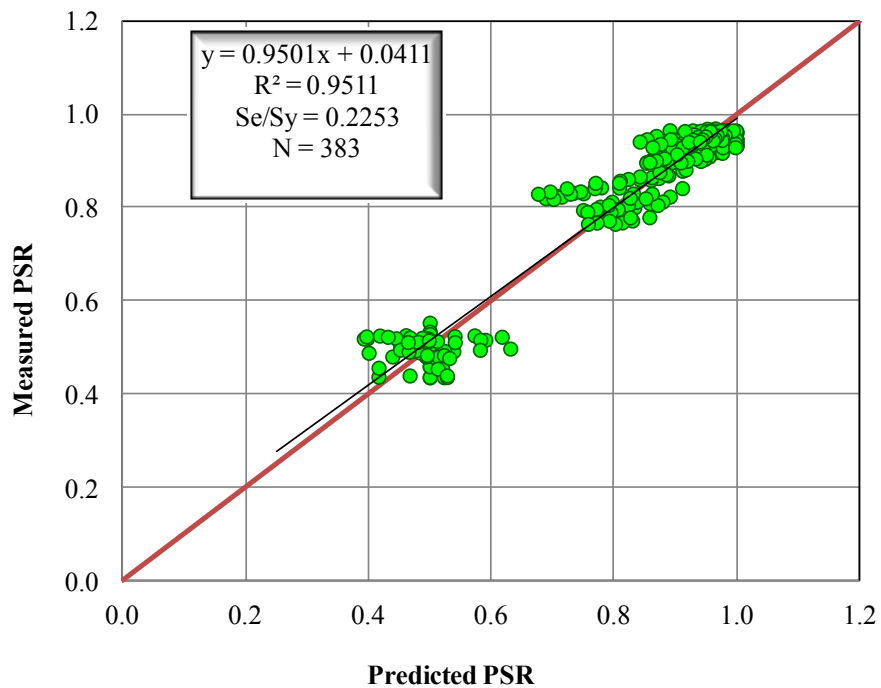


FIGURE 157 Measured versus predicted PSR for the second generation model.

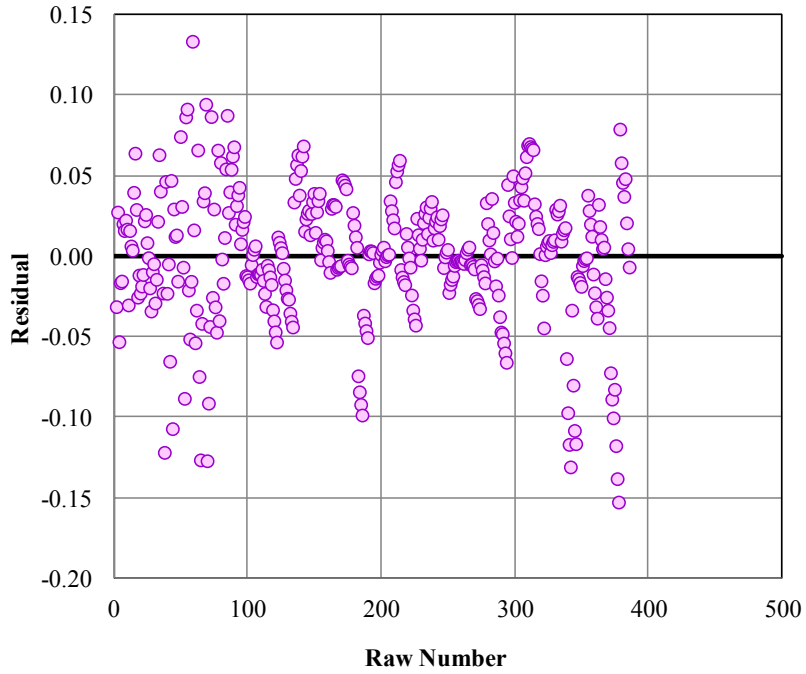


FIGURE 158 Residual versus raw number for the second generation model.

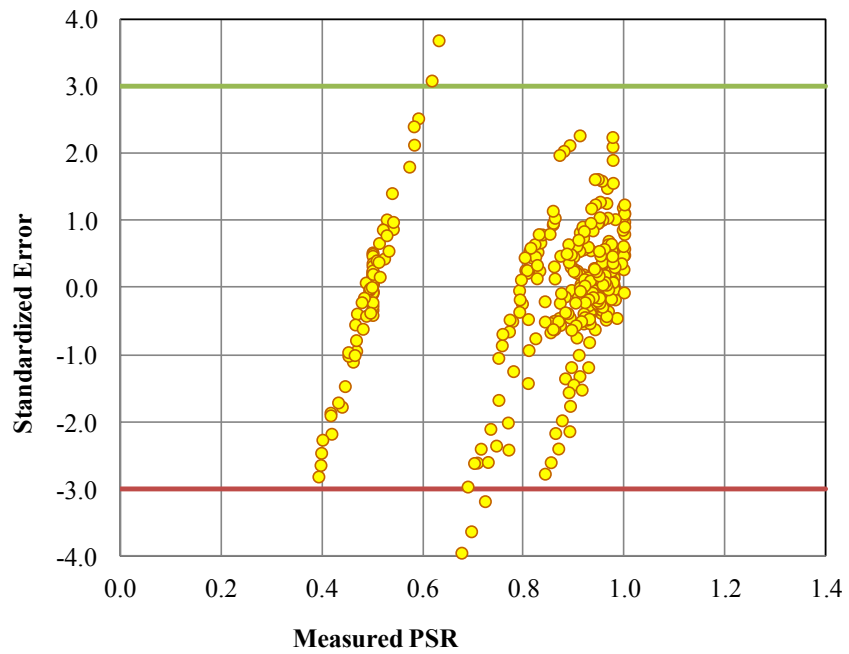


FIGURE 159 Standardized error versus measured PSR values.

8.3.1 Effect of Rest Period on PSR

FIGURE 160 shows the effect of rest period on the PSR, initial stiffness, and N values. The second generation model shows a similar trend for the effect of rest period compared to the first generation model. It is observed that increasing the rest period would increase the PSR until it reaches a maximum value, and does not change by increasing the rest period. An optimum rest period of 3 seconds (loading ratio of 30) for all the cases was obtained, which is the same compared to that generated by the first generation model.

8.3.2 Effect of N on PSR

Further analysis was conducted to investigate the effect of N on the PSR for the second generation model. The sensitivity analysis included plotting the PSR versus the tensile strain for different mixtures represented by the initial stiffness at rest periods of 1 and 10 seconds and N values of 25,000, 50,000, 100,000, and 200,000 loading cycles. The PSR-tensile strain relationships are presented in FIGURE 161 for the different cases. The analysis results showed that PSR-tensile strain relationships are not perfectly parallel at different N values when compared to the first generation model. Therefore, the effect of N will depend on the point of intersection. If the point of intersection is close enough to the horizontal line where $PSR = 1.0$, the N will not have any effect on the PSR and the calculation of the endurance limit. The N value seems to have an effect on the PSR if the intersecting point is distant from PSR value of 1.0. The N value of 20,000 cycles is recommended for the second generation PSR model.

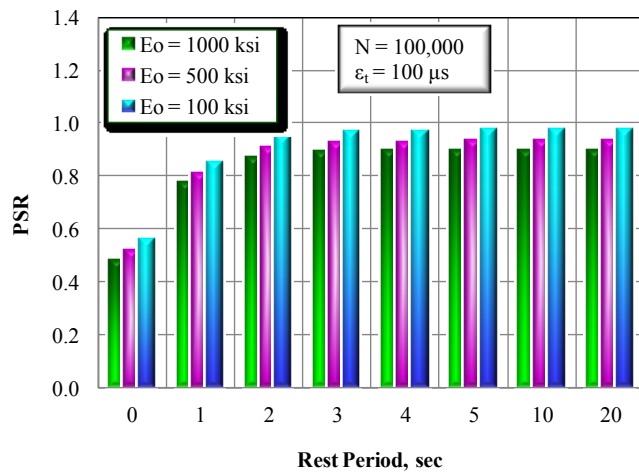
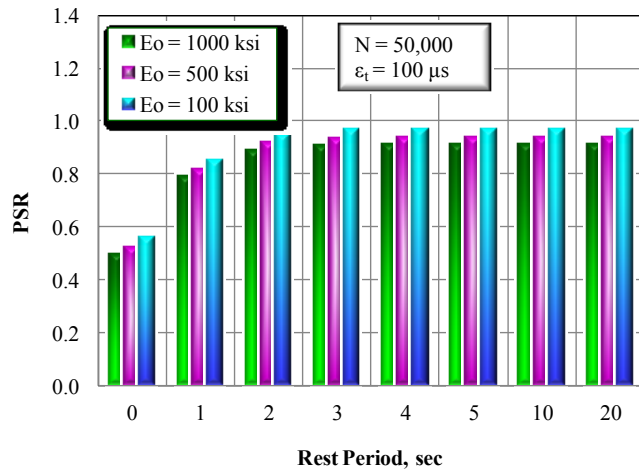
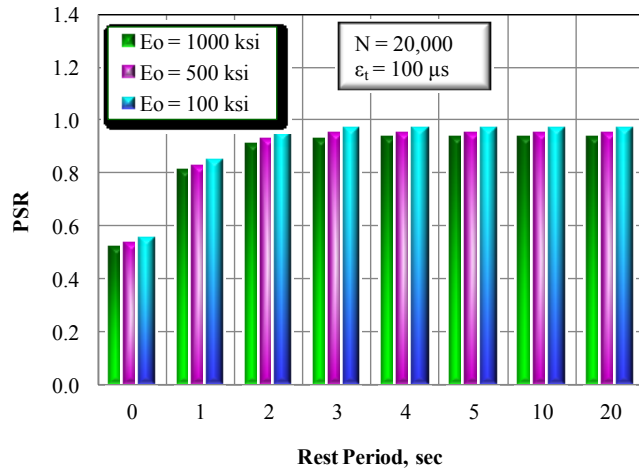


FIGURE 160 Effect of rest period on PSR at different N values.

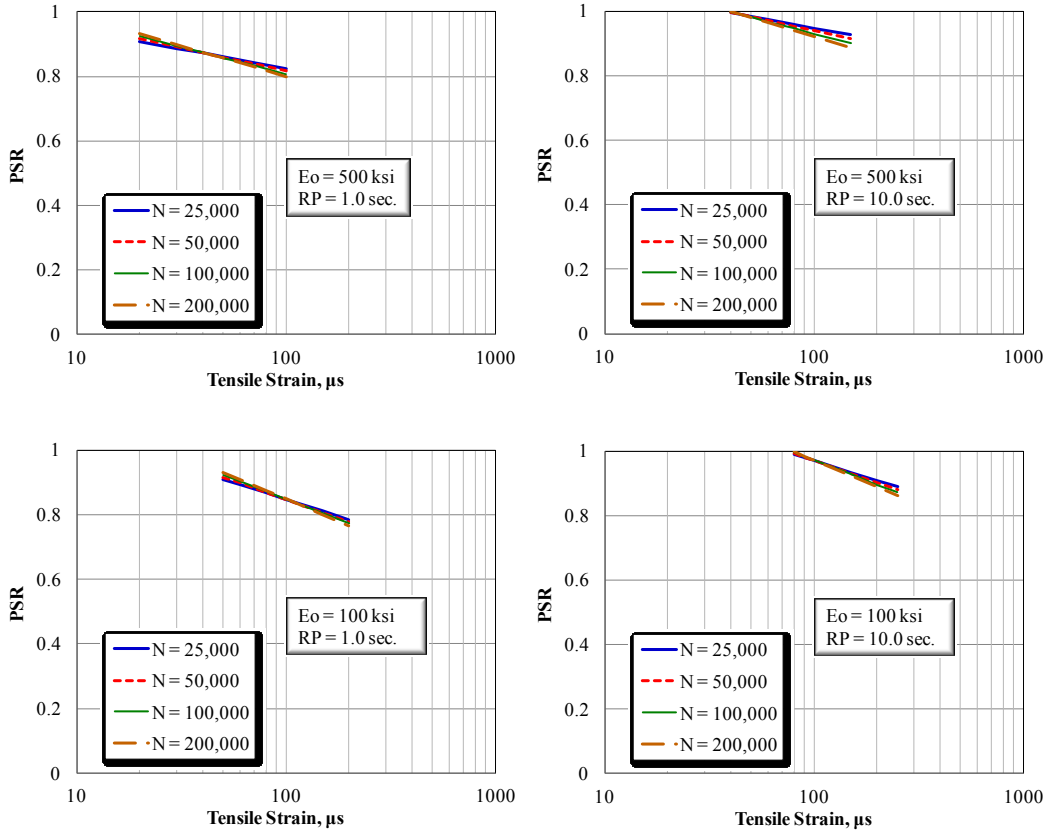


FIGURE 161 Effect of N on PSR at different initial stiffness and RP values.

8.3.3 Estimating Endurance Limits Using Second Generation PSR Model

Using the second generation PSR model, the PSR versus the tensile strain plots were established using several stiffness and rest period values at N of 200,000 loading cycles (FIGURES 162 to 166). It was observed that the relationship lines in case of the second model are intersecting, where they looked parallel for the first model. This is mainly because of using the stiffness in the model. For further elaboration, mixtures with high and low binder contents have a slight stiffness difference; however, their performance could be notably different. In addition, mixtures with high binder content and lower air voids showed similar stiffness to those that have higher air voids and lower binder, even though their

performance could be relatively dissimilar. Despite this concern, the model shows rational results and relationships. In addition, the simplicity of the model itself is an advantage compared to the form of the first generation PSR form. Based on relationships in FIGURES 162 to 166, the endurance limit is calculated as the tensile strain value where the PSR-tensile strain relationship meets a PSR value of 1.0.

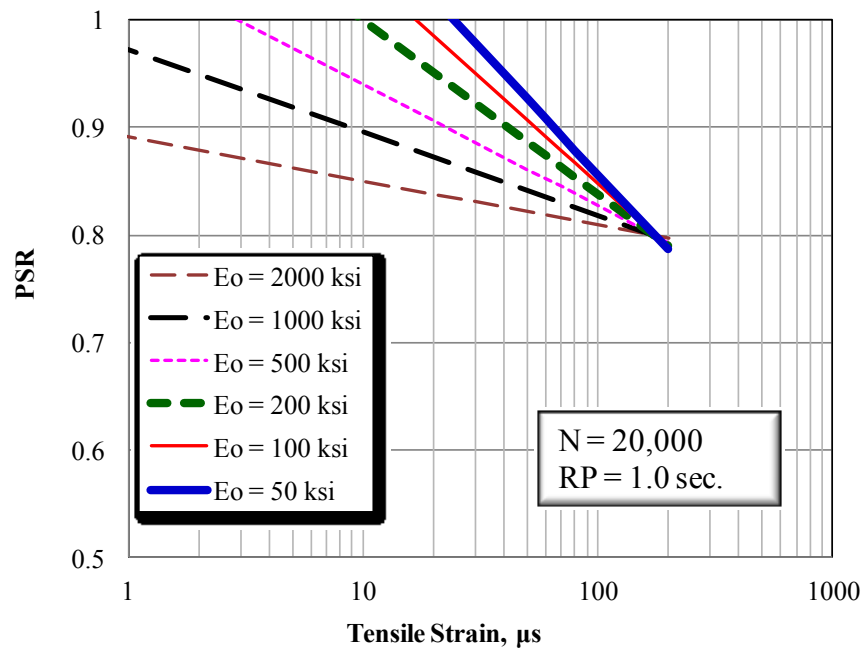


FIGURE 162 PSR versus tensile strain at different initial stiffness values (RP = 1.0 sec, N=20,000 cycles).

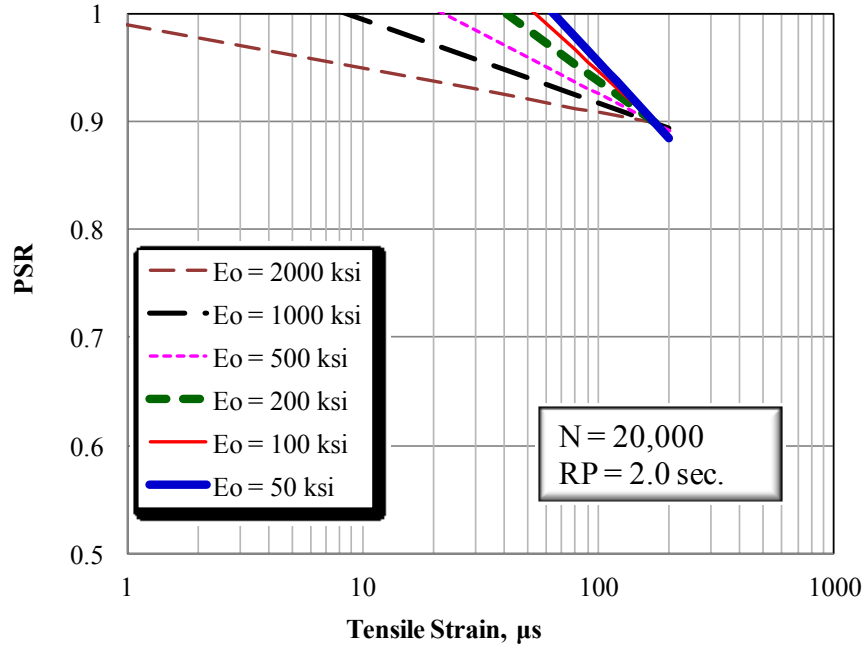


FIGURE 163 PSR versus tensile strain at different initial stiffness values (RP = 2.0 sec, N=20,000 cycles).

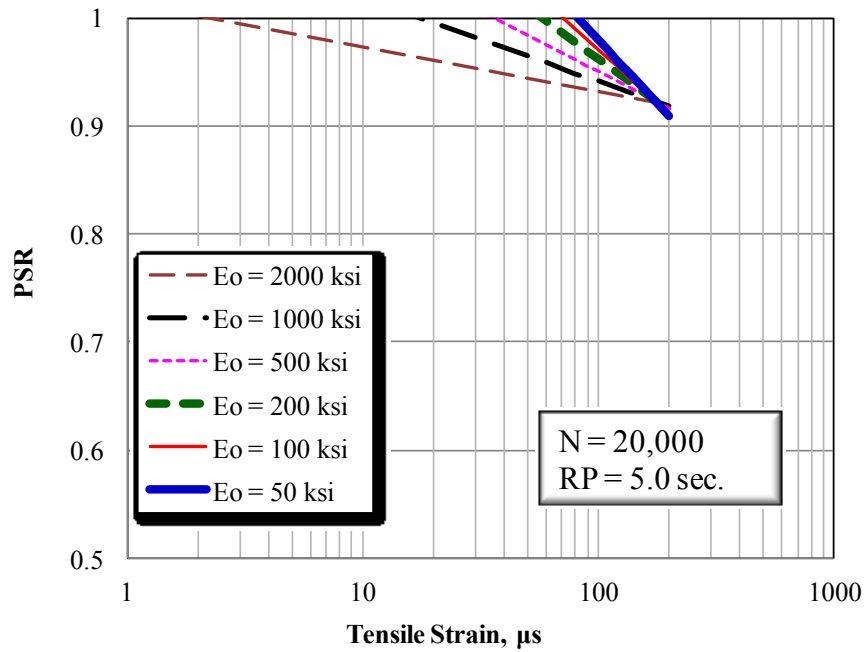


FIGURE 164 PSR versus tensile strain at different initial stiffness values (RP = 5.0 sec, N=20,000 cycles).

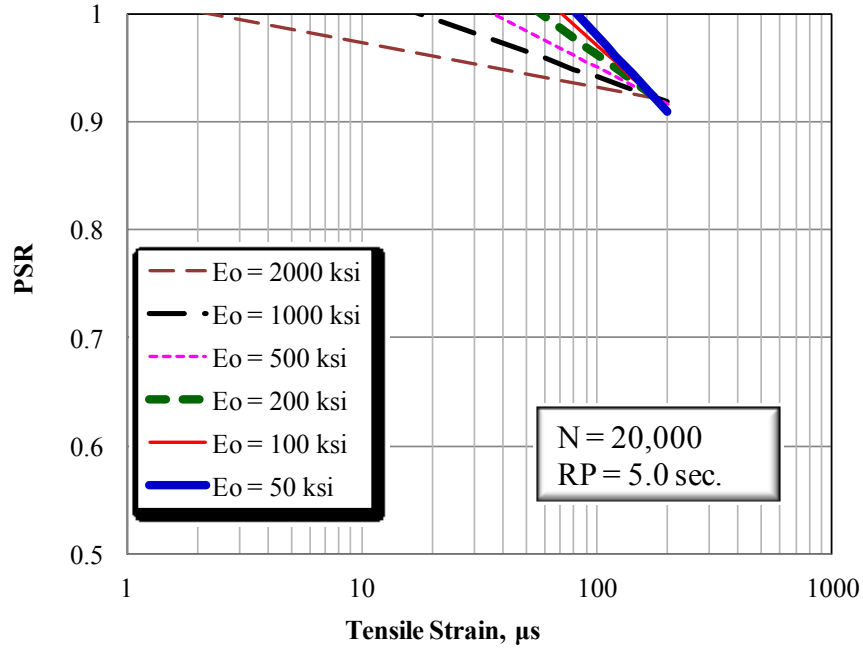


FIGURE 165 PSR versus tensile strain at different initial stiffness values (RP = 10.0 sec, N=20,000 cycles).

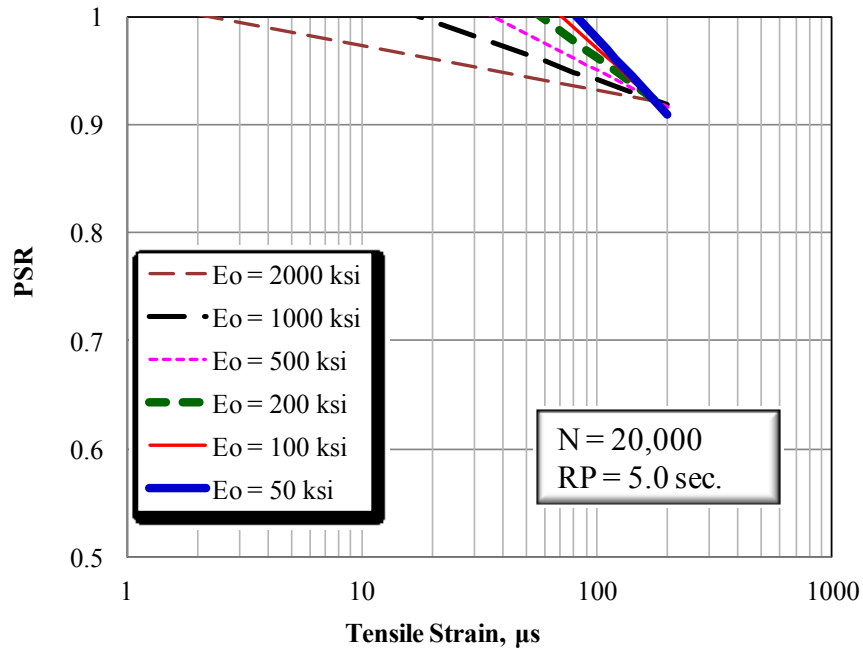


FIGURE 166 PSR versus tensile strain at different initial stiffness values (RP = 20.0 sec, N=20,000 cycles).

FIGURES 167 and 168 demonstrate the endurance limit values for different stiffness and rest period values at $N = 20,000$ and $100,000$ cycles respectively. It can be observed that the mixtures with higher stiffness showed lower endurance limit as expected. In addition, the endurance limit values were stable after 5 seconds rest period (loading ratio of 50). The N is having a slight effect on the endurance limit values, where higher N showed higher endurance limit values. The endurance limit values computed from the second model are slightly less compared to the ones from the first generation model at a comparable stiffness.

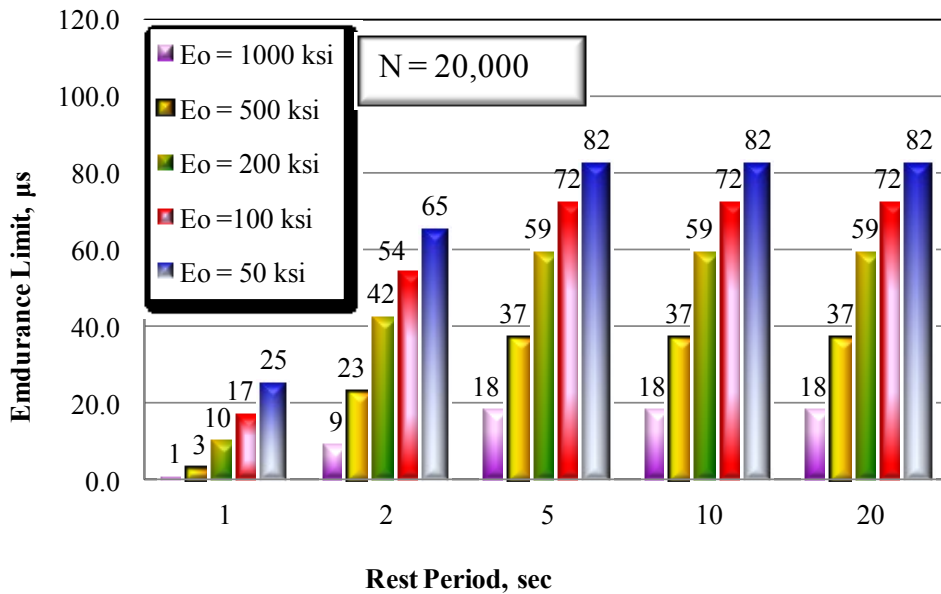


FIGURE 167 Endurance limit values at different rest periods and stiffness values using second generation model ($N = 20,000$).

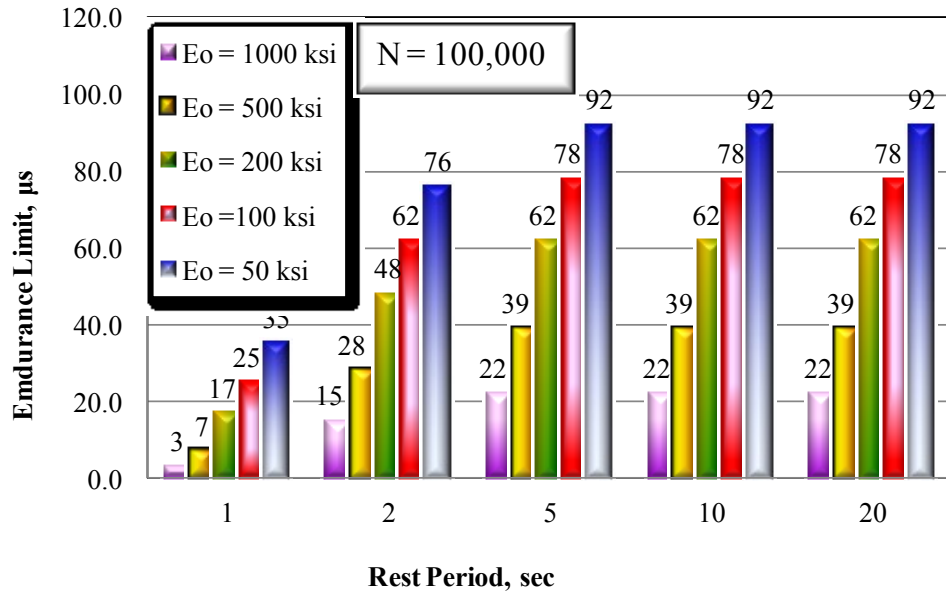


FIGURE 168 Endurance limit values at different rest periods and stiffness values using second generation model (N = 100,000).

8.4 Comparison of Endurance Limits Computed from Beam Fatigue Experiment

The beam fatigue data of the PG 64-22 mixture (Souliman, 2012) was used to develop the beam fatigue model to predict the Stiffness Ratio (SR). The procedure was similar to that of the first generation PSR model except that the initial stiffness was considered for beam fatigue results at 50th cycles. The model was developed based on the non-linear optimization techniques using the Solver and Evolver softwares. The sum of the square errors was minimized and the regression coefficients were determined. The regression coefficients are listed in TABLE 62 and the model form is presented in Equation 120.

FIGURE 169 presents the measured versus predicted SR using the SR model generation. FIGURE 170 shows the residual versus raw data plot. The standardized error versus the measured PSR plot is demonstrated in FIGURE 171.

The model shows high accuracy prediction presented by R^2_{adj} of 0.9471 and Se/Sy of 0.2502 using 231 data points.

TABLE 62 Regression coefficient values of first generation SR model using beam fatigue data for the PG 64-22 mixtures

Coefficient	Value	Coefficient	Value
a ₀	1.46723575	a ₁₈	0.00000000
a ₁	-0.00000627	a ₁₉	0.00000449
a ₂	0.00062326	a ₂₀	-0.00018445
a ₃	0.04017422	a ₂₁	-0.00011536
a ₄	-0.00592721	a ₂₂	-0.00001510
a ₅	-0.40039632	a ₂₃	0.00000000
a ₆	0.31492804	a ₂₄	0.00000000
a ₇	1.33934526	a ₂₅	-0.00003475
a ₈	-0.05944687	a ₂₆	-0.00006440
a ₉	0.00000000	a ₂₇	0.00000000
a ₁₀	0.00002984	a ₂₈	0.00000000
a ₁₁	-0.00000240	a ₂₉	-0.00012923
a ₁₂	0.00022569	a ₃₀	0.00000000
a ₁₃	0.00000388	a ₃₁	0.00000000
a ₁₄	-0.00021350	a ₃₂	-0.00002508
a ₁₅	0.00000000	a ₃₃	0.00000000
a ₁₆	0.00000000	a ₃₄	0.00000000
a₁₇	0.00000000		

$$\begin{aligned}
 SR = & 1.46723575 - 0.00000627 T^2 + 0.00062326 T + 0.04017422 AC - \\
 & 0.00592721 Va - 0.40039632 \log \epsilon_t + 0.31492804 \text{Tanh}(1.33934526 RP) \\
 & - 0.05944687 \log N + 0.00002984 T*AC - 0.00000240 T^2*Va + \\
 & 0.00022569 T*Va + 0.00000388 T^2*\log \epsilon_t - 0.00021350 T*\log \epsilon_t +
 \end{aligned}$$

$$\begin{aligned}
&0.00000449 T^2 \cdot \log N - 0.00018445 T \cdot \log N - 0.00011536 AC \cdot Va - \\
&0.00001510 AC \cdot \log \epsilon_t - 0.00003475 AC \cdot \log N - 0.00006440 Va \cdot \log \\
&\epsilon_t - 0.00012923 Va \cdot \log N - 0.00002508 \log \epsilon_t \cdot \log N \quad (120)
\end{aligned}$$

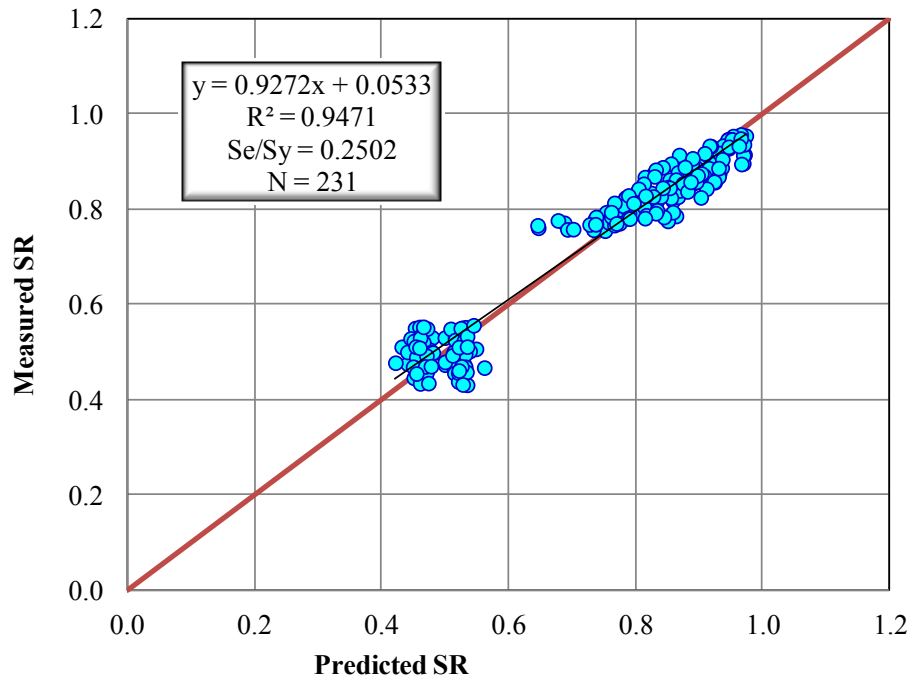


FIGURE 169 Measured versus predicted SR using the beam fatigue, PG 64-22 model.

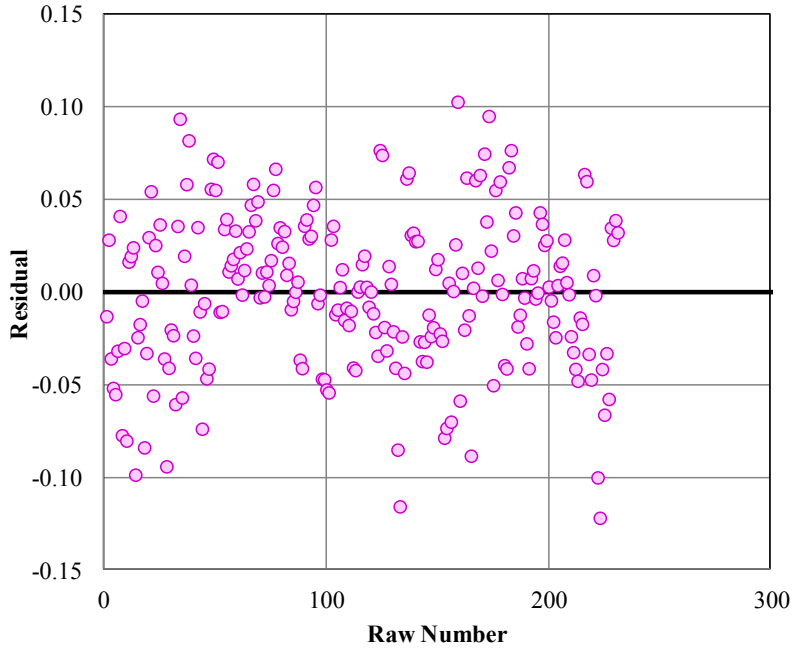


FIGURE 170 Residual versus raw number using the beam fatigue, PG 64-22 SR model.

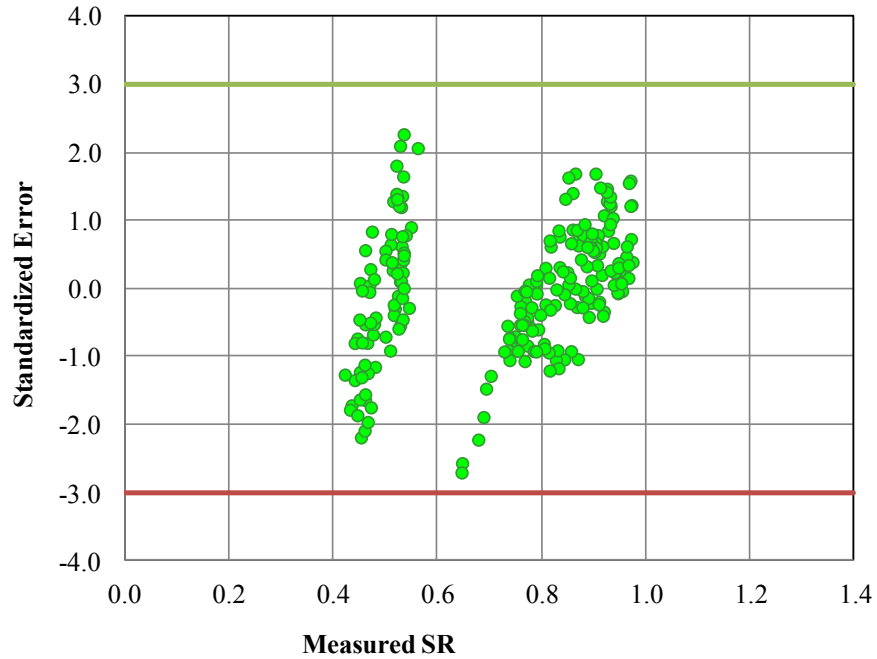


FIGURE 171 Standardized error versus measured SR values using the beam fatigue, PG 64-22 SR mode.

The effect of rest period on the SR values is shown in FIGURE 172 at different temperatures. The optimum rest period is 2.5 seconds (loading ratio of 25) compared to 3.0 seconds (loading ratio of 30) for the uniaxial fatigue test. The effect of N on the SR for the beam fatigue test is minimal especially at 100°F as shown in FIGURE 173. A value of N of 20,000 is recommended to avoid extrapolations as it represents the end of the fatigue tests with rest period.

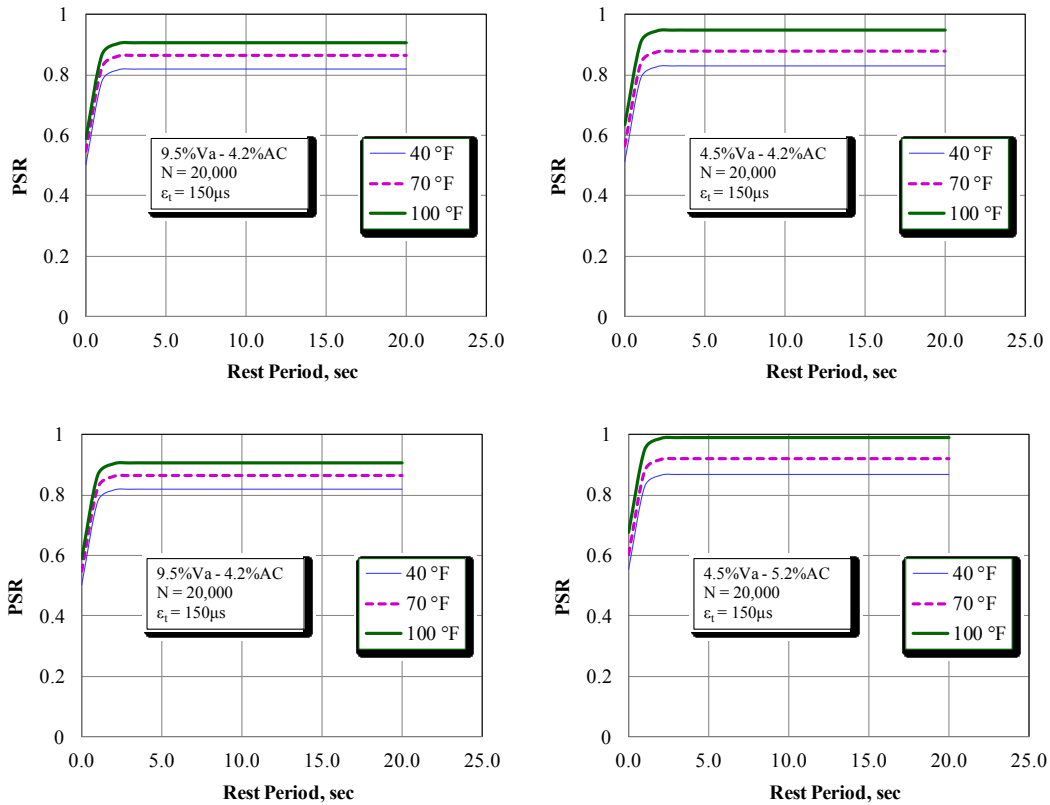


FIGURE 172 Effect N on SR- ϵ_t relationship at different RP and temperatures for the beam fatigue, PG 64-22, 4.5Va-4.2AC mixture.

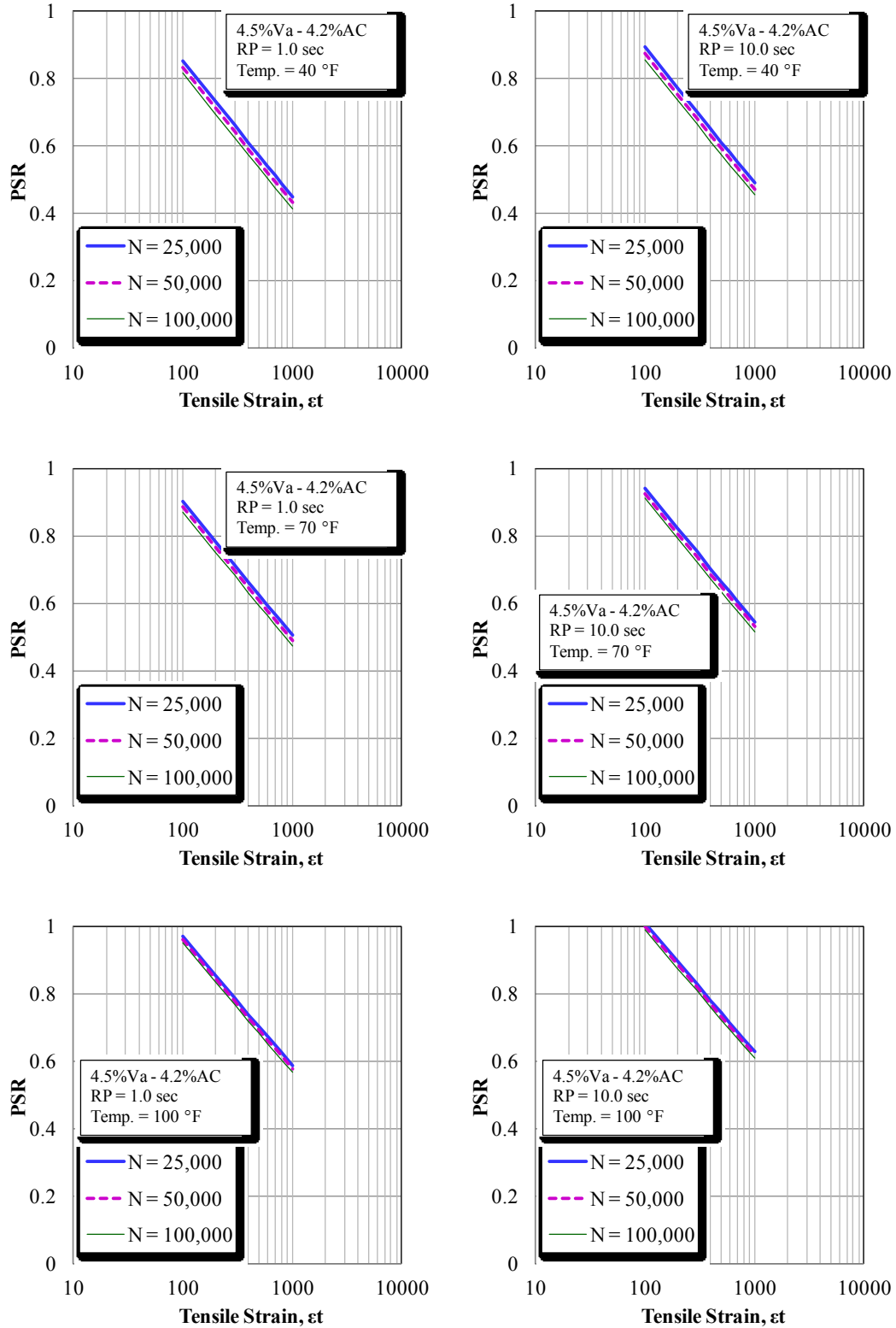


FIGURE 173 Effect N on SR- ϵ_t relationship at different RP and temperatures for the beam fatigue, PG 64-22, 4.5Va-4.2AC mixture.

The beam fatigue model was also used to predict the PSR values at different tensile strains values for each mixture type at different temperatures (4 mixtures \times 3 temperatures). FIGURES 174 to 176 show the relationship between the SR and the tensile strain for different mixtures. It is interesting that the SR- ϵ_t relationships of the beam fatigue tests show similar trends compared to those obtained in the uniaxial fatigue test. The mixtures with higher asphalt contents and lower air voids showed higher SR. In addition, the effect of asphalt content is higher compared to the effect of air voids.

The endurance limit values are calculated for mixtures at different temperatures when the SR- ϵ_t relationships intersect a SR value of 1.0. FIGURE 177 shows the endurance limit values at different temperatures for the 5 second rest period at 20,000 loading cycles. The mixtures with higher binder contents and lower air voids exhibited high endurance limit values at all test temperatures. The endurance limit values from the beam fatigue exhibits similar trends compared to those of the uniaxial fatigue test. However, the endurance limit values from beam fatigue are about 12% higher compared to those from the uniaxial fatigue test. This is an interesting finding knowing that the fatigue life using the beam fatigue test is much higher compared to the uniaxial fatigue test. This is mainly because the calculation of the endurance limit is based on healing; that is, by considering the changes of the stiffness or the pseudo stiffness and not the fatigue life extension. In addition, this comparison showed that, regardless of the fatigue test type, the asphalt mixtures are prone to heal in a similar fashion if left to rest.

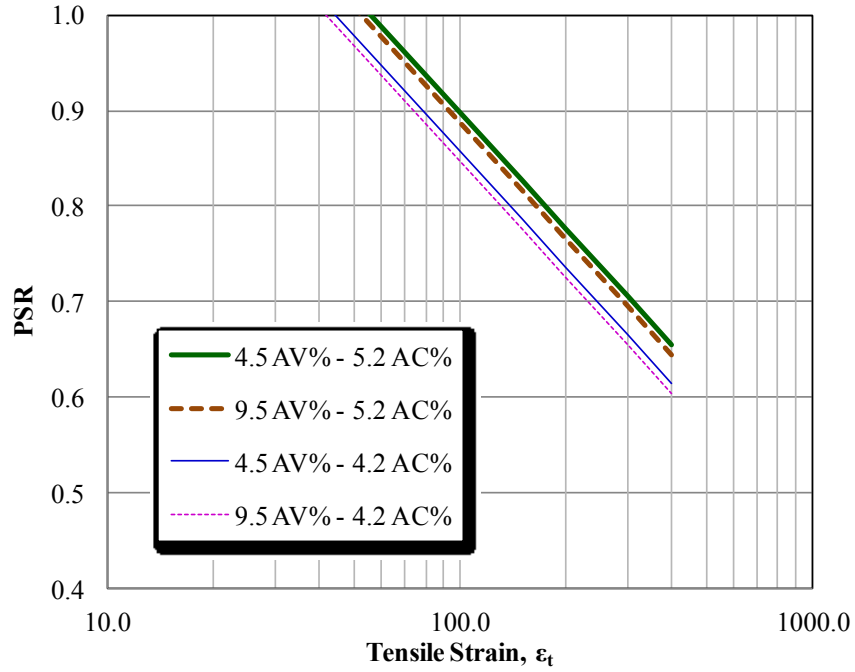


FIGURE 174 SR versus tensile strain for the beam fatigue, PG 64-22 mixtures at 40 °F (RP = 5.0 sec, and N = 20,000).

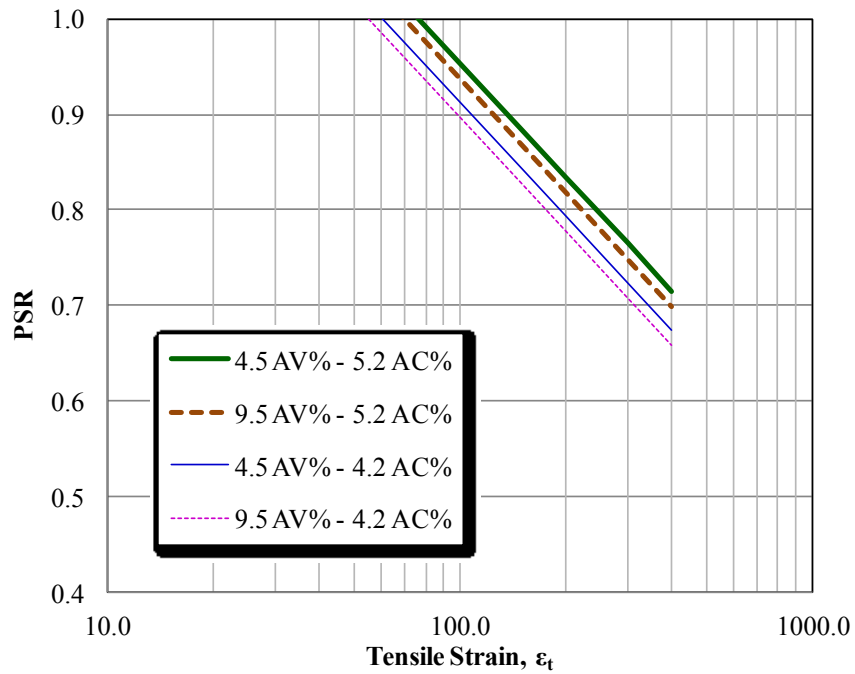


FIGURE 175 SR versus tensile strain for the beam fatigue, PG 64-22 mixtures at 70 °F (RP = 5.0 sec, and N = 20,000).

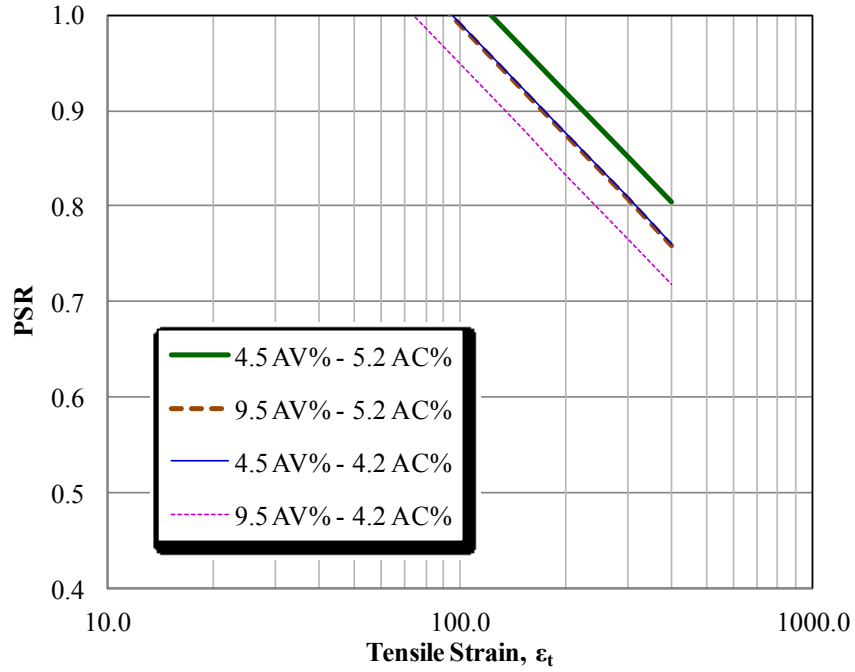


FIGURE 176 SR versus tensile strain for the beam fatigue, PG 64-22 mixtures at 100 °F (RP = 5.0 sec, and N = 20,000).

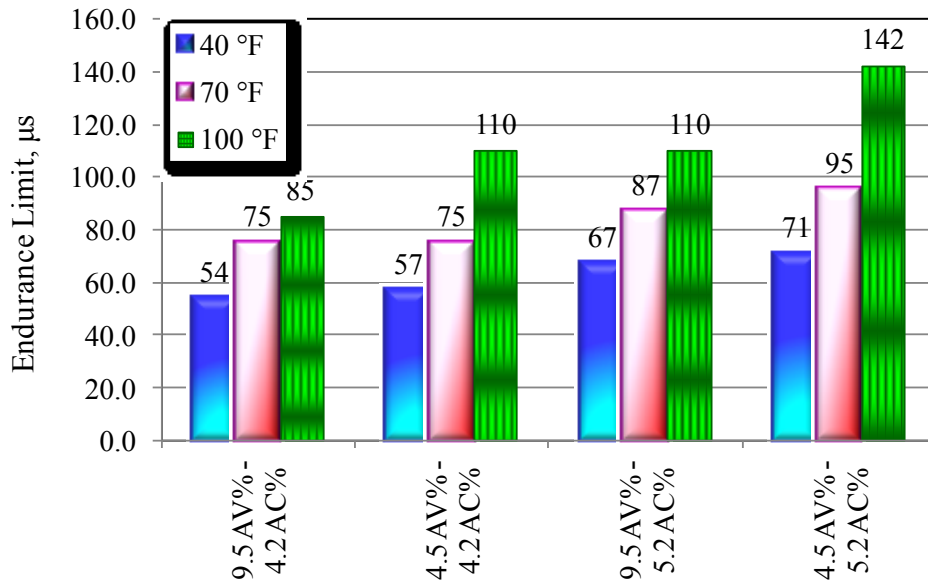


FIGURE 177 Endurance limit values for the beam fatigue, PG 64-22 mixtures at different temperatures using SR model (RP = 5 sec and N = 20,000 cycle).

FIGURE 178 includes a direct comparison of the endurance limit values obtained from the uniaxial fatigue model versus the beam fatigue model. These values were estimated for all mixtures at 5 seconds rest period, 200,000 loading cycles and three temperatures (40, 70, and 100°F). It is clear that there is a good correlation between the endurance limit values from both tests, which assures the robustness of the developed methodology to estimate the endurance limit of asphalt mixtures. The relationship between the two groups showed that the endurance limit calculated from the uniaxial fatigue test is almost 90% of the beam fatigue test values.

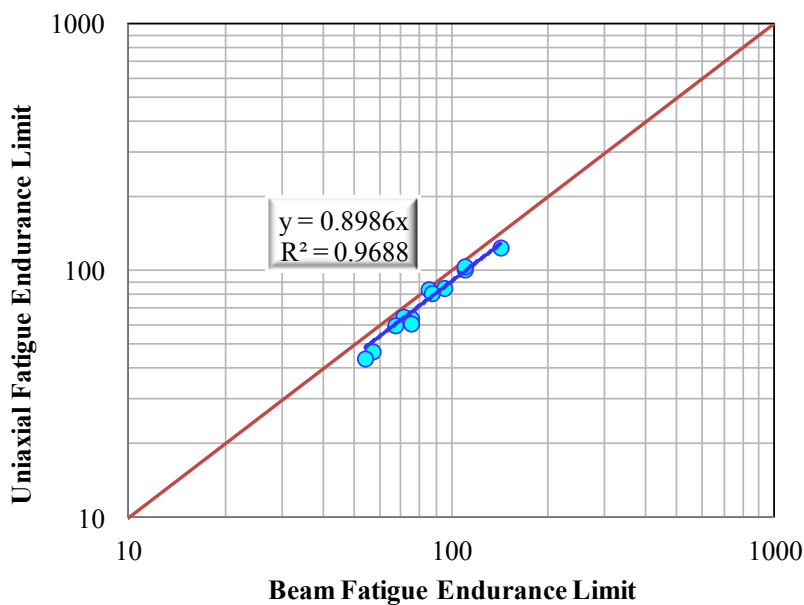


FIGURE 178 Comparison of endurance limit values for all mixtures using beam fatigue versus uniaxial fatigue test (PG 64-22, RP = 5 sec, N = 20,000 cycles).

8.5 Methodology for Incorporating the Endurance Limit into the DARWin-ME

Based on findings from the NCHRP 9-44A project, the fatigue endurance limit varies and depends on volumetric properties, stiffness of HMA and the frequency of the truck distribution. In other words, there is no single value of the endurance limit that can be input into the DARWin-ME software for all conditions. Knowing that, the current incorporation of the fatigue endurance limit in DARWin-ME software depends on inputting only one single value for all the different conditions. Therefore, the incorporation the endurance limit into DARWin-ME software requires an additional subroutine that calculates the endurance limit for the conditions used in the simulation and feeds it to the DARWin-ME software during the analysis process. The sections below discuss the proposed method for this purpose.

8.5.1 Calculation of Endurance Limit

The PSR model developed to estimate the endurance limit in the NCHRP 944-A project consists of five parameters as follows:

$$\text{PSR} = f(\varepsilon_t, E_o, N, \text{RP}) \quad (121)$$

where:

PSR = Pseudo stiffness ratio at number of cycles N

ε_t = Tensile strain, μs

E_o = Initial stiffness, ksi

N = Number of load cycles

RP = Rest period between load application, seconds

In Equation 123, when the PSR stiffness ratio is substituted with 1, the tensile strain becomes the endurance limit below which no fatigue damage occurs in the HMA layer. Although N is included in the PSR model, the results showed that N has little or no effect on the endurance limit values. A 20,000 loading cycles is recommended as a reasonable value.

The model parameters are dynamic and needs to be calculated by the DARWin-ME software for each simulation (every two hours during the pavement service life). The parameters included in the model are discussed below.

Pseudo Stiffness Ratio (PSR)

For the analysis of the fatigue endurance limit, the PSR value is always assumed to be 1.0 indicating full healing of the fatigue damage.

Initial Stiffness or Modulus (E_o)

The E_o value is a changeable parameter as the dynamic modulus (E^*) depending on the loading rate, temperature, volumetric properties. One of the differences between E_o and E^* is that E^* is measured at a strain range low enough not to induce damage (or completely healed during the rest period), where E_o is measured through a “damage” test with higher strain values. Due to damage that takes place in fatigue tests, E_o is always lower than the E^* for the same mixture. The difference between both parameters increases by increasing temperature and strain values. As the E^* is a key parameter in the calculations of DARWin-ME, it is more convenient and powerful to develop a correlation between E_o and E^* . Fortunately, and as explained before, the E^* values were measured for all the tests

using the finger print test before the uniaxial fatigue test. Using available data, an excellent relationship was found between E_o and E^* as shown in FIGURE 179. This relationship can be used to predict E_o from E^* values with high level of precision ($R^2 = 0.9875$).

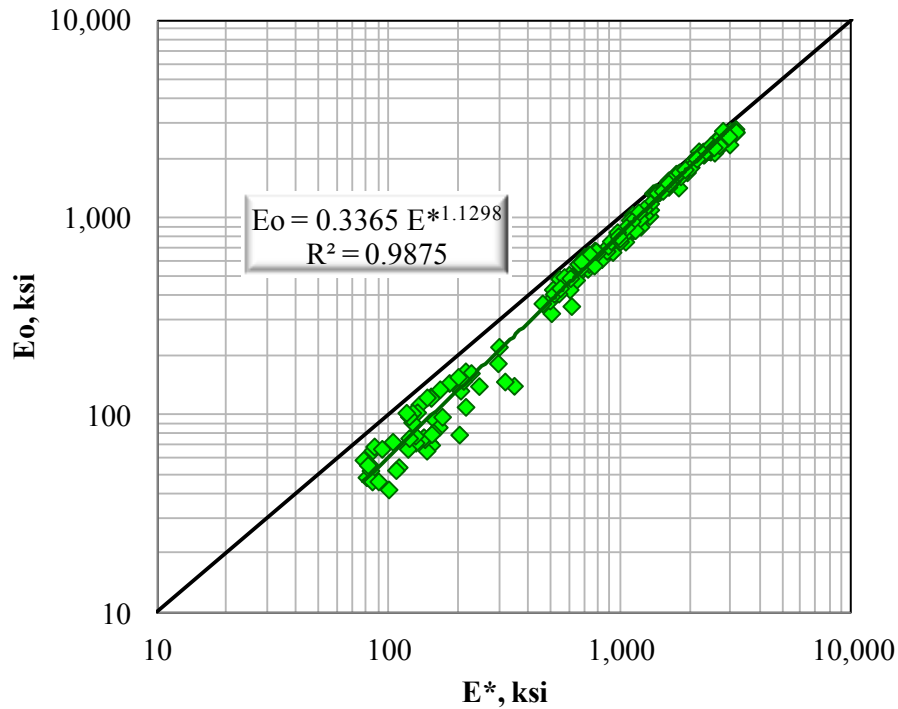


FIGURE 179 Relationship between initial stiffness and dynamic modulus using the uniaxial fatigue results.

Rest Period (RP)

The rest period between truck axles in seconds is calculated as an average value every two hours in the DARWin-ME simulations. This would require the calculation of the actual truck spectrum every 2 hours as shown in FIGURE 180.

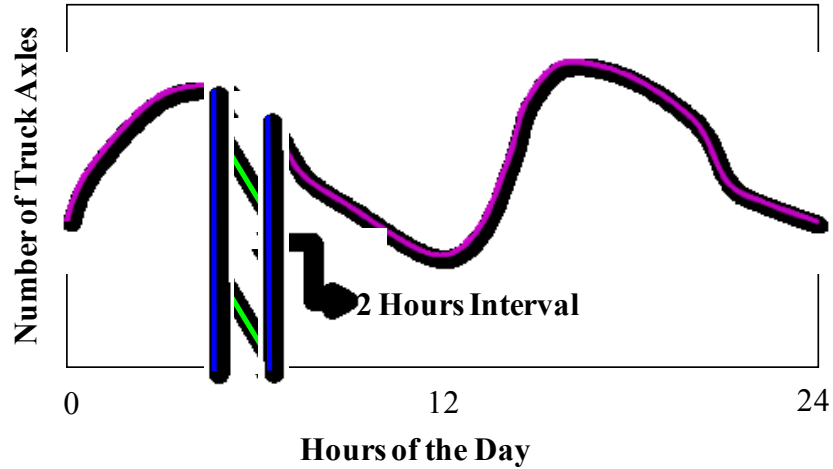


FIGURE 180 Assumed truck axle distribution during the 24 hours of the day.

The RP value in this case can be calculated as follows:

$$RP = 3,600 \times 2 / \sum(NT \cdot NA) \quad (122)$$

where,

NT = Number of trucks in the 2-hour increment considered in the analysis

NA = Average number of axles in each truck.

Once all the different parameters are calculated, the model in Equation 123 can be solved for the endurance limit, which is the strain at a stiffness ratio of 1. This calculation will be done every two hours during the DARWin-ME simulations.

8.5.2 Incorporating Endurance Limit into Fatigue relationships

The model used for the calculation of the fatigue damage in the DARWin-ME is as follows:

$$N_f = C \times k_1 (1/\epsilon_t)^{k_2} (1/E_o)^{k_3} \quad (123)$$

where:

- N_f = Number of repetitions to fatigue failure,
- ϵ_t = Tensile strain at the critical location,
- E_0 = Initial stiffness of the HMA,
- k_1, k_2, k_3 = Laboratory regression coefficients, and
- C = Laboratory to field adjustment factor.

The DARWin-ME divides the structural layers of the HMA layer into sub-layers. The JULEA program then calculates the critical tensile strain every two hours. The values K_1, K_2, K_3 calculated and calibrated based on the fatigue tests without rest period are used to determine the fatigue lives at different temperatures. The endurance limit approach developed in this study is based mainly on the fatigue healing using the results of the fatigue test with rest period. To incorporate the endurance limit concept with the fatigue lives used to calculate the fatigue damage in the DARWin-ME simulations, the fatigue lives are considered to be infinity when the strain level is equal to the endurance limit. This means the fatigue life versus the tensile strain relationship becomes a horizontal line at a strain value equal to the endurance limit. For each fatigue relationship, a corresponding endurance limit value is calculated at the same E_0 but at different rest periods using the second generation PSR model, which is a function of E_0 . FIGURES 181 to 183 show examples of incorporating of the endurance limit with fatigue relationships using different rest periods.

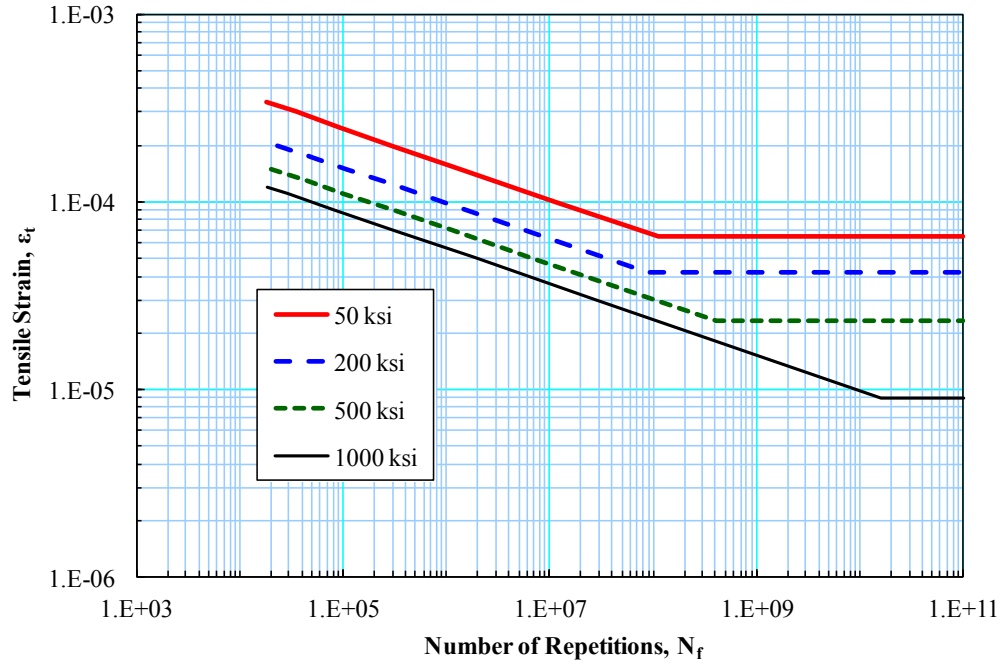


FIGURE 181 Fatigue relationships for different stiffness values at 2 second rest period.

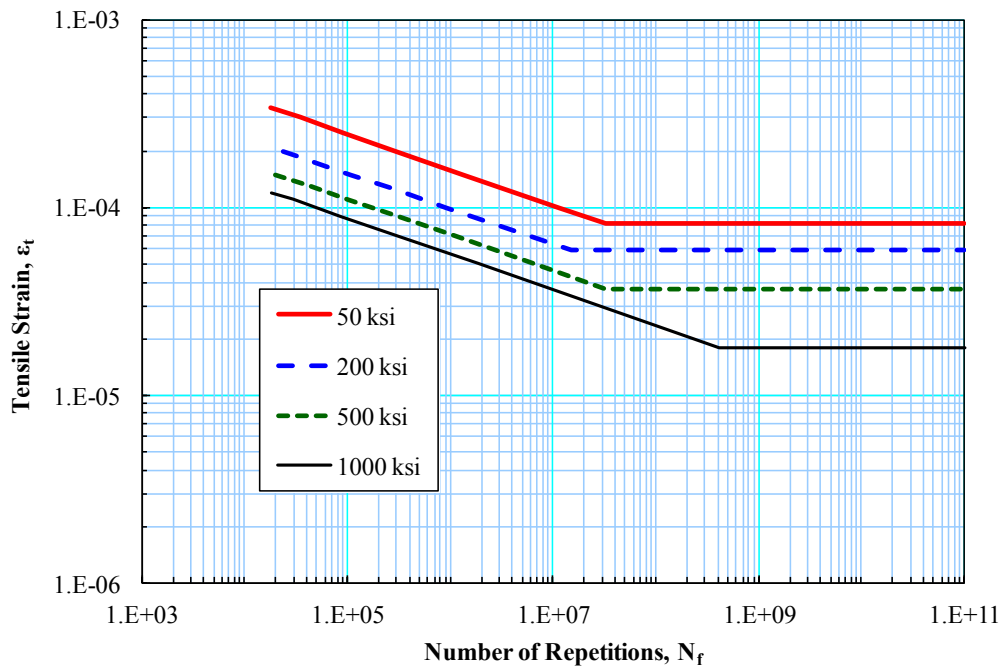


FIGURE 182 Fatigue relationships for different stiffness values at 5 second rest period.

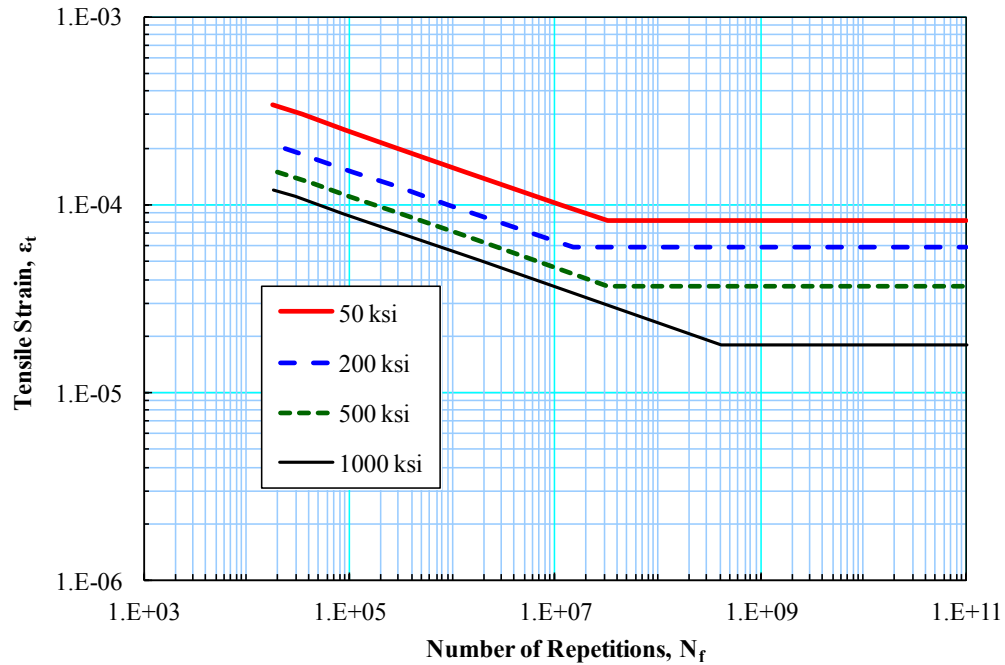


FIGURE 183 Fatigue relationships for different stiffness values at 20 second rest period.

8.5.3 Incorporating Endurance Limit into Fatigue Damage

The estimation of the fatigue damage in the DARWin-ME is based on Miner's law given by Equation 124.

$$D_i = \sum (n_i / N_i) \quad (124)$$

where:

D = Damage,

n_i = Actual traffic for period i, and

N_i = Traffic allowed under conditions prevailing in period i.

The endurance limit is calculated every two hours as discussed before. At the same time, the critical strain value of the HMA layer (or sub-layer) for each

truck axle is calculated using the JULEA program. If the critical strain calculated from the JULEA program is less than or equal to the fatigue endurance limit, the value of N_i calculated from the fatigue life relationships is equal to infinity, which means n_i/N_i is equal to zero. This means the fatigue damage inducted by that axle load is not counted in the analysis. However, if the critical strain is greater than the fatigue endurance limit, the axle is counted as causing fatigue damage.

CHAPTER 9

SUMMARY, CONCLUSIONS AND RECOMMENDATIONS FOR FUTURE RESEARCH

9.1 Summary

The main objective of this research was to validate and determine fatigue endurance limit models, based on uniaxial fatigue tests that can be used as input into the DARWin-ME software.

This study included testing of four HMA mixtures using two levels each of air voids and asphalt contents. Three asphalt binders (PG 58-28, PG 64-22 and PG 76-16) were used for the dynamic modulus test and one binder (PG 64-22) was used in the uniaxial fatigue test. One aggregate type and gradation was used in the study. The Superpave binder testing, aggregate testing, and Superpave mix design were conducted by MACTEC consulting company. Additional binder tests were conducted at the ASU laboratory.

The estimation of the endurance limit in this study was defined as the allowable tensile strains at which the micro-cracks damage due to load is balanced with the healing during the rest periods. To account for the damage and healing due to fatigue, the viscoelastic continuum damage analysis was applied. To determine the viscoelastic properties required for the viscoelastic continuum damage analysis, dynamic modulus tests were conducted according to the AASHTO TP 62-07 procedure, and the Proney's series coefficients were determined for the tested mixtures. An immense effort was done by conducting several essential studies to develop a proposed uniaxial fatigue test protocol that

accounts for tests conducted with and without rest periods. These studies included: specimen preparation and fixture adjustments, specimen geometry and air void distribution, strain control, and machine compliance. In addition, two new test software programs were developed through collaboration between ASU and IPC Company to conduct the tests with and without rest period.

Comprehensive laboratory uniaxial fatigue test experiments were conducted and included three major experiments. The first experiment was the fatigue life experiment. The main objective of this experiment was to establish the N_f - ϵ_t relationships at different temperatures to determine the proper strain levels for each asphalt mixtures that would fail specimens at 20,000 and 100,000 loading cycles. The second experiment was the main experiment to study the effect of five factors on the fatigue damage and healing by conducting uniaxial fatigue tests with and without rest periods. These factors were asphalt content, air voids, strain, rest period, and temperature. Each factor was represented by two levels except for temperature, where three levels were used. A third uniaxial fatigue experiment was introduced to account for additional strain levels and rest periods to study the non-linearity effects. A total of 54 dynamic modulus tests and 182 uniaxial fatigue tests were performed.

The data for the three uniaxial fatigue experiments were combined together to develop Pseudo Stiffness Ratio (PSR) models using a total number of 161 test results. Two PSR regression models were developed. The first PSR model included the main five factors plus one additional factor, which is the number of loading cycles N at which the PSR values were measured. The second

PSR regression model was developed by replacing three factors (air voids, asphalt content, and temperature) with the initial stiffness. The endurance limit was estimated using both models as the allowable tensile strain when PSR is equal to 1.0.

To compare the endurance limits from the uniaxial fatigue tests to those obtained from the beam fatigue tests, a stiffness ratio (SR) model was developed based on beam fatigue tests conducted in a companion study. The beam fatigue SR regression model included six factors similar to those of the uniaxial PSR regression model and the endurance limits were determined. The last task of this study was to demonstrate a process to incorporate the endurance limit calculated from the PSR model into fatigue analysis and damage using the DARWin-ME software.

9.2 Conclusions

The following conclusions were drawn from this research.

9.2.1 Viscoelastic Properties

- The effect of air voids on the dynamic modulus master curves was clear within the selected ranges, in which dynamic modulus master curves were shifted from each other in a parallel pattern. Increasing the air voids resulted in lowering the dynamic modulus master curves.
- There was no common trend for the effect of the binder content on the E^* master curves for all tested mixtures. However, a certain trend may be captured for each PG binder mixtures separately. For the PG 64-22 mixtures, the E^* master curves at different binder contents were overlapped

with no specific trend. In the case of PG 58-28 mixtures, the lower the binder content, the higher the E^* values. The master curves of the PG 76-16 mixtures at the optimum asphalt content (OAC) showed higher E^* values compared to those with $OAC \pm 0.5\%$.

- The effect of the asphalt content (OAC and $OAC \pm 0.5\%$) on the dynamic modulus master curves was less compared to the effect of the air void range (design value $\pm 2.5\%$ or $\pm 3.0\%$)
- The effect of changing air void and binder content on the E^* master curves was very accurately predicted using regression models that correlate both volumetric and sigmoidal parameters.
- The approach developed in this study can be applied to QA/QC analysis, especially if the project contract considered the pavement performance predicted by the MEPDG as a basis to penalties or bonuses. In this case, this approach would save extensive testing, and at the same time would accurately predict the dynamic modulus values due volumetric changes.

9.2.2 Development of Uniaxial Fatigue Protocol and Software

- The use of aluminum platens are better than steel in providing better cohesion between specimen and platens.
- Loctite metal/concrete epoxy, Loctite Fixmaster Superior Metal and Davcon plastic steel liquid (10210) are appropriate for 3-inch diameter specimens. ACE Plastic repair epoxy is suitable for 4-inch diameter specimen.

- Three inch diameter specimens have higher tendency to fail within the middle of the specimen, while the 4-inch diameter specimens usually fail more frequently near to the end platens.
- The thread locked joint is better than the slipped locked joint to decrease the machine compliance factor.
- Increasing the compaction height from 6.7-inch (170-mm) to 7.1-inch (180-mm) increases the chances of having a successful test where failure takes place in the middle of the specimen from 20 % to 83%.
- The on-specimen strain values using the crosshead controlled-strain method cannot be kept constant, but increase with time.
- Controlling the strain directly from the on-specimen LVDTs is unsafe. The wave shape of the load and strain waveform becomes distorted when the test is controlled by the average on-specimen LVDTs.
- The tension-compression test (sinusoidal) diminishes the permanent deformation compared to the direct-tension test (haversine).
- For the strain controlled uniaxial fatigue test, the haversine test condition cannot be maintained during the test, as it will switch quickly to a sinusoidal wave shape.

9.2.3 Results of the Uniaxial Fatigue Experiments

- The 50% stiffness reduction or pseudo stiffness reduction criterion seems to be an applicable definition for fatigue failure at all test temperatures. On the other hand, the definition of fatigue failure where there is a sharp decrease

of the phase angle is not usually valid as the test results at high temperatures (e.g., 100°F) did not show the behavior of phase angle sharp drop.

- The selection of initial stiffness to be at the 100th cycle significantly improved the fitting of the fatigue life relationships especially at 100°F compared to the initial stiffness at the 50th cycle.
- For all test temperatures, increasing the asphalt content by 1% (from 4.2 to 5.2) increased the fatigue life and k_2 values more compared to decreasing the air voids by 5% (from 9.5 to 4.5).
- For the generalized fatigue model, the lower the air voids the lower the k_2 and k_3 values. Also, increasing the asphalt content reduces both k_2 and k_3 values.
- For the individual fatigue lives, the k_2 values for uniaxial tension-compression fatigue test were higher compared to the historical beam fatigue test. This means that the fatigue damage caused by the uniaxial fatigue test is higher compared to the beam fatigue test.
- Based on test results, increasing the rest period from 5 to 10 seconds (50 to 100 loading ratio) did not show an increase in the healing value when comparing the PSR values for both rest periods.
- Introducing one second rest period showed around 50% increase on the PSR compared to the test without rest period.

9.2.4 Development of PSR Regression Models and Endurance Limit Analysis

- Regression PSR models developed by the non-linear optimization approach showed more accurate prediction compared to the models developed by the non-linear regression analysis.
- The Evolver® software reduced the sum of square error and increases the accuracy of the regression models compared to Solver® function and Statistica® Software to perform the non-linear optimization analysis.
- Using the tangent hyperbolic (Tanh) function to fit the PSR and rest period relationship increased the accuracy of the models.
- For the first and second generation PSR models, the optimum rest period values for all tested mixtures were 3 seconds (loading ratio of 30) for all test temperatures. This optimum rest period fits in the middle range of optimum rest periods (1 to 5 seconds or 10 to 50 loading ratio) collected from literature research work.
- The effect of N on the endurance limit value when PSR is equal to 1.0 was minimal.
- Mixtures with higher asphalt content and lower air voids exhibit higher endurance limit values.
- The effect of asphalt content is much more significant than the air voids on the fatigue healing and endurance limit.
- The endurance limits almost doubled by increasing the temperature from 40 to 70°F for the four asphalt mixtures.

- For the second generation PSR model, significant simplification was achieved by replacing the air voids, asphalt content, and temperature with the initial stiffness. In addition, the second generation PSR model is more compatible with the DARWin-ME software, where the pavement performance prediction is mainly driven by the dynamic modulus of the HMA mixture.
- The only concern in replacing the stiffness with the volumetric parameters is that a mixture with very high asphalt content that is stiff would show the same modulus for a mixture with very low asphalt binder that is soft. However, the expected fatigue damage and healing could be totally different. This even can be taken to the extreme by having the same stiffness from two mixtures. The first mixture is very rich with asphalt and well compacted; while the second mixture has low asphalt content and poorly compacted. The first mixture represents the best condition for fatigue resistance and healing, although the fatigue and healing performance of the second mixture should be the worst. The irregular stiffness effect can be reduced by having a data base with a larger number of factors.
- The endurance limits estimated by the second PSR model were 25% less compared to those of the first model.
- The endurance limit values determined from uniaxial and beam fatigue tests showed very high correlation with the fact that the uniaxial fatigue endurance limit is almost 10% less than that of the beam fatigue test.

- The incorporation of the developed methodology into DARWin-ME was successfully elaborated.

9.3 Recommendations for Future Research

Based on the main outcomes of this study, the following recommendations are made for future research:

- The laboratory experimental work of this study was conducted using only the PG 64-22 binder. Considering other PG binders is important to have the effect of the binder type on the fatigue healing and endurance limit. In addition, the effect of aggregate types and gradation requires further investigation.
- The effect of specimen geometry on the fatigue damage, healing, and endurance limit is need to be investigated further.
- With the high increase of using modified asphalt mixtures, it is important to replicate this study using different modified mixtures such as rubber-modified mixtures, polymer-modified mixtures, warm mix asphalt, and fiber-reinforced asphalt mixtures.
- The current study was based on laboratory tests only. Verification and calibration are still needed by either field observations or accelerated pavement testing.

REFERENCES

- American Association of State Highway and Transportation Officials. Bulk Specific Gravity of Bituminous Mixtures Using Saturated Surface Dry Specimens, Test Method AASHTO T 166 – 00, Standard Specifications for Transportation Materials and Methods of Sampling and Testing, *Part II – Tests*, Twentieth Edition, 2000.
- American Association of State Highway and Transportation Officials. Determining the Fatigue Life of Compacted Hot-Mix Asphalt (HMA) Subjected to Repeated Flexural Bending, Test Method T321-03, *AASHTO Provisional Standards*, Washington, D.C., 2003.
- American Association of State Highway and Transportation Officials. Determining Dynamic Modulus of Hot-Mix Asphalt Concrete Mixtures, Test Method AASHTO TP 62-03, *AASHTO Provisional Standards*, Washington D.C., 2006.
- American Association of State Highway and Transportation Officials. Theoretical Maximum Specific Gravity of Bituminous Mixtures, Test Method AASHTO T 209 – 00, Standard Specifications for Transportation Materials and Methods of Sampling and Testing, *Part II – Tests*, Twentieth Edition, 2000.
- Abojaradeh, M. *Predictive Fatigue Models for Arizona Asphalt Concrete Mixtures*, Ph.D. Dissertation, Arizona State University, Tempe AZ, December 2003.
- Advanced Asphalt Technologies, LLC, *Hot Mix Asphalt Endurance Limit Workshop: Executive Summary*, National Cooperative Highway Research Program Project 9-44, 2007.
- Aglan, H., and Figueroa, L. Technical Report, U.S Corps of Engineer, *Waterways Experiment Station*, Contact No: DACA39-90-K0023, December, 1991.
- Al-Khateeb, G., and Shenoy, A. A Simple Quantitative Method for Identification of Failure due to Fatigue Damage, *International Journal of Damage Mechanics*, Vol. 20, pp 3-21, 2011.
- Al-Khateeb, G., and Shenoy, A. *A Distinctive Fatigue Failure Criterion*, Journal of the Association of Asphalt Paving Technologists (AAPT), Vol. 73, pp. 585-622, 2004.

- Anderson, D.A., Christensen, D.W. and Bahia, H. Physical Properties of Asphalt Cement and the Development of Performance Related Specifications, *Journal of the Association of Asphalt Paving Technologists (AAPT)*, Vol. 60, pp. 437-475, 1991.
- Anderson, T.L. *Fracture Mechanics: Fundamentals and Applications*, CRC, Pr, 2nd Eddition, February, 1995.
- Asphalt Pavement Alliance (APA). *Perpetual Pavements: A Synthesis*, APA 101, Asphalt Pavement Alliance, Lanham, MD, 2002.
- Bahia, H., Zhai, H., Bonnetti, K., and Kose, S. Non-linear viscoelastic and fatigue properties of asphalt binders, *Journal of the Association of Asphalt Paving Technologists (AAPT)*, Vol. 68, pp. 1–34, 1999.
- Balbissi, A.H. *A comparative Analysis of the Fracture and Fatigue Properties of Asphalt Concrete and Sulphex*, Ph.D. Dissertation, Texas A&M University, College Station, Texas, 1983.
- Barksdale, R.D. and Miller, J. H., III. *Development of Equipment and Techniques for Evaluating Fatigue and Rutting Characteristics of Asphalt Concrete Mixes*, Report SCEGIT-77-147, School of Civil Engineering, Georgia Institute of Technology, Atlanta, 1977.
- Bazin, P., and Saunier, J. Deformability, Fatigue and Healing Properties of Asphalt Mixes, *Proceedings of the 2nd International Conference of Structural Design of Asphalt Pavements*, Ann Arbor, Michigan, pp. 553-569, 1967.
- Bhattacharjee, S., Swamy, A.K., and Daniel, J.S. *Application of the Elastic-Viscoelastic Correspondence Principle to Determine the Fatigue Endurance Limit of Hot Mix Asphalt*, Transportation Research Record 2126, Transportation Research Board of the National Academies, pp. 12-18, Washington D.C, 2009.
- Biligiri, K.P., Kaloush, K.E, and Uzan, j. Evaluation of Asphalt Mixtures' Viscoelastic Properties Using Phase Angle Relationships, *International Journal of Pavement Engineering*, Vol. 11, Issue 2, pp. 143-152, April 2010.

- Bonaquist, R.F. *Developing a Plan for Validating an Endurance Limit for HMA Pavements*, NCHRP 9-44, National Cooperative Highway Research Program, HMA Workshop Executive Summary, 2007.
- Bonnaure, F., Gravois A., and Udron, J. A New Method for Predicting The Fatigue Life of Bituminous Mixes, *Journal of the Association of Asphalt Paving Technologists (AAPT)*, Vol. 49 Proc., Louisville, KY, February 1980.
- Bonnaure, F., Huibers, A., and Boonders, A. A Laboratory Investigation of the Influence of Rest Periods on the Fatigue Characteristics of Bituminous Mixes, *Journal of the Association of Asphalt Paving Technologists (AAPT)*, Kansas City, Missouri, Vol.51, pp.104-128, 1982.
- Bonnot, J. *Asphalt Aggregate Mixtures*, Transportation Research Record 1096, Transportation Research Board of the National Academies, Washington, D. C., pp. 42-50, 1986.
- Breysse, D., Roche, C.D.L., Domee, V., and Chauvin, J. J. *Influence of Rest Time on Recovery and Damage during Fatigue Tests on Bituminous Composites*, Proceedings of 6th RILEM Symposium PTEBM' 03, Vol. 36, pp. 648-651, Zurich, 2003.
- Brown, E., Cooley, L., Hanson, D., Lynn, C., Powell, B., Prowell, B., and Watson, D. *NCAT Test Track Design, Construction, and Performance*, NCAT Report 2002-12, National Center for Asphalt Technology, Auburn University, 2002.
- Button, J.W., Little, D.N., Kim, Y., and Ahmed, S.J. Mechanistic evaluation of selected asphalt mixes, *Journal of the Association of Asphalt Paving Technologists (AAPT)*, Vol. 56, pp. 62-90, 1987.
- Carpenter, S. H., Ghuzlan, K, and Shen, S. *Fatigue Endurance Limit for Highway and Airport Pavements*, Transportation Research Record 1832, Journal of the Transportation Research Board, pp. 131-138, National Research Council, Washington D.C., 2003.
- Carpenter, S.H. *Fatigue Performance of IDOT Mixtures*, Civil Engineering Studies, Illinois Center for Transportation Series No 07.-007, University of Illinois at Urbana-Champaign, July, 2006.

- Carpenter, S.H., and Jansen, M. *Fatigue Behavior Under New Aircraft Loading Conditions*, Proceedings of Aircraft Pavement Technology in the Midst of Change, pp. 259- 271, 1997.
- Carpenter, S.H., and Shen, S. *Application of the Dissipated Energy Concept in Fatigue Endurance Limit Testing*, Transportation Research Record 1929, Transportation Research Board of National Academies, pp. 165-173, 2005.
- Carpenter, S.H., and Shen, S. *Dissipated Energy Approach to Study Hot-Mix Asphalt Healing in Fatigue*, Transportation Research Record 1970, Transportation Research Board of National Academies, Washington, D.C., 2006.
- Carpenter, S.H., Ghuzlan, K., and Shen, S. *Fatigue Endurance Limit for Highway and Airport Pavements*, Transportation Research Record 1832, Transportation Research Board of National Academies, Washington, DC., pp. 131-138, 2003.
- Castro, M. and Sanchez, J.A. Fatigue and Healing of Asphalt Mixtures: Discriminate Analysis of Fatigue Curves, *Journal of Transportation Engineering*, ASCE, Vol. 132, No. 2, pp. 168-174, 2006.
- Chehab, G., Kim, Y.R., Schapery, R.A., Witzack, M., and Bonaquist, R. Time-Temperature Superposition Principle for Asphalt Concrete Mixtures with Growing Damage in Tension State, *Journal of the Association of Asphalt Paving Technologists (AAPT)*, Vol. 71, pp. 559-593, 2002.
- Chehab, G.R. *Characterization of Asphalt Concrete in Tension Using a Viscoelastoplastic Model*, PhD Thesis, North Carolina State University, Raleigh, North Carolina, USA, 2002.
- Chehab, G.R., O'Quinn, E., and Kim, Y.R. *Specimen Geometry Study for Direct Tension Test Based on Mechanical Tests and Air Void Variation in Asphalt Concrete Specimens Compacted by SGC*. In Transportation Research Record 1723, Transportation Research Board of National academies, Washington D.C., pp. 125-1332, 2000.
- Chen, C.W. *Mechanistic Approach to The Evaluation of Microdamage in Asphalt Mixes*, PhD thesis, Texas A&M University, College Station, Texas, 1997.

- Chomton, J.S., and Valayer, P.J. *Applied Rheology of Asphalt Mixes, Practical Applications*, Proceedings of 3rd International Conference on the Structural Design of Asphalt Pavements, London, vol. I, 1972.
- Chowdary, V. *Experimental Studies on Healing Of Asphalt Mixtures*, International Symposium of Research Students on Materials Science and Engineering, Department of Metallurgical and Materials Engineering, Indian Institute of Technology Madras, India, 2004.
- Christensen, D.W., and Bonaquist, R.F. Practical Application of Continuum Damage Theory to Fatigue Phenomena in Asphalt Concrete Mixtures, *Journal of the Association of Asphalt Paving Technologists (AAPT)*, Vol. 74, , pp. 963–1002, 2005.
- Christensen, D.W., and Bonaquist, R.F. Analysis of HMA Fatigue Data Using the Concepts of Reduced Loading Cycles and Endurance Limit, *Journal of the Associations of Asphalt Paving Technologists (AAPT)*, vol. 78, pp. 377-416, 2009.
- Cowher, K. *Cumulative Damage of Asphalt Materials under Repeated-Load Indirect Tension*, Research Report Number 183-3, Center for Highway Research – University of Texas at Austin, Austin, TX, 1975.
- Cox W.P., and Merz, E.H. *Correlation of Dynamic and Steady Flow Viscosities*. *Journal of Polymer Sciences*, Vol. 28, pp. 619-622, 1958.
- Daniel, J.S., and Kim, Y.R. *Development of a Simplified Fatigue Test and Analysis Procedure Using a Viscoelastic, Continuum Damage Model*, *Journal of the Association of Asphalt Paving Technologists*, Vol. 71, Pp. 619–650, 2002.
- Daniel, J.S., and Kim, Y.R. *Laboratory Evaluation of Fatigue Damage and Healing of Asphalt Mixtures*, *Journal of Materials in Civil Engineering*, Vol. 13, No. 6, pp. 434–440, 2001.
- Daniel, J.S. *Development of a simplified fatigue test and analysis procedure using a viscoelastic, continuum damage model and its implementation to Westrack mixtures*, Ph.D. dissertation, North Carolina State University, Raleigh, 2001.

Douglas, R.A., and Holt, J.D. *Determining Length of Installed Timber Pilings by Dispersive Wave Propagation Methods*, Final Report Research Project 23241-92-2. North Carolina Department of Transportation, FHWA, U.S. Department of Transportation, June 1993.

El-Basyouny, M., and Witczak, M. *Development of the Fatigue Cracking Models for the 2002 Design Guide*, Presented at the 84th Annual Meeting of the Transportation Research Board, January 2005.

Elliot, R.P., and Thompson, M.R. *Mechanistic Design Concepts for Conventional Flexible Pavements*, Transportation Engineering Series No. 42, University of Illinois, Urbana, IL, February 1986.

Epps, J.A. and Monismith, C.L. Influence of Mixture Variables on the Flexural Fatigue Properties of Asphaltic Concrete, *Journal of the Association of Asphalt Paving Technologists (AAPT)*, Vol. 38, pp. 423-464, 1969.

Evolver Software, <http://www.palisade.com/evolver/>

Ferne, B. *Long-Life Pavements – A European Study by ELLPAG*, *International Journal of Pavement Engineering*, Vol. 7, No. 2, pp 91-100, 2006.

Ferry, J.D. *Viscoelastic Properties of Polymers*, 3rd edn. John Wiley and Sons, New York, 1980.

Finn, F., Saraf, C.L., Kulkarni, K., Nair, K., Smith, W., and Abdullah, A. *Development of Pavement Structural Subsystems*, Final Report, Project 1-10B, February 1977.

Franken, L. *Fatigue Performance of a Bituminous Road Mix under Realistic Test Condition*, Transportation Research Record 712, Transportation Research Board of National Academies, Washington D.C., pp. 30-36, 1979.

Freund, L.B., and Suresh, S. *Thin Film Materials: Stress, Defect Formation and Surface Evolution*, Cambridge, UK, Cambridge University Press, 2003.

Germann, F.P., and Layton, R.L. *Methodology for Predicting the Reflective Cracking Life of Asphalt Concrete Overlays*, Texas Transportation Institute, TTI-2-8-75-207-5, 1979.

- Ghuzlan, K.A. *Fatigue Damage Analysis in Asphalt Concrete Mixtures Based Upon Dissipated Energy Concepts*, Ph.D. Dissertation, University of Illinois at Urbana-Champaign, August 2001.
- Ghuzlan, K., and Carpenter, S.H. *An Energy-Derived/Damage-Based Failure Criteria for Fatigue Testing*, Transportation Research Record 1723, Transportation Research Board of the National Academies, pp. 131- 141, 2000.
- Griffith, A.A. *The Phenomena of Rupture and Flaw in Solids*, Philosophical Transactions of the Royal Society, London, Series A, Vol. 221, 1921.
- Harvey, J.T., Deacon, J.A., Taybali, A.A. , and Leahy, R.B. *A Reliability-Based Mix Design and Analysis System for Mitigating Fatigues Distress*. Proceedings of the 8th International Conference on Asphalt Pavements, Vol. 1. University of Washington, Seattle, WA, pp. 301-323, August 1997.
- Hilton, H.H., and Yi., S. Analytical Formulation of Optimum Material Properties for Viscoelastic Damping, *Journal of Smart Materials and Structures*, Vol. 1, pp. 113–122, 1992.
- Hopman, P.C., Kunst, P.A.J.C. and Pronk, A.C. *A Renewed Interpretation Method for Fatigue Measurements, Verification of Miner's Rule*, Proceedings of 4th Eurobitume Symposium in Madrid, Vol. 1, pp. 557-561, 1989.
- Hou, T. *Fatigue Performance Prediction of North Carolina Mixtures Using Simplified Viscoelastic Continuum Damage Model*, Ms.C Thesis, North Carolina State University, Raleigh, North Carolina, 2009.
- Hou, T., Underwood, B.S., and Kim, Y.R. Fatigue Performance Prediction of North Carolina Mixtures Using the Simplified Viscoelastic Continuum Damage Model, *Journal of the Association of Asphalt Paving Technologists (AAPT)*, Vol. 79, pp. 35-73, 2010.
- Hsu, T.W., and Tseng, K.H. Effect of Rest Periods on Fatigue Response of Asphalt Concrete Mixtures, *Journal of Transportation Engineering*, American Society of Civil Engineering, Vol. 122, No. 4, PP. 316-322, 1996.

- Huang, Y.H. *Material Characterization and Performance Properties of Superpave Mixtures*, Ph.D. Dissertation, North Carolina State University, Raleigh, 2004.
- Huang, Y.H. *Pavement Analysis and Design*. Prentice-Hall Englewood Cliffs, NJ, 1993.
- Jacobs, M. M. J. *Crack Growth in Asphaltic Mixes*, Ph.D. Thesis, Delft University of Technology, the Netherlands, 1995.
- Jacobs, M.M.J., Hopman, P. C. and Molenaar, A.A.A. Application of Fracture Mechanics Principles to Analyze in Asphalt Concrete, *Journal of the Association of Asphalt Paving Technologists (AAPT)*, Vol. 65, pp. 1-39, 1996.
- Jeong M.G. *Implementation of Simple Performance Test Procedure in Hot Mix Asphalt Quality Assurance Program*. Ph.D. Thesis, Arizona State University, Tempe, Arizona, 2010.
- JMP software, SAS Institute Inc, <http://www.jmp.com/>.
- Kallas, B. Dynamic Modulus of Asphalt Concrete in Tension and Tension-Compression, *Journal of the Association of Asphalt Paving Technologists (AAPT)*, vol. 39, pp. 1-20, 1970.
- Kaloush, K.E., Mello, L.G. *Continuum Damage Theory Applied for Asphalt Rubber Mixtures*, Report No. FHWA-AZ-08-644, Final Report Submitted to Arizona Department of Transportation, Arizona State University, Tempe, Arizona, USA, 2009.
- Kennedy, T.W. Characterization of asphalt pavement material using the indirect tensile test, *Journal of the Association of Asphalt Paving Technologists (AAPT)*, Vol. 46, 1977.
- Kim, Y. and Kim, Y.R. *In-Situ Evaluation of Fatigue Damage Growth and Healing of Asphalt Concrete Pavements Using Stress Wave Method*, Transportation Research Record 1568, National Research Council, Washington, D.C., pp. 106-113, 1997.

- Kim, Y.R. *Evaluation of Healing and Constitutive modeling of Asphalt Concrete by Means of the Theory of Nonlinear Viscoelasticity and Damage Mechanics*, Ph.D Dissertation, Texas A&M University, College Station, Tex, 1988.
- Kim, Y.R. *Mechanistic Fatigue Characterization and Damage Modeling of Asphalt Mixtures*, Ph.D. Dissertation, Texas A&M University, College Station, Texas, August 2003
- Kim, Y.R., Lee, H.J, Kim, Y, and Little, D.N. *Mechanistic Evaluation of Fatigue Damage Growth and Healing of Asphalt Concrete: Laboratory and field experiments*, Proceedings of the 8th International Conference on Asphalt Pavements, ISAP, Seattle, Washington, pp. 1089-1107, August 1997b.
- Kim, Y.R., Lee, H.J., and Little, D.N. Fatigue Characterization of Asphalt Concrete Using Visco-elasticity and Continuum Damage Theory, *Journal of the Association of Asphalt Paving Technologists (AAPT)*, Vol. 66, pp. 520-569, 1997a.
- Kim, Y.R., Little, D.N., and Benson, F. Chemical and Mechanical Evaluation on Healing Mechanism of Asphalt Concrete, *Journal of the Association of Asphalt Paving Technologists (AAPT)*, Vol. 59, pp.240-276, 1990.
- Kim, Y.R., Little, D.N., and Lytton, R.L. Fatigue and healing characterization of asphalt mixtures, *Journal of Materials in Civil Engineering*, ASCE, Vol. 15, No. 1, pp. 75-83, 2003.
- Kim, Y.R. *Modeling of Asphalt Concrete*, American Society of Civil Engineers (ASCE) Press, Reston, Virginia, 2009.
- Kim, Y.S. *Evaluation of Healing and Constitutive Modeling of Asphalt Concrete by Means of the Theory of Nonlinear Viscoelasticity and Damage Mechanics*, Ph.D. Dissertation, Texas A&M University, College Station, Texas, 1988.
- Kunst, P.A.J.C. *Surface Cracking on Asphalt Layers*, Working Committee B12, Hoevelaken, Holland, 1989.
- Leathy, R.B., Hicks, R.G., Monismith, C.L., and Finn, F.N. Framework for Performance—Based Approach to Mix Design and Analysis, *journal of the*

- Association of Asphalt Paving Technologists (AAPT)*, Vol. 64, pp. 431–473, Minneapolis, MN, 1995.
- Lee, H.J., and Kim, Y.R. A Uniaxial Viscoelastic Constitutive Model for Asphalt Concrete under Cyclic Loading, *ASCE Journal of Engineering Mechanics*, Vol. 124, No. 11, Pp. 1224-1232, 1998a.
- Lee, H.J., and Kim, Y.R. A Viscoelastic Continuum Damage Model of Asphalt Concrete with Healing, *ASCE Journal of Engineering Mechanics*, Vol. 124, No. 11, Pp. 1-9, 1998b.
- Lee, H.J. *Viscoelastic Constitutive Modeling of Asphalt Concrete Using Viscoelasticity and Continuum Damage Theory*, Ph.D. Dissertation, North Carolina State University, Raleigh, North Carolina, 1996.
- Lee, S. *Investigation of the Effects of Lime on the Performance of HMA using Advanced Testing and Modeling Techniques*, Ph.D. dissertation, North Carolina State University, Raleigh, North Carolina, USA, 2007.
- Liang, R.Y., and Zhou, J. Prediction of Fatigue Life of Asphalt Concrete Beams, *International Journal of Fatigue*, 19 (2), pp. 117-124, 1997.
- Little, D.N. *Investigation of Microdamage Healing in Asphalt and Asphalt Concrete*, Task K, Semi-Annual Technical Report Western research Institute, FHWA project DTFH61-92-C-00170- Fundamental Properties of Asphalts and Modified Asphalts, October, 1995.
- Little, D.N., Lytton, R.L., Williams, D., and Chen, C.W. *Microdamage Healing in Asphalt and Asphalt Concrete, Volume I: Microdamage and Microdamage Healing Project Summary Report*, Report Number FHWA-RD-98-141, Federal Highway Administration, Washington, D.C., June 2001.
- Little, D.N., R.L. Lytton, et al. An Analysis of the Mechanism of Microdamage Healing Based on the Applications of Micromechanics First Principles of Fracture and Healing, *Journal of the Association of Asphalt Paving Technologists (AAPT)*, Chicago, Illinois, Vol. 68, pp. 501 – 542, 1999.
- Lytton, R.L. *Characterizing asphalt pavements for performance*, Transportation Research Record 1723, TRB, National Research Council, pp. 5-16, 2000.

- Lytton, R.L., Chen, C.W., and Little, D.N. *Microdamage Healing in Asphalt and Asphalt Concrete, Volume III: A Micromechanics Fracture and Healing Model for Asphalt Concrete*, FHWA-RD-98-143, Texas A&M University, College Station, TX, 2001.
- Mahoney, J.P. *Study of Long-Lasting Pavements in Washington State, Perpetual Bituminous Pavements*, Transportation Research Circular 503. Transportation Research Board, National Research Council. Washington, D.C., pp. 88-95, 2001.
- Majidzadah, K., Kaufmann, E.M., and Saraf, C.L. Analysis of Fatigue of Paving Mixtures From the Fracture Mechanics Viewpoint, *Journal of Fatigue of Compacted Bituminous Aggregate Mixtures*, ASTM STP 508, pp. 67-83, 1972.
- Majidzadeh, K., Kauffmann, E.M., and Ramsamooj, D.V. Application of Fracture Mechanics in the Analysis of Pavement Fatigue, *Journal of Association of Asphalt Paving Technologists (AAPT)*, pp. 227-246, 1971.
- Mamlouk, M.S., Souliman, M.I., and Zeiada, W.A. *Optimum Testing Conditions to Measure HMA Fatigue and Healing Using Flexural Bending Test*. CR-ROM, Transportation Research Record 1266, Transportation Research Board of National Academies, Washington, DC, January 2012.
- Maupin, G.W. Jr. and J.R. Freeman, Jr. *Simple Procedure for Fatigue Characterization of Bituminous Concrete*, Final Report No. FHWA-RD-76-102, Federal Highway Administration, Washington, DC, 1976.
- McElvaney, J., and Pell, P.S. Fatigue Damage of Asphalt-Effect of Rest Periods, *Highway and Road Construction*, Vol. 41, No. 1776, pp. 16-20, 1973.
- Mello, L.G.R., Kaloush, K.E., and Farias, M.M. Damage Theory Applied to Flexural Fatigue Tests on Conventional and Asphalt Rubber Hot Mixes, *International Journal on Road Materials and Pavement Design*, Vol. 11(3), pp. 681-700, 2010.
- Souliman, M.I. *Integrated Predictive Model for Healing and Fatigue Endurance Limit for Asphalt Concrete*. Ph.D. Dissertation, Arizona State University, Tempe AZ, May 2012.

Minitab software, <http://www.minitab.com/en-US/default.aspx>

Monismith, C.L., and McLean, D.B. Structural Design Considerations, *Proceedings of the Association of Asphalt Paving Technologists (AAPT)*, Vol. 41, pp. 258-304, 1972.

Monismith, C.L., Epps, J.A., Kasianchuk, D.A., and Mclean, D.B. *Asphalt Mixture Behavior in Repeated Flexure*, Report No. TE 70-5, Institute of Transportation and Traffic Engineering, University of California, Berkeley, 1970.

Monismith, C.L., Secor, K.E., and Blackner, E.W. Asphalt Mixture Behavior in Repeated Flexure, *Proceedings of the Association of Asphalt Paving Technologists (AAPT)*, Vol. 30, pp. 188-222, 1961.

Monismith, C.L. *Fatigue of Asphalt Paving Mixtures*, Paper prepared for presentation at the First Annual Street and Highway Conference, University of Nevada, March 1966b..

Monismith, C.L., Epps, J.A., Kasianchuk, D.A., and McLean, D.B. *Asphalt Mixture Behavior in Repeated Flexure*, Report No. TE 70-5, Institute of Transportation and Traffic Engineering, University of California, Berkeley, 1970.

Montgomery, Douglas C., *Design and Analysis of Experiments*, Wiley, 2008.

Moore, R.K. and Kennedy, T. W. *Tensile Behavior of Subbase Materials under Repetitive Loading*, Research Report 98-12, Center for Highway Research, University of Texas at Austin, Austin, TX, 1971.

Navarro, D. and Kennedy, T. W. *Fatigue and Repeated-Load Elastic Characteristics of In-service Asphalt-Treated Pavement*, Research Report No.183-2, Center for Highway Research, the University of Texas at Austin, Austin, TX, 1975.

NCHRP Project 944-A. *Validating an Endurance Limit for HMA Pavements: Laboratory Experiment and Algorithm Development*, Quarterly Progress Report, Arizona State University, Tempe, Arizona, June, 2010.

- Nishizawa, T., Shimeno, S., and Sekiguchi, M. *Fatigue Analysis of Asphalt Pavements with Thick Asphalt Mixture Layer*, Proceedings of the 8th International Conference on Asphalt Pavements, Vol. 2, pp. 969–976, University of Washington, Seattle, WA, August 1996.
- Nunn, M. *Long-life Flexible Roads*. Proceedings of the 8th International Conference on Asphalt Pavements, Vol. 1, pp. 3–16, University of Washington, Seattle, WA, August 1997.
- Paris, P.C and Erdogan, F. A Critical Analysis of Crack Propagation Laws, *Journal of Basic Engineering, Transactions of ASME, Series D, Vol.85*, pp.528–534, 1963.
- Park, S.W. and Kim, Y.R. Fitting Prony-Series Viscoelastic Models with Power-Law Presmoothing, *Journal of Materials in Civil Engineering*, pp. 26-32, January/February 2001.
- Park, S.W., Kim, Y.R., and Schapery, R.A. A Viscoelastic Continuum Damage Model and Its Application to Uniaxial Behavior of Asphalt Concrete, *Mechanics of Materials*, No. 24, pp. 241-255, 1996.
- Park, S.W, and Schapery, R.A. Methods of Interconversion between Linear Viscoelastic Material Functions. Part I- a numerical method based on Prony series, *International Journal of Solids and Structures*, Vol. 36, pp. 1653-1675, 1999.
- Pell, P.S. and Hanson, J.M. Behavior of Bituminous Road Base Materials under Repeated Loading, *Proceedings of Association of Asphalt Paving Technologists (AAPT)*, pp. 201-229, 1973.
- Pell, P.S. *Fatigue of Asphalt Pavement Mixes*, Proceeding of the Second international Conference on the Structural Design of Asphalt Pavements, Ann Arbor, Michigan, pp. 577-594, 1967.
- Pell, P.S. and Cooper, K.E. The Effect of Testing and Mix Variables on The Fatigue Performance of Bituminous Materials, *Journal of the Association of Asphalt Paving Technologists (AAPT)*, Vol. 44, pp. 1-37, 1975.

- Pell, P.S. *Characterization of Fatigue Behavior*, Highway Research board Special Report No. 140, National Research Council, Washington, D.C., pp. 49-64, 1973.
- Pell, P.S. *Pavement Materials*, Sixth International Conference on the Structural Design of Asphalt Pavements, Vol. 2 Proceedings, Ann Arbor, Michigan, July 1987.
- Pellinen, T.K. *Investigation of the Use of Dynamic Modulus as an Indicator of Hot-Mix Asphalt Performance*, Ph.D. Dissertation, Arizona State University, Tempe, AZ, May 2001.
- Petersen, J.C. *Chemical Composition of Asphalt as Related to Asphalt Durability: State of Art*, Transportation Research Record 999, Transportation Research Board, Washington D.C., pp. 13-30, 1984.
- Peterson, R.L., Turner, P., Anderson, M., and Buncher, M. *Determination of Threshold Strain Level for Fatigue Endurance Limit in Asphalt Mixtures*, Proceedings of International Symposium on Design and Construction of Long Lasting Asphalt Pavements, National Center for Asphalt Technology, Auburn, pp. 385–410, AL, 2004.
- Phillips, M.C. *Multi-Step Models for Fatigue and Healing, and Binder Properties Involved in Healing*, Proceedings of Eurobitume Workshop on Performance Related Properties for Bituminous, Luxembourg, No. 115, 1998.
- Powell, W.D., Potter, J. F., Mayhew, H.C., and Nunn, M. E. *The Structural Design of Bituminous Roads*, Transportation and Road Research Laboratory (TRRL), Report No. 1132, pp. 62, 1984.
- Priest, A.L., and Timm, D.H. *Methodology and Calibration of Fatigue Transfer Functions for Mechanistic-Empirical Flexible Pavement Design*, Publication NCAT 06-03. National Center for Asphalt Technology, Auburn University, Auburn, Alabama, 2006.
- Pronk A.C., Poot, M. R., M. M. J. Jacobs, y R. F. Gelpke. *Haversine Fatigue Testing in Controlled Deflection Mode. Is it Possible?*, 89th Annual Meeting of the Transportation Research Board, Transportation Research Board of National Academies, Washington, DC, 2010.

- Pronk, A.C. Partial Healing in Fatigue tests on Asphalt Specimens, *International Journal of Road, Materials and Pavement Design (IJRMPD)*, Vol.4, No.4, 2001.
- Pronk, A.C. Partial Healing, A new approach for damage process during fatigue testing of asphalt specimen, *ASCE*, Geotechnical Special Publication No.146, pp. 83-94, Baton Rouge, 2005.
- Pronk, A.C. *PH Model in 4PB Tests with Rest Periods*, *International Journal of Road, Materials and Pavement Design (IJRMPD)*, Vol.10, No.2, pp. 417-426, 2009.
- Pronk, A.C. *Comparison of 2 and 4 point fatigue tests and healing in 4 point dynamic bending test based on the dissipated energy concept*, Proceedings of the 8th international conference on asphalt pavements, Seattle, Washington, pp. 987-994, 1997.
- Prowell B.D. and Brown, E.R. *Method of Determining Endurance Limit Using Beam Fatigue Tests*, International Conference on Perpetual Pavement. CD ROM 2006.
- Prowell, B., Brown, E.R., Anderson, R.M., Daniel, J.S., Swamy, A.K., Von Quintus, H., Shen, S., Carpenter, S.H., Bhattacharjee, S., and Maghsoodloo, S. *Validating the Fatigue Endurance Limit for Hot Mix Asphalt*, Final NCHRP Report 646, NCHRP 9-38 Project, National Cooperative Highway Research Program, Washington, D.C., 2010.
- Raithby, K.D. and Ramshaw, J.T. *Effect of Secondary Compaction on the Fatigue Performance of a Hot-Rolled Asphalt*, Transportation and Road Research Laboratory TRRL-LR 471, Crowthorne, England, 1972.
- Raithby, K.D. and Sterling, A.B. *Some effects of loading history on the fatigue performance of rolled asphalt*, Transport and Road Research Laboratory (TRRL), Report No. LR 496, Crowthorne, U.K, 1972.
- Raithby, K.D. and Sterling, A.B. *The Effect of Rest Periods on the Fatigue Performance of Hot-Rolled Asphalt under Reversed Axial Loading*, *Proceedings, The Association of Asphalt Paving Technologists (AAPT)*, Vol. 39, pp. 134-147, 1970.

- Reese, R. Properties of Aged Asphalt Binder Related to Asphalt Concrete Fatigue Life, *Journal of the Association of Asphalt Paving Technologists (AAPT)*, Vol. 66, pp. 604-632, 1997.
- Romanoschi S.A., Gisi, A. and Dumitru, C. *The dynamic response of Kansas Perpetual Pavements under vehicle loading*, Proceeding of the International Conference on Perpetual Pavement, Columbus, OH, September 13-15, 2006.
- Rowe, G.M. and Bouldin, M.G. *Improved Techniques to Evaluate the Fatigue Resistance of Asphaltic Mixtures*, Proceedings of 2nd Eurasphalt & Eurobitume Congress, Book 1, pp. 754-763, Barcelona, Spain, September, 2000.
- Rowe, G.M. Performance of Asphalt Mixtures in the Trapezoidal Fatigue Test, *Proceedings of Associations of Asphalt Paving Technologists (AAPT)*, Vol. 62, pp. 344-384, 1993.
- Rowe, G.M. Performance of Asphalt Mixtures in the Trapezoidal Fatigue Test, *Journal of the Association of Asphalt Paving Technologists (AAPT)*, Vol. 62, pp. 334-384, 1993.
- Said, S.F. *Variable in Roadbase Layer Properties Conducting Indirect Tensile Test*, 8th International Conference on The Structural Design of Asphalt Pavements, Vol. 2, Seattle, Washington, August 1997.
- Schapery, R.A. A Method for Predicting Crack Growth in Nonhomogeneous Visco-Elastic Media, *International Journal of Fracture*, Vol. 14, No. 3, pp. 293-309., 1978.
- Schapery, R.A. *A Theory of Crack Growth in Viscoelastic Media*, Research Report MM 2764-73-1, Mechanics and Materials Research Center, Texas A&M University, College Station, Texas, 1973.
- Schapery, R.A. Analysis of Damage Growth in Particulate Composites Using a Work Potential, *Composite Engineering*, Vol. 1(3) , pp. 167-182., 1991.
- Schapery, R.A. Correspondence Principles and a Generalized J Integral for Large Deformation and Fracture Analysis of Viscoelastic Media, *International Journal of Fracture*, Vol. 25, pp. 195-223., 1984.

- Schapery, R.A. A Theory of Mechanical Behavior of Elastic Media with Growing Damage and Other Changes in Structure, *Journal of Mechanics and Physics of Solids*, Vol. 38, pp.215-253, 1990.
- Schapery, R.A. *On The Mechanics of Crack Closing and Bonding in Linear Viscoelastic Media*, International Journal of Fracture, Vol. 39, pp. 163-189, 1989.
- Schapery, R.A., Park, S.W. Methods of Interconversion between Linear Viscoelastic Material Functions. Part II- An Approximate Analytical Method, *International Journal of Solids and Structures*, Vol. 36, pp. 1677-1699, 1999.
- Schutz, W. A history of fatigue, *Engineering Fracture Mechanics*, Vol. 54, No. 2, pp. 263-300, 1996
- Seo, Youngguk, and Kim, Y.R. Using Acoustic Emission to Monitor Fatigue Damage and Healing in Asphalt Concrete, *KSCE Journal of Civil Engineering*, Vol. 12, No. 4, pp. 237-243, 2008.
- Shell Pavement Design Manual. *Asphalt Pavements and Overlay for Road Traffic*, Shell International Petroleum Company Limited, London, 1978.
- Shen, S. and Carpenter, S.H. Development of an Asphalt Fatigue Model Based on Energy Principles, *Proceedings of The Association of Asphalt Paving Technologists (AAPT)*, Vol. 76, pp. 525- 574, 2007.
- Shen, S., and Carpenter, S.H. *Application of Dissipated Energy Concept in Fatigue Endurance Limit Testing*, Transportation Research Record 1929, Journal of Transportation Research Board, pp. 165-173, National Research Council, Washington D.C 2005.
- Shen, S. *Dissipated Energy Concepts for HMA Performance: Fatigue and Healing*, Ph.D. Dissertation, University of Illinois at Urban-Champaign, IL, 2006.
- Shen, S., Chiu, H., Huang, H. *Fatigue and Healing of Asphalt binders*, Transportation Research Record 1338, Transportation Research Board of National Academies, Washington, D.C., 2009.

SHRP A_404, *Fatigue Characteristics of Bitumen and Bituminous Mixes*, Asphalt research Program, Institute of transportation studies, University of California, Berkeley, Strategic Highway research Program, national research Council, 1994.

SHRP Designation: M-009. *Standard Method of Test for Determining the Fatigue Life of Compacted Bituminous Mixtures Subjected to Repeated Flexural Bending*.

SHRP, *Direct Tension Test Experiments*, SHRP-A -641, Strategic Highway Research Program, National Research Council, Washington, D.C. 1993.

Si, Z., Little, D.N., and Lytton, R.L. Characterization of Microdamage and Healing of Asphalt Concrete Mixtures. *Journal of Materials in Civil Engineering, ASCE*, Vol. 14, No. 6, pp. 461-470, 2002.

Si, Z. *Characterization of Microdamage and Healing of Asphalt Concrete Mixtures*, Ph.D. Dissertation, Texas A&M University, College Station, Texas, 2001

Soltani, A., and Anderson, D.A. New Test Protocol to Measure Fatigue Damage in Asphalt Mixtures, *Journal of Road Materials and Pavement Design*, Vol. 6, pp. 485-514, 2005.

Soltani, A., Solaimanian, M., and Anderson, D.A. *An Investigation of the Endurance Limit of Hot-Mix Asphalt Concrete Using a New Uniaxial Fatigue Protocol*. Final Report, Report Number FHWA-HIF-07-002, Federal Highway Administration (FHWA), Washington, D.C., 2006.

Sousa, J.B. *Dynamic Properties of Pavement Materials*, Ph.D. Thesis, University of California, Berkeley, 1986.

STATISTICA software, StateSoft, <http://www.statsoft.com/#>.

Suresh, S. *Fatigue of materials*. 2nd edition, Cambridge University Press, Cambridge, UK, 1998.

Tangella, S.R., Craus, J., Deacon, J.A., and Monismith, C.L. *Summary Report of Fatigue Response of Asphalt Mixtures*, Technical Memorandum No. TM-

UCB-A-003A-89-3M, prepared for SHRP Project A-003A, Institute of Transportation Studies, University of California, Berkeley, 1990.

Tayebali, A.A., Coplantz, J.S., Harvey, J.T., and Monismith, C.L. *Interim Report on Fatigue Response of Asphalt-Aggregate Mixtures*, SHRP project A-003A, TM-UCB-A-003A-92-1, Asphalt Research Program, Institute of Transportation Studies, University of California-Berkeley, Berkeley, CA, 1992.

Tayebali, A.A., Deacon, J.A., Coplantz, J.S., Harvey, J.T., and Monismith, C.L. Mix and Mode-of Loading Effects on Fatigue Response of Asphalt-Aggregate Mixes, *Proceedings of the Association of Asphalt Paving Technologists (AAPT)*, Vol. 63, pp. 118- 151, 1994.

Tayebali, A.A., Rowe, G.M. and Sousa, J.B. Fatigue Response of Asphalt-Aggregate Mixtures, *Journal of the Association of Asphalt Paving Technologists (AAPT)*, Vol. 61, pp. 333-360, 1992.

The Asphalt Institute. *Research and Development of The Asphalt Institute's Thickness Design Manual (MS-1) Ninth Edition*, Research Report No. 82-2, August 1982.

Thomson, M.R., and Carpenter, S.H. *Considering Hot-Mix-Asphalt Fatigue Endurance Limit in Full-Depth Mechanistic-Empirical Pavement Design*. CD-ROM, *Proceedings of the International Conference on Perpetual Pavements*. Columbus, Ohio, September 13-15, 2006.

Tsai, B.W., Harvey, J.T., and Monismith, C.L. High Temperature Fatigue and Fatigue Damage Process of Aggregate-Asphalt Mixes, *Journal of the Association of Asphalt Paving Technologists (AAPT)*, Vol. 71, pp. 345–385, 2002.

Tsai, B.W., Harvey, J.T., and Monismith, C.L. *Using the Three- Stage Weibull Equation and Tree-Based Model to Characterize the Mix Fatigue Damage Process*, Transportation Research Record 1929, *Journal of Transportation Research Board*, pp. 227-237, National Research Council, Washington D.C, 2005.

Tsai, B., Harvey, J.T., and Monismith, C.L. Two-Stage Weibull Approach for Asphalt Concrete Fatigue Performance Prediction, *Proceedings of the*

- Association of Asphalt Paving Technologists (AAPT)*, Vol. 73, pp. 200-228, 2004.
- Tschoegl, N.W. *The Phenomenological Theory of Linear Viscoelastic Behavior*, Springer-Verlag, Berlin, 1989.
- Underwood, B.S., Kim, Y.R., and Guddati, M.N. Characterization and Performance Prediction of ALF Mixtures Using a Viscoelastoplastic Continuum Damage Model, *Proceedings of the Association of Asphalt Paving Technologists (AAPT)*, Vol. 75, pp. 577-636, 2006.
- Underwood, B.S. and Kim, Y.R. *Analytical Techniques for Determining the Endurance Limit of Hot Mix Asphalt Concrete*, CD-ROM, International Conference on Perpetual Pavement, Columbus, Ohio, 2009.
- Underwood, B.S., Kim, Y.R., and Guddati, M.N. Improved Calculation Method of Damage Parameter in Viscoelastic Continuum Damage Model, *International Journal of Pavement Engineering*, Vol. 11, Issue 6, pp. 459 – 476, December 2010.
- Van Dijk, W. Practical Fatigue Characterization of Bituminous Mixes, *Proceedings, Journal of the Association of Asphalt Paving Technologists (AAPT)*, Vol. 44, p.38, Phoenix, Arizona, 1975.
- Van Dijk, W., and Visser, W. The Energy Approach to Fatigue for Pavement Design, *Proceedings of the Association of Asphalt Paving Technologists (AAPT)*, Vol. 46, pp.1-40, 1977.
- Van Dijk, W., Moreaud, H., Quedeville, A., and Uge, P. *The Fatigue of Bitumen and Bituminous Mixes*, *Proceedings, Third International Conference of Structural Design of Asphalt Pavements*, London, Vol. 1, pp. 354-366, September 1972.
- Verstraeten, j. *Aspects Divers de la Fatigue des Mélanges Bitumineux*. Report No. 170/Jv(1976), Center de Recherche Routières, Bruxelles, 1976.
- Walubita, L.F., Liu, W., Scullion, T., and Leidy, J. *Modeling Perpetual Pavements Using the Flexible Pavement System (FPS) Software*, CD-ROM, Transportation Research Record 2311, Transportation Research Board, Annual Meeting, Washington, D.C., 2008.

- Willis, J.R. *Field Based Strain Thresholds for Flexible Perpetual Pavement Design*. Ph.D. Dissertation, Auburn University, Auburn, Alabama, 2009.
- Witczak, M.W. *Development of relationships between binder viscosity and stiffness*. SUPERPAVE Support and Performance Models Contract, FHWA No. DTFH 61-94-R-00045, Team Technical Rep., University of Maryland, College Park, Md, 1998.
- Witczak, M.W., Hafez, I., Qi, X. *Laboratory characterization of Elvaloy modified asphalt mixtures: vol. I – Technical report*, College Park, Maryland, University of Maryland, 1995. Available from: <http://www.dupont.com/asphalt/link5.html>.
- Witczak, M.W., K. Kaloush, T.K. Pellinen, M. El-Basyouny, and H. Von Quintus. *Simple Performance Test for Superpave Mix Design*, NCHRP Report 465, National Cooperative Highway Research Program, Washington D.C, 2002.
- Witczak, M.W., Mamlouk, M., and Abojaradeh, M. *Flexural Fatigue Tests, NCHRP 9-19, Subtask F6 Evaluation Tests, Task F Advanced Mixture Characterization*. Interim Report, Arizona State University, Tempe, Arizona, July 2001.
- Wu, Z., Siddique, Z.Q. and Gisi, A.J. *Kansas Turnpike—An Example of Long Lasting Asphalt Pavement*, International Symposium on Design and Construction of Long Lasting Asphalt Pavements, pp. 859–879, International Society for Asphalt Pavements, Auburn, Alabama, 2004.
- Zhang, Z., Roque, R., Birgisson, B., and Sangpetngam, B. Identification and Verification of a Suitable Crack Growth Law, *Journal of the Association of Asphalt Paving Technologists (AAPT)*, Vol. 70, pp.206-241, 2001.

APPENDIX A

SUMMARY OF DYNAMIC MODULUS TEST RESULTS

Appendix A includes the complex modulus test results (dynamic modulus and phase angle) of three different mixtures based on the binder type. These binder types are PG 58-28, PG 64-22, and PG 76-16. For each mixture, a total of nine different mixtures were tested which represent nine different combinations of the air voids and the asphalt cement percent. The test results for each mixture combination were based on two replicates. The air voids and binder content levels were varying according the superpave mix design. For 64-22 asphalt mixture, the air voids values were the designed AV and $\pm 3\%$ ($7-3$, 7 , and $7+3 = 4$, 7 , and 10). The asphalt cement content values were the optimum AC and $\pm 0.5\%$ ($4.5-0.5$, 4.5 , and $4.5+0.5 = 4.0$, 4.5 , and 5). For both 58-28 and 76-16 mixtures, the air voids values were the designed AV and $\pm 2.5\%$ ($7-2.5$, 7 , and $7+2.5 = 4.5$, 7 , and 9.5). The asphalt cement content values were fixed for these two mixtures to be 4.2 , 4.7 , and 5.2% .

TABLES A.1 to A.27 summarized the complex modulus test results for a total of 27 different mixtures; nine for each mixture type representing nine different combinations of air voids and asphalt cement contents. Each table contains the dynamic modulus and phase angle of each replicate and the averages as well. To show the amount of variability between the replicates at different test temperatures and frequencies, standard deviation and coefficient of variation have been determined.

TABLE A.1 E* test results of PG 64-22 mixture at 4.0% AC and 10.0% Va

Temp (°F)	Freq (Hz)	Dynamic Modulus, E*					Phase Angle, ϕ				
		Repl. 1 6-105 (ksi)	Repl. 2 6-106 (ksi)	Average (ksi)	Std. Dev. (ksi)	Coeff. of Var.	Repl. 1 6-105 (Deg.)	Repl. 2 6-106 (Deg.)	Average (Deg.)	Std. Dev. (Deg.)	Coeff. of Var.
14	25	2482	2585	2533	73	2.9	5.0	5.2	5.1	0.1	2.1
	10	2381	2484	2432	73	3.0	6.0	7.7	6.8	1.2	17.9
	5	2268	2346	2307	55	2.4	6.3	8.7	7.5	1.7	22.7
	1	2104	2167	2136	45	2.1	7.3	9.1	8.2	1.3	15.8
	0.5	1997	2147	2072	106	5.1	7.8	11.0	9.4	2.2	23.5
	0.1	1764	1880	1822	82	4.5	9.2	11.1	10.1	1.3	13.3
40	25	1720	1691	1706	20	1.2	10.5	8.5	9.5	1.4	15.3
	10	1568	1573	1570	4	0.2	12.1	10.1	11.1	1.4	13.0
	5	1436	1460	1448	17	1.2	13.2	11.1	12.1	1.5	12.3
	1	1182	1218	1200	26	2.1	15.6	14.9	15.2	0.5	3.4
	0.5	1086	1096	1091	7	0.7	16.7	15.2	15.9	1.1	6.7
	0.1	848	851	849	2	0.3	20.3	16.4	18.4	2.7	14.9
70	25	862	903	882	29	3.3	18.5	19.2	18.9	0.5	2.8
	10	709	770	739	43	5.9	21.9	20.1	21.0	1.3	6.0
	5	610	673	642	44	6.9	23.2	23.0	23.1	0.1	0.5
	1	425	468	446	30	6.8	28.4	27.1	27.7	0.9	3.3
	0.5	359	408	383	35	9.1	30.8	28.1	29.4	1.9	6.4
	0.1	236	275	255	27	10.8	34.6	30.9	32.7	2.6	7.9
100	25	332	356	344	17	5.0	35.2	29.1	32.2	4.3	13.3
	10	245	285	265	28	10.5	34.6	29.0	31.8	4.0	12.5
	5	192	233	213	28	13.4	32.7	29.1	30.9	2.6	8.3
	1	120	153	137	23	17.2	30.7	26.8	28.7	2.8	9.6
	0.5	101	131	116	22	18.7	29.2	26.2	27.7	2.1	7.6
	0.1	76	77	77	1	1.0	27.6	23.3	25.5	3.1	12.0
130	25	113	120	117	5	4.4	32.4	25.2	28.8	5.1	17.6
	10	86	93	89	5	6.0	25.6	20.8	23.2	3.4	14.7
	5	68	77	72	6	8.3	25.2	18.2	21.7	5.0	22.9
	1	43	48	46	4	8.5	21.1	16.1	18.6	3.5	18.8
	0.5	35	40	37	3	8.6	17.8	14.3	16.0	2.5	15.7
	0.1	22	25	24	2	8.9	15.6	13.5	14.6	1.5	10.2

TABLE A.2 E* test results of PG 64-22 mixture at 4.0% AC and 7.0% Va

Temp (°F)	Freq (Hz)	Dynamic Modulus, E*					Phase Angle, ϕ				
		Repl. 1 6-703 (ksi)	Repl. 2 6-704 (ksi)	Average (ksi)	Std. Dev. (ksi)	Coeff. of Var.	Repl. 1 6-703 (Deg.)	Repl. 2 6-704 (Deg.)	Average (Deg.)	Std. Dev. (Deg.)	Coeff. of Var.
14	25	3265	3324	3295	42	1.3	4.8	5.2	5.0	0.3	5.4
	10	3218	3236	3227	13	0.4	7.7	6.2	7.0	1.1	15.7
	5	3145	3153	3149	6	0.2	8.3	8.4	8.3	0.0	0.3
	1	2918	2916	2917	1	0.0	8.8	8.5	8.6	0.3	2.9
	0.5	2859	2817	2838	30	1.0	9.0	7.7	8.4	0.9	10.7
	0.1	2553	2537	2545	11	0.4	8.1	9.8	8.9	1.2	13.4
40	25	2443	2237	2340	145	6.2	7.7	11.7	9.7	2.8	29.3
	10	2480	2261	2370	155	6.5	9.6	11.2	10.4	1.1	10.3
	5	2359	2171	2265	133	5.9	10.1	13.2	11.7	2.2	18.6
	1	2045	1886	1965	112	5.7	12.1	14.1	13.1	1.4	10.9
	0.5	1929	1778	1854	106	5.7	13.4	14.7	14.1	1.0	6.9
	0.1	1642	1520	1581	87	5.5	17.4	17.2	17.3	0.1	0.7
70	25	1311	1437	1374	89	6.5	13.1	11.8	12.4	0.9	7.6
	10	1255	1312	1283	40	3.1	16.3	14.2	15.2	1.5	9.9
	5	1118	1166	1142	34	3.0	17.5	17.2	17.3	0.2	1.3
	1	859	922	891	45	5.0	23.2	23.0	23.1	0.2	0.7
	0.5	767	762	764	3	0.5	26.3	25.6	25.9	0.5	1.8
	0.1	555	570	562	11	1.9	31.1	30.9	31.0	0.1	0.4
100	25	524	461	493	44	9.0	36.7	31.2	33.9	3.9	11.5
	10	381	344	362	26	7.3	35.5	32.4	34.0	2.1	6.3
	5	297	274	285	16	5.6	34.4	31.9	33.2	1.8	5.5
	1	183	170	176	10	5.5	34.0	31.7	32.8	1.7	5.0
	0.5	180	142	161	26	16.4	32.1	31.1	31.6	0.8	2.4
	0.1	113	103	108	7	6.6	29.7	29.1	29.4	0.4	1.3
130	25	190	145	167	31	18.7	26.5	30.0	28.2	2.4	8.6
	10	134	118	126	11	8.7	21.5	23.6	22.6	1.5	6.6
	5	108	107	107	1	0.7	19.8	21.4	20.6	1.2	5.6
	1	62	59	60	2	3.2	16.9	20.5	18.7	2.5	13.6
	0.5	49	47	48	1	2.9	15.3	19.2	17.3	2.8	16.1
	0.1	30	29	29	1	2.1	15.1	18.8	16.9	2.6	15.4

TABLE A.3 E* test results of PG 64-22 mixture at 4.0% AC and 4.0% Va

Temp (°F)	Freq (Hz)	Dynamic Modulus, E*					Phase Angle, ϕ				
		Repl. 1 6-404 (ksi)	Repl. 2 6-405 (ksi)	Average (ksi)	Std. Dev. (ksi)	Coeff. of Var.	Repl. 1 6-404 (Deg.)	Repl. 2 6-405 (Deg.)	Average (Deg.)	Std. Dev. (Deg.)	Coeff. of Var.
14	25	4642	5144	4893	355	7.3	5.4	4.3	4.8	0.8	16.2
	10	4526	5054	4790	373	7.8	6.8	7.6	7.2	0.5	7.4
	5	4395	4964	4679	403	8.6	7.0	7.5	7.3	0.4	5.4
	1	4041	4656	4349	434	10.0	5.5	6.6	6.0	0.8	13.4
	0.5	3976	4484	4230	359	8.5	7.5	7.9	7.7	0.3	3.7
	0.1	3569	4012	3790	313	8.3	9.1	8.2	8.6	0.7	7.8
40	25	3023	4839	3931	1284	32.7	8.9	5.0	6.9	2.8	40.1
	10	2953	4578	3766	1150	30.5	9.9	8.2	9.1	1.2	13.2
	5	2742	4235	3489	1056	30.3	11.6	10.9	11.3	0.5	4.1
	1	2411	3546	2978	803	27.0	12.2	11.4	11.8	0.6	4.7
	0.5	2251	3298	2775	740	26.7	14.3	12.6	13.5	1.3	9.3
	0.1	1794	2678	2236	625	28.0	16.1	15.3	15.7	0.6	3.8
70	25	1706	3133	2420	1009	41.7	15.3	14.5	14.9	0.6	3.9
	10	1485	2875	2180	983	45.1	19.4	18.6	19.0	0.6	2.9
	5	1317	2552	1935	873	45.1	21.0	21.1	21.1	0.0	0.2
	1	954	1875	1415	651	46.0	24.6	26.6	25.6	1.4	5.5
	0.5	820	1583	1202	539	44.9	27.3	29.9	28.6	1.9	6.5
	0.1	550	1106	828	393	47.5	29.4	30.4	29.9	0.7	2.3
100	25	654	758	706	73	10.4	29.1	31.7	30.4	1.8	6.1
	10	489	573	531	59	11.1	30.3	30.0	30.1	0.2	0.8
	5	388	454	421	47	11.1	29.9	30.6	30.3	0.5	1.6
	1	232	269	250	26	10.5	29.8	31.9	30.9	1.5	4.8
	0.5	186	217	201	22	10.8	29.5	31.0	30.2	1.1	3.5
	0.1	120	140	130	14	11.0	26.0	27.2	26.6	0.9	3.3
130	25	205	194	199	8	3.9	31.8	35.1	33.4	2.3	6.9
	10	148	139	144	7	4.7	29.5	29.9	29.7	0.2	0.8
	5	119	115	117	3	2.4	25.2	26.4	25.8	0.8	3.2
	1	69	68	68	0	0.3	20.8	20.3	20.6	0.3	1.7
	0.5	55	55	55	0	0.3	19.4	18.1	18.8	0.9	4.8
	0.1	34	34	34	0	0.3	14.8	15.7	15.2	0.7	4.5

TABLE A.4 E* test results of PG 64-22 mixture at 4.5% AC and 10.0% Va

Temp (°F)	Freq (Hz)	Dynamic Modulus, E*					Phase Angle, ϕ				
		Repl. 1 6O103 (ksi)	Repl. 2 6O104 (ksi)	Average (ksi)	Std. Dev. (ksi)	Coeff. of Var.	Repl. 1 6O103 (Deg.)	Repl. 2 6O104 (Deg.)	Average (Deg.)	Std. Dev. (Deg.)	Coeff. of Var.
14	25	2623	1769	2196	604	27.5	7.1	8.2	7.7	0.8	10.2
	10	2492	1802	2147	488	22.7	7.8	8.5	8.2	0.5	6.5
	5	2409	1741	2075	472	22.8	8.5	9.1	8.8	0.4	4.3
	1	2178	1569	1874	431	23.0	9.4	10.0	9.7	0.4	4.6
	0.5	2106	1504	1805	426	23.6	9.4	9.8	9.6	0.3	3.0
	0.1	1861	1347	1604	363	22.6	10.5	10.6	10.6	0.1	0.5
40	25	1424	1211	1318	150	11.4	10.5	10.9	10.7	0.3	2.7
	10	1319	1138	1229	128	10.4	12.2	13.0	12.6	0.6	4.9
	5	1221	1082	1152	98	8.5	14.2	14.0	14.1	0.1	1.0
	1	973	872	922	72	7.8	16.8	16.5	16.7	0.2	1.2
	0.5	880	793	836	61	7.3	17.2	18.2	17.7	0.7	4.1
	0.1	673	615	644	41	6.4	20.5	20.9	20.7	0.3	1.3
70	25	642	693	667	36	5.4	20.3	20.0	20.2	0.2	1.2
	10	533	565	549	23	4.2	23.0	23.5	23.2	0.4	1.6
	5	461	485	473	17	3.6	25.1	24.7	24.9	0.3	1.2
	1	315	336	326	15	4.5	29.6	29.0	29.3	0.5	1.6
	0.5	272	287	280	11	3.9	32.2	31.5	31.8	0.5	1.7
	0.1	186	197	191	8	4.1	37.5	36.5	37.0	0.7	2.0
100	25	271	258	264	10	3.6	30.4	33.3	31.8	2.1	6.6
	10	201	196	199	4	2.1	28.9	30.8	29.9	1.3	4.4
	5	169	160	165	7	4.2	29.0	30.2	29.6	0.8	2.9
	1	113	110	111	2	1.8	28.2	30.7	29.5	1.8	6.1
	0.5	102	95	98	4	4.4	26.6	29.6	28.1	2.1	7.5
	0.1	63	63	63	0	0.2	22.4	32.3	27.4	7.0	25.8
130	25	97	96	96	0	0.3	30.5	28.0	29.3	1.8	6.1
	10	76	76	76	0	0.0	23.8	23.2	23.5	0.4	1.6
	5	63	63	63	0	0.2	20.2	21.9	21.0	1.2	5.7
	1	41	41	41	0	0.7	16.6	20.2	18.4	2.6	13.9
	0.5	34	34	34	0	0.9	15.3	19.4	17.3	2.9	16.9
	0.1	22	22	22	0	1.4	12.7	17.3	15.0	3.2	21.7

TABLE A.5 E* test results of PG 64-22 mixture at 4.5% AC and 7.0% Va

Temp (°F)	Freq (Hz)	Dynamic Modulus, E*					Phase Angle, ϕ				
		Repl. 1 6O701 (ksi)	Repl. 2 6O702 (ksi)	Average (ksi)	Std. Dev. (ksi)	Coeff. of Var.	Repl. 1 6O701 (Deg.)	Repl. 2 6O702 (Deg.)	Average (Deg.)	Std. Dev. (Deg.)	Coeff. of Var.
14	25	4314	2714	3514	1131	32.2	6.6	5.9	6.2	0.5	7.6
	10	4053	2604	3328	1024	30.8	7.7	7.5	7.6	0.1	2.0
	5	3878	2498	3188	976	30.6	7.3	7.7	7.5	0.3	3.9
	1	3574	2318	2946	888	30.1	7.6	7.7	7.7	0.1	0.8
	0.5	3427	2232	2830	845	29.9	8.3	8.4	8.3	0.1	1.4
	0.1	2985	2018	2501	684	27.3	8.9	9.4	9.1	0.3	3.6
40	25	2971	2862	2917	77	2.6	11.5	9.8	10.7	1.2	11.3
	10	2783	2566	2674	153	5.7	13.8	13.5	13.6	0.3	1.9
	5	2568	2390	2479	126	5.1	14.1	14.3	14.2	0.2	1.1
	1	2122	1989	2056	94	4.6	15.3	15.3	15.3	0.0	0.2
	0.5	1956	1832	1894	88	4.6	16.0	16.3	16.1	0.2	1.2
	0.1	1524	1472	1498	36	2.4	19.4	19.4	19.4	0.0	0.1
70	25	1212	1140	1176	51	4.4	15.8	18.0	16.9	1.5	9.0
	10	1006	1028	1017	15	1.5	20.2	20.3	20.2	0.0	0.1
	5	884	920	902	25	2.8	21.5	21.8	21.6	0.2	1.0
	1	638	661	650	16	2.5	27.4	26.6	27.0	0.6	2.0
	0.5	551	571	561	14	2.5	30.5	28.9	29.7	1.1	3.9
	0.1	372	399	385	19	4.9	35.6	33.2	34.4	1.7	5.0
100	25	510	482	496	20	4.0	29.9	29.7	29.8	0.1	0.5
	10	372	349	360	16	4.5	28.1	28.4	28.3	0.2	0.8
	5	305	277	291	20	6.8	25.9	29.0	27.5	2.2	7.9
	1	189	171	180	13	7.2	23.9	29.6	26.7	4.0	15.1
	0.5	154	141	148	9	6.2	22.0	28.2	25.1	4.3	17.2
	0.1	95	100	98	3	3.5	22.5	25.9	24.2	2.4	9.9
130	25	154	148	151	4	2.6	29.7	26.9	28.3	1.9	6.9
	10	117	109	113	6	5.2	26.5	23.3	24.9	2.3	9.1
	5	95	92	94	2	1.8	22.2	21.3	21.7	0.7	3.0
	1	58	55	56	2	3.9	16.4	19.1	17.7	1.9	10.7
	0.5	47	44	45	2	3.8	12.3	17.7	15.0	3.9	25.7
	0.1	29	27	28	1	3.6	10.8	15.7	13.2	3.5	26.1

TABLE A.6 E* test results of PG 64-22 mixture at 4.5% AC and 4.0% Va

Temp (°F)	Freq (Hz)	Dynamic Modulus, E*					Phase Angle, ϕ				
		Repl. 1 6O401 (ksi)	Repl. 2 6O402 (ksi)	Average (ksi)	Std. Dev. (ksi)	Coeff. of Var.	Repl. 1 6O401 (Deg.)	Repl. 2 6O402 (Deg.)	Average (Deg.)	Std. Dev. (Deg.)	Coeff. of Var.
14	25	4591	4886	4738	208	4.4	5.7	8.0	6.8	1.6	23.5
	10	4515	4852	4684	238	5.1	8.9	8.0	8.4	0.7	7.9
	5	4451	4913	4682	327	7.0	8.8	11.9	10.4	2.2	21.2
	1	4115	4289	4202	123	2.9	8.7	12.4	10.5	2.6	24.7
	0.5	3970	4114	4042	102	2.5	9.4	13.4	11.4	2.8	24.5
	0.1	3542	3455	3499	62	1.8	9.0	14.1	11.6	3.6	31.1
40	25	4139	3109	3624	728	20.1	6.3	7.5	6.9	0.9	12.7
	10	3886	2953	3419	660	19.3	8.5	11.2	9.8	1.9	19.5
	5	3660	2821	3241	593	18.3	9.4	12.2	10.8	2.0	18.9
	1	3135	2338	2737	563	20.6	11.9	15.2	13.5	2.3	17.3
	0.5	2935	2176	2556	537	21.0	13.3	15.8	14.6	1.8	12.4
	0.1	2386	1774	2080	432	20.8	16.3	18.6	17.4	1.6	9.1
70	25	2191	2088	2139	73	3.4	15.5	14.4	15.0	0.8	5.3
	10	2035	1843	1939	136	7.0	20.4	23.0	21.7	1.8	8.5
	5	1798	1562	1680	167	9.9	22.9	25.0	23.9	1.5	6.4
	1	1311	1070	1190	170	14.3	29.7	29.5	29.6	0.2	0.6
	0.5	1087	904	995	129	13.0	32.5	31.1	31.8	1.0	3.0
	0.1	711	593	652	83	12.8	38.2	35.5	36.8	1.9	5.1
100	25	730	659	694	50	7.1	27.2	32.9	30.0	4.1	13.5
	10	523	473	498	35	7.1	27.6	35.1	31.3	5.3	16.8
	5	413	373	393	28	7.2	28.9	34.3	31.6	3.8	12.0
	1	257	214	236	31	13.1	30.0	35.5	32.7	3.9	11.9
	0.5	214	171	193	31	15.9	28.8	34.0	31.4	3.7	11.7
	0.1	151	122	136	21	15.5	25.9	29.2	27.6	2.3	8.3
130	25	164	162	163	2	0.9	34.4	40.6	37.5	4.4	11.6
	10	115	108	112	5	4.3	29.0	34.7	31.8	4.0	12.7
	5	97	89	93	6	6.1	24.7	31.9	28.3	5.1	18.1
	1	64	64	64	0	0.0	20.0	24.8	22.4	3.4	15.1
	0.5	52	52	52	0	0.0	16.5	22.1	19.3	4.0	20.5
	0.1	32	32	32	0	0.0	14.1	21.6	17.8	5.3	29.8

TABLE A.7 E* test results of PG 64-22 mixture at 5.0% AC and 10.0% Va

Temp (°F)	Freq (Hz)	Dynamic Modulus, E*					Phase Angle, ϕ				
		Repl. 1 6+105 (ksi)	Repl. 2 6+106 (ksi)	Average (ksi)	Std. Dev. (ksi)	Coeff. of Var.	Repl. 1 6+105 (Deg.)	Repl. 2 6+106 (Deg.)	Average (Deg.)	Std. Dev. (Deg.)	Coeff. of Var.
14	25	1933	1778	1855	110	5.9	4.8	7.1	5.9	1.6	27.9
	10	1982	1709	1845	193	10.5	7.4	8.4	7.9	0.7	8.7
	5	1924	1673	1799	178	9.9	7.4	9.5	8.5	1.5	18.2
	1	1776	1543	1659	164	9.9	8.1	11.2	9.6	2.1	22.1
	0.5	1714	1483	1598	163	10.2	9.2	11.2	10.2	1.4	13.7
	0.1	1529	1338	1434	135	9.4	10.9	12.3	11.6	1.0	8.7
40	25	1575	1468	1522	75	4.9	13.9	14.0	14.0	0.0	0.2
	10	1544	1321	1433	158	11.0	17.7	15.3	16.5	1.7	10.4
	5	1495	1231	1363	186	13.7	18.6	20.0	19.3	1.0	5.2
	1	1192	1030	1111	114	10.3	21.0	23.9	22.5	2.0	9.1
	0.5	1090	934	1012	110	10.9	23.0	24.9	24.0	1.4	5.7
	0.1	869	819	844	35	4.2	27.7	27.2	27.5	0.4	1.4
70	25	788	912	850	87	10.3	21.0	33.6	27.3	8.9	32.6
	10	735	823	779	62	8.0	24.8	36.5	30.6	8.2	26.8
	5	665	775	720	78	10.8	25.7	35.4	30.5	6.8	22.3
	1	449	585	517	97	18.7	31.5	39.5	35.5	5.6	15.9
	0.5	380	487	434	76	17.5	34.3	40.9	37.6	4.6	12.2
	0.1	244	298	271	38	14.0	42.0	43.0	42.5	0.7	1.7
100	25	300	307	304	5	1.6	37.7	37.9	37.8	0.1	0.4
	10	208	202	205	4	2.1	34.9	38.1	36.5	2.3	6.3
	5	173	161	167	8	4.8	31.4	35.1	33.2	2.6	7.8
	1	117	103	110	10	8.9	27.5	34.3	30.9	4.8	15.5
	0.5	106	89	97	12	12.2	24.6	32.2	28.4	5.4	19.1
	0.1	62	69	66	5	7.4	24.2	31.5	27.9	5.2	18.6
130	25	100	102	101	2	1.9	30.2	33.7	31.9	2.4	7.6
	10	76	78	77	1	1.7	26.3	31.8	29.0	3.9	13.5
	5	62	64	63	1	1.6	25.2	29.8	27.5	3.2	11.7
	1	38	39	39	0	1.2	24.2	26.4	25.3	1.5	6.1
	0.5	31	32	31	0	1.1	22.5	23.7	23.1	0.9	3.9
	0.1	19	20	19	0	0.8	20.5	21.9	21.2	1.0	4.8

TABLE A.8 E* test results of PG 64-22 mixture at 5.0% AC and 7.0% Va

Temp (°F)	Freq (Hz)	Dynamic Modulus, E*					Phase Angle, ϕ				
		Repl. 1 6+705 (ksi)	Repl. 2 6+706 (ksi)	Average (ksi)	Std. Dev. (ksi)	Coeff. of Var.	Repl. 1 6+705 (Deg.)	Repl. 2 6+706 (Deg.)	Average (Deg.)	Std. Dev. (Deg.)	Coeff. of Var.
14	25	3094	3593	3344	353	10.6	9.3	6.3	7.8	2.1	27.3
	10	3073	3450	3261	266	8.2	10.7	9.6	10.2	0.8	8.2
	5	2881	3327	3104	315	10.1	10.5	9.2	9.8	0.9	8.9
	1	2582	3001	2792	297	10.6	10.3	11.1	10.7	0.6	5.7
	0.5	2376	2848	2612	334	12.8	10.6	11.6	11.1	0.7	6.6
	0.1	2070	2495	2282	301	13.2	10.6	13.1	11.8	1.7	14.8
40	25	1633	2668	2151	732	34.0	8.5	14.3	11.4	4.1	35.5
	10	1580	2498	2039	649	31.8	10.2	16.9	13.5	4.7	35.0
	5	1493	2313	1903	580	30.5	11.3	17.9	14.6	4.7	31.9
	1	1251	1889	1570	451	28.7	13.7	20.5	17.1	4.8	28.2
	0.5	1159	1701	1430	383	26.8	15.4	21.5	18.5	4.3	23.2
	0.1	936	1296	1116	255	22.9	19.1	25.2	22.1	4.3	19.3
70	25	1058	1360	1209	214	17.7	24.9	16.0	20.5	6.3	30.8
	10	939	1137	1038	140	13.5	28.0	18.2	23.1	6.9	29.8
	5	849	1003	926	109	11.7	29.6	19.9	24.7	6.9	27.7
	1	594	739	667	103	15.4	35.7	26.7	31.2	6.4	20.5
	0.5	520	639	579	85	14.6	38.7	29.4	34.0	6.6	19.4
	0.1	349	422	386	52	13.4	43.2	36.5	39.8	4.8	11.9
100	25	423	432	428	7	1.5	37.0	39.0	38.0	1.4	3.6
	10	285	313	299	20	6.6	35.4	34.5	34.9	0.6	1.6
	5	227	251	239	17	7.1	34.0	32.1	33.0	1.3	4.0
	1	142	161	151	13	8.9	34.7	32.9	33.8	1.3	3.8
	0.5	117	139	128	15	12.1	31.7	30.3	31.0	1.0	3.2
	0.1	87	93	90	4	4.5	32.8	32.0	32.4	0.6	1.7
130	25	137	149	143	8	5.5	33.5	28.4	31.0	3.6	11.7
	10	108	113	111	4	3.8	26.8	22.2	24.5	3.3	13.3
	5	89	92	91	2	2.4	22.9	21.3	22.1	1.1	5.0
	1	57	57	57	0	0.9	18.7	20.8	19.7	1.5	7.8
	0.5	47	46	47	1	2.3	14.1	14.0	14.0	0.1	0.8
	0.1	31	28	29	2	5.5	13.2	13.5	13.4	0.2	1.4

TABLE A.9 E* test results of PG 64-22 mixture at 5.0% AC and 4.0% Va

Temp (°F)	Freq (Hz)	Dynamic Modulus, E*					Phase Angle, ϕ				
		Repl. 1 6+405 (ksi)	Repl. 2 6+406 (ksi)	Average (ksi)	Std. Dev. (ksi)	Coeff. of Var.	Repl. 1 6+405 (Deg.)	Repl. 2 6+406 (Deg.)	Average (Deg.)	Std. Dev. (Deg.)	Coeff. of Var.
14	25	4023	4197	4110	123	3.0	9.6	7.1	8.3	1.8	21.7
	10	3673	3737	3705	45	1.2	10.9	9.2	10.0	1.2	11.8
	5	3392	3445	3418	38	1.1	10.3	6.1	8.2	3.0	36.3
	1	3140	3245	3193	74	2.3	10.6	9.6	10.1	0.7	7.1
	0.5	3023	3061	3042	27	0.9	8.6	6.5	7.5	1.5	20.2
	0.1	2988	3022	3005	24	0.8	8.9	7.7	8.3	0.9	10.3
40	25	2649	2763	2706	81	3.0	13.0	9.8	11.4	2.3	19.8
	10	2517	2709	2613	135	5.2	14.6	13.0	13.8	1.1	8.2
	5	2351	2538	2445	132	5.4	16.1	13.8	14.9	1.6	10.8
	1	2005	2213	2109	147	7.0	17.2	15.3	16.2	1.3	8.1
	0.5	1853	2083	1968	163	8.3	17.4	16.0	16.7	1.0	6.1
	0.1	1508	1832	1670	229	13.7	19.5	18.7	19.1	0.6	3.1
70	25	1588	1756	1672	119	7.1	13.3	12.3	12.8	0.7	5.8
	10	1382	1602	1492	156	10.4	16.2	15.7	16.0	0.4	2.2
	5	1245	1458	1351	151	11.1	17.4	18.5	18.0	0.8	4.4
	1	919	1106	1012	132	13.0	23.5	23.9	23.7	0.3	1.2
	0.5	798	975	886	126	14.2	25.9	26.2	26.0	0.2	0.7
	0.1	542	712	627	120	19.2	32.7	32.6	32.7	0.1	0.2
100	25	622	650	636	20	3.2	32.9	31.2	32.1	1.2	3.7
	10	442	508	475	47	9.9	32.1	31.4	31.8	0.5	1.5
	5	358	387	373	20	5.4	30.6	29.9	30.2	0.5	1.8
	1	215	244	229	21	9.2	29.1	28.1	28.6	0.7	2.5
	0.5	174	199	186	17	9.4	27.6	24.6	26.1	2.1	8.0
	0.1	118	130	124	9	7.2	23.2	21.6	22.4	1.1	5.0
130	25	186	195	191	7	3.6	36.5	34.2	35.3	1.6	4.5
	10	139	155	147	11	7.3	35.2	26.0	30.6	6.5	21.3
	5	112	125	118	9	7.8	27.5	23.7	25.6	2.7	10.4
	1	67	77	72	7	10.4	21.3	20.0	20.6	0.9	4.4
	0.5	53	62	58	6	10.4	19.5	18.6	19.0	0.6	3.4
	0.1	32	37	34	4	10.4	16.6	17.7	17.2	0.7	4.3

TABLE A.10 E* test results of PG 58-28 mixture at 4.2% AC and 9.5% Va

Temp (°F)	Freq (Hz)	Dynamic Modulus, E*					Phase Angle, ϕ				
		Repl. 1 5-901 (ksi)	Repl. 2 5-902 (ksi)	Average (ksi)	Std. Dev. (ksi)	Coeff. of Var.	Repl. 1 5-901 (Deg.)	Repl. 2 5-902 (Deg.)	Average (Deg.)	Std. Dev. (Deg.)	Coeff. of Var.
14	25	3024	2259	2642	541	20.5	4.6	7.8	6.2	2.2	35.8
	10	2832	2222	2527	431	17.1	6.9	10.1	8.5	2.2	26.3
	5	2709	2111	2410	423	17.5	8.8	10.0	9.4	0.8	8.7
	1	2465	1904	2185	396	18.1	10.6	11.0	10.8	0.3	2.8
	0.5	2324	1835	2080	346	16.6	11.1	13.2	12.1	1.5	12.2
	0.1	1972	1642	1807	233	12.9	12.9	14.3	13.6	1.0	7.1
40	25	1801	1662	1732	98	5.7	11.5	8.8	10.2	1.9	18.6
	10	1601	1602	1602	1	0.0	17.3	11.3	14.3	4.2	29.7
	5	1459	1504	1482	31	2.1	20.1	13.7	16.9	4.6	27.1
	1	1129	1239	1184	78	6.5	22.0	14.8	18.4	5.1	27.9
	0.5	1016	1128	1072	79	7.4	22.9	16.6	19.7	4.4	22.3
	0.1	745	877	811	93	11.5	26.7	19.9	23.3	4.8	20.7
70	25	798	969	884	121	13.7	21.8	17.6	19.7	2.9	14.9
	10	675	786	730	78	10.7	23.0	21.7	22.3	1.0	4.3
	5	604	661	633	41	6.4	26.3	22.8	24.6	2.5	10.1
	1	413	451	432	27	6.3	31.2	28.1	29.7	2.2	7.4
	0.5	351	378	364	19	5.3	33.5	30.7	32.1	2.0	6.3
	0.1	232	244	238	8	3.4	34.4	33.4	33.9	0.7	2.1
100	25	283	243	263	29	10.9	31.0	32.6	31.8	1.1	3.5
	10	205	178	191	19	9.9	29.8	31.3	30.5	1.1	3.7
	5	167	142	154	18	11.4	29.3	30.6	30.0	0.9	2.9
	1	107	94	101	10	9.5	26.8	25.1	26.0	1.2	4.6
	0.5	91	83	87	6	6.5	24.8	23.0	23.9	1.2	5.2
	0.1	56	58	57	2	3.4	22.1	18.9	20.5	2.3	11.0
130	25	88	98	93	7	7.6	18.5	27.8	23.1	6.6	28.6
	10	65	75	70	8	10.8	19.3	26.9	23.1	5.4	23.2
	5	55	62	58	4	7.4	15.7	22.9	19.3	5.1	26.2
	1	36	38	37	2	4.5	12.2	19.6	15.9	5.2	32.8
	0.5	29	31	30	2	5.1	12.3	17.5	14.9	3.7	24.9
	0.1	18	20	19	1	6.3	11.4	17.6	14.5	4.3	30.0

TABLE A.11 E* test results of PG 58-28 mixture at 4.2% AC and 7.0% Va

Temp (°F)	Freq (Hz)	Dynamic Modulus, E*					Phase Angle, ϕ				
		Repl. 1 5-701 (ksi)	Repl. 2 5-702 (ksi)	Average (ksi)	Std. Dev. (ksi)	Coeff. of Var.	Repl. 1 5-701 (Deg.)	Repl. 2 5-702 (Deg.)	Average (Deg.)	Std. Dev. (Deg.)	Coeff. of Var.
14	25	3386	2399	2893	698	24.1	4.7	6.7	5.7	1.4	24.6
	10	3171	2365	2768	570	20.6	5.9	9.3	7.6	2.4	31.4
	5	3046	2274	2660	546	20.5	7.5	9.5	8.5	1.4	16.3
	1	2704	2029	2366	477	20.2	9.1	10.7	9.9	1.1	11.2
	0.5	2458	1929	2193	374	17.1	8.6	12.2	10.4	2.6	24.7
	0.1	2106	1645	1875	326	17.4	12.3	11.2	11.7	0.7	6.4
40	25	2654	2069	2361	413	17.5	10.8	8.4	9.6	1.7	17.6
	10	2486	2003	2244	342	15.2	14.9	11.2	13.1	2.7	20.3
	5	2227	1900	2063	231	11.2	18.1	13.0	15.5	3.6	23.2
	1	1685	1598	1641	62	3.7	20.7	14.7	17.7	4.2	24.0
	0.5	1486	1458	1472	20	1.3	21.8	15.2	18.5	4.6	25.1
	0.1	1050	1154	1102	73	6.6	26.6	19.9	23.3	4.7	20.4
70	25	1333	1173	1253	113	9.0	20.9	19.5	20.2	1.0	4.9
	10	1116	985	1051	92	8.8	24.1	21.7	22.9	1.7	7.4
	5	970	858	914	79	8.6	27.5	24.5	26.0	2.1	8.1
	1	643	586	614	40	6.5	33.8	30.2	32.0	2.6	8.0
	0.5	528	491	510	27	5.2	35.7	32.0	33.8	2.6	7.8
	0.1	329	321	325	6	1.9	39.3	35.0	37.2	3.0	8.0
100	25	347	295	321	37	11.5	37.3	31.9	34.6	3.9	11.1
	10	251	213	232	27	11.6	36.3	30.2	33.3	4.3	12.9
	5	194	171	183	17	9.2	35.3	30.2	32.7	3.6	10.9
	1	128	108	118	14	11.7	31.0	26.2	28.6	3.4	12.0
	0.5	108	91	100	12	12.1	27.9	24.5	26.2	2.4	9.2
	0.1	73	67	70	4	6.2	23.8	19.7	21.8	2.9	13.4
130	25	127	121	124	4	3.2	23.3	27.5	25.4	2.9	11.5
	10	96	94	95	2	1.8	21.1	22.9	22.0	1.2	5.6
	5	78	77	77	1	0.7	17.5	20.5	19.0	2.1	11.1
	1	47	49	48	1	1.9	14.9	15.6	15.2	0.5	3.1
	0.5	38	40	39	1	3.0	12.6	13.7	13.1	0.8	6.2
	0.1	24	25	24	1	5.5	7.2	13.0	10.1	4.1	40.2

TABLE A.12 E* test results of PG 58-28 mixture at 4.2% AC and 4.5% Va

Temp (°F)	Freq (Hz)	Dynamic Modulus, E*					Phase Angle, ϕ				
		Repl. 1 5-401 (ksi)	Repl. 2 5-402 (ksi)	Average (ksi)	Std. Dev. (ksi)	Coeff. of Var.	Repl. 1 5-401 (Deg.)	Repl. 2 5-402 (Deg.)	Average (Deg.)	Std. Dev. (Deg.)	Coeff. of Var.
14	25	3447	3730	3588	200	5.6	7.0	6.6	6.8	0.3	4.8
	10	3281	3614	3448	235	6.8	8.9	8.6	8.8	0.2	2.7
	5	3215	3482	3348	189	5.6	9.6	9.2	9.4	0.2	2.6
	1	2856	3109	2982	179	6.0	11.8	9.4	10.6	1.7	16.3
	0.5	2725	2978	2852	179	6.3	11.4	10.3	10.8	0.8	7.5
	0.1	2361	2600	2480	169	6.8	11.8	11.3	11.6	0.4	3.4
40	25	2864	2934	2899	49	1.7	9.7	9.1	9.4	0.4	4.6
	10	2488	2691	2590	143	5.5	12.0	11.5	11.8	0.3	2.8
	5	2270	2554	2412	201	8.3	13.5	13.8	13.6	0.2	1.5
	1	1864	2136	2000	192	9.6	15.8	15.7	15.7	0.1	0.5
	0.5	1703	1956	1830	179	9.8	17.3	16.1	16.7	0.8	5.1
	0.1	1317	1559	1438	171	11.9	19.2	20.7	19.9	1.1	5.3
70	25	1536	1581	1559	32	2.1	14.3	18.4	16.4	2.9	17.5
	10	1311	1417	1364	75	5.5	18.4	24.0	21.2	4.0	18.9
	5	1155	1271	1213	82	6.8	20.5	27.1	23.8	4.7	19.6
	1	814	858	836	31	3.7	25.3	31.3	28.3	4.3	15.1
	0.5	693	725	709	23	3.2	27.5	33.3	30.4	4.1	13.6
	0.1	462	472	467	7	1.6	30.6	37.0	33.8	4.5	13.3
100	25	437	454	445	12	2.8	30.3	32.5	31.4	1.6	5.0
	10	329	336	333	5	1.4	29.6	31.0	30.3	0.9	3.1
	5	263	268	266	4	1.5	29.8	30.4	30.1	0.4	1.4
	1	165	169	167	2	1.5	28.4	28.1	28.2	0.1	0.5
	0.5	137	142	140	3	2.3	26.6	25.9	26.3	0.4	1.7
	0.1	99	108	103	6	6.1	23.6	20.4	22.0	2.2	10.2
130	25	168	167	168	0	0.2	29.9	30.9	30.4	0.7	2.4
	10	128	127	127	1	0.8	25.0	25.6	25.3	0.5	1.8
	5	104	102	103	1	1.3	22.9	23.5	23.2	0.4	1.9
	1	64	62	63	1	2.3	17.9	18.0	18.0	0.1	0.5
	0.5	52	50	51	1	2.8	15.3	16.3	15.8	0.7	4.4
	0.1	33	31	32	1	3.9	12.8	12.3	12.6	0.4	3.2

TABLE A.13 E* test results of PG 58-28 mixture at 4.7% AC and 9.5% Va

Temp (°F)	Freq (Hz)	Dynamic Modulus, E*					Phase Angle, ϕ				
		Repl. 1 5O901 (ksi)	Repl. 2 5O902 (ksi)	Average (ksi)	Std. Dev. (ksi)	Coeff. of Var.	Repl. 1 5O901 (Deg.)	Repl. 2 5O902 (Deg.)	Average (Deg.)	Std. Dev. (Deg.)	Coeff. of Var.
14	25	2222	1734	1978	345	17.4	5.7	9.2	7.4	2.4	32.6
	10	2146	1717	1932	303	15.7	9.0	10.2	9.6	0.9	9.2
	5	2045	1661	1853	272	14.7	9.3	12.3	10.8	2.1	19.8
	1	1826	1508	1667	225	13.5	11.3	11.8	11.6	0.3	2.9
	0.5	1732	1409	1570	228	14.5	9.9	13.9	11.9	2.8	23.5
	0.1	1496	1235	1366	184	13.5	12.8	13.5	13.1	0.5	4.1
40	25	1712	1230	1471	341	23.2	14.3	12.9	13.6	1.0	7.1
	10	1549	1173	1361	266	19.6	16.5	15.0	15.7	1.1	6.7
	5	1409	1106	1258	214	17.0	19.2	16.4	17.8	2.0	11.2
	1	1078	859	969	155	16.0	22.8	18.6	20.7	3.0	14.4
	0.5	968	789	879	126	14.3	23.4	20.7	22.0	1.9	8.8
	0.1	679	592	636	62	9.8	28.3	24.3	26.3	2.8	10.8
70	25	845	743	794	72	9.1	21.2	24.4	22.8	2.2	9.7
	10	688	627	657	43	6.6	24.4	25.2	24.8	0.6	2.4
	5	578	531	554	34	6.1	28.1	28.9	28.5	0.6	2.1
	1	383	362	373	15	4.0	31.9	32.6	32.2	0.5	1.5
	0.5	320	303	311	12	3.8	33.4	35.1	34.2	1.2	3.5
	0.1	202	201	202	1	0.4	37.2	37.7	37.5	0.4	1.1
100	25	215	238	226	17	7.4	33.4	30.4	31.9	2.1	6.6
	10	160	182	171	15	8.9	33.8	29.6	31.7	3.0	9.4
	5	125	145	135	14	10.6	30.6	27.4	29.0	2.3	7.8
	1	82	102	92	14	15.3	28.2	26.2	27.2	1.5	5.4
	0.5	69	89	79	14	18.3	25.4	25.2	25.3	0.1	0.6
	0.1	51	58	54	5	9.0	20.5	24.7	22.6	3.0	13.1
130	25	93	96	94	2	2.2	30.6	23.3	27.0	5.2	19.1
	10	68	74	71	4	6.0	25.9	23.2	24.5	1.9	7.7
	5	59	61	60	2	2.6	22.6	21.3	22.0	0.9	4.2
	1	33	38	36	4	11.1	20.7	21.3	21.0	0.4	2.0
	0.5	27	32	29	3	11.7	18.0	19.7	18.9	1.2	6.1
	0.1	17	20	18	2	13.1	15.9	16.3	16.1	0.3	1.8

TABLE A.14 E* test results of PG 58-28 mixture at 4.7% AC and 7.0% Va

Temp (°F)	Freq (Hz)	Dynamic Modulus, E*					Phase Angle, ϕ				
		Repl. 1 5O702 (ksi)	Repl. 2 5O703 (ksi)	Average (ksi)	Std. Dev. (ksi)	Coeff. of Var.	Repl. 1 5O702 (Deg.)	Repl. 2 5O703 (Deg.)	Average (Deg.)	Std. Dev. (Deg.)	Coeff. of Var.
14	25	2986	3006	2996	14	0.5	9.7	4.4	7.0	3.7	53.0
	10	2868	2889	2878	15	0.5	11.2	6.3	8.8	3.5	40.0
	5	2771	2788	2779	12	0.4	10.9	7.0	9.0	2.8	31.3
	1	2447	2499	2473	37	1.5	11.1	8.4	9.8	1.9	19.5
	0.5	2358	2373	2365	11	0.5	11.6	9.0	10.3	1.8	17.5
	0.1	2043	2059	2051	11	0.6	13.4	10.8	12.1	1.8	14.7
40	25	2176	2079	2127	69	3.2	11.5	10.8	11.2	0.5	4.2
	10	1931	1861	1896	49	2.6	12.8	13.3	13.1	0.4	3.0
	5	1784	1677	1730	76	4.4	14.4	15.1	14.8	0.5	3.4
	1	1437	1320	1378	83	6.0	18.7	18.3	18.5	0.3	1.4
	0.5	1301	1177	1239	88	7.1	18.4	20.8	19.6	1.7	8.9
	0.1	994	856	925	98	10.6	23.1	24.2	23.7	0.7	3.1
70	25	1010	908	959	72	7.5	20.3	21.9	21.1	1.1	5.4
	10	836	735	785	71	9.1	23.2	25.7	24.4	1.7	7.1
	5	722	634	678	62	9.1	25.0	29.3	27.2	3.0	11.2
	1	486	390	438	68	15.4	29.7	33.3	31.5	2.6	8.2
	0.5	411	324	368	62	16.8	30.4	34.3	32.4	2.8	8.5
	0.1	272	198	235	52	22.1	31.4	35.6	33.5	3.0	9.0
100	25	373	258	316	81	25.8	31.8	32.4	32.1	0.4	1.2
	10	280	187	233	66	28.2	28.3	31.2	29.8	2.1	7.0
	5	227	149	188	55	29.5	28.5	30.2	29.4	1.2	4.1
	1	151	93	122	41	33.8	24.0	25.6	24.8	1.1	4.4
	0.5	123	79	101	31	31.2	22.6	23.4	23.0	0.5	2.4
	0.1	78	60	69	13	18.8	17.5	18.4	17.9	0.7	3.6
130	25	130	102	116	20	16.9	23.3	29.5	26.4	4.4	16.6
	10	100	78	89	16	17.7	20.5	24.3	22.4	2.7	12.0
	5	82	63	73	13	18.3	20.2	20.5	20.3	0.2	0.9
	1	52	39	45	9	19.6	16.9	16.2	16.5	0.5	3.2
	0.5	42	32	37	7	20.2	13.6	13.3	13.4	0.2	1.5
	0.1	27	20	23	5	21.6	13.3	7.7	10.5	4.0	37.9

TABLE A.15 E* test results of PG 58-28 mixture at 4.7% AC and 4.5% Va

Temp (°F)	Freq (Hz)	Dynamic Modulus, E*					Phase Angle, ϕ				
		Repl. 1 5O402 (ksi)	Repl. 2 5O403 (ksi)	Average (ksi)	Std. Dev. (ksi)	Coeff. of Var.	Repl. 1 5O402 (Deg.)	Repl. 2 5O403 (Deg.)	Average (Deg.)	Std. Dev. (Deg.)	Coeff. of Var.
14	25	3387	3306	3347	57	1.7	6.7	7.1	6.9	0.3	4.3
	10	3326	3240	3283	61	1.9	9.9	9.0	9.5	0.6	6.7
	5	3150	3153	3152	2	0.1	10.4	9.9	10.1	0.3	3.2
	1	2745	2847	2796	72	2.6	11.8	10.2	11.0	1.1	10.2
	0.5	2608	2733	2670	88	3.3	12.2	11.4	11.8	0.6	4.9
	0.1	2438	2408	2423	21	0.9	13.7	12.6	13.1	0.8	6.0
40	25	3265	1720	2493	1093	43.8	9.1	12.3	10.7	2.2	20.9
	10	3135	1701	2418	1014	41.9	11.2	14.2	12.7	2.1	16.8
	5	2942	1613	2277	939	41.2	13.7	15.6	14.6	1.3	9.1
	1	2373	1296	1835	761	41.5	16.6	18.1	17.4	1.1	6.1
	0.5	2118	1188	1653	658	39.8	16.6	19.8	18.2	2.3	12.5
	0.1	1701	915	1308	556	42.5	22.9	23.1	23.0	0.2	0.9
70	25	1759	1096	1427	468	32.8	20.1	23.0	21.6	2.1	9.5
	10	1500	907	1204	419	34.8	23.0	26.3	24.6	2.4	9.7
	5	1299	780	1039	367	35.3	26.2	27.1	26.6	0.7	2.5
	1	889	517	703	263	37.4	34.0	31.7	32.8	1.6	4.9
	0.5	731	420	576	220	38.2	34.8	31.6	33.2	2.2	6.7
	0.1	460	277	369	130	35.1	34.8	33.0	33.9	1.3	3.8
100	25	475	396	436	55	12.7	28.1	34.1	31.1	4.2	13.7
	10	345	301	323	31	9.6	28.5	31.9	30.2	2.4	8.1
	5	272	241	256	22	8.4	27.9	32.0	29.9	2.9	9.7
	1	176	161	169	10	6.1	25.1	29.3	27.2	3.0	10.9
	0.5	146	139	142	5	3.8	22.8	29.0	25.9	4.4	17.0
	0.1	88	81	85	5	6.2	17.8	24.5	21.2	4.7	22.4
130	25	163	137	150	19	12.5	26.0	28.9	27.4	2.0	7.3
	10	119	105	112	10	9.3	22.9	27.3	25.1	3.1	12.3
	5	94	85	90	6	6.8	20.8	22.2	21.5	1.0	4.5
	1	54	53	54	1	1.1	14.3	15.6	15.0	0.9	6.2
	0.5	43	43	43	1	1.3	12.4	14.0	13.2	1.1	8.6
	0.1	25	27	26	2	6.9	10.2	12.2	11.2	1.4	12.7

TABLE A.16 E* test results of PG 58-28 mixture at 5.2% AC and 9.5% Va

Temp (°F)	Freq (Hz)	Dynamic Modulus, E*					Phase Angle, ϕ				
		Repl. 1 5+901 (ksi)	Repl. 2 5+902 (ksi)	Average (ksi)	Std. Dev. (ksi)	Coeff. of Var.	Repl. 1 5+901 (Deg.)	Repl. 2 5+902 (Deg.)	Average (Deg.)	Std. Dev. (Deg.)	Coeff. of Var.
14	25	1883	1735	1809	104	5.7	6.8	7.1	6.9	0.2	2.7
	10	1791	1613	1702	126	7.4	8.2	8.6	8.4	0.3	3.8
	5	1710	1537	1624	122	7.5	10.5	8.2	9.4	1.6	17.1
	1	1503	1345	1424	111	7.8	11.4	11.9	11.7	0.4	3.1
	0.5	1420	1260	1340	113	8.4	11.8	11.6	11.7	0.2	1.3
	0.1	1187	1067	1127	85	7.5	14.8	14.3	14.5	0.3	2.4
40	25	1202	1242	1222	28	2.3	13.9	11.6	12.7	1.6	12.8
	10	1073	1207	1140	95	8.3	16.2	16.8	16.5	0.4	2.6
	5	978	1131	1055	108	10.2	18.6	20.4	19.5	1.3	6.7
	1	748	886	817	98	12.0	23.3	21.6	22.5	1.2	5.3
	0.5	662	791	727	91	12.6	24.7	23.3	24.0	0.9	3.9
	0.1	464	572	518	76	14.8	29.9	30.3	30.1	0.3	0.9
70	25	478	680	579	143	24.7	25.2	25.1	25.2	0.0	0.1
	10	376	602	489	160	32.7	27.7	26.2	26.9	1.1	4.1
	5	308	504	406	139	34.1	29.5	29.3	29.4	0.1	0.4
	1	194	331	262	96	36.7	33.4	35.7	34.5	1.6	4.6
	0.5	156	265	211	77	36.5	32.9	37.3	35.1	3.1	8.8
	0.1	95	166	131	50	38.1	32.5	41.9	37.2	6.6	17.9
100	25	150	152	151	1	0.6	31.7	34.0	32.8	1.6	4.9
	10	102	123	112	15	13.6	31.1	32.6	31.8	1.1	3.4
	5	82	114	98	22	22.7	27.8	29.4	28.6	1.1	3.9
	1	51	90	70	28	39.9	22.6	28.5	25.6	4.2	16.4
	0.5	44	85	64	29	45.5	21.5	27.5	24.5	4.3	17.5
	0.1	36	52	44	11	25.5	18.1	24.5	21.3	4.5	21.0
130	25	52	85	68	23	34.1	21.6	22.5	22.1	0.7	3.0
	10	39	66	53	19	36.3	20.2	19.1	19.7	0.7	3.7
	5	31	55	43	16	38.0	19.5	17.4	18.4	1.4	7.8
	1	19	35	27	11	41.8	17.1	14.5	15.8	1.8	11.6
	0.5	15	29	22	10	43.5	16.2	13.2	14.7	2.2	14.7
	0.1	9	19	14	7	47.2	14.5	11.5	13.0	2.1	16.5

TABLE A.17 E* test results of PG 58-28 mixture at 5.2% AC and 7.0% Va

Temp (°F)	Freq (Hz)	Dynamic Modulus, E*					Phase Angle, ϕ				
		Repl. 1 5+703 (ksi)	Repl. 2 5+704 (ksi)	Average (ksi)	Std. Dev. (ksi)	Coeff. of Var.	Repl. 1 5+703 (Deg.)	Repl. 2 5+704 (Deg.)	Average (Deg.)	Std. Dev. (Deg.)	Coeff. of Var.
14	25	2883	2059	2471	582	23.6	8.1	9.3	8.7	0.9	10.2
	10	2728	1971	2350	536	22.8	10.5	12.3	11.4	1.3	11.4
	5	2624	1898	2261	513	22.7	11.0	14.1	12.6	2.2	17.5
	1	2321	1661	1991	467	23.5	12.0	13.9	12.9	1.3	10.3
	0.5	2234	1569	1901	470	24.7	12.4	13.7	13.1	0.9	6.6
	0.1	1897	1287	1592	431	27.1	15.0	15.1	15.0	0.1	0.6
40	25	1700	1340	1520	255	16.8	13.2	13.7	13.4	0.4	2.7
	10	1574	1224	1399	247	17.7	16.1	15.2	15.6	0.7	4.3
	5	1437	1136	1286	213	16.5	17.9	17.8	17.8	0.0	0.2
	1	1125	880	1003	173	17.2	21.2	20.2	20.7	0.7	3.5
	0.5	1000	789	894	149	16.6	23.9	22.4	23.1	1.0	4.3
	0.1	729	590	660	99	15.0	29.2	27.6	28.4	1.1	4.0
70	25	769	596	683	122	17.9	25.6	25.6	25.6	0.0	0.0
	10	619	498	559	86	15.4	26.6	28.3	27.5	1.2	4.5
	5	517	430	473	62	13.0	29.0	29.3	29.2	0.2	0.7
	1	335	278	306	40	13.1	34.2	32.7	33.4	1.1	3.3
	0.5	276	233	254	30	11.9	34.8	33.4	34.1	0.9	2.8
	0.1	181	161	171	14	8.0	33.6	34.5	34.0	0.6	1.9
100	25	235	219	227	11	5.0	30.6	31.6	31.1	0.7	2.2
	10	162	176	169	10	6.0	27.7	30.2	28.9	1.7	6.0
	5	132	152	142	14	9.6	26.3	27.5	26.9	0.9	3.3
	1	86	110	98	17	16.9	21.2	22.8	22.0	1.1	5.2
	0.5	77	102	90	18	19.7	19.3	20.4	19.8	0.7	3.7
	0.1	67	61	64	4	6.4	17.3	15.8	16.5	1.0	6.3
130	25	104	97	101	5	4.9	19.7	20.7	20.2	0.7	3.5
	10	79	77	78	2	2.2	18.5	16.4	17.4	1.5	8.8
	5	64	64	64	0	0.1	16.3	15.2	15.7	0.8	5.2
	1	39	42	41	2	4.8	18.0	14.0	16.0	2.8	17.5
	0.5	32	35	33	2	6.9	17.2	13.2	15.2	2.9	18.8
	0.1	20	23	21	3	11.7	14.5	11.5	13.0	2.1	15.8

TABLE A.18 E* test results of PG 58-28 mixture at 5.2% AC and 4.5% Va

Temp (°F)	Freq (Hz)	Dynamic Modulus, E*					Phase Angle, ϕ				
		Repl. 1 5+401 (ksi)	Repl. 2 5+402 (ksi)	Average (ksi)	Std. Dev. (ksi)	Coeff. of Var.	Repl. 1 5+401 (Deg.)	Repl. 2 5+402 (Deg.)	Average (Deg.)	Std. Dev. (Deg.)	Coeff. of Var.
14	25	3444	3171	3307	193	5.8	8.1	5.2	6.7	2.0	30.4
	10	3340	3077	3208	186	5.8	12.1	7.7	9.9	3.1	31.7
	5	3253	2970	3111	200	6.4	13.3	7.9	10.6	3.8	35.4
	1	2880	2661	2771	155	5.6	14.5	9.3	11.9	3.7	31.1
	0.5	2689	2547	2618	100	3.8	15.3	10.6	12.9	3.3	25.7
	0.1	2304	2208	2256	67	3.0	14.4	12.3	13.4	1.5	11.0
40	25	2828	2482	2655	244	9.2	13.4	8.8	11.1	3.2	28.9
	10	2481	2353	2417	90	3.7	16.0	12.2	14.1	2.7	18.9
	5	2259	2080	2169	126	5.8	16.9	15.3	16.1	1.2	7.2
	1	1775	1664	1719	79	4.6	19.8	18.1	19.0	1.2	6.2
	0.5	1599	1496	1548	73	4.7	21.0	22.5	21.7	1.1	5.0
	0.1	1179	1070	1124	77	6.9	23.9	26.6	25.2	1.9	7.4
70	25	1294	1307	1300	10	0.7	22.5	25.6	24.1	2.2	9.1
	10	1188	1122	1155	47	4.0	27.9	29.6	28.8	1.2	4.3
	5	991	914	953	54	5.7	30.3	32.1	31.2	1.3	4.1
	1	631	568	600	45	7.4	35.3	36.6	36.0	0.9	2.5
	0.5	511	459	485	37	7.6	35.8	38.2	37.0	1.6	4.4
	0.1	322	275	298	33	11.1	37.9	40.3	39.1	1.7	4.2
100	25	344	312	328	22	6.9	31.5	34.3	32.9	2.0	6.1
	10	250	220	235	21	9.1	31.6	31.7	31.7	0.1	0.2
	5	203	173	188	22	11.5	29.9	30.2	30.0	0.2	0.6
	1	134	115	124	14	11.0	26.8	27.7	27.3	0.6	2.3
	0.5	120	100	110	14	12.7	24.1	24.8	24.5	0.5	1.9
	0.1	79	82	81	2	2.9	19.7	21.9	20.8	1.6	7.6
130	25	134	120	127	10	7.8	24.7	21.7	23.2	2.1	9.2
	10	103	92	97	8	8.0	20.9	18.1	19.5	2.0	10.1
	5	83	74	79	6	8.2	20.2	17.1	18.7	2.2	11.7
	1	51	46	49	4	8.6	18.5	17.0	17.7	1.0	5.8
	0.5	42	37	39	3	8.8	17.9	14.7	16.3	2.3	14.2
	0.1	26	23	25	2	9.2	16.6	13.5	15.0	2.2	14.5

TABLE A.19 E* test results of PG 76-16 mixture at 4.2% AC and 9.5% Va

Temp (°F)	Freq (Hz)	Dynamic Modulus, E*					Phase Angle, ϕ				
		Repl. 1 7-901 (ksi)	Repl. 2 7-902 (ksi)	Average (ksi)	Std. Dev. (ksi)	Coeff. of Var.	Repl. 1 7-901 (Deg.)	Repl. 2 7-902 (Deg.)	Average (Deg.)	Std. Dev. (Deg.)	Coeff. of Var.
14	25	3888	3225	3556	468	13.2	3.7	5.0	4.3	1.0	22.6
	10	3803	3153	3478	460	13.2	5.7	8.0	6.9	1.6	23.3
	5	3767	3035	3401	518	15.2	5.8	8.2	7.0	1.7	23.7
	1	3490	2820	3155	474	15.0	7.4	7.2	7.3	0.2	2.1
	0.5	3478	2721	3100	535	17.3	7.1	6.7	6.9	0.3	3.9
	0.1	3233	2446	2840	556	19.6	7.6	7.8	7.7	0.1	1.6
40	25	2961	2458	2709	356	13.1	5.9	8.2	7.1	1.6	23.2
	10	2824	2384	2604	311	12.0	6.3	9.6	7.9	2.3	29.1
	5	2710	2220	2465	346	14.1	8.4	10.5	9.5	1.5	15.7
	1	2420	1895	2158	372	17.2	9.5	11.9	10.7	1.7	15.6
	0.5	2278	1785	2031	349	17.2	10.1	13.1	11.6	2.1	17.8
	0.1	1990	1455	1723	378	22.0	13.5	14.6	14.0	0.8	5.8
70	25	1693	1585	1639	77	4.7	14.3	18.1	16.2	2.7	16.4
	10	1521	1330	1426	135	9.5	16.3	21.0	18.6	3.3	17.7
	5	1384	1177	1281	147	11.5	18.8	23.7	21.3	3.5	16.2
	1	1067	855	961	150	15.6	23.3	25.0	24.2	1.2	4.9
	0.5	933	749	841	130	15.4	25.4	27.3	26.3	1.3	4.9
	0.1	635	526	581	77	13.3	29.9	30.9	30.4	0.7	2.2
100	25	717	575	646	100	15.5	33.1	27.1	30.1	4.2	14.0
	10	507	441	474	46	9.8	35.3	28.7	32.0	4.7	14.7
	5	398	355	376	30	8.0	35.7	29.0	32.4	4.7	14.6
	1	226	223	225	2	1.0	35.9	29.4	32.6	4.6	14.1
	0.5	180	185	182	4	2.0	34.7	28.8	31.7	4.2	13.2
	0.1	113	126	120	9	7.5	29.9	27.5	28.7	1.7	6.1
130	25	223	177	200	33	16.4	32.5	34.4	33.5	1.3	3.9
	10	161	133	147	20	13.5	30.0	30.0	30.0	0.0	0.0
	5	136	112	124	17	13.9	26.9	27.6	27.3	0.5	1.8
	1	78	76	77	1	1.1	21.9	24.2	23.1	1.7	7.3
	0.5	62	59	61	2	3.4	20.7	22.5	21.6	1.3	5.8
	0.1	37	36	36	1	1.8	20.1	20.9	20.5	0.6	2.9

TABLE A.20 E* test results of PG 76-16 mixture at 4.2% AC and 7.0% Va

Temp (°F)	Freq (Hz)	Dynamic Modulus, E*					Phase Angle, ϕ				
		Repl. 1 7-703 (ksi)	Repl. 2 7-704 (ksi)	Average (ksi)	Std. Dev. (ksi)	Coeff. of Var.	Repl. 1 7-703 (Deg.)	Repl. 2 7-704 (Deg.)	Average (Deg.)	Std. Dev. (Deg.)	Coeff. of Var.
14	25	4015	4089	4052	52	1.3	5.8	5.2	5.5	0.5	8.6
	10	3934	4042	3988	76	1.9	6.9	7.3	7.1	0.3	4.5
	5	3857	3931	3894	52	1.3	7.0	7.6	7.3	0.4	5.6
	1	3633	3682	3658	35	1.0	6.7	7.5	7.1	0.5	7.7
	0.5	3518	3583	3550	46	1.3	7.1	8.1	7.6	0.7	9.6
	0.1	3266	3382	3324	82	2.5	6.9	10.7	8.8	2.6	29.8
40	25	2974	3107	3041	95	3.1	8.3	8.2	8.2	0.1	0.9
	10	2853	2936	2895	59	2.0	10.7	10.1	10.4	0.4	3.6
	5	2735	2717	2726	13	0.5	11.6	11.2	11.4	0.2	2.0
	1	2412	2386	2399	18	0.8	12.7	13.4	13.1	0.5	4.1
	0.5	2282	2245	2264	26	1.2	13.2	14.2	13.7	0.7	5.4
	0.1	1941	1977	1959	26	1.3	14.2	15.6	14.9	1.0	6.7
70	25	1647	2198	1922	390	20.3	12.2	11.9	12.0	0.2	1.6
	10	1476	1953	1715	338	19.7	15.0	15.9	15.4	0.6	4.1
	5	1337	1759	1548	298	19.3	16.7	16.2	16.4	0.3	2.1
	1	1029	1305	1167	195	16.7	21.1	21.7	21.4	0.4	1.9
	0.5	913	1141	1027	161	15.7	23.1	23.9	23.5	0.6	2.6
	0.1	655	801	728	104	14.2	28.0	29.0	28.5	0.7	2.3
100	25	789	945	867	110	12.7	25.9	27.6	26.7	1.2	4.6
	10	690	736	713	33	4.6	28.0	29.4	28.7	1.0	3.6
	5	569	608	588	27	4.6	29.2	30.4	29.8	0.8	2.8
	1	355	369	362	10	2.7	32.7	33.3	33.0	0.4	1.2
	0.5	282	292	287	7	2.5	33.5	34.5	34.0	0.7	2.2
	0.1	171	161	166	7	4.4	34.0	35.3	34.6	0.9	2.6
130	25	252	283	268	22	8.2	34.3	35.2	34.8	0.6	1.8
	10	196	216	206	14	7.0	31.8	33.3	32.6	1.1	3.3
	5	160	175	168	10	6.0	30.5	31.8	31.1	0.9	3.0
	1	100	105	102	4	3.7	26.6	28.0	27.3	1.0	3.8
	0.5	81	84	82	2	2.7	24.5	25.0	24.8	0.4	1.5
	0.1	49	50	50	0	0.3	19.6	20.3	19.9	0.5	2.7

TABLE A.21 E* test results of PG 76-16 mixture at 4.2% AC and 4.5% Va

Temp (°F)	Freq (Hz)	Dynamic Modulus, E*					Phase Angle, ϕ				
		Repl. 1 7-403 (ksi)	Repl. 2 7-404 (ksi)	Average (ksi)	Std. Dev. (ksi)	Coeff. of Var.	Repl. 1 7-403 (Deg.)	Repl. 2 7-404 (Deg.)	Average (Deg.)	Std. Dev. (Deg.)	Coeff. of Var.
14	25	4649	5325	4987	478	9.6	4.0	3.1	3.5	0.6	17.4
	10	4416	5060	4738	455	9.6	6.0	4.5	5.3	1.1	20.7
	5	4325	4892	4608	400	8.7	5.7	4.9	5.3	0.5	10.1
	1	4094	4597	4345	356	8.2	5.4	5.7	5.6	0.2	3.1
	0.5	3976	4503	4240	372	8.8	5.8	6.2	6.0	0.3	4.6
	0.1	3668	4083	3875	293	7.6	7.1	7.1	7.1	0.0	0.2
40	25	3476	3886	3681	290	7.9	6.2	5.4	5.8	0.6	10.0
	10	3288	3682	3485	279	8.0	8.7	7.8	8.3	0.7	8.2
	5	3148	3451	3299	215	6.5	7.3	8.3	7.8	0.7	8.7
	1	2760	2964	2862	145	5.1	10.1	10.4	10.3	0.2	2.1
	0.5	2551	2727	2639	124	4.7	11.0	11.8	11.4	0.6	4.8
	0.1	2168	2185	2176	12	0.6	13.6	14.8	14.2	0.9	6.0
70	25	2136	2207	2172	50	2.3	11.7	13.2	12.4	1.1	8.8
	10	1918	1886	1902	23	1.2	16.1	17.2	16.6	0.8	4.5
	5	1731	1667	1699	45	2.7	18.3	19.6	19.0	0.9	5.0
	1	1338	1221	1280	83	6.5	21.3	25.7	23.5	3.1	13.4
	0.5	1184	1044	1114	99	8.8	23.5	28.5	26.0	3.6	13.7
	0.1	857	705	781	108	13.8	30.3	34.7	32.5	3.1	9.4
100	25	940	894	917	33	3.6	26.6	29.3	27.9	1.9	6.8
	10	720	669	694	36	5.2	28.9	29.7	29.3	0.6	1.9
	5	591	553	572	27	4.7	29.8	28.8	29.3	0.7	2.3
	1	354	332	343	16	4.5	31.8	32.0	31.9	0.1	0.3
	0.5	284	267	275	12	4.5	31.4	32.8	32.1	1.0	3.1
	0.1	173	182	177	6	3.4	29.6	30.0	29.8	0.2	0.8
130	25	268	295	282	19	6.9	33.8	34.2	34.0	0.2	0.7
	10	201	234	218	23	10.7	28.3	32.0	30.2	2.7	8.8
	5	165	198	182	24	13.0	26.2	30.8	28.5	3.3	11.5
	1	115	111	113	3	2.5	20.1	24.3	22.2	3.0	13.4
	0.5	93	89	91	3	2.9	17.7	21.9	19.8	2.9	14.9
	0.1	57	54	56	2	3.9	13.0	22.1	17.5	6.4	36.5

TABLE A.22 E* test results of PG 76-16 mixture at 4.7% AC and 9.5% Va

Temp (°F)	Freq (Hz)	Dynamic Modulus, E*					Phase Angle, ϕ				
		Repl. 1 70903 (ksi)	Repl. 2 70904 (ksi)	Average (ksi)	Std. Dev. (ksi)	Coeff. of Var.	Repl. 1 70903 (Deg.)	Repl. 2 70904 (Deg.)	Average (Deg.)	Std. Dev. (Deg.)	Coeff. of Var.
14	25	2898	3814	3356	648	19.3	4.2	5.9	5.0	1.2	23.0
	10	2763	3649	3206	627	19.6	6.3	10.2	8.2	2.8	34.0
	5	2719	3537	3128	578	18.5	8.3	9.4	8.8	0.8	8.6
	1	2537	3339	2938	567	19.3	8.9	10.9	9.9	1.4	14.3
	0.5	2445	3189	2817	527	18.7	9.1	10.4	9.8	0.9	9.7
	0.1	2180	2882	2531	496	19.6	9.3	10.6	10.0	0.9	9.0
40	25	2722	2721	2722	1	0.0	8.4	8.0	8.2	0.3	3.2
	10	2543	2553	2548	7	0.3	11.2	10.2	10.7	0.7	6.3
	5	2410	2423	2417	9	0.4	11.9	11.7	11.8	0.1	1.1
	1	2065	2124	2094	41	2.0	13.8	11.5	12.7	1.6	12.8
	0.5	1925	2003	1964	55	2.8	12.9	13.0	13.0	0.1	0.5
	0.1	1603	1695	1649	64	3.9	14.6	14.5	14.6	0.0	0.2
70	25	1490	1445	1468	32	2.2	12.0	13.5	12.8	1.1	8.6
	10	1317	1290	1303	19	1.4	14.9	15.9	15.4	0.7	4.6
	5	1197	1160	1178	26	2.2	16.2	17.8	17.0	1.1	6.4
	1	920	895	907	17	1.9	20.4	21.9	21.1	1.0	4.9
	0.5	798	787	793	8	1.0	23.3	24.6	24.0	1.0	4.0
	0.1	557	564	561	5	1.0	27.4	30.7	29.0	2.3	7.9
100	25	548	584	566	25	4.4	25.1	29.0	27.0	2.8	10.4
	10	427	452	439	18	4.1	26.7	30.3	28.5	2.5	8.9
	5	354	372	363	13	3.5	28.8	30.9	29.9	1.5	5.0
	1	229	234	231	3	1.3	32.4	34.1	33.2	1.1	3.4
	0.5	190	192	191	1	0.8	33.1	33.3	33.2	0.1	0.3
	0.1	131	131	131	1	0.4	33.4	35.2	34.3	1.3	3.7
130	25	204	209	206	4	1.9	28.1	31.1	29.6	2.2	7.3
	10	159	166	162	5	2.9	28.5	29.4	29.0	0.6	2.1
	5	131	130	131	1	0.6	26.9	28.3	27.6	1.0	3.6
	1	82	77	80	4	4.7	22.2	26.5	24.3	3.1	12.6
	0.5	67	62	65	4	5.5	19.5	25.9	22.7	4.6	20.1
	0.1	42	37	40	3	7.5	17.1	25.6	21.3	6.0	28.2

TABLE A.23 E* test results of PG 76-16 mixture at 4.7% AC and 7.0% Va

Temp (°F)	Freq (Hz)	Dynamic Modulus, E*					Phase Angle, ϕ				
		Repl. 1 7O701 (ksi)	Repl. 2 7O702 (ksi)	Average (ksi)	Std. Dev. (ksi)	Coeff. of Var.	Repl. 1 7O701 (Deg.)	Repl. 2 7O702 (Deg.)	Average (Deg.)	Std. Dev. (Deg.)	Coeff. of Var.
14	25	4752	3803	4277	671	15.7	7.5	6.6	7.1	0.7	9.4
	10	4528	3529	4028	707	17.5	10.8	8.6	9.7	1.6	16.0
	5	4359	3441	3900	649	16.6	12.4	9.1	10.8	2.4	22.1
	1	3800	3166	3483	449	12.9	13.4	9.9	11.6	2.5	21.6
	0.5	3609	3047	3328	397	11.9	14.8	8.8	11.8	4.2	36.2
	0.1	3134	2791	2963	242	8.2	14.9	10.6	12.8	3.0	23.7
40	25	3040	3094	3067	38	1.3	10.6	8.5	9.5	1.5	15.5
	10	2860	2828	2844	22	0.8	14.8	11.1	12.9	2.6	20.1
	5	2788	2633	2710	110	4.0	15.9	13.0	14.4	2.1	14.4
	1	2325	2281	2303	31	1.3	17.4	12.6	15.0	3.5	23.1
	0.5	2132	2142	2137	7	0.3	18.7	13.3	16.0	3.8	23.7
	0.1	1752	1857	1805	74	4.1	19.9	12.8	16.3	5.0	30.5
70	25	2246	1825	2035	298	14.6	18.3	10.7	14.5	5.4	37.0
	10	2072	1737	1905	237	12.5	21.9	13.6	17.7	5.9	33.2
	5	1790	1602	1696	133	7.9	23.4	17.2	20.3	4.4	21.9
	1	1238	1259	1249	15	1.2	28.4	20.9	24.7	5.3	21.3
	0.5	1100	1106	1103	4	0.4	30.1	22.3	26.2	5.5	21.1
	0.1	748	823	786	53	6.7	33.7	26.1	29.9	5.4	18.0
100	25	921	633	777	204	26.3	31.9	24.6	28.2	5.1	18.2
	10	711	488	600	158	26.3	33.9	28.7	31.3	3.7	11.8
	5	596	411	503	130	25.9	34.5	28.4	31.4	4.3	13.6
	1	342	267	305	53	17.4	39.4	30.0	34.7	6.7	19.2
	0.5	289	227	258	43	16.8	39.4	29.6	34.5	6.9	20.1
	0.1	200	162	181	27	14.8	39.9	28.2	34.0	8.3	24.4
130	25	284	231	257	38	14.6	33.2	29.2	31.2	2.8	9.0
	10	215	175	195	28	14.5	29.0	25.5	27.2	2.5	9.3
	5	173	148	161	18	11.3	28.5	24.9	26.7	2.6	9.7
	1	103	97	100	4	4.2	24.8	20.1	22.4	3.3	14.8
	0.5	82	79	81	2	2.7	21.4	18.8	20.1	1.8	9.1
	0.1	48	49	48	0	0.9	20.9	19.0	19.9	1.3	6.7

TABLE A.24 E* test results of PG 76-16 mixture at 4.7% AC and 4.5% Va

Temp (°F)	Freq (Hz)	Dynamic Modulus, E*					Phase Angle, ϕ				
		Repl. 1 7O401 (ksi)	Repl. 2 7O403 (ksi)	Average (ksi)	Std. Dev. (ksi)	Coeff. of Var.	Repl. 1 7O401 (Deg.)	Repl. 2 7O403 (Deg.)	Average (Deg.)	Std. Dev. (Deg.)	Coeff. of Var.
14	25	4641	5346	4994	498	10.0	5.0	2.5	3.8	1.8	46.5
	10	4620	5260	4940	453	9.2	7.8	3.8	5.8	2.8	48.4
	5	4513	5183	4848	474	9.8	8.6	4.3	6.4	3.1	47.7
	1	4100	4870	4485	545	12.1	8.0	6.7	7.4	0.9	12.9
	0.5	3971	4709	4340	522	12.0	8.9	7.4	8.2	1.1	12.9
	0.1	3591	4324	3957	518	13.1	7.8	9.1	8.4	0.9	10.8
40	25	3404	3979	3692	407	11.0	7.1	5.6	6.3	1.1	16.9
	10	3192	3783	3487	418	12.0	8.9	7.6	8.2	0.9	11.3
	5	3028	3597	3313	403	12.2	9.6	8.1	8.9	1.0	11.8
	1	2663	3310	2987	458	15.3	10.5	10.2	10.4	0.2	2.2
	0.5	2529	3049	2789	368	13.2	11.0	12.1	11.6	0.8	7.2
	0.1	2183	2548	2365	258	10.9	12.6	15.7	14.1	2.2	15.6
70	25	2338	2115	2226	158	7.1	11.4	11.9	11.6	0.4	3.0
	10	2316	1944	2130	263	12.3	14.4	16.0	15.2	1.1	7.5
	5	2147	1690	1918	323	16.9	14.0	17.9	15.9	2.8	17.5
	1	1623	1264	1443	254	17.6	17.9	23.6	20.8	4.0	19.3
	0.5	1441	1112	1276	232	18.2	20.0	25.1	22.6	3.6	15.9
	0.1	1035	763	899	192	21.4	24.3	30.9	27.6	4.6	16.7
100	25	1074	1079	1077	4	0.4	23.7	25.8	24.8	1.5	5.9
	10	893	824	858	49	5.7	24.8	28.4	26.6	2.5	9.4
	5	776	682	729	67	9.2	25.8	28.6	27.2	2.0	7.4
	1	518	413	465	75	16.0	29.2	35.6	32.4	4.6	14.1
	0.5	439	325	382	80	20.9	30.0	36.3	33.2	4.5	13.4
	0.1	299	193	246	75	30.5	26.7	32.2	29.4	3.9	13.1
130	25	389	386	387	2	0.6	25.3	35.6	30.5	7.3	24.0
	10	313	270	291	30	10.3	24.6	32.9	28.8	5.9	20.5
	5	270	209	240	43	17.9	23.3	31.3	27.3	5.7	20.9
	1	167	125	146	30	20.3	20.3	25.1	22.7	3.4	15.0
	0.5	136	106	121	21	17.7	18.4	21.1	19.7	1.9	9.5
	0.1	84	68	76	11	14.7	15.9	15.0	15.4	0.6	4.1

TABLE A.25 E* test results of PG 76-16 mixture at 5.2% AC and 9.5% Va

Temp (°F)	Freq (Hz)	Dynamic Modulus, E*					Phase Angle, ϕ				
		Repl. 1 7+903 (ksi)	Repl. 2 7+904 (ksi)	Average (ksi)	Std. Dev. (ksi)	Coeff. of Var.	Repl. 1 7+903 (Deg.)	Repl. 2 7+904 (Deg.)	Average (Deg.)	Std. Dev. (Deg.)	Coeff. of Var.
14	25	2724	2331	2527	278	11.0	3.5	8.4	6.0	3.5	58.3
	10	2691	2222	2457	331	13.5	5.7	9.7	7.7	2.9	37.2
	5	2659	2140	2399	367	15.3	6.1	10.2	8.2	2.9	35.4
	1	2448	1975	2211	334	15.1	7.3	9.6	8.4	1.6	19.1
	0.5	2391	1923	2157	331	15.4	7.5	9.9	8.7	1.7	19.5
	0.1	2203	1725	1964	338	17.2	8.3	10.7	9.5	1.6	17.2
40	25	1999	1427	1713	404	23.6	7.7	8.3	8.0	0.4	5.6
	10	1921	1384	1652	380	23.0	10.8	9.0	9.9	1.3	12.7
	5	1825	1314	1570	362	23.1	12.3	11.5	11.9	0.6	4.9
	1	1571	1132	1351	311	23.0	13.1	11.9	12.5	0.8	6.6
	0.5	1490	1127	1309	256	19.6	13.2	12.1	12.7	0.7	5.9
	0.1	1233	886	1060	245	23.1	15.7	16.6	16.1	0.7	4.1
70	25	1101	774	937	231	24.6	13.9	17.6	15.7	2.6	16.6
	10	992	733	863	183	21.2	15.9	22.0	18.9	4.3	22.6
	5	910	672	791	168	21.3	18.0	22.8	20.4	3.4	16.7
	1	679	497	588	128	21.8	22.3	28.2	25.2	4.1	16.3
	0.5	591	430	511	114	22.2	24.3	31.4	27.8	5.0	18.1
	0.1	413	293	353	85	24.0	29.6	36.0	32.8	4.6	13.9
100	25	524	359	441	117	26.4	27.2	30.2	28.7	2.1	7.4
	10	398	278	338	85	25.0	28.2	29.6	28.9	1.0	3.4
	5	322	226	274	68	25.0	31.5	30.0	30.8	1.1	3.4
	1	193	140	166	38	22.8	32.5	31.6	32.0	0.6	2.0
	0.5	157	116	137	29	21.3	30.9	31.9	31.4	0.7	2.3
	0.1	104	80	92	17	18.4	29.4	32.7	31.0	2.3	7.5
130	25	165	142	154	16	10.4	33.3	34.3	33.8	0.7	2.1
	10	119	104	112	11	9.8	29.9	31.1	30.5	0.8	2.6
	5	96	87	91	6	6.7	27.8	27.4	27.6	0.3	1.2
	1	68	51	59	12	20.4	24.2	23.4	23.8	0.6	2.4
	0.5	60	41	51	14	26.6	22.8	21.2	22.0	1.1	5.2
	0.1	36	26	31	8	24.3	21.5	18.5	20.0	2.1	10.5

TABLE A.26 E* test results of PG 76-16 mixture at 5.2% AC and 7.0% Va

Temp (°F)	Freq (Hz)	Dynamic Modulus, E*					Phase Angle, ϕ				
		Repl. 1 7+703 (ksi)	Repl. 2 7+704 (ksi)	Average (ksi)	Std. Dev. (ksi)	Coeff. of Var.	Repl. 1 7+703 (Deg.)	Repl. 2 7+704 (Deg.)	Average (Deg.)	Std. Dev. (Deg.)	Coeff. of Var.
14	25	4181	3192	3687	699	19.0	4.5	5.4	4.9	0.7	13.6
	10	3983	3104	3543	622	17.5	5.0	7.8	6.4	1.9	30.2
	5	3863	2968	3415	633	18.5	5.7	8.2	7.0	1.8	25.3
	1	3578	2741	3160	592	18.7	6.9	9.8	8.3	2.0	24.1
	0.5	3442	2617	3029	584	19.3	6.8	9.3	8.0	1.8	22.8
	0.1	3043	2395	2719	458	16.8	6.8	10.0	8.4	2.3	27.0
40	25	2846	2333	2589	363	14.0	5.8	8.6	7.2	1.9	26.8
	10	2693	2268	2481	300	12.1	8.6	12.3	10.4	2.6	25.2
	5	2543	2137	2340	287	12.3	9.8	13.6	11.7	2.7	23.1
	1	2194	1840	2017	250	12.4	10.4	14.7	12.5	3.1	24.5
	0.5	2041	1717	1879	229	12.2	11.0	15.1	13.0	2.9	22.6
	0.1	1707	1422	1564	201	12.9	13.0	16.9	14.9	2.7	18.1
70	25	1684	1787	1735	73	4.2	13.1	14.8	14.0	1.2	8.4
	10	1494	1532	1513	27	1.8	17.9	20.0	18.9	1.5	7.9
	5	1340	1371	1356	22	1.6	18.3	22.2	20.2	2.8	13.7
	1	1005	979	992	18	1.8	24.2	27.1	25.7	2.1	8.0
	0.5	873	851	862	15	1.8	26.7	29.7	28.2	2.1	7.3
	0.1	596	558	577	27	4.6	32.9	34.5	33.7	1.1	3.3
100	25	702	715	709	10	1.3	26.6	29.4	28.0	2.0	7.1
	10	546	538	542	6	1.0	29.2	31.9	30.5	1.9	6.1
	5	444	427	435	12	2.7	30.4	32.5	31.4	1.5	4.7
	1	272	252	262	14	5.5	34.0	36.3	35.2	1.6	4.6
	0.5	218	199	209	14	6.5	34.5	35.7	35.1	0.9	2.5
	0.1	139	124	132	10	7.9	34.4	36.2	35.3	1.2	3.5
130	25	201	208	204	5	2.4	33.5	35.8	34.7	1.7	4.8
	10	147	147	147	0	0.2	30.8	32.7	31.8	1.4	4.3
	5	115	114	115	0	0.3	27.5	29.9	28.7	1.7	6.0
	1	77	75	76	1	1.4	22.5	25.7	24.1	2.3	9.4
	0.5	66	68	67	1	1.7	20.4	23.3	21.8	2.1	9.5
	0.1	38	42	40	2	6.2	17.7	23.6	20.6	4.2	20.2

TABLE A.27 E* test results of PG 76-16 mixture at 5.2% AC and 4.5% Va

emp (°F)	Freq (Hz)	Dynamic Modulus, E*					Phase Angle, ϕ				
		Repl. 1 7+401 (ksi)	Repl. 2 7+402 (ksi)	Average (ksi)	Std. Dev. (ksi)	Coeff. of Var.	Repl. 1 7+401 (Deg.)	Repl. 2 7+402 (Deg.)	Average (Deg.)	Std. Dev. (Deg.)	Coeff. of Var.
14	25	4765	4031	4398	519	11.8	6.1	5.6	5.8	0.4	6.2
	10	4742	3908	4325	590	13.6	6.4	6.6	6.5	0.2	2.5
	5	4613	3770	4191	596	14.2	6.2	7.3	6.7	0.8	11.2
	1	4322	3446	3884	619	15.9	7.6	6.7	7.1	0.7	9.4
	0.5	4175	3292	3733	624	16.7	8.3	6.7	7.5	1.2	15.4
	0.1	3821	3026	3423	562	16.4	9.5	8.2	8.9	0.9	10.4
40	25	3874	3498	3686	265	7.2	8.6	7.6	8.1	0.7	8.3
	10	3769	3488	3628	199	5.5	10.6	9.0	9.8	1.1	11.7
	5	3580	3341	3461	170	4.9	11.8	10.5	11.1	1.0	8.6
	1	3109	2954	3032	109	3.6	13.2	11.0	12.1	1.6	13.1
	0.5	2931	2775	2853	110	3.9	13.9	11.8	12.9	1.5	11.3
	0.1	2561	2373	2467	133	5.4	16.4	13.6	15.0	2.0	13.2
70	25	1778	1744	1761	24	1.3	14.5	10.7	12.6	2.6	20.9
	10	1567	1538	1552	21	1.3	18.7	14.1	16.4	3.2	19.7
	5	1413	1387	1400	19	1.3	19.9	14.9	17.4	3.5	20.4
	1	1081	1061	1071	14	1.3	24.5	18.2	21.4	4.5	21.0
	0.5	951	934	943	13	1.3	26.8	20.4	23.6	4.5	19.3
	0.1	687	674	680	9	1.3	31.9	25.5	28.7	4.5	15.7
100	25	795	711	753	60	8.0	29.4	27.6	28.5	1.2	4.3
	10	609	565	587	31	5.3	29.2	27.8	28.5	1.0	3.4
	5	481	469	475	9	1.8	29.9	29.1	29.5	0.6	2.0
	1	299	292	296	5	1.6	32.7	30.5	31.6	1.6	5.0
	0.5	244	242	243	2	0.7	31.3	30.9	31.1	0.3	0.9
	0.1	173	159	166	9	5.6	29.3	28.5	28.9	0.6	1.9
130	25	223	256	240	23	9.8	32.7	33.4	33.1	0.5	1.6
	10	159	184	172	18	10.3	27.7	30.5	29.1	2.0	6.8
	5	128	146	137	12	9.1	25.8	28.9	27.3	2.2	8.1
	1	94	97	96	2	2.4	20.3	24.6	22.4	3.0	13.6
	0.5	75	85	80	7	8.8	18.4	22.4	20.4	2.9	14.1
	0.1	44	49	47	4	8.3	16.6	18.4	17.5	1.3	7.3

APPENDIX B

PROPOSED UNIAXIAL FATIGUE TEST PROTOCOL

Proposed standard practice for

UNIAXIAL REPEATED FATIGUE TEST OF COMPACTED HOT-MIX ASPHALT (HMA)



AASHTO Designation: PP XX-XX

1. SCOPE

- 1.1. This test method covers procedures for preparing and testing asphalt concrete mixtures through the uniaxial cyclic fatigue tests.
- 1.2. This standard is applicable to laboratory prepared specimens of mixtures with nominal maximum size aggregate less than or equal to 37.5 mm (1.5 in.).
- 1.3. This standard may involve hazardous materials, operations, and equipment. This standard does not purport to address all of the safety problems associated with its use. It is the responsibility of the user of this procedure to establish appropriate safety and health practices and to determine the applicability of regulatory limitations prior to its use.

2. REFERENCED DOCUMENTS

- 2.1. AASHTO Standards:
 - TP-62 Determining Dynamic Modulus of Hot Mix Asphalt Concrete Specimens
 - R-30 Practice for Mixture Conditioning of Hot Mix Asphalt (HMA)
 - NCHRP 9-20 PP 01 Preparation of Cylindrical Performance Test Specimen using the Superpave Gyrotory Compactor
 - 2.2. ASTM Standards:
 - E4, Standard Practice for Force Verification and Testing Machine.
 - 2.3. Other Documents:
 - NCHRP 9-29 Equipment Specification for the Simple Performance Tester Version 3.
-

3. DEFINITIONS

- 3.1. Complex modulus (E^*)—a complex number that defines the relationship between stress and strain for a linear viscoelastic material where there is no or minimal damage takes place.
- 3.2. *Dynamic modulus* ($|E^*|$)—the normal value of the complex modulus calculated by dividing the maximum (peak-to-peak) stress by the recoverable (peak-to-peak) axial strain for a material subjected to sinusoidal loading.
- 3.3. *Phase angle* (ϕ)—the angle in degrees between a sinusoidal applied peak stress and the resulting peak strain in a controlled stress test.
- 3.4. *Stiffness* (E)—the measured moduli during the uniaxial fatigue test where the specimen is subjected to fatigue damage. The stiffness value at any cycle N is calculated by dividing the peak-to-peak stress by the recoverable peak-to-peak strain.
- 3.5. *Initial Stiffness* (E_0)—the stiffness measured at cycle number 100th.
- 3.6. *Fatigue life* (N_f)—the number of loading cycles until fatigue failure.

4. SUMMARY OF METHOD

- 4.1. The uniaxial fatigue test is strain-controlled and repeated sinusoidal cyclic loading that applied to a cylindrical asphalt concrete specimen until failure so that the average on-specimen axial strain is kept constant during the test. The applied stress and on-specimen axial strain response are measured and used to calculate the stiffness and the phase angle until failure. Figure 1 presents a schematic of the test setup for the fatigue test.

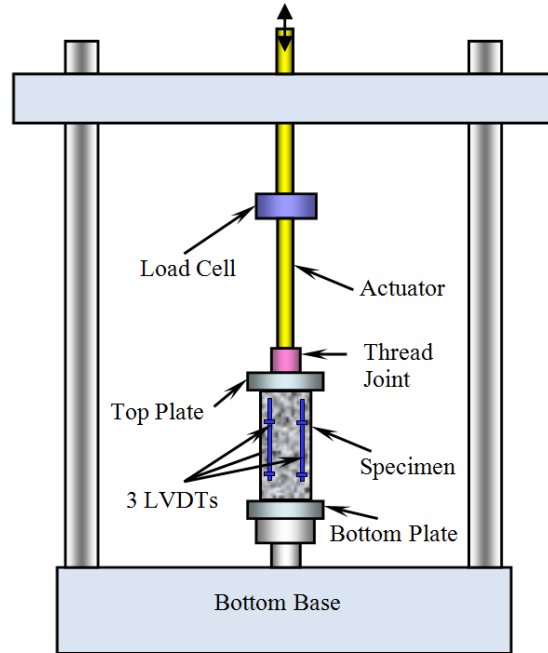


Figure 1—General schematic of the cyclic uniaxial fatigue test setup.

5. SIGNIFICANCE AND USE

- 5.1. This practice describes the procedure to run the uniaxial tension-compression (pull-push) fatigue test under a constant on-specimen strain-controlled condition until failure.

6. APPARATUS

- 6.1. *Uniaxial fatigue test system*—consists of a testing machine, environmental chamber, and measurement system.
- 6.2. *Testing machine*—A servo hydraulic testing machine capable of producing controlled sinusoidal tensile-compressive loading. The testing machine should have a capability of applying load over a range of frequencies from 1 to 10 Hz and stress level up to 2,800 kPa (400 psi).
- 6.3. *Conditioning chamber*—A chamber for controlling the test specimens to the desired testing temperature. The chamber shall be capable of controlling the temperature of the specimen over a temperature range of 0° to 40°C (32° to 104°F) to within $\pm 0.5^\circ\text{C}$ (1°F). The chamber shall be

large enough to accommodate at least a single test specimen and a dummy specimen with a temperature sensor mounted at the center and on the surface for temperature verification.

- 6.4. *Control and data acquisition system*—The system shall be fully computer-controlled and capable of measuring and recording the time history of the applied load and axial deformations. In addition, it shall be capable of adjusting the actuator deformation in order to keep the average on-specimen strain constant by time until the end of the test. The test system shall meet the minimum requirements specified in Table 1.

Table 1—Test System Minimum Requirements.

Measurement	Range	Accuracy	Resolution
Load	± 0.12 to ± 25 kN (± 25 to ± 5600 lb)	Error ≤ 1.0%	≤ 0.0012 kN
Deformation	At least 12 mm (0.5 in)	Error ≤ 0.03 mm	≤ 0.0025 mm
On-specimen Deformation	At least 7000 µε	Error ≤ 1.0%	≤ 7.5%
Frequency	1 to 10 Hz	≤ 0.01 Hz	≤ 0.005 Hz
Temperature	0° to 40°C (32° to 104°F)	± 0.5°C (± 1.0°F)	± 0.25°C (± 0.5°F)
Phase Lag between Load and Deformation	Not specified	Error ≤ 1.0 degree	Not specified

- 6.5. *Axial deformation measurements*—axial deformations shall be measured using linear variable differential transformers (LVDTs) mounted between gauge points glued to the specimen.

Note 1 —A gauge length range of 70 to 100 mm can be used. Longer gauge length improves the likelihood that cracking will develop within the gauge length range. Using three LVDTs set at 120° apart has an advantage over using other arrangements; it covers three different directions compared to only one and two directions in the case of the two and four LVDTs, respectively.

Note 2 – The LVDTs shall have a span length of $\pm 2.5 \text{ mm} \pm 0.01 \text{ mm}$. This span length is appropriate to cover a wide range of test temperatures and asphalt mixtures (Conventional and modified).

- 6.6. *Load measurement*—An electronic load cell shall be used to measure the load. The load measuring system shall have a minimum range of $\pm 25 \text{ kN}$ ($\pm 5600 \text{ lb}$).
- 6.7. *Loading platens*—Top and bottom loading platens are glued to the specimen to transfer the load from the testing machine to the specimen. Loading platens should be made of hardened or plated steel, or anodized high strength aluminum. Softer materials will require more frequent replacement. Materials that have linear elastic modulus properties and hardness properties lower than that of 6061-T6 aluminum shall not be used. To insure a better adhesion between the glue and the end platens, the face of each load platen shall be slightly ridged. The end platen shall be designed to be easily attached to the gluing jig and the loading machine.
- 6.8. *End plate gluing jig*—Gluing jig for gluing the end plates to the asphalt concrete specimen is crucial to achieve a good quality test results. The device should take care of centering the specimen within the end plates and ensure that no eccentricity exists between the specimen and end plates. The gluing jig shall have an alignment system to hold the specimen in an absolute vertical direction during the gluing. Figure 2 shows an example of a well-designed gluing jig.
- 6.9. *Compaction Machine*—Superpave Gyratory Compactor or any other standard compaction apparatus shall be used prepare laboratory specimens. The compactor shall be capable of compacting 180-mm (7.1-inch) high specimen.
- 6.10. *Coring Machine*—A coring machine with a cooling system and a diamond bit for coring 75-mm (3-inch) or 100-mm (4-inch) diameter shall be used.

A vertical feed speed of 0.5 mm/rev (0.002 inch/rev) and a rotational speed of 450RPM has been found to be satisfactory.

- 6.11. *Sawing Machine*—A saw with a cooling system shall be used to trim the specimen ends to the appropriate length. The saw shall have a diamond cutting edge and that appropriate for asphalt mixtures.

Note 3 – A cutting jig shall be used to hold the specimen tight and to ensure the cutting blade is perpendicular to the specimen edge.

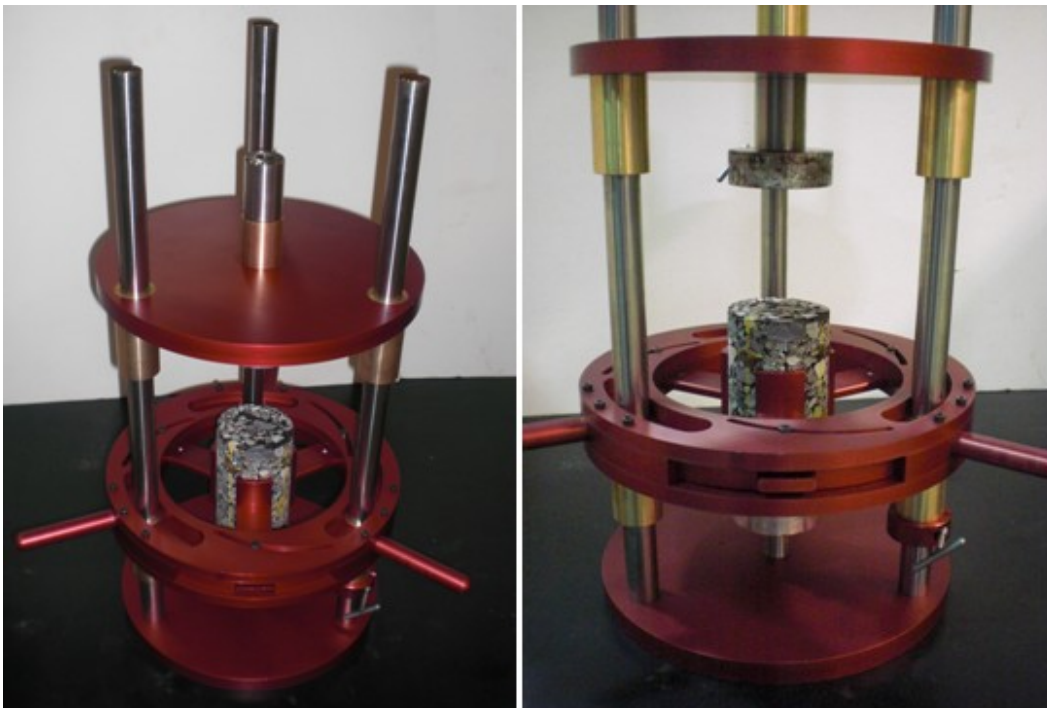


Figure 2—Axial gluing jig.

7. HAZARDS

- 7.1. This practice and associated standards involve handling of hot asphalt binder, aggregates and asphalt mixtures. It also includes the use of sawing and coring machinery and servo-hydraulic or pneumatic testing equipment. Use standard safety precautions, equipment, and clothing when handling hot materials and operating machinery.

8. TESTING EQUIPMENT CALIBRATION

- 8.1. The signal conditioning and data acquisition device of the testing system shall be verified to ensure that there is no excess phase shift between load and displacement channels.
- 8.2. The testing system shall be calibrated prior to initial use and at least once a year thereafter or per manufacturer requirements.
- 8.3. Check the capability of the environmental chamber to maintain the required temperature within the accuracy specified shall be verified.
- 8.4. The calibration of all the measurement components (such as the load cell and specimen deformation measurement device) of the testing system shall be verified.
- 8.5. If any of the verifications yield data that do not comply with the accuracy specified, the problem must be corrected prior to further testing.

9. TEST SPECIMEN

- 9.1. *Aging*—Laboratory-prepared mixtures shall be temperature-conditioned in accordance with the 4-hour short-term oven conditioning procedure outlined in AASHTO R-30. Field mixtures need not be aged prior to testing.
- 9.2. *Size*—Laboratory uniaxial tension-compression fatigue testing shall be performed on test specimens cored and cut from larger Superpave gyratory compacted specimens. Proper specimens for uniaxial fatigue test have been obtained from gyratory samples 150-mm (6-inch) in diameter and 180-mm (7.1-inch) in height. Test specimens shall be 75 ± 0.5 mm (3 ± 0.02 inch) or 100 ± 0.5 mm (4 ± 0.02 inch) in diameter with a standard deviation of 1.0 mm (0.04 inch). The average height of the test specimens shall be 150 ± 2.5 (6 ± 0.1 inch).

Note 1 –Specimens compacted using gyratory compactors tend to have non-uniform air void distribution with higher air voids at the core ends compared to the middle part. In addition, the top side of the cored specimen usually has higher air voids compared to the bottom side. The bottom side of the specimen refers to the bottom of the gyratory compaction mold. In order to have a more homogeneous air void distribution through the height of the specimen, certain portions have to be cut from the top and the bottom side of the cored specimen. For specimens compacted to a height of 180 mm, 18 mm should be cut from the top side of the specimen and 12 mm should be cut from the bottom side.

Note 2 –The target air void content should be representative of that expected to be obtained in the field with a reasonable air void tolerance for test specimen fabrication of $\pm 0.5\%$.

- 9.3. *Replicates*—three replicate specimens should be tested at each strain level.
- 9.4. *Sample storage*—If test specimens will not be tested within two days, the specimens shall be wrapped in polyethylene and stored in an environmentally protected storage area at temperatures between 5° and 25°C (40° and 77°F). Specimens shall not be stacked during storage.

Note 3 – To eliminate the effects of aging on the test results, it is recommended that specimens be stored no longer than one month prior to testing.

10. TEST SPECIMEN INSTRUMENTATION PROCEDURE

- 10.1. Clean the loading platens and the ends of the specimen from any residual dust using a towel or a brush. Screw the top and the bottom end platens into the gluing jig. Place the specimen roughly on the center of the bottom end platens. Tighten the gluing jig to hold the specimen vertically and to

place it exactly into the center of the bottom end platen. Move the upper part of the jig upward.

- 10.2. Weigh out an appropriate amount of glue for only the top end of the specimen.

Note 1 –The following epoxy types were found to be satisfactory for gluing the specimens without having any failure between the platens and the glue:

- Davcon plastic steel 5 minutes putty 10240 (2800 psi strength)
- Loctite metal /concrete epoxy (2700 psi strength)
- Loctite Fixmaster Superior Metal (5500 psi strength)
- ACE plastic repair epoxy (3431 psi strength)

Note 2 –approximately 35 grams epoxy was found to be enough for one side of 75 mm diameter specimen.

- 10.3. Mix the two components of the epoxy by the required percentages very well for 30 seconds until homogeneous putty is obtained. Take around 60% of the glue and spread it at the top surface of the specimens. Move the top part of the jig downward until the upper end platens rest on the upper surface of the specimen. Apply enough pressure on the top part of the jig to squeeze any extra glue between the top end platen and the top surface of the specimen. Use the other 40% plus the squeezed epoxy to glue the outer surface of the top end of the specimen and the top end platen to cover around 10 mm from each.

Note 3 –gluing about 10 mm from the outer surface at top and bottom of the specimen was found to decrease the opportunity of having edge failure.

- 10.4. Allow the adhesive to reach its initial set. Release the gluing jig then move the upper part upward with the upper end platens and the specimen.

Prepare the epoxy amount for the bottom side of the specimen. Spread 60% of the epoxy amount on the top of the lower end platens. Move down the upper part of the jig till the specimen rest on the upper end platen and finish the gluing of the lower end of the specimen as explained earlier for the top end. Leave the specimen until the initial set is reached then remove the specimen from the gluing jig.

- 10.5. After approximately two hours, attach the mounting studs for the axial LVDTs to the sides of the specimen using epoxy cement.

Note 4 –Davcon plastic steel 5 minutes putty 10240 was found to be efficient at a temperature range of -10° to 54°C (14° to 130°F).

- 10.6. The gauge length for measuring axial deformations of samples may be anywhere between $100\text{ mm} \pm 1\text{ mm}$ and $70\text{ mm} \pm 1\text{ mm}$ (between $4\text{ in.} \pm 0.04\text{ in.}$ and $2.75\text{ in.} \pm 0.04\text{ in.}$). The gauge length shall be measured between the stud centers.
- 10.7. Allow the glue to reach full cure before testing. Follow the manufacturer's recommendation to determine the time needed to full cure.

11. PROCEDURE

- 11.1. The test procedure consists of two tests. The first test is the non-destructive test to obtain fingerprint modulus at a specific temperature and frequency under the stress-controlled mode of loading. The second test is fatigue test, which is conducted under a constant on-specimen strain-control mode of loading at 10 Hz frequency until failure.
- 11.2. Insert the specimen into the environmental chamber of the test equipment.
- 11.3. Allow enough conditioning time for the specimen to reach the desired temperature $\pm 0.5^{\circ}\text{C}$ ($\pm 1^{\circ}\text{F}$) by monitoring the temperature probe instrumented on the dummy specimen.

Note 1 –when the dummy specimen is instrumented with only core temperature probe, allow more 30 minutes for equilibrium

once the core probe stabilized at the target test temperature. If the dummy specimen has skin as well as core temperature probe, monitor the specimen until the core probe temperature equilibrated at the target temperature and the temperature difference between both probes is not more than $\pm 1^{\circ}\text{C}$ ($\pm 2^{\circ}\text{F}$).

- 11.4. Zero the load cell in case if it is showing any readings which may be due to the weight of the actuator and the attachment joint.
- 11.5. Tighten the specimen securely to the bottom support and tighten the inner screw joint into the upper end platen. Bring the actuator to the specimen until inner screw joint get in contact with the outer screw joint attached to the end of the actuator. Tighten the inner and outer screw joints firmly.

Note 2 –After the specimen is tighten to the bottom base; if the testing machine has a mobile bottom base that can move up and down manually by hand or automatically by a motor, move the bottom base upward till the outer screw joint get in contact with the inner screw joint then tighten them. In this case, keep moving up the bottom base during tightening so that there is no compressive or tensile force applied to the specimen as showed by the software LEVELS screen. In case the testing machine have a fixed bottom base, switch the loading mode to a stress control with a very small compressive force of 10 Newtons so that the actuator moves down until the inner screw joint get in contact with the outer screw joint. Then tighten both joints together firmly.

- 11.6. Attach the LVDTs to the specimen and adjust them to be close as possible to the zero reading.
- 11.7. Reduce the specimen load to 0 Newtons (within ± 10 Newtons if this is possible with the equipment).
- 11.8. Allow the specimen time to come to equilibrium with the air temperature.

11.9. Perform a dynamic modulus fingerprint test at the target test temperature and at 10 Hz. Use the standard dynamic modulus protocol with the exception that a total of 50 cycles should be applied in tension-compression mode. In the first 10 cycles the load level should be adjusted so that the on specimen strains are 50–75 microstrains and in the final 40 cycles this load level should be consistently applied. The best way to achieve that is to assume as closely the expected fingerprint modulus at the test temperature, which can be estimated from experience. The software shall determine the required initial stress to achieve on-specimen strain in the middle of the desired strain range (62.5 microstrains). The software shall apply this stress value on the first cycle then the actual initial on-specimen strain and modulus shall be obtained. Based on how close the assumed modulus value is from the actual measured value, the Adaptive Level Control (ALC) option shall automatically change the stress level gradually to achieve as close strain within the desire range during the first 10 cycles. The obtained stress levels shall then fixed the remaining 40 cycles.

Note 3 –Alternatively one may apply a total of 50 cycles at a known stress input value (again tension-compression). This stress input value should yield on-specimen strain amplitude of 50-75 microstrains. If it does not then one may iterate until 50-75 microstrains is reached. At no time during these trials should the on-specimen strain amplitude exceed 150 microstrains.

11.10. The specimen should be allowed to rest for at least 2 minutes in case of repetition of the fingerprint modulus test.

11.11. Compute the dynamic modulus using the standard dynamic modulus protocol by using the final 5 test cycles results.

11.12. Return the dynamic modulus value, the phase angle value, and the machine compliance factor which should be calculated from Equation 1. Hold the machine compliance factor (MCF) in memory.

$$MCF = \frac{\varepsilon_{act}}{\varepsilon_{on-sp}} \quad (1)$$

where:

ε_{on-sp} = the peak-to-peak average on-specimen strain,

ε_{act} = the peak-to-peak actuator strain, calculated from Equation 2, and

MCF = the machine compliance factor.

$$\varepsilon_{act} = \frac{\Delta_{act}}{H_o} \quad (2)$$

where:

Δ_{act} = the peak-to-peak actuator displacement, and

H_o = the initial height of the specimen (150 mm).

$$\varepsilon_{on-sp} = \frac{\Delta_{on-sp}}{L_g} \quad (3)$$

where:

Δ_{on-sp} = the peak-to-peak average on-specimen displacement, and

L_g = Gauge length (70 to 100 mm).

11.13. Allow the specimen to rest for a period of 5 to 15 minutes with a load level of 0 Newtons (within ± 10 Newtons if this is possible with the equipment) before conducting the uniaxial tension-compression fatigue test.

11.14. Enter the target on-specimen strain into the software require to run the uniaxial tension-compression fatigue test.

Note 4 –If only one software is used to run both the fingerprint modulus as well as the uniaxial fatigue test, the target on-specimen strain shall be entered at the beginning and before running the finger print test.

- 11.15. Perform a strain-control actuator oscillation fatigue test at a frequency of 10 Hz.
- 11.16. The load shape for the actuator displacement will be repeating sinusoidal with positive-negative (tension-compression) movement.

Note 5 –Sinusoidal strain wave (tension-compression) is appropriate to minimize or eliminate the permanent deformation compared to the haversine strain wave (direct-tension) as shown in Figure 3. In addition, there is no existence for the haversine loading wave as it shall gradually change to sinusoidal wave after only few cycles due to the viscoelastic behavior of asphalt concrete mixture (Figure 4).

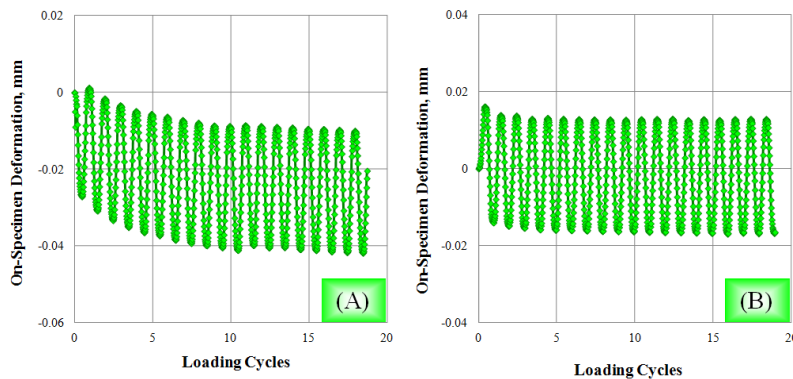


Figure 3—Typical on-specimen deformation wave shape over time; A) direct-tension and B) tension-compression.

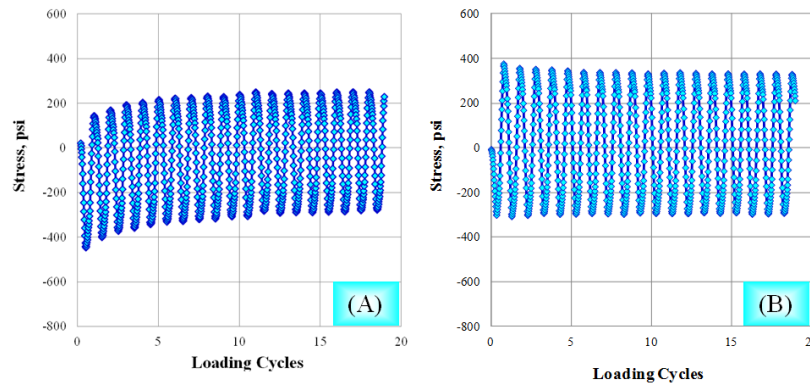


Figure 4—Typical stress wave shape over time; A) direct-tension and B) tension-compression.

11.17. At the first cycle, the software shall convert the initial target on-specimen strain (ϵ_{ost}) into actuator displacement (Δ_{act}) by using Equation 4.

$$\Delta_{act} = MCF \times L_g \times \epsilon_{ost} \quad (4)$$

11.18. Based on the calculated initial average on-specimen strain from the first cycle, the software shall have the capability to adjust the actuator strain to achieve the target average on-specimen strain by using a correction factor within the first 10 cycles. This can be achieved by having the adaptive strain control (ASC) option. Due to the fatigue damage as the test proceeds, the specimen stiffness shall reduce by time and decrease the machine compliance factor and increase the average on-specimen strain compared to the target value. To solve this issue, the software shall keep using the ASC option to readjust the actuator displacement every 10 cycles to keep the target on-specimen strain constant. Figure 5 shows typical relationships of actuator strain and on-specimen LVDTs strain versus loading cycles.

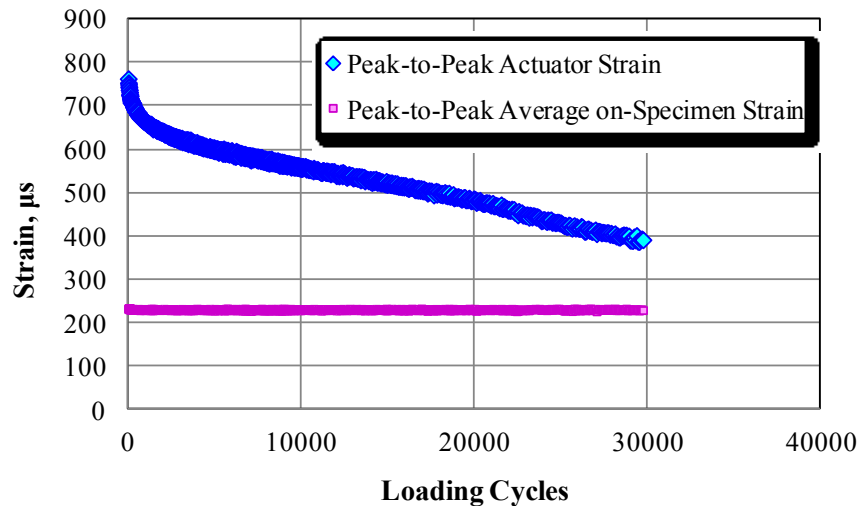


Figure 5 —Typical actuator strain and average on-specimen strain versus loading cycles relationships.

Note 6 –A correction factor of 0.5 was found to be good. The software shall automatically stop the test if the correction factor suddenly increased to 2.5, which mean that there is an issue with the test with it continuing the test is considered unsafe. These issues can be like a sudden failure of the specimen or one or more LVDTs might get stocked and stopped moving.

11.19. The test shall be run until failure or when the test reaches certain terminate condition.

Note 7 –The software shall have more than one option to automatically stop the test. These options are:

- Target number of loading cycles (i.e. 10,000 cycles),
- Target stiffness reduction (i.e. 50% reduction of the initial stiffness), and
- ALC limit (i.e. when the correction factor reaches 2.5).

11.20. The on-screen plots should include the following parameters as a function of cycle where the user can choose in-between to show from a dropping list:

- Modulus
- Phase angle
- Stresses (Minimum stress, maximum stress, and peak-to-peak stress)
- Strains (LVDTs individual strains, and the average strain)

11.21. These values can be determined by analysis or fitting of multiple cycles in a group, for example every 5 cycles or every 10 cycles or 20 cycles whatever is most currently used in the existing fatigue protocol should be sufficient.

12. DATA ACQUISITION AND SAVED DATA

12.1. Data should be acquired into three separate files.

12.2. In the first file the data from the dynamic raw data of the first cycle should be acquired at a rate of 1000 samples per second. The file should contain a header row with the column titles. The exact wording of these column headers is not important.

- Column 1 – Time (mseconds)
- Column 2 – Axial Stress (kilopascals)
- Column 3 –Actuator microstrain (mm/mm)
- Column 4 –Axial microstrain # 1 (mm/mm)
- Column 5 –Axial microstrain # 2 (mm/mm)
- Column 6 –Axial microstrain # 3 (mm/mm)
- Column 7 –Temperature (°C)
- Column 8 –Load (kN)
- Column 9 –Actuator (mm)
- Column 10 –Displacement #1 (mm)
- Column 11 –Displacement #2 (mm)
- Column 12 –Displacement #3 (mm)

12.3. In the second file the data from the remaining cycles should be stored. The contents and the order of data file are given below.

- Column 1 – Cycle
- Column 2 – Dynamic Modulus (MPa)
- Column 3 – Phase Angle (Degrees)
- Column 4 – Peak to Peak Stress (kPa)
- Column 5 – Maximum Stress (kPa)

- Column 6 – Minimum Stress (kPa)
- Column 7 – Peak to Peak Actuator Strain (micro-strain)
- Column 8 – Peak to Peak Average Strain (micro-strain)
- Column 9 – Peak to Peak Strain #1 (micro-strain)
- Column 10 – Peak to Peak Strain #2 (micro-strain)
- Column 11 – Peak to Peak Strain #3 (micro-strain)
- Column 12 – Maximum Actuator Strain (micro-strain)
- Column 13 – Minimum Actuator Strain(micro-strain)
- Column 14 – Maximum Strain #1 (micro-strain)
- Column 15 – Minimum Strain #1 (micro-strain)
- Column 16 – Maximum Strain #2 (micro-strain)
- Column 17 – Minimum Strain #2 (micro-strain)
- Column 18 – Maximum Strain #3 (micro-strain)
- Column 19 – Minimum Strain #3 (micro-strain)
- Column 20 – Column 7 –Temperature (°C)
- Column 21 – Peak to Peak Load (kN)
- Column 22 – Maximum Load (kN)
- Column 23 – Minimum Load (kN)
- Column 24 – Peak to Peak Actuator (mm)
- Column 25 – Peak to Peak LVDT #1 (mm)
- Column 26 – Peak to Peak LVDT #2 (mm)
- Column 27 – Peak to Peak LVDT #3 (mm)
- Column 29 – Maximum Actuator Displacement (mm)
- Column 30 – Minimum Actuator Displacement (mm)

- Column 31 – Maximum Displacement #1 (mm)
- Column 32 – Minimum Displacement #1 (mm)
- Column 33 – Maximum Displacement #2 (mm)
- Column 34 – Minimum Displacement #2 (mm)
- Column 35 – Maximum Displacement #3 (mm)
- Column 36 – Minimum Displacement #3 (mm)

12.3. The third data file shall be a runtime file that saves the raw dynamic data at a rate of 500 samples per second for every saved cycle in file 2. The saving of this shall be optional if the user decided to have these data as usually the size of this file is considerably high. The contents and the order of data file are given below.

- Column 1 – Cycle #
- Column 2 – Time (msecond)
- Column 3 – load (kN)
- Column 4 – Actuator (mm)
- Column 5 – LVDT #1 (mm)
- Column 6 – LVDT #2 (mm)
- Column 7 – LVDT #3 (mm)

The user should be able to select the spacing of data in the second and third file on the basis of cycle number. For example, if the user wants to store the output data for every 10 cycles there should be a location for them to enter the number “10”. If they want to store data every 30 cycles then in that same location they should enter “30”.

13. CALCULATIONS

13.1. Phase Angle (Degree):

$$\phi = 360 \times f \times t_l$$

where:

f = load frequency (Hz), and

t_l = time lag between maximum stress and maximum strain (seconds).

13.2. Maximum (Tensile) Stress (Pa, or psi):

$$\sigma_t = \frac{4 \times P_t}{\pi \times D^2}$$

where:

P_t = maximum (tensile) Load (N, or lb), and

D = specimen diameter (m, or inch).

13.3. Maximum (Tensile) Strain:

$$\varepsilon_t = \frac{\Delta_{t-avg}}{L_g}$$

where:

Δ_{t-avg} = Average maximum (tensile) deflection, (mm, or inch), and

L_g = gauge length (mm, or inch).

13.4. Stiffness (Pa, or psi):

$$E = \frac{\sigma_t}{\varepsilon_t}$$

- 13.5. Initial Stiffness (*Pa, or psi*): E_0 is defined as the stiffness at 100th loading cycle.

Note 1—It was found that E_0 at 100th cycle provided a more accurate fitting of the experimental data to establish the fatigue life ($\log N_f - \log \epsilon_t$) relationships compared to E_0 at 50th cycle.

- 13.6. Cycles to Failure (N_f): Fatigue failure is defined as the point at which the specimen is reduced to 50% of E_0 .

Note 2—Other definitions of fatigue failure can be used as there is no clear evidence about an ultimate definition of fatigue failure. Dissipated energy, phase angle, and pseudo stiffness are other candidate parameters to define fatigue failure.

14. REPORT

- 14.1. HMA Description: Mixture type, binder type, binder content, and air voids.
- 14.2. Specimen Dimension: Specimen height, and specimen diameter.
- 14.3. Test Conditions: Temperature, loading mode, and target peak-to-peak strain.
- 14.4. Finger Print Test: Dynamic modulus, phase angle, and machine compliance factor.
- 14.5. Uniaxial Fatigue Test: Initial modulus, initial phase angle, initial stress, cycles until failure, phase angle at failure, and stress at failure.

APPENDIX C

SUMMARY OF UNIAXIAL FATIGUE TEST RESULTS

Appendix C contains the results of the uniaxial tension compression fatigue test Experiments. Three uniaxial experiments were conducted. The first experiment is the fatigue lives experiment to determine the proper strain levels for each asphalt mixtures that fail the specimens at 20,000 and 100,000 loading cycles. The second experiment is the main experiment to study the effect of five factors on the fatigue damage and healing through the results of the tests without and with rest period respectively. A third uniaxial fatigue experiment called additional experiment was introduced to account for additional levels of the strain level and the rest period to account for the non-linearity effect of both factors. The data for the three uniaxial fatigue experiments were compiled together to developed PSR model using a total number of 161 test results. For the tests without rest period, only one PSR value was collected from each test at N_f . For the tests with rest periods, Four PSR values were collected from each test at 5000, 10000, 15000, 20000 cycles respectively to investigate the effect of N on the PSR for the tests with rest period which are of interest to determine the endurance limit. A total of 385 data point is summarized in TABLE C1.

The uniaxial fatigue experiments include the testing of four asphalt mixtures according to the asphalt content and air voids values (4.5 Va%&4.2 AC%, 9.5 Va%&4.2 AC%, 4.5 Va%&5.2 AC%, and 9.5 Va%&5.2 AC%). To estimate the healing of fatigue damage at different conditions, uniaxial fatigue tests were conducted at three temperatures (40, 70, and 100 °F) and at different strain values. The uniaxial fatigue software includes two tests. The first test is the

non-damage finger print test and the second test damage fatigue test. The next section showed the parameters of interest measured for each test.

Finger Print (FP) Modulus Test Results

- Stress-control test
- Sinusoidal wave form (tension-compression)
- 10 Hz frequency at fatigue test temperature

$$|E^*|_{fp} = \frac{\sigma_o}{\epsilon_o}$$

$$\phi = (t_i / t_p) \times (360^\circ)$$

Where:

E^*_{fp} = finger print modulus

ϕ = phase angle

σ_o = peak dynamic stress

ϵ_o = recoverable axial strain

t_i = time lag between a cycle of stress and strain (sec).

t_p = time for a stress cycle (sec).

Machine Compliance factor (MCF) = peak-to-peak actuator strain / average peak-to-peak on-specimen strain

Uniaxial Tension Compression Fatigue Test Results

- On-specimen strain-control test
- Tension-compression Sinusoidal wave form
- 10 Hz frequency

$|E_o|$ = initial modulus or stiffness measured at cycle number 100

Tensile strain = peak-to-peak on-specimen strain/2

S_o = tensile stress measured at cycle number 100

PSR = pseudo stiffness at cycle i divided by the initial pseudo stiffness at cycle number 100

$$PS = \frac{\sigma}{\varepsilon_{0,ta}^R \times DMR}$$

where:

PS = Pseudo stiffness at cycle i ,

σ = peak-to-peak stress at cycle i ,

$\varepsilon_{0,ta}^R$ = pseudo strain tension amplitude at cycle i ,

DMR = Dynamic Modular Ratio.

$$\left(\varepsilon_{0,ta}^R\right)_i = \frac{1}{E_R} \cdot \frac{\beta+1}{2} \left(\left(\varepsilon_{0,pp}\right)_i \cdot |E^*|_{LVE} \right)$$

where:

$\varepsilon_{0,pp}$ = peak-to-peak strain amplitude at cycle i ,

$|E^*|_{LVE}$ = the average representative dynamic modulus for the mixture of interest at the temperature and frequency of interest (kPa or psi).

$$\beta = \frac{Stress_{peak} + Stress_{vally}}{|Stress_{peak}| + |Stress_{vally}|}$$

$$DMR = \frac{|E^*|_{fp}}{|E^*|_{LVE}}$$

TABLE C.1 Summary of uniaxial fatigue test results

Serial Number	Specimen ID	Temperature, °F	PG Binder Grade	Asphalt Content (AC), %	Target Air Voids (Va), %	Actual Air Voids (Va), %	Tensile Strain (ϵ_t), μ s	Rest Period (RP), Sec	Finger Print Test			Uniaxial Tension-Compression Fatigue Test				
									FP Modulus (E_{LVE}), ksi	Phase Angle (ϕ), Degree	Machine Compliance Factor (MCF)	Initial Stiffness (E_o), ksi	Initial Tensile Stress (S_o), psi	Cycles to Failure at SR = 0.5, (N_f)	Cycle Number, N	Pseudo Stiffness Ratio (PSR) at N
1	D-412	40	64-22	4.20	4.50	4.84	95.0	0.0	2,573.7	9.32	11.89	2,394.0	211.5	9,470	9,470	0.500
2	D-449	40	64-22	4.20	4.50	4.48	62.5	0.0	2,624.7	11.51	12.00	2,527.5	156.2	254,100	254,100	0.500
3	D-404	70	64-22	4.20	4.50	4.08	145.0	0.0	1,307.4	32.99	6.23	1,105.8	149.3	3,430	3,430	0.500
4	D-405	70	64-22	4.20	4.50	4.33	105.0	0.0	1,333.3	31.87	6.03	1,020.7	102.8	27,400	27,400	0.500
5	D-432	70	64-22	4.20	4.50	4.03	105.0	0.0	1,344.1	22.59	6.70	1,099.8	111.5	27,340	27,340	0.500
6	D-407	100	64-22	4.20	4.50	4.09	255.0	0.0	346.8	39.76	2.45	140.7	45.2	15,930	15,930	0.500
7	D-408	100	64-22	4.20	4.50	4.63	175.0	0.0	316.6	41.57	2.46	147.9	35.1	147,895	147,895	0.500
8	D+442	40	64-22	5.20	4.50	4.79	87.5	0.0	2,129.4	11.75	9.67	2,044.7	158.2	130,320	130,320	0.500
9	D+443	40	64-22	5.20	4.50	4.20	100.0	0.0	2,440.5	12.84	14.21	2,164.2	197.3	74,710	74,710	0.500
10	D+445	40	64-22	5.20	4.50	4.37	137.5	0.0	2,648.4	13.16	11.99	2,263.6	285.3	9,470	9,470	0.500
11	D+402	70	64-22	5.20	4.50	3.46	105.0	0.0	1,038.9	28.18	4.80	843.0	92.6	218,000	218,000	0.500
12	D+403	70	64-22	5.20	4.50	3.63	145.0	0.0	1,049.1	30.46	5.25	757.0	109.4	50,500	50,500	0.500
13	D+404	70	64-22	5.20	4.50	3.37	175.0	0.0	924.0	30.18	4.41	670.7	119.2	30,000	30,000	0.500
14	D+430	100	64-22	5.20	4.50	4.89	250.0	0.0	149.4	47.59	1.75	72.5	21.9	64,570	64,570	0.500
15	D+438	100	64-22	5.20	4.50	3.99	450.0	0.0	201.2	45.71	1.77	79.6	38.3	8,810	8,810	0.500
16	D+440	100	64-22	5.20	4.50	4.46	200.0	0.0	157.7	49.80	1.74	94.4	21.4	245,470	245,470	0.500
17	D-959	40	64-22	4.20	9.50	9.65	75.0	0.0	1,936.5	12.96	12.92	1,701.0	119.4	17,920	17,920	0.500
18	D-972	40	64-22	4.20	9.50	9.49	70.0	0.0	1,595.3	14.37	7.38	1,478.5	83.9	57,250	57,250	0.500
19	D-946	70	64-22	4.20	9.50	9.22	87.5	0.0	648.0	27.52	3.46	514.7	47.1	94,770	94,770	0.500
20	D-947	70	64-22	4.20	9.50	8.52	125.0	0.0	827.6	25.16	4.27	617.1	75.3	22,260	22,260	0.500

21	D-951	70	64-22	4.20	9.50	9.31	100.0	0.0	724.3	25.42	3.86	596.8	59.5	84,000	84,000	0.500
22	D-962	100	64-22	4.20	9.50	9.28	225.0	0.0	152.3	31.39	2.10	70.5	24.9	32,030	32,030	0.500
23	D-963	100	64-22	4.20	9.50	9.91	275.0	0.0	145.5	34.78	1.95	65.9	26.7	7,100	7,100	0.500
24	D-964	100	64-22	4.20	9.50	9.49	175.0	0.0	164.2	37.97	2.03	86.9	24.3	168,530	168,530	0.500
25	D+959	40	64-22	5.20	9.50	9.10	100.0	0.0	1,443.4	12.21	7.92	1,332.3	126.1	53,760	53,760	0.500
26	D+958	40	64-22	5.20	9.50	8.80	112.5	0.0	1,777.4	14.38	8.19	1,423.6	143.3	17,380	17,380	0.500
27	D+962	40	64-22	5.20	9.50	9.40	130.0	0.0	1,610.6	14.10	8.15	1,434.7	172.7	8,320	8,320	0.500
28	D+943	70	64-22	5.20	9.50	9.52	95.0	0.0	516.6	28.26	2.85	409.4	40.2	372,300	372,300	0.500
29	D+944	70	64-22	5.20	9.50	8.92	125.0	0.0	643.5	24.11	3.57	484.05	60.2	63,910	63,910	0.500
30	D+948	70	64-22	5.20	9.50	9.34	200.0	0.0	613.2	26.83	3.93	356.9	71.7	4,070	4,070	0.500
31	D+949	70	64-22	5.20	9.50	9.99	187.5	0.0	502.6	31.81	2.97	328.4	65.1	9,740	9,740	0.500
32	D+952	100	64-22	5.20	9.50	9.66	200.0	0.0	110.2	34.25	1.59	54.4	20.2	357,550	357,550	0.500
33	D+953	100	64-22	5.20	9.50	9.25	350.0	0.0	99.7	37.08	1.76	42.0	24.0	13,560	13,560	0.500
34	D+956	100	64-22	5.20	9.50	9.77	250.0	0.0	107.2	30.34	1.78	52.6	22.7	74,140	74,140	0.500
35	D-442	40	64-22	4.20	4.50	3.81	87.5	0.0	3,144.6	11.52	12.70	2,711.8	237.3	21,660	16,147	0.735
36	D-440	40	64-22	4.20	4.50	4.39	87.5	0.0	2,700.7	10.74	12.21	2,394.1	209.5	15,810	16,147	0.497
37	D-446	40	64-22	4.20	4.50	4.82	87.5	0.0	2,955.7	11.32	14.42	2,353.5	205.9	10,970	16,147	0.398
38	D-443	40	64-22	4.20	4.50	4.06	70.0	0.0	3,049.7	12.72	13.43	2,751.3	192.6	71,160	61,921	0.539
39	D-452	40	64-22	4.20	4.50	4.52	70.0	0.0	2,969.2	10.64	12.95	2,755.8	192.9	56,700	61,921	0.469
40	D-455	40	64-22	4.20	4.50	4.46	70.0	0.0	3,136.6	12.22	13.09	2,823.4	197.6	57,903	61,921	0.487
41	D-436	70	64-22	4.20	4.50	4.92	115.0	0.0	974.9	23.89	4.33	814.0	93.6	12,090	15,253	0.461
42	D-437	70	64-22	4.20	4.50	5.09	115.0	0.0	1,133.2	26.63	5.53	862.0	99.1	22,620	15,253	0.573
43	D-488	70	64-22	4.20	4.50	4.99	115.0	0.0	1,220.3	23.34	5.01	901.2	97.6	11,050	15,253	0.418
44	D-427	100	64-22	4.20	4.50	3.85	195.0	0.0	295.6	42.37	1.77	183.1	35.7	85,770	77,083	0.508
45	D-467	100	64-22	4.20	4.50	4.12	195.0	0.0	244.7	51.49	1.77	140.3	27.3	71,340	77,083	0.493
46	D-466	100	64-22	4.20	4.50	4.50	195.0	0.0	203.6	50.02	1.51	132.9	25.9	74,140	77,083	0.495
47	D+452	40	64-22	5.20	4.50	3.75	112.5	0.0	2,385.6	10.92	11.97	2,183.8	245.7	17,340	17,270	0.501
48	D+453	40	64-22	5.20	4.50	4.51	112.5	0.0	2,542.2	13.34	11.16	2,139.1	240.6	11,200	17,270	0.250
49	D+459	40	64-22	5.20	4.50	4.79	112.5	0.0	2,291.3	11.17	10.86	2,095.3	235.7	23,270	17,270	0.591
50	D+449	70	64-22	5.20	4.50	4.79	122.5	0.0	872.0	30.02	4.31	679.4	83.2	129,320	98,157	0.524

51	D+455	70	64-22	5.20	4.50	4.01	122.5	0.0	959.1	24.88	4.84	784.7	96.1	88,450	98,157	0.483
52	D+492	70	64-22	5.20	4.50	4.63	122.5	0.0	1,035.6	26.13	4.27	824.1	96.8	76,700	98,157	0.400
53	D+457	100	64-22	5.20	4.50	4.63	357.5	0.0	142.7	51.90	1.26	75.4	27.0	29,520	24,897	0.523
54	D+465	100	64-22	5.20	4.50	4.78	357.5	0.0	140.7	50.87	1.26	77.0	27.5	28,400	24,897	0.528
55	D+463	100	64-22	5.20	4.50	4.86	357.5	0.0	155.3	49.98	1.32	81.5	29.1	16,770	24,897	0.417
56	D-993	40	64-22	4.20	9.50	9.14	62.5	0.0	1,734.7	10.84	8.25	1,673.9	104.6	86,210	104,943	0.452
57	D-988	40	64-22	4.20	9.50	8.93	62.5	0.0	2,175.1	12.95	9.29	2,175.1	135.9	90,280	104,943	0.478
58	D-987	40	64-22	4.20	9.50	9.01	62.5	0.0	2,065.9	12.66	9.13	1,960.0	122.5	138,340	104,943	0.631
59	D-969	70	64-22	4.20	9.50	9.52	115.0	0.0	538.4	24.58	2.83	433.6	49.9	31,150	25,753	0.541
60	D-984	70	64-22	4.20	9.50	8.76	115.0	0.0	720.8	24.46	3.56	551.1	63.4	21,990	25,753	0.468
61	D-981	70	64-22	4.20	9.50	8.73	115.0	0.0	729.5	28.92	3.58	583.2	67.1	24,120	25,753	0.487
62	D-977	70	64-22	4.20	9.50	9.25	90.0	0.0	716.6	23.16	3.36	627.9	56.5	146,780	86,893	0.583
63	D-978	70	64-22	4.20	9.50	9.45	90.0	0.0	672.8	24.26	3.45	557.3	50.2	61,820	86,893	0.445
64	D-983	70	64-22	4.20	9.50	9.32	90.0	0.0	768.8	27.53	4.26	572.5	51.5	52,080	86,893	0.393
65	D-985	100	64-22	4.20	9.50	8.84	237.5	0.0	130.5	51.65	1.29	72.4	17.2	9,810	13,897	0.439
66	D-986	100	64-22	4.20	9.50	9.17	237.5	0.0	120.7	49.30	1.25	67.3	16.0	15,530	13,897	0.514
67	D-992	100	64-22	4.20	9.50	9.05	237.5	0.0	169.7	46.54	1.37	98.0	23.3	16,350	13,897	0.523
68	D+971	40	64-22	5.20	9.50	9.16	112.5	0.0	1,628.6	12.51	6.92	1,490.3	167.7	20,580	14,723	0.617
69	D+968	40	64-22	5.20	9.50	9.98	112.5	0.0	1,470.8	12.21	6.73	1,348.4	151.7	11,220	14,723	0.397
70	D+967	40	64-22	5.20	9.50	9.04	112.5	0.0	1,612.1	11.74	7.72	1,510.0	169.9	12,370	14,723	0.432
71	D+965	40	64-22	5.20	9.50	9.38	82.5	0.0	1,379.5	12.16	5.97	1,334.0	110.1	93,810	119,010	0.452
72	D+936	40	64-22	5.20	9.50	9.79	82.5	0.0	1,408.0	12.36	6.37	1,345.4	111.0	156,080	119,010	0.582
73	D+935	40	64-22	5.20	9.50	9.26	82.5	0.0	1,598.6	11.87	7.90	1,531.4	126.3	107,140	119,010	0.466
74	D+961	70	64-22	5.20	9.50	9.66	155.0	0.0	603.4	30.02	3.50	433.1	67.1	25,910	20,377	0.541
75	D+974	70	64-22	5.20	9.50	9.61	155.0	0.0	459.6	29.08	2.55	368.3	57.1	18,060	20,377	0.481
76	D+9B2	70	64-22	5.20	9.50	9.34	155.0	0.0	540.3	27.94	2.66	412.9	62.5	17,160	20,377	0.464
77	D+985	100	64-22	5.20	9.50	9.41	252.5	0.0	129.8	43.41	1.33	78.6	19.8	126,870	97,217	0.521
78	D+989	100	64-22	5.20	9.50	9.89	252.5	0.0	80.0	56.86	1.21	48.4	12.2	58,440	97,217	0.417
79	D+984	100	64-22	5.20	9.50	9.39	252.5	0.0	122.3	44.21	1.21	76.4	19.3	106,340	97,217	0.513
80	D-490	70	64-22	4.20	4.50	4.44	90.0	0.0	1,118.4	26.32	4.55	961.4	83.4	53,570	50,355	0.512

81	D-491	70	64-22	4.20	4.50	4.48	90.0	0.0	1,058.1	23.50	4.50	896.7	76.8	47,140	50,355	0.499
82	D-9A7	100	64-22	4.20	9.50	8.87	280.0	0.0	214.2	38.94	1.51	110.0	32.5	6,050	6,390	0.495
83	D-9B3	100	64-22	4.20	9.50	8.83	280.0	0.0	152.7	46.54	1.44	80.0	24.5	6,730	6,390	0.532
84	D+9B3	100	64-22	5.20	9.50	8.87	342.5	0.0	84.6	51.32	1.17	46.0	17.3	16,350	14,175	0.528
85	D+9B5	100	64-22	5.20	9.50	8.83	343.5	0.0	90.0	52.38	1.41	46.1	17.6	12,000	14,175	0.467
86	D-475	40	64-22	4.20	4.50	4.62	70.0	5.0	3,145.4	11.51	14.20	2,731.2	191.2		5,000	1.000
87	D-475	40	64-22	4.20	4.50	4.62	70.0	5.0	3,145.4	11.51	14.20	2,731.2	191.2		10,000	1.000
88	D-475	40	64-22	4.20	4.50	4.62	70.0	5.0	3,145.4	11.51	14.20	2,731.2	191.2		15,000	1.000
89	D-475	40	64-22	4.20	4.50	4.62	70.0	5.0	3,145.4	11.51	14.20	2,731.2	191.2		20,000	1.000
90	D-478	40	64-22	4.20	4.50	4.26	70.0	5.0	2,691.0	11.37	10.63	2,567.8	179.7		5,000	0.980
91	D-478	40	64-22	4.20	4.50	4.26	70.0	5.0	2,691.0	11.37	10.63	2,567.8	179.7		10,000	0.978
92	D-478	40	64-22	4.20	4.50	4.26	70.0	5.0	2,691.0	11.37	10.63	2,567.8	179.7		15,000	0.977
93	D-478	40	64-22	4.20	4.50	4.26	70.0	5.0	2,691.0	11.37	10.63	2,567.8	179.7		20,000	0.976
94	D-495	40	64-23	4.20	4.50	3.99	70.0	5.0	2,763.7	9.85	10.20	2,763.7	193.5		5,000	0.968
95	D-495	40	64-23	4.20	4.50	3.99	70.0	5.0	2,763.7	9.85	10.20	2,763.7	193.5		10,000	0.962
96	D-495	40	64-23	4.20	4.50	3.99	70.0	5.0	2,763.7	9.85	10.20	2,763.7	193.5		15,000	0.959
97	D-495	40	64-23	4.20	4.50	3.99	70.0	5.0	2,763.7	9.85	10.20	2,763.7	193.5		20,000	0.956
98	D-465	70	64-22	4.20	4.50	4.54	90.0	5.0	1,126.1	22.43	5.01	1,036.4	93.3		5,000	0.955
99	D-465	70	64-22	4.20	4.50	4.54	90.0	5.0	1,126.1	22.43	5.01	1,036.4	93.3		10,000	0.943
100	D-465	70	64-22	4.20	4.50	4.54	90.0	5.0	1,126.1	22.43	5.01	1,036.4	93.3		15,000	0.934
101	D-465	70	64-22	4.20	4.50	4.54	90.0	5.0	1,126.1	22.43	5.01	1,036.4	93.3		20,000	0.927
102	D-468	70	64-22	4.20	4.50	3.95	90.0	5.0	1,343.3	24.12	5.81	1,183.2	106.5		5,000	0.961
103	D-468	70	64-22	4.20	4.50	3.95	90.0	5.0	1,343.3	24.12	5.81	1,183.2	106.5		10,000	0.955
104	D-468	70	64-22	4.20	4.50	3.95	90.0	5.0	1,343.3	24.12	5.81	1,183.2	106.5		15,000	0.951
105	D-468	70	64-22	4.20	4.50	3.95	90.0	5.0	1,343.3	24.12	5.81	1,183.2	106.5		20,000	0.948
106	D-493	70	64-22	4.20	4.50	4.25	90.0	5.0	1,261.7	23.77	5.03	1,110.0	100.0		5,000	0.954
107	D-493	70	64-22	4.20	4.50	4.25	90.0	5.0	1,261.7	23.77	5.03	1,110.0	100.0		10,000	0.944
108	D-493	70	64-22	4.20	4.50	4.25	90.0	5.0	1,261.7	23.77	5.03	1,110.0	100.0		15,000	0.937
109	D-493	70	64-22	4.20	4.50	4.25	90.0	5.0	1,261.7	23.77	5.03	1,110.0	100.0		20,000	0.932
110	D-471	70	64-22	4.20	4.50	4.66	115.0	5.0	1,208.7	26.62	5.25	987.8	113.6		5,000	0.955

111	D-471	70	64-22	4.20	4.50	4.66	115.0	5.0	1,208.7	26.62	5.25	987.8	113.6		10,000	0.935
112	D-471	70	64-22	4.20	4.50	4.66	115.0	5.0	1,208.7	26.62	5.25	987.8	113.6		15,000	0.919
113	D-471	70	64-22	4.20	4.50	4.66	115.0	5.0	1,208.7	26.62	5.25	987.8	113.6		20,000	0.905
114	D-473	70	64-22	4.20	4.50	4.83	115.0	5.0	1,095.5	25.15	4.77	975.4	112.2		5,000	0.958
115	D-473	70	64-22	4.20	4.50	4.83	115.0	5.0	1,095.5	25.15	4.77	975.4	112.2		10,000	0.942
116	D-473	70	64-22	4.20	4.50	4.83	115.0	5.0	1,095.5	25.15	4.77	975.4	112.2		15,000	0.929
117	D-473	70	64-22	4.20	4.50	4.83	115.0	5.0	1,095.5	25.15	4.77	975.4	112.2		20,000	0.919
118	D-494	70	64-22	4.20	4.50	4.34	115.0	5.0	1,195.7	20.98	4.75	1,066.6	122.3		5,000	0.930
119	D-494	70	64-22	4.20	4.50	4.34	115.0	5.0	1,195.7	20.98	4.75	1,066.6	122.3		10,000	0.909
120	D-494	70	64-22	4.20	4.50	4.34	115.0	5.0	1,195.7	20.98	4.75	1,066.6	122.3		15,000	0.894
121	D-494	70	64-22	4.20	4.50	4.34	115.0	5.0	1,195.7	20.98	4.75	1,066.6	122.3		20,000	0.882
122	D-472	100	64-22	4.20	4.50	4.25	242.5	5.0	213.9	45.34	1.48	166.6	40.4		5,000	0.933
123	D-472	100	64-22	4.20	4.50	4.25	242.5	5.0	213.9	45.34	1.48	166.6	40.4		10,000	0.918
124	D-472	100	64-22	4.20	4.50	4.25	242.5	5.0	213.9	45.34	1.48	166.6	40.4		15,000	0.908
125	D-472	100	64-22	4.20	4.50	4.25	242.5	5.0	213.9	45.34	1.48	166.6	40.4		20,000	0.900
126	D-474	100	64-22	4.20	4.50	4.68	242.5	5.0	226.1	47.19	1.56	163.3	39.6		5,000	0.913
127	D-474	100	64-22	4.20	4.50	4.68	242.5	5.0	226.1	47.19	1.56	163.3	39.6		10,000	0.895
128	D-474	100	64-22	4.20	4.50	4.68	242.5	5.0	226.1	47.19	1.56	163.3	39.6		15,000	0.882
129	D-474	100	64-22	4.20	4.50	4.68	242.5	5.0	226.1	47.19	1.56	163.3	39.6		20,000	0.872
130	D-497	100	64-22	4.20	4.50	5.00	242.5	5.0	182.0	46.39	1.28	145.4	31.9		5,000	0.892
131	D-497	100	64-22	4.20	4.50	5.00	242.5	5.0	182.0	46.39	1.28	145.4	31.9		10,000	0.873
132	D-497	100	64-22	4.20	4.50	5.00	242.5	5.0	182.0	46.39	1.28	145.4	31.9		15,000	0.861
133	D-497	100	64-22	4.20	4.50	5.00	242.5	5.0	182.0	46.39	1.28	145.4	31.9		20,000	0.853
134	D+473	40	64-22	5.20	4.50	4.57	82.5	5.0	2,268.8	10.51	11.49	2,168.4	178.9		5,000	0.997
135	D+473	40	64-22	5.20	4.50	4.57	82.5	5.0	2,268.8	10.51	11.49	2,168.4	178.9		10,000	0.997
136	D+473	40	64-22	5.20	4.50	4.57	82.5	5.0	2,268.8	10.51	11.49	2,168.4	178.9		15,000	0.997
137	D+473	40	64-22	5.20	4.50	4.57	82.5	5.0	2,268.8	10.51	11.49	2,168.4	178.9		20,000	0.997
138	D+476	40	64-22	5.20	4.50	4.22	82.5	5.0	2,889.4	11.81	13.29	2,540.8	209.6		5,000	1.000
139	D+476	40	64-22	5.20	4.50	4.22	82.5	5.0	2,889.4	11.81	13.29	2,540.8	209.6		10,000	1.000
140	D+476	40	64-22	5.20	4.50	4.22	82.5	5.0	2,889.4	11.81	13.29	2,540.8	209.6		15,000	1.000

141	D+476	40	64-22	5.20	4.50	4.22	82.5	5.0	2,889.4	11.81	13.29	2,540.8	209.6		20,000	1.000
142	D+491	40	64-22	5.20	4.50	4.95	82.5	5.0	2,402.4	12.55	9.21	2,180.0	196.4		5,000	0.979
143	D+491	40	64-22	5.20	4.50	4.95	82.5	5.0	2,402.4	12.55	9.21	2,180.0	196.4		10,000	0.972
144	D+491	40	64-22	5.20	4.50	4.95	82.5	5.0	2,402.4	12.55	9.21	2,180.0	196.4		15,000	0.967
145	D+491	40	64-22	5.20	4.50	4.95	82.5	5.0	2,402.4	12.55	9.21	2,180.0	196.4		20,000	0.963
146	D+464	40	64-22	5.20	4.50	5.00	112.5	5.0	2,275.6	12.25	8.80	2,090.4	235.2		5,000	0.978
147	D+464	40	64-22	5.20	4.50	5.00	112.5	5.0	2,275.6	12.25	8.80	2,090.4	235.2		10,000	0.973
148	D+464	40	64-22	5.20	4.50	5.00	112.5	5.0	2,275.6	12.25	8.80	2,090.4	235.2		15,000	0.971
149	D+464	40	64-22	5.20	4.50	5.00	112.5	5.0	2,275.6	12.25	8.80	2,090.4	235.2		20,000	0.969
150	D+477	40	64-22	5.20	4.50	4.54	112.5	5.0	2,664.1	11.86	11.30	2,330.6	262.2		5,000	0.979
151	D+477	40	64-22	5.20	4.50	4.54	112.5	5.0	2,664.1	11.86	11.30	2,330.6	262.2		10,000	0.974
152	D+477	40	64-22	5.20	4.50	4.54	112.5	5.0	2,664.1	11.86	11.30	2,330.6	262.2		15,000	0.970
153	D+477	40	64-22	5.20	4.50	4.54	112.5	5.0	2,664.1	11.86	11.30	2,330.6	262.2		20,000	0.968
154	D+489	40	64-22	5.20	4.50	4.36	112.5	5.0	2,299.3	11.18	8.90	2,147.2	243.9		5,000	0.962
155	D+489	40	64-22	5.20	4.50	4.36	112.5	5.0	2,299.3	11.18	8.90	2,147.2	243.9		10,000	0.952
156	D+489	40	64-22	5.20	4.50	4.36	112.5	5.0	2,299.3	11.18	8.90	2,147.2	243.9		15,000	0.945
157	D+489	40	64-22	5.20	4.50	4.36	112.5	5.0	2,299.3	11.18	8.90	2,147.2	243.9		20,000	0.940
158	D+468	70	64-22	5.20	4.50	4.39	197.5	5.0	1,155.8	24.00	5.15	865.7	171.0		5,000	0.964
159	D+468	70	64-22	5.20	4.50	4.39	197.5	5.0	1,155.8	24.00	5.15	865.7	171.0		10,000	0.940
160	D+468	70	64-22	5.20	4.50	4.39	197.5	5.0	1,155.8	24.00	5.15	865.7	171.0		15,000	0.922
161	D+468	70	64-22	5.20	4.50	4.39	197.5	5.0	1,155.8	24.00	5.15	865.7	171.0		20,000	0.908
162	D+471	70	64-22	5.20	4.50	4.61	197.5	5.0	883.4	26.83	4.10	719.9	142.2		5,000	0.982
163	D+471	70	64-22	5.20	4.50	4.61	197.5	5.0	883.4	26.83	4.10	719.9	142.2		10,000	0.967
164	D+471	70	64-22	5.20	4.50	4.61	197.5	5.0	883.4	26.83	4.10	719.9	142.2		15,000	0.956
165	D+471	70	64-22	5.20	4.50	4.61	197.5	5.0	883.4	26.83	4.10	719.9	142.2		20,000	0.948
166	D+495	70	64-22	5.20	4.50	4.68	197.5	5.0	907.5	24.99	3.82	761.8	142.7		5,000	0.944
167	D+495	70	64-22	5.20	4.50	4.68	197.5	5.0	907.5	24.99	3.82	761.8	142.7		10,000	0.928
168	D+495	70	64-22	5.20	4.50	4.68	197.5	5.0	907.5	24.99	3.82	761.8	142.7		15,000	0.918
169	D+495	70	64-22	5.20	4.50	4.68	197.5	5.0	907.5	24.99	3.82	761.8	142.7		20,000	0.912
170	D+466	100	64-22	5.20	4.50	4.57	232.5	5.0	151.6	51.59	1.44	124.3	28.9		5,000	0.966

171	D+466	100	64-22	5.20	4.50	4.57	232.5	5.0	151.6	51.59	1.44	124.3	28.9		10,000	0.955
172	D+466	100	64-22	5.20	4.50	4.57	232.5	5.0	151.6	51.59	1.44	124.3	28.9		15,000	0.948
173	D+466	100	64-22	5.20	4.50	4.57	232.5	5.0	151.6	51.59	1.44	124.3	28.9		20,000	0.941
174	D+470	100	64-22	5.20	4.50	4.13	232.5	5.0	209.6	48.89	1.71	149.0	34.6		5,000	0.919
175	D+470	100	64-22	5.20	4.50	4.13	232.5	5.0	209.6	48.89	1.71	149.0	34.6		10,000	0.906
176	D+470	100	64-22	5.20	4.50	4.13	232.5	5.0	209.6	48.89	1.71	149.0	34.6		15,000	0.899
177	D+470	100	64-22	5.20	4.50	4.13	232.5	5.0	209.6	48.89	1.71	149.0	34.6		20,000	0.893
178	D+493	100	64-22	5.20	4.50	4.70	232.5	5.0	165.9	52.00	1.41	135.1	27.5		5,000	0.947
179	D+493	100	64-22	5.20	4.50	4.70	232.5	5.0	165.9	52.00	1.41	135.1	27.5		10,000	0.929
180	D+493	100	64-22	5.20	4.50	4.70	232.5	5.0	165.9	52.00	1.41	135.1	27.5		15,000	0.916
181	D+493	100	64-22	5.20	4.50	4.70	232.5	5.0	165.9	52.00	1.41	135.1	27.5		20,000	0.906
182	D-9A4	40	64-22	4.20	9.50	9.05	80.0	5.0	1,665.5	10.81	6.92	1,527.8	122.2		5,000	0.891
183	D-9A4	40	64-22	4.20	9.50	9.05	80.0	5.0	1,665.5	10.81	6.92	1,527.8	122.2		10,000	0.869
184	D-9A4	40	64-22	4.20	9.50	9.05	80.0	5.0	1,665.5	10.81	6.92	1,527.8	122.2		15,000	0.854
185	D-9A4	40	64-22	4.20	9.50	9.05	80.0	5.0	1,665.5	10.81	6.92	1,527.8	122.2		20,000	0.842
186	D-9B9	40	64.22	4.20	9.50	9.29	80.0	5.0	1,720.4	11.68	7.13	1,604.8	128.4		5,000	0.928
187	D-9B9	40	64.22	4.20	9.50	9.29	80.0	5.0	1,720.4	11.68	7.13	1,604.8	128.4		10,000	0.911
188	D-9B9	40	64.22	4.20	9.50	9.29	80.0	5.0	1,720.4	11.68	7.13	1,604.8	128.4		15,000	0.899
189	D-9B9	40	64.22	4.20	9.50	9.29	80.0	5.0	1,720.4	11.68	7.13	1,604.8	128.4		20,000	0.890
190	D-9C8	40	64.22	4.20	9.50	9.04	80.0	5.0	1,608.9	12.28	6.52	1,492.8	130.6		5,000	0.967
191	D-9C8	40	64.22	4.20	9.50	9.04	80.0	5.0	1,608.9	12.28	6.52	1,492.8	130.6		10,000	0.957
192	D-9C8	40	64.22	4.20	9.50	9.04	80.0	5.0	1,608.9	12.28	6.52	1,492.8	130.6		15,000	0.950
193	D-9C8	40	64.22	4.20	9.50	9.04	80.0	5.0	1,608.9	12.28	6.52	1,492.8	130.6		20,000	0.944
194	D-997	70	64-22	4.20	9.50	9.25	90.0	5.0	772.9	24.22	3.61	682.8	61.5		5,000	0.952
195	D-997	70	64-22	4.20	9.50	9.25	90.0	5.0	772.9	24.22	3.61	682.8	61.5		10,000	0.946
196	D-997	70	64-22	4.20	9.50	9.25	90.0	5.0	772.9	24.22	3.61	682.8	61.5		15,000	0.942
197	D-997	70	64-22	4.20	9.50	9.25	90.0	5.0	772.9	24.22	3.61	682.8	61.5		20,000	0.939
198	D-9A1	70	64-22	4.20	9.50	9.29	90.0	5.0	699.1	25.54	2.34	636.1	57.3		5,000	0.965
199	D-9A1	70	64-22	4.20	9.50	9.29	90.0	5.0	699.1	25.54	2.34	636.1	57.3		10,000	0.961
200	D-9A1	70	64-22	4.20	9.50	9.29	90.0	5.0	699.1	25.54	2.34	636.1	57.3		15,000	0.959

201	D-9A1	70	64-22	4.20	9.50	9.29	90.0	5.0	699.1	25.54	2.34	636.1	57.3		20,000	0.957
202	D-9C5	70	64-22	4.20	9.50	9.10	90.0	5.0	728.2	25.49	3.31	652.4	58.0		5,000	0.966
203	D-9C5	70	64-22	4.20	9.50	9.10	90.0	5.0	728.2	25.49	3.31	652.4	58.0		10,000	0.960
204	D-9C5	70	64-22	4.20	9.50	9.10	90.0	5.0	728.2	25.49	3.31	652.4	58.0		15,000	0.955
205	D-9C5	70	64-22	4.20	9.50	9.10	90.0	5.0	728.2	25.49	3.31	652.4	58.0		20,000	0.952
206	D-996	100	64-22	4.20	9.50	9.28	187.5	5.0	135.2	47.45	1.35	113.0	21.2		5,000	0.965
207	D-996	100	64-22	4.20	9.50	9.28	187.5	5.0	135.2	47.45	1.35	113.0	21.2		10,000	0.952
208	D-996	100	64-22	4.20	9.50	9.28	187.5	5.0	135.2	47.45	1.35	113.0	21.2		15,000	0.942
209	D-996	100	64-22	4.20	9.50	9.28	187.5	5.0	135.2	47.45	1.35	113.0	21.2		20,000	0.934
210	D-999	100	64-22	4.20	9.50	9.47	187.5	5.0	151.9	46.67	1.46	122.1	22.9		5,000	0.977
211	D-999	100	64-22	4.20	9.50	9.47	187.5	5.0	151.9	46.67	1.46	122.1	22.9		10,000	0.977
212	D-999	100	64-22	4.20	9.50	9.47	187.5	5.0	151.9	46.67	1.46	122.1	22.9		15,000	0.977
213	D-999	100	64-22	4.20	9.50	9.47	187.5	5.0	151.9	46.67	1.46	122.1	22.9		20,000	0.976
214	D-9C9	100	64-22	4.20	9.50	8.64	187.5	5.0	145.9	50.02	1.37	122.9	21.9		5,000	0.923
215	D-9C9	100	64-22	4.20	9.50	8.64	187.5	5.0	145.9	50.02	1.37	122.9	21.9		10,000	0.911
216	D-9C9	100	64-22	4.20	9.50	8.64	187.5	5.0	145.9	50.02	1.37	122.9	21.9		15,000	0.904
217	D-9C9	100	64-22	4.20	9.50	8.64	187.5	5.0	145.9	50.02	1.37	122.9	21.9		20,000	0.899
218	D-995	100	64-22	4.20	9.50	9.08	237.5	5.0	132.4	50.69	1.24	103.4	24.5		5,000	0.928
219	D-995	100	64-22	4.20	9.50	9.08	237.5	5.0	132.4	50.69	1.24	103.4	24.5		10,000	0.911
220	D-995	100	64-22	4.20	9.50	9.08	237.5	5.0	132.4	50.69	1.24	103.4	24.5		15,000	0.899
221	D-995	100	64-22	4.20	9.50	9.08	237.5	5.0	132.4	50.69	1.24	103.4	24.5		20,000	0.890
222	D-9A2	100	64-22	4.20	9.50	9.48	237.5	5.0	126.0	48.24	1.21	92.0	21.8		5,000	0.888
223	D-9A2	100	64-22	4.20	9.50	9.48	237.5	5.0	126.0	48.24	1.21	92.0	21.8		10,000	0.870
224	D-9A2	100	64-22	4.20	9.50	9.48	237.5	5.0	126.0	48.24	1.21	92.0	21.8		15,000	0.860
225	D-9A2	100	64-22	4.20	9.50	9.48	237.5	5.0	126.0	48.24	1.21	92.0	21.8		20,000	0.853
226	D-9C7	100	64-22	4.20	9.50	9.35	237.5	5.0	126.3	47.27	1.13	102.6	21.3		5,000	0.937
227	D-9C7	100	64-22	4.20	9.50	9.35	237.5	5.0	126.3	47.27	1.13	102.6	21.3		10,000	0.918
228	D-9C7	100	64-22	4.20	9.50	9.35	237.5	5.0	126.3	47.27	1.13	102.6	21.3		15,000	0.905
229	D-9C7	100	64-22	4.20	9.50	9.35	237.5	5.0	126.3	47.27	1.13	102.6	21.3		20,000	0.894
230	D+996	40	64-22	5.20	9.50	8.84	82.5	5.0	2,009.5	13.08	8.37	1,807.2	149.1		5,000	0.975

231	D+996	40	64-22	5.20	9.50	8.84	82.5	5.0	2,009.5	13.08	8.37	1,807.2	149.1		10,000	0.972
232	D+996	40	64-22	5.20	9.50	8.84	82.5	5.0	2,009.5	13.08	8.37	1,807.2	149.1		15,000	0.969
233	D+996	40	64-22	5.20	9.50	8.84	82.5	5.0	2,009.5	13.08	8.37	1,807.2	149.1		20,000	0.968
234	D+9A0	40	64-22	5.20	9.50	9.06	82.5	5.0	1,616.3	10.55	7.08	1,552.9	128.1		5,000	0.979
235	D+9A0	40	64-22	5.20	9.50	9.06	82.5	5.0	1,616.3	10.55	7.08	1,552.9	128.1		10,000	0.977
236	D+9A0	40	64-22	5.20	9.50	9.06	82.5	5.0	1,616.3	10.55	7.08	1,552.9	128.1		15,000	0.975
237	D+9A0	40	64-22	5.20	9.50	9.06	82.5	5.0	1,616.3	10.55	7.08	1,552.9	128.1		20,000	0.974
238	D+9C0	40	64-22	5.20	9.50	9.32	82.5	5.0	1,427.9	12.31	5.65	1,350.5	119.3		5,000	0.976
239	D+9C0	40	64-22	5.20	9.50	9.32	82.5	5.0	1,427.9	12.31	5.65	1,350.5	119.3		10,000	0.972
240	D+9C0	40	64-22	5.20	9.50	9.32	82.5	5.0	1,427.9	12.31	5.65	1,350.5	119.3		15,000	0.969
241	D+9C0	40	64-22	5.20	9.50	9.32	82.5	5.0	1,427.9	12.31	5.65	1,350.5	119.3		20,000	0.967
242	D+995	40	64-22	5.20	9.50	9.66	112.5	5.0	1,443.9	13.08	5.96	1,336.3	150.3		5,000	0.975
243	D+995	40	64-22	5.20	9.50	9.66	112.5	5.0	1,443.9	13.08	5.96	1,336.3	150.3		10,000	0.968
244	D+995	40	64-22	5.20	9.50	9.66	112.5	5.0	1,443.9	13.08	5.96	1,336.3	150.3		15,000	0.963
245	D+995	40	64-22	5.20	9.50	9.66	112.5	5.0	1,443.9	13.08	5.96	1,336.3	150.3		20,000	0.960
246	D+997	40	64-22	5.20	9.50	9.54	112.5	5.0	1,704.5	10.00	7.10	1,614.1	181.6		5,000	0.957
247	D+997	40	64-22	5.20	9.50	9.54	112.5	5.0	1,704.5	10.00	7.10	1,614.1	181.6		10,000	0.948
248	D+997	40	64-22	5.20	9.50	9.54	112.5	5.0	1,704.5	10.00	7.10	1,614.1	181.6		15,000	0.941
249	D+997	40	64-22	5.20	9.50	9.54	112.5	5.0	1,704.5	10.00	7.10	1,614.1	181.6		20,000	0.936
250	D+9B0	40	64-22	5.20	9.50	8.77	112.5	5.0	1,543.5	12.23	5.98	1,427.1	164.0		5,000	0.941
251	D+9B0	40	64-22	5.20	9.50	8.77	112.5	5.0	1,543.5	12.23	5.98	1,427.1	164.0		10,000	0.931
252	D+9B0	40	64-22	5.20	9.50	8.77	112.5	5.0	1,543.5	12.23	5.98	1,427.1	164.0		15,000	0.925
253	D+9B0	40	64-22	5.20	9.50	8.77	112.5	5.0	1,543.5	12.23	5.98	1,427.1	164.0		20,000	0.921
254	D+991	70	64-22	5.20	9.50	8.73	112.5	5.0	656.7	26.28	3.13	584.1	65.7		5,000	0.958
255	D+991	70	64-22	5.20	9.50	8.73	112.5	5.0	656.7	26.28	3.13	584.1	65.7		10,000	0.950
256	D+991	70	64-22	5.20	9.50	8.73	112.5	5.0	656.7	26.28	3.13	584.1	65.7		15,000	0.944
257	D+991	70	64-22	5.20	9.50	8.73	112.5	5.0	656.7	26.28	3.13	584.1	65.7		20,000	0.940
258	D+992	70	64-22	5.20	9.50	8.97	112.5	5.0	543.3	26.54	2.77	491.4	55.3		5,000	0.960
259	D+992	70	64-22	5.20	9.50	8.97	112.5	5.0	543.3	26.54	2.77	491.4	55.3		10,000	0.951
260	D+992	70	64-22	5.20	9.50	8.97	112.5	5.0	543.3	26.54	2.77	491.4	55.3		15,000	0.945

261	D+992	70	64-22	5.20	9.50	8.97	112.5	5.0	543.3	26.54	2.77	491.4	55.3		20,000	0.940
262	D+9B4	70	64-22	5.20	9.50	9.35	112.5	5.0	570.7	27.69	2.77	501.2	56.0		5,000	0.961
263	D+9B4	70	64-22	5.20	9.50	9.35	112.5	5.0	570.7	27.69	2.77	501.2	56.0		10,000	0.956
264	D+9B4	70	64-22	5.20	9.50	9.35	112.5	5.0	570.7	27.69	2.77	501.2	56.0		15,000	0.952
265	D+9B4	70	64-22	5.20	9.50	9.35	112.5	5.0	570.7	27.69	2.77	501.2	56.0		20,000	0.950
266	D+983	70	64-22	5.20	9.50	9.77	155.0	5.0	606.7	25.46	2.93	494.4	76.6		5,000	0.949
267	D+983	70	64-22	5.20	9.50	9.77	155.0	5.0	606.7	25.46	2.93	494.4	76.6		10,000	0.936
268	D+983	70	64-22	5.20	9.50	9.77	155.0	5.0	606.7	25.46	2.93	494.4	76.6		15,000	0.927
269	D+983	70	64-22	5.20	9.50	9.77	155.0	5.0	606.7	25.46	2.93	494.4	76.6		20,000	0.920
270	D+988	70	64-22	5.20	9.50	8.76	155.0	5.0	782.0	20.20	3.65	676.8	104.9		5,000	0.930
271	D+988	70	64-22	5.20	9.50	8.76	155.0	5.0	782.0	20.20	3.65	676.8	104.9		10,000	0.914
272	D+988	70	64-22	5.20	9.50	8.76	155.0	5.0	782.0	20.20	3.65	676.8	104.9		15,000	0.903
273	D+988	70	64-22	5.20	9.50	8.76	155.0	5.0	782.0	20.20	3.65	676.8	104.9		20,000	0.895
274	D+9B1	70	64-22	5.20	9.50	9.65	155.0	5.0	509.8	27.66	2.53	433.4	65.7		5,000	0.948
275	D+9B1	70	64-22	5.20	9.50	9.65	155.0	5.0	509.8	27.66	2.53	433.4	65.7		10,000	0.932
276	D+9B1	70	64-22	5.20	9.50	9.65	155.0	5.0	509.8	27.66	2.53	433.4	65.7		15,000	0.921
277	D+9B1	70	64-22	5.20	9.50	9.65	155.0	5.0	509.8	27.66	2.53	433.4	65.7		20,000	0.912
278	D+993	100	64-22	5.20	9.50	9.43	342.5	5.0	84.9	54.36	1.20	66.2	22.7		5,000	0.912
279	D+993	100	64-22	5.20	9.50	9.43	342.5	5.0	84.9	54.36	1.20	66.2	22.7		10,000	0.889
280	D+993	100	64-22	5.20	9.50	9.43	342.5	5.0	84.9	54.36	1.20	66.2	22.7		15,000	0.873
281	D+993	100	64-22	5.20	9.50	9.43	342.5	5.0	84.9	54.36	1.20	66.2	22.7		20,000	0.860
282	D+999	100	64-22	5.20	9.50	9.43	342.5	5.0	103.7	52.46	1.27	73.2	25.1		5,000	0.917
283	D+999	100	64-22	5.20	9.50	9.43	342.5	5.0	103.7	52.46	1.27	73.2	25.1		10,000	0.885
284	D+999	100	64-22	5.20	9.50	9.43	342.5	5.0	103.7	52.46	1.27	73.2	25.1		15,000	0.862
285	D+999	100	64-22	5.20	9.50	9.43	342.5	5.0	103.7	52.46	1.27	73.2	25.1		20,000	0.842
286	D+9B8	100	64-22	5.20	9.50	8.98	342.5	5.0	77.6	51.23	1.14	59.3	18.5		5,000	0.874
287	D+9B8	100	64-22	5.20	9.50	8.98	342.5	5.0	77.6	51.23	1.14	59.3	18.5		10,000	0.842
288	D+9B8	100	64-22	5.20	9.50	8.98	342.5	5.0	77.6	51.23	1.14	59.3	18.5		15,000	0.823
289	D+9B8	100	64-22	5.20	9.50	8.98	342.5	5.0	77.6	51.23	1.14	59.3	18.5		20,000	0.810
290	D-484	40	64-22	4.20	4.50	4.11	100.0	5.0	2,928.6	11.17	11.10	2,586.5	261.6		5,000	0.915

291	D-484	40	64-22	4.20	4.50	4.11	100.0	5.0	2,928.6	11.17	11.10	2,586.5	261.6		10,000	0.892
292	D-484	40	64-22	4.20	4.50	4.11	100.0	5.0	2,928.6	11.17	11.10	2,586.5	261.6		15,000	0.876
293	D-484	40	64-22	4.20	4.50	4.11	100.0	5.0	2,928.6	11.17	11.10	2,586.5	261.6		20,000	0.863
294	D-476	100	64-22	4.20	4.50	4.07	195.0	1.0	298.6	39.64	1.97	221.8	41.3		5,000	0.858
295	D-476	100	64-22	4.20	4.50	4.07	195.0	1.0	298.6	39.64	1.97	221.8	41.3		10,000	0.828
296	D-476	100	64-22	4.20	4.50	4.07	195.0	1.0	298.6	39.64	1.97	221.8	41.3		15,000	0.807
297	D-476	100	64-22	4.20	4.50	4.07	195.0	1.0	298.6	39.64	1.97	221.8	41.3		20,000	0.791
298	D-482	100	64-22	4.20	4.50	4.35	195.0	1.0	199.0	47.06	1.37	156.1	26.7		5,000	0.859
299	D-482	100	64-22	4.20	4.50	4.35	195.0	1.0	199.0	47.06	1.37	156.1	26.7		10,000	0.833
300	D-482	100	64-22	4.20	4.50	4.35	195.0	1.0	199.0	47.06	1.37	156.1	26.7		15,000	0.816
301	D-482	100	64-22	4.20	4.50	4.35	195.0	1.0	199.0	47.06	1.37	156.1	26.7		20,000	0.803
302	D+478	40	64-22	5.20	4.50	4.33	112.5	10.0	2,456.8	10.77	9.37	2,338.2	261.6		5,000	0.985
303	D+478	40	64-22	5.20	4.50	4.33	112.5	10.0	2,456.8	10.77	9.37	2,338.2	261.6		10,000	0.982
304	D+478	40	64-22	5.20	4.50	4.33	112.5	10.0	2,456.8	10.77	9.37	2,338.2	261.6		15,000	0.979
305	D+478	40	64-22	5.20	4.50	4.33	112.5	10.0	2,456.8	10.77	9.37	2,338.2	261.6		20,000	0.977
306	D+483	40	64-22	5.20	4.50	4.44	112.5	10.0	2,528.3	11.16	9.72	2,277.3	256.9		5,000	0.999
307	D+483	40	64-22	5.20	4.50	4.44	112.5	10.0	2,528.3	11.16	9.72	2,277.3	256.9		10,000	0.999
308	D+483	40	64-22	5.20	4.50	4.44	112.5	10.0	2,528.3	11.16	9.72	2,277.3	256.9		15,000	0.998
309	D+483	40	64-22	5.20	4.50	4.44	112.5	10.0	2,528.3	11.16	9.72	2,277.3	256.9		20,000	0.998
310	D+485	40	64-22	5.20	4.50	4.70	125.0	1.0	2,130.5	10.98	8.47	1,991.3	257.7		5,000	0.911
311	D+485	40	64-22	5.20	4.50	4.70	125.0	1.0	2,130.5	10.98	8.47	1,991.3	257.7		10,000	0.891
312	D+485	40	64-22	5.20	4.50	4.70	125.0	1.0	2,130.5	10.98	8.47	1,991.3	257.7		15,000	0.880
313	D+485	40	64-22	5.20	4.50	4.70	125.0	1.0	2,130.5	10.98	8.47	1,991.3	257.7		20,000	0.871
314	D+472	70	64-22	5.20	4.50	4.24	197.5	1.0	995.2	25.12	4.26	758.5	139.3		5,000	0.862
315	D+472	70	64-22	5.20	4.50	4.24	197.5	1.0	995.2	25.12	4.26	758.5	139.3		10,000	0.837
316	D+472	70	64-22	5.20	4.50	4.24	197.5	1.0	995.2	25.12	4.26	758.5	139.3		15,000	0.822
317	D+472	70	64-22	5.20	4.50	4.24	197.5	1.0	995.2	25.12	4.26	758.5	139.3		20,000	0.811
318	D+475	70	64-22	5.20	4.50	4.18	197.5	1.0	991.3	24.17	4.27	783.8	145.1		5,000	0.831
319	D+475	70	64-22	5.20	4.50	4.18	197.5	1.0	991.3	24.17	4.27	783.8	145.1		10,000	0.797
320	D+475	70	64-22	5.20	4.50	4.18	197.5	1.0	991.3	24.17	4.27	783.8	145.1		15,000	0.778

321	D+475	70	64-22	5.20	4.50	4.18	197.5	1.0	991.3	24.17	4.27	783.8	145.1		20,000	0.750
322	D+474	70	64-22	5.20	4.50	4.24	122.5	10.0	967.5	24.86	4.24	845.6	101.4		5,000	0.963
323	D+474	70	64-22	5.20	4.50	4.24	122.5	10.0	967.5	24.86	4.24	845.6	101.4		10,000	0.955
324	D+474	70	64-22	5.20	4.50	4.24	122.5	10.0	967.5	24.86	4.24	845.6	101.4		15,000	0.950
325	D+474	70	64-22	5.20	4.50	4.24	122.5	10.0	967.5	24.86	4.24	845.6	101.4		20,000	0.946
326	D+479	70	64-22	5.20	4.50	4.17	122.5	10.0	977.0	29.22	4.56	807.9	98.1		5,000	0.964
327	D+479	70	64-22	5.20	4.50	4.17	122.5	10.0	977.0	29.22	4.56	807.9	98.1		10,000	0.956
328	D+479	70	64-22	5.20	4.50	4.17	122.5	10.0	977.0	29.22	4.56	807.9	98.1		15,000	0.951
329	D+479	70	64-22	5.20	4.50	4.17	122.5	10.0	977.0	29.22	4.56	807.9	98.1		20,000	0.946
330	D-9B2	40	64-22	4.20	9.50	9.32	62.5	5.0	1,790.5	13.25	7.38	1,699.1	104.7		5,000	0.994
331	D-9B2	40	64-22	4.20	9.50	9.32	62.5	5.0	1,790.5	13.25	7.38	1,699.1	104.7		10,000	0.981
332	D-9B2	40	64-22	4.20	9.50	9.32	62.5	5.0	1,790.5	13.25	7.38	1,699.1	104.7		15,000	0.977
333	D-9B2	40	64-22	4.20	9.50	9.32	62.5	5.0	1,790.5	13.25	7.38	1,699.1	104.7		20,000	0.976
334	D-9B6	40	64-22	4.20	9.50	9.08	62.5	5.0	1,896.4	11.26	7.52	1,759.4	111.8		5,000	0.974
335	D-9B6	40	64-22	4.20	9.50	9.08	62.5	5.0	1,896.4	11.26	7.52	1,759.4	111.8		10,000	0.968
336	D-9B6	40	64-22	4.20	9.50	9.08	62.5	5.0	1,896.4	11.26	7.52	1,759.4	111.8		15,000	0.964
337	D-9B6	40	64-22	4.20	9.50	9.08	62.5	5.0	1,896.4	11.26	7.52	1,759.4	111.8		20,000	0.961
338	D-9B8	40	64-22	4.20	9.50	9.30	80.0	1.0	1,520.3	13.21	6.14	1,369.7	114.6		5,000	0.779
339	D-9B8	40	64-22	4.20	9.50	9.30	80.0	1.0	1,520.3	13.21	6.14	1,369.7	114.6		10,000	0.734
340	D-9B8	40	64-22	4.20	9.50	9.30	80.0	1.0	1,520.3	13.21	6.14	1,369.7	114.6		15,000	0.708
341	D-9B8	40	64-22	4.20	9.50	9.30	80.0	1.0	1,520.3	13.21	6.14	1,369.7	114.6		20,000	0.689
342	D-9C0	40	64-22	4.20	9.50	9.13	80.0	1.0	1,610.5	12.07	6.42	1,497.5	120.0		5,000	0.809
343	D-9C0	40	64-22	4.20	9.50	9.13	80.0	1.0	1,610.5	12.07	6.42	1,497.5	120.0		10,000	0.750
344	D-9C0	40	64-22	4.20	9.50	9.13	80.0	1.0	1,610.5	12.07	6.42	1,497.5	120.0		15,000	0.715
345	D-9C0	40	64-22	4.20	9.50	9.13	80.0	1.0	1,610.5	12.07	6.42	1,497.5	120.0		20,000	0.702
346	D-9A8	70	64-22	4.20	9.50	9.69	115.0	5.0	737.4	23.00	3.46	651.3	76.0		5,000	0.950
347	D-9A8	70	64-22	4.20	9.50	9.69	115.0	5.0	737.4	23.00	3.46	651.3	76.0		10,000	0.938
348	D-9A8	70	64-22	4.20	9.50	9.69	115.0	5.0	737.4	23.00	3.46	651.3	76.0		15,000	0.929
349	D-9A8	70	64-22	4.20	9.50	9.69	115.0	5.0	737.4	23.00	3.46	651.3	76.0		20,000	0.922
350	D-9B0	70	64-22	4.20	9.50	9.76	115.0	5.0	678.1	23.90	3.29	599.3	70.1		5,000	0.957

351	D-9B0	70	64-22	4.20	9.50	9.76	115.0	5.0	678.1	23.90	3.29	599.3	70.1		10,000	0.949
352	D-9B0	70	64-22	4.20	9.50	9.76	115.0	5.0	678.1	23.90	3.29	599.3	70.1		15,000	0.944
353	D-9B0	70	64-22	4.20	9.50	9.76	115.0	5.0	678.1	23.90	3.29	599.3	70.1		20,000	0.940
354	D-9B5	100	64-22	4.20	9.50	9.46	237.5	10.0	122.0	47.36	1.37	98.3	20.8		5,000	0.951
355	D-9B5	100	64-22	4.20	9.50	9.46	237.5	10.0	122.0	47.36	1.37	98.3	20.8		10,000	0.933
356	D-9B5	100	64-22	4.20	9.50	9.46	237.5	10.0	122.0	47.36	1.37	98.3	20.8		15,000	0.920
357	D-9B5	100	64-22	4.20	9.50	9.46	237.5	10.0	122.0	47.36	1.37	98.3	20.8		20,000	0.909
358	D-9C1	100	64-22	4.20	9.50	9.13	237.5	10.0	118.8	46.88	1.34	102.7	21.1		5,000	0.903
359	D-9C1	100	64-22	4.20	9.50	9.13	237.5	10.0	118.8	46.88	1.34	102.7	21.1		10,000	0.882
360	D-9C1	100	64-22	4.20	9.50	9.13	237.5	10.0	118.8	46.88	1.34	102.7	21.1		15,000	0.869
361	D-9C1	100	64-22	4.20	9.50	9.13	237.5	10.0	118.8	46.88	1.34	102.7	21.1		20,000	0.858
362	D+9A5	70	64-22	5.20	9.50	9.35	207.5	1.0	516.2	27.11	2.55	412.2	83.4		5,000	0.852
363	D+9A5	70	64-22	5.20	9.50	9.35	207.5	1.0	516.2	27.11	2.55	412.2	83.4		10,000	0.823
364	D+9A5	70	64-22	5.20	9.50	9.35	207.5	1.0	516.2	27.11	2.55	412.2	83.4		15,000	0.807
365	D+9A5	70	64-22	5.20	9.50	9.35	207.5	1.0	516.2	27.11	2.55	412.2	83.4		20,000	0.795
366	D+997	70	64-22	5.20	9.50	9.54	207.5	1.0	548.2	27.59	2.78	440.2	86.8		5,000	0.826
367	D+997	70	64-22	5.20	9.50	9.54	207.5	1.0	548.2	27.59	2.78	440.2	86.8		10,000	0.791
368	D+997	70	64-22	5.20	9.50	9.54	207.5	1.0	548.2	27.59	2.78	440.2	86.8		15,000	0.771
369	D+997	70	64-22	5.20	9.50	9.54	207.5	1.0	548.2	27.59	2.78	440.2	86.8		20,000	0.757
370	D+9A6	100	64-22	5.20	9.50	9.42	450.0	5.0	82.1	50.96	1.13	56.3	24.0		5,000	0.809
371	D+9A6	100	64-22	5.20	9.50	9.42	450.0	5.0	82.1	50.96	1.13	56.3	24.0		10,000	0.769
372	D+9A6	100	64-22	5.20	9.50	9.42	450.0	5.0	82.1	50.96	1.13	56.3	24.0		15,000	0.745
373	D+9A6	100	64-22	5.20	9.50	9.42	450.0	5.0	82.1	50.96	1.13	56.3	24.0		20,000	0.729
374	D+9A7	100	64-22	5.20	9.50	8.91	450.0	5.0	81.0	49.30	1.21	55.8	23.1		5,000	0.770
375	D+9A7	100	64-22	5.20	9.50	8.91	450.0	5.0	81.0	49.30	1.21	55.8	23.1		10,000	0.723
376	D+9A7	100	64-22	5.20	9.50	8.91	450.0	5.0	81.0	49.30	1.21	55.8	23.1		15,000	0.696
377	D+9A7	100	64-22	5.20	9.50	8.91	450.0	5.0	81.0	49.30	1.21	55.8	23.1		20,000	0.676
378	D+9A8	100	64-22	5.20	9.50	9.06	252.5	1.0	86.4	51.22	1.15	69.3	15.3		5,000	0.858
379	D+9A8	100	64-22	5.20	9.50	9.06	252.5	1.0	86.4	51.22	1.15	69.3	15.3		10,000	0.830
380	D+9A8	100	64-22	5.20	9.50	9.06	252.5	1.0	86.4	51.22	1.15	69.3	15.3		15,000	0.814

381	D+9A8	100	64-22	5.20	9.50	9.06	252.5	1.0	86.4	51.22	1.15	69.3	15.3		20,000	0.802
382	D+9A9	100	64-22	5.20	9.50	9.11	252.5	1.0	93.2	51.05	1.47	67.4	15.4		5,000	0.827
383	D+9A9	100	64-22	5.20	9.50	9.11	252.5	1.0	93.2	51.05	1.47	67.4	15.4		10,000	0.792
384	D+9A9	100	64-22	5.20	9.50	9.11	252.5	1.0	93.2	51.05	1.47	67.4	15.4		15,000	0.772
385	D+9A9	100	64-22	5.20	9.50	9.11	252.5	1.0	93.2	51.05	1.47	67.4	15.4		20,000	0.758